AFRL-ML-WP-TR-1999-4049

MECHANICAL BEHAVIOR OF ADVANCED AEROSPACE MATERIALS

N.E. ASHBAUGH
R. JOHN
W.J. PORTER
B.D. WORTH

UNIVERSITY OF DAYTON RESEARCH INSTITUTE
STRUCTURAL INTEGRITY DIVISION
300 COLLEGE PARK
DAYTON, OHIO 45469-0128

JUNE 1997

INTERIM REPORT FOR 05/25/1996 – 05/24/1997

APPROVED FOR PUBLIC RELEASE; DISTRIBUTION UNLIMITED

MATERIALS AND MANUFACTURING DIRECTORATE
AIR FORCE RESEARCH LABORATORY
AIR FORCE MATERIEL COMMAND
WRIGHT-PATTERSON AIR FORCE BASE OH 45433-7750

DTIC QUALITY INSPECTED 4

19991115 075

NOTICE

WHEN GOVERNMENT DRAWINGS, SPECIFICATIONS, OR OTHER DATA ARE USED FOR ANY PURPOSE OTHER THAN IN CONNECTION WITH A DEFINITELY GOVERNMENT-RELATED PROCUREMENT, THE UNITED STATES GOVERNMENT INCURS NO RESPONSIBILITY OR ANY OBLIGATION WHATSOEVER. THE FACT THAT THE GOVERNMENT MAY HAVE FORMULATED OR IN ANY WAY SUPPLIED THE SAID DRAWINGS, SPECIFICATIONS, OR OTHER DATA, IS NOT TO BE REGARDED BY IMPLICATION OR OTHERWISE IN ANY MANNER CONSTRUED, AS LICENSING THE HOLDER OR ANY OTHER PERSON OR CORPORATION, OR AS CONVEYING ANY RIGHTS OR PERMISSION TO MANUFACTURE, USE, OR SELL ANY PATENTED INVENTION THAT MAY IN ANY WAY BE RELATED THERETO.

THIS REPORT IS RELEASABLE TO THE NATIONAL TECHNICAL INFORMATION SERVICE (NTIS). AT NTIS, IT WILL BE AVAILABLE TO THE GENERAL PUBLIC, INCLUDING FOREIGN NATIONS.

THIS TECHNICAL REPORT HAS BEEN REVIEWED AND IS APPROVED FOR PUBLICATION.

JAY R. JIRA, Project Engineer
Ceramics, Development, & Materials
Behavior Branch
Metals, Ceramics & NDE Division

ALLAN P. KATZ, Acting Chief
Ceramics, Development, & Materials
Behavior Branch
Metals, Ceramics & NDE Division

GERALD J. PETRAK, Asst. Chief
Metals, Ceramics & Nondestructive
Evaluation Division
Materials and Manufacturing Directorate

IF YOUR ADDRESS HAS CHANGED, IF YOU WISH TO BE REMOVED FROM OUR MAILING LIST, OR IF THE ADDRESSEE IS NO LONGER EMPLOYED BY YOUR ORGANIZATION, PLEASE NOTIFY, AFRL/MLLN, WRIGHT-PATTERSON AFB OH 45433-7817 TO HELP US MAINTAIN A CURRENT MAILING LIST.

COPIES OF THIS REPORT SHOULD NOT BE RETURNED UNLESS RETURN IS REQUIRED BY SECURITY CONSIDERATIONS, CONTRACTUAL OBLIGATIONS, OR NOTICE ON A SPECIFIC DOCUMENT.

REPORT DOCUMENTATION PAGE	Form Approved OMB No. 0704-0188

Public reporting burden for this collection of information is estimated to average 1 hour per response, including the time for reviewing instructions, searching existing data sources, gathering and maintaining the data needed, and completing and reviewing the collection of information. Send comments regarding this burden estimate or any other aspect of this collection of information, including suggestions for reducing this burden, to Washington Headquarters Services, Directorate for Information Operations and Reports, 1215 Jefferson Davis Highway, Suite 1204, Arlington, VA 22202-4302, and to the Office of Management and Budget, Paperwork Reduction Project (0704-0188), Washington, DC 20503.

1. AGENCY USE ONLY *(Leave blank)*	2. REPORT DATE	3. REPORT TYPE AND DATES COVERED
	JUNE 1997	INTERIM REPORT FOR 05/25/1996 - 05/24/1997

4. TITLE AND SUBTITLE
MECHANICAL BEHAVIOR OF ADVANCED AEROSPACE MATERIALS

5. FUNDING NUMBERS
C F33615-94-C-5200
PE 62102
PR 2302
TA B1
WU 06

6. AUTHOR(S)
N.E. ASHBAUGH, R. JOHN
W.J. PORTER, AND B.D. WORTH

7. PERFORMING ORGANIZATION NAME(S) AND ADDRESS(ES)
UNIVERSITY OF DAYTON RESEARCH INSTITUTE
STRUCTURAL INTEGRITY DIVISION
300 COLLEGE PARK
DAYTON, OH 45469-0128

8. PERFORMING ORGANIZATION REPORT NUMBER

9. SPONSORING/MONITORING AGENCY NAME(S) AND ADDRESS(ES)
MATERIALS AND MANUFACTURING DIRECTORATE
AIR FORCE RESEARCH LABORATORY
AIR FORCE MATERIEL COMMAND
WRIGHT-PATTERSON AFB, OH 45433-7750
POC: JAY JIRA, AFRL/MLLN, 937-255-1358

10. SPONSORING/MONITORING AGENCY REPORT NUMBER
AFRL-ML-WP-TR-1999-4049

11. SUPPLEMENTARY NOTES

12a. DISTRIBUTION AVAILABILITY STATEMENT
APPROVED FOR PUBLIC RELEASE, DISTRIBUTION UNLIMITED.

12b. DISTRIBUTION CODE

13. ABSTRACT *(Maximum 200 words)*

The effect of microstructure, environment, and coatings on mechanisms of fatigue and fatigue crack initiation and growth in TiAl intermetallic alloys has been investigated. For a gamma titanium aluminide alloy, the coarse and refined lamellar materials with colony sizes equal to 700 and 280 μm, respectively, have substantially greater crack growth resistance than does the fine duplex material with approximately 20 μm grain size. The influence of laboratory air on a wrought gamma TiAl alloy produces crack growth rates more than an order of magnitude higher than those observed in ultra high vacuum environment at temperatures ranging from ambient to 800°C. A two-phase glass coating that exhibits a reduction in oxidation rate of an orthorhombic titanium aluminide, which was used as the matrix in a composite, fails to produce any enhancement in fatigue life.

An extensive investigation involving fatigue, fatigue crack growth, mechanisms, modeling, and metallurgy of titanium matrix composites (TMC) is being conducted. Life models for isothermal and thermomechanical fatigue and crack propagation have been developed using concepts based on the maximum fiber stress, life fraction for time and cycle dependent response, matrix stress-life behavior, and fiber bridging. A model was developed for deformation, damage evolution, and failure of unidirectional TMC under sustained load. Effects of heat treatments on tensile and creep behavior of an orthorhombic neat matrix and on several continuous SiC fibers have been evaluated.

Thermally induced stresses and damage progression in ceramic matrix composites due to fatigue and fracture are being studied. In monolithic materials, effects of stress ratio on FCG in an Al-alloy in the absence of closure and prediction of residual stress in Ti-6Al-4V generated by laser shock peening have been investigated.

14. SUBJECT TERMS
Titanium aluminides, gamma, orthorhombic, titanium matrix composites, ceramic matrix composites, turbine blade materials, high cycle fatigue, fatigue crack growth, elevated temperatures, SiC fibers, creep, thermal fatigue, thermomechanical fatigue, nickle-base superalloys, mixed-mode, stress intensity factors, finite element analysis, nondestructive evaluation

15. NUMBER OF PAGES
324

16. PRICE CODE

17. SECURITY CLASSIFICATION OF REPORT	18. SECURITY CLASSIFICATION OF THIS PAGE	19. SECURITY CLASSIFICATION OF ABSTRACT	20. LIMITATION OF ABSTRACT
UNCLASSIFIED	UNCLASSIFIED	UNCLASSIFIED	SAR

Standard Form 298 (Rev. 2-89) (EG)
Prescribed by ANSI Std. 239.18
Designed using Perform Pro, WHS/DIOR, Oct 94

TABLE OF CONTENTS

PAGE

1.0 EXECUTIVE SUMMARY 1

1.1 γ TiAl-BASE ALUMINIDES 1

1.2 Ti-MATRIX AND Ti-ALUMINIDE COMPOSITES 2

1.3 CERAMIC MATRIX COMPOSITES 3

1.4 ENGINE BLADE MATERIALS 3

1.5 DEVELOPMENT OF EXPERIMENTAL PROCEDURES, METHODOLOGIES AND LABORATORY ENHANCEMENTS 4

2.0 INTRODUCTION 6

2.1 BACKGROUND 6

2.2 PROGRAM OBJECTIVES 6

2.3 REPORT ORGANIZATION 6

3.0 DAMAGE TOLERANCE STUDIES OF γ TiAl-BASE TITANIUM ALUMINIDE 8

3.1 LIFE PREDICTION METHODOLOGY FOR TiAl-BASE TITANIUM ALUMINIDES 8

3.1.1 Mechanisms and Mechanics of Crack Initiation and Growth From Small Notches in γ-TiAl Alloys 8

3.1.2 Effect of Environment on the Life Prediction of Gamma Titanium Aluminides and the Implications for Life Prediction 8

3.2 MECHANISMS OF FATIGUE CRACK INITIATION IN TiAl INTERMETALLIC ALLOYS 9

3.2.1 Threshold Crack Growth Behavior of the Gamma Titanium Aluminide Alloy Ti-46.5Al-3Nb-2Cr-0.2W Under High Cycle Fatigue Conditions **[C1]** 9

3.2.2 Temperature and Stress Ratio Dependence on the High Cycle Fatigue Behavior of Ti-46Al-2Nb-2Cr-1Mo-0.2W 9

3.3 EFFECTS OF MICROSTRUCTURE, TEMPERATURE AND ENVIRONMENTAL ON FATIGUE CRACK GROWTH IN Ti-46.5Al-3Nb-2Cr-0.2W γ TITANIUM ALUMINIDE **[C2]** 10

3.4 MULTILAYER COATING FOR THE OXIDATION PROTECTION OF ORTHORHOMBIC TITANIUM ALUMINIDES DURING FATIGUE **[C3]** 10

4.0 DAMAGE ACCUMULATION AND FAILURE OF Ti-MATRIX AND Ti-ALUMINIDE-MATRIX COMPOSITES 11

4.1 TMF AND FCG BEHAVIOR 11

4.1.1 Influence of Temperature and Stress Ratio on the Low-Cycle Fatigue Behavior of Trimarc-1™/Ti-6Al-2Sn-4Zr-2Mo **[C4]** 11
4.1.2 HCF Behavior of Trimarc-1™/Ti-6Al-2Sn-4Zr-2Mo 11
4.1.3 Micromechanical Analysis and Life Prediction of Titanium Matrix Composites **[C5]** 12
4.1.4 TMF and Sustained Load Damage in SCS-6/Ti-6Al-4V 13
4.1.5 Mechanical Properties Assessment of an Ultra SCS®/Ti-22Al-23Nb 13
4.1.6 Determination of Crack Bridging Stresses From Crack Opening Profiles **[C6]** 14
4.1.7 FCG Behavior of SCS-6/Ti-6Al-4V 14
4.1.8 Effect of Stress and Geometry on Fatigue Crack Growth Perpendicular to Fibers in Ti-6Al-4V Reinforced with SiC Fibers **[C7]** 15
4.1.9 Effect of Temperature on Fiber/Matrix Interfacial Sliding in SCS-6/TIMETAL®21S 15
4.1.10 FCG of Trimarc-1™/Ti-6Al-2Sn-4Zr-2Mo 16

4.2 TENSILE AND CREEP BEHAVIOR 17

4.2.1 Creep Behavior of Ti-6Al-4V and SCS-6/Ti-6Al-4V 17
4.2.2 Creep Behavior of Neat Ti-22Al-26Nb 18
4.2.3 Modeling the Deformation and Failure of a Unidirectional Metal Matrix Composite Under Sustained Load [C8] 18
4.2.4 Tensile and Creep Behavior of Trimarc-1™/Ti-6Al-2Sn-4Zr-2Mo 18

4.3 DEVELOPMENT OF ADVANCED ORTHORHOMBIC MATRIX 20

4.3.1 The Effect of Heat Treatment on the Tensile and Creep Behavior of Neat Matrix Ti-22Al-23Nb [C9] 20
4.3.2 Thermal Stability of Neat Ti-22Al-23Nb Neat Matrix Material 20

4.4 CHARACTERIZATION OF CONSTITUENTS 21

4.4.1 Constitutive Model of Neat Ti-6Al-4V 21
4.4.2 FCG of Neat Ti-6Al-4V 23
4.4.3 Heat Treatment Effects on SiC Fiber [C10] 23
4.4.4 Heat Treatment Effects on SiC (Trimarc-1™) Fiber Tensile Properties 24
4.4.5 Modulus and Density Measurement of Ti-22Al-23Nb 25

5.0 DAMAGE ACCUMULATION AND FAILURE OF CERAMIC MATRIX COMPOSITES (CMC) 27

5.1 CHARACTERIZATION OF DAMAGE PROGRESSION IN CERAMIC MATRIX COMPOSITES USING AN INTEGRATED NDE/MECHANICAL TESTING SYSTEM 27

5.2 FRACTURE BEHAVIOR OF NEXTEL610/ALUMINOSILICATE 28

5.3 FATIGUE CRACK GROWTH BEHAVIOR OF NEXTEL610/ALUMINOSILICATE 29

5.4 STRESSES DUE TO TEMPERATURES IN CMC AEROSPACE COMPONENTS **[C11]** 30

5.5 TRANSTHICKNESS TENSILE TESTING OF CMC 30

6.0 INITIATION AND GROWTH OF FATIGUE CRACKS IN ENGINE MATERIALS 32

6.1 HIGH CYCLE FATIGUE OF TITANIUM ALLOYS 32

6.1.1 Development of the Modified Goodman Curve for HCF Ti-6Al-4V 32
6.1.2 Mean Stress and Frequency Effects on Ti-6Al-4V 33
6.1.3 Effect of Prior Torsion of HCF Life of Ti-6Al-4V 33
6.1.4 Effect of Fretting on HCF Life of Ti-6Al-4V 34
6.1.5 HCF/LCF Interaction on Life in Ti-6Al-4V 35
6.1.6 High Cycle Fatigue and Fatigue Crack Growth of Ti-6Al-2Sn-4Zr-6Mo 36

6.2 THE EFFECT OF STRESS RATIO ON FATIGUE CRACK GROWTH RATE IN THE ABSENCE OF CLOSURE **[C12]** 37

6.3 MIXED-MODE CRACK GROWTH IN Ti-6Al-4V and Ni-BASE SUPERALLOY 38

6.4 EFFECT OF LASER SHOCK PEENING ON CRACK GROWTH IN Ti-6Al-4V 38

6.4.1 Weight Function For A Tapered Three-Point Bend Specimen 38
6.4.2 Prediction Of Crack Growth In A Laser Shock Peened Zone [C13] 39

7.0 DEVELOPMENT OF EXPERIMENTAL PROCEDURES, METHODOLOGIES AND LABORATORY ENHANCEMENTS 40

7.1 INFRARED CRACK DETECTION SYSTEM 40

7.2 CHARACTERIZATION OF THE STABILITY OF ULTRASONIC COUPLANTS AS A FUNCTION OF RELATIVE HUMIDITY 40

7.3 CAPABILITY OF EDDY CURRENT NONDESTRUCTIVE EVALUATION FOR DETECTING CRACKS IN MMC SPECIMENS 42

7.4 MANUAL FOR FIDEP2 47

7.5 EXTENSOMETER USE IN ELEVATED TEMPERATURE TESTING 47

7.6 LEFM SOLUTION FOR NEW FCG SPECIMENS 48

7.6.1 Effect Of Height To Width Ratio On K And CMOD Solutions For A Single Edge Cracked Geometry With Clamped Ends [C14] 48

7.6.2 Stress Intensity Factor And Compliance Solutions For An Eccentrically Loaded Single Edge Cracked Geometry [C15] 48

7.7 FABRICATION AND OPERATION OF NEW SHAKER BASED HCF TEST SYSTEMS 49

7.8 DATA ARCHIVAL AND STATUS OF KEYSERVER® 49

8.0 REFERENCES 51

COMPENDIUM OF MANUSCRIPTS 53

LIST OF FIGURES

4.1-1 S-N data from C20 tests 12
4.1-2 (a)da/dN versus ΔK_a for two TMC, (b) a versus N at 23°C and 371°C for Trimarc-1™/Ti-6Al-2Sn-4Zr-2Mo 17
5.2-1 Stress intensity factor and applied stress vs. Crack mouth opening displacement (CMOD) for 23°C and 950°C fracture tests 29
6.1-1 Modified Goodman Curve for Ti6Al-4V 34
6.1-2 Schematic of Fretting Fatigue Grips 35
6.1-3 Modified Goodman Curve for Ti-6Al-2Sn-4Zr-6Mo 36
6.1-4 Room Temperature Fatigue-Crack-Growth Rate Data for Ti-6Al-2Sn-4Zr-6Mo 37
7.2-1a Ultrasonic surface wave amplitudes using different couplants (low lab humidity) 42
7.2-1b Ultrasonic surface wave amplitudes using different couplants (high lab humidity) 42
7.3-1 Eddy current image of a specimen containing many matrix cracks 44
7.3-2 The eddy current images show the initiation and progression of edge cracks before, during, and after TMF testing 46

LIST OF TABLES

4.2-1 Test Martix for Trimarc-1™/Ti-6Al-2Sn-4Zr-2Mo 19
4.4.5-1 Calculated Values for Ti-22Al-23Nb Specimens 25
5.5-1 Results of Transthickness Tension Tests on Nicalon/MAS-5 31
7.2-1 Properties of Couplants 41

FOREWORD

The work described in this report was performed at the Ceramics Development and Materials Behavior Branch, Metals, Ceramics, and NDE Division, Materials and Manufacturing Directorate, Air Force Research Laboratory (AFRL/MLLN) under Contract No. F33615-94-C-5200, "Mechanical Behavior of Advanced Aerospace Materials." The contract is administered under the direction of AFRL by Mr. Jay R. Jira. The program is being conducted by the Structural Integrity Division, University of Dayton Research Institute, Dayton, Ohio with Dr. Noel E. Ashbaugh and Mr. Robert J. Andrews acting as the Principal Investigator and Program Manager, respectively. This report is an interim report on the progress of the 4-year contract effort.

Investigations were directed and conducted by Drs. Reji John, Andrew Rosenberger, and Brian Worth, and Messrs. Dennis Buchanan, Richard Goodman, George Hartman, Joseph Kroupa, David Maxwell, W. John Porter, and David Stubbs, and Mrs. Alisha Hutson, and graduate students Ms. Victoria Kramb, and Messrs. Roger Gural and Stetson Planck. Mrs. Jacqui Hawkins was responsible for coordinating the input and typing of this document. This work was performed during the period of 25 May 1996 to 24 May 1997.

SECTION 1

EXECUTIVE SUMMARY

1.1 γ-TIAL-BASE ALUMINIDES

The Air Force Materials and Manufacturing Directorate (AFRL/MLLN), Propulsion and Power Directorate (AFRL/PR), and Air Force Office of Scientific Research (AFOSR), as well as the Navy, NASA, and industrial IRAD, continue to fund research aimed at the material and design methodology development of gamma TiAl-base titanium aluminides. The goal of this research is to use gamma to replace nickel base superalloys in high temperature structural components for higher thrust-to-weight gas turbine engines in support of Integrated High Performance Turbine Engine Technology (IHPTET). These applications include both static components (e.g. compressor stators and guide vanes) and fracture critical, rotating components (e.g. compressor and low pressure turbine blades, compressor disks, and slot covers). The highest payoff will come from the fracture critical rotating components where the low density of gamma alloys can be utilized to the greatest potential. The use of gamma engine components, however, is currently limited by the lack of design data and a clear design methodology for the utilization of low toughness, brittle intermetallics. Current efforts are aimed at understanding, more completely, the influence of microstructure, temperature, and environment on the cyclic properties of gamma alloys -- and the development of a damage tolerant design methodology for any low toughness, brittle intermetallic.

Gamma alloys have two distinct characteristics of their fatigue behavior that prove to be challenging for design; 1) a steep crack growth rate curves that exhibit a narrow interval between the threshold stress intensity range, ΔK_{th}, and the apparent fracture toughness KQ, and 2) smooth bar fatigue behavior (S-N) that contains the ultimate tensile strength and fatigue runout ($>10^7$ cyclic life) over only a narrow interval of stress. Though the fatigue behavior is attractive from a fail-safe point of view, standard damage tolerant design methods, utilizing fracture mechanics concepts, appear to be unusable [Larsen, et al., 1996]. As a result, a new damage tolerant design methodology is required that may make use of ΔK_{th} values to ensure usable life. Such an approach requires accurate determination of the threshold behavior of gamma materials and especially the threshold behavior of small cracks emanating from microstructural or damage details.

1.2 Ti-MATRIX AND Ti-ALUMINIDE COMPOSITES

Metal matrix composites have great potential for application in gas turbine engines due to their high specific-strength-to-weight ratio and elevated temperature capabilities. IHPTET, Titanium Matrix Composite Turbine Engine Components Consortium (TMCTECC), and F-22 Advanced Tactical Fighter programs have targeted advanced titanium matrix composites (TMC) for specific applications such as blings, blades and actuator rods, respectively. The MMC Life Prediction Cooperative (MMCLPC) is developing a comprehensive state-of-the-art code to predict the life of these TMC components. During this reporting period, substantial efforts were directed towards supporting the IHPTET, TMCTECC, MMCLPC and F-22 Advanced Tactical Fighter programs.

Extensive testing of Trimarc-1™/Ti-6Al-2Sn-4Zr-2Mo and SCS-6/Ti-6Al-4V was conducted in support of the F-22 Advanced Tactical Fighter and MMCLPC programs, respectively, to evaluate the damage tolerance under simulated service loading conditions. Testing of Ultra SCS®/Ti-22Al-26Nb was also initiated in support of the IHPTET program. The effect of temperature and stress ratio on the fatigue behavior of Trimarc-1™/Ti-6Al-2Sn-4Zr-2Mo was successfully modeled using the Walker-Parameter model. Viscoplastic constitutive models for neat Ti-6Al-4V were developed and used to determine the constituent stresses in SCS-6/Ti-6Al-4V after processing and during TMF and creep loading. The predicted stresses were used to predict the life under fatigue and TMF loading. Studies were conducted to determine the conditions under which through and surface cracks in SCS-6/Ti-6Al-4V will be bridged by unbroken fibers. A shear lag model was successfully used to predict fully bridged and partially bridged crack growth in SCS-6/Ti-6Al-4V under a wide range of stress levels at room temperature. The influence of temperature on the fiber/matrix interfacial shear stress (τ) during crack growth in a TMC was also determined from crack opening displacements (COD). A unique optimization technique was also developed to deduct the bridging stress distributions from COD measured during crack growth.

Extensive testing was conducted characterize the creep and tensile behavior of neat Ti-6Al-4V, SCS-6/Ti-6Al-4V, neat Ti-22Al-26Nb and Trimarc-1™/Ti-6Al-2Sn-4Zr-2Mo. A new model based on the statistical variation of the fiber strength was developed to predict the deformation and failure of unidirectionally reinforced TMC subjected to sustained loading. In addition, due to the increased creep resistance of orthorhombic titanium matrices, a large effort was devoted to developing advanced orthorhombic matrices through alloy additions and heat treatments.

Life prediction of the TMC components requires the characterization of the individual constituents. Tensile, creep and FCG experiments were conducted to generate the baseline data for the neat matrices. Ultrasonic NDE method was also used to determine the modulus of thin foils of Ti-22Al-23Nb. Failure of the TMC component during longitudinal loading is controlled by the fracture strength of the fibers. Hence, extensive testing of fibers extracted from the composite was conducted to evaluate the detrimental effect of consolidation and post-consolidation heat treatment on the *in situ* strength of the fibers in the composite.

1.3 CERAMIC MATRIX COMPOSITES

Ceramic matrix composites (CMC) have been identified as potential replacement materials for critical low load components in gas turbine engines. To aid development of damage-based life prediction models for CMC, the efficacy of a unique integrated NDE/Mechanical testing system was investigated. Techniques based on surface replicates and *in situ* high-magnification photography were used to establish the relationship between the formation of cracks and the changes in the wave signals. The growth of these cracks can lead to eventual failure of the CMC. Hence, fracture and FCG tests were conducted at room temperature and 950°C to understand the effect of elevated temperature on crack growth from notches in advanced CMC systems.

During service, CMC components such as engine flaps and seals are subjected to severe temperature gradients. An analytical procedure was developed to predict the thermal stresses in CMC that exhibit non-linear temperature-dependent stress-strain behavior. This effort supports the tests being conducted on Nextel610/AS and Nextel720/AS using a thermal gradient testing system. Some of these CMC components are typically held in place using special attachments that are molded in the component. A unique transthickness testing system was developed and used to determine the transthickness tensile strength of a Nextel720/AS in support of developing a design procedure of such attachments.

1.4 ENGINE BLADE MATERIALS

High cycle fatigue (HCF) is one of the most important problems effecting the readiness of the Air Force fleet. To understand this problem and to develop life prediction models, tests must be conducted in the laboratory for lives greater than 10^6 cycles. An effective test method must be applied to produce fatigue life data. A step stress test method has been developed and evaluated for Ti-6Al-4V and Ti-6Al-2Sn-4Zr-6Mo for fatigue lives at 10^7 cycles. Goodman curves have been generated for stress ratio values from –1 to 0.90. Test systems and

methodology are being developed to evaluate the influence of (a) mean stress and frequency, (b) prior torsional fatigue, (c) fretting, and (d) low cycle fatigue (LCF) interaction with HCF of Ti-6Al-4V.

Crack growth behavior is strongly influenced by crack closure and other factors. A fractographic study of naturally initiated cracks indicated that the growth of cracks as small as 20μm in an Al-alloy were affected by applied mean stress as well as stress range. In this study, the stress ratio values were high enough to avoid crack closure.

Crack growth in structures is also complicated by stresses that produce a sliding mode of deformation and by residual stresses that modify the applied stress field at the crack tip. Under mixed-mode loading the results of a fatigue crack growth study in Ti-6Al-4V show that initiation angles and crack propagation paths can be predicted using available mixed-mode theories for isotropic materials. Residual stresses produced by laser shock peening (LSP) can be an effective method to reduce fatigue crack growth rates in engine blades. Data from a crack growth investigation and a weight function analysis were used to deduce the residual stress distribution generated by the LSP process.

Also, changes in microstructure can alter crack growth behavior. Preliminary results indicate that resistance to mixed-mode crack growth at 593°C of a new microstructure of Ni-base superalloys is significantly superior compared to that at room temperature.

1.5 DEVELOPMENT OF EXPERIMENTAL PROCEDURES, METHODOLOGIES AND LABORATORY ENHANCEMENTS

Maintaining excellence in material behavior research requires that the staff have the best possible tools and procedures for monitoring damage and specimen response to the imposed test conditions. For the nondestructive evaluation, an infrared crack detection system has been designed and software layouts have been completed for early detection of cracks. The effects of local humidity on the response of couplants used in the detection of material damage have been assessed to avoid false damage indications due to changes in couplant composition. An investigation of some new eddy current instrumentation indicated that the eddy current imaging technique is viable for the detection and characterization of matrix cracks in metal matrix composite specimens.

For measuring the specimen deformation, a Linear Variable Displacement Transducer (LVDT) based extensometer has been designed to minimize some of the problems associated with an expensive strain gage based high temperature extensometer. Current extensometers have registered over 500 microstrain variations with changes in laboratory air environment. The

new LVDT-based extensometer should be insensitive to lab air variations and provide as good electrical stability.

In analytical methodology, a manual has been completed for the description of a PC-compatible code for the analysis of micromechanical stresses in metal matrix composites under complex thermal and mechanical loadings. Expressions have been provided for the evaluation of stress intensity factor and crack mouth opening of a single edge cracked geometry with uniform end displacement. Also, expressions have been determined for stress intensity factor and compliance of eccentrically pin-loaded single edge cracked geometry.

The in-house test capability for the HCF test program is being augmented by the design and construction of two new electromagnetic shaker systems. The current electronic data archival system has been enhanced with a faster computer system and the addition of multiple 4 GB drives. A Keyserver® system was installed to provide controlled access to licensed software for Window and Macintosh platforms.

SECTION 2

INTRODUCTION

2.1 BACKGROUND

Lighter-weight higher-strength damage-tolerant materials must be used to achieve the Air Force goals for future aircraft and engines. The durability and damage tolerance analysis requirements defined in the Aircraft Structural Integrity Program (ASIP) and the Engine Structural Integrity Program (ENSIP) standards guide the design of Air Force vehicles. Engine performance goals have been set forth in the Integrated High Performance Turbine Engine Technology (IHPTET) program. A new program has been initiated to improve the design methodology being applied to engine components that are subjected to high cycle fatigue. To apply the advanced materials effectively, a thorough understanding of the material behavior must be obtained and a methodology for life prediction of these materials must be developed.

2.2 PROGRAM OBJECTIVES

The objectives of this program are to (a) obtain experimental data on the material behavior of current and advanced aerospace materials (b) develop state-of-the-art techniques for determining mechanical properties of materials under simulated engine service conditions (c) develop the methodology for a damage tolerant design approach and durability analysis for application of these materials (d) analyze experimental results and governing microstructure mechanisms and (f) transition the findings to the scientific and design communities.

2.3 REPORT ORGANIZATION

This third interim annual report presents the research conducted on the material behavior and modeling of advanced aerospace materials under contract within the Materials Behavior Branch of the Metals and Ceramics Division of the Materials Directorate at Wright-Patterson Air Force Base. This effort was conducted from 25 May 1996 to 24 May 1997. The investigations that have been completed and were in progress during the reporting year of the contract will be discussed.

The completed efforts are summarized in this report. Copies of the manuscripts which have been written on these efforts are provided in the compendium for the convenience of readers who wish to have more detailed information of the investigations readily available.

Extended discussions of the work-in-progress are presented to provide as much information as possible about the current investigations.

In Sections 3, 4, 5, and 6, the material properties and damage assessment for γ-titanium aluminides, TMC, CMC, and engine blade materials, respectively, are discussed. The development of experimental procedures and test techniques, methodologies, and laboratory enhancements are presented in Section 7.

SECTION 3

DAMAGE TOLERANCE STUDIES OF γ TiAl-BASE TITANIUM ALUMINIDE

3.1 LIFE PREDICTION METHODOLOGY OF γ TiAl-BASE TITANIUM ALUMINIDES

3.1.1 Mechanisms and Mechanics of Crack Initiation and Growth from Small Notches in γ-TiAl Alloys

Research has been initiated to study the initiation and growth of cracks from small notches in a gamma TiAl alloy having the nominal composition Ti-46.5Al-3Nb-2Cr-0.2W (at%) having a refined lamellar microstructure. Fatigue tests have been conduced on samples containing twelve electrodischarge machined (EDM) notches that are uniformly and symmetrically located on the gage length. Notches were machined to an approximately semicircular shape (a=c) with depths of 80, 100, and 180 μm. Fatigue runouts (cyclic life > 10^7) were plotted on a Kitagawa diagram [Kitagawa and Takahashi, 1976] and exhibited behavior similar to that predicted by the fatigue endurance limit and the effective threshold stress intensity range, $\Delta k_{th\ eff}$. Additional effort is required to measure and predict the growth rate of the small cracks that emanate from the notches.

3.1.2 Effect of Environment on the Life Prediction of Gamma Titanium Aluminides and the Implications for Life Prediction

Fatigue crack growth tests conducted in ultra high vacuum in a gamma TiAl alloy having the nominal composition Ti-46.5Al-3Nb-2Cr-0.2W (at%) exhibit better crack growth resistance as compared to tests conducted in laboratory air -- over the examined temperature range of 23° to 800°C. Equations were fit to the data, and life integrations were performed by integrating up the curves from an assumed initial crack size. A comparison of the crack propagation lives for the air and UHV crack growth curves show that in all instances, the life is longer for cracks growing in UHV than in laboratory air. This indicates that component failure should be controlled by surface connected cracks. Internal cracks, due to processing or inclusions should be benign which means that components can be inspected for damage on the surface only.

3.2 MECHANISMS OF FATIGUE AND FATIGUE CRACK INITIATION IN TiAl INTERMETALLIC ALLOYS

3.2.1 THRESHOLD CRACK GROWTH BEHAVIOR OF THE GAMMA TITANIUM ALUMINIDE ALLOY Ti-46.5Al-3Nb-2Cr-0.2W UNDER HIGH CYCLE FATIGUE CONDITIONS [C1]

To date, there is a limited understanding of the mechanics of cyclic damage in gamma TiAl intermetallic alloys. The available studies indicate that the fatigue strength for this class of alloys typically exceeds 80 percent of the material's monotonic yield strength. Such data suggest the possibility of using a safe-life fatigue design at relatively high stresses. However, a safe-life design scheme does not account for the possible existence of intrinsic material defects or service-induced damage, both of which must be addressed in order to ensure reliability in fracture-critical applications. Previous results have shown that the long-crack growth rates in materials of both fully lamellar and duplex microstructures are highly sensitive to the level of applied loading. As a result, it appears likely that a fracture-mechanics-based approach to life prediction must assure that conditions for crack growth remain below the threshold stress intensity factor range, ΔK_{th}. The current study examined the smooth and notched high cycle fatigue behavior of representative TiAl-based alloys to develop a better understanding of the events that lead to fatigue crack initiation and growth. The results of the study were used to identify the key parameters that should be addressed in order to develop reliable life prediction models of this class of alloys in fracture critical applications in turbine engines.

3.2.2 Temperature and Stress Ratio Dependence on the High Cycle Fatigue Behavior of Ti-46Al-2Nb-2Cr-1Mo-0.2B (at%)

A study has been initiated to examine the fatigue behavior of a gamma titanium aluminide, having a composition of Ti-46Al-2Nb-2Cr-1Mo-0.2B (at%), as a function of temperature and stress ratio. Baseline tests will be conducted at room temperature, 540C and 760C with a stress ratio of 0.1. Select tests will be conducted at higher stress ratios in order to determine the fatigue behavior under conditions amenable to rotating structures in gas turbine engines. A quartz lamp heating system is used for the elevated temperature tests that allowed rapid cooling of the specimen after failure in order to obtain accurate measurements of the size and shape of the heat-tinted cracks. The goal of this study is to characterize the high cycle fatigue behavior of this alloy, the cyclic stress-strain response, damage mechanisms, and crack growth that leads to failure. These results will help exploit the high fatigue strength of this class of alloys while allowing damage tolerance, residual life management.

3.3 EFFECTS OF MICROSTURCTURE, TEMPERATURE AND ENVIRONMENTAL ON FATIGUE CRACK GROWTH IN Ti-46.5Al-3Nb-2Cr-0.2W γ TITANIUM ALUMINIDE [C2]

The influence of environment on the fatigue crack growth in a gamma titanium aluminide alloy was examined through a comparison of crack growth behavior in laboratory air and ultra high vacuum (UHV). Specimens of wrought Ti-46.5Al-3Nb-2Cr-0.2W (at %) were tested in duplex, refined lamellar and coarse lamellar microstructures at temperatures ranging from ambient to 800°C. A pronounced environmental effect was observed at all temperatures, with crack growth rates more than an order of magnitude lower in vacuum than in air. The poorest crack growth resistance was observed in air at an intermediate temperature, however in a UHV environment, no anomalous temperature dependence on fatigue crack growth was observed. This temperature effect was shown to be the result of an environmental embrittlement that is mitigated by the increase in ductility at higher temperatures. A careful examination of crack closure levels supported this conclusion. Subtle fractographic differences in crack growth mode were observed in the two environments but were not sufficient to cause the dramatic changes in fatigue crack growth resistance.

3.4 MULTILAYER COATING FOR THE OXIDATION PROTECTION OF ORTHORHOMBIC TITANIUM ALUMINIDES DURING FATIGUE [C3]

The effect of a $TiAl_3$ + two-phase glass coating on the fatigue performance of unidirectionally reinforced orthorhombic based titanium aluminide composites (SCS-6/Ti-22Al-23Nb $[0]_4$) was examined. Though the coating system exhibited a reduction in oxidation rate, it failed to produce any enhancement in fatigue life. In fact, a reduction in life was found for the isothermal fatigue condition examined. The probable reasons for this are discussed based on the current understanding of the damage mechanisms in orthorhombic titanium matrix composites. It must be note that the coating system was not tailored for either the orthorhombic alloy or the temperature range utilized in the current study. An improvement in fatigue performance may be achieved with an optimization of the coating system.

SECTION 4

DAMAGE ACCUMULATION AND FAILURE OF Ti-MATRIX AND Ti-ALUMINIDE-MATRIX COMPOSITES

4.1 TMF AND FCG BEHAVIOR

4.1.1 Influence Of Temperature and Stress Ratio On The Low-Cycle Fatigue Behavior Of Trimarc-1™/Ti-6Al-2Sn-4Zr-2Mo [C4]

The results of an experimental investigation of load-controlled isothermal low-cycle fatigue behavior of a titanium matrix composite (TMC) are discussed in this paper. The TMC was composed of Ti-6Al-2Sn-4Zr-2Mo matrix (wire) reinforced with silicon-carbide (Trimarc-1™) fibers. The composite panels were constructed using alternating layers of matrix wire and fiber using a wire winding technique. The panels were unidirectional with a $[0]_{10}$ layup and fiber volume fraction $\approx$ 0.29. Fatigue tests were conducted at temperatures of 23°C, 163°C and 371°C at stress ratios of -1.3 and 0.1 for longitudinal tests and 0.1 for transverse tests at a frequency of 3 Hz. The longitudinal fatigue data showed good correlation with other TMC systems at both positive and negative stress ratios. The maximum fiber stress versus cycles to failure for several unidirectional TMC systems at similar test conditions consolidate to a narrow band indicating that the life is fiber dominated. A transverse fatigue model was used to predict the cycles to failure of the TMC using the monolithic S-N data and a net-section based the unit cell.

4.1.2 HCF Behavior of Trimarc-1™/Ti-6Al-2Sn-4Zr-2Mo:

The purpose of this study was to evaluate material proposed for use in the actuator rod component of the F22 airframe and F119 powerplant. The material under consideration was Trimarc-1™/Ti-6Al-2Sn-4Zr-2Mo, a wire wound metal matrix composite produced by Textron. Straight-sided specimens were cut from 2 mm thick panels. Nominal specimen dimensions were 100 mm X 8 mm. These specimens were fatigue tested, using an electromagnetic shaker system, at 380 Hz, 163°C, and a stress ratio of 0.1, at stresses ranging from 300 MPa to 700 MPa, to evaluate the total life of the material. Two batches of specimens were tested, and indicated in Figure 4.1-1 by "phase 1" and "phase 2". One test from phase 2, indicated by hollow diamonds, was step tested. The test was started with an initial stress of 300 MPa. When the specimen had not failed after 175 million cycles, the stress was raised to 325 MPa. It was then allowed to run for another 100 million cycles before the stress was increased again.

The stress was raised a total of five times before the specimen finally failed in the grips. Attempts are being made to repeat the results at 400MPa.

The trend for the C20 results is not definitive because of the large number of grip failures, designated in Figure 4.1-1 by symbols with an arrow. The grip failures were largely a product of fretting occurring in the grips. With no stress concentrator in the gage section the specimens' weakest points occurred at the edge of the grip section. A few straight specimens have been remachined into dogbone specimens. Testing to confirm current results is underway.

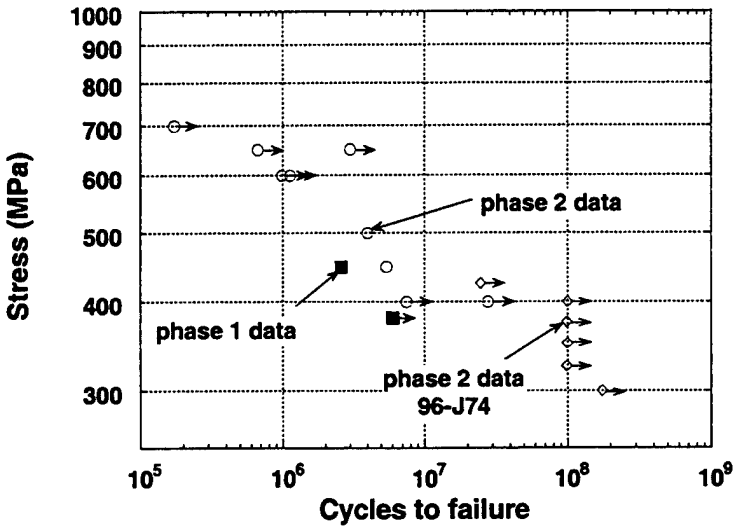


Figure 4.1-1

SN Data from C20 Tests.

4.1.3 Micromechanics Analysis and Life Prediction of Titanium Matrix Composites [C5]

The response of a unidirectional SCS-6/Ti-6Al-4V composite is evaluated under a range of isothermal fatigue (IF) and thermomechanical fatigue (TMF) conditions. Both processing and thermomechanical test conditions are simulated using a cylinder in cylinder code, FIDEP, which treats the fiber as thermoelastic while the matrix is characterized using a recent version of the Bodner-Partom constitutive law. Computed stresses and strains in the constituents are obtained after 10 cycles of loading and are used as input into a new and simpler version of a life fraction model. Applied stress at temperature and computed matrix strains are used for the time-dependent and matrix fatigue terms in the model, respectively. Cyclic stress-strain behavior of the matrix material is also computed and used, together with fatigue life data, to

identify the governing mechanisms and to explain the observed trends in fatigue life as a function of frequency and applied stress level. Comparisons of fatigue behavior with that of SCS-6/Timetal®21S illustrate differences when tested under nominally similar conditions.

4.1.4 Advanced NDE Techniques Applied to Monitor Damage during TMF and Sustained Load of SCS-6/Ti-6Al-4V Composites

SCS-6/Ti-6Al-4V composites subjected to sustained load and in-phase TMF were examined with the aid of *in situ* NDE techniques in order to verify any similarities in the damage mechanisms or their accumulation under the dissimilar loading spectra. Ultrasonic longitudinal bulk rod wave and modal acoustic emission analyses were applied to detect damage during testing. Sustained load tests were conducted at 427°C with stresses ranging from 1000 to 1150 MPa. In-phase TMF tests were conducted with a temperature range of 23°C to 427°C, at a frequency of 0.01 Hz, a stress ratio of 0.05, and maximum cyclic stress ranging from 1000 to 1150 MPa.

Ultrasonic modulus was found to be insensitive to the damage accumulation under either test type while ultrasonic amplitude was found to decrease with time or cycles during the sustained load and in-phase TMF tests, respectively. A direct relationship between the decrease in ultrasonic amplitude and level of damage was not attained in this study. Modal acoustic emission techniques indicated that under the two test types, damage progressed through a series of fiber fractures until ultimate failure of the composite. Using this technique it was found that fiber fractures characteristically had high amplitude emissions with a substantial level of energy at frequencies higher than 1 MHz.

The NDE techniques and postmortem examinations of the specimens indicated that under the higher stress conditions of this study, the failure mechanisms during sustained load and in-phase TMF testing were identical. Under these test conditions, the time to failure of a sustained load specimen was found to be equal to the effective time to failure of an in-phase test conducted at the same maximum stress. The effective time to failure of the in-phase TMF cycling was found to be approximately 15% of the total time to failure. At the lowest stress conditions, however, a contribution of matrix fatigue was found under the in-phase TMF cycling that caused a more rapid accumulation of damage as compared to sustained load.

4.1.5 Preliminary Mechanical Properties Assessment of an Ultra-SCS®/Ti-22Al-23Nb Composite

The mechanical performance of an orthorhombic based titanium matrix composite (OTMC) reinforced with Ultra SCS® silicon fiber monofilament was investigated. Tensile,

creep, isothermal and thermomechanical fatigue were examined over the temperature range from 20 to 760°C, with the bulk of the testing at the higher end of this range to more fully characterize the high temperature performance of this composite system. A comparison was made with similar OTMCs reinforced with SCS-6 and Trimarc-1™ silicon carbide fibers where data was available. In general, the longitudinal properties were increased as a result of the higher strength Ultra SCS® fiber. Both cyclic properties, isothermal fatigue and in-phase thermomechanical fatigue, as well as static properties, tensile and creep were improved. However, out-of-phase thermomechanical fatigue, which demonstrates the importance of matrix as well as fiber, showed a slight debit in the Ultra SCS® composite. The transverse properties are similar to that of the other composites which was not surprising due to their strong dependence on the matrix mechanical properties. The improvement in longitudinal properties makes the Ultra SCS® composites better suited for gas turbine engine applications, however, improvements in transverse properties may still be required for some applications.

4.1.6 Determination of Crack Bridging Stresses From Crack Opening Profiles [C6]

This paper discusses the development of an optimization procedure to deduce the bridging stress from the crack opening displacements (COD) measured during fatigue crack growth. Finite element analysis was conducted using the center-cracked geometry to verify the optimization procedure. The proposed procedure successfully predicted the bridging stress distributions with zero stresses at the crack tip and the bridging stress distributions with non-zero stresses at the crack tip. The results also showed that COD measurements spaced at ≈ 0.8-1.0 mm are sufficient for reliable prediction of bridging stresses. Accurate prediction of bridging stresses near the crack tip required COD data within ≈ 0.1 mm from the crack tip. The application of the proposed procedure to a metal matrix composite (SCS-6/Timetal®21S) is also discussed.

4.1.7 FCG Behavior of SCS-6/Ti-6Al-4V

Extensive testing was conducted to characterize the through and surface crack growth behavior of SCS-6/Ti-6Al-4V in support of the PRDAIV program. Tests were conducted at stress ratios, R = 0.1, 0.5 and 0.7 and at 23, 177 and 316°C. The number of through and surface crack specimens tested were 21 and 7, respectively. The layup of the through and surface crack specimens were 8 and 24, respectively. During some of the tests, the crack opening displacement (COD) profile was measured using the laser interferometric displacement

gage (IDG) system. The COD measurements from the surface crack specimens indicated that the extent of bridging by the fibers is similar to that in the through crack specimens. The crack growth rate (da/dN) versus applied stress intensity factor range (ΔK_a) behavior of the surface crack specimen tested at 600 MPa was similar to the through crack specimen tested at 400 MPa. The analysis of the through crack growth behavior at room temperature is discussed in the next section. The analysis of the through crack growth behavior at elevated temperatures and the surface crack growth behavior is in progress.

4.1.8 Effect of Stress and Geometry on Fatigue Crack Growth Perpendicular to Fibers in Ti-6Al-4V Reinforced with SiC Fibers [C7]

Critical turbine engine and aircraft components fabricated from continuous fiber reinforced metal matrix composite (MMC) will experience cyclic loads during service, and many of these components typically contain crack initiators. Hence, extensive characterization of the fatigue crack growth behavior of a model MMC ($[0]_8$ SCS-6/Ti-6Al-4V) was initiated by the USAF Wright Laboratory. This paper discusses some of the results of the experimental and analytical investigation of fatigue crack propagation in $[0]_8$ SCS-6/Ti-6Al-4V. Automated fatigue crack growth tests were conducted using middle tension, M(T) specimens at 23°C with stress ratio of 0.1. During some of the tests, the crack opening displacement profile was measured to verify the stress distributions predicted by the fiber bridging models. The results are also compared with those available for SM1240/Ti-6Al-4V under tension and bending fatigue loading. This study showed that the shear lag model assuming a constant value of τ can be used to predict bridged crack growth perpendicular to fibers in SCS-6/Ti-6Al-4V and SM1240/Ti-6Al-4V over a wide range of stress levels, and under tension and bending fatigue loading conditions. The predictions of partially-bridged and unbridged crack growth, crack opening displacements and slip lengths correlated well with the data. The value of the fiber/matrix interfacial shear stress, τ was the same for SCS-6/Ti-6Al-4V and SM1240/Ti-6Al-4V implying that the bridging mechanism of the SM1240 fiber is identical to that of the SCS-6 fiber at room temperature. The results also indicate that the onset of fiber failure could be predicted using the bundle strength as the critical value.

4.1.9 Effect of Temperature on Fiber/Matrix Interfacial Sliding in SCS-6/Timetal®21S

A model of fiber/matrix interface behavior as a function of test temperature, excluding environmental effects, was developed by relating crack opening displacement, measured during a tension-tension fatigue test, to a shear lag model. Four ply unidirectional SCS-6/Timetal®21S

was selected for the study. Crack length measurements were made with an optical microscope, and with electric potential calibrated against *in situ* photographs throughout the precrack portion of the test. A rotating mirror IDG was used to measure crack opening displacement on a 4 mm long crack while temperature was varied. τ was evaluated for each temperature step. The results were compared with analytical τ values derived from the fiber clamping stress values determined via finite difference analysis. τ appears to decrease with temperature as a result of thermal expansion of the matrix reducing the residual stress state of the material. This trend can be predicted using the fiber clamping stresses and a constant coefficient of friction. The model derived here can be incorporated with other models to provide accurate predictions of fatigue life for specimens at all temperatures between room temperature and 500°C, and can be used to extrapolate effects of elevated temperature beyond 500°C on the composite, excluding thermal degradation due to carbon burnout.

4.1.10 FCG Behavior of Trimarc-1™/Ti-6Al-2Sn-4Zr-2Mo

The fatigue crack growth tests were performed at temperatures (23°C, 163°C, 371°C), maximum stresses (400 MPa, 700 MPa) and stress ratios (0.1, 0.5, 0.7) for $[0]_{10}$ orientations. Figure 4.1-2a shows that for identical test conditions, Trimarc-1™/Ti-6Al-2Sn-4Zr-2Mo is less resistant to crack growth than SCS-6/Ti-6Al-4V. This lower resistance can be attributed to a lower average fiber strength, 3100 and 4000 MPa, for Trimarc-1™ and SCS-6, respectively, and a lower fiber volume fraction in the composite, 0.29 and 0.33, for Trimarc-1™/Ti-6Al-2Sn-4Zr-2Mo and SCS-6/Ti-6Al-4V, respectively. The effects of temperature on crack growth rate are shown in Figure 4.1-2b. The number of cycles to failure at 371°C is approximately a quarter of the cycles to failure at 23°C.

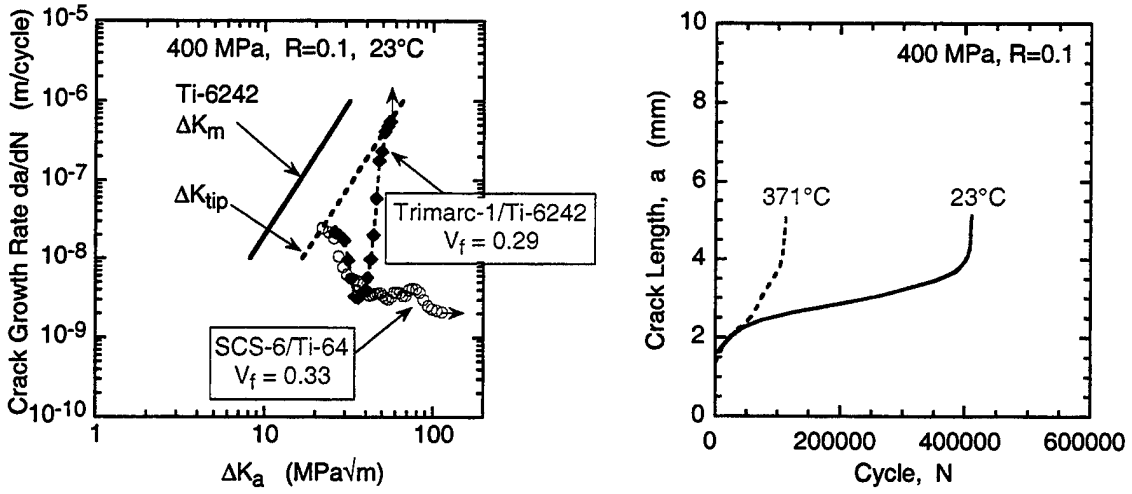


Figure 4.1-2

(a) da/dN Versus ΔK_a for Two TMC, (b) a Versus N at 23°C and 371°C for Trimarc-1™/Ti-6Al-2Sn-4Zr-2Mo.

4.2 TENSILE AND CREEP BEHAVIOR

4.2.1 Creep Behavior of Ti-6Al-4V and SCS-6/Ti-6Al-4V

As part of the characterization of neat Ti-6Al-4V and SCS-6/Ti-6Al-4V, creep tests of neat matrix and [90] composite were completed. The creep tests on the [90] composite specimens have been conducted in laboratory air. The behavior could have been influenced by the exposure of the cut fiber ends, in the heated section of the specimen, to laboratory air. Since the anticipated application of composite does not involve exposed fiber ends, the influence on the behavior of the composite, due to exposure of the ends to an aggressive environment, was investigated.

To evaluate the environmental effect, a test at 538°C and 110 MPa in a vacuum ($\approx 10^{-6}$ torr) was conducted and the results compared to a previous test conducted in laboratory air. The specimen tested in a vacuum exhibited almost three times to rupture life and, interestingly, about a third of the strain at failure as the specimen in laboratory air. Due to some data acquisition problems, a second vacuum test was also performed. Rupture time and strain to failure for the second vacuum specimen were similar to the first. Additional interrupted tests in both laboratory air and vacuum will be conducted to evaluate data scatter.

For the [0] composite, several creep/sustained load test conditions and ten step-stress test conditions have yet to be investigated. These tests have been delayed to allow for the

evaluation of sensors and development of waveguides for an acoustic emission (AE) system that can reliably detect individual breaks in fibers during the test.

In previous applications of a LOCAN AE system, the hits or indications of fiber breaks was a factor of five larger than the actual count of fiber breaks in an interrupted creep test. Knowing the number of fiber breaks and the time when these breaks occur during the test, are important factors in understanding the damage accumulation and thus, the behavior of these composites. More sophisticated AE systems, which provide details on the acoustic events such as the signal trace of each of the hits, have been evaluated. Also, due to the small size of the specimen and thus, the relative inaccessibility of the specimen when mounted in the test frame, a wave guide will be developed to transport the acoustic event signals to the AE sensors.

4.2.2 Creep Behavior of Neat Ti-22Al-26Nb

A project has been initiated to evaluate the behavior of neat Ti-22Al-26Nb. Creep behavior will be evaluated over 482° to 749°C. These results will be used to develop a constitutive model that will be used in the analysis of composite response.

4.2.3 Modeling the Deformation and Failure of a Unidirectional Metal Matrix Composite Under Sustained Load [C8]

A creep model utilizing the two bar composite representation was developed in order to characterize the deformation and failure of a unidirectionally reinforced SCS-6/Ti-6Al-4V composite. This model is capable of simulating loading, taking into account residual stresses in the composite and allowing for fiber failure according to Weibull statistical strength distribution. The validity of the model was evaluated by comparing predicted strains and lifetimes to measurements of strains and lifetimes taken from a range of creep tests. The model's sensitivity was also investigated using a parameter study. Through extensive fiber tracking of an interrupted creep test, the model's primary assumptions were evaluated and found to be true.

4.2.4 Tensile, Creep and Fatigue Crack Growth Behavior of Trimarc-1™/Ti-6Al-2Sn-4Zr-2Mo

The tensile and compressive tests were completed at temperatures (23°C, 163°C, 371°C) for $[0]_{10}$ and $[90]_{10}$ orientations. The creep tests were performed at temperatures (427°C, 482°C, 538°C) and stresses (760 MPa, 900 MPa, 1035 MPa) for $[0]_{10}$ are on schedule and almost complete.

The ultimate strength and elastic modulus properties for $[0]_{10}$ tests of the Trimarc-1™/Ti-6Al-2Sn-4Zr-2Mo system are generally lower than other systems such as SCS-6/Ti-6-4 and SCS-6/Ti-15-3. This has been attributed to the lower average strength of the Trimarc-1™ fiber compared to the SCS-6 fiber, 3100 MPa and 4300 MPa, respectively and the low volume fraction of the composite (0.29) compared to (0.33-0.35) for the other TMC systems.

Four neat panels made from the Ti-6Al-2Sn-4Zr-2Mo wire have recently been received from the manufacturer. The neat material behavior in creep, fatigue and fatigue crack growth is required for the development of life prediction models. A cut-out plan is currently being developed to provide the required number of specimens for tension, creep, relaxation and fatigue crack growth tests to determine the material constants needed for the life prediction models.

The objective of this program is to replace current stainless steel (PH13-8Mo) piston rods used in both the F-22 airframe actuators and the F119 engine actuators with lighter weight titanium matrix composite piston rods. The approach was a three phase program where the first phase was a development phase to validate the material and manufacturing process by verifying that the material meets minimum allowables used in the design of the piston rod. The second phase, which is near completion, was a demonstration phase that provided additional data to satisfy the minimum mechanical property requirements for the design and examined lot to lot variations in the mechanical properties from the manufacturing process. The final phase will be a production phase that will provide data for damage tolerance based design systems.

Table 4.2-1

Test Matrix for Trimarc-1™/Ti-6Al-2Sn-4Zr-2Mo

Test Type	Orientation	Number of Specimens		
		(23°C) 72°F	(163°C) 325°F	(371°C) 700°F
Tension	Longitudinal	9	18	15
	Transverse	9	12	9
Compression	Longitudinal	6	6	6
	Transverse	6	6	6
LCF	Longitudinal (R=-1.3)	18	18	18
	Longitudinal (R=0.1)	10	9	9
	Transverse (R=0.1)	7	6	7
HCF	Longitudinal (R=0.1)		12	
FCG	Longitudinal (R=0.1)	4	2	2
	Longitudinal (R=0.5)	1		
	Longitudinal (R=0.7)	2	2	2
		(427°C) 800°F	(482°C) 900°F	(538°C) 1000°F
Creep	Longitudinal	7	6	3

The characterization of the TMC included tension, compression, sustained-load creep, low-cycle fatigue, high-cycle fatigue and fatigue crack growths tests for a total of 281 specimens. Based on the actuator service environment, three temperatures (23°C, 163°C, 371°C) and two stress ratios (0.1, -1.3) were prescribed as conditions for the fatigue tests. The fatigue behavior characterization [Buchanan et al. (1997)] determined that the data fall within a 2X variation in life and that the 0° maximum fiber stress versus cycles to failure for several TMC systems collapse together.

4.3 DEVELOPMENT OF ADVANCED ORTHORHOMBIC MATRIX

4.3.1 The Effect of Heat Treatment on the Tensile And Creep Behavior of 'Neat' Matrix Ti-22Al-23Nb [C9]

A study has been conducted to examine the effect of post-consolidation heat treatment on the longitudinal tensile and creep properties of an orthorhombic-based titanium aluminide, Ti-22Al-23Nb(a%), in neat matrix form. Heat treatment parameters were selected such that they would be consistent with future inclusion into the consolidation cycle for the fabrication of continuously-reinforced orthorhombic titanium matrix composites (O TMC's). The effects of heat treatment on microstructural evolution, including type and morphology of the phase constituents, was examined via scanning secondary electron microscopy and quantitative image analysis. Variations in microstructural features were correlated with resulting room temperature tensile properties including: ultimate tensile strength (UTS), yield strength (YS), total elongation (%El) and modulus (E), as well as isothermal creep response at 650°C/172MPa.

4.3.2 Thermal Stability of Ti-22Al-23b 'Neat' Matrix Material

Orthorhombic titanium matrix composites (OTMC's) are being considered for long-life applications at temperatures exceeding 600°C. It is necessary that the matrix microstructure be stable during long time exposures at these temperatures. The purpose of this work is to ascertain the stability of the microstructure at elevated temperatures and to determine the effects of extended exposure on the mechanical properties. The matrix material was neat, Ti-22Al-23Nb that had been sub-transus heat treated at 1125°C/2hr and cooled at 2.8°C/ min to 815°C/8hr/FC. This heat treatment yields a three-phase structure of globular alpha-2, surrounded by a rim orthorhombic phase, with acicular or needle-like orthorhombic contained in a beta matrix.

Test samples were held for 50, 200 and 500 hours at 600° and 750°C, respectively. The samples were encased in evacuated quartz tubes prior to exposure to minimize environmental effects. Following exposure, small pieces were cut from the grip section and mounted for metallographic analysis. The 50-hour samples showed no signs of microstructural instability, regardless of exposure temperature. However, material exposed at both 600 and 750°C for 200 and 500 hours showed formation of a fourth phase at the rim orthorhombic/beta boundary. Backscatter electron microscopy shows this new phase to be darker in contrast than the surrounding material, indicating a low density constituent. Transmission electron microscopy studies on similar phases in other orthorhombic alloys are currently underway.

The exposed samples are currently awaiting tensile and creep testing to determine the effects of this fourth phase on mechanical behavior.

4.4 CHARACTERIZATION OF CONSTITUENTS

4.4.1 Constitutive Model of Neat Ti-6Al-4V

Recent work at WL/MLLN in the area of analytical modeling of creep in titanium and titanium matrix composites has been based on unified viscoplastic models, notably the Bodner-Partom model [Chan et al. (1988)]. The ultimate goal has been a single model capable of capturing both the quasi-static plasticity behavior and high-temperature creep with reasonable accuracy. However, attempts to model both primary and secondary creep, even at constant stress, have had limited success.

A study was undertaken to optimize the Bodner-Partom model parameters, and determine whether the Bodner-Partom model's failure to capture both phases of creep behavior is a fundamental limitation. The standard of comparison used to evaluate model accuracy was a selection of creep and quasi-static tension data for neat Ti-6Al-4V at 427 °C. As part of this study, some numerical experimentation with power law and other more conventional creep models was been performed.

Material constants for the Bodner-Partom model have been optimized both manually, one parameter at a time, and numerically using function minimization routines to minimize the error for selected test data. The property optimization procedure was carried out using the tensile and creep data mentioned above.

Using the optimized material constants, the Bodner-Partom model gives reasonable secondary creep rates, but fails to capture the primary creep behavior. Thus, the total creep

strains exhibit significant error. We have found that the model could be optimized for primary creep but the resulting secondary creep rates were extremely inaccurate.

The failure of the Bodner-Partom model to capture both primary and secondary creep responses accurately is that only one "mode" of time dependence is present in the model. So, the model is limited in transitioning from relatively high primary creep rates to significantly lower steady creep rates. The evolution equations in the Bodner-Partom model key on the plastic work and two hardening variables (isotropic and kinematic). The plastic work and the isotropic hardening parameter control the tensile creep response; both are monotonically increasing quantities that change according to decaying exponential evolution equations. This mathematical form appears impossible to tune properly to capture the transition from primary to secondary creep. The remaining hardening parameter is important for cyclic behavior only, and contributes nothing in the way of improving the creep prediction.

We should emphasize that the Bodner-Partom model remains an excellent choice for quasi-static plasticity and cyclic deformation (although the numerical behavior is troublesome at times). However, the ability of the model to reproduce the important features of creep response in titanium is limited. The model may still be useful for the analysis of metal matrix composites in which primary creep of the matrix is not a crucial factor in the overall creep response; thus far we have not attempted a head-to-head comparison with other models to resolve this question.

A limited number of numerical experiments have been performed using power law creep models (actually, a power law for primary creep, and hyperbolic sine law for secondary creep). This model did an accurate job of predicting both primary and secondary creep response and the fitting of the model parameters was extremely simple. The secondary creep term was fit first from experimentally determined steady creep rates versus stress. Next, holding the secondary creep terms fixed, the power law parameters for primary creep could be determined accurately within a few minutes using a simple spreadsheet model.

For creep at several stress levels at 427 °C, the power law creep model was extremely accurate for both primary and secondary creep. For a stepped-strain test resulting in relaxation, the power law model with the material constants based on creep data predicted stress levels which were generally within five to ten percent, and the relaxation rates were very reasonable.

The power law model is being extended to provide cyclic creep predictions. The predictions will be compared to results from cyclic creep tests under strain control at 1 Hz and 0.01 Hz.

4.4.2 FCG Behavior of Neat Ti-6Al-4V

The FCG behavior of neat Ti-6Al-4V was characterized in support of the analysis of the FCG behavior of SCS-6/Ti-6Al-4V under the PRDAIV program. Tests were conducted using the single edge cracked geometry with clamped ends at stress ratios, R=0.1 and 0.7 at 23°C and at R=0.1 at 316°C. The load versus crack mouth opening displacement (CMOD) response was measured periodically to characterize the closure behavior at room and elevated temperatures. The closure-corrected effective stress intensity factor in the matrix, $\Delta K_{m,eff}$ was calculated as,

$$\Delta K_{m,eff} = K_{max} - K_{cl} \ , \qquad \text{(Eq. 4.4.2-1)}$$

where K_{cl} = stress intensity factor corresponding to the closure load. The crack growth rate (da/dN) versus $\Delta K_{m,eff}$ was obtained as,

$$\log\left(\frac{da}{dN}\right) = C_1(\sinh(C_2(\log(\Delta K_{m,eff}) + C_3))) + C_4 \ . \qquad \text{(Eq. 4.4.2-2)}$$

where C_1 = 1.4474, C_2 = 2.0000, C_3 = -1.0822, and C_4 = -7.1261 at 21°C, and C_1 = 1.1985, C_2 = 2.0000, C_3 = -0.9690, and C_4 = -7.4317 at 316°C, da/dN is in m/cycle and ΔK_m is in MPa$\sqrt{m}$. The data indicated negligible difference between the crack growth behavior at 23 and 316°C. The above equations are being used to analyze the through- and surface-crack growth in SCS-6/Ti-6Al-4V.

4.4.3 Heat Treatment Effects On SiC Fiber [C10]

The Wright Laboratory Materials Directorate at Wright-Patterson AFB has been spearheading the development and evaluation of a new class of metal matrix composites based upon continuous SiC fiber reinforcement of orthorhombic phase containing titanium aluminide matrices. These composites (O TMCs) will be necessarily subjected to thermal exposures during primary and secondary component processing, and possibly also to optimize matrix-dominated mechanical performance through heat treatment. It is imperative that such thermal excursions do not degrade the SiC fiber reinforcement, hence compromising resulting composite properties. As such, a study has been undertaken to examine the effects of heat treatment on the room temperature tensile strength of continuous SiC fibers. The fibers examined in the subject investigation included: Trimarc-1™, SCS-6, Ultra SCS®, and an

experimental large diameter version of Ultra SCS®. The fibers were subjected to two heat treatment conditions being below (subtransus) and above (supertransus) the beta solvus temperature of the orthorhombic matrix alloy utilized for this study, Ti-22Al-23Nb (at%). The fibers were evaluated for ambient temperature tensile strength in the following conditions: 1) as-received; 2) heat treated in vacuum; and 3) consolidated into Ti-22Al-23Nb, heat treated in vacuum, and chemically extracted. Fiber microstructure and fracture analysis was accomplished via secondary scanning electron microscopy (SEM). In addition, chemical reactions between fiber core and the SiC, and between the SiC fiber and the Ti-22Al-23Nb matrix, were also studied using SEM analysis.

4.4.4 Heat Treatment Effects on SiC (Trimarc-1™) Fiber Tensile Properties

Advanced gas turbine engine components and hypersonic airframe applications require materials with significantly improved specific property performance at elevated temperature. Titanium aluminide-based metal matrix composites have thus received considerable attention in recent years. A new class of titanium aluminides based upon the Ti2AlNb "orthorhombic" (O) phase has emerged as a particularly promising matrix for continuous fiber reinforcement. Most recent results for the Ti-22Al-23Nb (at%) O-phase composition indicate that it offers many advantages as a composite matrix when compared to the Ti3Al-based (alpha-2) composition, Ti-24Al-11Nb (at%). These advantages include reduced fiber/matrix reactivity, increased elevated temperature strength, improved creep resistance and improved short-term resistance to interstitial embrittlement. However, in the as-fabricated condition, the non-optimized microstructure results in property levels, particularly creep, which still fall short of anticipated performance requirements. Recent studies have indicated that neat matrix and matrix-dominated composite properties can be improved through post-consolidation thermal treatments that alter microstructural features of the matrix. However, these thermal exposures (as well as subsequent component processing) may have a deleterious effect on fiber strength due to inherent fiber instability or excessive reaction at the fiber/matrix interface, and hence, on fiber dominated composite properties.

The subject study was undertaken to investigate the effect of heat treatment on the strength retention of continuous SiC fibers. The principle fiber studied was a tungsten core SiC fiber with a carbon coating produced by Amercom Inc. (Trimarc-1™). The fiber was evaluated in the as-received condition and after heat treatment. Heat treatments incorporated a subtransus or supertransus solution treatment followed by a controlled slow cooling to a direct aging condition. These treatments were conducted on bare as-received fiber, and on fibers

within an orthorhombic matrix (Ti-22Al-23Nb at%) which were then chemically extracted. Characterization included room temperature tensile testing, evaluation of fiber/matrix interfacial reaction zone growth (and corresponding carbon coating depletion), fiber microstructure and fracture, and matrix microstructure. Tensile data was plotted based upon a probability to survive at a given strength level, and analyzed using Weibull statistical analyses. The results indicate that the Trimarc-1™ fiber examined in this study is degraded by the heat treatment. This degradation appears to be the result of a tungsten core/SiC reaction and by internal defects which are accentuated by compressive residual stresses in the composite. Results for the Trimarc-1™ fiber are briefly compared to those of carbon core SiC fibers (i.e. SCS-6 and Ultra SCS®) neither of which are degraded by heat treatment.

4.4.5 Modulus and Density Measurements of Ti-22Al-23Nb

Determination of elastic modulus and mass density values for new materials is necessary to support various modeling efforts and mechanical tests. The modulus of a monolithic material can be calculated from measurements of the ultrasonic rod wave velocity and the mass density [Ashbaugh et al (1996)]. This method is especially useful for thin foils as accurate measurements of applied loads and resulting displacements are difficult using mechanical test systems. The rod wave velocity can be accurately measured using thin (0.5 mm) strips of the material and 1 MHz ultrasound. Measuring the density of small, irregularly-shaped specimens can be difficult. Thus, large samples of a material, especially if the shape allows straight-forward measurement of dimensions, are desirable for accurate density calculations.

Table 4.4.5-1

Calculated Values for Ti-22Al-23Nb Specimens

Specimen	Length (mm)	TOF (usec)	# Echoes	Velocity (mm/usec)	Density (g/cc)	Modulus (GPa)
96516	56.67	25.2	1	4.50	5.19	105.0
96518	48.78	22.0	1	4.43	5.19	102.1
96520	57.57	50.2	2	4.59	5.19	109.2
96522	53.81	47.2	2	4.56	5.19	107.9
96524	58.00	50.0	2	4.64	5.19	111.7
					Average =	107.2
					S.D. =	2.1
Note: Density value obtained from measurements on large O-Ti panel						

A large panel (approximately 830 x 300 x 0.5 mm) of Ti-22Al-23Nb was obtained that was to be cut up into many mechanical test specimens. Several different methods of measuring the panel thickness and/or volume were tried with the two most precise being a high resolution micrometer (resolution = 0.001 mm) and dial indicator (0.002 mm). Thickness measurements were made at 50 mm intervals along the length and width of the entire surface of the panel. The width and length of the panel were measured several times with a metal scale having a resolution of 0.050 mm. The mass of the panel was measured on a calibrated electronic balance with a resolution of 0.1 g. The calculated density for the panel was 5.19 ± 0.02 g/cc.

Ultrasonic rod wave velocities were calculated by measuring the time-of-flight of 1 Mhz ultrasound through the length of the specimens. When possible several passages of the sound within the specimen were measured which resulted in more accurate velocity calculations. The ultrasonic rod wave velocity calculations for several Ti-22Al-23Nb specimens are listed in Table 4.4.5-1 along with the calculated elastic moduli. The average modulus value for the five specimens was 107 GPa with a standard deviation of 2 GPa.

SECTION 5

DAMAGE ACCUMULATION AND FAILURE OF CERAMIC MATRIX COMPOSITES (CMC)

Ceramic matrix composites (CMC) are considered to be potentially useful as hot-section components in advanced engines and structures in aerospace vehicles. Damage tolerance based design of CMC components for structural applications requires the knowledge of damage initiation and progression under service load conditions. Non-structural applications such as flaps and seals in the engines require the knowledge of the behavior of CMC under severe temperature gradients. In addition, such CMC components typically damage initiators such as holes resulting in crack growth under cyclic mechanical and thermal loading. In some applications, the CMC components contain attachments that generate significant tensile loads across the thickness. To address these issues, the UDRI conducted extensive experimental and analytical investigations in the areas of characterization of damage progression using an integrated NDE/Mechanical testing system, fracture and fatigue crack growth behavior of an advanced CMC, stresses due to temperature gradients, and development of a test technique to determine the transthickness strength of advanced CMC. These activities are discussed in the following sections.

5.1 CHARACTERIZATION OF DAMAGE PROGRESSION IN CERAMIC MATRIX COMPOSITES USING AN INTEGRATED NDE/MECHANICAL TESTING SYSTEM

The objective of this investigation was to develop an *in situ* ultrasonic evaluation technique to monitor damage initiation and accumulation in advanced ceramic matrix composites. The research focused upon correlating the amount of detected microcracks to the changing wave characteristics of an ultrasonic surface wave signal. The wave speed, frequency content, and amplitude of the ultrasonic signal were monitored as it propagated along the specimen. The experimental setup was designed to allow the continuous characterization of damage under applied loads. Accumulated damage was monitored optically and by other available nondestructive techniques. A 35-mm camera with microscope attachment allowed the inspection of the specimen edge at high magnification under load. These tests were conducted at room temperature in lab air.

The material used was Barium-Magnesium Aluminosilicate reinforced with Silicon Carbide fibers in a $[0/90]_{3S}$ layup. Before testing, immersion C-scans of each specimen were

made using both surface waves and gated reflector plate scans. Edge replicates were also taken to document surface features prior to loading. Specimens were loaded in tension using a servohydraulic testing machine. An extensometer was used to measure strain. An external function generator was used to ramp the specimen up to peak load, pausing at discrete intervals to acquire ultrasonic wave data. At peak load, the specimen edge was examined under high magnification and cracks were photographed using the 35-mm camera. Edge replicates were also taken at peak load and later examined for damage features.

The onset of matrix cracking was found to occur at 60 MPa. This stress level coincided with the material's proportional limit as well as a sudden decrease in ultrasonic surface wave amplitude. The matrix cracks found were generally within the first three plies from the specimen surface. This depth is well within the area interrogated by the ultrasonic surface wave. Future work will focus on a quantitative measurement of crack depth and density. Fatigue and sustained loading tests at room and elevated temperatures (1000°C) will also be conducted.

5.2 FRACTURE BEHAVIOR OF NEXTEL 610/ALUMINOSILICATE

The fracture behavior of Nextel 610/Aluminosilicate (N610/AS) was investigated using the modified single edge notched geometry, MSE(T), at room temperature and 950°C in lab air. Load versus crack mouth opening displacement (CMOD) data were acquired continuously throughout the testing. Damage assessment was made through optical inspection, ultrasonic C-scans, changes in specimen compliance, loadbearing capacity and CMOD during testing. Results of the fracture tests indicate that the N610/AS composite is notch sensitive at room temperature and 950°C. For all tests, the peak net section stress of the notched specimens was less than 60% of the ultimate tensile strength of the unnotched composite. A comparison of the RT and elevated temperature fracture data showed a decrease of 50% in the peak stress intensity factor as temperature increased from 23°C to 950°C, Figure 5.2.1. The result is in sharp contrast to the unnotched tensile behavior, which shows only a 15% drop in tensile strength. Fracture tests conducted at 950°C showed no effect of load-line displacement rate or unloading loops on the peak stress intensity factor. During the room temperature fracture test a single dominant matrix crack could not be identified on the specimen surface. Ultrasonic C-scans of the intact fracture specimen after the peak load, however, showed increased ultrasonic attenuation ahead of the notch tip which was distributed above and below the notch plane. At 950°C, matrix crack growth from the saw-cut notch tip was measured and correlated with the ultrasonic attenuation, which was concentrated in the plane of the notch. Fracture surface profiles of failed specimens supported the C-scan results with fibers extending from the

fracture surface up to 3 mm at room temperature and a maximum extension of 0.5 mm at 950°C.

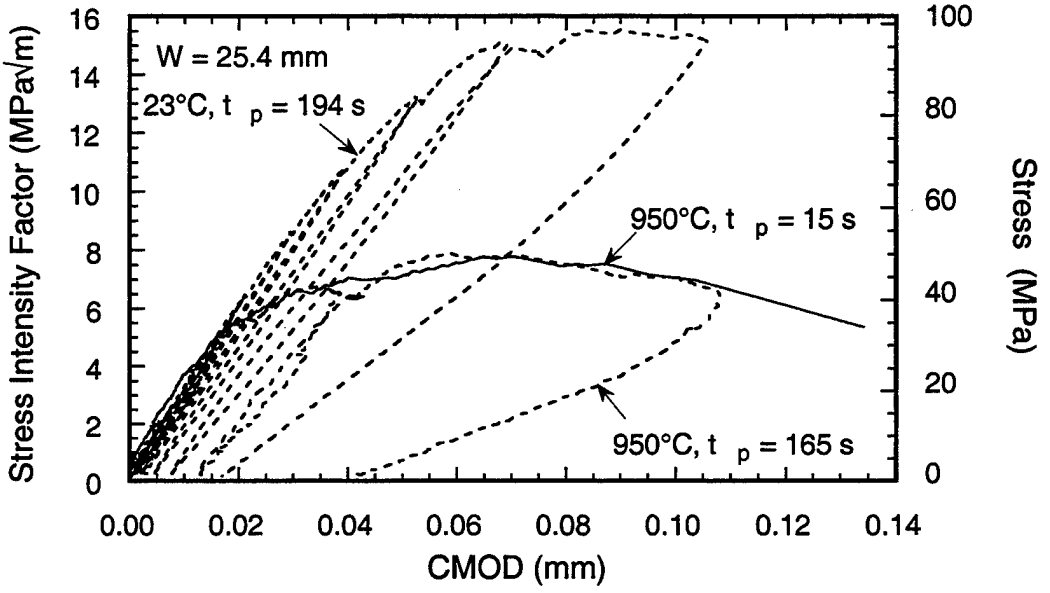


Figure 5.2-1

Stress Intensity Factor and Applied Stress vs. Crack Mouth Opening Displacement (CMOD) for 23°C and 950°C Fracture Tests

5.3 FATIGUE CRACK GROWTH BEHAVIOR OF NEXTEL 610/ALUMINOSILICATE

The fatigue crack growth behavior of N610/AS composite was investigated using the MSE(T) geometry at room temperature (RT) and 950°C in lab air. Crack arrest conditions were identified during testing by constant maximum CMOD values with applied cycles while progressive damage accumulation resulted in continually increasing maximum CMOD values. Similar to the fracture test results, peak stress intensity factor leading to specimen failure was reduced by 50% when temperature was increased from 23°C to 950°C. At RT and 950°C an applied maximum stress, $\sigma_{a,max}$ = 23 MPa resulted in constant CMOD values, consistent with no evidence of ultrasonic attenuation ahead of the notch tip. Cycling at $\sigma_{a,max}$ = 41 MPa produced no changes in ultrasonic attenuation or CMOD with applied cycles at RT, but at 950°C ultrasonic attenuation increased in the notch plane and CMOD increased slowly with applied cycles. Cycling at $\sigma_{a,max}$ = 48 MPa, 950°C, resulted in high attenuation ahead of the notch tip and eventual specimen failure. At 950°C a dominant matrix crack was identified on the specimen surface prior to failure, during fatigue cycling at the peak applied stress. The length

of the optically measured crack length was consistent with the length of the C-scan damage region. At RT, cycling at applied stresses above 93 MPa resulted in specimen failure, with a C-scan indicated damage region that extended above and below the notch plane.

Fatigue crack growth tests were conducted at RT on specimens 12.7 mm, 19.0 mm and 25.4 mm in width, at applied stress ratios (R) of 0.1 and 0.5. Peak applied stress levels leading to specimen failure varied by 10% between the 3 specimen widths. For a given specimen width, increasing stress ratio from 0.1 to 0.5 resulted in reduced cycles to failure.

5.4 STRESSES DUE TO TEMPERATURES IN CMC AEROSPACE COMPONENTS [C11]

Ceramic matrix composites (CMC) are being considered as replacement materials for divergent flaps and seals in advanced aerospace turbine engines. During service, these components are subjected to severe temperature gradients across the width of the flaps. This paper discusses an analytical procedure to estimate the stresses generated in the CMC flaps due to the temperature gradients. The analytical procedure can be used for a material with non-linear temperature-dependent stress-strain behavior. This procedure was used to predict the thermal stresses in four candidate CMC systems due to temperature gradients. The thermal stresses along the edges typically exceed the proportional limit, and sometimes the fatigue limit of the CMC.

5.5 TRANSTHICKNESS TENSILE TESTING OF CMC

Current designs for using CMCs in advanced turbine engines require attachment features that produce tensile loads across the thickness of the component. The successful design of these attachments require extensive characterization of the transthickness behavior of the CMC.

To address this issue, a servo-hydraulic test machine was configured for conducting transthickness tensile tests on an advanced CMC. The material was $[0/90]_{4S}$ Nicalon/MAS-5. Two specimen geometry's were investigated, round and square. The square specimens were selected because they minimize machine costs, however they have corners that act as stress risers which could effect the results. The tests were performed at room temperature using FM®1000 adhesive film to attach the specimens to the fixturing. Lamps were used for the elevated temperature (175°C/ 60 minutes) curing of the adhesive. A loading rate of 2 MPa/second was applied to the specimens until specimen fracture.

A total of 36 specimens were tested, 18 round and 18 square. The dimensions of the square and round specimens were 16.8mm x 16.8mm and 19mm diameter, respectively. 33 specimens (16 round and 17 square) fractured within the thickness. Three specimens were discarded, two because of failure at the adhesive line, and one because of specimen misalignment. Results of the 33 specimens are shown in Table5.5-1.

Table 5.5-1

Results of Transthickness Tension Tests on Nicalon/MAS-5

Geometry	Mean Strength (MPa)	Standard Deviation (MPa)
Round	20.9	3.4
Square	19.9	2.5

No statistically significant differences were found between the test results of the round and square specimens.

SECTION 6

INITIATION AND GROWTH OF FATIGUE CRACKS IN ENGINE MATERIALS

6.1 HIGH CYCLE FATIGUE OF TITANIUM ALLOYS

6.1.1 Development of the Modified Goodman Curve for HCF Ti-6Al-4V

A rapid test method is applied for generating data points for a modified Goodman Curve (alternating stress v. mean stress) for Ti-6Al-4V at 70 Hz under high cycle fatigue conditions (HCF). The method involves subjecting a specimen to 10^7 fatigue cycles at a particular value of R at a stress level that is below the anticipated level to cause failure. If failure does not occur after 10^7 cycles, the stress level is increased 5% and the test is repeated on the same specimen. The procedure is repeated until failure occurs within a loading block before 10^7 cycles.

The fatigue stress is determined using a linear interpolation scheme. The stress level of the prior block (σ_{i-1}) in which failure did not occur, the stress level of the present block (σ_i) where failure occurred, and the number of cycles to failure in the present block (N_i) yield the failure stress for 10^7 cycles:

$$\sigma_f = \sigma_{i-1} + \frac{N_i}{10^7}(\sigma_i - \sigma_{i-1}) \qquad \text{(Eq. 6.1.3-1)}$$

The failure stresses yield alternating and mean stresses at 10^7 cycles that are plotted as a Goodman Curve.

The test method is applied to Ti-6Al-4V for stress ratios from R=-1 to R=0.9. The validity of the method is confirmed by comparing data with those obtained using the conventional S-N approach for values of R=0.1, 0.5, and 0.8.

Cylindrical specimens were machined from random length, 1.75 inches in diameter, Ti-6Al-4V forging bars. Fatigue tests were conducted under constant stress intensity conditions using a closed-loop computer controlled servo-hydraulic test machine. All tests were conducted at room temperature in laboratory air at a frequency of 70 Hz. The data are plotted as alternating stress versus mean stress as shown in Figure 6.1-1.

The rapid testing technique is extended to the generation of a modified Goodman Curve for the same material subjected to prior low cycle fatigue (LCF) at 1 Hz for ten percent of its LCF life. The prior LCF damage is shown to have no degradation of the HCF life under several conditions as determined from subsequent HCF testing using the rapid testing technique. To

further understand and explain observed behavior under HCF, particularly at high values of R, a method for representing data corresponding to constant life (or endurance limit) is introduced. The "Nicholas-Haigh Diagram" presents maximum stress, as well as alternating stress as a function of mean stress. Inclusion of maximum stress as a design criterion is found to limit some high mean stress conditions that would otherwise be considered to be in the safe operation region.

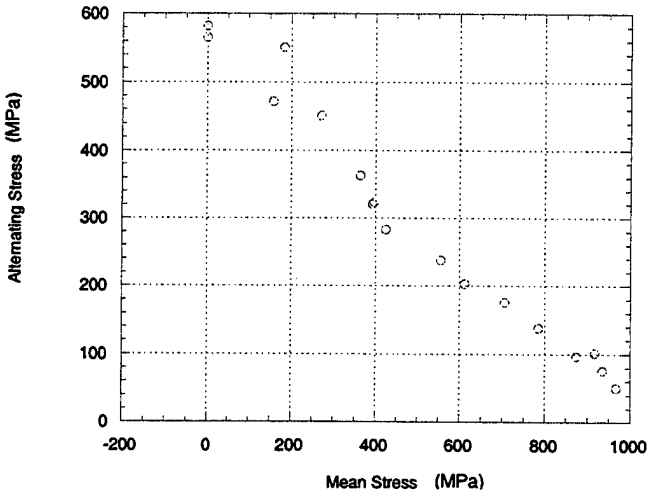


Figure 6.1-1

Modified Goodman Curve for Ti-6Al-4V

6.1.2 Mean Stress and Frequency Effects on Ti-6Al-4V

Contractor supported initial experiments in a program to determine the effect of LCF on HCF life of Ti-6Al-4V. The C10 HCF test system, which had been dormant for several years, was renovated with a new amplifier, Woods metal alignment fixture and an improved load train. Grips and specimens were designed for the new load train. Frequency scans revealed a useable frame resonance with high loading capability at 400 Hz. Room temperature baseline tests were conducted at stress ratios of 0.8, 0.7 and 0.5 at frequencies of 400 Hz and 70 Hz. Fixturing and software were designed and fabricated for incorporating the Laser-Mic into the C10 system in order to monitor specimen elongation as a function of fatigue life.

6.1.3 Effect of Prior Torsion Fatigue on HCF Life of Ti-6Al-4V

A project has been initiated to determine if an interaction exists between damage introduced by a torsion fatigue and a uniaxial tension fatigue. Axial fatigue is applied to

specimens that have been subjected to various fractions of torsion fatigue life. If the reduction in uniaxial fatigue life is significant, additional tests would be conducted and models would be developed to understand the effect. Tests were conducted to characterize the torsion stress-strain behavior. Then, torsion fatigue tests were conducted on a combined torsion/axial fatigue test system. Unfortunately, the load control of the test system was not adequate to maintain the desired test conditions. To minimize expenses, a torsion fatigue system has been designed and components will be assembled in the laboratory. Currently, this project is awaiting the completion of the test system.

6.1.4 Effect of Fretting on HCF Life of Ti-6Al-4V

An extensive search of the literature for publications on fretting fatigue of plate to plate contact indicated a lack of published data in this area [Hills & Nowell 1994; Hoeppner, 1994; Papanikos & Meguid; Ruiz & Chen; Ruiz, et. al.]. Most of the studies on fretting have focused on fretting wear, or gross slip [Fayeulle, et. al.; Nowell & Hills; Saritas, et. al.; Soderberg, et. al.; Waterhouse, 1984; Waterhouse, 1992]. The studies conducted on fretting fatigue, or slip-stick, have addressed either line or Hertzian contact [Adibnarazi & Hoeppner, 1992, 1993, 1994; Blanchard, et. al.; Del Puglia, et. al.; Endo & Goto; Fannes; Kuno, et. al.; Vincent; Waterhouse, et. al.]. While these types of contact are easier to model, they provide very little data that is directly applicable to evaluating the fretting damage seen in turbine engine blade attachment joints.

A study to simulate fretting damage as seen in turbine engine components is under way. The fretting fatigue grips, straight-sided specimens, and fretting pads have been designed, and manufactured (Figure 6.1-2). Load washers were ordered along with pairs of concave and convex washers for centering the load washers. FM1000 adhesive for isolating vibration between the grips and the fretting pads was obtained. The grips and pads have been assembled. Testing should begin as soon as the furnace, used to cure the adhesive, is repaired.

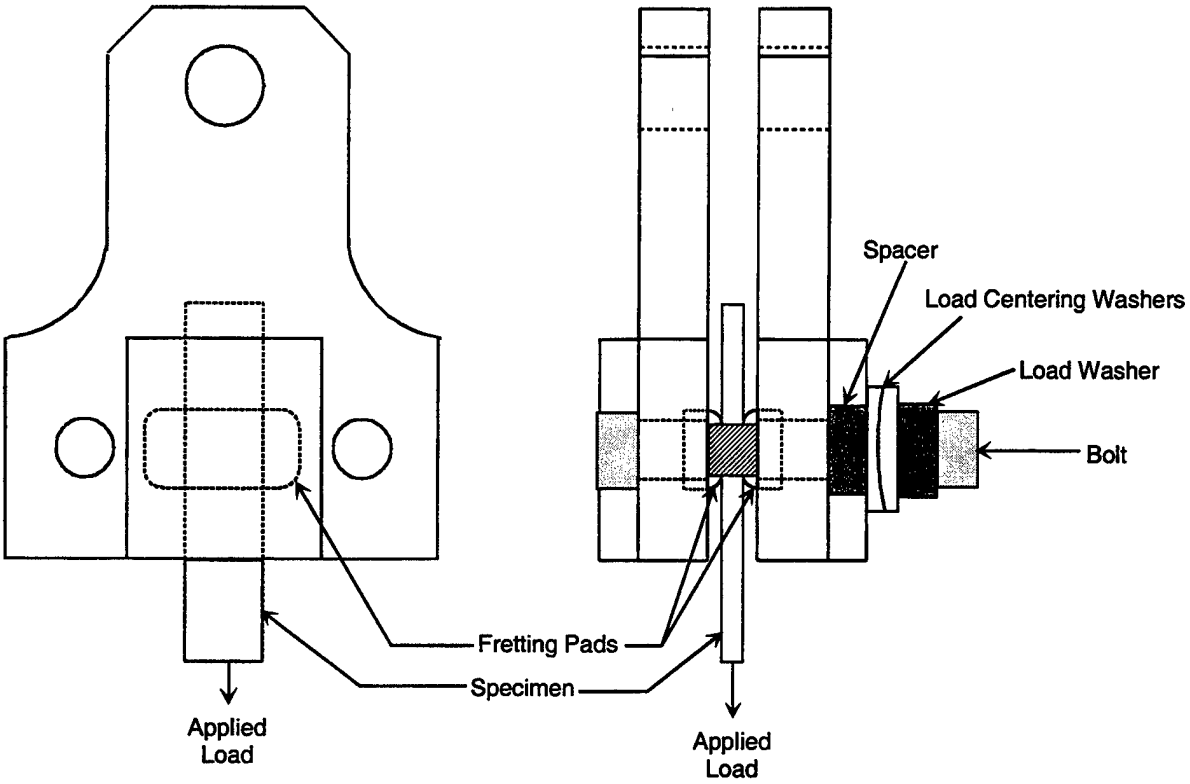


Figure 6.1-2

Schematic of Fretting Fatigue Grips

6.1.5 HCF/LCF Interaction on Life in Ti-6Al-4V

This program has been designed to study the micro-mechanical basis for any observed effects of prior and/or concurrent LCF on HCF life. Real-time observations of the specimen surface using an infrared imaging system will be performed to identify highly localized regions of damage evolution at the earliest possible stage. Subsequent metallographic examination should reveal at least some of the major contributions to the damage and, perhaps, the sequence of damage events.

The illness and death of the lead researcher, Dr. Brian Worth, have delayed the start of this project. Despite this demoralizing setback, we have been able to identify the test matrix, establish the methodology to be used, reduce the observation procedure to practice, and obtain the required equipment. The remaining tasks are to write and debug the computer code required to obtain the data, integrate and check out the complete system, perform the experiments, and analyze the data. We anticipate that experimental work will begin during the first quarter of 1998 and that results will become available during the third quarter of 1988.

The types of damage evolution observed in related research programs (described elsewhere in this report) have guided the steps taken so far in this project. Future work will

concentrate on areas of interest identified in these related programs with an emphasis on providing experimental evidence to explain the damage observations.

6.1.6 High Cycle Fatigue and Fatigue Crack growth of Ti-6Al-2Sn-4Zr-6Mo.

A modified Goodman curve was developed for stress ratios from -1 to 0.90 for Ti-6Al-2Sn-4Zr-6Mo. Hourglass specimens were machined from a 18 inch diameter by 2 inch thick pancake forging. The specimens were low stress ground and electropolished. Fatigue tests were conducted under constant stress intensity conditions using a closed-loop computer controlled servo-hydraulic test machine. All tests were conducted at room temperature in laboratory air at a frequency of 60 Hz.

The tests were conducted in the manner described in Section 6.1.3. The failure stress for 10^7 cycles over a range of stress ratios from -1 to 0.90 was determined Eq. 6.1.3-1. The results of the modified Goodman tests are shown in Figure 6.1-3.

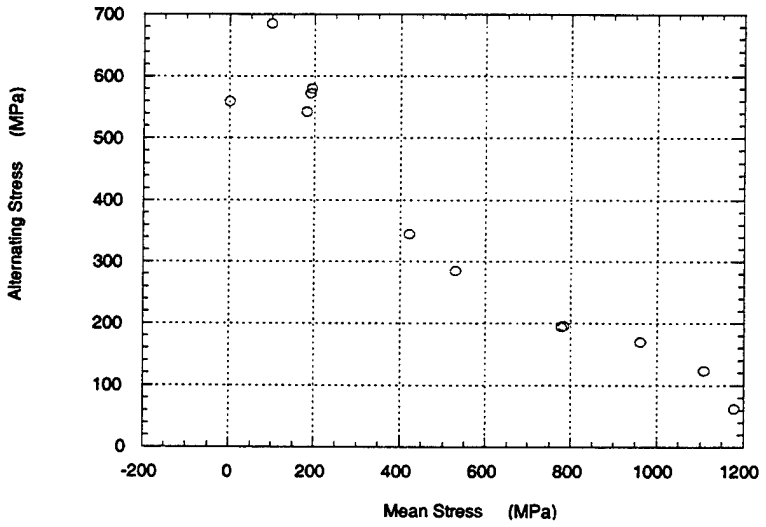


Figure 6.1-3

Modified Goodman Curve for Ti-6Al-2Sn-4Zr-6Mo

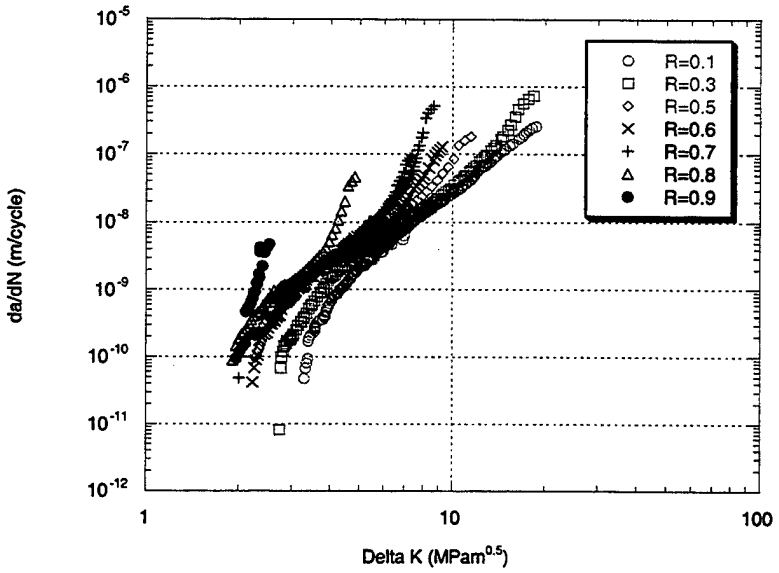


Figure 6.1-4

Room Temperature Fatigue-Crack-Growth Rate Data for Ti-6Al-2Sn-4Zr-6Mo

Fatigue-crack-growth rate tests were conducted using ASTM E647 (1997) procedures and 40 mm compact tension, C(T), specimens. The tests were conducted at 60 Hz in laboratory air at room temperature under stress ratios ranging from 0.1 to 0.9. The crack growth data were acquired under decreasing stress-intensity factor range fatigue followed by constant-load-amplitude fatigue. The resulting fatigue-crack-growth rate data are shown in Figure 6.1-4.

6.2 THE EFFECT OF STRESS RATIO ON FATIGUE CRACK GROWTH RATE IN THE ABSENCE OF CLOSURE [C12]

A fractographic study was performed on Al-alloy fatigue fracture surfaces produced by programmed load sequences. The load sequences included steps of constant amplitude cycles at three different stress ratios, each step is preceded by a small number of high amplitude cycles designed to avoid the influence of crack closure and to serve as fractographic markers. The experiments were conducted on different specimen geometries to produce conditions associated with a long crack under *fully elastic* conditions and a short crack in a notched coupon seeing *high local post yield* stress conditions. Crack sizes, covered in the study, ranged from 0.02 to 12 mm and growth rates ranged from $2x10^{-7}$ to $4x10^{-5}$ mm/cycle. Fractographic

evidence from the study suggests that crack growth rate can vary by up to a factor of five with applied stress ratio change from 0.64 to 0.73. In the case of the long crack, the effect is less noticeable or totally absent. In the case of naturally initiating notch root cracks, the effect is more pronounced at higher stress level and lower crack growth rate.

6.3 MIXED-MODE CRACK GROWTH IN Ti-6Al-4V and Ni-BASE SUPERALLOY

The mixed-mode crack growth behavior of Ti-6Al-4V was investigated using the centrally notched disk geometry, DM(C). The disks were oriented such that the initial machined flaw was inclined at 16° or 27° to the loading axis. These orientations ensured that the ratio of mode II stress intensity factor, K_{II}, to mode I stress intensity factor, K_I, was > 0 at the crack tip. Some of the specimens were precracked under mode I conditions prior to mixed-mode testing. All the tests were conducted at room temperature in lab air. The results showed that crack initiation angles and crack propagation paths could be predicted using mixed-mode theories for materials with isotropic behavior.

The effect of microstructure and temperature on the mixed-mode crack growth behavior of Ni-base superalloys was also investigated. The specimens with the new microstructure exhibited mixed-mode crack growth rates that were ≈10X slower than that observed in the standard microstructure. Thus, the heat treatment used to obtain the new microstructure can be utilized in manufacturing engine components that are resistant to mixed-mode crack growth. Preliminary elevated temperature tests indicate that the resistance to mixed-mode crack growth at 593°C is significantly superior to that at room temperature. Additional tests are required to confirm this behavior.

6.4 EFFECT OF LASER SHOCK PEENING ON CRACK GROWTH IN Ti-6Al-4V

6.4.1 Weight Function For A Tapered Three-Point Bend Specimen, TSE(B)

The UDRI continued to provide analytical support to the investigation of the efficacy of the laser shock peening (LSP) process in improving the damage tolerance of Ti-6Al-4V. The geometry used is a tapered three-point bend specimen, TSE(B) simulating the leading edge of an engine blade. Three dimensional finite element analysis was used to generate the stress intensity factors (K_I) and crack mouth opening displacement (CMOD) as a function of crack length for the edge cracked specimen. Expressions were developed for K_I and CMOD. Additional finite element analysis was also conducted to generate K_I and CMOD corresponding to constant and non-uniform stress distributions on the crack surface. These results were used

to develop and verify a weight function for the TSE(B) geometry. This weight function was used to analyze the crack growth behavior of Ti-6Al-4V subjected to the LSP process as discussed in the next section.

6.4.2 Prediction Of Crack Growth In A Laser Shock Peened Zone [C13]

This paper describes an analytical investigation of the effect of the laser shock peening (LSP) process on crack growth behavior of Ti-6Al-4V. A notched three-point bend specimen with varying thickness was used to simulate the leading edge of a fan blade. Data from constant amplitude crack growth tests and the weight function method were used to deduce the residual stress distribution generated due to the LSP process.

SECTION 7

DEVELOPMENT OF EXPERIMENTAL PROCEDURES, METHODOLOGIES AND LABORATORY ENHANCEMENTS

A number of tasks have been completed or are currently underway to address the experimental needs of the laboratory. These tasks span a wide range of subjects and incorporate expert input from staff members in a number of disciplines. The following subsections detail the tasks associated with improving the experimental capability of the laboratory.

7.1 INFRARED CRACK DETECTION SYSTEM

A prototype for an infrared crack detection system has been designed and software layouts have been completed. The system will allow the operator to compare instantaneous thermal images of the specimen from various points in the loading cycle. These comparisons can be made in real-time to quickly show any local areas experiencing cyclic temperature changes. Thus, adiabatic changes in local temperature caused by thermo-elastic or thermo-plastic behavior can be observed. In particular, a surface connected crack will produce a local disturbance in the elastic stress field and a region of intense plasticity. Although the temperature changes associated with these local disturbances are small, the system uses a high-resolution, high-sensitivity infrared camera capable of detecting changes as small as 0.04C without software enhancement and as small as 0.001C with enhancement.

Features such as multiple cycle image averaging, digital image sharpening, and nearest-neighbor aberration reduction have been designed into the system. We expect to be checking out system components in the fourth quarter of 1997 and have the complete prototype on-line the second quarter of 1998.

7.2 CHARACTERIZATION OF THE STABILITY OF ULTRASONIC COUPLANTS AS A FUNCTION OF RELATIVE HUMIDITY

One of the experimental techniques used for *in situ* detection of damage during mechanical tests was surface wave ultrasonics. Using this method, ultrasonic surface waves were coupled to test specimens using acrylic wedges and coupling fluids or gels ("couplants"). During the past year several fatigue tests using *in situ* ultrasonics produced data that indicated the couplants were affecting the surface wave data during tests that lasted more than a few hours. Tests were conducted to examine the stability of several ultrasonic couplants over

periods of several days. Descriptions and selected properties for each of the four couplants tested are listed in Table 7.2-1.

Table 7.2-1

Properties of Couplants

Name	Supplier	Physical Description	Working Temperature Range	Solubility in Water
Ultragel II®	Echo Ultrasound	light blue gel, bland odor	Room Temperature	Complete
Sono 600	Sonotech	pale yellow, oily fluid or gel, odorless	10 to 260 EC	Insoluble
Sono 950	Sonotech	light brown paste, odorless	315 to 385EC	Insoluble
Thermasonic 7	Sonotech	clear golden gel, bland odor	-18 to 162EC	40%

The couplant stability tests were conducted using equipment and fixtures identical to those used during actual mechanical tests. A metal matrix composite specimen was placed in hydraulic friction grips. A pitch-catch ultrasonic propagation mode was set up using two 5 MHz transducers screwed into acrylic, mode conversion wedges and the wedges were attached to the specimen using spring-loaded clamps. The received signal from the Panametrics PR5052 pulser/receiver was sent to a Signatec Dasp500 analog-to-digital converter for digitizing at 500 MHz with 8-bit resolution. The maximum peak-to-peak amplitude of the pitch-catch signal was recorded at various time intervals for test durations as long as eight days.

The peak-to-peak amplitudes of the surface waves coupled through the various couplants are plotted in Figures 7.2-1a and 7.2-1b. Figure 7.2-1a contains data acquired during winter months in which the laboratory relative humidity varied from 14% to 40%. Figure 7.2-1b shows data from similar tests conducted during summer months in which the laboratory relative humidity varied from 42% to 54%. All data are normalized to the peak-to-peak amplitude of the surface wave signal at the beginning of the test.

The test data acquired using one of the couplants, Ultragel II®, showed significant degradation over time periods as short as one day. The degradation was thought to be due to the couplant's high solubility in water. (Separate studies of the couplants to monitor mass loss due to evaporation showed that Ultragel II® lost over 50% of its mass in one week.) The other

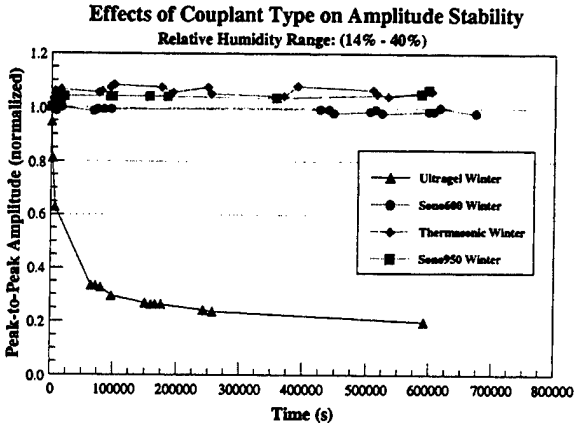


Figure 7.2-1a

Ultrasonic surface wave amplitudes using different couplants (low lab humidity).

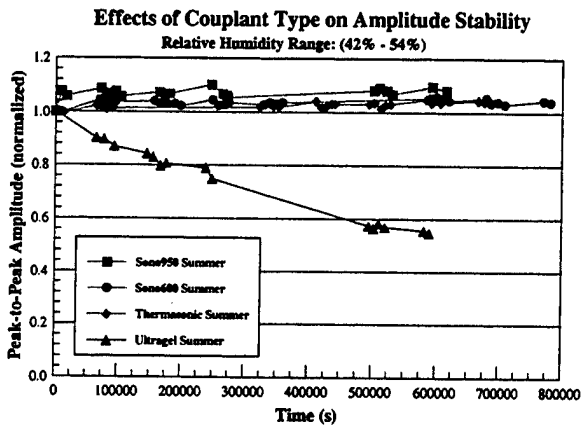


Figure 7.2-1b

Ultrasonic surface wave amplitudes using different couplants (high lab humidity).

three couplants did not seem to degrade the surface wave signals. Except for the Sono 600 data acquired during the winter months (Figure 7.2-1a), the peak-to-peak amplitudes of the surface waves coupled using the Sono 600, Sono 950, and Thermasonic® couplants increased slightly during the first 25,000 seconds. The increases were between 2% and 8%.

The conclusion obtained from the couplant tests was that it is necessary to verify the stability of an ultrasonic couplant, over an appropriate time period, prior to use. Specifically, Ultragel II®, a couplant that is very soluble in water, should not be used except for very short (less than one hour) tests. The other three couplants appear to cause a 2% to 8% increase in the surface wave amplitude during the first few hours of testing, however, the amplitudes remain very constant after the first day.

7.3 CAPABILITY OF EDDY CURRENT NONDESTRUCTIVE EVALUATION FOR DETECTING CRACKS IN MMC SPECIMENS

One approach UDRI has pursued for acquiring information about damage initiation and propagation in advanced composites during mechanical testing has been to apply various sensing methods traditionally not used in the mechanical testing laboratory. Specifically, several NDE methods have been investigated including ultrasonic surface waves, fluid penetrants, X-ray radiography, and eddy current imaging, that can detect small cracks in the matrix layers of metal matrix composites (MMCs). Of primary interest are methods that are adaptable for *in situ* use in the mechanical test systems. *In situ* techniques are desirable to avoid the delays of removing, scanning and reloading the specimen and prevent alignment errors introduced by regripping the specimen.

For the present study an NDE technique was needed to detect initiation and propagation of surface cracks in MMCs during 180° out-of-phase thermomechanical fatigue (TMF) testing. The technique had to have sufficient sensitivity and resolution to detect cracks less than 500 microns in length and be suitable for eventual *in situ* use. Although very few publications describing its application to MMCs were available, eddy current imaging was selected as the most promising NDE technique to evaluate. The evaluation was conducted using an eddy current imaging system to detect surface-initiated matrix cracks created in MMC specimens during thermomechanical fatigue testing. While the goal was to evaluate techniques for eventual *in situ* use, all of the eddy current imaging for this project was done with the specimen removed from the fatigue test system to simplify the evaluation of the technique.

The MMC composite specimens were cut from a six-ply, unidirectional BP Sigma-1240 SiC/Titanium-6Al-2Sn-4Zr-2Mo panel with a fiber volume percentage of 24.5 ± 0.2%, manufactured by Howmet. The dogbone-shaped specimens, cut with an abrasive water jet, maintained a longitudinal fiber orientation, which also became the loading direction for all of the mechanical testing

The eddy current imaging system consisted of a UniWest 450 eddy current instrument, a five axis scanning system, and differential eddy current probes. The eddy current probes contained a 0.06" diameter transmit coil surrounding two D-shaped receiver coils. The receiver coils were wound in opposition to cancel out the effects of probe lift-off from the specimen. The coils were held in a polymer shoe that was attached to the probe body by a copper leaf spring. The spring coupling kept the shoe in contact with the specimen compensating for slight variations in the specimen as the probe was raster scanned across the gage section of the specimen. This probe design was created for the U.S. Air Force's automated engine component inspection systems and has proved to be very effective for minimizing lift-off signals and maximizing small crack detection.

Prior to evaluating the MMC specimens the eddy current instrument and scanning system were set up to provide a sensitivity sufficient to detect a 0.2 x 0.1 mm rectangular EDM notch in a Waspaloy calibration block.

Data were taken at 0.25 mm intervals in the scanning (specimen length) direction and 0.05 mm intervals in the index (specimen width) direction. The rectangular scanning area covered most of the specimen gage with only a slight loss of detail near the edges of the specimen in the widest region of the dogbone shape. The scanning area extended from one corner of the gage section of the specimen to the opposite corner, but the width was limited by the narrowest portion of the specimen.

The magnitude of the differential impedance of the probe's receiver coils was recorded and displayed as an 8-bit color pixel on the system display as the probe was raster-scanned over the specimen's gage section. The resulting image was similar to the standard ultrasonic C-scan, with the difference being that each pixel represented electrical impedance values rather than ultrasonic echo amplitude values. The images can be interpreted as follows. A large change in the impedance of the receive coils is recorded as either a black or a white color, the extreme of the color spectrum for these images. Black and white indications generally appear next to each other in the images. This is because the eddy current probe is a differential probe with the two receive coils wound in opposition. Thus, in the presence of a large defect, one receive coil produced a signal of maximum response while the other produced a signal with nearly equal but opposite sign. The spatial offset between the two signals on the resulting image approximately corresponds to the distance between the coils.

Figure 7.3-1 shows an eddy current image of the gage section of specimen 94-017 after 10,000 out-of-phase TMF cycles. The parameters for this test were σ_{max} = 540 MPa, r = 0.1, cyclic frequency = 0.01 Hz, ΔT = 400°C, and T_{max} = 500°C. Many cracks are visible in the eddy current image, appearing as dark/white lines emanating from the specimen edge. At least twelve cracks are indicated in Figure 7.3-1. Three cracks have been labeled for easy identification. Crack "1", the shorter black line of the pair of indications near the "1" in the figure, was measured to be 0.45 mm in length using an optical microscope. The dark lines beside the "2" in Figure 7.3-1 resulted from a long crack extending to almost the center of the specimen. Optical evaluation indicated this crack was actually two cracks propagating out from opposite sides of a thermocouple weld and extending greater than 2 mm from tip to tip. The crack labeled "3" in the figure was optically measured to be 0.60 mm in length.

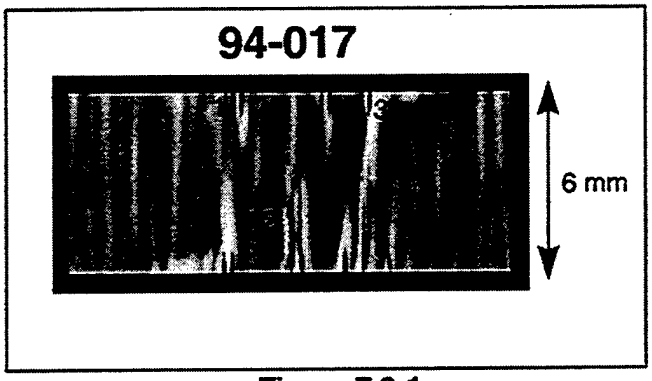


Figure 7.3-1

Eddy current image of a specimen containing many matrix cracks.

Figure 7.3-2 contains eddy current images acquired at various times during the TMF of specimen 94-021. The fatigue test parameters for specimen 94-021 were σ_{max} = 840 MPa, r =

0.1, frequency = 0.01 Hz, ΔT = 400°C, and T_{max} = 500°C. The data acquisition for all of the images shown in Figure 7.3-2 was performed with the specimen removed from the fatigue test machine. The objective was to show progression of damage caused by TMF testing. Eddy current imaging data collected before fatigue testing, after 2000 cycles, and after failure (2476 cycles) show the initiation and progression of cracks forming at the specimen edges. Figure 7.3-2A shows the eddy current image acquired before any fatigue cycling of the specimen. In Figure 7.3-2B eddy current indications of fatigue cracks forming at the edges of the specimen are clearly seen as white/black pairs of lines pointed towards the center of the specimen. Based on the correlation of crack length from other eddy current images and optical microscopy, the cracks in Figure 7.3-2B were approximately 0.5 to 1.0 mm in length. The specimen failed in the region where the dark and white lines transverse the width of the specimen in Figure 7.3-2C. The eddy current images indicate that the edge cracks in the fracture region grew substantially between 2000 cycles and failure while the other edge cracks experienced very little growth.

Based on the limited data acquired during this project the eddy current imaging technique appears to be valuable for detecting and characterizing matrix cracks in MMC specimens. While the data recorded during this study were not acquired *in situ,* adapting the eddy current imaging method to *in situ* use will be straightforward. UDRI personnel have conducted *in situ* eddy current evaluations to image the growth of cracks in aluminum specimens during fatigue tests in other Air Force sponsored programs and anticipate similar success in developing an *in situ* eddy current system for the MLLN laboratories.

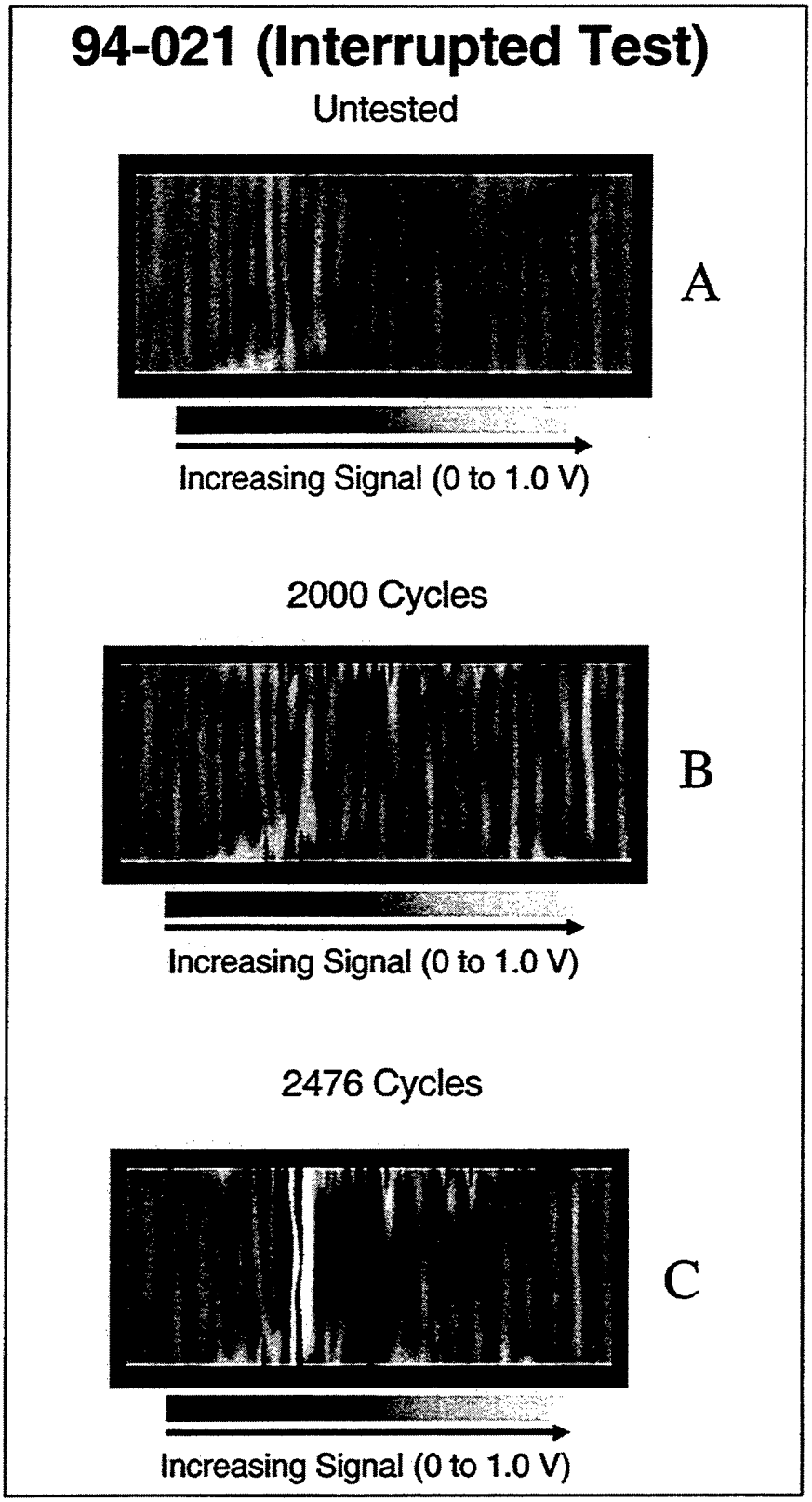


Figure 7.3-2

The eddy current images show the initiation and progression of edge cracks before, during, and after TMF testing.

7.4 MANUAL FOR FIDEP2

FIDEP2 (**FI**NITE-**D**IFFERENCE CODE FOR **E**LASTIC-VISCO-**P**LASTIC ANALYSIS) is a PC-compatible, user-friendly computer code developed in-house at the Materials Directorate, Wright Laboratory, Wright-Patterson AFB, Ohio. The program [Coker et al., 1997] is capable of predicting micromechanical stresses in metal matrix composites under complex thermal and mechanical loading histories. FIDEP2 is a generalized version of FIDEP program [Coker and Ashbaugh, 1992] which was limited by the concentric cylindrical geometry and elastic-plastic constitutive model. The program FIDEP2 incorporates different loading histories, micromechanical models, and constitutive models in a modular form to allow for easy implementation of new requirements.

Operation of FIDEP2 program is straightforward, requiring a loading history file and a material properties data file. Input data are in free format and some descriptive titles are allowed. The referenced source describes the program in more detail and addresses the following:

- The FIDEP2 program operation is described in sufficient detail to allow the reader to begin to use the program.
- Demonstration problems are discussed to provide the user with examples of input and output information.
- Verification problems are presented to evaluate the accuracy of the numerical algorithms.
- A detailed description of FIDEP2 is provided so that an advanced user can make substantial modifications to the material and loading data files.
- The micromechanical models, the available constitutive models, and the numerical integration schemes that are implemented in the FIDEP2 code are summarized.

7.5 EXTENSOMETER USE IN ELEVATED TEMPERATURE TESTING

During the last several years, the following problems with strain measurements were observed during elevated temperature material testing:

1. Extensometers mounted on opposite sides of the same test specimen would often show significant differences (10% or more) in measured strains, even in the elastic region.
2. During low strain rate creep tests (less then 10^{-8} m/m/s), the strain readings displayed a tendency to drift (up to .0003 m/m) during testing.

Investigation of the strain differences between two extensometers on opposite sides revealed some sources of error in strain measurement. These include: 1) use of slotted extensometer rod tips, 2) cracking of quartz rod inside mounting clamps, 3) use of alumina extensometer rods for TMF and CTE tests. Corrections have been made to procedures to eliminate these problems, and other possible sources of error are being examined.

The strain variations observed during low strain rate creep tests appear to be more related to the operational limits of the extensometer strain gages. Under low strain rate conditions these extensometers are extremely sensitive to changes in room temperature and air currents around the extensometer body. Controlling the environment around the extensometer body appears to be the best way to decrease drift at low strain rates with these extensometers.

Alternative methods of measuring strain were also evaluated for use in our testing applications. These included laser extensometers, high temperature strain gages and an LVDT based extensometer. The LVDT based extensometer shows some promise in reducing drift at low strain rates, but will have to be studied further.

7.6 LEFM SOLUTION FOR NEW FCG SPECIMENS

7.6.1 Effect of Height to Width Ratio on K and CMOD Solutions For a Single Edge Cracked Geometry With Clamped Ends [C14]

Series expressions for the stress intensity factor (K) and crack mouth opening displacement (CMOD) were developed for a single edge cracked geometry with clamped ends using finite element analysis. The solutions are valid for crack length to width ratio (a/W) in the range $0 \leq a/W \leq 0.9$ and height to width ratio (H/W) in the range $2 \leq H/W \leq 10$. Experiments conducted using MSE(T) specimens with H/W = 3, 6 and 9 and compact tension specimens verified the applicability of the proposed solutions.

7.6.2 Stress Intensity Factor and Compliance Solutions For an Eccentrically Loaded Single Edge Cracked Geometry [C15]

Eccentrically pin-loaded single edge cracked geometries are an excellent alternative to compact tension type geometries for testing some advanced composite materials. This paper discusses the development of stress intensity factor and compliance solutions for an eccentrically pin-loaded single edge cracked geometry, ESE(T).

7.7 FABRICATION AND OPERATION OF NEW SHAKER BASED HCF TEST SYSTEMS

Design and drawings were completed for two new electromagnetic shaker-based HCF test systems similar to the "C20 System". The drawings were submitted to machine shops and some components have been completed. The shakers ordered for these systems are Unholtz-Dickie model SA15-S202-XB which are efficient, reliable and factory equipped with custom mounts for the pneumatic loading chambers. They are rated for 4100 LB dynamic load (the C20 is 3600 LB). The systems will be capable of HF loads of 15 kN at frequencies up to 400 Hz with de-rated loading at frequencies up to 1 kHz. Static or low frequency loads of 22 kN will be possible. Projected completion date of these systems is September 1997.

7.8 DATA ARCHIVE AND KEYSERVER® STATUS

The Data Archive is a central computer on which all test data generated by AFRL/MLLN Research Group is stored and indexed. Its purpose is to prevent the loss of valuable test data and provide independent user access within AFRL/MLLN Research Group. The framework for the archive was established in 1995. No fundamental changes have been implemented since it was established; however, the hardware has been updated to keep pace with current technology and user demands on the system. A faster computer system was purchased and installed, and a third 4 GB drive was added to provide additional storage space. The Windows NT operating system was maintained to facilitate user access from multiple platforms. During the past year, a large volume of test data has been added to the archive, and administrative support has been maintained.

The archive is organized in the following manner. Test data from the 1990 to 1997 fiscal years and the index, which tracks material pedigree and test conditions, are located on one disk. Test data from 1981 to 1989 are located on a second disk. Users submit data to be archived on a third disk. AFRL/MLLN Research Group users have read access to archived test data and its index.

The archive structure has been expanded to allow the storage of fiber test data, which was generated to evaluate the strength of reinforcing fibers used in metal matrix composites. A separate indexing system was created for the fiber data. Fiber batches were assigned numbers according to fiscal year, and the data for each batch was tracked with test and fiber conditions according to its number. A separate file to be stored with the test data was created for each batch. It tracks the condition of failure for each tested fiber. The index for all fiber tests to date

has been completed and the data has been organized for archival. The archived test data will be stored with the 1981 to 1989 standard test data.

A system, called a Keyserver®, has also been established to provide hands-off control of commercial software licenses. This system controls the number of copies of a software package that can run at a given time by requiring the software to contact the Keyserver® over the network to see if a license is available. All AFRL/MLLN Research Group computers, not used for data acquisition, were installed with the Keyserver® access software. All software packages that could support the Keyserver® received the necessary modifications at that time. Pre-modified software for the Macintosh platform was copied to the third data archive disk, and detailed instructions were generated to step users through the installation process. Periodic reports of Keyserver® software usage were created and used to evaluate the number of copies of various software upgrades to purchase.

8.0 REFERENCES

Adibnarazi, S. and Hoeppner, D. W., "Characteristics of the Fretting Fatigue Damage Threshold," Wear, Vol. 159, 1992, pp. 43-46.

Adibnarazi, S. and Hoeppner, D. W., "A fretting fatigue normal pressure threshold concept", Wear, Vol. 160, 1993, pp. 33-35.

Adibnarazi, S. and Hoeppner, D. W., "The role of normal pressure in modeling fretting fatigue", Fretting Fatigue, ESIS 18 (Edited by R. B. Waterhouse and T. C. Lindley), 1994, Mechanical Engineering Publications, London, pp. 125-133.

Ashbaugh, N.E., John, R., Porter, W.J., and Worth, B.D., "Mechanical Behavior of Advanced Aerospace Materials," WL-TR-96-4087, Annual Report for Period 25 May 1995 - 24 May 1996, June 1996, pp 21-22.

Blanchard, P., et. al., "Material effects in fretting wear - application to iron, titanium, and aluminum alloys", Metallurgical Transaction A, Vol. 22A, July 1991, pp. 1535-1544.

Buchanan, D.J., John, R., and Johnson, D.A., "Determination of Crack Bridging Stresses from Crack Opening Displacement Profiles," accepted for publication in International Journal of Fracture, University of Pittsburgh, Pittsburgh, PA, March 1997.

Chan, K.S., Bodner, S.R., and Lindholm, U.S., "Phenomenological Modeling of Hardening and Thermal Recovery in Metals," ASME Journal of Engineering Materials and Technology, Vol. 110, 1988, pp. 1-8.

Cocker, D. And Ashbaugh, N.E, "Elastic-Plastic Finite Difference Analysis of Unidirectional Composites Subjected to Thermomechanical Cyclic Loading, WL-TR-93-4043, Wright-Patterson AFB, Materials Directorate, Wright Laboratory, 1992.

Coker, D., Frank Boller, Joseph Kroupa, and Noel Ashbaugh, "FIDEP2 User Manual to Micromechaical Models for Thermoviscoplastic Behavior of Metal Matrix Composites", submitted as technical report, WL-TR-98-XXXX, Wright Laboratories, Wright-Patterson Air Force Base, Ohio, 1998.

Del Puglia, A., Pratesi, F., and Zonfrillo, G., "Experimental procedure and parameters involved in fretting fatigue tests", Fretting Fatigue, ESIS 18 (Edited by R. B. Waterhouse and T. C. Lindley), 1994, Mechanical Engineering Publications, London, pp. 219-238.

Endo, K. and Goto, H. "Initiation and propagation of fretting fatigue cracks", Wear, Vol. 38, 1976, pp. 311-324.

Fannes, S., "Inclined cracks in fretting fatigue", Engineering Fracture Mechanics, Vol. 52, No. 1, 1995, pp. 71-82.

Fayeulle, S., Blanchard, P., and Vincent, L., "Fretting behavior of titanium alloys", Tribology Transactions, Vol. 36, No. 2, 1993, pp. 267-275.

Hills, D. A. and Nowell, D., "A Critical analysis of fretting fatigue experiments", Fretting Fatigue, ESIS 18 (Edited by R. B. Waterhouse and T. C. Lindley), 1994, Mechanical Engineering Publications, London, pp. 171-182.

Hills, D. A. Nowell, D., and Sackfield, A., "Surface fatigue considerations in fretting", Interface Dynamics, 1987.

Hoeppner, D. W., "Mechanisms of Fretting fatigue" , Fretting Fatigue, ESIS 18 (Edited by R. B. Waterhouse and T. C. Lindley), 1994, Mechanical Engineering Publications, London, pp. 3-19.

Kitagawa, H., and Takahashi, (1976) Proceedings of the Second International Conference on Mechanical Behavior of Materials, pp. 627-631.

Kuno, M. et. al., "Initiation and growth of fretting fatigue cracks in the partial slip regime", Fatigue Fract. Engng. Mater. Struct., Vol. 12, No. 5, 1989, pp. 387-398.

Larsen, J.M., Worth, B.D., Balsone, S.J., and Rosenberger, A.H., (1996) "Reliability Issues Affecting the Implementation of Gamma Titanium Aluminides in Turbine Engine Applications," in Titanium '95: Science and Technology, P.A. Blenkinsop, W.J. Evans, and H.M. Flower, eds., Institute of Metals, London, pp. 113-120.

Nowell, D. and Hills, D. A., "Crack initiated criteria in fretting fatigue", Wear, Vol. 136, 1990, pp. 329-343.

Papanikos, P., and Meguid, S. A., "Theoretical and experimental studies of fretting-initiated fatigue failure of aerospace compressor discs", Fatigue Fract. Engng. Mater. Struct., Vol. 17, No. 5, 1994, pp. 539-550.

Ruiz, C. and Chen, K. C., "Life Assessment of dovetail joints between blades and disks in aero-engines", International Conference of Fatigue of Engineering Materials and Structures, Vol. 1, pp. 187-194.

Ruiz, C., Boddington, P. H. B., and Chen, K. C., "An investigation of fatigue and fretting in a dovetail joint", Experimental Mechanics, September 1984, pp. 208-217.

Saritas, S., Procter, R., and Grant, W. A., "Effect of ion implantation of fatigue, fretting and fretting corrosion of Ti-6Al-4V", Materials Science and Engineering, Vol. A115, 1989, pp. 307-314.

Soderberg, S., Bryggman, U., and McCullough, T., "Frequency effects in fretting wear", Wear, Vol. 110, 1986, pp. 19-34.

Vincent, L., "Materials and fretting", Fretting Fatigue, ESIS 18 (Edited by R. B. Waterhouse and T. C. Lindley), 1994, Mechanical Engineering Publications, London, pp. 323-337.

Waterhouse, R. B., "Fretting wear", ASM Handbook, Vol. 18, 1992, pp. 242-256.

Waterhouse, R. B., "Fretting wear", Wear, Vol. 100, 1984, pp. 107-118.

Waterhouse, R. B., Dutta, M. K., and Swallow, P. J., "Fretting Fatigue in Corrosive Environments", Mechanical Behavior of Materials, Proceedings of the International Conference on Mechanical Behavior of Materials, 1971, pp. 292-298.

COMPENDIUM OF MANUSCRIPTS

LIST OF MANUSCRIPTS

C1 Threshold Crack Growth Behavior of the Gamma Titanium Aluminide Alloy Ti-46.5Al-3Nb-2Cr-0.2W Under High Cycle Fatigue Conditions, B.D. Worth, J.M. Larsen, and A.H. Rosenberger 55

C2 Effects of Microstructure, Temperature and Environmental on Fatigue Crack Growth in Ti-46.5Al-3Nb-2Cr-0.2W γ Titanium Aluminide, A.H. Rosenberger, B.D. Worth, and J.M. Larsen 67

C3 Multilayer Coating for the Oxidation Protection of Orthorhombic Titanium Aluminides During Fatigue, A.H. Rosenberger, S. Sankaran, P.R. Smith, D. Glass, and D. Rice..... 81

C4 Influence of Temperature and Stress Ratio on the Low-Cycle Fatigue Behavior of Trimarc-1™/Ti-6Al-2Sn-4Zr-2Mo, D.J. Buchanan, R. John, and K.E. Goecke 91

C5 Micromechanics Analysis and Life Prediction of Titanium Matrix Composites, T. Nicholas, and J.L. Kroupa..... 113

C6 Determination of Crack Bridging Stresses from Crack Opening Displacement Profiles, D.J. Buchanan, R. John, and D.A. Johnson 127

C7 Effect of Stress and Geometry on Fatigue Crack Growth Perpendicular to Fibers in Ti-6Al-4V Reinforced with Unidirectional SiC Fibers, R. John, J.R. Jira, and J.M. Larsen 149

C8 Modeling the Deformation and Failure of a Unidirectional Metal Matrix Composite Under Sustained Load, J. Metzcar..... 175

C9 The Effect of Heat Treatment on the Tensile and Creep Behavior of 'Neat' Matrix Ti-22Al-23Nb, P.R. Smith and W.J. Porter 219

C10 Heat Treatment Effects on SiC Fiber, P.R. Smith, M.L. Gambone, D.S., Williams, and D.I. Garner 231

C11 Stresses Due to Temperature Gradients in CMC Aerospace Components, R. John, L.P. Zawada, and J.L. Kroupa..... 257

C12 The Effect of Stress Ratio on Fatigue Crack Growth Rate in the Absense of Closure, R. Sunder, W.J. Porter, and N.E. Ashbaugh 283

C13 Prediction of Crack Growth in a Laser Shock Peened Zone, C. Lykins and R. John 299

C14 Effect of Height to Width Ratio on K and CMOD Solutions for a Single Edge Cracked Geometry with Clamped Ends, R. John and B. Rigling 305

C15 Stress Intensity Factor and Compliance Solutions for an Eccentrically Loaded Single Edge Cracked Geometry, R. John 321

Reference: B.D. Worth, J.M. Larsen, and A.H. Rosenberger, "Threshold Fatigue Crack Growth Behavior of the Gamma Titanium Aluminide Alloy Ti-46.5Al-3Nb-2Cr-0.2W Under High Cycle Fatigue Conditions," in Structural Intermetallics, eds. M.V. Nathal, et al., pp. 563-569, TMS Warrendale, PA (1997).

THRESHOLD CRACK GROWTH BEHAVIOR OF THE GAMMA TITANIUM ALUMINIDE ALLOY Ti-46.5Al-3Nb-2Cr-0.2W UNDER HIGH CYCLE FATIGUE CONDITIONS

Brian D. Worth*, James M. Larsen, and Andrew H. Rosenberger
Air Force Research Laboratory – Materials Directorate
Wright-Patterson Air Force Base, Ohio 45433, USA

* The University of Dayton Research Institute
Dayton, Ohio 45419, USA

Abstract

To date, there is a limited understanding of the mechanics of cyclic damage in gamma TiAl intermetallic alloys. The available studies indicate that the fatigue strength for this class of alloys typically exceeds 80 percent of the material's monotonic yield strength. Such data suggest the possibility of using a safe-life fatigue design at relatively high stresses. However, a safe-life design scheme does not account for the possible existence of intrinsic material defects or service-induced damage, both of which must be addressed in order to ensure reliability in fracture-critical applications. Previous results have shown that the long-crack growth rates in materials of both fully lamellar and duplex microstructures are highly sensitive to the level of applied loading. As a result, it appears likely that a fracture-mechanics-based approach to life prediction must assure that conditions for crack growth remain below the threshold stress intensity factor range, ΔK_{th}. The current study examined the smooth and notched high cycle fatigue behavior of representative TiAl-based alloys to develop a better understanding of the events that lead to fatigue crack initiation and growth. The results of the study were used to identify the key parameters that should be addressed in order to develop reliable life prediction models of this class of alloys in fracture critical applications in turbine engines.

Introduction

In the continuing effort to develop improved aerospace materials for turbine engine applications, considerable attention is being given to intermetallic alloys based on the ordered TiAl phase. These alloys, known as gamma titanium aluminides, have attractive mechanical properties that include high specific strength, specific modulus, and specific creep resistance, combined with good oxidation/hot-corrosion resistance [1-3]. Current gamma TiAl alloys appear to possess useful mechanical properties up to a temperature of approximately 760°C, which significantly exceeds the capability of conventional titanium-base materials and offers the potential to replace nickel-base superalloys used in some turbine engine applications with a material of one-half the density. However, the attractive high temperature properties of gamma alloys are accompanied by relatively low levels of room temperature ductility, fracture toughness, fatigue crack growth resistance, and impact resistance.

The effective use of gamma TiAl alloys in the more aggressive turbine engine applications will require new approaches to structural design. Although gamma alloys exhibit smooth-bar fatigue limits approaching their monotonic yield strength, the tolerance of these materials to defects and service-induced damage is a key concern for fracture-critical components. In turbine engines, damage may result from high-velocity impacts by foreign objects in the gas flow path and from fretting fatigue in airfoil attachment regions. In addition, many turbine engine components experience combinations of low- and high-cycle fatigue, which may cause the initiation and growth of cracks in otherwise undamaged material.

Table I. Mechanical Properties of Alloy K5 (Ti-46.5Al-3Nb-2Cr-0.2W)

Microstructure	Processing	Y.S. (MPa)	U.T.S. (MPa)	Elongation (%)	Fracture Toughness (MPa•m)	Fatigue Strength ($\bullet\sigma$; R = 0.1, 10^7
Duplex	Forged + 1270°C/2 h/ FC to 900 °C + 900°C / 8 h/ AC	460	550	1.7	K_{ic} = 11	405
Refined Fully Lamellar (RFL)	Forged + 1260C/10 min/ to 1355 °C/ 4 min / to 1100 °C/ AC	479	547	1.0	——	392
Lamellar	Forged + 1340°C/0.6 h/ FC to 900 °C	375	450	0.9	K_{ic} = 16.5	331

FC: Furnace Cooled; AC: Air cooled

To predict the useful lifetime of gamma alloys used in many turbine engine applications requires consideration of damage tolerance. Fracture critical components in Air Force turbine engines are designed and life-managed under the Engine Structural Integrity Program (ENSIP) [4] which specifically requires a damage tolerance approach wherein intrinsic or service-induced defects are assumed to exist. Moreover, the problem of high cycle fatigue (HCF) of turbine engine airfoils has recently gained considerable attention [5-7], and efforts are underway to extend the ENSIP requirement to address HCF.

It is clear that gamma alloys will need to satisfy any new high cycle fatigue requirements if these alloys are to replace the existing materials in engines. However, fatigue crack growth rate curves for gamma TiAl alloys exhibit a narrow interval between the threshold stress intensity factor range, ΔK_{th}, and the apparent fracture toughness, K_Q [8-13], suggesting that the fraction of the total fatigue life associated with crack propagation is small. As a result, damage tolerant design of these materials is expected to require the use of ΔK_{th} as a life-management criterion. This paper examines the damage tolerance fatigue capability of a representative gamma titanium aluminide alloy in three microstructural conditions. The role of the fatigue-crack-growth-rate threshold is examined for material usage conditions that are likely to be life-limiting for turbine engine components.

Material

The experimental results to be presented are from an alloy developed by Kim [3], Ti-46.5Al-3Nb-2Cr-0.2W, designated K5. This material was forged and heat treated to produce three microstructures: duplex, refined fully lamellar (RFL), and fully lamellar. The heat treatment conditions for the three microstructures are given in Table I, along with a summary of mechanical properties. Optical micrographs of the three microstructures are presented in Fig. 1. The duplex microstructure was composed of a mixture of equiaxed gamma ($L1_0$ structure) grains and fine colonies of lamellar gamma plus alpha-2 phase (DO_{19} structure). The refined and coarse lamellar microstructures were composed of lamellar colonies of approximate diameters of 280 and 700 μm, respectively. The average lamellae thickness in the RFL microstructure was also less than that of the coarse lamellar material. As indicated in Table I, the coarse lamellar microstructure had a lower strength than either the RFL microstructure or duplex microstructure. Although the duplex microstructure exhibited a higher ductility than its lamellar counterparts, the duplex material also had a lower initiation fracture toughness than either of the lamellar microstructures.

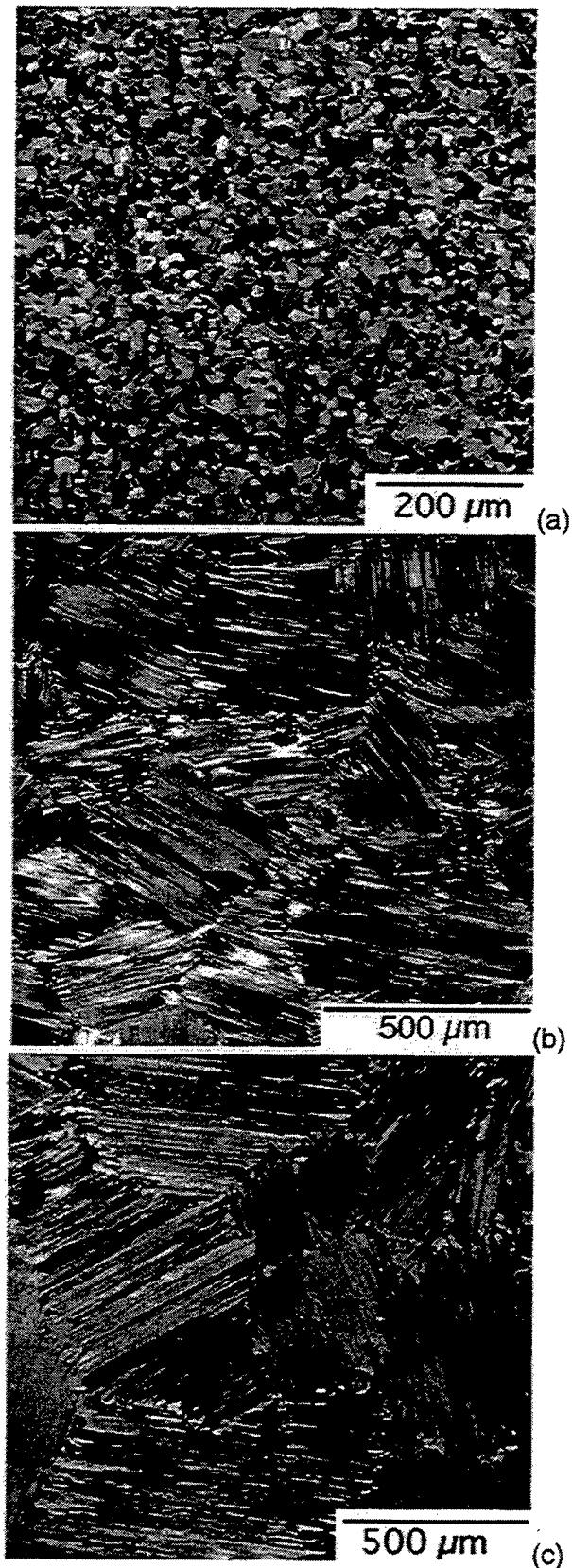


Fig. 1 – Microstructures of the alloy Ti-46.5Al-3Nb-2Cr-0.2W:
(a) duplex, (b) refined fully lamellar, and (c) coarse fully lamellar.

Experimental Procedure

Fatigue and fatigue crack growth experiments were performed at room temperature on specimens of the three microstructures. The fatigue specimens were smooth bars, nominally 9.5 mm in diameter, having diametrically opposed flat sides that reduced the gage section to 25 mm^2 producing a 25 mm long uniform gage that was subsequently electropolished to remove surface residual stresses. The fatigue tests were performed in air at 40 Hz under a stress ratio ($R = s_{min}/s_{max}$) of 0.1. In addition, to characterize sensitivity of the materials to small surface defects, fatigue tests were performed on smooth-bar specimens that had been fabricated with a series of equally spaced, semicircular, electro-discharge-machined surface notches. The details of this test method will be discussed later.

Fatigue crack growth experiments were performed on the three microstructures using standard procedures and compact type, C(T), specimens of width 20 mm and thickness 5 mm. These tests were conducted at 20 Hz, in laboratory air at room temperature, under a stress ratio of 0.1. The crack growth data were acquired under decreasing stress-intensity-factor range, ΔK, fatigue followed by constant-load-amplitude fatigue. For all of the data to be presented, crack arrest occurred at the minimum crack growth rate, *da/dN*, shown. Crack-opening-compliance measurements obtained using a crack-mouth extensometer provided measurements of crack length, and these data were analyzed to determine levels of crack closure, K_{cl}, which were used to calculate the effective stress intensity factor range $\Delta K_{eff} = K_{max} - K_{cl}$.

Results

Fatigue Crack Growth

Fatigue crack growth rate data for the three microstructures are plotted versus ΔK in Fig. 2. The fine duplex microstructure offered the least resistance to fatigue crack growth. The slope of the $da/dN\Delta K$ data for this microstructure was extremely steep, and this material had lowest value of threshold stress-intensity-factor range, ΔK_{th}, and the lowest apparent toughness, K_Q, of the three materials. In comparison to the duplex material, the two lamellar microstructures exhibited much greater crack growth resistance. Although the average colony sizes of the two lamellar microstructures differed by a factor of 2.5, their crack growth rate behavior was equivalent in all but the near-threshold region. The crack growth rate data from each of the materials were regressed with an equation of the form

$$\log(da/dN) = C_1\{\text{arctanh}(C_2[\log(\Delta K)+C_3])\}+C_4 \quad (1)$$

which provided a good representation of the behavior over the full range of the data.

As noted earlier, the damage tolerance approach to life management requires that fracture critical components be assumed to contain initial defects or damage. Generally, the scale of the assumed damage is defined by the detection limit of some nondestructive inspection method. In this case the detection limit is the *maximum* crack size, a_i, that can be *missed* by the inspection, and this size is dependent on a variety of factors. Damage tolerance life predictions are performed by calculating the number of cycles required to propagate a crack of initial size a_i to failure. This crack propagation lifetime is given by

$$N_p = \int_{a_i}^{a_c} \frac{da}{f(\Delta K)} \quad (2)$$

where a_C is the critical crack length corresponding to the material's effective fracture toughness in fatigue (K_Q), $f(\Delta K)$ is a crack-growth-rate function such as Eq. 1, and ΔK is defined for a specific crack geometry and loading history. In the example to follow, the crack was assumed to be a semicircular surface flaw of depth *a*, which is a crack geometry commonly observed in actual components.

To illustrate the effect of the assumed initial crack size on the calculated crack propagation lifetime, Eq. 2 was solved numerically to construct the remaining-life plot shown in Fig. 3. For a given initial crack size, a_i, the integrated remaining fatigue crack propagation life, N_p, is simply given by the ordinate of the plot. The lamellar microstructures clearly exhibit much more attractive damage tolerance than does the duplex material. For turbine engine components that are life-limited by low cycle fatigue, the maximum number of fatigue cycles is typically less than 10,000. Thus, for either of the lamellar materials, a cracked component could spend the majority of its fatigue life propagating a crack of initial depth equal to a millimeter, which is a crack size that is readily detectable by advanced methods of nondestructive evaluation. In the case of the duplex material, however, catastrophic failure would occur at a crack depth less than approximately 0.4 mm, making reliable, early crack detection extremely difficult or impossible.

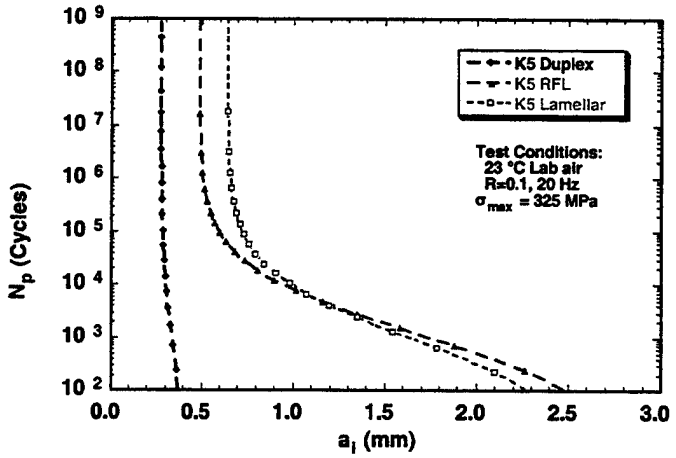


Fig. 3 – Remaining crack propagation lifetime, N_p, plotted versus initial crack size, a_i, for fatigue under conditions of $R = 0.1$ and $s_{max} = 325$ MPa.

As shown in the figure, each of the materials exhibits a critical crack depth, corresponding to ΔK_{th}, below which the remaining crack propagation lifetime is effectively infinite. For the duplex, RFL, and lamellar materials, this crack size was 0.27, 0.49, and 0.64 mm, respectively. The general trends of the curves indicate that ΔK_{th} is the dominate

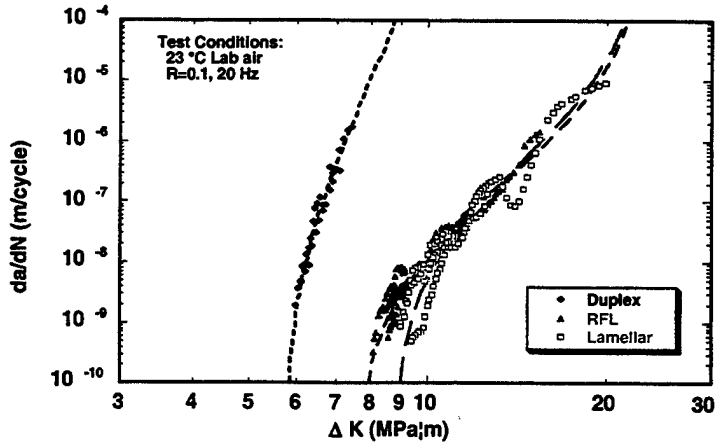


Fig. 2 – Fatigue crack growth behavior from tests of C(T) specimens in air at room temperature; R = 0.1.

consideration for lifetimes exceeding approximately 10^5 cycles. Components that are subjected to high cycle fatigue may be expected to experience fatigue loadings greatly in excess of 10^5 cycles, highlighting the critical nature of the fatigue crack growth threshold, ΔK_{th}, for life prediction under high cycle fatigue conditions.

Although it may be attractive to use the large-crack ΔK_{th} as a life-management criterion, it is well known that data of large fatigue cracks may not accurately represent the behavior of small fatigue cracks in that occur actual structures [15,16]. One view of this issue follows from the original work of Kitagawa and Takahashi [17] who showed that threshold crack growth rate data display a dependence on crack size that is related to the material's fatigue strength, ΔS_e, and ΔK_{th}. As shown schematically in Fig. 4, a plot can be constructed that combines fatigue crack initiation and propagation concepts. Considering crack initiation, and disregarding the possibility of a preexisting crack, specimen failure should occur only if the applied stress range exceeds ΔS_e, which is represented by the horizontal line in the figure. Alternatively, considering a fracture mechanics approach, crack growth should occur only if the applied ΔK exceeded ΔK_{th}, which is represented by the solid line of slope –1/2 on the figure. Thus, the utility of ΔK_{th} as a "material property" appears to be limited to cracks of approximate length greater than that given by the intersection of the two lines (a_0). For many materials, a_0 appears to provide a rough approximation of the crack size below which small-crack effects become potentially significant. If, as has been frequently suggested, a small crack has not yet developed the full level of crack closure that exists for large fatigue cracks, then the limiting small-crack threshold condition may be more accurately represented by a closure-free condition, defined as $\Delta K_{eff,th} = \Delta K_{max,th} - \Delta K_{op,th}$, corresponding to the threshold crack growth rate. In this situation, the solid line of slope –1/2 in the figure would be displaced to the left in Fig. 4 (assuming $\Delta K_{eff,th} < \Delta K_{th}$).

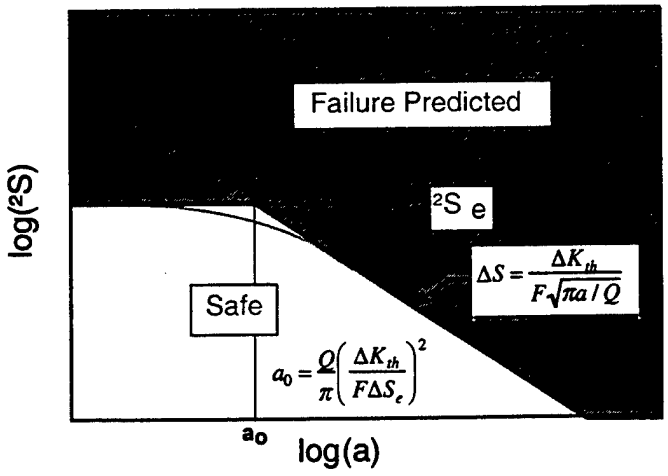


Fig. 4 – Schematic "Kitagawa plot" of threshold fatigue conditions in terms of crack size and stress range.

Notch Fatigue Behavior

To examine the feasibility of using a threshold crack growth approach to deal with occasional sources of damage, such as foreign object impacts, the influence of damage size on residual fatigue strength was examined. Previous research [18] had indicated that, in the coarse lamellar microstructure, the effective initial crack size was determined by the colony size. Thus, the superior crack growth resistance of the lamellar, versus the duplex, microstructure can be

misleading. The large initiation crack size in the coarse lamellar microstructure far outweighed the beneficial effects of the superior crack growth resistance and higher ΔK_{th} of this material. For this reason, it was of interest to gain an understanding of the influence of notch size on residual fatigue strength in a lamellar microstructure with a refined colony size, which also has more attractive monotonic properties than a coarse lamellar microstructure. Thus, the refined fully lamellar material was selected for study.

In previous testing of materials with lamellar microstructures, it was found that when a single notch was machined into a specimen, fatigue failure to often occurred at a location away from the notch, which appeared to result from the coarse, anisotropic nature of the microstructure. To increase the chances of finding the 'weak link' of the structure, twelve equivalent notches were machined into each sample. The test method involved using electro-discharge machining (EDM) to produce twelve, well-separated semicircular notches of equal size on the surface of electropolished fatigue samples. Specimens were produced with three notch sizes, ranging in depth from 80 μm to 400 μm. The height of the notches was approximately 75 μm. As noted earlier, the average colony size of the materials with the refined lamellar microstructure was 280 μm, which meant that the notch depth ranged from 30 to 150 percent of the colony size. These specimens were then tested under constant-load-amplitude fatigue to determine the threshold stress range required to produce failure. Using this test method, failure always originated at a notch. A typical failure site is pictured in Fig. 5, which shows a site of interlamellar fracture at the depth of the EDM notch.

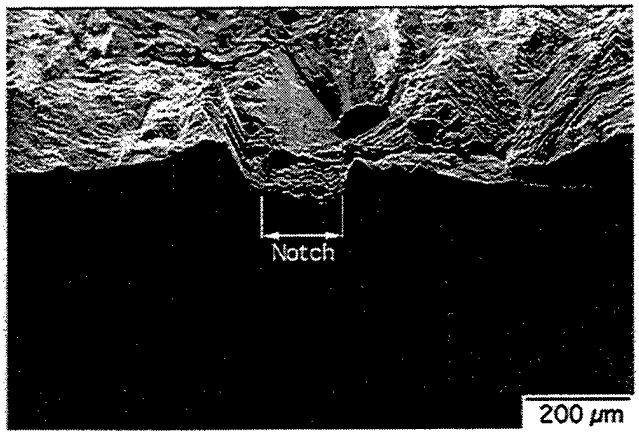


Fig. 5 – Fracture surface of a refined lamellar specimen showing the origin of the failure at a 80 μm deep semicircular notch.

The 10^7-cycle fatigue strengths for the three notch depths are listed in Table II. As shown in Fig. 6, when these results are plotted on a Kitagawa diagram, it is seen that the residual fatigue strength was below that predicted based on the large-crack ΔK_{th} for all notch sizes, and this disparity increased as the notch size is decreased. The data for the notched-threshold conditions fall near the line corresponding to $\Delta K_{eff,th}$, but this large-crack parameter still overestimates the data from the 80 μm deep notch. It should be noted that the latter notch size is well below the average colony diameter (see Fig. 5) and that this threshold condition was probably controlled by the microstructural dimension rather than by the notch size, as was shown previously for the coarse lamellar material [13]. In a similar lamellar alloy, Campbell, et al [19] noted that the rapid growth of small fatigue cracks persisted up to a crack size approximately equal to the colony size. The trend in the notched-threshold data is also consistent with the smooth transition in threshold behavior depicted in Fig. 4 as the behavior becomes dominated by the fatigue-limit stress range, ΔS_e.

Table II. Notch Fatigue Results (R = 0.1)

Notch Depth (a; μm)	Stress Range, Δs (MPa)	s_{max}/s_{YS} (MPa)
Smooth Bar	392	0.91
80	340	0.79
200	270	0.63
400	225	0.52

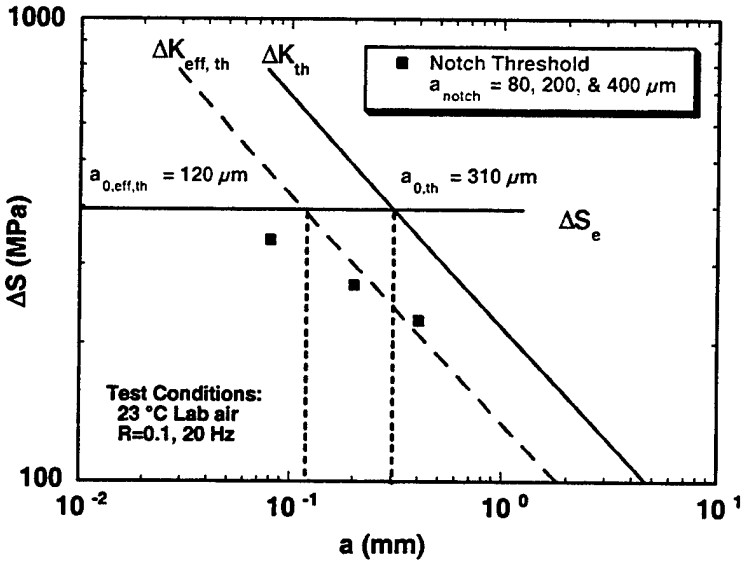


Fig. 6 – Plot of threshold fatigue conditions in terms of crack size and stress range for the RFL microstructure showing the threshold conditions for crack propagation from small semicircular notches.

An additional advantage of the multiple notch sample was that an indication of the fatigue crack propagation mechanisms could be obtained by using periodic optical microscopy to examine the crack growth that occurred at unfailed notches. In several instances non-catastrophic cracks were observed from notches other than the notch from which failure occurred. As shown in Fig. 7 crack growth tended to occur preferentially along interfaces in the lamellar microstructure. It was also observed that crack growth was intermittent. Testing conducted at 400 MPa on samples with 80 μm notches showed that cracks initiated from two notches after 25,000 cycles. One of these cracks continued to propagate for the next 50,000 cycles and then arrested at a colony boundary. The second crack arrested at a colony boundary after 30,000 cycles and showed no visible growth for the next 120,000 cycles (150,000 total cycles). Failure subsequently occurred from this crack after a total of 165,000 cycles.

The subcritical crack shown in Fig. 7 gives a good indication of the strong influence that local microstructural orientation had on the growth of small cracks - in this case, small cracks growing from a notch. It appears that a ligament bridge formed between the crack that had grown from the notch and the crack that is growing in an adjacent colony. Ligament bridging may, in fact, be active in small cracks due to the generally lower crack tip opening displacements that would be found at small crack lengths and the stronger influence of the

microstructure. Bridging may have lead to the arrest of the crack in Fig. 7, however, the chronology of the cracking at the notch tip would have to be determined, as would the three dimensional nature of the cracking. A reduction in the crack tip K by as much as 2 MPa÷m during fatigue crack growth in a XD™ gamma alloy was reported by Campbell [20], and this was attributed to ligament bridging. However, other researchers [14], have failed to find any indication of ligament bridging during fatigue crack growth in a coarse lamellar gamma alloy. The disparity in these findings indicates an obvious area for future work.

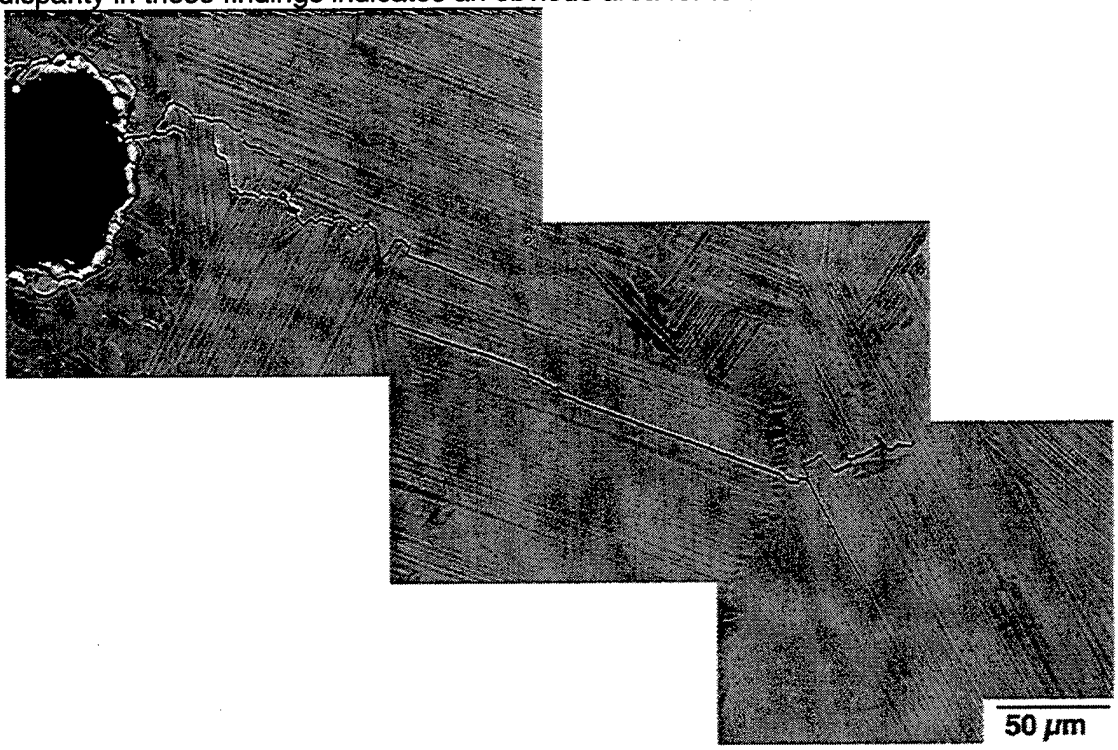


Fig. 7 Typical cracking from the notch tip showing the early states of ligament formation associated with surface cracking.

Discussion

Gamma titanium aluminide alloys have a variety of extremely attractive properties in demanding applications such as in gas turbine engines. The performance and fuel economy of turbine engines can be improved significantly by replacing existing alloys with less-dense, TiAl alloys for a number of components. Static components provide the opportunity to introduce these alloys into service with relatively low risk. However, the greatest payoff will occur when gamma alloys demonstrate capabilities suitable for fracture critical applications. Given their unusual balance of properties, it appears that the widespread use of these low-ductility materials will depend on (*i*) tailoring their properties to meet specific application needs and (*ii*) demonstrating reliability under actual service conditions.

A key aspect of a component's service requirements is defined by its imposed time-temperature-stress spectrum, which may contain significant levels of both low- and high-cycle fatigue. In addition, the material must be able to tolerate the existence of occasional intrinsic material defects and secondary damage from factors such as foreign object impacts and fretting fatigue. To ensure the long term reliability of TiAl alloy components in service, a life-prediction system capable of accurately predicting the effects of complex loading and secondary damage must be available.

Consistent with previous results, the current findings show that lamellar microstructures tend to be much more resistant to crack propagation than is material of a fine duplex

microstructure. While the scale of the coarse lamellar and refined lamellar microstructures that were tested differed by a factor of 2.5, the fatigue crack growth behavior of these two materials was essentially equivalent in all but the near-threshold crack growth regime. Although ΔK_{th} decreased with decreasing colony size, the overall fatigue resistance improved as colony size decreased. This behavior is believed to be associated with the reduced size of the initiated crack, which scaled with the colony size. The effect of this initiated crack size appears to far outweigh the benefits of improved crack growth resistance in the coarse lamellar microstructure. Further refinement in lamellar colony size should have a modest effect on overall crack growth resistance but may impart significant additional improvements in strength and resistance to fatigue crack initiation. Moreover, the evidence thus far suggests that a reduction in colony size would also reduce the minimum crack size for which the large-crack ΔK_{th} may apply.

The data and analyses presented here show that a crack growth approach is useful for life management under low cycle fatigue, but that the typical crack propagation lifetimes are insufficient under the number of cycles expected under high cycle fatigue. Recognizing that crack formation due to a variety of potential mechanisms cannot be avoided, it appears that an effective damage tolerance life prediction system must focus on the conditions necessary for threshold crack growth. This will require understanding the small-crack ΔK_{th} as a function of residual stress, mode of crack formation, mission spectra, crack geometry, temperature, and material and microstructural characteristics.

Conclusions

Based on the results presented on the alloy gamma titanium aluminide alloy Ti-46.5Al-3Nb-2Cr-0.2W, the following conclusions are drawn:

- The coarse and refined lamellar materials, having lamellar colony sizes equal to 700 and 280 μm, respectively, had substantially greater crack growth resistance than did the fine duplex material (grain size approximately 20 μm.
- The crack growth resistance of the two lamellar materials was equivalent in all but the near-threshold region, where ΔK_{th} in the refined lamellar microstructure was slightly below that of the coarse lamellar material.
- Analysis of the crack propagation behavior indicated that a crack growth approach to life prediction is feasible for low cycle fatigue but that the crack propagation lifetimes appear to be insufficient to satisfy high cycle fatigue requirements. As a result, a fracture mechanics life prediction approach will probably require the use some form of threshold condition for the growth of small fatigue cracks.

Acknowledgments

This research was performed in the Materials Directorate, Air Force Research Laboratory, Wright-Patterson Air Force Base, OH and was supported by the Air Force Office of Scientific Research under Task 2302BW. B. D. Worth gratefully acknowledges the support of Air Force contract F33615-94-C-5200. The authors would also like to thank Y.-W. Kim of Universal Energy Systems, Dayton, OH for providing the K5 alloy.

References

1. Y-W. Kim, "Intermetallic Alloys Based on Gamma Titanium Aluminide," JOM, Vol. 41, No. 7, (1989) 24-30.
2. Y-W. Kim and D. M. Dimiduk, "Progress in the Understanding of Gamma Titanium Aluminides," JOM, Vol. 43, No. 8, (1991) 40-47.
3. Y.-W. Kim, "Ordered Intermetallic Alloys, Part III: Gamma Titanium Aluminides," JOM, Vol. 46, No. 7, (1994) 30-40.

4. U.S. Air Force, Engine Structural Integrity Program. Military Standard 1783, Aeronautical Systems Division, Wright-Patterson Air Force Base, OH, (1984).
5. T. Nicholas and J. R. Zuiker, "On the Use of the Goodman Diagram for High Cycle Fatigue Design," Int. J. Fract., 80, (1996) 219-235.
6. B. A. Cowles, "High Cycle Fatigue in Aircraft Gas Turbines - An Industry Perspective," Int. J. Fract., Vol. 80., (1996) 147-163.
7. J. M. Larsen, B. D. Worth, C. G. Annis, Jr., and F. K. Haake, "An Assessment of the Role of Near-Threshold Crack Growth in High-Cycle-Fatigue Life Prediction of Aerospace Titanium Alloys Under Turbine Engine Spectra," Int. J. Fract., Vol. 80, (1996) 237-255.
8. S. J. Balsone, J. W. Jones, D. C. Maxwell, "Fatigue Crack Growth in a Cast Gamma Titanium Aluminide Between 25 and 954°C," in Fatigue and Fracture of Ordered Intermetallic Materials, W. O. Soboyejo and T. S. Srivatsan, eds., TMS, Warrendale, PA. (1994).
9. S. J. Balsone, J. M. Larsen, D. C. Maxwell, and J. W. Jones, "Effect of Microstructure and Temperature on Fatigue Crack Growth in the TiAl Alloy Ti-46.5Al-3Nb-2Cr-0.2W," Mater. Sci. Eng., A192/193, (1995) 457-464.
10. K. T. Venkateswara Rao, Y-W. Kim, and R. O. Ritchie, "High-Temperature Fatigue-Crack Growth Behavior in a Two-Phase ($g + a_2$) TiAl Intermetallic Alloy," Scr. Metall. Mater., Vol. 33, No. 3, (1995) 459-464.
11. J. M. Larsen, B. D. Worth, S. J. Balsone, and J. W. Jones, "An Overview of the Structural Capability of Available Gamma Titanium Aluminide Alloys," in Gamma Titanium Aluminides, Y-W. Kim, R. Wagner, and M. Yamaguchi, eds., TMS/ASM International, Warrendale, PA, (1995) 821-834.
12. P. Bowen, R. A. Chave, and A. W. James, "Cyclic Crack Growth in Titanium Aluminides," Mater. Sci. Eng., A192/193, (1995) 443-456.
13. J. M. Larsen, B. D. Worth, S. J. Balsone, A. H. Rosenberger, and J. W. Jones, "Mechanisms and Mechanics of Fatigue Crack Initiation and Growth in TiAl Intermetallic Alloys," FATIGUE '96, Vol. III, Elsevier Science Ltd., Oxford, U.K., (1996) 1719-1730.
14. B. D. Worth, J. M. Larsen, S. J. Balsone, and J. W. Jones, "Mechanisms of Ambient Temperature Fatigue Crack Growth in Ti-46.5Al-3Nb-2Cr-0.2W", Met. Mat. Trans., Vol. 28A, (1996) 825-835.
15. R. O. Ritchie and J. Lankford, eds., Small Fatigue Cracks, The Minerals, Metals, and Materials Society, Warrendale, PA (1986).
16. K. J. Miller and E. R. de los Rios, Short Fatigue Cracks, Mechanical Engineering Publications Limited, London, UK, (1992).
17. H. Kitagawa and S. Takahashi, "Applicability of Fracture Mechanics to Very Small Cracks or the Cracks in the Early Stage," in Proceedings of the Second International Conference on Mechanical Behavior of Materials, Boston, MA, (1976) 627-631.
18. J. M. Larsen, B. D. Worth, S. J. Balsone, and A. H. Rosenberger, "Reliability Issues Affecting the Implementation of Gamma Titanium Aluminides in Turbine Engine Applications," in Titanium '95, Vol. I, The Institute of Materials, U. K., (1996) 113-120.
19. J. P. Campbell, J. J. Kruzic, S. Lillibridge, K. T. Venkateswara Rao, and R. O. Ritchie, "On the Growth of Small Fatigue Cracks in g-Based Titanium Aluminides," Scr. Matell. Mater., submitted, (1997).
20. J. P Campbell, M. S. Thesis, University of California, Berkeley, CA (1996).

This page intentionally left blank

Reference: A.H. Rosenberger, B.D. Worth, and J.M. Larsen, "Effects of Microstructure, Temperature, and Environmental on Fatigue Crack Growth in Ti-46.5Al-3Nb-2Cr-0.2W • Titanium Aluminide," in Structural Intermetallics, eds. M.V. Nathal, et al., pp. 555-561, TMS Warrendale, PA (1997).

EFFECTS OF MICROSTURCTURE, TEMPERATURE AND ENVIRONMENTAL ON FATIGUE CRACK GROWTH IN Ti-46.5Al-3Nb-2Cr-0.2W γ TITANIUM ALUMINIDE

A.H. Rosenberger[1], B.D. Worth[2], and J.M. Larsen[1]

[1]Air Force Research Laboratory – Materials Directorate
Wright-Patterson Air Force Base, Ohio 45433-7817, USA
[2]The University of Dayton Research Institute
Dayton, Ohio 45419-0128, USA

Abstract

The influence of environment on the fatigue crack growth in a gamma titanium aluminide alloy was examined through a comparison of crack growth behavior in laboratory air and ultra high vacuum (UHV). Specimens of wrought Ti-46.5Al-3Nb-2Cr-0.2W (at %) were tested in duplex, refined lamellar and coarse lamellar microstructures at temperatures ranging from ambient to 800°C. A pronounced environmental effect was observed at all temperatures, with crack growth rates more than an order of magnitude lower in vacuum than in air. The poorest crack growth resistance was observed in air at an intermediate temperature, however in a UHV environment, no anomalous temperature dependence on fatigue crack growth was observed. This temperature effect was shown to be the result of an environmental embrittlement that is mitigated by the increase in ductility at higher temperatures. A careful examination of crack closure levels supported this conclusion. Subtle fractographic differences in crack growth mode were observed in the two environments but were not sufficient to cause the dramatic changes in fatigue crack growth resistance.

Introduction

Gamma titanium aluminide alloys, which are based on the TiAl intermetallic phase, are candidates for use as structural materials in advanced gas turbine engines. Currently, however, there is a limited understanding of the influence of environment on mechanical properties of this class of alloys over the typical range of application temperatures. An effect of environment on the fatigue crack growth behavior of a cast gamma alloy was found by Mabru, et al., [1]. Here, near threshold, crack growth rates were two orders of magnitude slower in a vacuum and merged with the growth behavior in air at higher crack growth rates. Liu and Kim [2] also found an increase in ductility at 25°C in a duplex microstructure in vacuum and oxygen environments. Oh *et al.* [3] demonstrated a large, room temperature environmental effect on the tensile properties in polysynthetically twinned TiAl. Crystals oriented in a 'soft' orientation exhibited more translamellar fracture at low strain rates, but the orientation-dependent differences in fracture mode and ductility diminished at progressively higher strain rates. A decrease in fatigue crack growth rates was found in vacuum at 700°C in an "as cast" TiAl material by James and Bowen [4]. However, these researchers found similar crack growth behavior in air and vacuum in duplex and near-gamma heat treated conditions. Balsone *et al.* [5] reported that the fatigue crack growth behavior of an alloy having a duplex microstructure was relatively insensitive to temperature over the range of 25 to 954°C. The highest crack growth rates, however, were found at the intermediate temperature of 425°C. This was attributed to environmentally-assisted crack growth that occurs at elevated temperatures below the ductile-to-brittle transition temperature. More recent work on a wrought gamma alloy in both fine

duplex and fully lamellar microstructural conditions [6], and a fine lamellar XD alloy [7], have shown that the minimum in fatigue crack growth resistance occurred at a temperature of approximately 600°C. Generally, environmental effects on gamma materials have not been studied over a temperature range large enough to document the level of environmentally-assisted crack growth or to determine the cause of the poor crack growth resistance at intermediate temperatures.

The objective of this study was to perform fatigue crack growth experiments in an ultra high vacuum (UHV) environment and compare these results with those obtained in laboratory air [6] in order to characterize environmentally-assisted crack growth phenomena for temperatures ranging from ambient to 800°C. Levels of crack closure were measured and analyzed to help determine the relative influences of crack shielding and environmental attack on fatigue crack growth behavior as a function of temperature. This analysis was complemented by scanning electron microscopy of the fracture surfaces which was used to characterize the modes of crack advance.

Materials and Experimental Procedure

The gamma titanium aluminide alloy investigated in this study was a wrought material developed by Kim [8] of nominal composition Ti-46.5Al-3Nb-2Cr-0.2W (atomic %). This material, also designated as alloy K5, was tested in the three microstructural conditions: duplex, refined lamellar, and coarse lamellar (Fig. 1). Additional information on the processing, heat treatment, and microstructures of these materials may be found in [9].

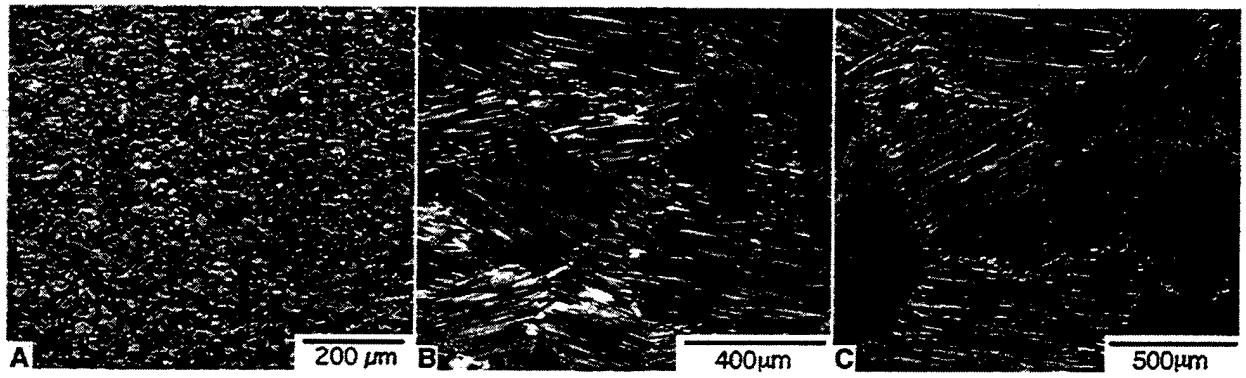


Fig. 1. Microstructures of the gamma titanium aluminides: a) duplex, b) refined lamellar, and c) coarse lamellar Ti-46.5Al-3Nb-2Cr-0.2W.

Fatigue crack growth tests were conducted on the three microstructures at temperatures of RT, 600, and 800°C in laboratory air and UHV. Compact tension specimens, C(T), of width equal to 20 mm and thickness of 5 mm, were tested under load-shedding (decreasing DK) and constant-load-amplitude (increasing DK) fatigue using a computer controlled servohydraulic test machine. A relatively high cyclic frequency of 10 or 20 Hz was used to minimize creep-fatigue interactions and thereby promote an examination of the effects of microstructure, temperature, and environment on the mechanisms of pure fatigue crack growth. A stress ratio ($R = s_{min}/ s_{max}$) of 0.1 was used on all tests. Crack lengths and crack closure loads were determined from measurements of crack mouth opening displacements. The level of crack closure was calculated from the load-displacement data using the slope-intercept method, which produced repeatable results on these low-R tests.

The refined lamellar material was subjected to an additional examination of the effects of temperature on crack growth behavior. Using a constant K_{max} = 10 MPa$\sqrt{m}$ with R = 0.1, the crack growth rate in this material was measured in laboratory air over the temperature range from ambient to 800°C, in temperature increments of 100°C or less. During each increment, the crack was allowed to extend 0.5 mm or more before switching to a higher temperature. This

allowed several increments of crack growth (several temperatures) to be examined on a single specimen. The crack growth threshold was also determined as a function of temperature in the refined lamellar microstructure by generating only the lower portion of the curve in a decreasing-DK test. A number of different, temperature-dependent threshold levels were determined from a single test specimen.

Ultra high vacuum crack growth tests were conducted on a servohydraulic test machine fitted with a vacuum chamber evacuated by a two-stage turbomolecular pumping system. This chamber is capable of maintaining a vacuum of 3×10^{-7} Pa, with predominantly water vapor, nitrogen, and oxygen as the residual gasses, having partial pressures of approximately 9×10^{-8}, 1×10^{-8} and 3×10^{-9} Pa, respectively. Elevated temperature tests were conducted in UHV using a tungsten mesh hot zone which had no appreciable influence on the vacuum level or residual impurities. Fatigue crack growth rate curves were generated in UHV for the coarse lamellar and duplex microstructures only. Closure measurements were obtained using the same technique as used in the laboratory air experiments (quartz rod extensometer on the crack mouth).

Results

Fatigue Crack Growth

The fatigue crack growth behavior of the coarse lamellar and duplex microstructures tested at the temperatures of RT, 600, and 800°C are shown in the form of crack growth rate as a function of applied stress intensity factor range, DK, in Figs. 2-3. In the laboratory air environment, the minimum crack growth rates represent crack arrest, while no cessation of crack growth was found in the UHV environment.

Over the temperature range from RT to 800°C, there was a significant reduction of crack growth rates in the coarse lamellar microstructure material under the UHV conditions, Fig. 2. The crack growth rate behavior in UHV of the lamellar material at room temperature and 600°C was nearly identical, while faster fatigue crack growth rates were evident at 800°C. This behavior in vacuum is consistent with the decrease in strength and elastic modulus that occurs with increasing temperature. Notice that the increased crack growth rate observed in air at 600°C was not present in vacuum, which lends credibility to the argument of an environment-assisted crack growth at elevated temperatures that are still below the ductile to brittle transition temperature [6]. In the UHV environment, over the temperature range RT-600°C, the crack growth thresholds were higher than in air by approximately 5 MPa$\sqrt{m}$, which is significant considering the apparent arrest of crack growth in air. At 800°C, the UHV threshold was lower than in air, due to the lack of crack arrest, but the growth rate at the same value of DK was almost two orders of magnitude slower.

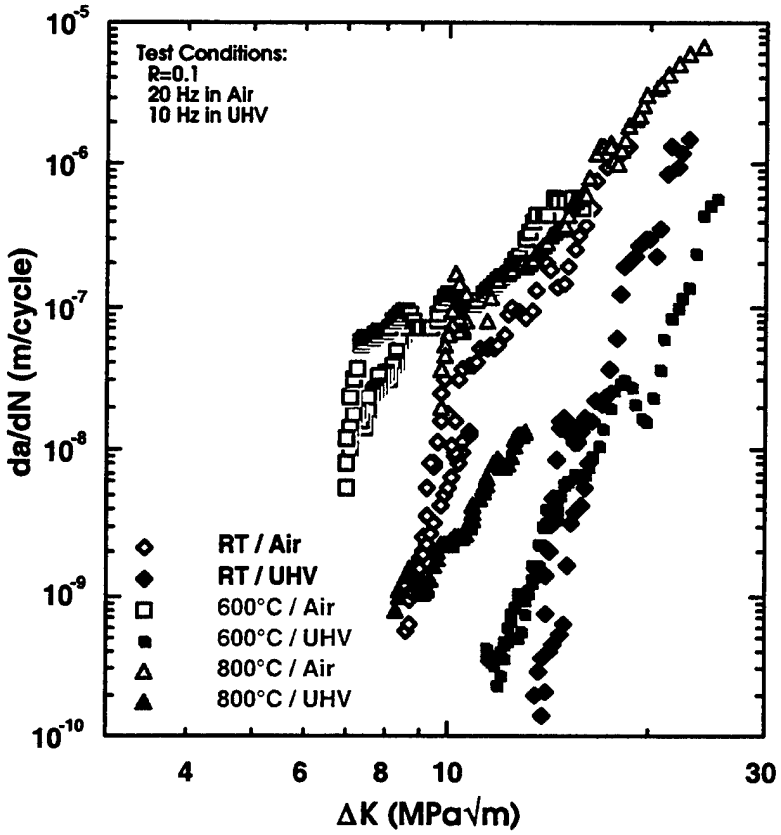


Fig. 2. Fatigue crack growth behavior of coarse lamellar K5 at RT, 600, and 800°C in air and UHV.

Crack growth rate curves for the duplex material, Fig 3, showed trends similar to those of the coarse lamellar material presented in Fig 2. There was, again, an obvious decrease in the crack growth rates by over an order of magnitude at all temperatures in the UHV compared to the air environment. The shift in DK_{th} at the lower temperatures, RT and 600°C, was less dramatic than in the lamellar material. However, the crack growth curves were over two orders of magnitude slower in UHV as compared to air. Notice, also that at RT and 600°C the apparent toughness, K_Q, was independent of environment. This resulted in steeper crack growth curves in UHV; for example, at room temperature, the exponent of a Paris equation fit was approximately 40! At 800°C, as in the lamellar material, DK_{th} in UHV was lower than in air, but this was, again, a result of the arrest in air and the continued growth at low crack growth rates in UHV.

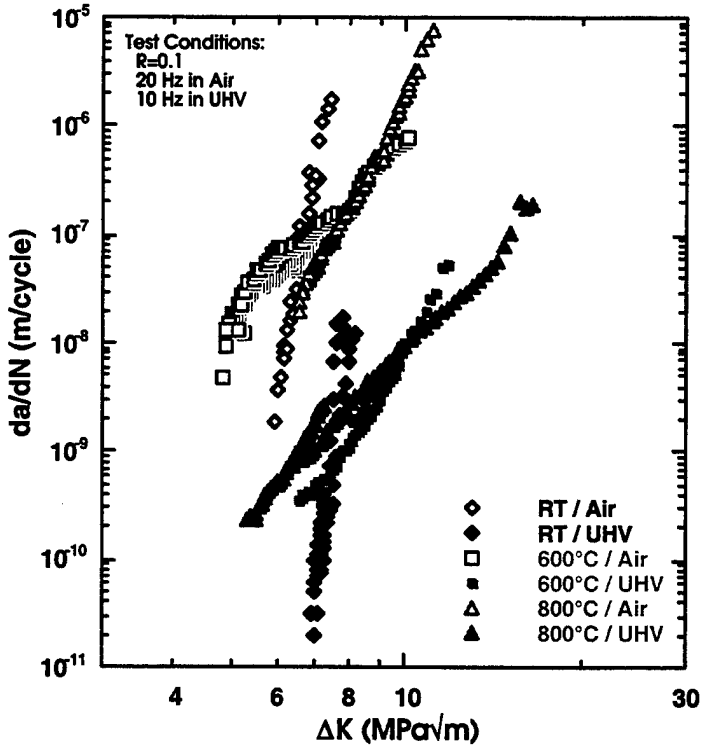


Fig. 3. Fatigue crack growth behavior of duplex K5 at RT, 600, and 800°C in air and UHV.

The crack growth behavior of the refined lamellar material in laboratory air was similar to that seen in the coarse lamellar material [9] and is not shown here. The decrease in the scale of the microstructure, apparent in Fig. 1, did not have a large influence on the fatigue crack growth resistance. It is expected that the refined lamellar microstructure would have a environmental influence on crack growth behavior similar to that of the duplex and coarse lamellar microstructures.

Crack Closure Corrected Crack Growth

It has been suggested that the anomalous temperature dependence on crack growth rate that has been observed in a number of gamma alloys [7, 6] is due to an extrinsic mechanism (i.e. oxide induced closure) [7] and not only a result of the changes in the deformation character and environmental attack that accompany the increase in temperature. This theory was investigated by a careful examination of the closure behavior of the coarse lamellar and duplex K5 materials, shown in Figs. 4 and 5, respectively. The level of closure may be represented by the U ratio, $U = (P_{max}-P_{op})/(P_{max}-P_{min}) = DK_{eff}/DK$ [10] and was described as a function of DK. In the present results, closure was monitored during both the decreasing-DK and constant-DP portions of the test and appeared to follow the same dependence on DK for both of these loading histories.

As shown in Fig. 4, closure in the coarse lamellar material displayed little variation with temperature in the air environment - U generally had a value of 0.8 to 0.9, though slightly lower at the lowest DK levels at room temperature. However, U tended to be lower in UHV than in air at room temperature and higher in UHV than in air at the highest temperature. This suggests that closure was dominated by fracture surface roughness at low temperatures and included a contribution due to oxide wedging at higher temperatures. More discussion of these observations follows in later sections.

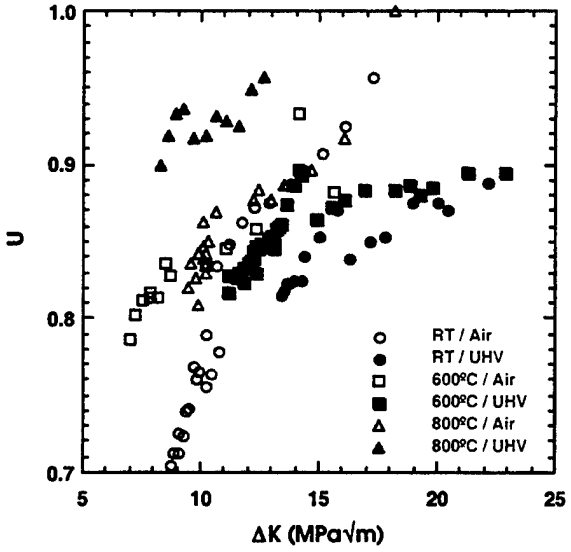


Fig. 4. U as a function of applied stress intensity factor range in coarse lamellar K5 at RT, 600, and 800°C in air and UHV.

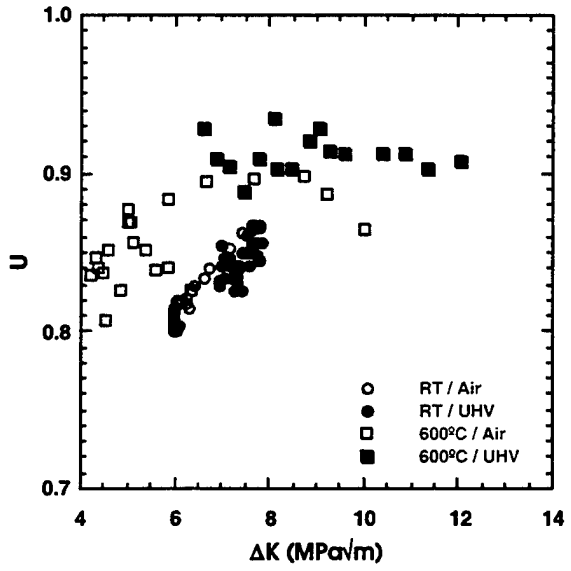


Fig. 5. U as a function of applied stress intensity factor range in duplex K5 at RT and 600°C in air and UHV. No closure was detected in either environment at 800°C.

In duplex K5, there was little influence of environment on the closure behavior. There was a general increase in U as the temperature increased. At 800°C (not shown in Fig. 5) the cracks were fully open over the full range of DK (i.e. U=1). The temperature dependence of closure is likely due to a decrease in roughness of the fracture surface at the lower temperatures and a lack of any closure at the highest temperature, due to creep and/or blunting at the crack tip. A comparison of the closure behavior in the coarse lamellar and duplex materials, Figs. 4 & 5 respectively, showed that U was generally higher in the duplex material. As discussed later (and in [11]), the main influence of microstructure on closure was probably due to differences in fracture surface morphology and roughness of the two materials.

Especially notable was that at 800°C in air, no unusual increase in the level of crack closure was observed that could be linked to oxide wedge formation.

Closure corrected crack growth curves are shown in Figs. 6 and 7 for the coarse lamellar and duplex microstructural conditions, respectively. Here, the crack growth rate was correlated with DK_{eff} where $DK_{eff} = K_{max}-K_{op}$. The correction for closure generally shifted the crack growth rate curves to the left, however, the magnitude of the temperature-dependent layering and environmental influence of the data was unchanged.

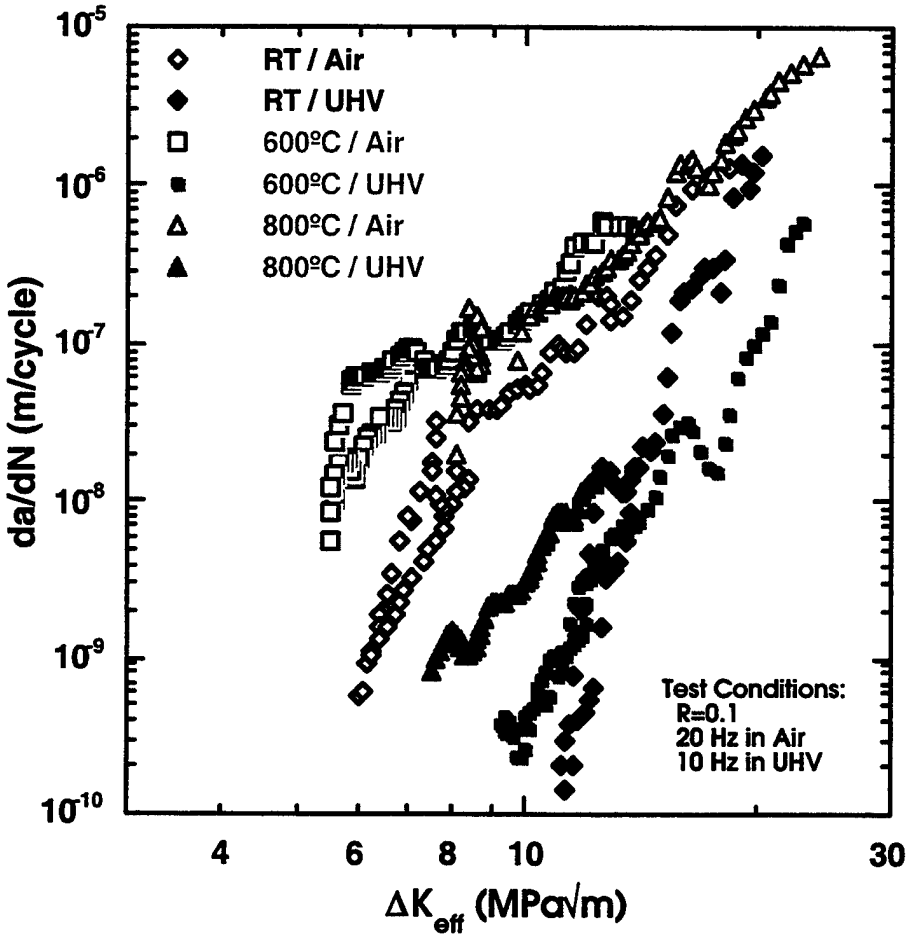


Fig. 6. Closure corrected fatigue crack growth behavior of coarse lamellar K5 at RT, 600, and 800°C in air and UHV.

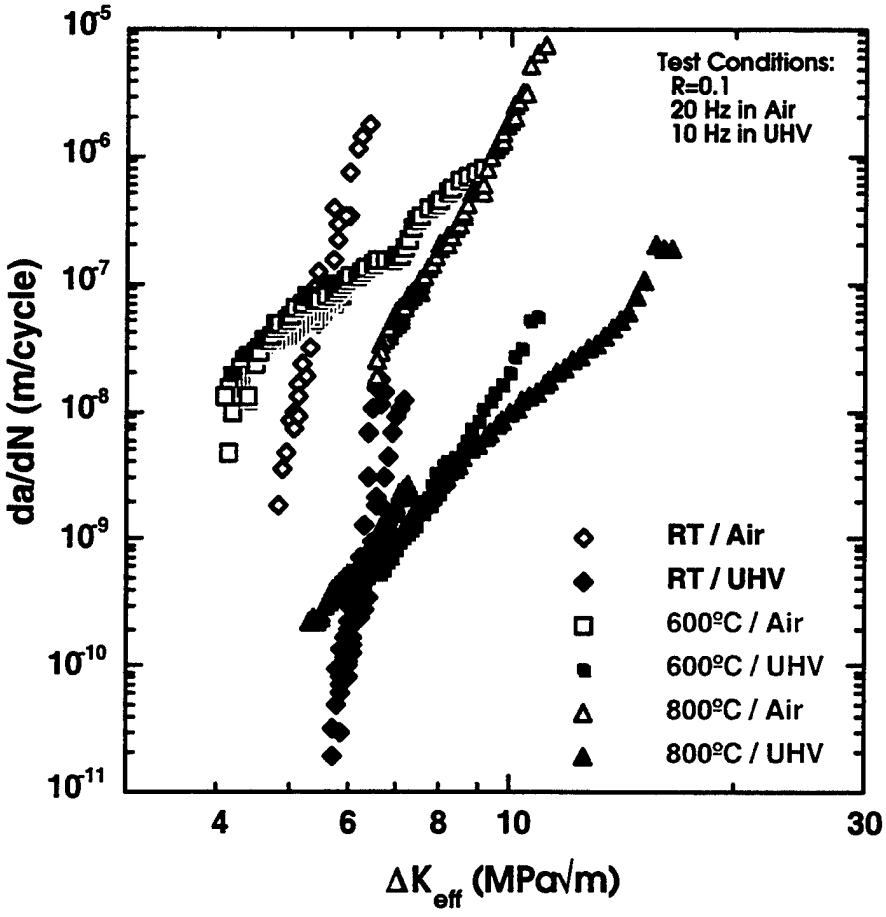


Fig. 7. Closure corrected fatigue crack growth behavior of duplex K5 at RT, 600, and 800°C in air and UHV.

Temperature Dependence of Fatigue Crack Growth

The fatigue crack growth behavior of the refined lamellar material was examined in more detail as a function of temperature. Using a small number of specimens, the crack growth rate under constant-DK conditions was determined over the range of temperatures shown in Fig. 8. It is apparent that there was a gradual increase in growth rate as the temperature increased from 200 to 600°C, followed by a steep decline in growth rate at higher temperatures. No crack growth was measured at 800°C, which indicated that the growth rate was lower than 10^{-10} m/cycle. Notice that the crack growth rates at the temperatures of RT, 600, and 800°C compare well with the curves for the coarse lamellar material presented in Fig. 2.

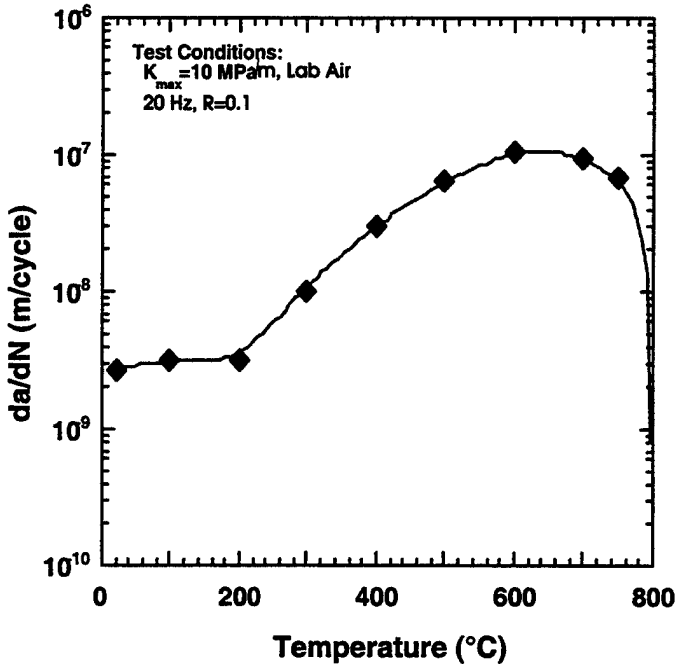


Fig. 8. Fatigue crack growth rate under constant-DK conditions plotted as a function of temperature for the refined lamellar material.

Closure measurements were obtained during each of the crack growth increments in Fig. 8. The closure levels were measured in the manner described earlier and are shown in terms of U as a function of temperature in Fig. 9. The trend of these closure measurements was similar to the associated crack growth rate behavior shown Fig. 8. That is, a peak in U was observed at approximately 650°C, followed by a steep drop at higher temperatures. This indicated that the variation in crack growth rate was influenced by crack closure, but the overall change in closure level at this value of DK was only 10% (i.e. U changing from 0.8 to 0.9). This change in driving force would influence the room temperature crack growth behavior the most, as this test condition had the steepest crack growth rate curve. In this case a decrease in DK of 10% would change the crack growth rate by a factor of 5, which is much less than the nearly 50x change in da/dN seen in Fig. 8. At the higher temperatures, where the crack growth curves are less steep, the variation in crack growth rate due to a 10% change in driving force would be even more limited.

Additional samples of the refined lamellar material were used to determine the crack growth thresholds and the influence of closure over the temperature range from 500 to 800°C. The variation in DK_{th} and U, at threshold, are represented as a function of temperature in Fig. 10. The threshold levels in this figure do not represent growth at a fixed growth rate of, say, 10^{-10} m/cycle, but represent the DK at apparent crack growth arrest. This arrest occurred at growth rates between 1×10^{-8} and 4×10^{-8} m/cycle. The values of U in this figure are similar to, or lower than, the measurements of U obtained under constant-DK conditions (Fig. 9). This trend in U is consistent with the closure conditions that would be expected at the crack growth threshold (or arrest). It is interesting to note that the minimum DK_{th} does not correspond to the maximum U. In fact, highest values of U occurred over the temperature interval from 650 to 750°C which showed a steep increase in threshold, indicating that closure was not the cause of the increase.

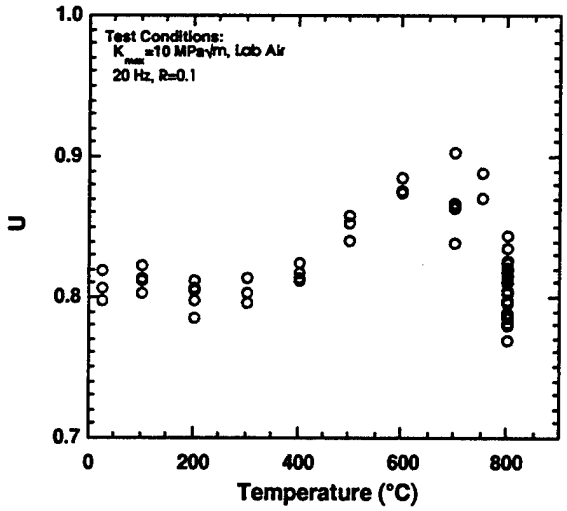


Fig. 9. U versus temperature corresponding to the constant-DK fatigue crack growth data presented in Fig. 8 for the refined lamellar material.

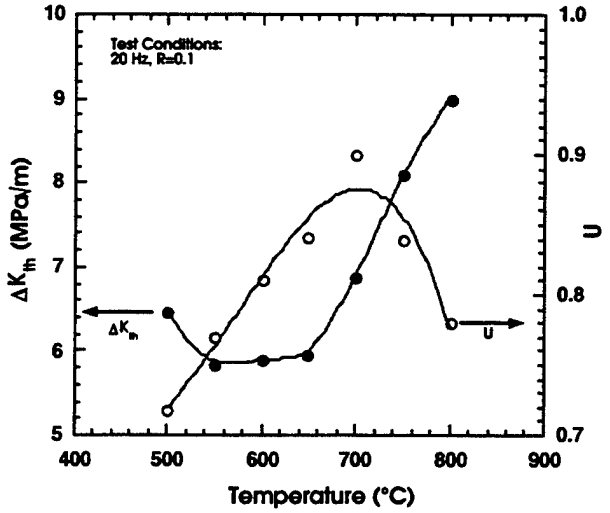


Fig. 10. DK_{th} and U as a function of temperature in the refined lamellar material.

Fractography

Examinations of the fracture surfaces of the specimens revealed only subtle differences in the modes of fracture. However, the main fracture features were relatively unaffected by the test environment. The thick oxide layer on specimens tested at 800°C in air prevented observation of their fracture modes, but the specimens tested at 600°C in air had only a light surface oxide. The specimens tested in UHV retained their pristine condition, and no oxidation was apparent even at the highest temperature.

Crack advance in the coarse lamellar material was strongly dependent on the underlying microstructure and tended to produce a tortuous crack path. At room temperature, the specimen tested in air produced a predominantly translamellar fracture with occasional inter- and intralamellar facets, Fig. 11(a). Under UHV conditions, the fracture surface appeared rougher, with more interlamellar fracture facets and a mixture of inter- and translamellar fracture within a single colony, Fig. 11(b). These subtle differences were present at both the near-

threshold and the mid-10^{-8} m/cycle crack growth regimes. Preliminary measurements of the fracture surface roughness using scanning confocal laser microscopy indicated an appreciably greater asperity height in UHV as compared to the surface produced in the air environment. This increase in roughness likely resulted in the lower values of U in the UHV environment, Fig. 4. Increasing the temperature to 600°C had little effect on the fracture behavior. The specimens tested in air and UHV had slightly flatter fracture surfaces that were less sensitive to the colony orientation. The specimen that was tested in UHV did, however, have more interlamellar fracture facets, similar to the room temperature specimen. At high levels of DK, the specimen tested in UHV exhibited more secondary interlamellar splitting than the specimen tested in air. At 800°C, the air-tested specimen was too oxidized to examine, but the specimen tested in UHV exhibited evidence of ductile intralamellar and translamellar fracture and a macroscopically flatter fracture surface.

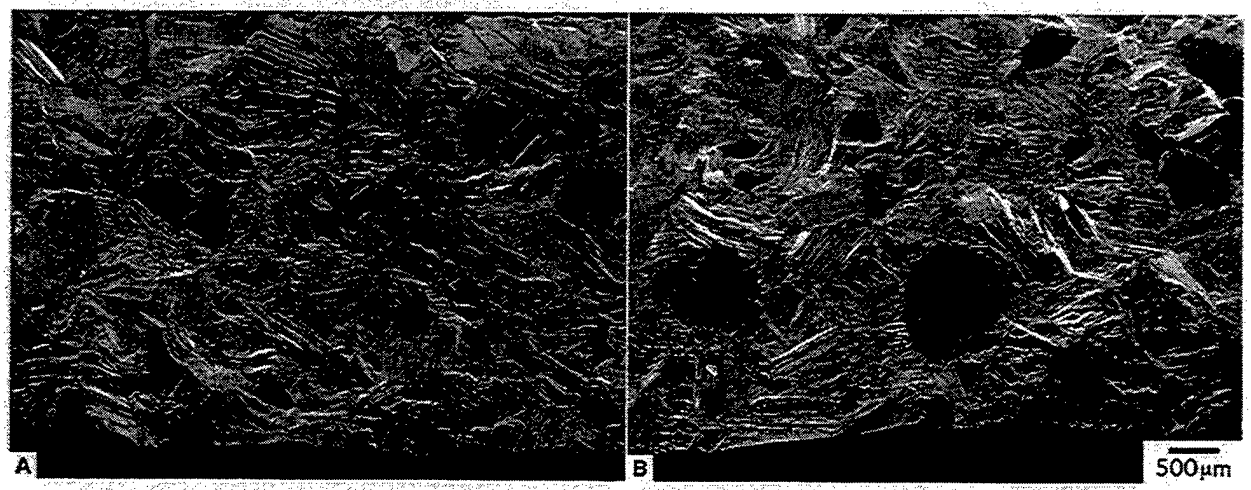


Fig. 11. Fracture behavior of lamellar Ti-46.5Al-3Nb-2Cr-0.2W at RT in: (a) air, and (b) UHV.

The fine grain size of the duplex material promoted a smooth fracture surface in both air and UHV. The dominant fracture mode at room temperature was transgranular cleavage or microcleavage. Here, no differences were observed between the specimen tested in air and UHV. At 600°C, however, the specimen tested in air exhibited a small amount of intergranular fracture at DK_{th} that increased to approximately 20 percent of the total fracture at high growth rates near K_Q. In UHV, the fracture mode was completely transgranular cleavage in the threshold regime, but intergranular fracture accounted for approximately 10 percent of the fracture near K_Q. Overall, the differences in fracture behavior in air and UHV were small for the three materials tested and would not account for the large environmental influence on the crack growth behavior.

Discussion

Over the entire temperature range examined in this study, crack growth rates were over an order of magnitude slower than in UHV as compared to lab air. This effect is believed to be due to a moisture-induced hydrogen embrittlement mechanism [2,3] at ambient temperatures. The likely mechanism of hydrogen generation by the reaction between moisture and an active metal, either aluminum or titanium in this case, was discussed by Liu and Kim [2]. However, the exact mechanism of the embrittlement is poorly understood. Hino and coworkers [12] measured a release of hydrogen at the moment of tensile fracture in a TiAl alloy indicating that hydrogen has some role in the failure of gamma alloys. The similarity in the K_Q values in UHV and air in this study and that of Mabru, et al. [1] indicated that the embrittlement was time dependent or was controlled by a diffusion process. Tensile tests at different strain rates by Oh, et al. [3] also support this.

The increase in fracture surface roughness observed in the UHV environment in the coarse lamellar gamma alloy indicates that a change in the deformation mode occurred, and this change may be due to an increase in ductility or slip length causing failure at strong boundaries within the microstructure. This would promote interlamellar fracture at lamella boundaries rather than the transgranular microcleavage observed in air. Confirmation of this interpretation was beyond the scope of this study and would require careful TEM work to study the slip character.

At elevated temperatures, the environmental effect is most likely caused by an oxygen embrittlement mechanism that is most virulent at temperatures high enough to cause oxygen diffusion but below the ductile to brittle transition temperature (DBTT). At temperatures above the DBTT, the crack growth rates are reduced, partly due to extrinsic oxide wedging, but mainly due to the intrinsic changes in the crack tip deformation that are brought about by the increase in ductility. The lack of an environmental influence on the fracture features at elevated temperatures, in both this study and that of James and Bowen [4], indicates that the deformation modes must be similar.

The measurements conducted in this study indicated that the only significant environmental influences on closure occurred in the lamellar microstructure at ambient and 800°C. At room temperature, the higher closure was consistent with the rougher fracture surface and the larger size of the facets. Given the low ductility of gamma alloys, it is unlikely that a mechanism other than roughness induced closure occurred at room temperature. At 800°C in the lamellar microstructure material, the higher level of closure in air compared to the UHV environment could signify an oxide contribution to closure, since the fracture surfaces of specimens tested in air had a oxide layer that was sufficiently thick to obscure most of the fracture features. However, the closure levels at 800°C in air were the same as those measured at 600°C. This indicated that any increase in closure at the higher temperature, due to oxide scale growth, was negated by the concomitant increase in crack tip opening due to creep and strength reductions. The duplex microstructure material did not exhibit closure at 800°C, indicating that creep and/or blunting increased the crack tip opening faster than the formation of an oxide layer would tend to decrease it. The UHV crack growth results, in general, showed that the fatigue crack resistance of the gamma alloys decreases with an increase in temperature. This, with the measured closure behavior, shows that the poorest, intermediate temperature, crack growth resistance in air is due to an environmental assist.

The examination of the crack growth rate as a function of temperature in the refined lamellar material showed (for K_{max} = 10 MPa$\sqrt{m}$) that the highest crack growth rates occurred at 600° to 650°C and were greater than could be expected based on closure corrections alone. The decrease in closure (increase in U, Fig. 9) that occurred over the 200° to 600°C temperature interval was most likely due to the decrease in fracture surface roughness that occurred over this temperature range. The variation in closure at DK_{th}, Fig. 10, was greater than that observed at a higher K_{max}, Fig. 9, indicating that the arrest at the lower temperatures, 500°-600°C was likely associated with the high closure levels. However, the crack growth thresholds at these temperatures were lower than those found at 700° and 750°C, where U was 10 to 20% higher. This temperature dependence on DK_{th} was most likely caused by the similar environmental effect that was observed in the duplex and coarse lamellar materials and is not due to closure alone.

The increased DK_{th} and crack growth resistance observed in vacuum indicated that failure of actual high-temperature components due to sub-surface defects should be extremely unlikely, since surface initiated cracks would propagate much faster than internally initiated cracks. This preference for surface cracks would facilitate damage detection and monitoring using conventional nondestructive techniques. Also, the decrease in crack growth rates in the UHV environment would have a significant effect on the integrated component life - if such a life prediction scheme is applicable to this intermetallic material.

The poorest crack growth resistance at intermediate temperatures below the ductile to brittle transition temperate may represent the most critical design hurdle for the implementation of gamma alloys in fracture critical applications. The mechanism of crack growth arrest that was observed in air but not in UHV raises questions whether the behavior of small cracks would be similar to that of the measured long crack thresholds, or would fundamentally differences in behavior exist? The pronounced environmental effect that was observed in crack growth rate also raises questions with regard to the fatigue and crack initiation performance of this class of alloys after prolonged, high-temperature service exposure.

Conclusions

The crack growth behavior of three different variations of a gamma titanium aluminide were examined over a wide range of temperatures in aggressive and inert environments. Several conclusions can be drawn from this study.

- The environment has a major effect on the crack growth rates in gamma titanium aluminides at temperatures ranging from ambient to 800°C. Lower crack growth rates, by over an order of magnitude, were found in the UHV environment.
- The highest crack growth rates were observed in air at temperatures within the 600° to 700°C range. Crack growth at these temperatures in air was enhanced by environmental attack, which diminished as the temperature was increased above the ductile to brittle transition temperature.
- Crack closure had only a limited influence on the trends of crack growth behavior in air or UHV environments at any of the temperatures examined.
- Only minor changes in the mode of fracture occurred with changes in test environment.

Acknowledgments

This research was performed in the Materials Directorate, Air Force Research Laboratory, Wright-Patterson Air Force Base, OH and was supported by the Air Force Office of Scientific Research under Task 2302BW. B.D. Worth gratefully acknowledges the support of Air Force contract F33615-94-C-5200. The authors would also like to thank Y.-W. Kim of UES, Dayton, OH for the K5 alloy.

References

1. C. Mabru, G. Henaff, and J. Petit, "Fatigue Crack Propagation Behavior of a Lamellar Ti-Al Alloy in Air and Vacuum," in Proceedings of the Sixth International Fatigue Congress Fatigue '96, G. Lutjering and H. Nowack, eds, Pergamon, Oxford, (1996) 1749-1754.

2. T. Liu and Y.-W. Kim, "Room-Temperature Environmental Embrittlement in a TiAl Alloy," Scr. Metall. Mater., 27, (1992) 599-603.

3. M.H. Oh, H. Inui, M. Misaki, and M. Yamaguchi, "Environmental Effects on the Room Temperature Ductility of Polysynthetically Twinned (PST) Crystals of TiAl," Acta Metall. Mater., Vol. 41, No. 7, (1993) 1939-1949.

4. A.W. James and P. Bowen, "Elevated Temperature Crack Growth Resistance of TiAl Under Monotonic and Cyclic Loading," Mater. Sci. Eng., A153, (1992) 486-492.

5. S.J. Balsone, J.W. Jones, D.C. Maxwell, "Fatigue Crack Growth in a Cast Gamma Titanium Aluminide Between 25 and 954°C," in Fatigue and Fracture of Ordered Intermetallic Materials, W.O. Soboyejo and T.S. Srivatsan, eds., TMS, Warrendale, PA. (1994).

6. S.J. Balsone, J.M. Larsen, D.C. Maxwell, and J.W. Jones, "Effect of Microstructure and Temperature on Fatigue Crack Growth in the TiAl Alloy Ti-46.5Al-3Nb-2Cr-0.2W," Mater. Sci. Eng., A192/193, (1995) 457-464.

7. A.L. McKelvey, J.P. Campbell, K.T. Venkateswara Rao, and R.O. Ritchie "High Temperature Fatigue Crack Growth Behavior in an XD™ g-TiAl Intermetallic Alloy," in Proceedings of the Sixth International Fatigue Congress Fatigue '96, G. Lutjering and H. Nowack, eds, Pergamon, Oxford, (1996) 1743-1748.

8. Y.-W. Kim, "Ordered Intermetallic Alloys, Part III: Gamma Titanium Aluminides," JOM, Vol. 46, No. 7, (1994) pp. 30-40.

9. B.D. Worth, J.M. Larsen, and A.H. Rosenberger, "Threshold Crack Growth Behavior of the Gamma Titanium Aluminide Alloy Ti-46.5Al-3Nb-2Cr-0.2W Under High Cycle Fatigue Conditions," in Second International Symposium on Structural Intermetallics, this proceedings, Seven Springs Resort, Champion, PA, (1997).

10 W. Elber, "The Significance of Crack Closure," in Damage Tolerance in Aircraft Structures ASTM STP 486, ASTM, PA, (1971) 230-242.

11.J.M. Larsen, B.D. Worth, S.J. Balsone, A.H. Rosenberger, and J.W. Jones, "Mechanisms and Mechanics of Fatigue Crack Initiation and Growth in TiAl Intermetallic Alloys," in Proceedings of the Sixth International Fatigue Congress Fatigue '96, G. Lutjering and H. Nowack, eds, Pergamon, Oxford, (1996) 1719-1730.

12.T.H. Hino, Okada, M. Kanno, "Analysis of Hydrogen Evolved from Fracture Surfaces of a TIAl Alloy," Scr. Metall. Mater., Vol. 29, (1993) 1029-1033.

Reference: A.H. Rosenberger, S. Sankaran, P.R. Smith, D. Glass, and D. Rice, "Multilayer Coating for the Oxidation Protection of Orthorhombic Titanium Aluminides During Fatigue," in Orthorhombic Titanium Matrix Composites II, WL-TR-97-4082, P.R. Smith, ed., pp. 368-378 (1997).

MULTILAYER COATING FOR THE OXIDATION PROTECTION OF ORTHORHOMBIC TITANIUM ALUMINIDES DURING FATIGUE

A.H. Rosenberger[1], S. Sankaran[2], P.R. Smith, D. Glass[2], and D. Rice[2]

Wright Laboratory Materials Directorate, Wright-Patterson AFB, OH 45433
[1]University of Dayton Research Institute, Dayton, OH 45469
[2]Analytical Services and Materials, Inc. Hampton, VA 23666

ABSTRACT

The effect of a $TiAl_3$ + two-phase glass coating on the fatigue performance of unidirectionally reinforced orthorhombic based titanium aluminide composites (SCS-6/Ti-22Al-23Nb $[0]_4$) was examined. Though the coating system exhibited a reduction in oxidation rate, it failed to produce any enhancement in fatigue life. In fact, a reduction in life was found for the isothermal fatigue condition examined. The probable reasons for this are discussed based on the current understanding of the damage mechanisms in orthorhombic titanium matrix composites. It must be note that the coating system was not tailored for either the orthorhombic alloy or the temperature range utilized in the current study. An improvement in fatigue performance may be achieved with an optimization of the coating system.

INTRODUCTION

There is ample evidence of the detrimental effects of a high temperature oxidizing environment on the fatigue performance of many titanium and titanium aluminide alloys [1-4]. It is now understood that protection from oxidation damage involves more than just protection from structural material loss due to oxidation, but also protection from interstitial oxygen embrittlement that has a deleterious effect on the both fatigue and tensile properties [2, 3]. The protection of high temperature gas turbine components from this embrittlement using coating systems is not currently envisioned to provide primary life, but to provide a life extension. Such a coating scheme could also be utilized for titanium matrix composites which have a demonstrated debit in high temperature fatigue performance due to environment [1, 4].

The purpose of this study was to use a multilayer coating system that has a demonstrated reduction in oxidation weight gain in a number of titanium alloys [2] and asses its applicability as a life enhancement coating for the SCS-6/Ti-22Al-23Nb (at%) $[0]_4$ composite system. This multilayer coating system is identical to that used in a study to protect monolithic Timetal21S and SCS-6 / Timetal®21S composites [2]. These Timetal®21S composites were envisioned for use in a hypersonic vehicle where service would periodically include brief excursions up to 800°C. SCS-6/Ti-22Al-23Nb composites are envisioned for use in the structural reinforcement of gas turbine engine components where the maximum temperature will be limited to approximately 650°C for long times. No attempt was made to refine the coating system to specifically protect the orthorhombic composite under the anticipated application stress and temperature conditions.

This report contains the results of isothermal and thermomechanical fatigue tests on the coated and uncoated specimens. The following section describes the experimental techniques used in the investigation including a description of the coating system, materials, and test techniques. The next section describes the baseline fatigue behavior and damage mechanisms from two studies by Russ, et al., [1, 5] that help to elucidate the tests chosen for the coated specimens. The final section contains results of the fatigue tests on the coated specimens as well as observations of the damage mechanisms and the coating performance.

EXPERIMENTAL

Multilayer Coating System

The multilayer coating system, developed by Analytical Services and Materials, Inc., incorporates a reaction barrier overcoated by an oxygen diffusion barrier as shown in Figure 1. In this case, the reaction barrier is an EB-PVD aluminum layer that is deposited onto the surface of the composite and converted to $TiAl_3$ by a proprietary diffusion anneal process. The oxygen diffusion barrier is a two phase glass (TPG) layer applied by the sol-gel process. The TPG layer has two immiscible glass phases that result in a rigid glass matrix surrounding droplets of fluid glass, Figure 2. The rigid glass matrix resists oxygen diffusion while the fluid glass phase resist cracking. Also, the lower melting point second phase glass 'heals' damage or cracks by flowing to and filling cracks, Figure 3. The combination of the diffusion barrier and the TPG is used to prevent a deleterious reaction that could occur if the TPG is applied directly to the orthorhombic alloy. The total thickness of the multilayer coating system is approximately 2 to 4 mm.

Material

The material used in this study was a unidirectional orthorhombic-based titanium aluminide composite, SCS-6 / Ti-22Al-23Nb (at%) $[0]_4$ identical to that used in the study by Russ, et al. [1]. 127 mm x 152 mm composites panels were manufactured using the foil/fiber/foil technique incorporating the orthorhombic foil and woven fiber mats using Ti-Nb crossweave in order to maintain uniform fiber spacing. $[0]_4$ specimens were machined with overall dimensions of 150 x 16 mm and a 150 mm radius to a reduced gage section, nominally 20 x 10 mm. The composite had a fiber volume fraction of 0.33.

Testing

The mechanical testing of the coated and uncoated specimens was conducted using a computer controlled servo hydraulic test machine orientated in the horizontal position in order to minimize thermal chimney effects [6-7]. The specimens were loaded using precisely-aligned hydraulic friction grips. Strain was monitored via a high temperature quartz rod extensometer. Specimens were heated by a unit containing two banks of four quartz lamps running perpendicular to the loading axis, one above and one below the specimen. Four thermocouples were welded to the uncoated specimens providing four zones of temperature control with two lamps each. A beaded, wired, and

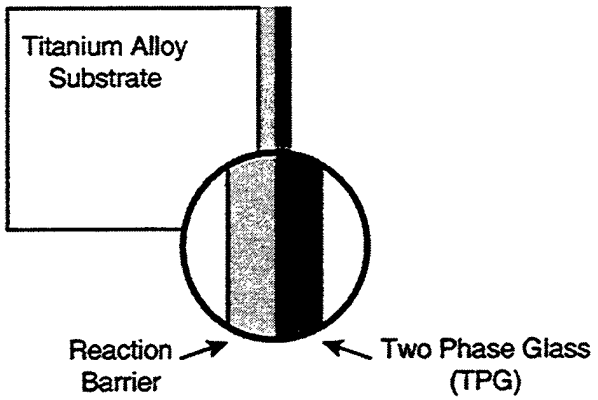


Figure 1. Multilayer coating system for the prevention of oxidation and oxygen embrittlement of orthorhombic matrix composites.

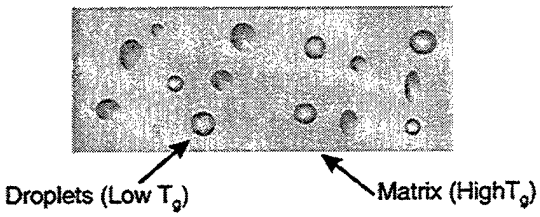


Figure 2. The oxygen diffusion barrier is a two phase glass applied by the sol-gel process.

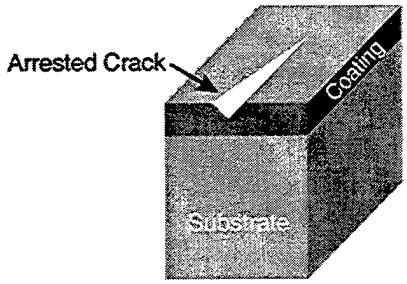


Figure 3. The two phase glass is self healing - the low T_g phase fills and arrests cracks.

bonded thermocouple technique was developed for testing the coated specimens that resulted in reliable, repeatable temperature measurement without damaging the multilayer coating. With both thermocouple techniques, a length of about 25 mm in the center of the specimens was heated uniformly, while the ends of the specimen, clamped in the water-cooled grips, remained near room temperature. The temperature within the 25 mm central portion of the specimen was within ±5°C of the setpoint under isothermal and thermomechanical fatigue conditions. All testing was conducted in laboratory air using testing software described elsewhere [8].

All isothermal fatigue tests were run in load-control with a triangular waveform, a stress ratio of 0.1, a frequency of 0.1 Hz, and a temperature of 650°C. Thermomechanical fatigue tests were run in load control with a stress ratio of 0.1 and a frequency of 0.0056 Hz (180 seconds per cycle). The temperature was cycled, out of phase with the load, with a maximum of 650 °C and minimum of 150°C.

FATIGUE RESULTS AND DAMAGE MECHANISMS IN UNCOATED OTMCs

In order to assess the protection offered by a coating system, it was necessary to understand damage mechanisms in uncoated specimens and chose fatigue conditions that have a known matrix-dominated damage mode or a strong environmental dependence. The conditions of interest are shown below in Table 1 along with the results of the individual tests.

Table 1. Comparison of Baseline Fatigue Results for Uncoated SCS-6/Ti-22Al-23Nb $[0]_4$ Composites.

Spec. #	Test Type	Temp (°C)	s_{max}* (MPa)	n (Hz)	Environment	Nf
94-107	OP-TMF	150-650	780	0.006	Lab Air	1517
95-045	Iso Fatigue	650	900	0.1	Lab Air	11805
95-035	Iso Fatigue	650	900	0.1	Lab Air	7414
95-049	Iso Fatigue	650	900	0.1	Vacuum	90708

**Stress Ratio = 0.1 in all cases*

The out-of-phase thermomechanical fatigue (OP-TMF) condition chosen for this study, 150°-650°C / 780 MPa / R=0.01 / 0.006 Hz, led to the initiation and growth of many cracks within the matrix of the composite [5]. This is due to the high matrix stress range typical of OP-

TMF in a titanium matrix/SiC fiber composite. Using a concentric cylinder model with elastic fibers and an elastic-plastic matrix, SCS-6 and Ti-22Al-23Nb, respectively, the matrix stress range for the above condition is 569 MPa with a slightly compressive stress ratio (R= -1.036). The mechanical strain range, in this case, is 0.45% but the total strain range would be even less due to the competition between the mechanical and thermal strains (i.e. minimum thermal strain at the time of the maximum mechanical strain). However the stress or strain range is, apparently, sufficient to produce rapid crack initiation and drive the crack growth into the matrix of the composite. The fracture surface of this specimen showed that the crack penetration was nearly complete - only a small portion of the cross section failed by tensile overload (less than 10%). This indicates that the crack growth constituted a large portion of the total TMF life and any benefit provided by the coating in crack prevention may have a limited impact. Generally, any coating system should be able to protect the composite from OP-TMF or pure thermal fatigue that causes similar matrix cracking and damage.

A study by Russ, et.al. [2] examined the damage mechanisms of the SCS-6 / Ti-22Al-23Nb $[0]_4$ composites under several isothermal fatigue conditions. Under the condition chosen for the present study, 650°C / 900 MPa / R=0.01 / 0.1 Hz, it was observed that the specimens failed due to the growth of a single crack that lead to catastrophic failure of the composite. Examination of the fracture surface and metallographic sections of the specimens showed little evidence of high temperature damage in the form of burning of the SCS-6 coating or carbon core. This indicated that the portion of life attributed to crack propagation is small - that is, crack initiation (nucleation) was the life limiting fatigue process. An identical test conducted under high vacuum conditions lead to an order of magnitude increase in fatigue life, Table 1, showing the strong influence of environment on fatigue life. In addition to the increase in fatigue life, there is a change in the form of damage observed in a vacuum environment. Several cracks were found that did not lead to failure of the specimen. This indicated that in a vacuum environment, crack growth constituted a greater portion of the fatigue life (slower crack growth rates) and possibly the life limiting process (this is a change in the dominate damage mechanism found in laboratory air). The findings of this study are also supported by fatigue crack growth studies conducted by Jira and Larsen [9]. Here a study of crack initiation and growth in notched SCS-6/Ti-22Al-23Nb $[0]_4$ composites showed a decreasing beneficial effect of the reinforcing fibers as the maximum cyclic stress increased. The repeated isothermal tests, specimens 95-045 and 95-035, show that the differences in composite panels lead to some variation in fatigue life, but only on the order of 2x (or less).

FATIGUE RESULTS AND DAMAGE MECHANISMS IN COATED OTMCs

A significant reduction in oxygen weight gain is apparent for Timetal21S [2] and Ti-22Al-23Nb exposed at 800°C when the multilayer coating system is used, Figure 4a & b. The rate of weight gain of the coated orthorhombic alloy is similar to that of the Timetal21S for which the coating system had been optimized. This indicates that the static oxidation protection of the coating system for orthorhombic composites would be good, however, the performance under fatigue conditions is equally important.

Based on the understanding of the isothermal fatigue and OP-TMF tests discussed in the previous section, the influence of the experimental coating on fatigue life was assessed. Table 2 shows the fatigue life results on coated and one uncoated specimen from the same panel.

A comparison of the fatigue results in Tables 1 and 2 shows that there is no difference in OP-TMF performance in coated and uncoated specimens. However, under the isothermal fatigue condition chosen, there is a obvious degradation in life due to the coating system. The uncoated specimen in Table 2 is from the same composite panel as the coated specimens and shows good correlation with the results from tests on specimens from two other panels (Table 1). The shorter fatigue life of the coated specimen suggests that crack initiation occurred earlier improve the static oxidation performance of the orthorhombic alloy, but under fatigue conditions.

it appears to lead to premature crack initiation and a reduction in fatigue life. The OP-TMF results tentatively support the isothermal fatigue performance. Damage in the case of OP-TMF is rapid matrix crack initiation and growth with a slower evolution of damage in the reinforcing fibers (failure may occur due to a degradation of the fiber strength caused by coating burning and subsequent rubbing damage). Based on the high matrix stress (and strain) range of OP-TMF, crack initiation in the matrix may be more influenced by the loading mechanics than the environment. In this case, the coating may, at best, have little influence on the OP-TMF life, and could produce a life debit if a test is conducted in which the matrix crack initiation occurs only late in life.

Table 2. Fatigue test results comparing coated and uncoated SCS-6/Ti-22Al-23Nb $[0]_4$ composites.

Spec. #	Test Type	Temp (°C)	s_{max}* (MPa)	n (Hz)	Coating	Nf
95-027	OP-TMF	150-650	780	0.006	$TiAl_3$ + glass	1586
95-026	Iso Fatigue	650	900	0.1	$TiAl_3$ + glass	2178
95-025	Iso Fatigue	650	900	0.1	$TiAl_3$ + glass	1504
95-024	Iso Fatigue	650	900	0.1	none	7626

**Stress Ratio = 0.1 in all cases*

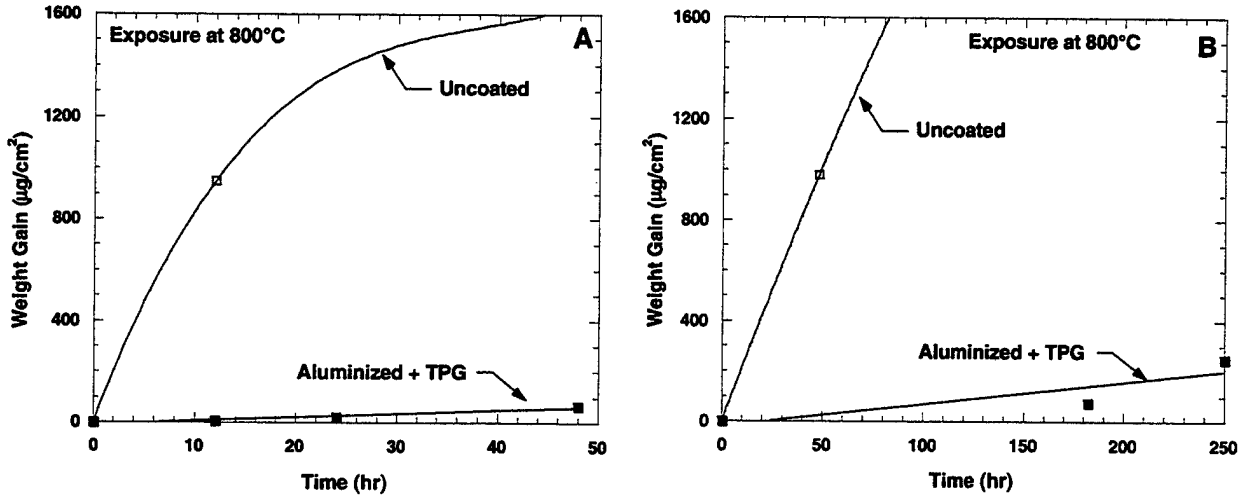


Figure 4, TGA oxidation weight gain during an 800°C air exposure of; a) Timetal21S both uncoated and with the multilayer coating [2], and b) Ti-22Al-23Nb, uncoated and with the multilayer coating.

The evolution of maximum and minimum strain, filled and open symbols respectively, for the isothermal fatigue tests is shown below in Figure 5. It can be seen that the strain accumulation is very similar for specimens from different panels w/ and w/o coating. Generally the specimens attained 0.7% maximum strain which may be high enough to cause cracking of the coating and subsequent crack growth. The concentric cylinder model of this test condition showed that the matrix stress range was only 209 MPa (with a slightly compressive ratio of -0.029) and had a cyclic strain range of 0.52 %. On all fracture surfaces examined, the crack growth area was approximately 10 to 20% of the cross sectional area and only one crack composed the fracture surface.

Polished longitudinal cross sections of specimen No. 95-026 show that the $TiAl_3$ coating is not of uniform thickness, Fig. 6. This would help in the adherence of the coating, however, the axial stress may be non uniform which could lead to crack initiation. Crack initiation occurs

in the coating and then propagates into the specimen. Figures 7 a&b show typical cracks in the glass and $TiAl_3$ coating. Only a few coating cracks appear to have propagated into the matrix on the specimen, but the results of this would be devastating. Near the fracture surface, the crack density in the coating increased yet matrix crack initiation was similar as in the lower strained portion of the gage section. Obviously the coating has a much lower strain to failure than the base orthorhombic alloy. No evidence of coating 'healing' was found in any of the specimens tested under isothermal fatigue.

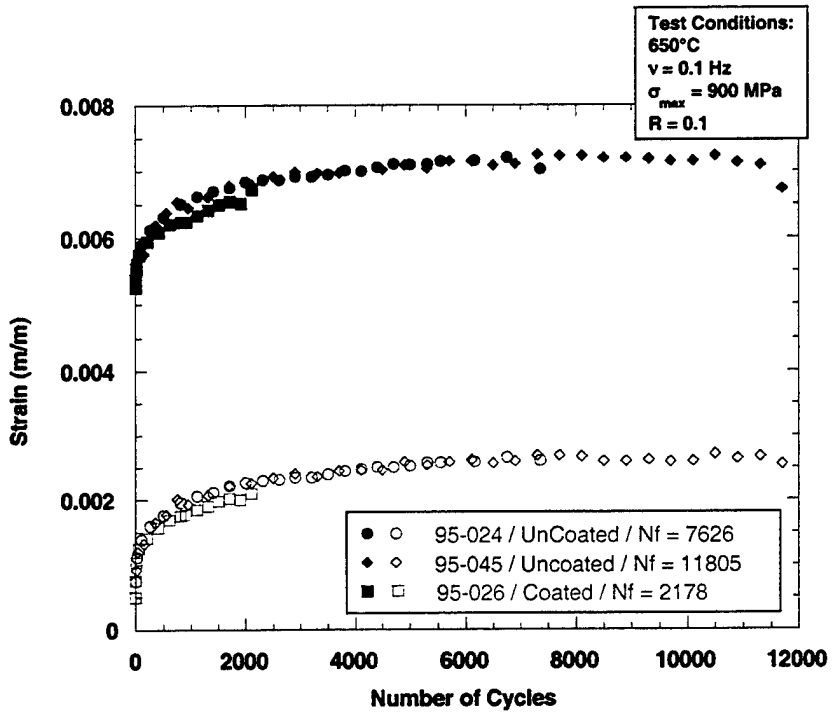


Figure 5, Maximum and minimum strain accumulation for coated and uncoated SCS-6/Ti-22Al-23Nb $[0]_4$ composites under isothermal fatigue loading at 650°C.

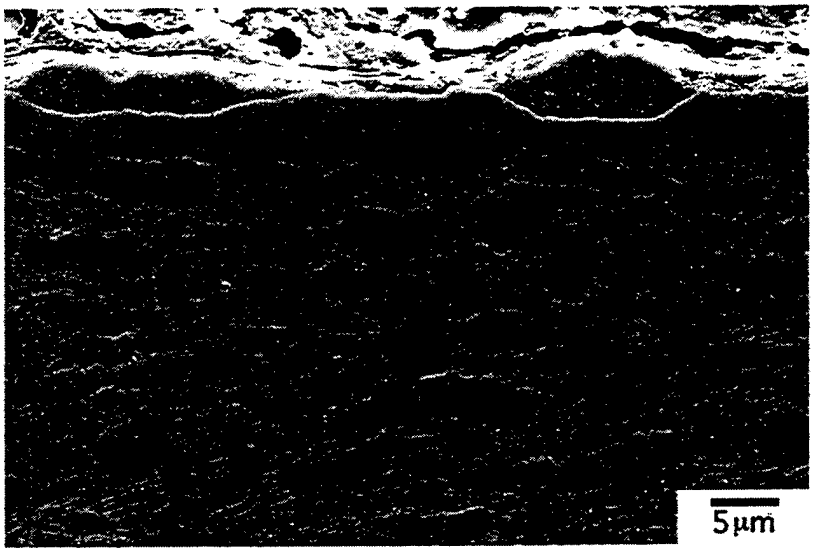


Figure 6. Typical, poor uniformity of $TiAl_3$ coating on SCS-6/Ti-22Al-23Nb $[0]_4$ composite. This may be due to initial non-uniformity of the composite panel surface.

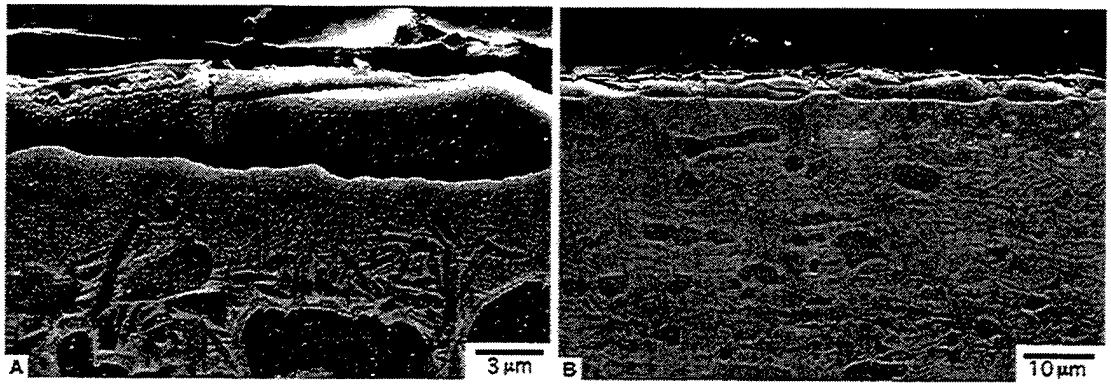


Figure 7. Typical coating cracks in isothermal fatigue specimen 95-026; a) crack in the $TiAl_3$ layer, and b) crack propagation into the orthorhombic matrix.

Under OP-TMF cycling, the overall damage mechanisms were similar in coated and uncoated specimens - that is, many matrix cracks were found and the fracture surface was nearly covered by matrix crack growth. A micrograph of the exposed surface of the coated specimen, 95-027, is shown in Figure 8. Here it can be seen that large matrix cracks are found throughout the gage section of the specimen as well as numerous smaller 'craze' cracks in the coating.

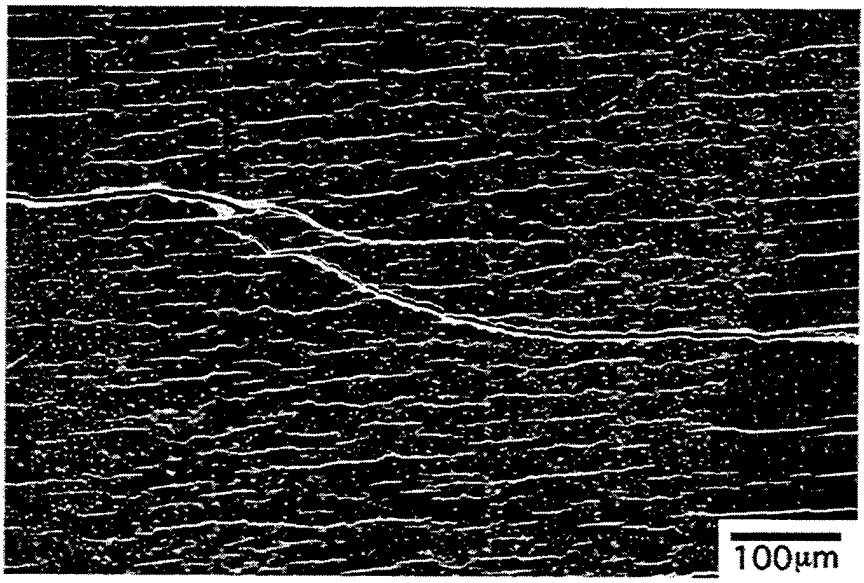


Figure 8. Matrix crack and numerous smaller 'craze' cracks on the OP-TMF specimen, loading direction is vertical.

A polished longitudinal cross section of 95-027 shows the depth of crack propagation and numerous smaller cracks, Figure 9. A closer view of the $TiAl_3$ coating, Figure 10a, shows that crack initiation likely occurred within this coating. The crack is then exposed to the air and sealed, either by the glass or a titanium aluminide of higher aluminum content, Figure 10b. The fill material then cracks and leads to cracking within the matrix, Figure 10c. These pictures are not from different stages of interrupted tests and therefore, do not offer proof of the progression of damage but represent the most likely means of damage progression.

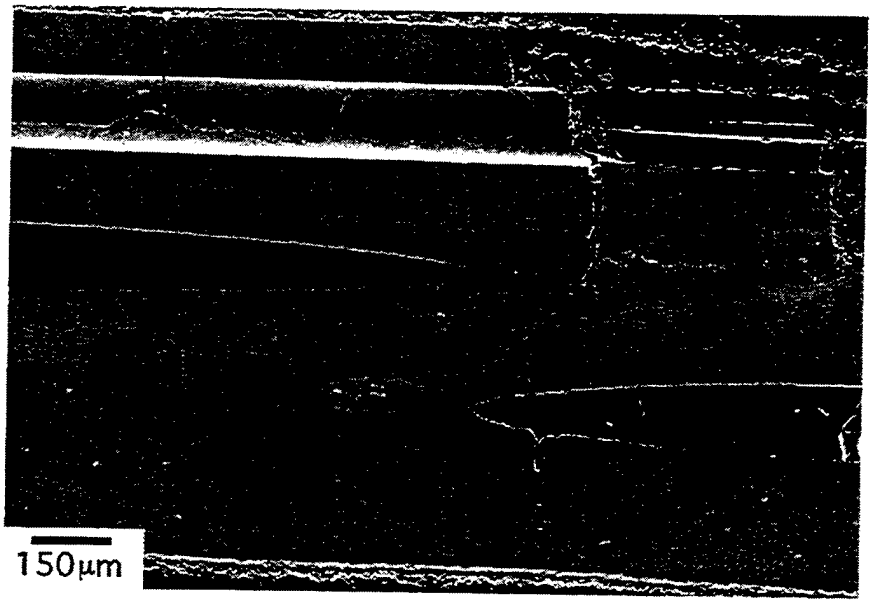


Figure 9. Typical damage in a coated SCS-6/Ti-22Al-23Nb $[0]_4$ composite subjected to OP-TMF. The fracture surface is to the right.

SUMMARY AND COMMENTS

In general, the coating system is protective under static oxidation conditions, however, its protection under cyclic stress is less than desirable. Healing of the coating appears to occur under cyclic temperature but not isothermal conditions. The cause for the different behavior is puzzling. It may be due to the fact that the crack initiated late in life of the isothermal fatigue specimens and there was not sufficient time to allow crack healing. In any case, the "healed" coating did not prevent later cracking and failure of the coating/specimen. The coating, however, remained adherent after both isothermal and thermomechanical fatigue cycling and showed no spalling damage after the conclusion of the tests.

The coating system has been shown to provide a life extension in a SCS-6 / Timetal21S composite under room temperature fatigue after a long 800°C exposure in air [10]. Also, under thermal fatigue, the prevention of cracking was found using the coating system. The fatigue conditions chosen for this study, however, may be the most severe for any coating system - especially one that has been formulated for higher temperature applications. The combination of a lower test temperature that would prevent healing of cracks by the TPG layer, and high temperature environment to assist the growth of cracks, once they have initiated, may prove to be the most difficult test environment for any protective coating system.

One important criteria of a coating system suitable for fatigue applications is the prevention of crack initiation. This may be achieved with coatings having a higher ductility than the base material. Another desirable property, besides ductility, is resistance to crack initiation under low cycle fatigue conditions with high stress and/or strain ranges - not necessarily high maximum strains.

It must be remembered that this coating system was not optimized for the current application. A multilayer coating system, however, may be able to provide protection under fatigue loading if changes were made to the diffusion barrier and TPG layers. A different or thinner diffusion barrier layer may prove to be more ductile or provide less of a starter crack for matrix crack initiation. Also, the TPG layer could be formulated with lower melting point glasses that would flow easier in the lower temperature applications of this orthorhombic alloy.

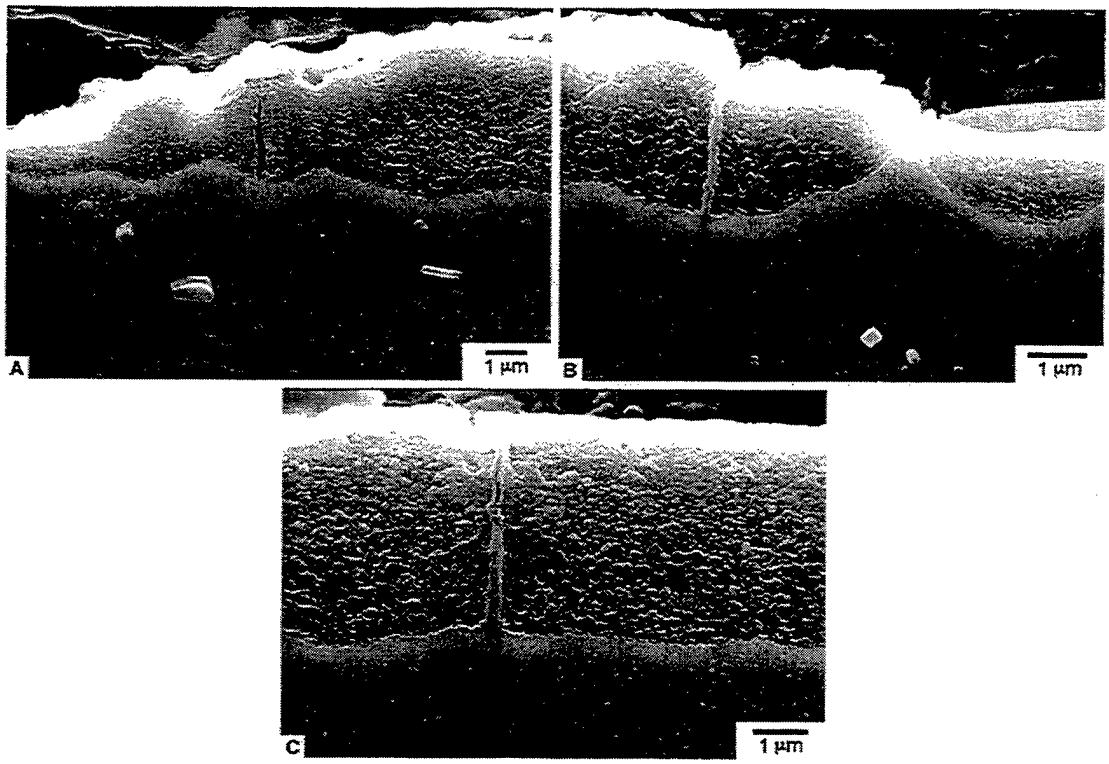


Figure 10. Probable progression of damage in OP-TMF specimens with a coating.

REFERENCES

[1] Russ, S.M., A.H. Rosenberger, and D.A. Stubbs, "Isothermal Fatigue of a SCS-6/Ti-22Al-23Nb Composite in Air and Vacuum," in *Recent Advances in Composite Materials*, S.R. White, H.T. Hahn, and W.F. Jones, Eds. American Society of Mechanical Engineers, New York, pp. 13-22, (1995).

[2] Wiedemann, K.E., R.K. Bird, T.A. Wallace, and R.K. Clark, "Mechanical Properties of Coated Titanium Beta-21S After Exposures to Air at 700 and 800°C, in *Titanium '92 Science and Technology*, F.H. Froes and I. Caplan, eds., The Minerals, Metals & Materials Society, Warrendale, PA, pp. 2185-2192, (1993).

[3] Rosenberger, A.H., "Preliminary Assessment of the Environmental Sensitivity of Ti-22Al-23Nb (a/o) Neat Laminates", in *Orthorhombic Titanium Matrix Composites*, WL-TR-95-4068, P.R. Smith, ed., WPAFB, OH, pp. 41-51, (1995).

[4] Brindley, W.J., T.P. Gabb, and J.W. Smith, "Embrittlement of the Surfaces and Crack Faces of TMC's During Fatigue," in *Orthorhombic Titanium Matrix Composites*, WL-TR-95-4068, P.R. Smith, ed., WPAFB, OH, pp. 52-63, (1995).

[5] Russ, S.M., P.R. Smith, and J.M. Larsen, "Mechanical Property Assessment of SCS-6/Ti-22Al-23Nb," in *Orthorhombic Titanium Matrix Composites*, WL-TR-95-4068, Wright Laboratory Materials Directorate, WPAFB, OH, pp. 162-179, (1995).

[6] Hartman, G. A. and S.M. Russ, "Techniques for Mechanical and Thermal Testing of Ti_3Al/SCS-6 Metal Matrix Composites," *Metal Matrix Composites: Testing, Analysis and Failure Modes, ASTM STP 1032*, W. S. Johnson, Ed., American Society for Testing and Materials, Philadelphia, pp. 43-53, (1989).

[7] Hartman, G.A. and D.J. Buchanan, "Methodologies for Thermal and Mechanical Testing of TMC Materials," in *Characterization of Fiber Reinforced Titanium Matrix Composites*, AGARD Report 796, pp. 12.1-12.9, 1994.

[8] Hartman, G. A. and N.E. Ashbaugh, "A Fracture Mechanics Test Automation System for a Basic Research Laboratory," in *Applications of Automation Technology to Fatigue and Fracture Testing, ASTM STP 1092*, A. A. Braun, N. E. Ashbaugh, and F. M. Smith, Eds., American Society for Testing and Materials, Philadelphia, pp. 95-110, (1990).

[9] Jira, J.R., and J.M. Larsen, "The contribution of Matrix Alloy to the Fatigue Crack Growth Resistance of Three Classes of Titanium Matrix Composites, " in *Fatigue '96, Proceedings of the Sixth International Fatigue Congress*, G. Lütjering & H. Nowack, eds. Pergamon Press, Oxford, Vol. III, pp. 1463-1468, (1996).

[10] Sankaran, S.N., Unpublished data, Analytical Services and Materials, Inc., Hampton, VA, (1996).

Dennis J. Buchanan[1], Reji John[2] and Kenneth E. Goecke[3]

INFLUENCE OF TEMPERATURE AND STRESS RATIO ON THE LOW-CYCLE FATIGUE BEHAVIOR OF TRIMARC-1/Ti-6Al-2Sn-4Zr-2Mo

REFERENCE: Buchanan, D.J., John, R. and Goecke, K. E., **"Influence of Temperature and Stress Ratio on the Low-Cycle Fatigue Behavior of Trimarc-1/Ti-6Al-2Sn-4Zr-2Mo,"** Seventh Symposium on Composites: Fatigue and Fracture, ASTM STP 1330, Ronald B. Bucinell, Ed., American Society for Testing and Materials, Philadelphia, PA, 1997.

ABSTRACT: The results of an experimental investigation of load-controlled isothermal low-cycle fatigue behavior of a titanium matrix composite (TMC) are discussed in this paper. The TMC was composed of Ti-6Al-2Sn-4Zr-2Mo matrix (wire) reinforced with silicon-carbide (Trimarc-1™) fibers. The composite panels were constructed using alternating layers of matrix wire and fiber using a wire winding technique. The panels were unidirectional with a $[0]_{10}$ layup and fiber volume fraction ≈ 0.29. Fatigue tests were conducted at temperatures of 23°C, 163°C and 371°C at stress ratios of -1.3 and 0.1 for longitudinal tests and 0.1 for transverse tests at a frequency of 3 Hz. The longitudinal fatigue data showed good correlation with other TMC systems at both positive and negative stress ratios. The maximum fiber stress versus cycles to failure for several unidirectional TMC systems at similar test conditions consolidate to a narrow band indicating that the life is fiber dominated. A transverse fatigue model was used to predict the cycles to failure of the TMC using the monolithic S-N data and a net-section based the unit cell.

KEYWORDS: titanium matrix composite, isothermal, low-cycle fatigue, mechanical testing, Trimarc-1, Ti-6Al-2Sn-4Zr-2Mo, wire winding, longitudinal, transverse, fatigue, TMC

INTRODUCTION

Engine and airframe systems of advanced aircraft require materials with high modulus, relatively low density and elevated temperature capability. Continuous reinforced titanium matrix composites (TMC) have been identified as a replacement material for some applications currently using conventional monolithic materials. The process of evaluating the mechanical behavior of the TMC requires numerous mechanical tests to fully characterize the composite performance in tension, compression, fatigue and creep. This paper will focus on the longitudinal and transverse fatigue results at three temperatures and two stress ratios.

Several investigators have studied fatigue damage initiation and evolution in continuous fiber reinforced metal matrix composites (MMC) [1-11]. Many have shown that the reduction in the stiffness is a useful parameter for indication of initiation and accumulation of damage in the composite [1,2,5]. A variety of failure modes and damage accumulation theories have also been identified. A common approach that several researchers have utilized as a method to analyze the data was to calculate the stress range or maximum stress in the 0° fibers. This method has been shown to consolidate fatigue data of composites with varied fiber orientations and layups [1,2]. Another approach used was to compare different materials systems on a density corrected basis [15]. This is an effective way to compare composite materials with monolithic nickel-base alloys.

Primarily, most of the fatigue research on TMC systems available in the literature has been done for positive stress ratios, R, particularly at R = 0.1. Several reasons exist for this such as the difficulty of developing test fixtures for compressive loading. Another is that the low value of R provides the largest stress or strain range possible without approaching zero or compressive loads. The tensile mean stresses are representative of what a component may experience in service and tend to be the most damaging to the fatigue life which can provide a

worst case scenario. Finally the composites panels that are available are often comprised of eight or less plys, resulting in a moment of inertia that can only support compressive loads of less than half the yield strength without the benefit of antibuckling fixtures. All these support the limited amount of data in the literature on negative stress ratio tests on TMC. To overcome these problems, Lerch and Halford [11] conducted tests using a 32 ply unidirectional TMC over a wide range of R (-1.0 to 0.7) for both stress and strain control at 427°C. Their [11] results showed that tensile mean stresses for a given stress or strain range are detrimental to the fatigue life. Lerch and Halford [11] also concluded that the Soderberg method which normalizes the mean stress by the yield strength was able to correlate all the data.

This investigation will discuss the fatigue behavior data from the evaluation of two stress ratios (R = -1.3, 0.1) and three temperatures (T = 23, 163, 371°C) and compare the results to other TMC references in the literature.

EXPERIMENTAL PROCEDURE

Material and Specimens

The TMC evaluated during this study was a Ti-6Al-2Sn-4Zr-2Mo matrix reinforced with Trimarc-1™(SiC) fibers. The fiber is manufactured by silicon carbide deposition on a tungsten monofilament core with a subsequent deposition of approximately 3 mm of carbon in a three layered outer coating. The composite is not constructed by the traditional foil-fiber-foil layup, but is fabricated using a wire winding methodology. The wires and the fibers are co-wound around a large cylinder using a small amount of binder as Fig. 1. The nominal fiber and wire diameter are approximately 127 mm and 178 mm, respectively. The composite panels have a unidirectional fiber orientation in a 10 ply layup. The fiber spacing was 130 fibers/in and the computed fiber volume fraction based on specimen thickness was determined to be approximately 0.29.

C-Scans of the panels made prior to machining the specimens showed relatively few points of high attenuation which corresponded to exposed fibers. Hence, he specimen machining plan was modified to avoid the regions of high attenuation and exposed fibers. Longitudinal and transverse specimens were water-jet cut from 150 mm x 230 mm panels and low-stress ground to final dimensions while maintaining the thickness in the as received condition. Straight sided along with some dogbone specimens were used in this study primarily due to the expense of manufacturing the composite panels and the large test matrix that was needed to evaluate the material behavior. Both the straight sided and dogbone specimens had a minimum » 8 mm width in the gage section, resulting in an average of 410 fibers in the gage section. The specimens were nominally 2 mm thick and 119 mm long. Virgin and tested specimens revealed that fiber spacing varied from a nearly perfect rectangular array to having multiple pairs and strings of fiber touches (Fig. 2).

Mechanical Test Setup

The schematic of the mechanical test set up is shown in Figure. 3 [10]. A horizontal test frame [12,13] with commercial hydraulic wedge grips and a quartz lamp heating system [14] were used to provide uniform specimen heating for the elevated temperature tests. The quartz lamps were positioned above and below the test specimen to provide a uniform heated zone. Thermal mapping demonstrated a controlled heated zone of 13 mm with less than 0.5% variation over the entire length. Three thermocouples were used inside the gage section to control the three independent temperature control zones.

The combination of straight sided specimens and room temperature tests required silicon carbide matting and brass tabs in the grip section to reach the required test loads and to reduce the likelihood of failures in the grips. The negative stress ratio tests subjected the specimens to compressive loads, 827 MPa, which is greater than the Euler buckling load of 773 MPa. Therefore an anti-buckling fixture was developed to prevent buckling of the test specimen

during the compressive portion of the loading cycle (Fig. 3). The anti-bucking guides were attached to the test frame supports with threaded rods. The threaded rods were screwed into the support to eliminate the space between the specimen and the buckling guide. A 25 mm x 13 mm x 50 mm stiffener was used to increase the moment of inertia of the buckling guides to reduce transverse deformation. The buckling guides consisted of a cylindrical piece of alumna, 3 mm in diameter and 25 mm long, that was placed in contact with the test specimen. This allowed a line contact along the length of the test specimen equal to the width of the buckling guide. A point contact was not sufficient due to the large deformation that that specimen traverses from maximum to minimum load. A high temperature lubricant was used in conjunction with the alumna rod to minimize friction between the specimen and rod. The quartz rods of the extensometer contacted the specimen on the outside of the buckling guide (Fig. 3). A commercial 12 mm gage length high temperature extensometer was modified with bent quartz rods to achieve a 37 mm gage length between tips.

All fatigue tests followed the same procedure prior to the fatigue cycling. After the specimen was mounted on the grips three thermocouples were attached to the specimen (Fig. 4). One thermocouple was attached near the top edge of specimen at the center of the specimen's length and two thermocouples were placed 5 mm from the center near the bottom edge. The buckling guides were then positioned in place and tightened simultaneously to minimize transverse displacement and transverse force in the system. A room temperature modulus measurement was completed at a low stress as a check on the setup and as a comparison to monotonic test results. After successful completion of the modulus check the temperature was raised to the test temperature over a 10 min period. The specimen was held at temperature with zero applied load for another 15 minutes for the entire system to stabilize. Another modulus check was completed at a low stress and compared to monotonic test results. After completion of the modulus check at test temperature the first ten load-displacement cycles at full load were taken and recorded at 1 Hz to capture any initial damage. The load-displacement sampling interval was set to collect approximately 50 data acquisition cycles (DAC) for the entire test. The automated test control and data acquisition were achieved using personal computers.

Test Matrix

The low cycle fatigue test matrix is shown in Table 1. The focus was to characterize the longitudinal and transverse stress-life behavior at three test temperatures; T=23°C, 163°C and 371°C. Two stress ratios, R = -1.3, 0.1 were evaluated for the longitudinal specimens and one, R = 0.1 for the transverse specimens. At each temperature, stress ratio and orientation three different stress levels, (s_i) were chosen so that the of cycles to failure, (N_f) ranged from 50,000 to 400,000 cycles. As shown later, multiple tests were conducted at most of the test conditions.

EXPERIMENTAL RESULTS

Longitudinal Fatigue

The maximum applied stress versus cycles to failure curve for the negative stress ratio, R = -1.3, and positive stress ratio, R = 0.1, tests at the three test temperatures are shown in Figs. 5a and 5b, respectively. The lines shown in the figures are power law curve fits to the data and are represented by the solid, dashed and dotted lines for the tests at T = 23°C, 163°C and 371°C, respectively. All the fatigue data at a given stress level, stress ratio and temperature were within a factor or 2 from the mean value except for the data obtained at T = 23°C, 398 MPa and R = -1.3. There was one runout test data that fell outside the factor of 2 scatter band.

Effect of Temperature

The data in Fig. 5a show that the slope of the isothermal S-N curves for stress ratio, R =

-1.3, increase with an increase in the test temperature. At the lowest stress, 398 MPa the fatigue life decreases with increasing temperature. The curve fits for Fig. 5a indicate that there was a slight increase in the number of cycles to failure with an increase in temperature at the highest stress 636 MPa. This behavior has been observed in some low carbon steels at moderately elevated temperatures. The increase in fatigue strength for the low carbon steels at elevated temperatures were attributed to strain-aging which increased the yield strength in load-controlled cyclic testing caused by the reduction in cyclic plasticity [17]. There is not enough data to make any conclusions about the increase in life at the 636 MPa stress level in the TMC without the benefit of any matrix material characterization.

The data in Fig. 5b show that the slope of the three curve fits stress ratio, R = 0.1, increase with an increase in the test temperature. At both the 398 and 636 MPa stresses the fatigue life decreases with increasing temperature. At the 530 MPa stress the data fall in narrow regime without a well defined trend. The curve fits for the lower two temperatures is reasonable well described by the power law expression. The T = 371°C data show an increase in fatigue life at the 530 MPa stress condition from the power law fit. The increase in life fall outside of the factor of two accepted scatter in fatigue results. Further conclusions cannot be made without the support of matrix material characterization.

The effects of temperature on the unloading modulus and maximum and minimum strain with applied cycles are shown in Fig. 6a and Fig. 6b, respectively for R = -1.3 at s_{max} = 398 MPa. The room temperature test showed no change in either the unloading modulus or the maximum an minimum strain for the first 400,000 cycles. After that point there was indications of damage initiation and accumulation in the unloading modulus and the maximum strain. The specimen failed after 967,853 cycles, outside the gage section and consequently the data shown is not an accurate representation of the material behavior at those test conditions. The elevated temperature test failed inside the gage section after 301,188 cycles. The unloading modulus shows a gradual decline, » 4.2 % over the first » 200,000 cycles. The remaining life, » 100,000 cycles shows a sharp drop in unloading modulus, » 12.6 %. The maximum and minimum strain also show the acceleration in degradation at » 200,000 cycles. The minimum strain show a slight decrease and the maximum shows no change prior to » 200,000 cycles.

Effect of Stress Ratio

The maximum applied stress versus cycles to failure curve for the three temperatures T=23°C, 163°C and 371°C at the two stress ratios are shown in Figs. 7a, 7b and 7c, respectively. The lines shown in the figures are power law curve fits to the data and are represented by the solid and dashed lines for the tests at R = -1.3 and 0.1, respectively.

The data in Figs. 7a, 7b and 7c show that there is a large difference in cycles to failure between the two stress ratios for a given maximum stress. For example in Figs. 7a and 7b at 636 MPa there is greater than an order of magnitude difference in cycles to failure between the two stress ratios. In Fig. 7c at 371°C the difference is only a factor five increase between the R= -1.3 and R = 0.1 curve at 636 MPa.

The effects of stress ratio on the unloading modulus and maximum and minimum strain with applied cycles are shown in Fig 8a and Fig 8b, respectively for T = 371°C and s_{max} = 636 MPa. The unloading modulus for the negative stress ratio test shows a slight decreasing trend to » 10,000 cycles after which the curve sharply drops until failure. This test specimen failed outside the gage section which is evident from the decrease in the maximum and minimum strain curves in Fig. 8a. The decrease in final unloading modulus was » 3.7 % from the initial measurement. The unloading modulus for the R = 0.1 shows a slight increase to » 10,000 after which the curve sharply drops until failure with a final decrease of 9.0 % from the initial measurement. The maximum and minimum strain provide no indication of damage prior to » 100,000 cycles.

Comparison with other TMC Systems

The stress range in the fiber ($\Delta\sigma_f$) versus cycles to failure (N_f) data are plotted in Fig. 9 from the tests at 371°C. For a given $\Delta\sigma_f$, R=-1.3 yields longer life than R=0.1. This implies that the higher mean stress at R=0.1 results in decrease of fatigue life. Similar trends were also observed at 23 and 163°C. Based on tests at R=-1.0 to 0.7, Lerch and Halford [11] also reported the same behavior for SCS-6/Ti-15-3 tested at 427°C. The data from Lerch and Halford [11] for R=0.0 and -1.0 are also plotted in Fig. 9. These stress ratios are close to the R tested in this study. Even though, SCS-6/Ti-15-3 was tested at a higher temperature and different stress ratios, the data from this composite are consistent with the trend observed for Trimarc-1/Ti-6-2-4-2.

Figure 10 shows the maximum fiber stress versus cycles to failure for $[0]_{10}$ Trimarc-1/Ti-6Al-2Sn-4Zr-2Mo and for other titanium matrices reinforced with SCS-6 fibers. The 6 ply layups of SCS-6/Ti-15-3, SCS-6/Ti-6-4 and SCS-6/Ti-25-10 were tested by Jeng et al. [2] at R=0.1 and 23°C. $[0]_8$ SCS-6/Ti-15-3 was tested by Johnson [1] at R=0.1 and 23°C and $[0]_{32}$ was tested by Lerch and Halford [11] at R=0.0 and 427°C. Interestingly, the maximum fiber stress for all the composites follow the same trend. The contribution of the Trimarc-1™ fibers appears to be similar to that of the SCS-6 fibers, at least at these temperatures. The trend shown in Fig. 10 is also consistent with the fiber dominated failure observed in layups with 0° fibers. Figure 10 is similar to the plot used by Johnson [1] to compare the 0° fiber stresses in different layups of SCS-6/Ti-15-3. The data shown in Fig. 10 indicates an apparent *in situ* fatigue limit of ≈ 1200 MPa for the SCS-6 and Trimarc-1 fibers at temperatures ≤ 427°C.

Correlation of Data Obtained at Two Stress Ratios

We used the Walker-Parameter [18] approach in attempt to correlate and predict the data obtained during this study. The Walker-Parameter, W_P is given by,

$$W_p = \sigma_{max}(1-R)^m = \Delta\sigma_a^m \sigma_{max}^{1-m}. \qquad (1)$$

where m is a fit parameter ranging from 0.3 to 0.7 for metals [22]. W_p was related to N_f using the following equation.

$$\log(N_f) = A_1 + A_2 \log(W_p). \qquad (2)$$

Figure 11 shows Eqn. (2) applied to the data obtained at 23°C for R=-1.3, 0.1. The constants A_1, A_2 and m, obtained using the R=-1.3, 0.1 data, are reported in Table 2 for the three temperatures. The values of m are 0.47, 0.51 and 0.39 for the data at 23°C, 163°C and 371°C, respectively. These values are within the range reported for metals [22]. In contrast, Lerch and Halford [11] reported a low value of m=0.12 for SCS-6/Ti-15-3 tested at 427°C. The correlation and predictive capabilities of Eqn. (2) are shown in Figs. 12(a)-12(c) for temperatures 23°C, 163°C and 371°C, respectively. The solid line corresponds to a perfect prediction and the dashed lines correspond to 2X variation in fatigue life. In Figs. 12(b) only one data point fell outside a 2X variation from the prediction. In Fig. 12(a) and 12(c) all the data points fell inside the 2X variation from the prediction. The constants obtained from the R=-1.3, 0.1 data were used to predict the cycles to failure for the R=0.5 at 163°C and R=0.7 at 371°C as shown in Figs. 12(b) and 12(c), respectively. Additional tests are required at different stress ratios to verify the true predictive capabilities of Eqn. (2) at other temperatures.

Transverse Fatigue

Figure 13 is a plot of maximum applied stress versus cycles to failure for the transverse specimens at the three test temperatures for stress ratio, R = 0.1. There are several instances were there was a factor of three or larger difference in the cycles to failure for identical test

conditions. Often the low cycles to failure data can be explained by extremely poor fiber spacing as shown in Fig. 2b.

John et al. [19-21] showed that the creep-rupture and fatigue crack growth behavior of unidirectionally reinforced MMC subjected to transverse loading can be predicted using a net-section based model. The model is based on the assumption that the fibers in MMC subjected to transverse loading are essentially ineffective during the majority of the life. A schematic of the transverse model is shown in Fig. 14. The matrix stress in the ligament between the fibers can be calculated as,

$$\Delta\sigma_{lig} = \frac{\Delta\sigma_{90}}{F_n}, \qquad (3)$$

where

$$F_n = 1 - \frac{2R_f}{B_p}, \qquad (4)$$

$\Delta\sigma_{90}$ = applied far-field stress range for the [90] composite, $\Delta\sigma_{lig}$= stress range in the matrix ligament between the fibers, R_f= fiber radius (=64 μm), B_p=average ply thickness = B/n, B= thickness of composite, and n=number of plies. Using the geometry shown in Fig. 14, Eqn. (4) can also written as [20],

$$F_n = 1 - \sqrt{\frac{4 V_f s}{\pi B_p}}, \qquad (5)$$

where s = center-center fiber spacing along the length of the [90] composite = 0.195 mm. Equation (5) reduces to the expression derived by Walls et al. [23] for a square array, i.e. when $s=B_p$. Thus, by equating $\Delta\sigma_{lig}$ to the matrix behavior, $\Delta\sigma_{90}$ can be predicted.

The maximum stress, σ_{max} versus N_f data for neat (fiberless) Ti-6-2-4-2 and $[90]_{10}$ Trimarc-1/Ti-6-2-4-2 is shown in Fig. 15 from tests conducted at 163°C with R=0.1. Note that the matrix data was obtained from specimens which were prepared such that the matrix wires were oriented perpendicular to the loading axis. The following expression [21] was used to represent the matrix behavior.

$$\sigma_{max} = \sigma_{m,th} + \left(\sigma_{m,u} + \sigma_{m,th}\right) e^{p(\log N_f)^q} \qquad (6)$$

where $\sigma_{m,u}$ = ultimate matrix stress = 840 MPa, $\sigma_{m,th}$= threshold matrix stress = 325 MPa, and p and q are fit constants. For the fit of the matrix data shown in Fig. 15, p = -0.054 and q = 2.75. Using Eqns. (5) and (6), and assuming $\Delta\sigma_{lig} = \Delta\sigma_m = \sigma_{max}^*(1-R)$, the composite fatigue behavior, i.e. $\Delta\sigma_{90}$ versus N_f was predicted and plotted as a solid line in Fig. 15. The prediction correlates well with the overall trend of the data. The tensile strength of the composite (N_f=1) and the threshold regime are predicted satisfactorily [21]. The model correctly predicts the near-flat S-N behavior for stresses ≤ 200 MPa exhibited by the data. Figure 15 also shows that the fatigue behavior occurs over a small range of stress for the $[90]_{10}$ composite, i.e the S-N curve is not conducive to a design based on cycle dependent "design" stress. In contrast, a threshold type approach, i.e. design stress < σ_{th} appears to be more appropriate.

The model assumes that the fibers are located in a straight row. Hence, the assumed fracture plane is always perpendicular to the applied load and follows the narrowest matrix ligament between the fibers. But, in actual practice, the arrangement of the fibers maybe staggered and consequently, the fracture surface could be tortuous as shown in Figs. 16(a)-16(d). The dashed lines close to the prediction correspond to the fatigue behavior predicted for

±10% variation in $\Delta\sigma_{lig}$. These predictions highlight the large variations in predicted N_f due to small changes in $\Delta\sigma_{lig}$ for stress levels ≤ 200 MPa.

As seen in Fig. 15, the data for $[90]_{10}$ composite shows significant scatter for stresses ≤ 200 MPa. This regime coincides with the predicted threshold-type behavior as given by the solid line in Fig. 15. Figure 16 shows the edge view of the fracture surface of specimens 96-K39 and 96-K43 both tested at s_{max} = 190 MPa and T = 163°C in Figs. 16(a)-(b) and 16(c)-(d), respectively. The specimen 96-K43 failed at 40,846 cycles while the specimen 96-K39 actually lasted almost 10X longer. Comparing the Figs. 16(a)-16(d), we see that the fracture surface of 96-K39 is more tortuous than that of 96-K43. Hence the effective fracture surface area of the matrix ligament between the fibers in 97-K39 could be higher than that of 97-K43. Hence, the effective $\Delta\sigma_{lig}$ for 97-K43 could be lower than that of 97-K39. As shown by the model predictions (dashed lines) in Fig. 15, such small variations in stress can easily translate to large variations in N_f. Hence, establishing a σ_{th} value for design will require numerous tests.

Detailed examinations of the fracture surface and characterization of the variations in fibers spacing, fiber touches etc. are in progress to determine their effect on the cycles to failure. Preliminary results appear to indicated that an excessive amount of fiber touches does reduce the fatigue life of the transverse specimens.

CONCLUSIONS

An experimental investigation of the low-cycle fatigue behavior of the Trimarc-1/Ti-6Al-2Sn-4Zr-2Mo unidirectional composite were conducted at temperatures of 23°C, 163°C and 371°C at stress ratios -1.3 and 0.1 for longitudinal tests and 0.1 for transverse tests at a frequency of 3 Hz. The data for different stress ratios was combined using the Walker [18] approach and shown to fall within a 2X variation in fatigue life for the three test temperatures. The results of these tests, along with comparisons to other TMC systems demonstrated that fatigue data collapse together for a 0° fiber stress range or maximum versus cycles to failure plot. A net-section model [19-21] using the matrix S-N data predicted the fatigue response of the [90] composite. The model and the data showed that small variations in the stress can produce large variations in the cycles to failure of the [90] composite.

ACKNOWLEDGMENT

This research was conducted at Wright Laboratory (WL/MLLN), Materials Directorate, Wright-Patterson Air Force Base, OH 45433-7817, USA. D. J. Buchanan, R. John and K. E. Goecke were supported under on-site contract number F33615-94-C-5200. The authors gratefully acknowledge the efforts Mr. M. J. Shepard for his many hours on the SEM photographing fracture surfaces.

REFERENCES

[1] Johnson, W. S., "Fatigue Testing and Damage Development in Continuous Fiber Reinforced Metal Matrix Composites," Metal Matrix Composites: Testing, Analysis, and Failure Modes, ASTM STP 1032, W. S. Johnson, Ed., American Society for Testing and Materials, Philadelphia, PA, USA, 1989, pp. 194-221.

[2] Jeng, S. M., Wang, P. C. and Yang, J. -M., "Fatigue Damage Evolution and Degradation of Mechanical Properties in Silicon-Carbide (SiC) Fiber-Reinforced Titanium Matrix Composites," Life Prediction Methodology for Titanium Matrix Composites, ASTM STP 1253, W. S. Johnson, J. M. Larsen and B. N. Cox, Eds., American Society for Testing and Materials, Philadelphia, PA, USA, 1996, pp. 377-394.

[3] Bakuckas, J. G., Jr., and Johnson, W. S., "A Methodology to Predict Damage Initiation, Damage Growth, and Residual Strength in Titanium Matrix Composites," Life Prediction Methodology for Titanium Matrix Composites, ASTM STP 1253, W. S. Johnson, J. M. Larsen and B. N. Cox, Eds., American Society for Testing and Materials, Philadelphia, PA, USA, 1996, pp. 497-519.

[4] Harmon, D. M. and Saff, C. R., "Damage Initiation and Growth in Fiber Reinforced Metal Matrix Composites," Metal Matrix Composites: Testing, Analysis, and Failure Modes, ASTM STP 1032, W. S. Johnson, Ed., American Society for Testing and Materials, Philadelphia, PA, USA, 1989, pp. 237-250.

[5] Wang, P. C., Jeng, S. M., Yang, J. -M. and Russ, S. M., "Fatigue Damage Evolution and Property Degradation of SCS-6/Ti-22Al-23Nb Orthorhombic Titanium Aluminude Composite," Acta Metallurgica, Vol. 44, No. 8, 1996, pp. 3141-3156.

[6] Wang, P. C., Jeng, S. M., Yang, J. -M. and Mall, A. K., "Fatigue Life Prediction of Fiber-Reinforced Titanium Matrix Composites," Acta Metallurgica, Vol. 44, No. 3 1996, pp. 1097-1108.

[7] Neu, R. W. and Nicholas, T., "Methodologies for Predicting the Thermomechanical Fatigue Life of Unidirectional Metal Matrix Composites," Advances in Fatigue Lifetime Predictive Techniques: 3rd Volume, ASTM STP 1292, M. R. Mitchell and R. W. Landgraf, Eds., American Society for Testing and Materials, Philadelphia, PA, USA, 1996, pp. 1-23.

[8] Nicholas, T., "Fatigue Life Prediction in Titanium Matrix Composites," Transactions of the ASME, Vol. 117, 1995, pp. 440-447.

[9] Nicholas, T. and Kroupa, J. L., "Micromechanics Analysis and Life Prediction of Titanium Matrix Composites," Submitted for publication in Journal of Composites Technology & Research, 1996.

[10] Blatt, A, P. and Stevens, K. A., "Unpublished Work," Materials Directorate, Wright Laboratory, Wright-Patterson Air Force Base, 1995.

[11] Lerch, B. and Halford, G., "Fatigue Mean Stress Modeling in a $[0]_{32}$ Titanium Matrix Composite," Proceedings of the 7th Annual HITEMP Review, Vol. II, Paper No. 21, 1996, pp. 1-10.

[12] Hartman, G. A., III and Russ, S. M., "Techniques for Mechanical and Thermal Testing of Ti_3Al/SCS-6 Metal Matrix Composites," Metal Matrix Composites: Testing, Analysis, and Failure Modes, ASTM STP 1032, W. S. Johnson, Ed., American Society for Testing and Materials, Philadelphia, PA, USA, 1989, pp. 43-53.

[13] Hartman, G. A., and Buchanan, D. J., "Methodologies for Thermal and Mechanical Testing of TMC Materials," Characterisation of Fibre Reinforced Titanium Matrix Composites, 77th Meeting of the AGARD Structures and Materials Panel, AGARD Report 796, Bordeaux, France, 27-28 September 1993.

[14] Hartman, G. A., III, "A Thermal Control System for Thermal/Mechanical Cycling," Journal of Testing and Evaluation, JTEVA, Vol. 13, No. 5, September 1985, pp. 363-366.

[15] Larsen, J. M., Russ, S. M. and Jones, J. W., "An Evaluation of Fiber-Reinforced Titanium Matrix Composites for Advanced High-Temperature Aerospace," Metallurgical and Materials Transactions, Vol 26A, December 1985, pp. 3211-3223.

[16] Hartman, G. A., Ashbaugh, N. E., and Buchanan, D. J., "A Sampling of Mechanical Test Automation Methodologies Used in a Basic Research Laboratory," Automation in Fatigue and Fracture: Testing and Analysis, ASTM STP 1231, C. Amzallag, Eds., American Society for Testing and Materials, Philadelphia, PA, USA, 1994, pp. 36-50.

[17] Sandor, B. I., "Achievement of High Fatigue Resistance in Metals and Alloys," ASTM STP 467, American Society for Testing and Materials, Philadelphia, PA, USA, 1970, pp. 254-275.

[18] Walker, K, "The Effect of Stress Ratio During Crack Growth Propagation and Fatigue for 2024-T3 and 7075-T6 Aluminum," ASTM STP 462, American Society for Testing and Materials, Philadelphia, PA, USA, 1970, pp. 1-14.

[19] John, R., Lackey, A. F., and Ashbaugh, N. E., "Fatigue Crack Growth Parallel to Fibers in Unidirectionally Reinforced SCS-6/TIMETAL®21S," Scripta Materialia, Vol. 35, No. 6, 1996, pp. 711-716.

[20] John, R., Khobaib, M., and Smith, P. R., "Prediction of Creep-Rupture Life of Unidirectional Titanium Matrix Composites Subjected to Transverse Loading," Metallurgical and Materials Transactions, Vol. 27A, October 1996, pp. 3074-3080.

[21] John, R., Larsen, J. M., Buchanan, D. J., and Hall, J., "Prediction of Fatigue Strength of Unidirectional Titanium Matrix Composites Subjected to Transverse Loading," To be submitted for publication, 1997.

[22] Military Standardization Handbook, Metallic Materials and Elements for Aerospace Vehicle Structures, MIL-HDBK-5E, Vols. 1 & 2, 1987.

[23] Walls, D. P., Bao, G., and Zok, F. W., "Mode I Fatigue Cracking in a Fiber Reinforced Metal Matrix Composite," Acta Metallurgica et Materialia, Vol. 41, No. 7, 1993, pp. 2061-2071.

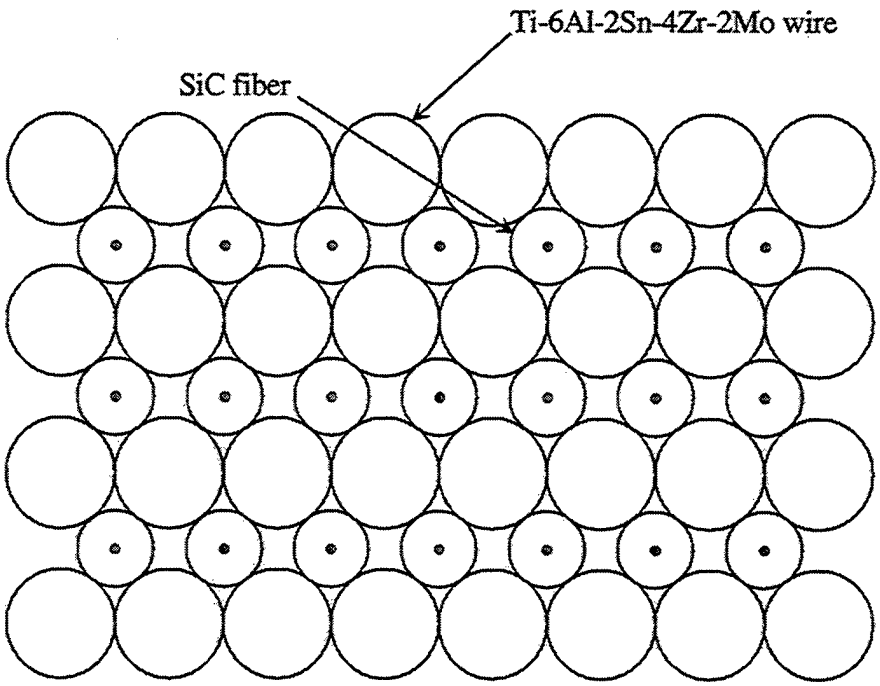


Figure 1. Schematic showing the co-wound SiC fibers and the titanium wires for the 10 ply layup of the unidirectional Trimarc-1/Ti-6Al-2Sn-4Zr-2Mo composite.

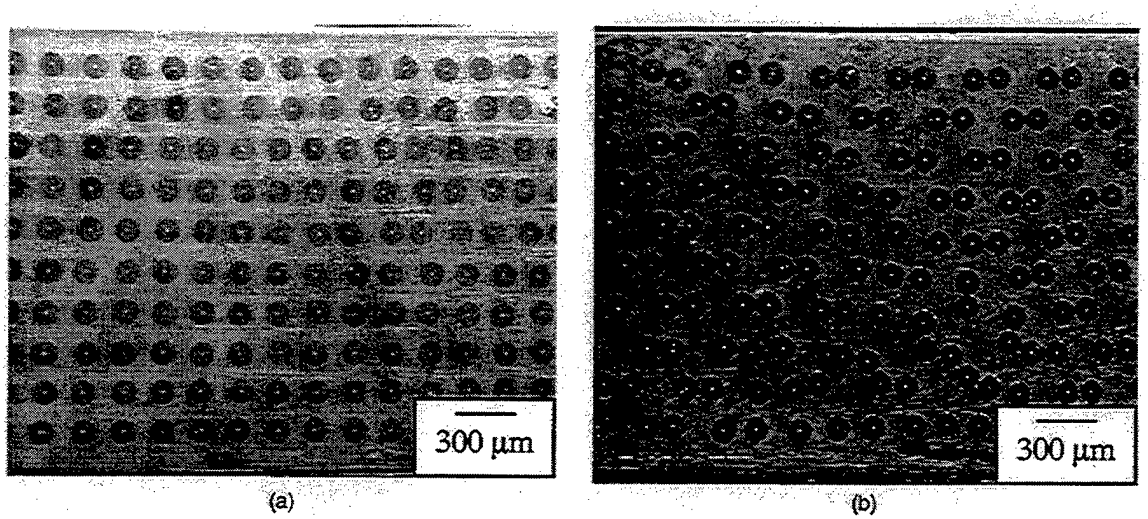


Figure 2. Photomicrographs showing variation in fiber spacing observed in Trimarc-1/Ti-6Al-2Sn-4Zr-2Mo composite specimens.

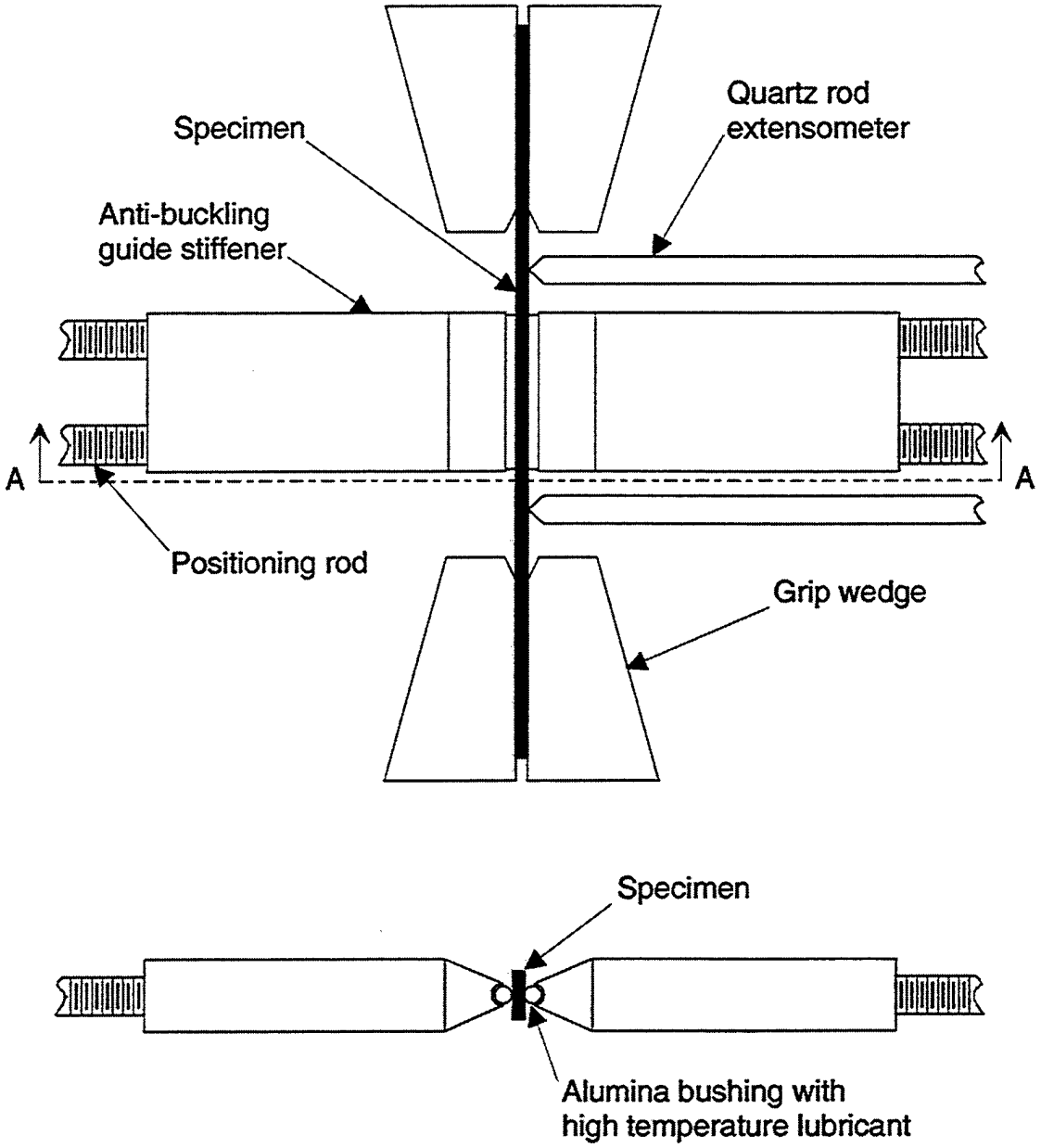


Figure 3. Schematic of anti-buckling guide setup for negative stress ratio tests.

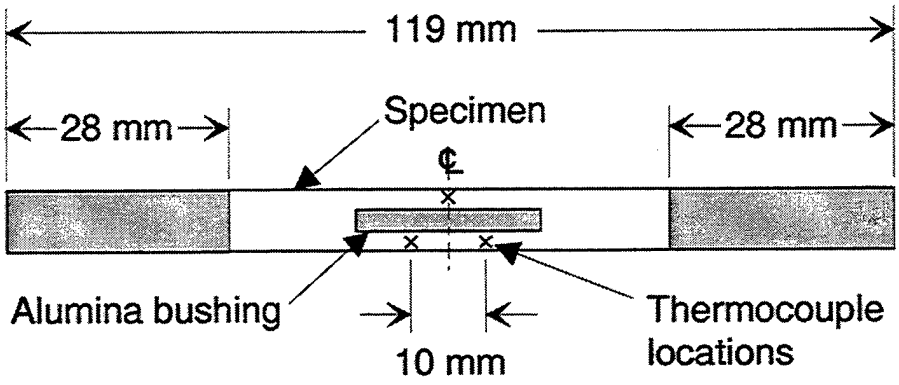


Figure 4. Schematic of test specimen with placement of thermocouple locations and alumina bushing for negative stress ratio tests.

Orientation	Stress Ratio	Stress Levels, σ_i (MPa)								
		23°C			163°C			371°C		
		σ_1	σ_2	σ_3	σ_1	σ_2	σ_3	σ_1	σ_2	σ_3
$[0]_{10}$	-1.3	398	530	636	398	530	636	398	530	636
$[0]_{10}$	0.1	724	827	900	636	827	900	636	827	900
$[90]_{10}$	0.1	150	160	170	180	190	200	140	150	160

Table 1. Test matrix for the load controlled isothermal fatigue tests on Trimarc-1/Ti-6Al-2Sn-4Zr-2Mo composite.

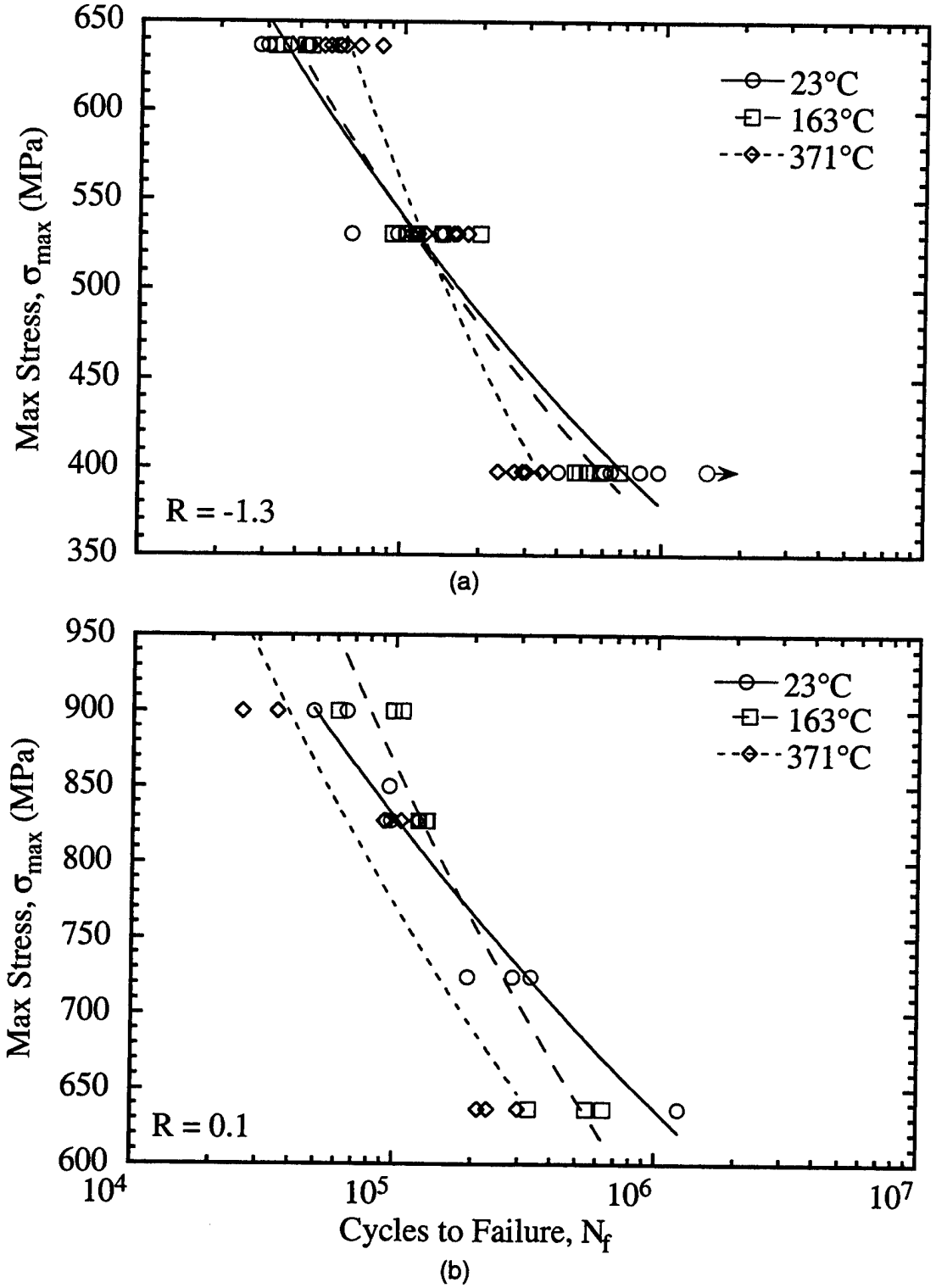


Figure 5. Effects of temperature on S-N behavior of $[0]_{10}$ Trimarc-1/Ti-6Al-2Sn-4Zr-2Mo for (a) R = -1.3 and (b) R = 0.1.

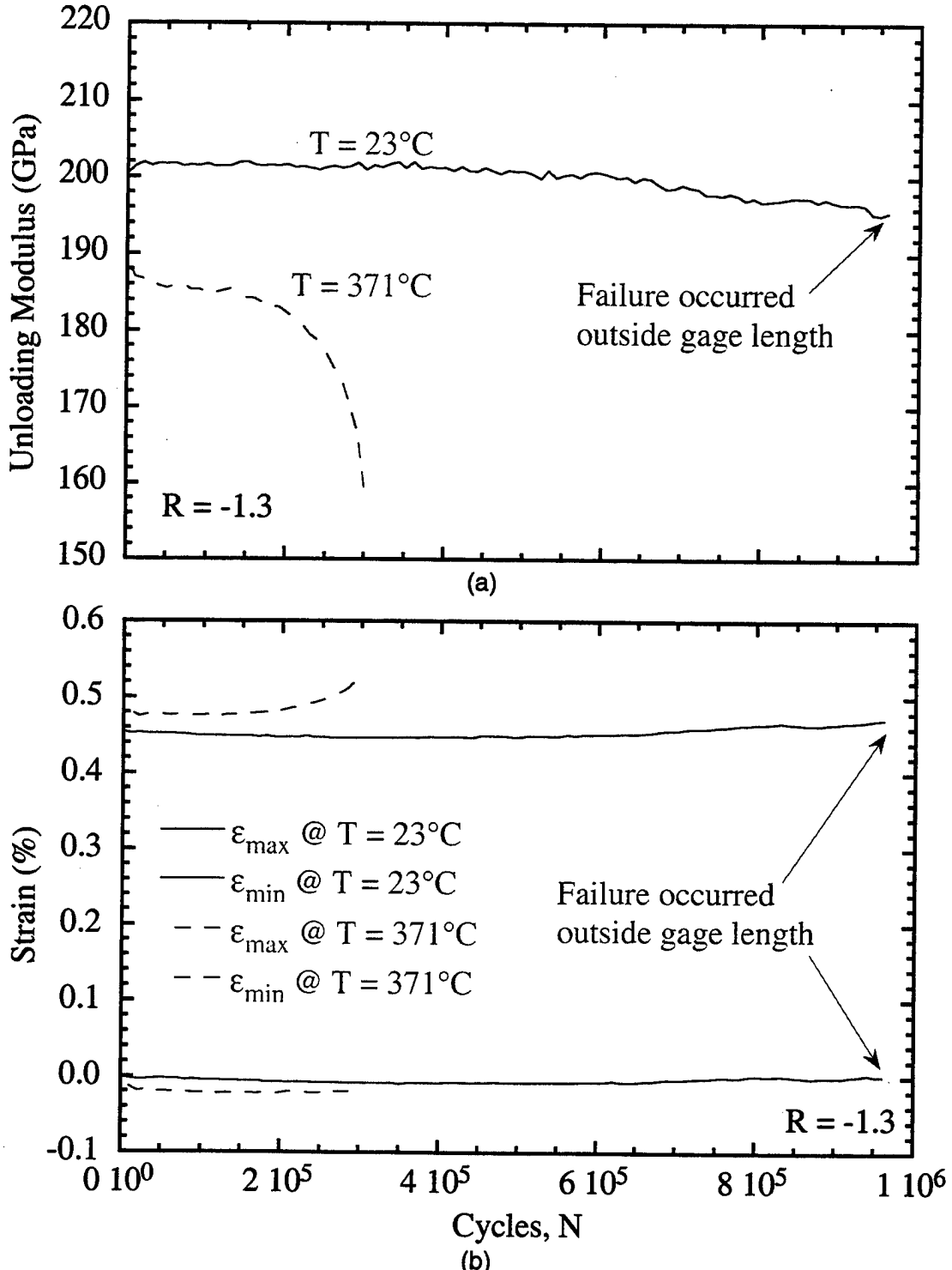


Figure 6. Effects of temperature on (a) maximum and minimum strain and (b) unloading modulus versus applied fatigue cycles for $[0]_{10}$ Trimarc-1/Ti-6Al-2Sn-4Zr-2Mo for R = -1.3, s_{max} = 397.8 MPa at T = 23°C and 371°C.

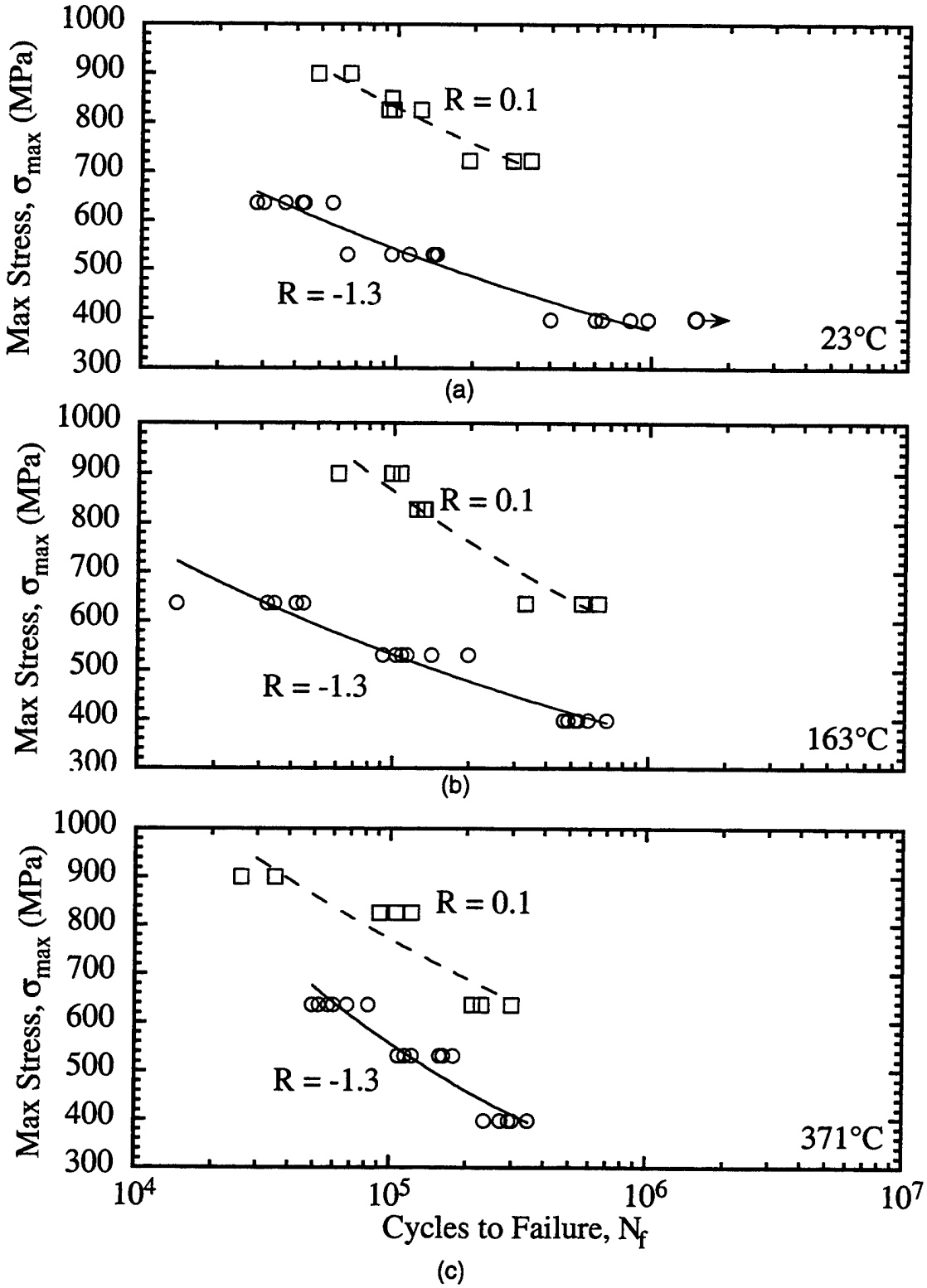


Figure 7. Effects of stress ratio on S-N behavior of $[0]_{10}$ Trimarc-1/Ti-6Al-2Sn-4Zr-2Mo for (a) T=23°C, (b) T=163°C and (c) T=371°C.

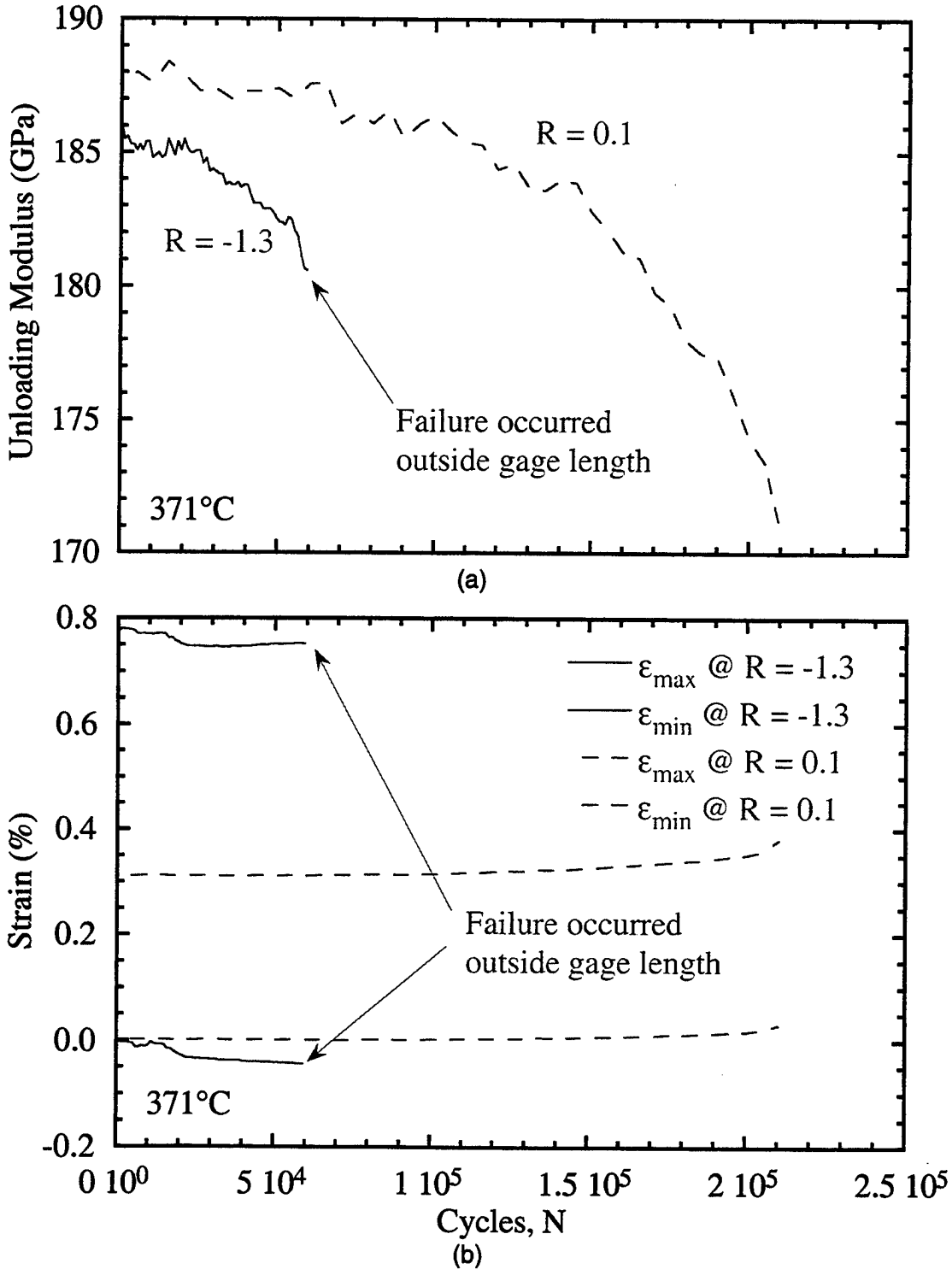


Figure 8. Effects of stress ratio on (a) maximum and minimum strain and (b) unloading modulus versus applied fatigue cycles for $[0]_{10}$ Trimarc-1/Ti-6Al-2Sn-4Zr-2Mo for T = 371°C, s_{max} = 636.4 MPa.

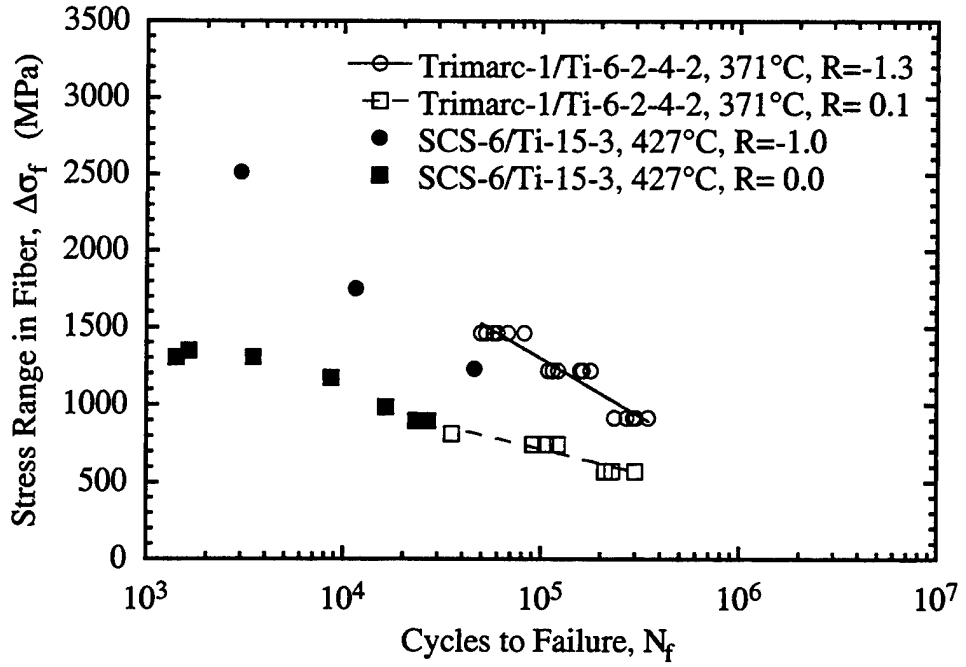


Figure 9. Stress range versus cycles to failure for two material systems, Trimarc-1/Ti-6Al-2Sn-4Zr-2Mo and SCS-6/Ti-15-3.

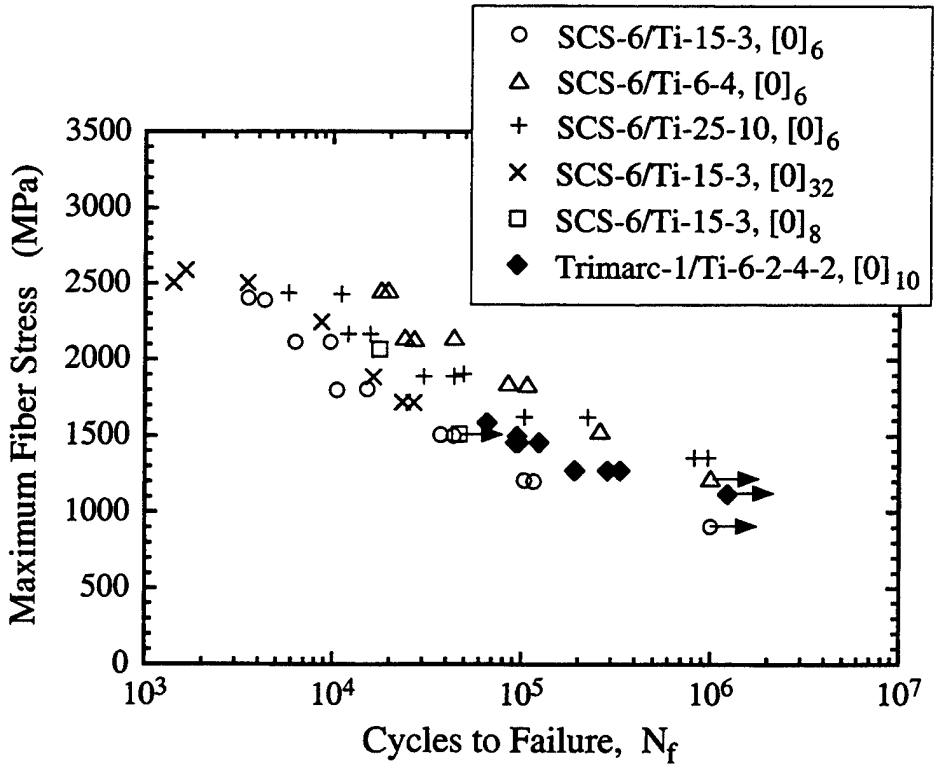


Figure 10. Maximum fiber stress in 0° fibers versus cycles to failure for $[0]_{10}$ Trimarc-1//Ti-6Al-2Sn-4Zr-2Mo and other titanium matrices reinforced with SCS-6 fibers.

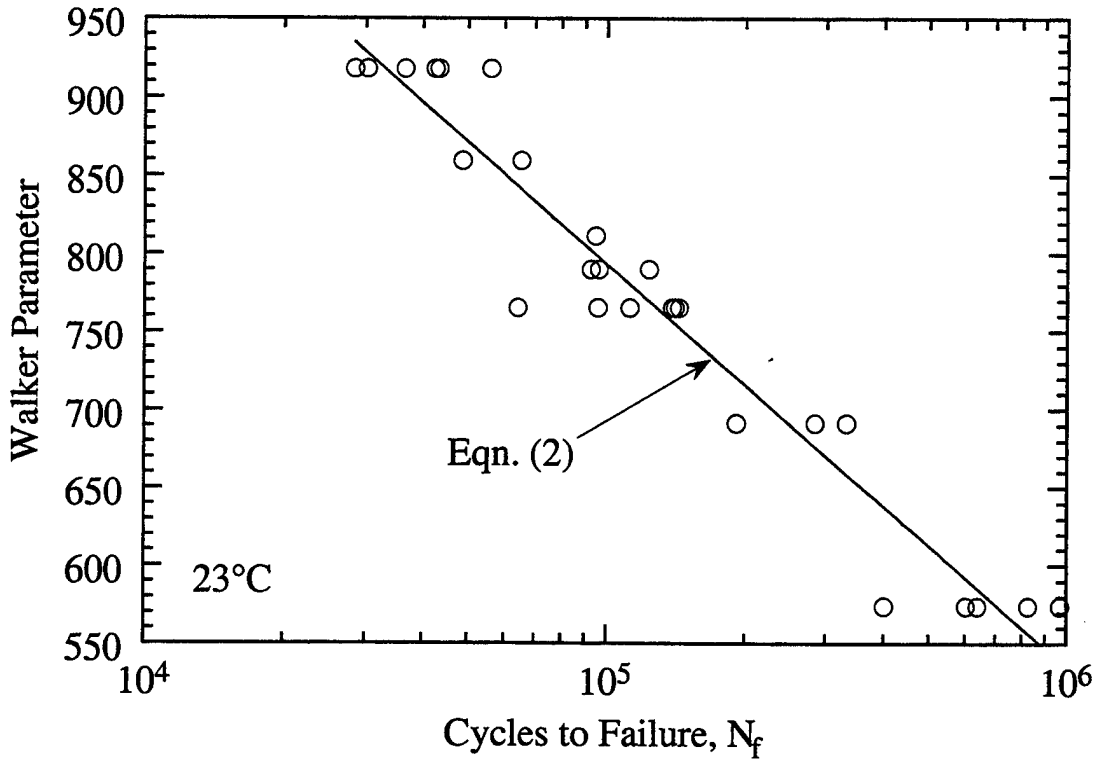


Figure 11. Walker-Parameter versus cycles to failure for Trimarc-1/Ti-6Al-2Sn-4Zr-2Mo at T = 23°C, R = -1.3, 0.1.

T (°C)	A_1	A_2	m
23	23.57	-6.39	0.47
163	21.68	-5.73	0.51
371	15.04	-3.48	0.39

Table 2. Walker-Parameter coefficients for Trimarc-1/Ti-6Al-2Sn-4Zr-2Mo at T = 23°C, 163°C and 371°C at R = -1.3, 0.1.

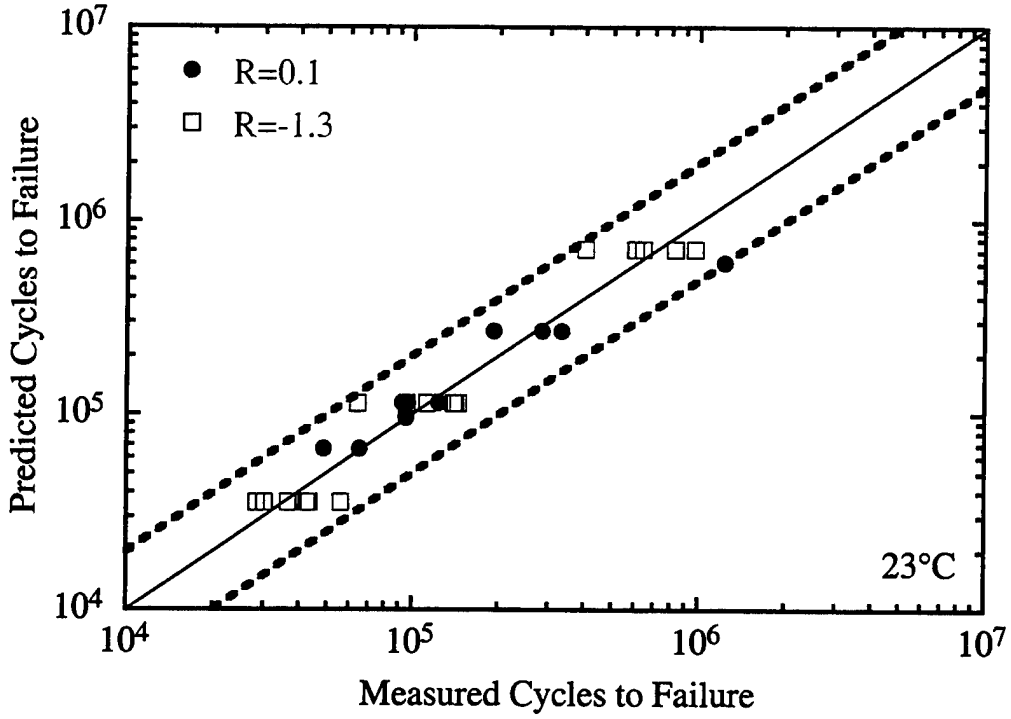


Figure 12(a). Predicted versus measured cycles to failure using the Walker-Parameter approach for $[0]_{10}$ Trimarc-1/Ti-6Al-2Sn-4Zr-2Mo at 23°C for R = -1.3, 0.1

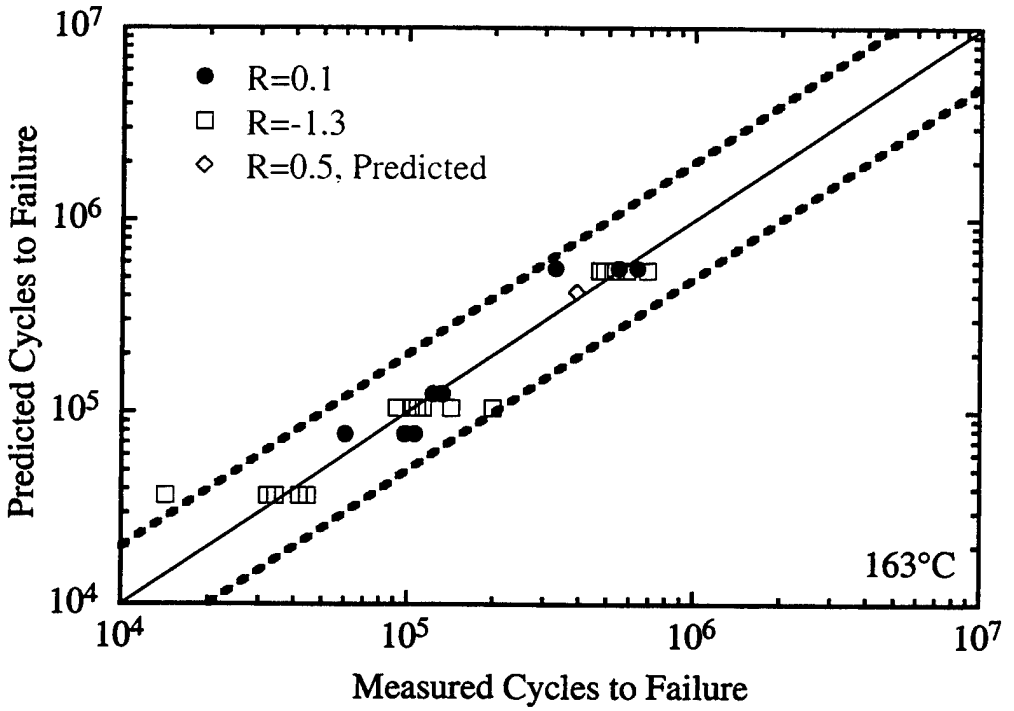


Figure 12(b). Predicted versus measured cycles to failure using the Walker-Parameter approach for $[0]_{10}$ Trimarc-1/Ti-6Al-2Sn-4Zr-2Mo at 163°C for R = -1.3, 0.1 and 0.5.

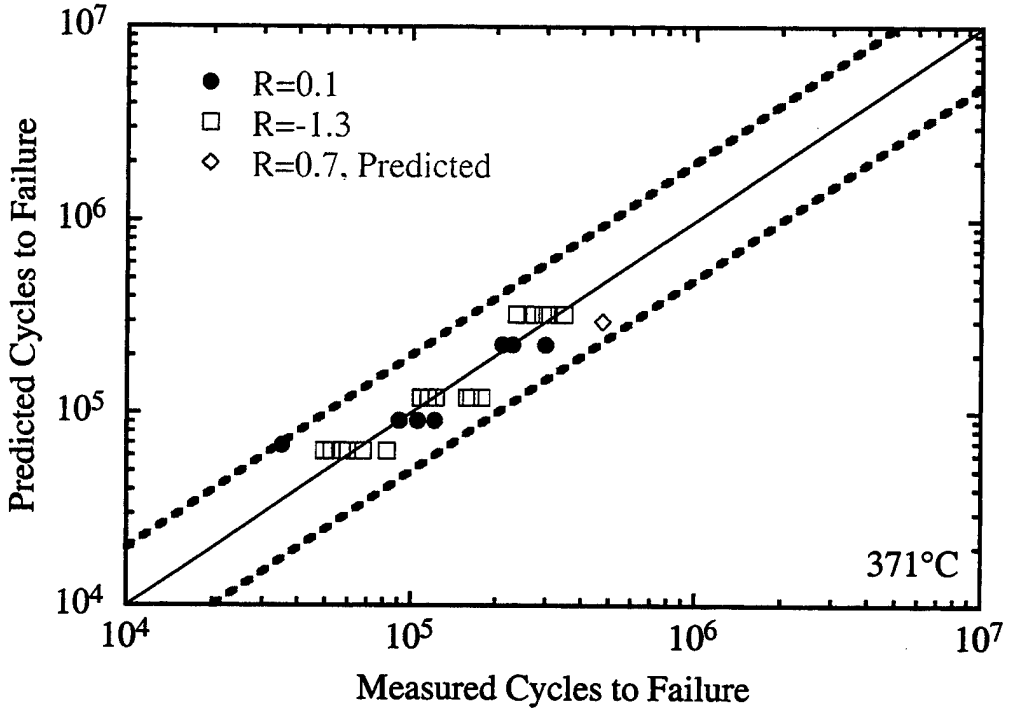


Figure 12(c). Predicted versus measured cycles to failure using the Walker-Parameter approach for $[0]_{10}$ Trimarc-1/Ti-6Al-2Sn-4Zr-2Mo at 371°C for R = -1.3, 0.1 and 0.7.

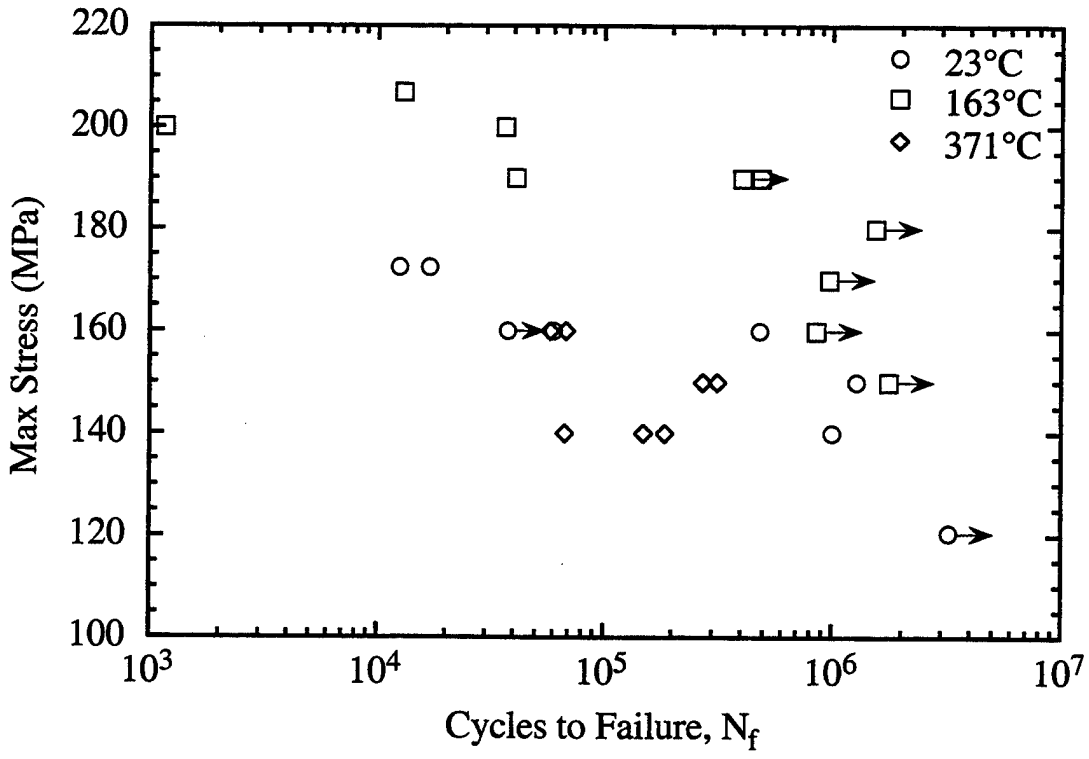


Figure 13. Effects of temperature on cycles to failure of $[90]_{10}$ Trimarc-1/Ti-6Al-2Sn-4Zr-2Mo for R = 0.1.

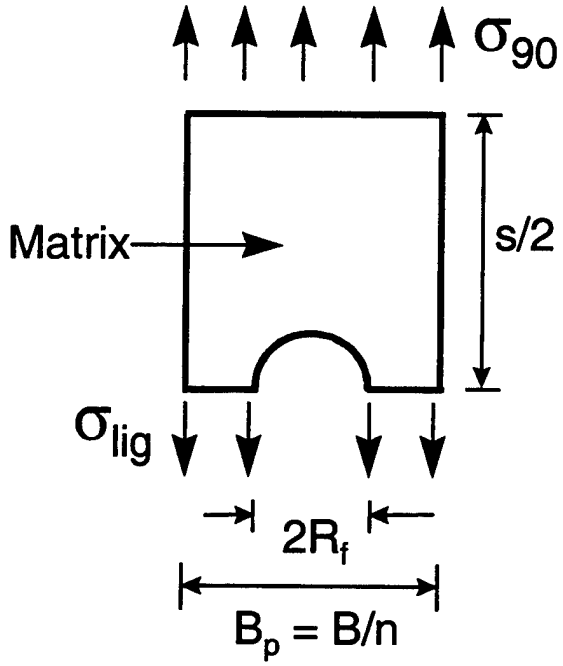


Figure 14. Schematic diagram of rectangular net section model used for the life prediction of the unidirectional [90] orientation composite.

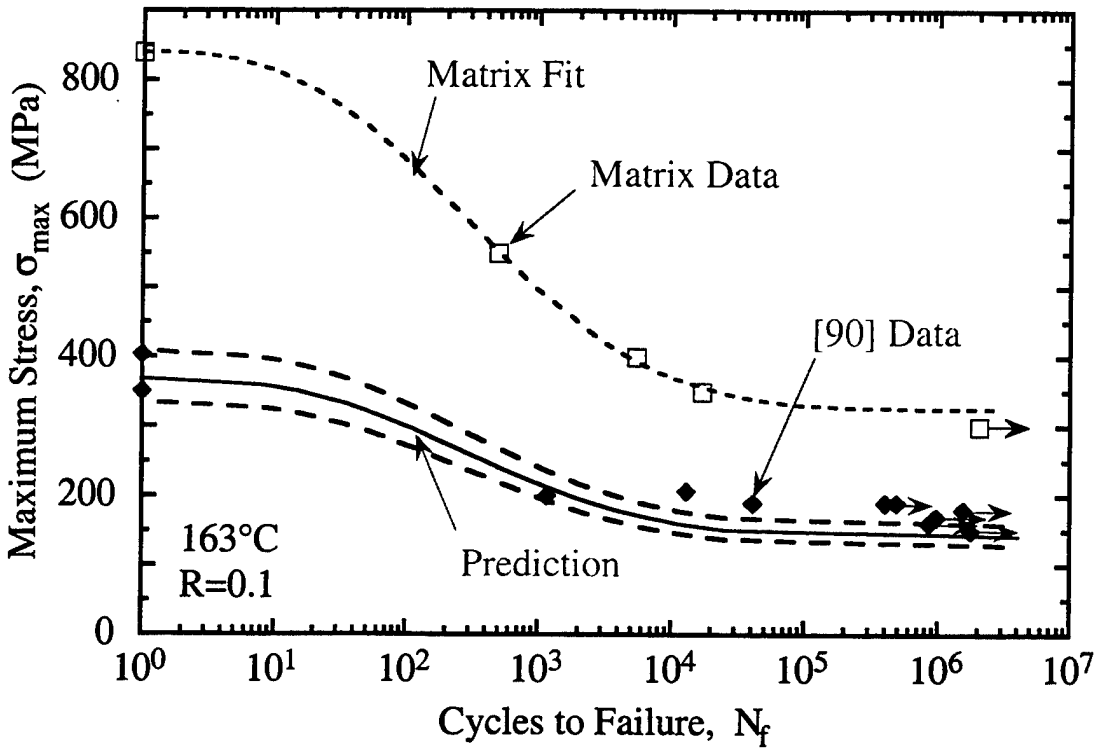
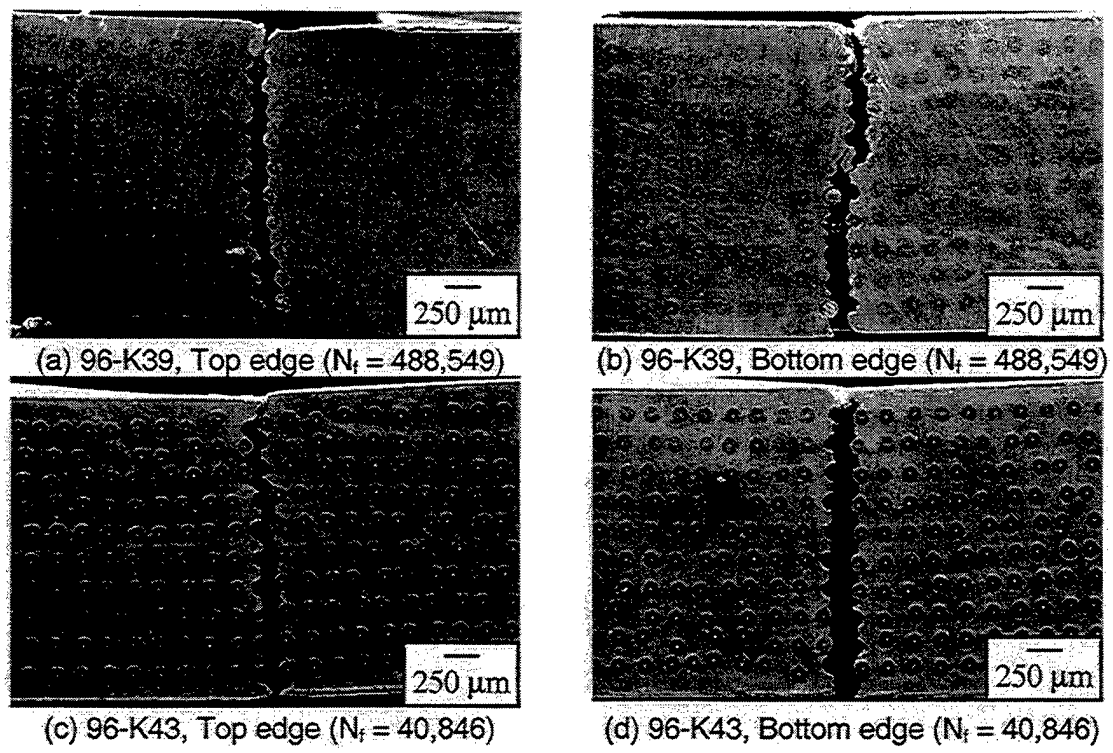


Figure 15. Prediction of $[90]_{10}$ S-N behavior from neat Ti-6Al-2Sn-4Zr-2Mo for R = 0.1 at T = 163°C.



(a) 96-K39, Top edge (N_f = 488,549)
(b) 96-K39, Bottom edge (N_f = 488,549)
(c) 96-K43, Top edge (N_f = 40,846)
(d) 96-K43, Bottom edge (N_f = 40,846)

Figure 16. Photomicrographs of fracture planes for two $[90]_{10}$ Trimarc-1/Ti-6Al-2Sn-4Zr-2Mo specimens at identical test conditions: s_{max} = 190 MPa, R = 0.1 and T = 163°C with an order of magnitude difference in their cycles to failure.

This page intentionally left blank

Reference: Nicholas, T., and Kroupa, J.L., "Micromechanics Analysis and Life Prediction of Titanium Matrix Composites," J. of Composites Technology & Research, JCTRER, V.20, No. 2, pp. 79-88.

T. Nicholas[1] and J. L. Kroupa[2]

Micromechanics Analysis and Life Prediction of Titanium Matrix Composites

ABSTRACT: The response of a unidirectional SCS-6/Ti-6Al-4V composite is evaluated under a range of isothermal fatigue (IF) and thermomechanical fatigue (TMF) conditions. Both processing and thermomechanical test conditions are simulated using a cylinder in cylinder code, FIDEP, which treats the fiber as thermoelastic while the matrix is characterized using a recent version of the Bodner-Partom constitutive law. Computed stresses and strains in the constituents are obtained after 10 cycles of loading and are used as input into a new and simpler version of a life fraction model. Applied stress at temperature and computed matrix strains are used for the time-dependent and matrix fatigue terms in the model, respectively. Cyclic stress-strain behavior of the matrix material is also computed and used, together with fatigue life data, to identify the governing mechanisms and to explain the observed trends in fatigue life as a function of frequency and applied stress level. Comparisons of fatigue behavior with that of SCS-6/Timetal 21S illustrate differences when tested under nominally similar conditions.

KEYWORDS: metal matrix composites (MMCs), micromechanics, life prediction, thermomechanical fatigue, constitutive model

[1] Senior scientist, USAF Wright Laboratory, Wright-Patterson AFB, OH
[2] Senior engineer, Research Applications Inc., Dayton, OH

Titanium matrix composites, which have received considerable attention in recent years for high temperature aerospace applications, exhibit complex behavior under the most general combinations of thermal and mechanical loading conditions.. To develop life prediction methodologies and to understand the controlling mechanisms, micromechanics analyses have been utilized to describe the constituent behavior. These analyses have to take into account the thermoviscoplastic properties of the matrix in order to provide realistic solutions for the behavior of the composite as well as the stress states within the constituents. In processing alone, very large residual stresses can result from the cool down cycle. Under thermal cycling, significant stresses can arise because of the coefficient of thermal expansion (CTE) mismatch between fiber and matrix. Under creep, isothermal fatigue, and thermomechanical fatigue (TMF), complex stress histories are produced in the fiber and matrix from the combination of applied loads as well as thermal histories. In these situations, the matrix material can undergo creep, stress relaxation, and cyclic inelastic deformation. It is important to capture this behavior in a robust constitutive model in order to adequately represent the composite response. The constituent behavior can then be used as input to a life prediction model. Because of the variety of mechanisms which are reported to control fatigue life in TMCs [1,2], models containing more than one term or parameter have been found necessary to describe the fatigue life accurately under a wide variety of loading conditions.

Neu and Nicholas [3] presented two fatigue life prediction methods which assume that life depends on at least two fatigue damage mechanisms and, therefore, must consist of at least two terms. They showed that a single parameter cannot be used in collapsing fatigue data from a variety of IF and TMF conditions because the mechanisms are different for each type of test, frequency, stress ratio, temperature, etc. Several parameters and models to correlate the cycles to failure of a unidirectional metal matrix composite (SCS-6/Timetal®21S) undergoing

thermal and mechanical loading were examined. Using a large body of fatigue data on that composite covering maximum temperatures up to 815°C, a single parameter based on either the fiber or matrix behavior was unable to collapse all of the fatigue life data. In the present investigation, a new version of a life fraction model is used to consolidate data on a unidirectional SCS-6/Ti-6Al-4V composite under IF conditions at several frequencies and R values as well as under both in-phase (IP) and out-of-phase (OP) TMF conditions.

Experiments

The experimental data were provided from an in-house investigation at Wright Laboratory whose details are reported elsewhere [4,5]. The IF tests were conducted at 427°C at frequencies ranging from 0.01 to 10 Hz at R=0.05 and at 1 Hz at R=0.5. The TMF tests were conducted under IP and OP conditions at 0.01 Hz, R=0.05, from 23°C to 427°C. Additional IF tests were conducted at several other temperatures ranging from 23°C to 538°C. In general, these test conditions are less aggressive than those used on SCS-6/Timetal 21S composites. All tests were conducted on fatigue machines which consist of a servo hydraulic load frame positioned horizontally and utilizes quartz lamp heating units containing two banks of four quartz lamps running perpendicular to the loading axis, one above and one below the specimen. Four thermocouples are attached to the specimen with each actively controlling two lamps, thereby providing four zones of temperature control. A length of about 30 mm in the center of the specimen is heated uniformly, while the ends of the specimen, clamped in the water-cooled grips, remain near room temperature. In order to perform TMF tests where the minimum temperature of the cycle was room temperature (23°C), a special cooling apparatus using compressed air that was passed through a coil submerged in a methanol bath held at -50°C was used. Axial strain was monitored throughout the tests using a high temperature extensometer with quartz extension rods placed on the edge of the specimen. Symmetric triangular wave forms were used for both load and temperature for TMF tests. The test conditions and cycles to failure are summarized in Table 1.

Analysis

Each of the experimental conditions was simulated numerically using a concentric cylinder model embedded in a finite difference code FIDEP [6]. The finite difference equations of the cylinder in cylinder loaded unidirectionally are solved using the equations presented by Coker et al. [7]. The inner cylinder, which represents the SiC fiber, is treated as an elastic material with temperature-dependent properties. The outer cylinder, which represents the Ti-6-4 matrix, is treated as a thermoviscoplastic material using a recently modified version of the Bodner-Partom flow law [8]. The residual stresses due to the CTE mismatch between the fiber and matrix during processing are included in the analysis. The modeling approach uses the micromechanical stresses from the tenth cycle, after the majority of initial stress redistribution has taken place due to creep in the matrix. Additionally, the stress-strain response of the matrix material was obtained.

In order to determine the micromechanical stresses in the composite accurately, the complex inelastic behavior of the matrix material under TMF cycling must be represented accurately [9]. For the temperature and time dependence, as well as the strain-rate sensitivity, the response of the Ti-6Al-4V matrix is characterized with the viscoplastic theories of Bodner and Partom (B-P). The theory used in the present paper is a recently modified version [8] of the basic theory presented by Neu [10] which, in turn, is rooted in the isotropic nonisothermal formulation of Chan et al. [11]. A brief description of the basic theory along with the recent modifications are given here.

The material behavior is represented by the Bodner-Partom (B-P) flow law which decomposes total strain rate into the sum of elastic, thermal and inelastic components,

$$\dot{\varepsilon}_{ij}^{tot} = \dot{\varepsilon}_{ij}^{el} + \dot{\varepsilon}_{ij}^{th} + \dot{\varepsilon}_{ij}^{in} \tag{1}$$

The elastic strains, ε_{ij}^{el}, depend on the current stress state, elastic modulus, E, and Poisson's ratio, n. The thermal strain components, ε_{ij}^{th}, equal the product of the coefficient of thermal expansion and the difference between the current and reference temperatures. The inelastic strain rate (dots denote derivatives with respect to time) is given by the B-P flow law as

$$\dot{\varepsilon}_{ij}^{in} = D_0 \exp\left[-\frac{1}{2}\left(\frac{Z^2}{3J_2}\right)^n\right]\frac{s_{ij}}{\sqrt{J_2}} \tag{2}$$

where D_0 is a limiting strain rate, s_{ij} are the components of deviatoric stress, and J_2 equals the summation $s_{ij}\, s_{ij}/2$. Z, which represents the hardening of the material, is composed of the sum of two components, Z^I and Z^D

$$Z = Z^I + Z^D \tag{3}$$

which quantify the isotropic and directional hardening, respectively. The evolution equations of Z^I and Z^D have similar empirical forms. Each equation consists of a hardening, thermal recovery, and temperature rate term. The isotropic component is written as

$$\dot{Z}^I = m_1\left(Z_1 - Z^I\right)\dot{W}^{in} - A_1 Z_1\left(\frac{Z^I - Z_2}{Z_1}\right)^{r_1} + \left(\frac{Z_1 - Z^I}{Z_1 - Z_2}\right)\frac{\partial Z_2}{\partial T}\dot{T} \tag{4}$$

where $\dot{W}^{in}$ is the inelastic work rate

$$\dot{W}^{in} = \sigma_{ij}\,\dot{\varepsilon}_{ij}^{in} \tag{5}$$

The initial value of the isotropic hardening, $Z^I(0)$, is Z_0. The material parameters associated with isotropic hardening are m_1, Z_0, Z_1, Z_2, A_1, and r_1. The thermal differential term $\frac{\partial Z_2}{\partial T}$ appropriately scales the isotropic hardening variable Z^I when inelastic deformation and thermal recovery occur under nonisothermal conditions.

An equation similar to (4) describes the directional hardening whose magnitude can be written as a scalar product of a state variable, b_{ij}, and a unit vector u_{ij} in the s_{ij} direction.

$$Z^D = \beta_{ij} u_{ij} \tag{6}$$

where

$$\dot{\beta}_{ij} = m_2\dot{W}^{in}\left(Z_3 u_{ij} - \beta_{ij}\right) - A_2 Z_1\left(\frac{\sqrt{\beta_{kl}\beta_{kl}}}{Z_1}\right)^{r_2} v_{ij} + \frac{\beta_{ij}}{Z_3}\frac{\partial Z_3}{\partial T}\dot{T} \tag{7}$$

$$u_{ij} = \frac{\sigma_{ij}}{\sqrt{\sigma_{kl}\sigma_{kl}}} \tag{8}$$

$$v_{ij} = \frac{\beta_{ij}}{\sqrt{\beta_{kl}\beta_{kl}}} \tag{9}$$

The initial directional hardening variables, $b_{ij}(0)$ are set equal to zero. The material constants associated with directional hardening are m_2, Z_3, A_2, and r_2. The temperature differential term $\frac{\partial Z_3}{\partial T}$ appropriately scales the directional hardening variable when inelastic deformation and thermal recovery occur under nonisothermal conditions.

A more recent modification of the present theory to better represent creep data, proposed by Neu and Bodner [8], allows much more flexibility in characterizing a larger range of strain-rates than previously possible. The proposed changes are similar to the approach taken by Bodner and Lindenfeld [12] and Bodner and Rubin [13]. The first modification assumes that the constant m_1 now becomes a variable. In particular, the hardening rate term m_1 is proposed to be an exponential function of the state variable Z';

$$m_1 = m_{1b} + \left(m_{1a} - m_{1b}\right) \exp\left[-m_{1c}\left(Z' - Z_0\right)\right] \tag{10}$$

The two new material constants m_{1a} and m_{1b} represent, respectively, the initial and final (saturated) values of m_1. The material constant m_{1c} controls the saturation rate of m_1.

The second modification is made to constant A_1 in Eq (4), which also becomes a function of the hardening variable Z'

$$A_1 = A_{1b} + \left(A_{1a} - A_{1b}\right) \exp\left[-A_{1c}\left(Z' - Z_2\right)\right] \tag{11}$$

where A_{1a} and A_{1b} are, respectively, the initial and saturated values of A_1. Similar to m_{1c} in Eq (10), A_{1c} controls the saturation rate of A_1.

In modifying the theory, two temperature-dependent material constants are transformed into six constants. The increased number of material constants allows much more flexibility in representing the viscoplastic, time- and temperature-dependent response. Although a similar form for m_2 and A_2 could be proposed, there is no experimental evidence or rationale that supports such a form.

Bodner-Partom Parameters for Ti-6Al-4V

To produce a microstructure similar to that found in the composite, fiberless panels of layered Ti-6Al-4V foils were processed in the same manner as the composite. The resultant fiberless material was tested in tension, creep and stress relaxation at several temperatures from 23°C to 800°C [14]. The corresponding Bodner-Partom material parameters (Table 1) were determined by an iterative process of comparing the Bodner-Partom model response to the experimental measurements. As shown in Fig. 1, the model and corresponding Ti-6Al-4V parameters are able to characterize material behavior over a very large range of strain-rates (10^{-2}/s to 10^{-10}/s) and stress levels (10 MPa to 1000 MPa) over a broad range of temperatures from 23°C to 800°C. The data compiled in Fig. 1 depict minimum creep rates from creep tests and saturated stresses from tensile tests. Thus, the Bodner-Partom constants were primarily fit to the minimum creep rate and the ultimate strength. The secondary fitting was done to characterize hardening rates and primary creep rates.

Further evidence of the capability of these equations to represent the matrix material is illustrated in Figs. 2 and 3 where, at 538°C, experimental creep and stress-relaxation data, respectively, are compared with model predictions. The model is able to represent the data quite well in both cases. While the characterization of primary creep at 538°C is not optimal (Fig. 2), the model parameters accurately capture the secondary creep rate. In an out-right prediction, the constants do a very nice job of modeling the stress relaxation experiment at

538°C, as shown in Fig. 3. The high quality of characterization of both secondary creep and stress-relaxation are suitably accurate for the analysis conducted here.

These comparisons with experimental data illustrate that the enhanced Bodner-Partom model and the material parameters of Table 2 accurately characterize the strain-rate sensitivity and time-dependent response of this Ti-6Al-4V alloy at several temperatures. The incorporation of the improved viscoplastic model within the finite difference code FIDEP2 results in a very powerful analytical tool. For the analysis conducted here, this tool is well suited to determine the thermomechanical response of the SCS-6/Ti-6Al-4V composite.

Life Prediction Model

A review of the life fraction modeling for predicting elevated temperature fatigue life of MMCs is presented by Nicholas [15]. In that paper, modeling approaches developed by the author involving concepts of both linear and non-linear summation of damage from cycle-dependent as well as time-dependent mechanisms are summarized. The analyses utilize the micro-mechanical stresses in the constituents as parameters in various versions of life fraction models. Such modeling has been applied to isothermal fatigue at different frequencies and temperatures, and TMF under both in-phase and out-of-phase loading conditions at different temperature ranges and maximum temperatures.

The model considers cyclic and time-dependent damage accumulation in the form

$$\frac{N}{N_c} + \left(\frac{N}{N_t}\right)^{0.5} = 1 \qquad (12)$$

where N_C represents the cycles to failure due to cyclic damage and N_t is the cycles to failure due to time-dependent damage mechanisms. In this type of model, damage is considered to accumulate simultaneously due to independent mechanisms, each represented in the model by a life fraction. When the sum of the damage induced by all mechanisms equals one, failure is predicted. In practice, one damage mode typically dominates in an individual test, so that the life-fraction concept becomes more of a discrimination test of the dominant mechanism, and life is then governed by the related term.

With increased understanding of the dominant mechanisms which has been gained over the last several years, a new and simpler version of the life fraction model is presented here. Only two mechanisms of failure are accounted for here, matrix fatigue and time-dependent failure. Matrix fatigue is assumed to be governed by the strain range in the matrix material, as opposed to the stress range which was used in prior investigations. To account for mean strain or R_ε (ratio of minimum to maximum strain) which has been shown to affect fatigue life significantly [16], an effective strain range in the matrix is utilized in the form

$$\Delta\varepsilon_{m,eff} = \Delta\varepsilon\,(1-R_\varepsilon)^{p-1} \qquad (13)$$

where p is a parameter which can vary from 0 to 1: p=0 corresponds to ε_{max} as the governing parameter, p=1 corresponds to Δe.

$$N_m = B\left(\Delta\varepsilon_{m,eff}\right)^{-n} \qquad (14)$$

The time-dependent term (N_t) in Eq (12) is obtained by integrating the incremental damage using time to failure, t_c, as a function of stress,

$$t_c = A\,\sigma^{-m} \qquad (15)$$

which produces the following expression

$$\frac{1}{N_t} = \frac{1}{f\sigma_{max}(1-R)} \int_{R\sigma_{max}}^{\sigma_{max}} \frac{d\sigma}{A\sigma^{-m}} \tag{16}$$

Carrying out the integration for a triangular wave form results in the following term for use in Eq (12).

$$N_t = \frac{A f (m+1) (1-R)}{\sigma_{max}^{\ m}\left(1-R^{m+1}\right)} \tag{17}$$

where s is applied stress, s_{max} is its maximum value, f is cycle frequency, R is stress ratio, and A and m are empirical constants in Eq (15).

In order to account for differences in fiber volume fraction in the various specimens, an effective stress is used in place of the applied stress in computations involving the time-dependent term [17]. The effective stress produces the same stress in the composite as would be obtained in a composite whose fiber volume fraction were 0.35, the average value for this material. For small variations from 0.35, the effective stress can be accurately represented as

$$\sigma_{eff} = \sigma_{appl}\left(\frac{V_f}{0.35}\right)^{0.718} \tag{18}$$

This equation provides a convenient method for normalizing fatigue data having small variations in fiber volume fraction. For the cycle-dependent term which utilized matrix strains, the computations are carried out using the actual fiber volume fraction for each specimen evaluated.

For cases where the isothermal data are obtained at a number of different temperatures, temperature dependence of the matrix strain term, and the time-dependent or environmental term is introduced in the following manner [15]:

$$B = B_1\left(1+\frac{B_2}{T_{abs}}\right) \tag{19}$$

$$A = \frac{A_1}{\exp\left(\frac{-A_2}{T_{abs}}\right)} \tag{20}$$

where B, and A are now the temperature-dependent terms in Eqs (14) and (15), respectively, and T_{abs} is absolute temperature (T_{abs} = T°C + 273).

For TMF computations, the integration of the time-dependent term, Eq (16), using Eq (20) for temperature dependence, becomes unwieldy since the term "A" is now temperature dependent, and can only be performed numerically. Following the procedure of Nicholas et al. [17], a simple method is adapted which allows for a closed form solution to the integration. For this purpose, the temperature-dependent form of the constant in Eq (16) is taken as

$$A(T) = \frac{A\left(T_{max} - T_{min}\right)}{T - T_{min}} \tag{21}$$

for all TMF computations. Carrying out the procedure, the following equation is obtained:

$$\frac{1}{N_t} = \frac{\sigma_{max}^{\ m}}{f A (1-R)^2} F \qquad (22)$$

where the function, F, is given very accurately for m > 2 and R=0.05 (all TMF tests were conducted with mechanical cycles of R=0.05) as

$$F = \frac{1}{m+2} - \frac{R}{m+1} \quad \text{for in-phase TMF} \qquad (23a)$$

$$F = \frac{1}{m+1} - \frac{1}{m+2} \quad \text{for out-of-phase TMF} \qquad (23b)$$

with the terms f, A, m, and R as previously defined. For the limiting cases where $T_{max}=T_{min}$, these expressions reduce to Eq (17) in the limit for the isothermal case.

For modeling of the 427°C isothermal and TMF data, the following constants were obtained in a prior investigation [18]. These provided the best correlation between experimental and predicted lives based on a least squares error minimization scheme of (log) fatigue life: A=3.325 E+27, m=7.425, B=5.144 E-09, n=5.831, p=0.650. These constants are based on stress and time given in units of MPa and seconds, respectively. In the present investigation, isothermal data at other temperatures were included in the data base. This required the introduction of Eqs (19) and (20) in order to characterize the temperature dependence of the material. Using this complete set of data, the following constants were obtained: A_1=3.325 E+27, A_2=13517, m=10.287, B_1=5.144 E-09, B_2=126.1, n=5.613, p=0.944.

Results and Discussion

In comparing IF at the maximum temperature of a TMF cycle to IP TMF, the stress-strain behavior of the matrix material provides useful information. Figure 4 presents such a plot for unidirectional SCS-6/Ti-6Al-4V based on micromechanical computations using the modeling described above. For comparison, similar curves are shown in Fig. 5 for unidirectional SCS-6/Timetal®21S under typical loading conditions for that material. For the Timetal composite, it is clear that the hysteresis loop of the matrix material under isothermal fatigue is much larger than that obtained under IP TMF. What cannot be determined from the calculations alone is whether the hysteresis loop is large enough to produce matrix fatigue before the strain ratchetting and associated stress redistribution causes fiber fracture. In the case presented, the maximum fiber stress is 2477 MPa under IF and 2579 MPa under IP TMF. Such high fiber stresses usually lead to fiber fracture, most likely before matrix fatigue occurs in this material. These curves can be compared to the ones for the Ti-6Al-4V composite of Fig. 4 which are obtained under a less aggressive temperature environment than that used for the Timetal composite. It can be seen that the there is very little hysteresis in the matrix under IF or IP TMF in the Ti-6Al-4V composite, but the maximum applied stress is higher than in the Timetal composite. Further, the maximum fiber stresses are lower; 2104 and 2063 for IF and IP TMF, respectively. One should expect more of a tendency for matrix fatigue to occur rather than fiber breakage in this composite compared to the observed response of the Timetal composite for the conditions evaluated. This issue is addressed again later.

The capability of the model to represent the isothermal fatigue data at 427°C and the TMF data (23°C-427°C) is illustrated in Figs. 6 and 7, respectively. It can be seen that the isothermal data of Fig. 6 are well predicted by the model which produces nominally the same slope for all frequencies and stress ratios. The data at R=0.5 (the only ones at any value of R other than 0.05) seem to imply that the slope could change at high R or the time-dependent part of the model should have more of an effect than it now produces. Given the limited data at other R, combined with a error minimization scheme which is biased towards the majority of the

data points, it is not surprising that the R=0.5 are not as well represented by the model and associated constants developed for this data base.

In addition to the isothermal data of Fig. 6, data obtained under isothermal conditions at other temperatures were used in calibrating the model. Some of the data, at applied stress levels of 800 and 1050 MPa and a frequency of 10 Hz, are shown in Fig. 8 as a function of reciprocal absolute temperature. While the model captures the general trend of the data, the temperature-dependent constants of Eqs (19) and (20) are not sufficient to match the data very accurately. At all temperatures including the highest at 538°C, these 10 Hz data are dominated by the cycle-dependent term in the model based on strain in the matrix, particularly at this high frequency. This would imply that the form of the temperature dependence chosen in Eq (19), which governs the cycle-dependent term, N_m, is not optimum for capturing the temperature-dependent behavior of the matrix fatigue. Because of the limited data available at temperatures other than 427°C, no attempt was made to improve the ability of the model to represent the variation in matrix dominated fatigue life with temperature.

The IP TMF data, shown in Fig. 7, show good correlation with the model except for the two data points showing very low life at high applied stresses. These data points are clearly within Region 1 of a Talreja diagram (statistical fiber failure) and, as mentioned previously, do not lend themselves to extended life prediction. Rather, they fall within a range of parameters which produce early failure and were not used in determining the constants in the model. For these particular data points, the fiber stress ranges are in excess of 2700 MPa and maximum fiber stresses are in excess of 2400 MPa. These values of fiber stress have been shown to produce early failure in SiC fiber reinforced TMCs [19,20] and could be used to sort out the early failure conditions for design purposes. In a similar fashion, the three OP TMF data at the highest applied stresses (1150 and1200 MPa without the V_f correction) produce the shortest lives and show what appears to be the start of a horizontal cutoff. In these cases, the effective strain ranges in the matrix are the highest of any of the conditions evaluated and occur in combination with fiber stress ranges of nearly 1600 MPa. If the matrix cracks significantly, the fiber stresses can be expected to increase. While no account is taken of this in the model because of limited data, this could easily form the basis for a criterion to indicate early failure. With the exception of horizontal cutoff lines to represent these limits, not drawn in the figure, the remaining TMF data are predicted adequately by the model, again given the limited data available for calibrating the model.

The overall capability of the model to correlate the entire isothermal fatigue and TMF data base is illustrated in Fig. 9 where the predicted number of cycles is compared with the experimental results. As noted above, the two IP TMF data points were not used in determining the model constants and are not correlated with the model. In the figure, the straight line represents perfect correlation of model with experiment. With the exception of these points, the entire data base is predicted quite well for all of the conditions tests.

The present model utilizes only two terms to capture the fatigue mechanisms leading to failure, a matrix strain range cyclic term and a time-dependent stress relaxation term which accounts for stress redistribution due to applied stress at high temperature. Prior work using a life fraction model utilized fiber stress, matrix stress range, and applied stress as input in order to account for fiber dominated, matrix fatigue dominated, and time-dependent failure modes, respectively. Evaluation of the individual terms which govern life led to observations such as those of Nicholas and Johnson [19] that creep, in-phase TMF, hold-time fatigue loading and low frequency IF are all governed by a time-dependent mechanism. The mechanism is simply the relaxation of stress in the matrix which, in turn, produces fiber stresses above the strength of the weakest fibers and the subsequent failure of a bundle of fibers. The results indicated that there is essentially no fatigue involved in the cases studied and the data are indicative of a statistical process more than a deterministic one. Further, the time-dependent nature of the observed behavior is due to the time required for relaxation to occur and is related to applied stress and time. Higher applied stresses produce both higher fiber stresses and faster

relaxation rates in the matrix which, in turn, increase the fiber stresses even more. Lower applied stresses result in lower fiber stresses and lower matrix stresses which take longer to relax and trasfer their load to the fibers. The attainment of a critical value of fiber stress under these circumstances results in failure only within a narrow band of applied stresses. High applied stresses can cause immediate failure while lower ones may never produce the required stress in the fibers for failure to occur. Under these conditions, the degradation of strength with continued time of exposure is not found to be a dominant issue. The time-dependent term of the present model is based on applied stress and attempts to capture the mechanism of fiber failure. The very short life data are captured by this term and seem to represent the equivalent of Region 1 of a Talreja diagram [21] which is governed by the statistical failure of fibers due to fiber stresses which are sufficiently high to cause initiation and propagation of failure of a bundle of fibers. A similar observation made from analysis of a large body of IP TMF data over a wide range of conditions from several lay ups of SCS-6/Timetal®21S shows that a maximum fiber stress of slightly more than 2000 MPa correlates fatigue lives from 10 to 10^4 cycles to failure [22]. The authors note that the best correlation between fiber stress and fatigue life would be a horizontal line which, though not useful for predicting lives, could be a useful tool for design by establishing an upper limit for fiber stress. This cutoff line is not incorporated in the present model, but should be used instead as a screening rule to eliminate short life conditions.

In comparing IP TMF behavior in SCS-6/Ti-6-4 with that in SCS-6/Timetal 21S (Figs. 4 and 5), it should be noted that in addition to the differences in the hysteretic energy in the matrix material, the numerical results from the Ti-6-4 model indicate that both terms, fiber dominated from stress applied at temperature over time, and matrix dominated from fatigue in the matrix, contribute in similar quantities to the failure prediction. This is in contrast to results for the Timetal composite [3] where IP TMF is dominated by stress at temperature or fiber failure. While the hysteresis loop is large in the Timetal composite, it apparently does not contribute significantly to matrix fatigue. Rather, it appears to contribute to redistribution in stress from matrix to fiber in the composite, resulting ultimately in high fiber stresses leading to failure of the fiber bundle. In a similar fashion, the low frequency tests at high temperature all produce matrix stress-strain behavior which leads to matrix fatigue because of the large matrix strain ranges. A major difference between the Ti-6-4 composite compared to the Timetal composite is the maximum temperature at which the composites have been studied. Ti-6-4 composites have been studied primarily at 427°C, with only a few tests conducted at 538°C. Timetal composites, on the other hand, have been evaluated primarily at 650°C, with some tests conducted as high as at 815°C. It is important to note, based on micromechanical computations, that the higher temperature will produce lower stresses in the matrix and higher stresses in the fiber for a given applied maximum stress because of the thermal stress contribution to the overall behavior. Stated otherwise, as the maximum temperature is decreased, the matrix develops tension while the fiber tends towards compression. Thus, the different behavior of the two matrix materials is probably due to the temperature at which the behavior is being compared under IF and IP TMF, not the fatigue or environmental resistance of the matrix. Thus, it is not surprising to find that the model predicts matrix fatigue contributions to total life in Ti-6-4 composites, while matrix fatigue does not appear to influence such behavior in Timetal composites at low frequencies. Recent fractographic and NDI results in the Ti-6-4 composite system [23] appear to confirm the observation that failure under IP TMF involves not only fiber failure but matrix fatigue cracking as well.

Conclusions

The life fraction model does a good job of representing fatigue data in a MMC when the constitutive behavior of the matrix is adequately represented. The modified Bodner-Partom model fulfills this require-ment for the range of matrix behavior encountered in these experiments. The two terms in the life fraction model, matrix strain range and time at applied stress, appear to capture the dominant mechanisms governing the observed behavior. Under

loadings which lead to high fiber stresses, behavior is dominated by statistical fiber failure which should be used as a cutoff criterion in a more robust life prediction model. Differences between SCS-6/Ti-6-4 and SCS-6/Timetal composites are not well characterized in this investigation because the different maximum temperatures influence the response more than the matrix fatigue resistance.

References

[1] Gabb, T.P., Gayda, J., Bartolotta, P.A. and Castelli, M.G., "A Review of Thermomechanical Fatigue Damage Mechanisms in Titanium and Titanium Aluminide Matrix Composites," *International Journal of Fatigue*, 15, 1993, pp. 413-422.

[2] Jeng, S.M., Yang, J.-M. and Aksoy, S., "Damage Mechanisms of SCS-6/Ti-6Al-4V Composites Under Thermal-Mechanical Fatigue," *Materials Science and Engineering*,, A156, 1992, pp. 117-124.

[3] Neu, R.W. and Nicholas, T., "Methodologies for Predicting the Thermomechanical Fatigue Life of Unidirectional Metal Matrix Composites," *Advances in Fatigue Lifetime Predictive Techniques: 3rd Volume, ASTM STP 1292*, M.R. Mitchell and R.W. Landgraf, Eds., American Society for Testing and Materials, Philadelphia, 1996, pp. 1-23.

[4] Pittman, R.N., Sanders, B.P. and Mall,S., "Frequency Effects on Fatigue Behavior of a Unidirectional Metal Matrix Composite at Elevated Temperature," *Proceedings of the American Society for Composites: 11th Technical Conference*, W. S. Johnson, Ed., Technomic, Lancaster PA, 1996, pp 253-261.

[5] Rosenberger, A.H., Wright Laboratory, unpublished data.

[6] Coker, D., Ashbaugh, N.E. and Nicholas, T., "Analysis of the Thermo-mechanical Fatigue Behavior of [0] and [0/90] SCS-6/TIMETAL®21S Composites," *Thermomechanical Behavior of Advanced Structural Materials*, AD-Vol. 34, AMD-Vol. 173, W.F. Jones, Ed., American Society of Mechanical Engineers, New York, 1993, pp. 1-16.

[7] Coker, D. Ashbaugh, N.E. and Nicholas, T., "Analysis of Thermomechanical Cyclic Behavior of Unidirectional Metal Matrix Composites," *Thermomechnical Fatigue Behavior of Materials, ASTM STP 1186*, H. Sehitooglu, Ed., American Society for Testing and Materials, Philadelphia, 1993, pp. 50-69.

[8] Neu, R.W., and Bodner, S.R., "Contributive Research and Development, Volume 6, Determination of the Material Constants of Timetal®21S for a Constitutive Model," SYSTRAN report under contract #F33615-94-C-5804 for Wright Laboratory, Wright-Patterson AFB, OH, 45433, 1995.

[9] Neu, R.W., Coker, D. and Nicholas, T., "Cyclic Behavior of Unidirectional and Cross-Ply Titanium Matrix Composites," *International Journal of Plasticity*, 12, 1996, pp. 361-385.

[10] Neu, R.W., "Nonisothermal Material Parameters for the Bodner-Partom Model,", *Material Parameter Estimation for Modern Constitutive Equations*, L.A. Bertram, S.B. Brown, and A.D. Freed, Eds., MD-Vol. 43/AMD-Vol. 168, ASME, 1993, pp. 211-226.

[11] Chan, K.S., Bodner, S.R., and Lindholm, U.S., "Phenomenological Modeling of Hardening and Thermal Recovery in Metals," *ASME Journal of Engineering Materials and Technology*, Vol. 110, January 1988, pp. 1-8.

[12] Bodner, S.R. and Lindenfeld, A., "Constitutive Modeling of the Stored Energy of Cold Work Under Cyclic Loading," *European Journal of Mechanics and Solids*, Vol. 14, No. 3, 1995, pp. 333-348.

[13] Bodner, S.R., and Rubin, M.B., "On the Representation of Rate Dependence of Hardening and Non-Proportional Loading Effects by a Viscoplastic Model, ICES, 1995.

[14] Ashbaugh, N.E. and Knapke, D., University of Dayton Research Institute, unpublished data.

[15] Nicholas, T. "An Approach to Fatigue Life Modeling in Titanium Matrix Composites," *Materials Science and Engineering*, A200, 1995, pp. 29-37.

[16] Lerch, B. and Halford, G., "Effects of Control Mode and R-ratio on the Fatigue Behavior of a Metal Matrix Composite," *Materials Science and Engineering*,, A200, 1995, pp. 47-54.

[17] Nicholas, T., Russ, S.M., Neu, R.W. and Schehl, N., "Life Prediction of a [0/90] Metal Matrix Composite Under Isothermal and Thermomechanical Fatigue," *Life Prediction Methodology for Titanium Matrix Composites*, ASTM STP 1253, W. S. Johnson, J.M. Larsen and B.N. Cox, Eds., American Society for Testing and Materials, Philadelphia, 1996, pp. 595-617.

[18] Nicholas, T. and Kroupa, J.L., "The Role of Inelastic Deformation in the Analysis and Life Prediction of Titanium Matrix Composites," *Proceedings of International Symposium on Inelastic Deformation, Damage and Life Analysis '97*, San Jose, Costa Rica, May 1997.

[19] Nicholas, T. and Johnson, D.A., "Time- and Cycle-Dependent Aspects of Thermal and Mechanical Fatigue in a Titanium Matrix Composite," *Thermo-Mechanical Fatigue Behavior of Materials, ASTM STP 1263*, M.J. Verrilli and M.G. Castelli, Eds., American Society for Testing and Materials, Philadelphia, 1996, pp. 331-351.

[20] Mirdamadi, M. and Johnson, W.S., "Modeling and Life Prediction Methodology for Titanium Matrix Composites Subjected to Mission Profiles," *Life Prediction Methodology for Titanium Matrix Composites, ASTM STP 1253*, W.S. Johnson, J.M. Larsen and B.N. Cox, Eds., American Society for Testing and Materials, Philadelphia, 1996, pp. 573-594.

[21] Talreja, R., "Fatigue of Composite Materials: Damage Mechanisms and Fatigue Life Diagrams," *Proceedings of the Royal Society of London*, Vol. A378, 1981, pp. 461-475.

[22] Calcaterra, J.R., Johnson, W.S. and Neu, R.W., "A Comparison of Life Prediction Methodologies for Titanium Matrix Composites Subjected to Thermomechanical Fatigue," *13th Symposium on Composite Materials: Testing and Design*, American Society for Testing and Materials, Philadelphia, 1996 (accepted for publication).

[23] Clemons, G.S., "In Situ Nondestructive Evaluation of In-Phase Thermomechanical Fatigue and Sustained Load Damage in an SCS-6/Ti-6Al-4V Metal Matrix Composite," M.S. thesis, University of Dayton, 1997.

Table 1: Summary of Experimental Conditions for SCS-6/Ti-6Al-4V $[0]_8$

Specimen ID	Vf	s max appl	T_{min}	T_{max}	Freq	R	Cyc to failure
Isothermal fatigue							
95-712	0.328	900	427	427	0.01	0.05	10,827
95-702	0.340	1050	427	427	0.01	0.05	2,889
95-701	0.345	1200	427	427	0.01	0.05	1,747
95-708	0.336	800	427	427	0.10	0.05	90,434
95-700	0.343	1050	427	427	0.10	0.05	13,620
95-730	0.371	1200	427	427	0.10	0.05	10,700
95-697	0.346	800	427	427	1.00	0.05	130,707
95-698	0.343	1050	427	427	1.00	0.05	23,096
95-725	0.353	800	427	427	10.00	0.05	163,029
95-723	0.359	1050	427	427	10.00	0.05	26,252
95-711	0.331	1200	427	427	10.00	0.05	12,911
95-740	0.34	1050	427	427	1.00	0.5	59,333
95-741	0.342	900	427	427	1.00	0.5	299,730
95-742	0.349	800	427	427	1.00	0.5	**1,123,000**
95-726	0.361	800	23	23	10	0.05	411,562
95-728	0.367	1050	23	23	10	0.05	95,634
95-735	0.343	800	260	260	10	0.05	367,486
95-736	0.336	1050	260	260	10	0.05	51,374
95-696	0.343	800	370	370	1	0.05	134,467
95-739	0.333	800	370	370	1	0.05	99,175
95-699	0.341	1050	370	370	1	0.05	33120
95-727	0.363	800	370	370	10	0.05	327,666
95-722	0.347	1050	370	370	10	0.05	22,131
95-737	0.336	800	538	538	10	0.05	96,643
95-738	0.336	1050	538	538	10	0.05	11,260
95-709	0.336	800	538	538	0.1	0.05	22,704
95-710	0.335	1050	538	538	0.1	0.05	2,624
In-Phase TMF							
95-A23	0.348	1200	23	427	0.01	0.05	4
95-A24	0.344	1200	23	427	0.01	0.05	5
95-A25	0.34	1050	23	427	0.01	0.05	14,240
95-A27	0.344	1150	23	427	0.01	0.05	6,567
Out of Phase TMF							
95-A21	0.342	1200	23	427	0.01	0.05	1,297
95-A22	0.352	1200	23	427	0.01	0.05	2,208
95-A26	0.337	1050	23	427	0.01	0.05	11,637
95-A60	0.323	1150	23	427	0.01	0.05	2,987

Table 2: B-P Constants for Ti-6Al-4V

Temperature-Independent Constants

$n = 0.31$
$Z_1 = 2500$ MPa
$m_{1b} = 1.5$ $(MPa)^{-1}$
$A_{1c} = 0.003$
$r_1 = r_2 = 2.7$

Temperature-Dependent Constants

T (°C)	E(GPa)	CTE* $(10^6C)^{-1}$	$Z_0=Z_2$ (MPa)	Z_3 (MPa)	n	m_{1a} $(MPa)^{-1}$	m_{1c}	m_2 $(MPa)^{-1}$
23	120	9.976	2450	450	1.74	1.5	0	0.01
260	103	10.45	2350	450	1.315	1.8	0.00005	0.04
316	100	10.57	2250	450	1.285	6	0.00015	0.07
427	94	10.79	290	280	1.17	10	0.001	0.08
482	80	10.90	200	190	1.12	25	0.00155	0.08
538	74	11.01	130	125	1.04	35	0.0018	0.08
598	71.9	11.13	65.7	58.7	0.95	82.1	0.00201	0.08
650	70	11.24	10	1.2	0.87	110	0.0022	0.08
725	60	11.39	7.5	1.1	0.7875	165	0.00233	0.08
800	50	11.54	3	1	0.71	220	0.0025	0.08
825	25	11.59	2.5	0.75	0.67	232	0.00252	0.08
850	5	11.64	2	0.5	0.63	250	0.00258	0.08

*(T_{ref}=25°C)

$a_{1a} = 118.3X10^9 \exp(-23902/(T+273.))$, T in °C
$a_{1b} = a_2 = 5.914 \times 10^9 \exp(-23902/(T+273.))$, T in °C

Figure Captions

Fig. 1 Comparison of experimental steady-state (saturation) stress and B-P model calibration.

Fig. 2 Comparison of experimental data and B-P model calibration for creep.

Fig. 3 B-P model prediction of stress relaxation at 538°C.

Fig. 4 Matrix stress-strain behavior for unidirectional SCS-6/Ti-6Al-4V after 10 cycles.

Fig. 5 Matrix stress-strain behavior for unidirectional SCS-6/Timetal®21S after 10 cycles.

Fig. 6 427°C isothermal S-N data and model predictions.

Fig. 7 TMF S-N data and model predictions.

Fig. 8 Cycles to failure as function of reciprocal absolute temperature for tests conducted at 10 Hz.

Fig. 9 Predicted and experimental fatigue life comparison for all isothermal and TMF tests.

Reference: Buchanan, D.J., John, R., and Johnson, D.A., "Determination of Crack Bridging Stresses from Crack Opening Displacement Profiles," International Journal of Fracture, V. 87, No. 2, pp. 101-117.

Determination of Crack Bridging Stresses from Crack Opening Displacement Profiles

Dennis J. Buchanan[1], Reji John[1] and David Alan Johnson[2], USAF Wright Laboratory, Materials Directorate, WL/MLLN, Wright-Patterson AFB, OH 45433-7817

[1]Advanced Materials Characterization Group
Structural Integrity Division
University of Dayton Research Institute
Dayton, OH 45469-0128
[2]Graduate Research Assistant
Division of Engineering and Applied Sciences
Harvard University
Cambridge, MA 02138

Abstract

This paper discusses the development of an optimization procedure to deduce the bridging stress from the crack opening displacements (COD) measured during fatigue crack growth. Finite element analysis was conducted using the center-cracked geometry to verify the optimization procedure. The proposed procedure successfully predicted the bridging stress distributions with zero stresses at the crack tip and the bridging stress distributions with non-zero stresses at the crack tip. The results also showed that COD measurements spaced at ≈ 0.8-1.0 mm are sufficient for reliable prediction of bridging stresses. Accurate prediction of bridging stresses near the crack tip required COD data within ≈ 0.1 mm from the crack tip. The application of the proposed procedure to a metal matrix composite (SCS-6/TIMETAL®21S) is also discussed.

1. Introduction

A variety of models have been developed to describe bridging in concrete, ceramics, ceramic matrix composites (CMC) and metal matrix composites (MMC) during crack growth under monotonic and cyclic loading [1-23]. In monolithic and short fiber reinforced concrete and ceramics [17-23], increasing crack opening displacement (COD) results in an initial increase, followed by a decrease of the bridging stress. In contrast, continuously reinforced CMC and MMC [1-16,24,25] exhibit continuously increasing bridging stress with increasing COD in the bridged region. In these materials the bridging mechanisms were modeled as a distributed closing pressure exerted on the crack surface with the applied load in the direction of the fibers (Fig. 1). The models used to describe crack growth in continuously reinforced CMC and MMC include shear lag [1-11,13-15], constant bridging stress distributions [8,9,11] and fiber pressure models [7]. These fiber bridging models for continuously reinforced CMC and MMC predict a wide range of bridging stress distributions as shown in Fig. 2. The shear lag models developed by Marshall et al. [1] and McCartney [2] enforce zero bridging stress at the crack tip (Fig. 2a). In contrast, the shear lag models proposed by Danchaivijit and Shetty [5], Chiang et al. [6] and Majumdar et al. [3] predict non-zero bridging stress at the crack tip. All these models show a similar trend of an increase in bridging stress with an increase in distance away from the crack

tip (Fig. 2a and 2b). Similar to the latter shear lag models, the fiber pressure [7] and constant bridging stress [8,9,11] models predict non-zero bridging stress at the crack tip (Fig. 2c).

Based on analysis of data from SCS-6/Ti-24Al-11Nb, John et al. [9] concluded that even though the different bridging models can be used to describe the fatigue crack growth behavior, the resulting fiber bridging stress distributions are significantly dissimilar in shape and magnitude. Consequently, prediction of onset of fiber breakage and eventual failure of the composite would require values of fiber strength which depend on the fiber bridging model used during the analysis.

An independent verification of the fiber bridging stress distribution can be achieved by direct comparison of the predicted COD profile with the measured COD data [7-9,11,15,17-25]. The weight function approach [28,29] is commonly used to predict the COD due to arbitrary stress distributions along the bridged crack. Recently, many investigators [13,17-25] have used the measured COD profile to deduce the bridging stress, s_b as a function of COD and location along the crack in various materials. Rödel et al. [17] used a deconvolution approach to deduce the grain bridging stress distribution from COD profiles measured during crack extensions in an alumina ceramic specimen under monotonic loading. Du et al. [20] and Guo et al. [21] deduced the aggregate bridging stresses from COD profiles in concrete using the weight function approach and finite element analysis. Fett et al. [18,19] used COD data to determine fiber and grain bridging stresses in SiC_w/Al_2O_3 and Al_2O_3, respectively. These results from unreinforced and reinforced concrete and ceramic materials [17-23] correspond to monotonic loading. During fatigue loading, Zheng and Ghonem [13] and John et al. [24,25] used COD data to deduce the fiber bridging stress distribution in continuously reinforced MMC systems SM1240/TIMETAL®21S and SCS-6/TIMETAL®21S, respectively. Zheng and Ghonem [13] reported non-zero bridging stress at the crack tip, with a linear or near-constant distribution along the crack. John et al. [24,25] concluded from multiple stress ratio tests on SCS-6/TIMETAL®21S at one crack length that the magnitude of the bridging fiber stress range was proportional to the applied stress range. The bridging stress range was near-linear with non-zero stress at the crack tip [24,25].

The above studies [13,17-25] were based on COD measured at discrete locations along the crack. The number of locations of measurement depend on the crack length and the technique used to measure the COD. The use of scanning electron microscope (SEM) [17] and Moiré interferometry [20,21] yield numerous COD data along the crack. During crack growth in MMC, the load versus COD response at various locations along the crack enables the deduction of the effect of cyclic loading on the bridging mechanism. The laser interferometric displacement gage (IDG) system [26,27] enables such measurements. Zheng and Ghonem [13] and John et al. [24,25] used the laser IDG system to obtain the COD data during crack growth in MMC systems. The laser IDG method typically results in 3 to 6 locations of COD measurements along the crack. The influence of the number of locations of COD data and the proximity to the crack tip on the deduced bridging stress is not precisely known. This paper describes the development of a procedure to deduce the bridging stress distribution from limited COD data. This paper also discusses verification of the procedure using finite element analysis, sensitivity of results to location of COD location and application of the procedure to a metal matrix composite subjected to fatigue loading.

2. Experimental Procedure and Results

The material tested was TIMETAL®21S matrix reinforced with unidirectional silicon carbide (SCS-6) fibers in a $[0]_4$ layup. The volume fraction of fibers, V_f was approximately 0.33. The middle tension M(T) geometry shown in Fig. 3 was used in this study with width, W=19.0 mm, thickness, B=0.95 mm and initial notch, a_o=1.9 mm, produced by electrical discharge machining (EDM). The specimen was fatigue loaded at maximum stress level, $s_{a,max}$ of 270 MPa after initial cycling at 100 and 120 MPa up to » 1.5×10^6 cycles . The applied stress ratio,

R ($=s_{a,min}$ / $s_{a,max}$) was equal to 0.1 and the frequency of loading was 1 Hz. The test was conducted at room temperature in laboratory air.

The crack length as a function of the number of applied cycles is shown in Fig. 4 for the left and right sides. The reported crack length for each side is the average of the corresponding front and back crack lengths. The crack length versus cycle count response is typical of fully bridged crack growth exhibiting decreasing crack growth rate (da/dN) with increasing crack length [4,7-9,11,24-25]. The test was stopped at » 7.87 x 10^6 cycles, COD profiles measured and the matrix removed using an etchant. There were no broken fibers confirming fully bridged crack growth [24,25].

During the crack growth tests, the COD profile was measured at different crack lengths using a laser IDG system [26,27]. This technique has been used to measure COD during crack growth in SCS-6/Ti-24Al-11Nb [8,9], SM1240/TIMETAL®21S [13] and SCS-6/TIMETAL®21S [15,24,25]. The crack lengths at which the COD profiles were measured is shown in Fig. 4. Figure 5 shows a schematic highlighting the location of the COD measurements along the crack. The locations were typically spaced 0.8 mm apart with the last set of indents usually less than 0.1 mm behind the crack tip. The measured COD profiles are shown in Fig. 6. The COD profiles show a steep increase near the machined notch tip which is attributed to lack of bridged fibers between those locations and the center of the machined notch.

As shown in Fig. 4, at any given cycle count the crack length on the left side was slightly different from that on the right side. The measured crack lengths were corrected to the average optical crack length to enable the analysis of the average response of the specimen. The locations of the COD measurement were also corrected proportionally, while the COD values were not corrected. The resulting COD data corrected to average crack length are shown as symbols in Fig. 7. The procedure to deduce the bridging stress distribution from these COD data is discussed next.

3. Analytical Procedure

This section describes the optimization procedure to deduce the bridging stress distribution from measured COD profiles. The procedure was developed based on the weight function method [24,25,28,29] and verified using finite element analysis as discussed below.

3.1 Weight Function Method

The weight function method as given by Eqn. (1) was used to calculate the COD range due to an arbitrary stress distribution on the crack surface.

$$\Delta v(x) = \frac{1}{E_o}\int_x^a \left[\int_0^{\bar{a}} h(\bar{x},\bar{a})\,\Delta\sigma_s\,d\bar{x}\right] h(x,\bar{a})\,d\bar{a} \qquad (1)$$

where

$\Delta v(x)$ = half crack opening displacement range, (see Fig. 3),

E_o = orthotropic modulus [12,30],

$h(x,a)$ = weight function, and

$\Delta\sigma_s$ = surface stress range.

In general, Ds_s can be calculated as

$$Ds_s = Ds_a - Ds_b \qquad (2)$$

where

Ds_a = applied stress range, and

Ds_b = bridging stress range.

The applied stress range was, $Ds_a = s_{a,max} - s_{a,min}$ where $s_{a,max}$ = maximum applied stress and $s_{a,min}$ = minimum applied stress. Note that Ds_a was constant along the surface in the crack

plane. The bridging stress range, Ds_b is the closing stress on the crack due to the interfacial sliding between the fiber and the matrix and is active only in the range a_o £ x £ a.

h(x,a) is the weight function for a central crack in a plate with finite width as shown in Fig. 3. During this study, a new weight function was developed using the procedure proposed by Wu and Carlsson [31]. The expression for the weight function is given in the Appendix.

3.2 Fiber Bridging Stress From COD

The algorithm to deduce the fiber bridging stress was based on the weight function method to calculate the half COD range, Dv(x) at the location of the COD measurements along the crack plane. The bridging stress range was chosen to be a function of three undetermined coefficients (A_0, A_1, A_2) and the normalized crack length, r, as given by Eqn. (3), where x, a, a_0 in Eqn. (4) are defined in Fig. 3. John et al. [24,25] used Eqn. (3) for deducing fiber bridging stress distributions in a MMC. Fett et al. [18,19] used a similar form (up to 10 constants) to deduce the bridging stress distribution in a ceramic and a CMC.

Equation (3) does not imply any predefined shape because A_i can be positive, negative or zero. Therefore Eqn. (3) can accommodate increasing or decreasing Ds_b with increasing distance away from the crack tip. Note that the crack tip is r = 0 and the initial machined notch tip is r = 1. Equation (3) also allows the bridging stress distribution to assume several stress profiles and crack tip stress conditions.

$$\Delta\sigma_b = A_0 + A_1\sqrt{\rho} + A_2\rho \qquad (3)$$

where

$$\rho = \frac{a - x}{a - a_o}. \qquad (4)$$

A_0 corresponds to the bridging stress range at the crack tip and the sum of the coefficients, $\sum_{i=0}^{2} A_i$ to the bridging stress range at the initial machined notch tip.

The coefficients (A_0, A_1, A_2) are not known *a priori* and must be determined such that the square of the normalized difference between the measured and the calculated half-COD is minimized as given by Eqn. (5). An IMSL optimization routine [34] was incorporated to determine the values of A_i in Eqn. (3) that minimize the sum in Eqn. (5).

$$\sum_{i=1}^{n}\left[\frac{\Delta\bar{v}(x)_i^{measured} - \Delta\bar{v}(x)_i^{calculated}}{\Delta\bar{v}(x)_i^{measured}}\right]^2 = \text{minimum} \qquad (5)$$

The number of locations of COD measurements, n ranged from 3 to 6 depending on the crack length. The optimization of the constants, A_i, was terminated when the normalized sum of squares reached a specified tolerance of 1×10^{-6}. Knowing Ds_b, the fiber stress range, Ds_f can be calculated as

$$\Delta\sigma_f = \frac{\Delta\sigma_b}{V_f} \qquad (6)$$

where V_f = volume fraction of fibers in the composite. The verification of the optimization procedure is described next.

4. Verification Using Finite Element Analysis

4.1 Finite Element Analysis

The finite element (FE) software package ADINA [35] was used to evaluate the efficacy of the proposed procedure to deduce the bridging stress distribution from COD data. Several finite element models using 8-node quadrilateral elements were developed to evaluate the accuracy of the weight function, and to verify the optimization procedure for several types of distributions. In all cases the initial unbridged notch length was $2a_o = 0.22W$, and the specimen width was, W = 18.9 mm. The FE mesh used approximately 200-500 nodes along the crack surface with quarter-point collapsed quadrilateral elements at the crack tip.

Figure 8 shows the three bridging stress distributions that were prescribed on the crack surface as a function of the normalized location along the crack, r. Note that r = 0 is the crack tip and r = 1 is the initial machined notch tip. Case 1 had a crack-tip stress of 150 MPa with the stress increasing as a function of $\sqrt{\rho}$ to 250 MPa at the initial notch tip. Case 2 also had a crack-tip stress of 150 MPa but the stress increased linearly to 250 MPa at the initial notch tip. Case 3 had a zero crack-tip stress with the stress increasing as function of $\sqrt{\rho}$ to 250 MPa at the initial notch tip. During this study two crack lengths were evaluated, 2a/W = 0.40 and 2a/W = 0.69. The orthotropic modulus, E_o = 176.66 GPa and remote stress, s_a = 218 MPa was used to obtain the COD profile. The number of nodes along the crack at which FE COD values are available was 196 and 514 for 2a/W = 0.40 and 2a/W = 0.69, respectively. As discussed earlier, experimental COD data is available only at discrete locations spaced approximately 0.8 mm apart resulting in 3 to 6 locations along the crack depending on the crack length. Hence finite element COD values from only a few locations were used to deduce the bridging stress distribution as discussed in detail in the next section.

4.2 Verification of Deduced Bridging Stress Distribution

To accurately correlate the FE analysis with data from experimental results the distance between the COD locations were spaced consistent with the locations of COD measurements used on the specimen. The discrete COD data from the finite element analysis was used to determine A_0, A_1, and A_2 in Eqn. (3). The results for the optimized COD profiles for 2a/W = 0.40 and 0.69 are shown in Figs. 9 and 10, respectively. The symbols represent the displacements profiles from the FE model and the solid lines the optimized half-COD profile obtained using Eqns. (1) and (3). The solid symbols (inverted triangles) represent the finite element COD values used in the optimization procedure. The optimized COD profiles show very good agreement with the FE results for all the cases in Figs. 9 and 10.

The deduced bridging stress distributions and the prescribed distributions input into the FE models for 2a/W = 0.40 and 0.69 are shown in Fig. 11. The symbols represent the prescribed bridging stress profile input into the FE model at the crack plane and the solid lines are the bridging stress profiles deduced using the proposed optimization procedure. The inverted triangles show the location of the selected finite element COD points used as input for the optimization procedure. The deduced bridging stress profiles show very good agreement with the FE results for all the cases especially at the crack tip where zero and non-zero bridging stresses were prescribed. Hence, the optimization procedure can be expected to predict accurate bridging stress distributions based on only a few COD data points along the crack.

4.3 Sensitivity of Bridging Stress to Location of Near-Tip Data

The shape and magnitude of the deduced bridging stress profile can be expected to depend on the location of the COD data which is closest to the crack tip. Different near-tip COD data points were used from the FE COD profile to check the influence of the distance (L) between crack tip and near-tip COD data on the deduced bridging stress. The bridging stress distribution identified as case 2 in Fig. 8 was used for this sensitivity study. The distance

between the near-tip COD and the crack tip was varied from 0.04 mm to 0.50 mm for 2a/W = 0.4 and 2a/W = 0.69. The near-tip COD data correspond to the last set of indents shown in the inserts of Figs. 12 and 13.

Figures 12 and 13 show plots of the error in the deduced bridging stress at the initial notch tip and crack tip as a function of L, for 2a/W = 0.4 and 2a/W = 0.69, respectively. The dashed line is the error in deduced bridging stress at the initial machined notch tip. This location is far from the crack tip and hence is not strongly influenced by the location of the near-tip COD data. The solid line is the error in deduced bridging stress at the crack tip. The absolute error in the deduced Ds_b at the crack tip is higher than that at the initial notch tip. The error increases rapidly as L decreases from 0.05 mm to 0, i.e., as the near-tip COD location is moved closer to the crack tip for 2a/W = 0.40 (Fig. 12) in contrast to the results for 2a/W = 0.69 (Fig. 13). This increase in error could be attributed to the decreased number of nodes along the crack for 2a/W = 0.40. Figures 12 and 13 show that the error in deduced Ds_b along the crack length is within ±1.1% for L ranging from 0.05 to 0.18 mm. As discussed earlier, the available COD data near the crack tip was typically measured at » 0.075 mm from the crack tip. Hence, the near-tip stress distribution deduced from the COD data should be sufficiently accurate.

5. Bridging Stress Distribution in SCS-6/TIMETAL®21S

The application of the proposed optimization procedure to deduce the bridging stress distribution during crack growth in SCS-6/TIMETAL®21S is described in this section. For the specimen tested in this study, Ds_a = 243 MPa, $2a_o/W$ = 0.2, E_f = 393 GPa, $E_c = E_fV_f + E_m(1-V_f)$ = 206 GPa and E_o = 178 GPa. The measured COD data and the COD profile (solid line) obtained using the optimization procedure are shown in Figs. 7(a), 7(b) and 7(c) for crack lengths 2a/W = 0.38, 2a/W = 0.62 and 2a/W = 0.73, respectively. The optimized fit is very close to the data except near the initial notch tip, where there is a large discrepancy in the measured COD data.

The corresponding bridging stress range distribution for the three crack lengths is shown in Fig. 14. For all the crack lengths, the bridging stress distributions exhibits a non-zero crack-tip stress condition which is similar to the models proposed by Majumdar et al. [3], Danchaivijit and Shetty [5], Chiang et al. [6], Ghosn et al. [7], John et al. [24,25], Davidson [11] and Zheng and Ghonem [13]. The bridging stress increases with increasing COD as we move away from the crack tip. The stress range in the fiber at the crack tip (» 545 MPa) appears to be independent of crack length. The maximum fiber stress range at the initial notch tip is » 1210 MPa which is less than the reported failure strength (» 3750 MPa) of the fibers. This is also consistent with the observation of fully bridged crack growth in the composite devoid of broken fibers [24,25]. The bridging fiber stress at the initial notch-tip does not increase with increasing crack length. Since the fiber stresses at the initial notch-tip are less than the failure strength of the fibers, the strength of the fiber could be degrading due to an increase in the applied cycles [8,9].

Majumdar et al. [3], Danchaivijit and Shetty [5] and Chiang et al. [6] assumed that the fiber bridging stress range at the crack tip, $Ds_{f,tip}$ is equal to that under remote loading. $Ds_{f,tip}$ is given by [3,5,6]

$$\Delta\sigma_{f,tip} = \frac{\Delta\sigma_a}{\left(1-\frac{2a_o}{W}\right)}\frac{E_f}{E_c}. \qquad (7)$$

Equation (7) yields, $Ds_{f,tip} \approx 580$ MPa for the specimen tested in this study. Figure 14 shows that the deduced Ds_f at the crack tip is ≈ 518-574 MPa, which is close to that calculated using Eqn. (7).

Figure 15 shows the deduced bridging stress range, Ds_b as a function of normalized location along the crack length, r. Interestingly, the bridging stress range distributions for

different crack lengths collapse to a single curve. The constant bridging stress range predicted by the fiber pressure model [7] can be calculated as the net-section stress range = $Ds_a/(1-2a_o/W)$ » 304 MPa, which is also shown in Fig. 15. The bridging stress distribution predicted by the fiber pressure model is close to an average representation of Ds_b deduced from measured COD profiles. The relationship of Ds_b deduced from measured COD profiles to the various bridging models is discussed by John and Buchanan [36].

6. Summary

An optimization routine using the weight function method was developed to deduce the fiber bridging stress distribution from the measured crack opening displacement profiles. The optimization procedure was validated using finite element analysis for a variety of bridging stress profiles, crack-tip stress conditions and crack lengths. A few locations of COD data, typically 3-6, were sufficient to deduce the bridging stress distribution. The bridging stress deduced at the crack tip is sensitive to the location of COD data near the crack tip. If the distance between the near-tip COD data and the crack tip is ≈ 0.07-0.10 mm from the crack tip, then the error in the predicted bridging stress can be expected to be within ± 0.5% for the range of crack lengths used during this study. During fatigue crack growth in $[0]_4$ SCS-6/TIMETAL®21S, the bridging stress distribution increases with increasing crack opening displacement and is non-zero at the crack tip. The maximum fiber stress at the initial notch-tip is independent of crack length.

Acknowledgment

The research was conducted at the Materials Directorate, Wright Laboratory, Wright-Patterson Air Force Base, OH 45433-7817, USA under the contract number F33615-94-C-5200. The authors gratefully acknowledge the assistance of Mr. A. F. Lackey in conducting the detailed experiments.

Appendix

Weight Function For a Middle Tension Geometry, M(T)

The weight function, h(x,a) for the middle tension geometry shown in Fig. 2 was derived using the procedure proposed by Wu and Carlsson [31]. h(x,a) can be expressed as a series expression given by the following equation.

$$h(x,a)=\frac{1}{\sqrt{\pi a}}\sum_{i=1}^{4}\beta_i\left[1-\left(\frac{x}{a}\right)^2\right]^{i-3/2}$$

in which,

$$\beta_1 = 2\ ,$$

$$\beta_2 = \frac{1}{F_r}\left[\alpha F_1^{'} + 3F_2\right]\ ,$$

$$\beta_3 = \frac{1}{F_r}\left[\alpha F_2^{'} - 2F_2 + 5F_3\right]\ , \text{ and}$$

$$\beta_4 = \frac{1}{F_r}\left[\alpha F_3^{'} - 4F_3\right]\ .$$

The functions F_j and the corresponding derivatives, $F_j^{'}$ are defined as,

$$F_1 = 2F_r\ ,$$

$$F_2 = 32\varphi - 6F_r - 5G_r\ ,$$

$$F_3 = -32\varphi + 4F_r + 6G_r\ ,$$

$$F_j^{'} = \frac{\partial F_j}{\partial \alpha}\ ,\ i = 1,2,3\ ,$$

where the crack length to width ratio, α = 2a/W. In the above equations, F_r and G_r are the nondimensionalized functions for the stress intensity factor [31] and crack mouth opening displacement [32], respectively, for a middle tension geometry subjected to tension loading. The expressions for F_r [31] and G_r [32] are,

$$F_r = \frac{1}{\sqrt{1-\alpha}}\left[1 - 0.5\,\alpha + 0.4707\,\alpha^2 - 0.3662\,\alpha^3 + 0.3550\,\alpha^4 - 0.1730\,\alpha^5 + 0.0440\,\alpha^6\right],$$

and

$$G_r = -0.142 - 1.070\,\alpha + 0.338\,\alpha^2 - 0.180\,\alpha^3 + 0.040\,\alpha^4 - \frac{2.142}{\alpha}\ln(1-\alpha)\ .$$

F_r and G_r are valid for any α ($0 \le \alpha \le 1$) within 0.1% and 0.6%, respectively. Wu and Carlsson [31] defined φ as,

$$\varphi = \frac{1}{\alpha^2}\int_0^{\alpha} \alpha\, F_r^2\, d\alpha\ .$$

During this study, the above integral was evaluated numerically and an expression for φ was obtained as,

$$\varphi = \frac{1}{(1-\alpha)^{3/2}} \sum_{i=1}^{8} p_i \, \alpha^{i-1},$$

with $p_1 = 0.5$, $p_2 = -0.7626$, $p_3 = 0.5979$, $p_4 = -0.7827$, $p_5 = 0.7879$, $p_6 = -0.2171$, $p_7 = -0.3575$, and $p_8 = 0.2322$. The use of the series expression for φ instead of the integral greatly enhances the computation speed of the double integral, Eqn. (1) to calculate the crack opening displacement profile. This series expression for φ was fit for α ranging from 0.0 to 0.95 within ±0.5%. A similar approach was successfully used by John et al. [33] in developing a weight function for the single edge cracked geometry with clamped ends.

Note that the derivatives F_r', G_r' and φ' can be easily derived as,

$$F_r' = \frac{\partial F_r}{\partial \alpha},$$

$$G_r' = \frac{\partial G_r}{\partial \alpha}, \text{ and}$$

$$\varphi' = \frac{\partial \varphi}{\partial \alpha} = \frac{1}{\alpha}\left[-2\varphi + F_r^2\right].$$

References

1. D. B. Marshall, B. N. Cox and A. G. Evans, *Acta Metalllurgica*, 33 (1985) 2013-2021.
2. L. N. McCartney, *Proceedings of Royal Society of London*, A 429 (1987) 329-350.
3. B. S. Majumdar, G. M. Newaz and A. R. Rosenfield, Advances in Fracture Research, Proceedings of the 7th International Conference on Fracture, Vol. 4 Houston, Texas (1989) 2805-2814.
4. R. M. McMeeking and A. G. Evans, *Mechanics of Materials*, 9 (1990) 217-227.
5. S. Danchaivijit and D. K. Shetty, *Journal of the American Ceramic Society*, 76 (1993) 2497-2504.
6. Y. -C. Chiang, A. S. D. Wang, and T. -W. Chou, *Journal of the Mechanics and Physics of Solids*, 41 (1993) 1137-1154.
7. L. J. Ghosn, J. Telesman, P. Kantos, *Fatigue 93*, Vol. II, Engineering Materials Advisory Services Ltd., West Midlands, U. K., (1993) 1231-1238.
8. R. John, J. R. Jira, J. M. Larsen and N. E. Ashbaugh, *Fatigue 93*, Vol. II, Engineering Materials Advisory Services Ltd., West Midlands, U. K., (1993) 1091-1096.
9. R. John, S. G. Kaldon and N. E. Ashbaugh, Titanium Metal Matrix Composites II, WL-TR-93-4105, Wright Laboratory, Wright-Patterson AFB, OH 45433 (1993) 270.
10. J. W. Hutchinson and H. M. Jensen, *Mechanics of Materials*, 9 (1990) 139-163.
11. D. L. Davidson, *Metallurgical Transactions*, 23A (1992) 865-879.
12. B. N. Cox and D. B. Marshall, *International Journal of Fracture*, 49 (1991) 159-176.
13. D. Zheng and H. Ghonem, "Life Prediction Methodology of Titanium Matrix Composites," ASTM STP 1253, Philadelphia, PA, (1996) 137-163.
14. J. G. Bakuckas and W. S. Johnson, "Life Prediction Methodology of Titanium Matrix Composites," ASTM STP 1253, Philadelphia, PA, (1996) 497-519.
15. J. M. Larsen, J.R. Jira, R. John and N. E. Ashbaugh, "Life Prediction Methodology of Titanium Matrix Composites," ASTM STP 1253, Philadelphia, PA, (1996) 114-136.
16. B. N. Cox, "Life Prediction Methodology of Titanium Matrix Composites," ASTM STP 1253, Philadelphia, PA, (1996) 552-572.
17. J. Rödel, J. F. Kelly and B. R. Lawn, *Journal of the American Ceramic Society*, 73 (1990) 3313-3318.
18. T. Fett, D. Munz, C. T. Yu, and A. S. Kobayashi, *Journal of the American Ceramic Society*, 77 (1994) 3267-3269.
19. T. Fett, D. Munz, J. Seidel, M. Stech, and J. Rödel, *Journal of the American Ceramic Society*, 79 (1996) 1189-1196.
20. J. J. Du, A. S. Kobayashi and N. M. Hawkins, *Journal of Engineering Mechanics*, 116 (1990) 605-619.
21. Z. K. Guo, A. S. Kobayashi and N. M. Hawkins, *Engineering Fracture Mechanics*, 46 (1993) 1041-1049.
22. J. C. Hay and K. W. White, *Journal of the American Ceramic Society*, 76 (1993) 1025-1032.
23. J. C. Hay and K. W. White, *Journal of the American Ceramic Society*, 78 (1995) 1849-1854.
24. R. John, P. R. Stibich, D. A. Johnson, N. E. Ashbaugh and A. F. Lackey, *Proceedings of Ninth Annual Technical Conference, American Society for Composites,* Technomic Publishing Co., Inc., Lancaster, PA, (1994) 515-522.
25. R. John, P. R. Stibich, D. A. Johnson and N. E. Ashbaugh, *Scripta Metallurgica et Materialia*, 33 (1995) 75-80.
26. G. A. Hartman and T. Nicholas, *Experimental Mechanics*, SEM, 2 (1987) 24-26.
27. W. N. Sharpe, J.R. Jira and J. M. Larsen, "Small-Crack Test Methods," ASTM STP 1149, Philadelphia, PA, (1992) 92-115.
28. H. Bueckner, *Angew. Math. Mech.*, 50 (1970) 529-546.
29. J. R. Rice, *International Journal of Solids and Structures*, 8 (1972) 751-758.
30. P. C. Paris and G. C. Sih, "Fracture Toughness Testing and Its Applications," ASTM STP 381, Philadelphia, PA. (1964) 30-81.

31. X. -R. Wu and A. J. Carlsson, "Weight Functions and Stress Intensity Factor Solutions," Pergamon Press, Inc., Elmsord, New York, USA (1991).
32. H. Tada, P. C. Paris and G. R. Irwin, "The Stress Analysis of Cracks Handbook," Paris Productions Inc., St. Louis, MO, 1985.
33. R. John, S. G. Kaldon, D. A. Johnson and D. Coker, *International Journal of Fracture*, 72 (1995) 145-158.
34. IMSL, Problem-Solving Software Systems, User's Manual, Math/Library Version 2.0, Houston, TX, USA (1996).
35. ADINA - A Finite Element Program for Automatic Dynamic Incremental Nonlinear Analysis, Report ARD 89-1, ADINA R&D, Inc., Watertown, Massachusetts, USA 1989.
36. R. John and D. J. Buchanan, *to be submitted for publication,* (1996).

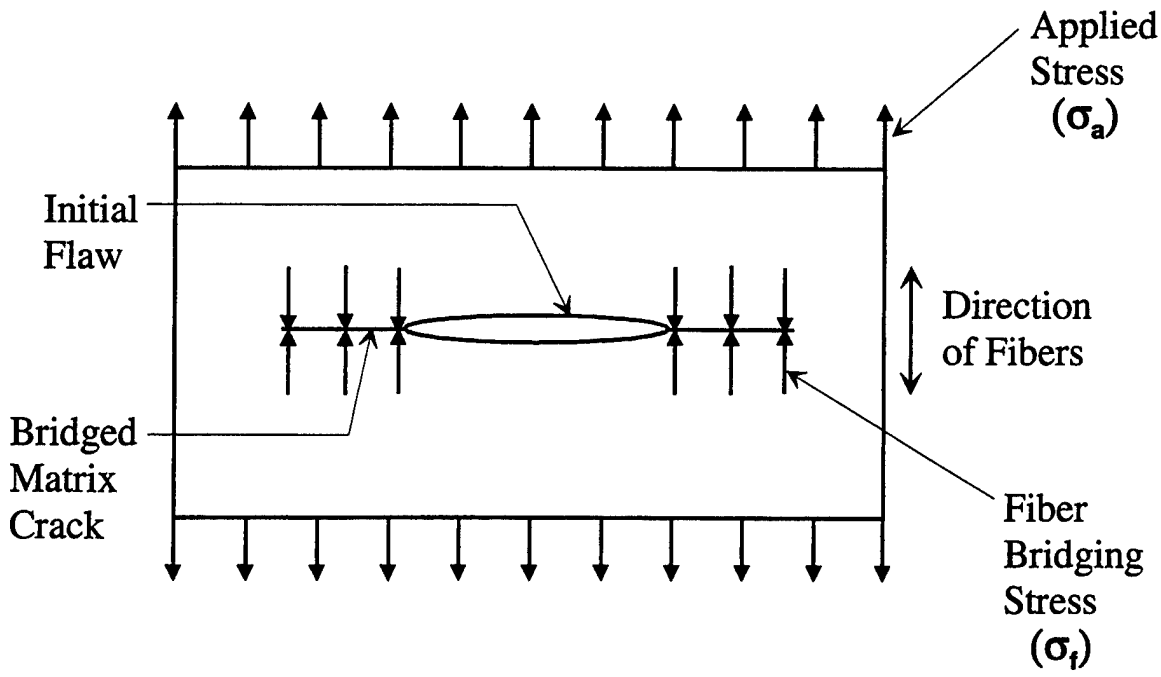


Figure 1. Schematic of fiber bridged crack growth in an unidirectional reinforced composite.

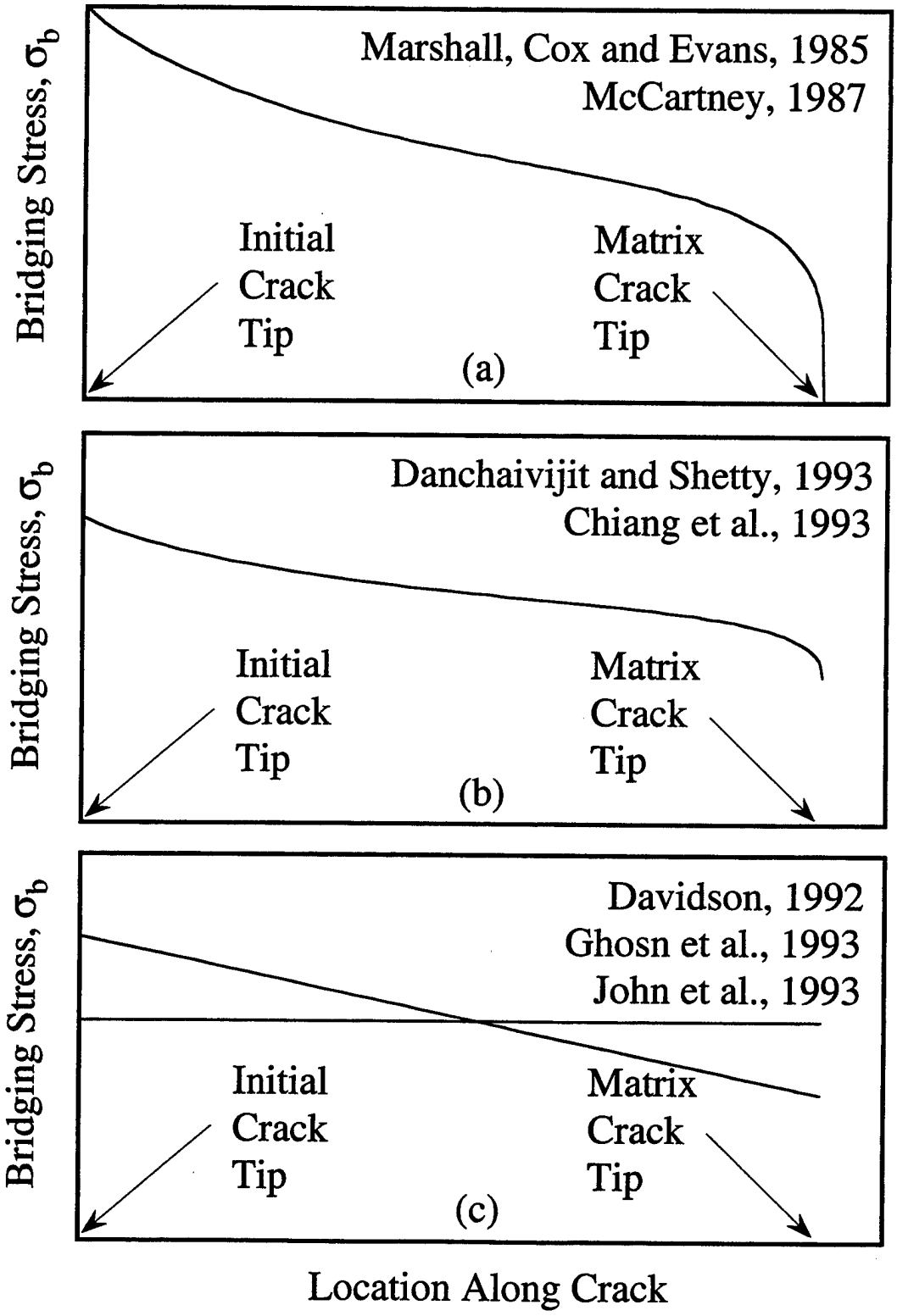


Figure 2. Schematic showing different bridging stress distributions.

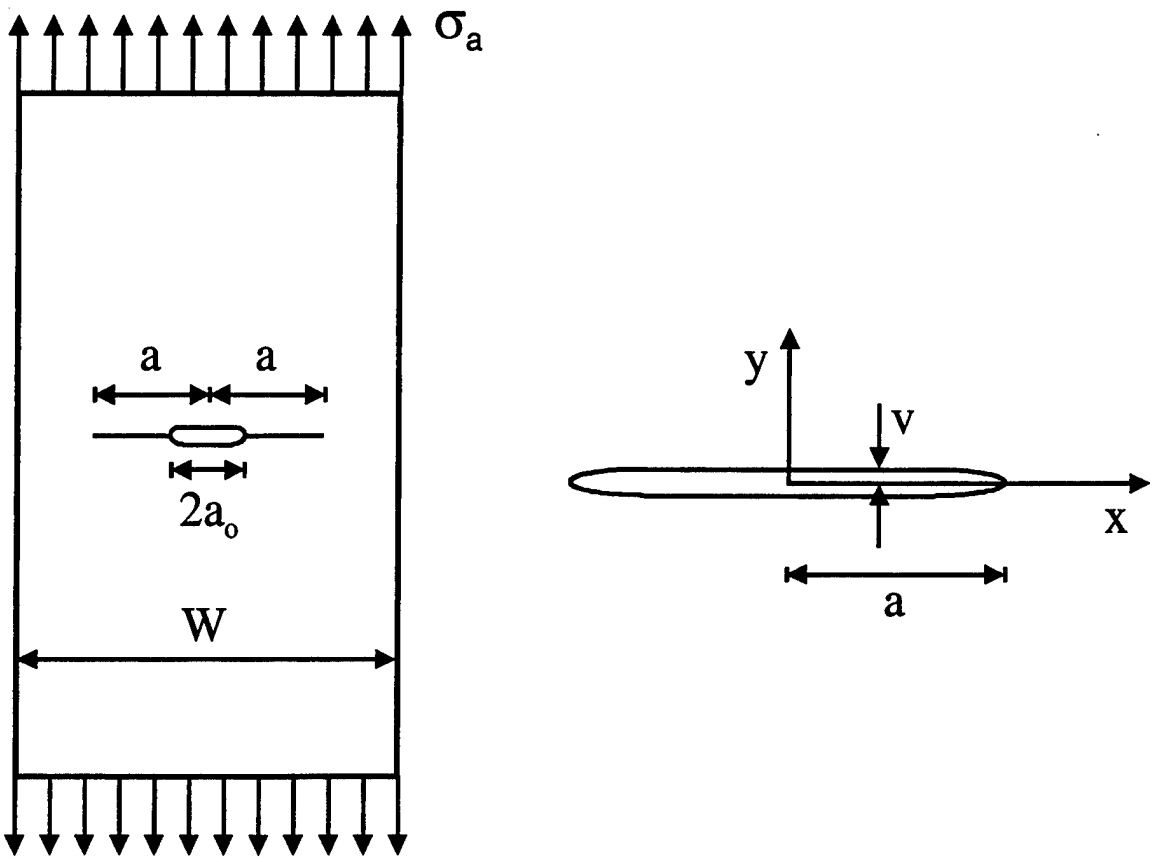


Figure 3. Schematic of M(T) geometry.

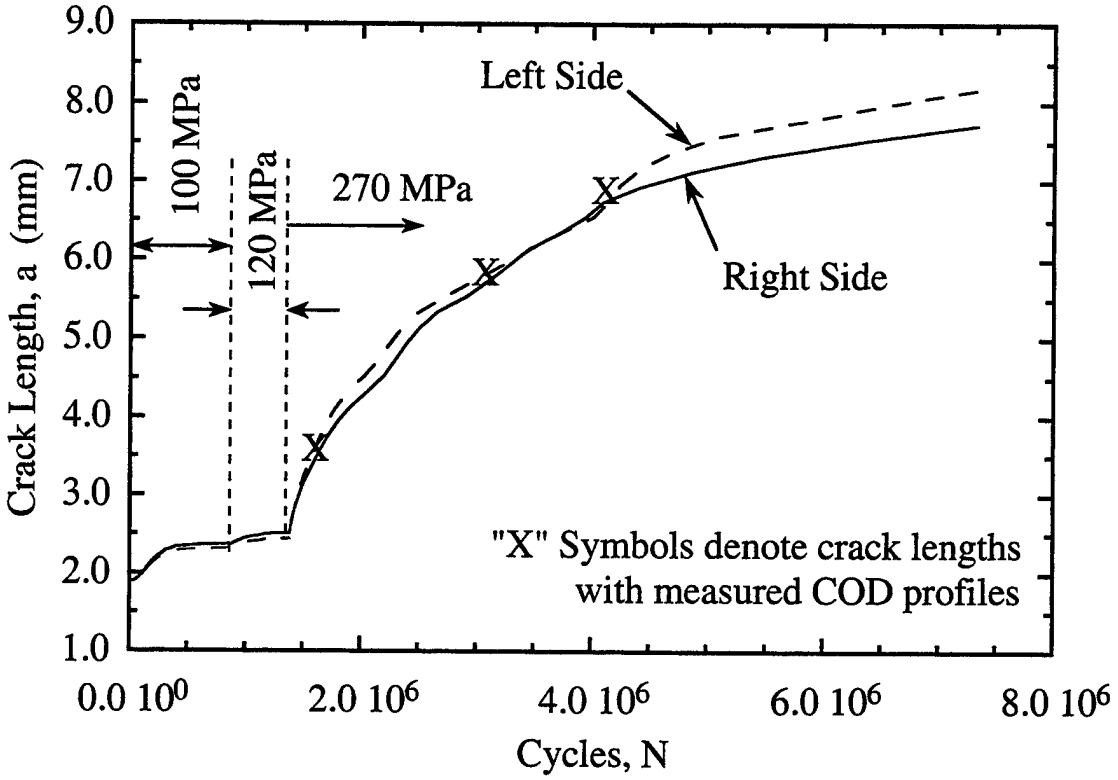


Figure 4. Crack length versus cycles response for $[0]_4$ SCS-6/TIMETAL®21S tested at room temperature.

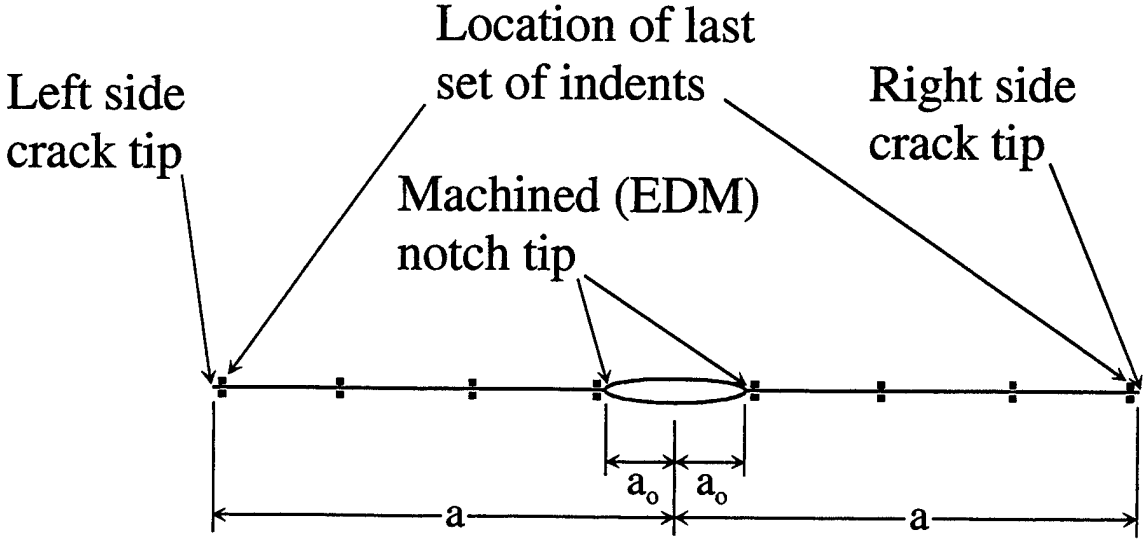


Figure 5. Schematic of COD locations during crack growth in SCS-6/TIMETAL®21S.

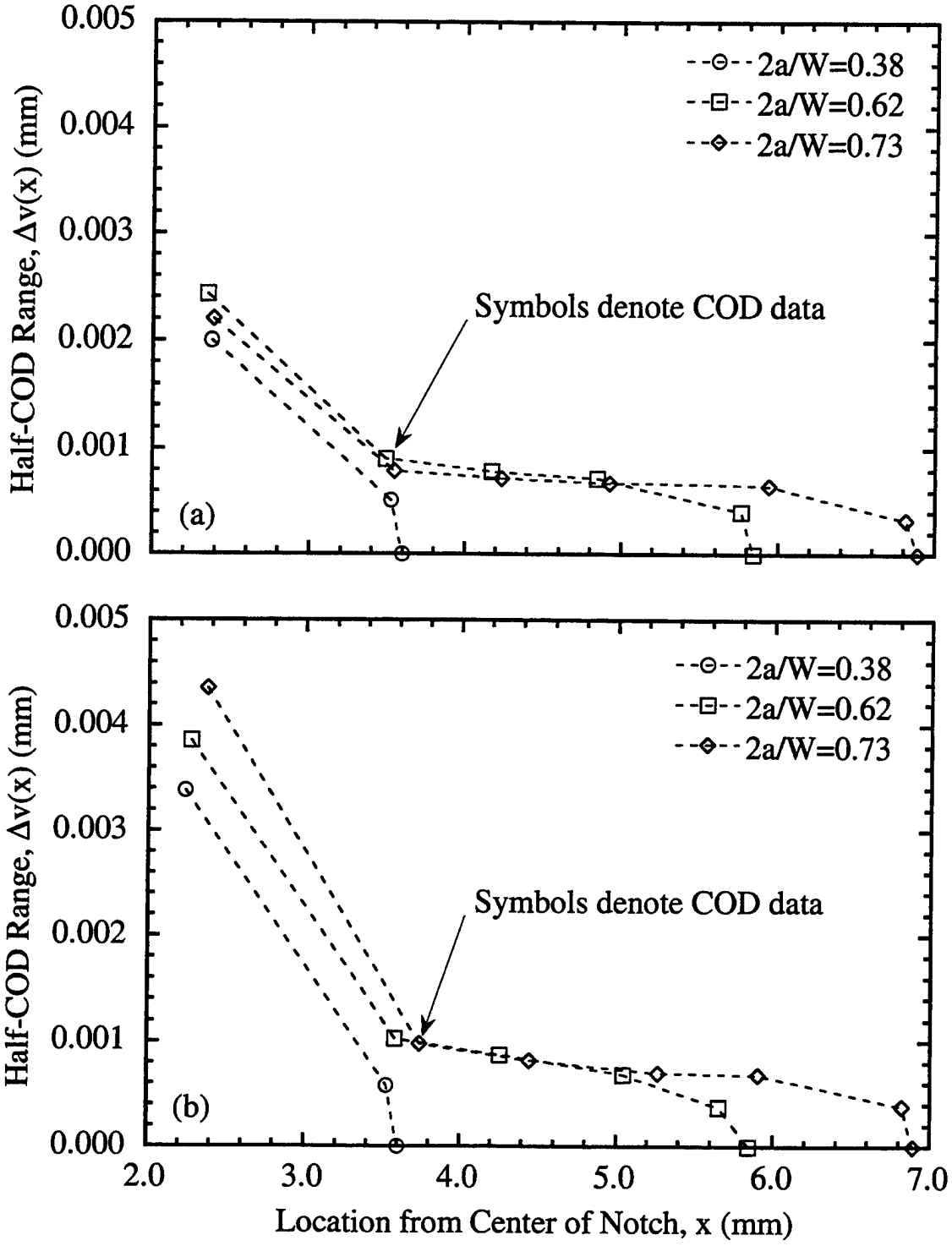


Figure 6. Half-COD range as a function of location for 3 crack lengths (a) Left side, (b) Right side.

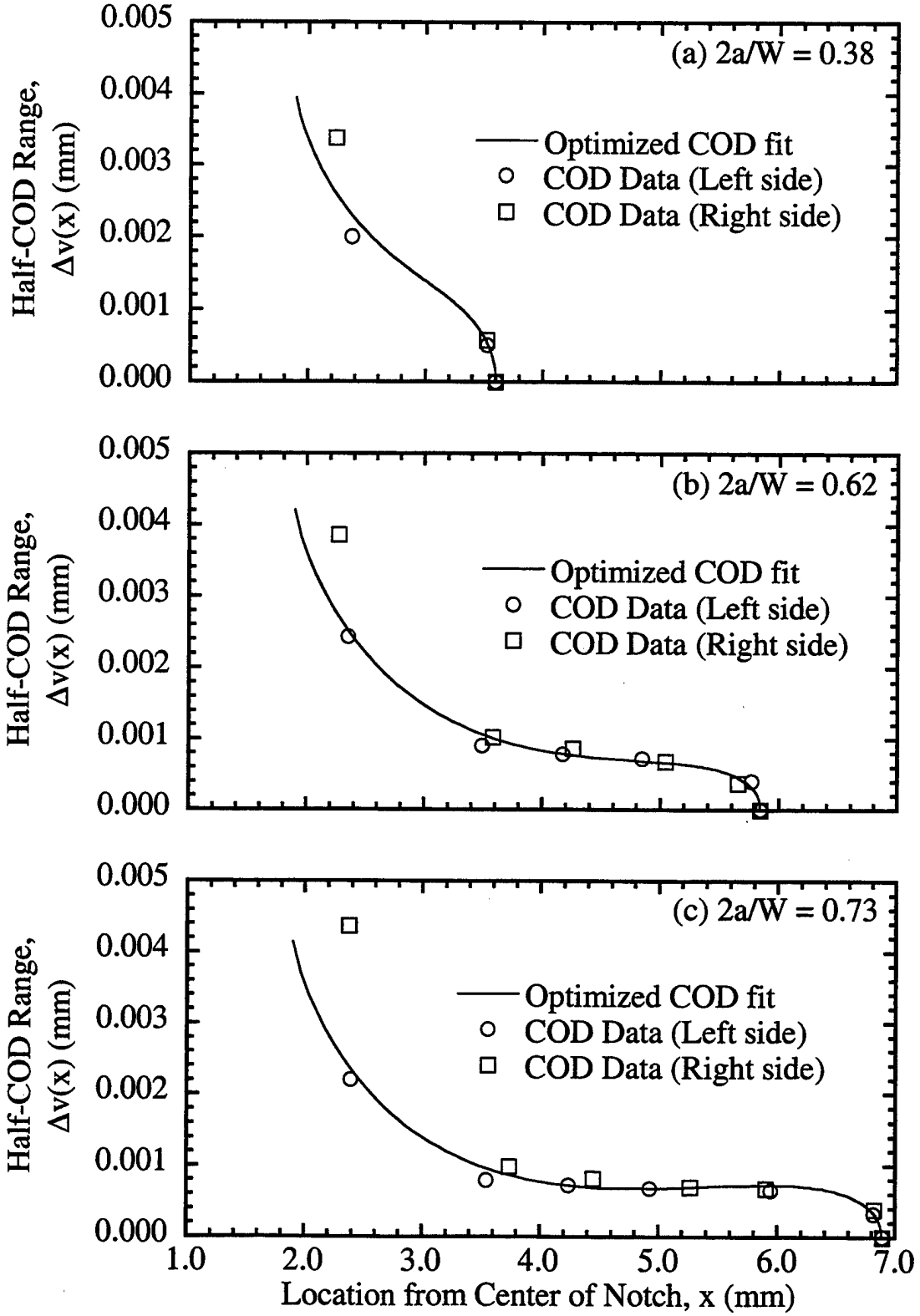


Figure 7. Comparison of optimized half-COD profile and measured COD Data.

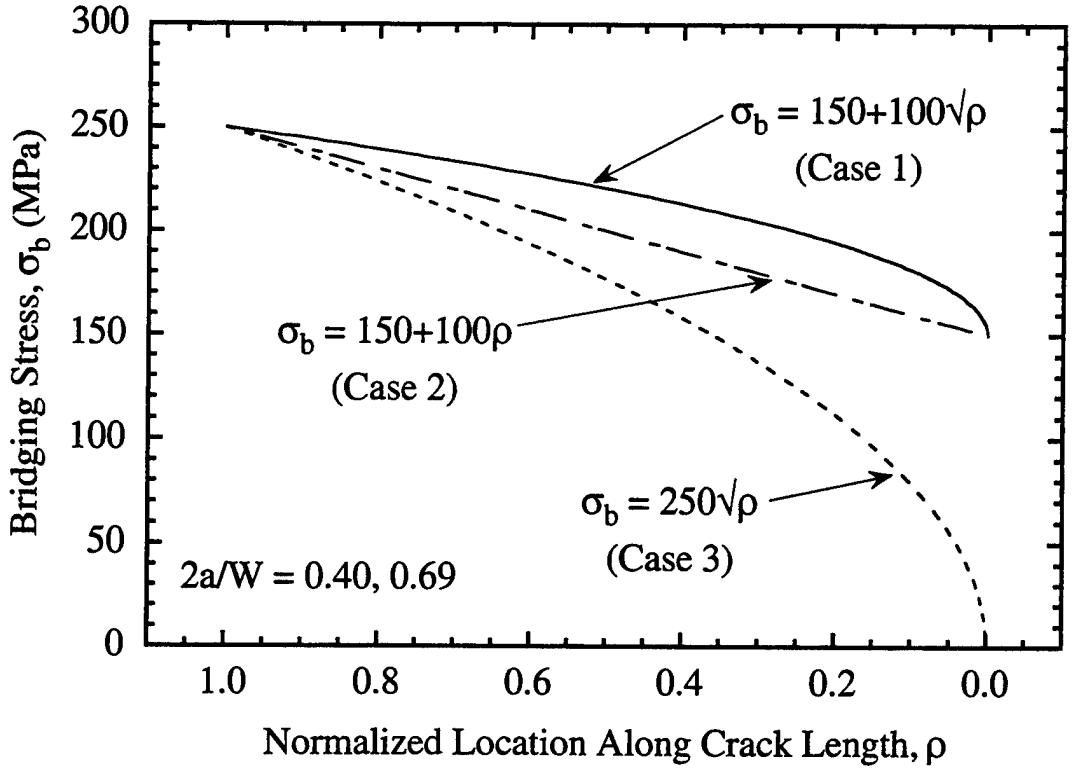


Figure 8. Bridging stress distributions used in the finite element analysis.

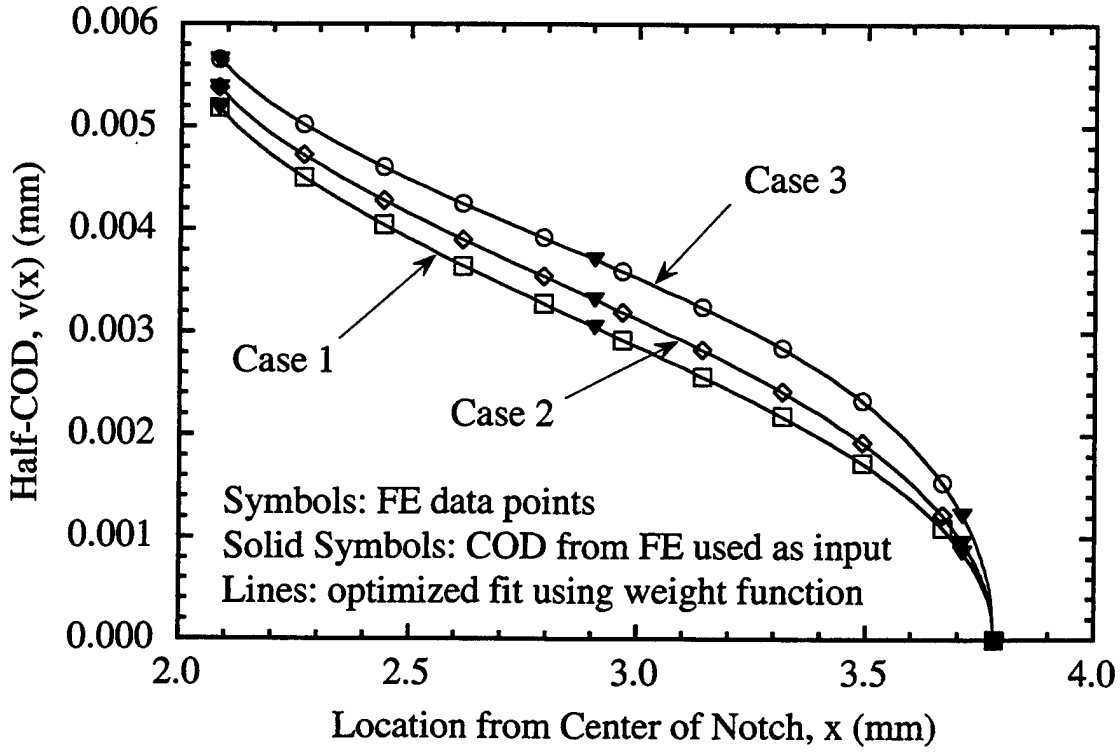


Figure 9. Comparison of optimized COD profile with FE results for 2a/W=0.40.

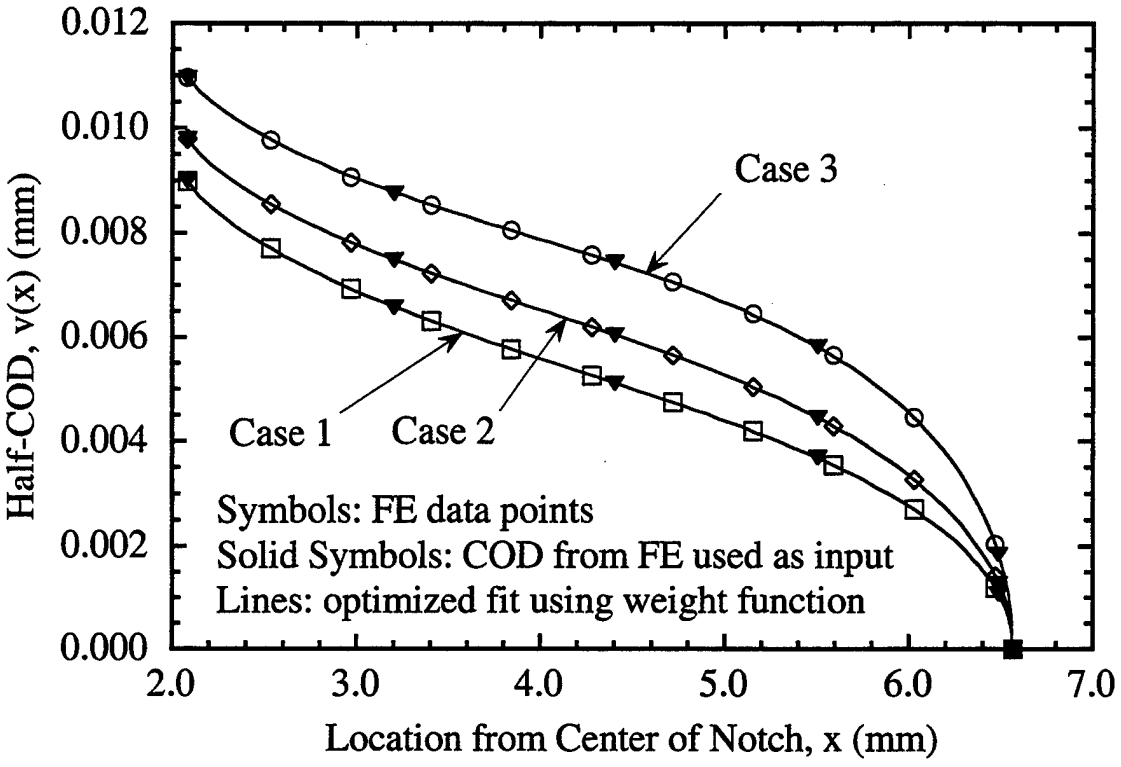


Figure 10. Comparison of optimized COD profile with FE results for 2a/W=0.69.

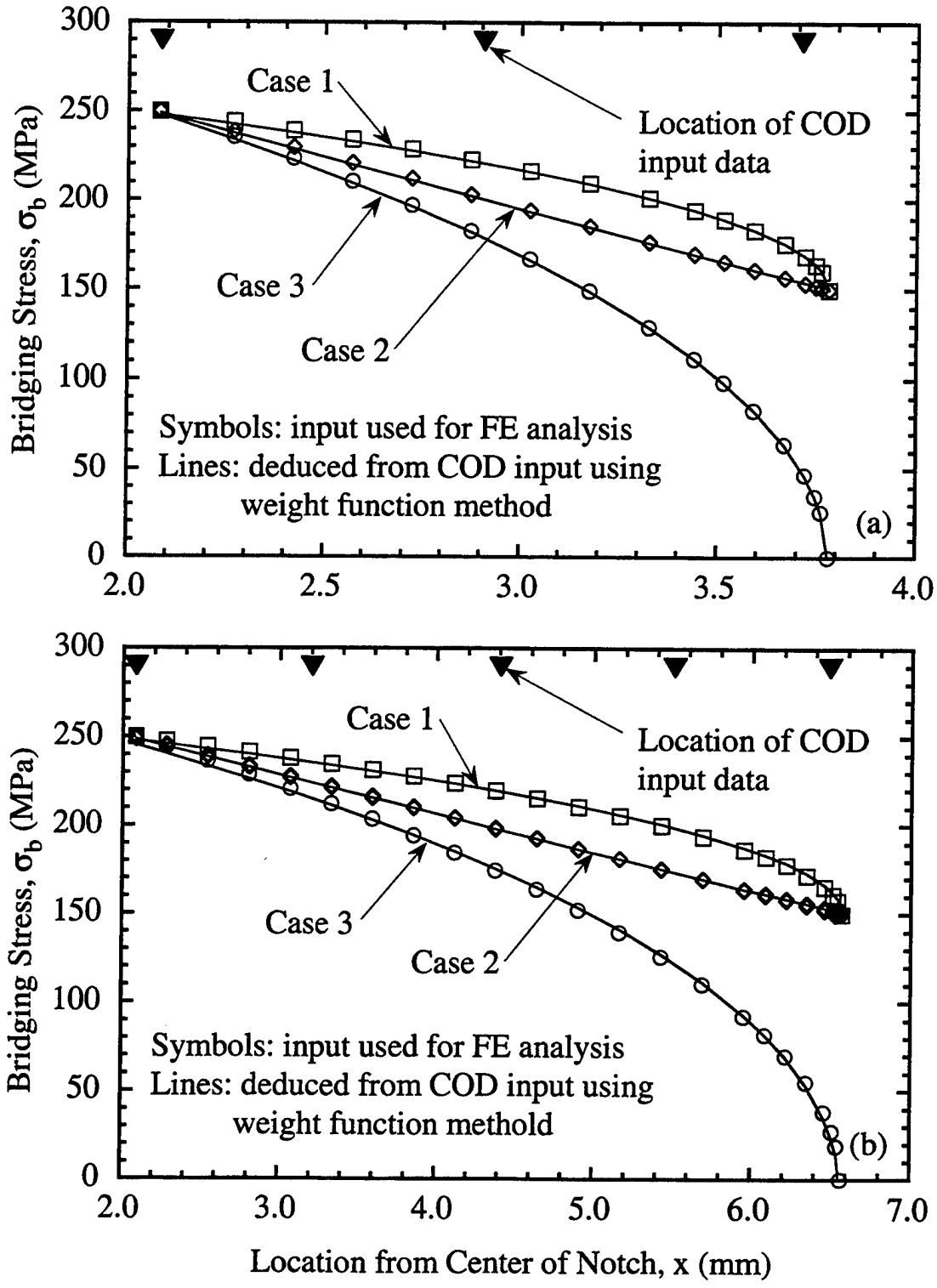


Figure 11. Comparison of bridging stress deduced using WF method with input used for FE analysis for (a) 2a/W=0.40 and (b) 2a/W=0.69.

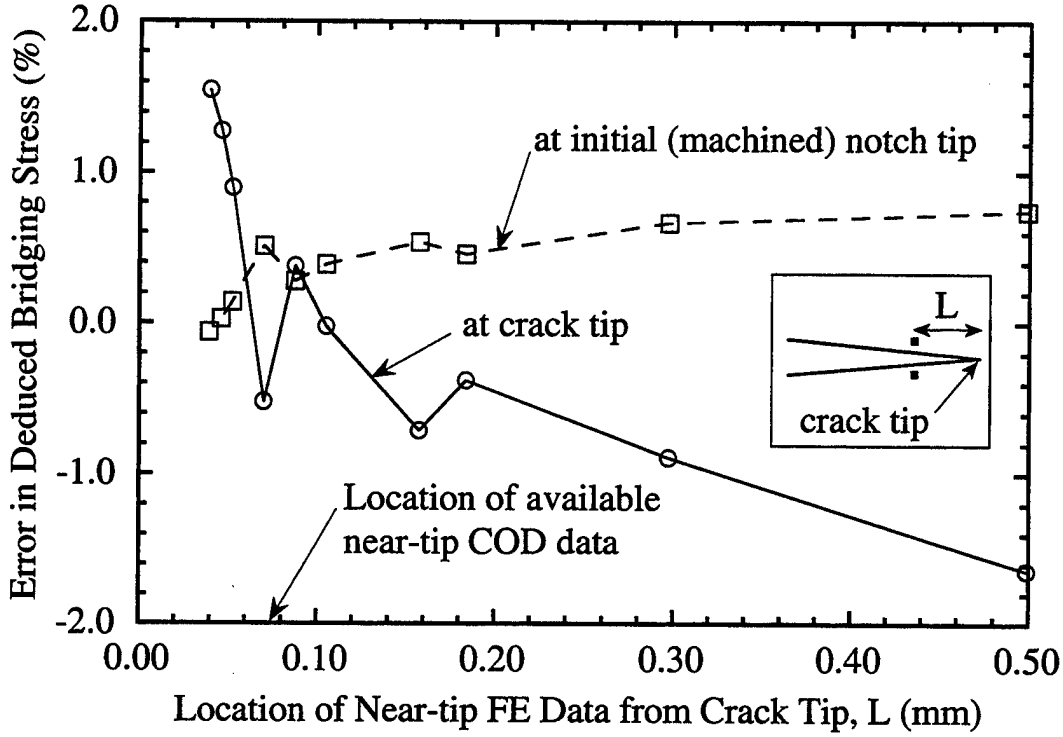


Figure 12. Effect of location of near-crack tip COD measurement on deduced bridging stress distribution for 2a/W=0.40.

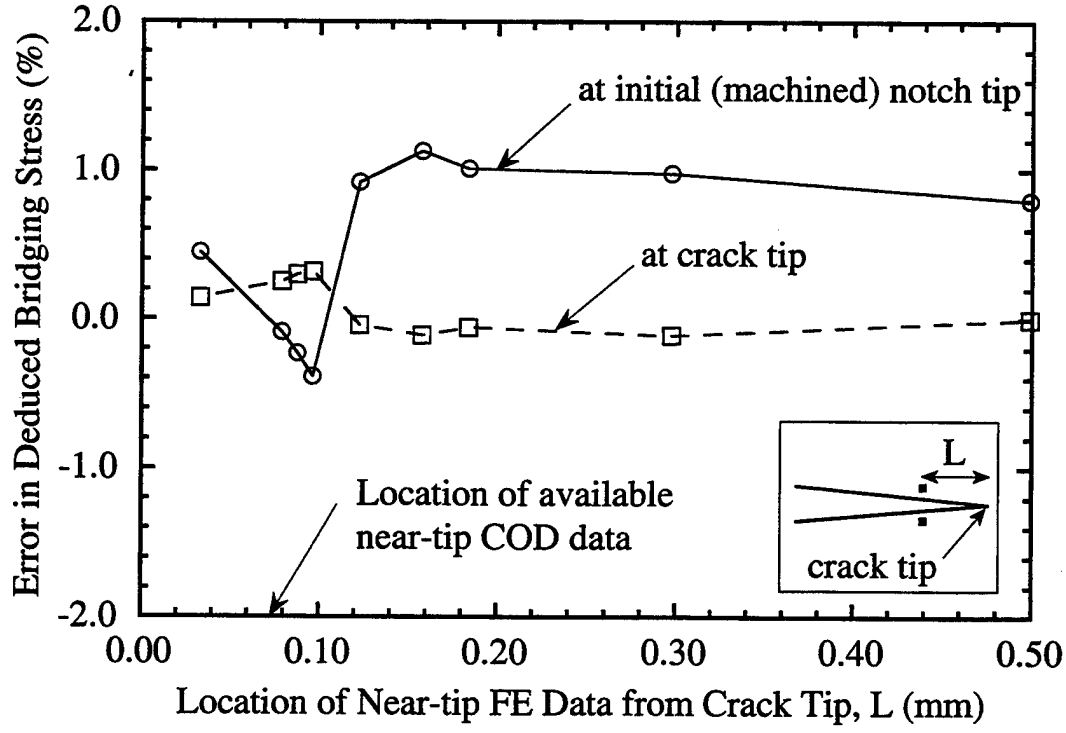


Figure 13. Effect of location of near-crack tip COD measurement on deduced bridging stress distribution for 2a/W=0.69.

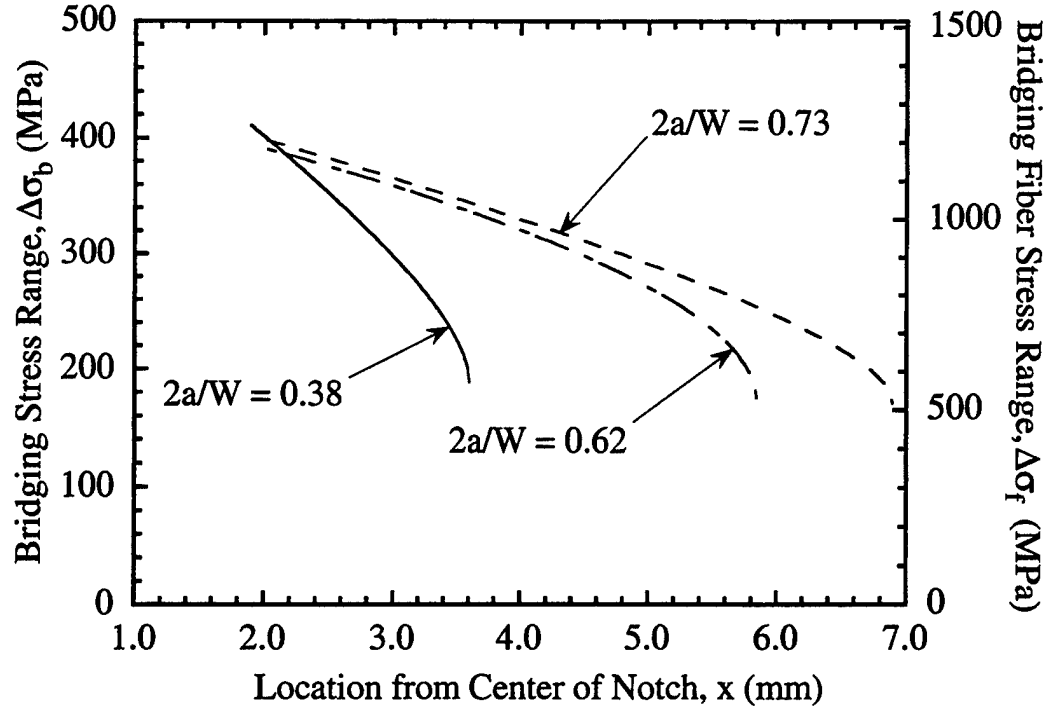


Figure 14. Deduced bridging stress distribution in SCS-6/TIMETAL®21S.

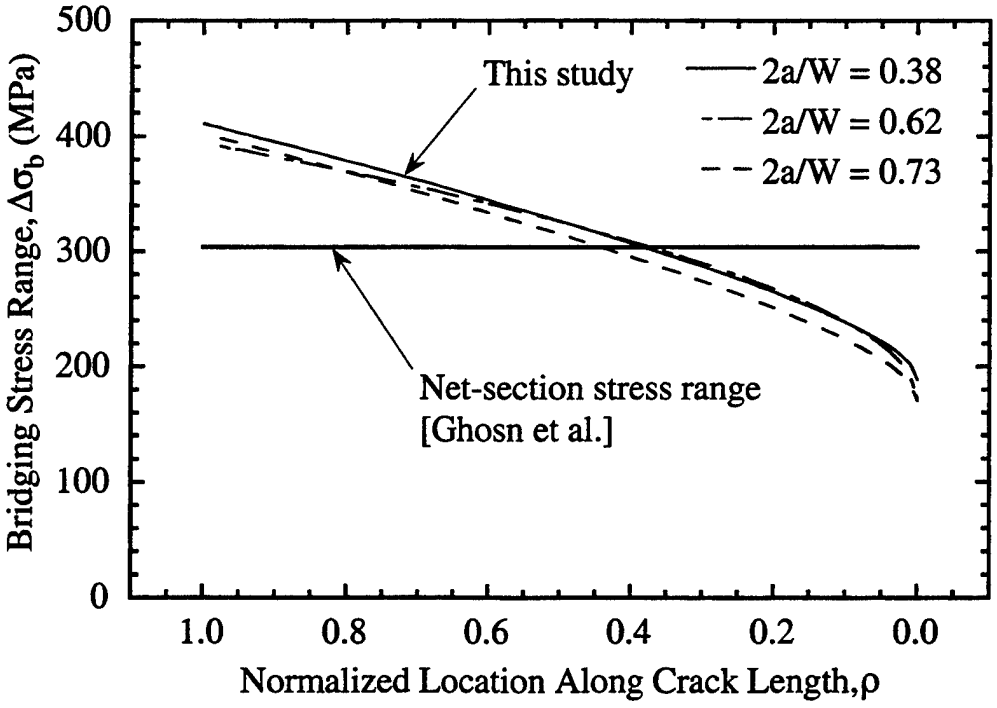


Figure 15. Deduced bridging stress distribution as a function of normalized location along crack length in SCS-6/TIMETAL®21S.

Reference: John, R., Jira, J.R., and Larsen, J.M., "Effect of Stress and Geometry on Fatigue Crack Growth Perpendicular to Fibers in Ti-6Al-4V Reinforced with Unidirectional SiC Fibers," Seventh Symposium on Composites: Fatigue and Fracture, ASTM STP 1330, American Society for Testing and Materials, May 1997. (Paper ID # 1199)

Effect of Stress and Geometry on Fatigue Crack Growth Perpendicular to Fibers in Ti-6Al-4V Reinforced with Unidirectional SiC Fibers

Reji John[1], Jay R. Jira and James M. Larsen
Wright Laboratory (WL/MLLN), Materials Directorate
Wright-Patterson Air Force Base, OH 45433-7817, USA.

[1]University of Dayton Research Institute, Dayton, OH 45469-0128, USA.

ABSTRACT

Critical turbine engine and aircraft components fabricated from continuous fiber reinforced metal matrix composite (MMC) will experience cyclic loads during service, and many of these components typically contain crack initiators. Hence, extensive characterization of the fatigue crack growth behavior of a model MMC ($[0]_8$ SCS-6/Ti-6Al-4V) was initiated by the USAF Wright Laboratory. This paper discusses some of the results of the experimental and analytical investigation of fatigue crack propagation in $[0]_8$ SCS-6/Ti-6Al-4V. Automated fatigue crack growth tests were conducted using middle tension, M(T), specimens at 23°C with a stress ratio of 0.1. During some of the tests, the crack opening displacement profile was measured to verify the stress distributions predicted by fiber bridging models. The results are also compared with those available for SM1240/Ti-6Al-4V under tension and bending fatigue loading. This study showed that the shear lag model assuming a constant value of τ can be used to predict bridged crack growth perpendicular to fibers in SCS-6/Ti-6Al-4V and SM1240/Ti-6Al-4V over a wide range of stress levels and under tension and bending fatigue loading conditions. The predictions of partially-bridged and unbridged crack growth, crack opening displacements and slip lengths correlated well with the data. The value of the fiber/matrix interfacial shear stress, τ, was the same for SCS-6/Ti-6Al-4V and SM1240/Ti-6Al-4V, implying that the bridging mechanism of the SM1240 fiber is identical to that of the SCS-6 fiber at room temperature. The results also indicate that the onset of fiber failure could be predicted using the bundle strength as the critical value.

KEYWORDS: bridging stress intensity factor, center-crack, crack growth rate, crack opening displacement, cyclic loading, fatigue crack growth, fiber bridging, life prediction, metal matrix composite, shear lag model, titanium matrix composite

INTRODUCTION

Titanium alloy matrix composites (TMC) are targeted for use in many aerospace applications which require high specific strength and stiffness at elevated temperatures [1,2]. Critical turbine engine and aircraft components fabricated from continuous fiber reinforced TMC will experience cyclic loads during service, and many of these components typically contain crack initiators. Hence, many investigations [3-25] have been conducted to characterize the fatigue crack growth behavior of titanium matrix composites such as SCS-6/Ti-24Al-11Nb, SCS-6/TIMETAL®21S, SM1240/Ti-6Al-4V, SM1240/TIMETAL®21S, SCS-6/Ti-15V-3Cr-3Al-3Sn and SCS-6/Ti-6Al-4V. The matrix crack growth in these composites is typically dominated by fiber bridging, resulting in decreasing crack growth rate with increasing crack length [3-22]. This behavior has been generally modeled as fully bridged crack growth using various fiber bridging models such as shear lag models [4-7,11,13-15,18-25], fiber pressure models [7] and constant

bridging stress models [6,14,15]. Most of the available data have been restricted to one or two stress levels. Jira and Larsen [12] and Larsen et al. [13] provided extensive data under a wide range of stress levels for crack growth from holes in $[0]_8$ SCS-6/Ti-24Al-11Nb and various layups of SCS-6/TIMETAL®21S, respectively. Larsen et al. [13,26] showed that the shear lag model could be used to predict the crack growth in various layups of SCS-6/TIMETAL®21S over a wide range of stress levels, and at room and elevated temperatures. The fiber/matrix interfacial stress, τ, in the shear lag models was found to be independent of applied stress and decreased with increasing temperature [13,27]. The effect of temperature on τ is similar to the results reported by Bakuckas and Johnson [8,25] and Connell and Zok [21].

All these investigations essentially determined τ as a fitting parameter based on the measured crack length versus cycles response and the constituent properties. As shown by Bakuckas and Johnson [8] and Larsen et al. [13], the value of τ deduced from crack growth data depends on the fiber bridging model, and the assumed relationship between the effective stress intensity factor range at the matrix crack tip in the composite and the neat (fiberless) matrix. Many attempts [4-8,13-16,18,20] have been made to relate the τ required to predict the crack growth behavior to that obtained from push-out tests. But, the wide range of values reported for τ appears to indicate the futility of such a correlation. Cox [19], in discussing the limitations and applicability of the existing fiber bridging models, suggested the deduction of the bridging law (and associated parameters) directly from critical experiments. This is consistent with deducing τ as a fit parameter. Thus, determination of the parameters required for developing a comprehensive life prediction model requires extensive testing and critical measurements.

An extensive characterization of the fatigue crack growth behavior of a model TMC was initiated by the USAF Wright Laboratory under the Metal Matrix Composite (MMC) Life Prediction Cooperative Program. The model TMC system chosen by the Cooperative was $[0]_8$ SCS-6/Ti-6Al-4V. The test program included a wide range of loading conditions such as low to high stress levels, stress ratios from 0.1 to 0.7 and temperatures from 23 to 316°C. This papers discusses the results from the tests on $[0]_8$ SCS-6/Ti-6Al-4V conducted under tension fatigue loading at room temperature with a stress ratio of 0.1. These results are compared with the results available in the literature for $[0]_4$ SCS-6/Ti-6Al-4V [6] and $[0]_6$ SM1240/Ti-6Al-4V [20,21] under tension loading and $[0]_6$ SM1240/Ti-6Al-4V under three-point bend loading [9]. The ability of a shear lag model to predict the crack growth in these composites under a wide range of stress levels is also discussed.

EXPERIMENTAL PROCEDURE

Material

The composite consisted of the Ti-6Al-4V matrix reinforced with continuous SiC fibers (SCS-6™). The composite panels were manufactured by Textron Specialty Materials Division (SMD) by hot isostatic pressing alternating layers of woven fiber mat and matrix foil. The Textron SCS-6 fiber is produced by chemical vapor deposition on a carbon monofilament core. The fiber has a nominal diameter of 142 μm and possesses a double-pass, carbon-rich outer coating. The fiber mat was woven with a fiber spacing equivalent to 129 fibers per 25.4 mm. The thickness of the 8-ply panels ranged from 1.82 to 1.94 mm. Knowing the thickness of the composite and the fiber spacing, the volume faction of the fibers, V_f, can be calculated as

$$V_f = \frac{\pi R_f^2}{B_p s}, \qquad (1)$$

in which R_f = fiber radius, B_p = average ply thickness = B/n, B = thickness of composite, n = number of plies, s = fiber spacing = 25.4/129 = 0.197 mm in this case. Thus, V_f for the specimens ranged from 0.32 to 0.35. Following consolidation, the composite was aged in

vacuum for 8 hours at 621°C to stabilize the matrix prior to testing. The properties of the constituent materials can be found in Refs. [28,29].

In this paper, the crack growth behavior of $[0]_8$ SCS-6/Ti-6Al-4V is compared with that obtained from $[0]_4$ SCS-6/Ti-6Al-4V [6] and $[0]_6$ SM1240/Ti-6Al-4V [9,20,21]. The loading conditions, geometric parameters, material constituents, and stress levels are listed in Table I. All these tests were conducted at R=0.1 in laboratory air. Note that the stress levels shown in Table I are the maximum far-field stresses for the center-cracked geometry and the maximum stresses in the outer layer for the bending geometry.

The SCS-6 and SM1240 are essentially SiC fibers with carbon and tungsten cores, respectively. The SCS-6 and SM1240 fibers are coated with two layers of carbon-rich coating (≈1μm thick/layer). SM1240 has an additional coating of TiB_2 on the outer layer. The presence of the carbon layers promotes the fiber/matrix interfacial sliding required to generate fiber bridging across the crack. After consolidation, significant residual stresses exist in SCS-6/Ti-6Al-4V [28] and SM1240/Ti-6Al-4V due to the mismatch of the coefficient of thermal expansion (CTE) between the fibers and the matrix. A finite-difference based non-linear code, FIDEP2 [29], was used to estimate the residual stresses in these composites. For $V_f \approx 0.32$, the radial residual stress in matrix at the fiber/matrix interface ≈ -260 MPa and -235 MPa for SCS-6/Ti-6Al-4V and SM1240/Ti-6Al-4V, respectively. Since, the fibers contain similar carbon coatings and are subjected to similar radial residual stresses, the fiber/matrix frictional shear stresses opposing the crack opening in the matrix may be expected to be similar.

Testing

A schematic of the center-cracked-tension specimen, M(T) is shown in Fig. 1. Typically, width, W, is 19.0 mm, thickness, B, is 1.82-1.94 mm, and initial notch to width ratio, $2a_0/W \approx 0.11$. The dimensions of the specimens corresponding to the tested stress levels are shown in Table I. The initial notches, created using electrical discharge machining (EDM), were ≈0.3 mm wide. The notches were oriented perpendicular to the fibers. The specimens were ≈152 mm long with a clear distance of ≈ 102 mm between the clamped ends. Automated fatigue crack growth tests were conducted with stress ratio, R (=minimum stress/maximum stress) of 0.1 and loading frequency of 1 Hz. During the tests, crack extension from the machined notch was monitored using the direct current electric potential (DCEP) technique. Periodic optical measurements of the four crack tips enabled verification and subsequent correction of the DCEP response. During some of the tests, the crack opening displacement (COD) profile was measured along both cracks on one side of the specimen using the laser interferometric displacement gage (IDG) system [30].

In addition to the tests on composites, fatigue crack tests were also conducted on the neat (fiberless) Ti-6Al-4V, which was consolidated from matrix alloy foils into 1.44 mm thick panels using the composite material processing and aging conditions. The single edge-cracked geometry with clamped ends [31,32] was used to conduct threshold-type and constant-load tests at R = 0.1 and 0.7. All the tests were conducted with a loading frequency of 1 Hz. During these tests, crack length and closure behavior were determined from crack mouth opening compliance measurements made using an extensometer.

EXPERIMENTAL RESULTS

Crack Growth in Neat Ti-6Al-4V

The crack growth rate (da/dN) versus effective stress intensity factor range ($\Delta K_{m,e}$) behavior of neat Ti-6Al-4V is shown in Fig. 2. The data from the tests at R=0.1 exhibited closure stress intensity factor, K_{cl} of ≈ 0.3-0.5 K_{max} where K_{max} = maximum stress intensity factor. Thus, $\Delta K_{m,e} = K_{max} - K_{cl}$. The tests at R=0.7 were devoid of closure. As shown in Fig. 2, the closure corrected data obtained at R=0.1 correlated well with the data obtained at R=0.7. These data can be represented by the following expression:

$$\log\left(\frac{da}{dN}\right) = C_1\left(\sinh\left[C_2\left\{\log\left(\Delta K_{m,e}\right) + C_3\right\}\right]\right) + C_4 \qquad (2)$$

where C_1 = 1.4474, C_2 = 2, C_3 = -1.0822, and C_4 = -7.1261, $\Delta K_{m,e}$ is in MPa$\sqrt{m}$, and da/dN is in m/cycle. This equation, which is valid for growth rates ranging from 5 x 10^{-10} to 3 x 10^{-6} m/cycle, is shown as a solid line in Fig. 2. Three other lines corresponding to the matrix behavior assumed by Davidson [6], Zok et al. [20] and Connell and Zok [21] are also shown in Fig. 2. These Paris-law type equations are close to the data obtained during this study for neat Ti-6Al-4V. Davidson's [6] equation is based on test data from recrystallization annealed (RA) Ti-6Al-4V. The equation by Connell and Zok [21] was deduced by fitting the fatigue crack growth data from $[0]_6$ SM1240/Ti-6Al-4V.

Crack Growth in $[0]_8$ SCS-6/Ti-6Al-4V

The crack growth response obtained from specimens tested at 400 MPa and 700 MPa are shown in Figs. 3 and 4, respectively. The specimens tested at 400 MPa exhibited decreasing crack growth rate (da/dN) with increasing cracking length, consistent with the phenomenon of fully bridged crack growth [4]. One specimen was stopped after ≈1.2x10^6 cycles, and the other was tested until the crack tips were close to the edges of the specimen. As shown in the figure, the V_f of these two specimens are different because they were obtained from different plates. There is a minor difference in the crack growth response for the two specimens, i.e. difference of ≈1 mm after 10^6 cycles. Not surprisingly, the specimen with the lower V_f shows faster crack growth rate. Figure 4 shows the data obtained at 700 MPa. The crack growth response is distinctly different from that shown in Fig. 4. The specimen failed at ≈7200 cycles, which is three orders of magnitude lower than the cycle count achieved at 400 MPa without failure.

Comparison of Crack Growth in $[0]_8$ SCS-6/Ti-6Al-4V and $[0]_6$ SM1240/Ti-6Al-4V

The crack growth behavior of $[0]_8$ SCS-6/Ti-6Al-4V is compared with that of $[0]_6$ SM1240/Ti-6Al-4V [9,20,21] in Figs. 5 and 6, respectively. As shown in Table I, V_f for these specimens ranges from 0.31 to 0.35. Figure 5 compares the crack growth rate (da/dN) versus applied stress intensity factor range (ΔK_a) obtained at similar maximum stress levels of ≈400 MPa under tension fatigue loading and bending fatigue loading. Interestingly, under tension fatigue loading, the data from $[0]_8$ SCS-6/Ti-6Al-4V are close to those obtained from $[0]_6$ SM1240/Ti-6Al-4V. This similarity is also seen in the crack extension versus cycles response as shown in Fig. 6. The similarity in the crack growth behavior implies that, at room temperature, the bridging contribution of the SCS-6 fibers is similar to that of SM1240 fibers. This can possibly be attributed to the presence of similar carbon layers on the fibers and near-identical radial compressive stresses at the fiber/matrix interface (also discussed in section "Material"). The crack growth behavior of neat Ti-6Al-4V is also shown in Fig. 5. The crack growth rate in the composite is ≈ 2-3 orders of magnitude slower than in neat Ti-6Al-4V, highlighting the significantly higher damage tolerance of the composite.

The data from SM1240/Ti-6Al-4V [9] subjected to bending fatigue loading are also shown in Figs. 5 and 6. During the initial stages, i.e. when $\Delta K_a \leq 40$ MPa$\sqrt{m}$, the crack growth rates are similar to those under tension fatigue loading. With increase in crack length, the crack growth rate under bending decreases rapidly and appears to exhibit near-crack arrest conditions at $\Delta K_a \approx 50$ MPa$\sqrt{m}$. In contrast, under tension fatigue loading, the crack growth rate is ≈ an order of magnitude higher at the same ΔK_a, and for $\Delta K_a \geq 50$ MPa$\sqrt{m}$ the crack growth rate is nearly constant. Similar differences in crack growth rate behavior can be seen in the data reported by Ghosn et al. [7] for SCS-6/Ti-15V-3Cr-3Al-3Sn. Figure 6 clearly shows the difference in crack extension from the notch under tension and bending fatigue loading. Under bending, the crack extended only ≈1.23 mm [9] prior to near-arrest condition, while under

tension, the crack continued to extend at a near-constant rate. The distinct difference in the crack growth behavior of the composite under different types of loading implies that the use of a threshold ΔK, ΔK_{th}, type approach for design should account for the loading condition.

The crack growth behavior of the composites at high stress levels is compared with that of neat Ti-6Al-4V in Fig. 7. Also shown is the predicted behavior of the crack tip in the composite given by Eqn. (3).

$$\Delta K_{tip} = F_s \, \Delta K_{m,e} \ , \text{ where } \ F_s = \frac{E_c}{E_m} \qquad (3)$$

ΔK_{tip} = ΔK at the crack tip in the composite, E_c = elastic modulus of the composite in the direction of loading, E_m = elastic modulus of the matrix, and F_s = shielding factor [13]. Equation (3) was first proposed by Marshall, Cox and Evans [34] to predict matrix cracking in ceramic matrix composites. Larsen et al. [13] showed that Eqn. (3) can be used to predict the unbridged crack growth behavior in SCS-6/TIMETAL®21S. Equation (3) implies that the damage tolerance of the composite is higher than that in the matrix even when the fibers are not bridging the crack. This can be attributed to the shielding effect of the fiber in reducing the effective stress in the matrix. Typically, E_c / $E_m \approx 2$ at room temperature. Figure 7 shows that Eqn. (3) predicts the crack growth rate behavior of SM1240/Ti-6Al-4V at 844 and 889 MPa satisfactorily. This correlation between Eqn. (3) and the composite data is consistent with crack growth devoid of fiber bridging as reported by Zok et al. [20]. The data from SCS-6/Ti-6Al-4V at 700 MPa shows an initial region of bridged crack growth followed by increasing crack growth rate. Since the da/dN of this specimen is slower than that given by Eqn. (3), partial fiber bridging may be active during crack growth. The analysis and prediction of the effect of stress and type of loading on the crack growth behavior of SCS-6/Ti-6Al-4V and SM1240/Ti-6Al-4V are discussed in the following section.

ANALYTICAL PROCEDURE

The result of fiber bridging is the reduction of the effective ΔK at the matrix crack tip in the composite. This phenomenon is typically modeled as

$$\Delta K_{tip} = \Delta K_a - \Delta K_b \ , \qquad (4)$$

where ΔK_{tip} = ΔK at the crack tip in the composite and ΔK_b = bridging stress intensity factor range. ΔK_b is calculated using the weight function method given by Eqn. (5).

$$\Delta K_b = \int_{a_0}^{a} \Delta\sigma_b \, h(x,a) \, dx \ , \qquad (5)$$

where $\Delta\sigma_b$ = bridging stress range, h(x,a) = load-independent weight function, and a_0, x and a are defined in Fig. 1. $\Delta\sigma_b$ is generated by the fibers bridging along the crack wake. Various expressions for $\Delta\sigma_b$ are available in the literature [4-7,14-18,34,35]. The shear lag model, developed by Marshall, Cox and Evans [34] provided an expression for σ_b as given by Eqn. (6).

$$\sigma_b = \beta \sqrt{v} \ , \qquad (6)$$

where

$$\beta = \left[\frac{4 V_f^2 E_c E_f \tau}{(1 - V_f) E_m R_f} \right]^{1/2} \ , \qquad (7)$$

R_f = fiber radius, E_f = elastic modulus of the fiber, τ = frictional shear stress at the fiber/matrix interface, v = half-crack opening displacement as defined in Fig. 1, and other parameters were defined earlier. For cyclic loading, $\Delta\sigma_b$ is defined as [36]

$$\Delta\sigma_b = \beta\sqrt{2\,\Delta v}\,, \tag{8}$$

where Δv = half-crack opening displacement range. Using the weight function method, Δv can also be calculated as

$$\Delta v(x) = \frac{1}{E_o}\int_x^a \left[\int_0^{\bar{a}} h(\bar{x},\bar{a})\left\{\Delta\sigma_a(\bar{x}) - \Delta\sigma_b(\bar{x})\right\} d\bar{x}\right] h(x,\bar{a})\, d\bar{a}\,, \tag{9}$$

where $\Delta\sigma_a(x)$ = is the applied stress range, and E_o = effective elastic modulus for a transversely isotropic material [37]. In the above calculations, $\Delta\sigma_b = 0$ for $x < a_0$. Knowing $\Delta\sigma_b$, the maximum stress in the fibers bridging the crack can be calculated as

$$\sigma_{f,max} = \frac{\Delta\sigma_b}{V_f\,(1-R)}\,. \tag{10}$$

Thus, for a given crack length, knowing the constituent properties, τ and ΔK_a, the quantities ΔK_b and ΔK_{tip} can be calculated using Eqns. (5)-(9). Knowing ΔK_{tip} and using Eqns. (2) and (3), the crack growth da/dN can be calculated at the current crack tip. Hence, using crack length or cycle increments, Eqns. (2)-(9) can be used to predict the crack growth behavior of the composite. Equations (8) and (9) imply that an iterative scheme is required to predict the crack growth under cyclic loading. To overcome this problem, Cox and Lo [38] developed simplified non-dimensionalized solutions for ΔK_b. ΔK_b was expressed as

$$\Delta K_b = \Delta K_a\,\xi\left(\psi, \frac{2a_0}{W}, \frac{2a}{W}\right), \tag{11}$$

where

$$\psi = \frac{2\,\Delta\sigma_a\,\pi\,E_o}{4W\beta^2}, \tag{12}$$

and ξ is expressed as a canonical function [38]. Equation (11) can be used in place of Eqns. (5)-(9), thus increasing the computation speed significantly. Cox and Lo [38] provided expressions for ξ for the center-cracked, single-edge cracked and double-edge cracked geometries subjected to far-field tension loading. During this study, Eqns. (2)-(4), (11) and (12) were used to predict the crack growth behavior of the M(T) geometry. The rigorous method using Eqns. (2)-(9) were used to predict the crack opening displacement profiles for specific crack lengths for the M(T) geometry and to predict the da/dN versus ΔK_a behavior of the SE(B) geometry.

The above equations are applicable for analyzing fully bridged crack growth behavior with all the fibers intact during the entire crack growth, i.e, a_0 does not change during the crack growth. The bridged length, L_{br}, for a crack extending from the initial unbridged notch is defined as

$$L_{br} = a - a_0\,. \tag{13}$$

During fully bridged crack growth, L_{br} increases linearly with increase in crack extension, $\Delta a = a - a_0$. For unbridged crack growth $L_{br} = 0$. When L_{br} = constant, $a_0 = a - L_{br}$, i.e., the unbridged notch size is increased during the analysis, thus simulating a constant bridged length behind the

crack tip. This assumption implies that as the crack advances, the fibers are continuously failing at a distance equal to L_{br} behind the crack tip. As discussed later, a constant value of L_{br} was used to predict the crack growth at high stress levels in SCS-6/Ti-6Al-4V. The available solutions [39] for the M(T) and SE(B) geometries were used to calculate ΔK_a. The method proposed by Wu and Carlsson [40] were used to derive the weight functions for the M(T) and SE(B) geometries. The weight function used for the M(T) geometry is also reported in Ref. [17]. The constituent properties used in the analysis are reported in Table II. The predictions of crack growth in SCS-6/Ti-6Al-4V and SM1240/Ti-6Al-4V are discussed next.

PREDICTION OF CRACK GROWTH IN SCS-6/Ti-6Al-4V AND SM1240/Ti-6Al-4V

Bridged Crack Growth Under Tension Fatigue Loading

Using the simplified analytical procedure described in the previous section, the crack growth response of $[0]_8$ SCS-6/Ti-6Al-4V was predicted for the specimen tested at 400 MPa with $V_f = 0.35$ for various values of τ. As shown in Fig. 3, the prediction using $\tau = 9$ MPa correlated well with the data. Using this value of τ, the crack growth response was predicted for the specimen with $V_f = 0.33$. The prediction agrees well with the data up to $\approx 1.8 \times 10^6$ cycles. The analysis was stopped when the ratio 2a/W exceeded 0.8. Hence, the shear lag model is able to predict the minor differences in crack growth behavior due to small changes in V_f. Using the same value of τ, the crack growth behavior of $[0]_4$ SCS-6/Ti-6Al-4V tested at 171 MPa by Davidson [6] was predicted as shown in Fig. 8. The prediction agrees well with the limited data, confirming the applicability of the proposed analytical procedure for very low stress levels. Note that the crack extension was only ≈0.4 mm from the notch. Figure 9 shows our predictions of crack extension in $[0]_6$ SM1240/Ti-6Al-4V reported by Connell and Zok [21] for stress levels ranging from 222 to 444 MPa. These predictions were performed using the same value of $\tau = 9$ MPa. The good agreement between the predicted and measured crack growth response for SM1240/Ti-6Al-4V confirms the earlier observation (Figs. 5 and 6) that at room temperature SM1240/Ti-6Al-4V and SCS-6/Ti-6Al-4V show similar crack growth behavior. Note that τ obtained from a single specimen was used to predict the trends in Figs. 3, 8 and 9. The value of τ used in this study is close to the value of 10 MPa reported by Connell and Zok [21].

Bridged Crack Growth Under Bending Fatigue Loading

Using the weight function for the SE(B) geometry [40], the crack growth behavior of $[0]_6$ SM1240/Ti-6Al-4V under bending fatigue loading was predicted with $\tau = 9$ MPa. The predictions are compared with the data from Cardona et al. [9] in Figs. 6 and 10. The stress levels shown in Figs. 6 and 10 for bending fatigue loading correspond to the maximum stress at the bottom edge of the "uncracked" composite. The predictions were performed assuming that the cracks were fully bridged during crack growth. The predictions agree well with the data obtained at maximum stresses of 330 and 404 MPa during the initial growth region. In Fig. 10, the predictions underestimate the crack growth rate at growth rates $< 10^{-9}$ m/cycle, i.e. under near-arrest conditions. As shown in Fig. 2, the matrix crack growth behavior was not adequately characterized for growth rates $< 10^{-9}$ m/cycle. Hence, crack growth predictions under near-arrest (near-threshold) conditions may not be accurate. As discussed earlier, the crack is arrested soon after initiation under bending fatigue loading, while the crack grows at a constant rate under tension fatigue loading. This trend is predicted accurately by the proposed analytical procedure as shown in Fig. 6.

At the highest stress level (453 MPa), the prediction assuming fully bridged crack growth agrees with data up to $\Delta K_a \approx 40$ MPa$\sqrt{m}$. The composite exhibits near-constant growth rate when $\Delta K_a \geq 40$ MPa$\sqrt{m}$. Based on observations under tension fatigue loading [12-15], we can conclude that the change in crack growth behavior could be attributed to the onset of non-catastrophic fiber failure. This behavior is discussed later in terms of predicted fiber stresses.

Partially-Bridged and Unbridged Crack Growth Under Tension Fatigue Loading

The crack growth behavior of SCS-6/Ti-6Al-4V at 700 MPa was predicted using three assumptions: (1) unbridged crack growth with $\tau = 0$, (2) partially bridged crack growth with $\tau = 9$ MPa and $L_{br} = 0.35$ mm, and (3) fully bridged crack growth with $\tau = 9$ MPa. These three predictions are compared with the data in Fig. 4. The prediction assuming partially bridged crack growth agrees well with the data. The specimen failed after ≈7200 cycles which is almost thrice the life predicted (≈2500) for unbridged crack growth. Note that the bridged length, L_{br} = 0.35 mm, is ≈ twice the fiber spacing. Hence even a few fibers bridging behind the crack tip increases the crack growth life significantly.

Figure 11 compares the predictions with the data for unbridged crack growth in SM1240/Ti-6Al-4V at stress levels of 844 and 889 MPa. The predictions, using Eqn. (3) and assuming $\tau = 0$, agree well with the data. The scatter in the data highlights the very small crack extensions that can be expected under such high stress levels. The predictions ignoring the shielding effect of the fibers, i.e. assuming $\Delta K_{tip} = \Delta K_{m,e}$, i.e. $F_s = 1$, are also shown in Fig. 11. As shown in Fig. 11, if unreinforced matrix properties were used, the predicted life would be ≈ 25 and 10 cycles for the tests conducted at 844 and 889, respectively. But, as predicted using Eqn. (3) and confirmed by the data, the actual lives were about 5X-10X higher. Evidently, the assumption of $F_s = 1$, grossly underestimates the damage tolerance of the unbridged composite. Hence, Eqn. (3) should be used to accurately predict the unbridged crack growth in the composite [13,41].

Crack Opening Displacements and Slip Lengths Along the Crack

The above predictions for SCS-6/Ti-6Al-4V and SM1240/Ti-6Al-4V are based on $\tau = 9$ MPa. This value of τ is generally lower than the values obtained from push-out tests [5-8,13-15,21,27]. As discussed earlier, Connell and Zok [21] reported a value of $\tau = 10$ MPa for $[0]_6$ SM1240/Ti-6Al-4V based on correlation with the crack growth response and cyclic load-COD data from through-cracked (edge-to-edge) samples cut out from the interrupted fatigue tests. The hysteresis loop method proposed by Connell and Zok [21] used extensometers with gage lengths ≈10 mm to measure the crack opening displacement. This implies that the measured data could be dominated by the elastic displacement of the intact material within the gage length.

Alternate methods of more accurate measurements include *in situ* testing using special stages in a scanning electron microscope (SEM) [6,7] and direct measurements using the laser interferometric displacement gage (IDG) system [30]. We used the laser IDG system to measure the COD during some of the tests on SCS-6/Ti-6Al-4V. The laser IDG method has been successfully used to measure COD during crack growth in SCS/Ti-24Al-11Nb [14], SCS-6/TIMETAL®21S [13,15] and SM1240/TIMETAL®21S [18]. This method uses indents that are placed within about 50μm from the crack surface. Hence the measured values are dominated by the COD at the location. As the crack grows, additional indents can be added and COD profiles obtained as functions of crack lengths and cycles.

The half-COD range (Δv) profile obtained from $[0]_8$ SCS-6/Ti-6Al-4V tested at 400 MPa is shown in Fig. 12. The displacements range from ≈0.5 μm near the crack-tip to ≈3.2 μm near the machined notch-tip. Such small displacements highlight the need to measure COD accurately and as close to the crack surface as possible. These values are similar to those reported for SCS-6/Ti-6Al-4V [6], SCS-6/Ti-24Al-11Nb [14], SCS-6/Ti-15V-3Cr-3Al-3Sn[7] and SM1240/TIMETAL®21S [18]. As discussed earlier, the rigorous method of analysis was used to predict the half-COD range using $\tau = 9$ MPa. The predictions agree well with the measured profile as shown in Fig. 12. The bridging model was also used to predict the half-COD profile for $[0]_4$ SCS-6/Ti-6Al-4V [6] corresponding to the data shown in Fig. 8. The COD data reported in Ref. [6] correspond to the maximum stress. The residual COD (under zero load) was also

reported in Ref. [6] as a function of cycles, maximum stresses and crack length. Using the maximum COD, COD_{max} and residual COD, COD_r the half-COD range, Δv for the test conducted at R=0.1 was obtained as

$$\Delta v = \frac{COD_{max} - COD_r}{2(1-R)}. \qquad (14)$$

The data deduced using Eqn. (14) agree well with the prediction as shown in Fig. 13. The good correlation between the measured and predicted COD profiles as shown in Figs. 12 and 13 validates $\Delta\sigma_b$ and ΔK_b predicted by the shear lag model.

The shear lag model can also be used to predict the debond or slip length along the fiber, l_s, the region along which τ is active. Marshall et al. [34] derived an expression for l_s as

$$l_s = \sqrt{\frac{R_f E_f E_m (1-V_f)}{\tau E_c}}\sqrt{\Delta v}\ . \qquad (15)$$

The slip length predicted by Eqn. (15) is shown in Fig. 14 along with the data from Davidson [6]. The data [6] shown in Fig. 14 were based on the damaged regions on the fiber coating visible after the matrix was removed. Reliable measurements of slip length are extremely difficult, but the damaged regions on the coating indicate the minimum lengths along which the fiber/matrix slip was active. All the data available in the literature (for example Ref. [13]) indicate that such damaged zones are visible only behind the crack tip, consistent with the assumption that the fiber/matrix slip is active only along the crack. Hence, the data [6] shown in Fig. 14 are expected to indicate only the range of values to be expected. As shown in Fig. 14, the predicted $l_s \approx 1$ mm for $\Delta v \approx 1\mu m$, is consistent with the data.

Maximum Fiber Stresses at the Machined Notch Tip

The failure of the composite is governed by the strength of the fiber. Hence, during bridged crack growth analysis, the stresses in the fibers bridging the crack should be monitored. The maximum fiber stress, $\sigma_{f,max}$ occurs at the machined notch tip, i.e. at $x = a_0$ [34,35]. The predicted $\sigma_{f,max}$ for SCS-6/Ti-6Al-4V and SM1240/Ti-6Al-4V subjected to tension fatigue loading is shown in Fig. 15 for tests conducted at $\sigma_{a,max}$ = 400, 700 and 844 MPa. As expected, $\sigma_{f,max}$ increases with increase in crack extension, Δa, and the rate of increase of $\sigma_{f,max}$ depends on the applied stress and crack extension. For the specimen tested at $\sigma_{a,max}$ = 400 MPa, $\sigma_{f,max}$ never exceeded ≈2300 MPa, consistent with the bridged crack growth behavior shown in Fig. 3. When $\sigma_{a,max}$ = 700 MPa, $\sigma_{f,max}$ increases rapidly with increasing crack extension. As shown in Figs. 4 and 7, this specimen showed a sudden change in the crack growth rate at $\Delta a \approx 0.6$ mm. This corresponds to $\sigma_{f,max} \approx 2750$ MPa, which is lower than the reported mean fiber strength of 3700 MPa for SCS-6 fibers [42]. Using a Weibull distribution to represent the strength variation, Ashbaugh [43] reported a bundle strength, $\sigma_{f,uB} \approx$ 2600-3200 MPa for the SCS-6 fibers extracted from SCS-6/Ti-6Al-4V composites. Interestingly, the critical $\sigma_{f,max}$ for the test at 700 MPa is within this range.

The predicted $\sigma_{f,max}$ for SM1240/Ti-6Al-4V tested at 844 MPa is also shown in Fig. 15. Soon after crack initiation, $\sigma_{f,max}$ increases rapidly to stress levels > 3000 MPa, which exceeds the bundle strength (≈2800 MPa) [21] of the SM1240 fibers. In fact, $\sigma_{f,max}$ is already close to the reported mean tensile strength (≈3300 MPa) [42] of the SM1240 fibers. Hence, the shear lag model correctly predicts the unbridged crack growth behavior of SM1240/Ti-6Al-4V for stress levels ≥ 844 MPa as shown in Fig. 11.

$\sigma_{f,max}$ predicted for SM1240/Ti-6Al-4V under bending fatigue loading is shown in Fig. 16 for different maximum stresses. For the tests conducted at 330 and 404 MPa, $\sigma_{f,max}$ was less

than the bundle strength of 2800 MPa, consistent with the fully bridged crack growth behavior shown in Figs. 6 and 10. When the stress level was increased to 453 MPa, a change in the crack growth trend was observed at $\Delta K_a \approx 40$ MPa$\sqrt{m}$ as indicated by the bold arrow in Fig. 10. This value of ΔK_a corresponds to a crack extension of ≈ 0.7 mm. Interestingly, as shown in Fig. 16, $\Delta a \approx 0.7$ mm corresponds to predicted $\sigma_{f,max} \approx 2800$ MPa, which is equal to the bundle strength [21] of the SM1240 fibers. Hence, the shear lag model correctly predicts the onset of fiber failure and increase in crack growth rate in SM1240/Ti-6Al-4V under bending fatigue loading. Comparing Figs. 15 and 16, we can conclude that, for similar stress levels and crack lengths, the bridging fiber stresses under bending fatigue are ≈30-35% higher than that under tension fatigue loading.

DISCUSSION

Surprisingly, the data at room temperature indicate that the crack growth behavior of SCS-6/Ti-6Al-4V is similar to that of SM1240/Ti-6Al-4V. As discussed earlier, this similarity may be attributed to the nearly identical stiffnesses of the fibers, dual carbon coatings on the fibers and radial compressive stresses at the fiber/matrix interface. Since the processing conditions can be expected to be different, the crack growth behavior of the matrix in these composites could be different. Connell and Zok [21] represented the matrix crack growth behavior as

$$\frac{da}{dN} = \eta \left(\Delta K_{m,e}\right)^{3.8} . \qquad (16)$$

Using τ and η as fitting parameters, Connell and Zok [21] determined various combinations of τ and η which successfully predicted the crack behavior of SM1240/Ti-6Al-4V, i.e. the data shown in Fig. 9. As discussed earlier, cyclic load tests were conducted on through-cracked specimens and τ deduced from the hysteresis loops. Thus, the corresponding value of η was also determined. Using this value of η, the deduced matrix behavior was plotted in Fig. 2. As seen in the figure, the deduced crack growth behavior of the matrix in SM1240/Ti-6Al-4V is close to the neat Ti-6Al-4V obtained during this study. Thus, the similarity between the fibers and the matrix enabled us to successfully predict the crack growth behavior of SCS-6/Ti-6Al-4V and SM1240/Ti-6Al-4V using the same value of τ.

The value of τ used in this study compares well with that reported by Connell and Zok [21], but it is lower than the results generally reported from push-out tests. The effect of fatigue loading has been suggested as a possible reason for the low value of τ [44]. An important point to be noted is that all models and experiments indicate that the slip length ≈1-2 mm at room temperature. This implies that the correct value of τ can be deduced only if a push-out or pull-out test is conducted on specimens in which the fatigued slip zone is interrogated. In general, such specimens (from within 1-2 mm from the crack surface) are nearly impossible to obtain. Most of the reported data are based on specimen sections that were located at distances > 2-5 mm from the crack surfaces. Hence, it is not surprising that the push-out results tend to yield higher values of τ. Alternate methods include cyclic-load tests with COD measurements, from which τ can be deduced. As shown during this study (Fig. 12) and by Larsen et al. [13], the COD measurements near the crack surface yield values of τ which correlate well with the crack growth behavior.

During this study and in Ref. [13], we used Eqn. (3) to relate ΔK_{tip} at the crack tip in the composite to the neat matrix behavior. This study showed that the use of Eqn. (13) along with the shear lag model of Marshall et al. [34], is able to successfully predict the crack growth behavior and related parameters such as crack opening displacements, slip length and fiber stresses. Larsen et al. [13] and John et al. [14,15] showed that the crack growth behavior can also be predicted assuming $F_s = 1$ with higher values of τ. But the resulting predictions of the COD profile are lower than those measured during the crack growth tests.

Cox [19] suggested that the COD data from small crack extensions may not be sensitive enough to deduce the applicability of the shear lag models. Tests on very large (and expensive) specimens are required to verify the bridging relationship given by Eqn. (6). As shown during this study, and in Refs. [13] and [41], Eqn. (3) can also be used to predict the unbridged crack growth in the composites.

The results from this study indicate that the use of the bundle strength of fibers extracted from the composite can be used to predict the onset of fiber failure. We should note that the use of $F_s = 1$ will necessitate the use of higher strength values. The analyses of Bakuckas and Johnson [8,25], Larsen et al. [13], John et al. [14,15], and Connell and Zok [21] support the use of a fiber strength that is lower than the mean strength based on tests on fibers prior to consolidation. In typical composites, depending on the layup, ≈8-30 fibers can be expected to exist adjacent to the crack tip within a fiber spacing. This number, coupled with the expected degradation of the fiber/matrix interface during fatigue, could justify the use of the bundle strength to predict fiber failure.

SUMMARY

This study showed that the shear lag model assuming a constant value of τ can be used to predict bridged crack growth perpendicular to fibers in SCS-6/Ti-6Al-4V and SM1240/Ti-6Al-4V over a wide range of stress levels and under tension and bending fatigue loading conditions. The model predicted partially-bridged and unbridged crack growth, as well as crack opening displacement and slip length measurements. Analysis of the bending fatigue loading data confirmed that under bending fatigue loading the crack growth arrested soon after initiation, in contrast to the continued growth under tension fatigue loading. The bridging fiber stresses under bending fatigue are ≈30-35% higher than those under tension fatigue loading. The value of τ was the same for SCS-6/Ti-6Al-4V and SM1240/Ti-6Al-4V, implying that the bridging mechanism of the SM1240 fiber is identical to that of the SCS-6 fiber at room temperature. The results also indicate that the onset of fiber failure could be predicted using the bundle strength as the critical value.

ACKNOWLEDGMENT

This research was conducted at Wright Laboratory (WL/MLLN), Materials Directorate, Wright-Patterson Air Force Base, OH 45433-7817. R. John was supported under on-site contract number F33615-94-C-5200. The authors gratefully acknowledge the assistance of R. Kleismit and A. F. Lackey in conducting the experiments.

REFERENCES

1. Larsen, J. M., Williams, K. A., Balsone, S. J., and Stucke, M. A., "Titanium Aluminides for Aerospace Applications," *High Temperature Aluminides and Intermetallics*, S. H. Whang, C. T. Liu, D. P. Pope, J. O. Stiegler, Eds., The Minerals, Metals & Materials Society, Warrendale, PA, 1990, pp. 521-556.
2. Larsen, J. M., Russ, S. M., and Jones, J. W., "An Evaluation of Fiber-Reinforced Titanium Matrix Composites for Advanced High-Temperature Aerospace Applications," *Metallurgical and Materials Transactions A*, Vol. 26A, 1995, pp. 3211-3223.
3. Bain, K. R. and Gambone, M. L., "Fatigue Crack Growth of SCS-6/Ti-64 Metal Matrix Composite", *Fundamental Relationships Between Microstructure and Mechanical Properties of Metal Matrix Composites*, P. K. Liaw and M. N. Gungor, Eds., The Minerals, Metals, and Materials Society, 1990, pp. 459-469.
4. McMeeking, R. M. and Evans, A. G., "Matrix Fatigue Cracking in Fiber Composites," *Mechanics of Materials*, Vol. 9, No. 3, 1990, pp. 217-227.

5. Sensmeier, M. D. and Wright, P. K., "The Effect of Fiber Bridging on Fatigue Crack Growth in Titanium Matrix Composites," *Fundamental Relationships Between Microstructure and Mechanical Properties of Metal Matrix Composites*, The Metallurgical Society, Inc., Warrendale, PA, 1990, pp. 441-450.
6. Davidson, D. L., "The Micromechanics of Fatigue Crack Growth at 25°C in Ti-6Al-4V Reinforced with SCS-6 Fibers," *Metallurgical and Materials Transactions A*, Vol. 23A, 1992, pp. 865-879.
7. Ghosn, L. J., Telesman, J., and Kantzos, P., "Specimen Geometry Effects on Fiber Bridging in Composites," *FATIGUE 93, Vol. 2*, J.-P. Bailon and I. J. Dickson, Eds., Engineering Materials Advisory Services, Ltd., U. K., 1993, pp. 1231-1238.
8. Bakuckas, J. G. Jr. and Johnson, W. S., "Application of Fiber Bridging Models to Fatigue Crack Growth in Unidirectional Titanium Matrix Composites," NASA Technical Memorandum 107588, NASA Langley, Hampton, VA, July 1992.
9. Cardona, D. C., Barney, C., and Bowen, P., "Modeling and Prediction of Crack Arrest in Fiber Reinforced Composites," *Life Prediction Methodology for Titanium Matrix Composites, ASTM STP 1253*, W.S. Johnson, J.M. Larsen, and B.N. Cox, Eds., American Society for Testing and Materials, West Conshohocken, PA, USA, 1996, pp. 164-181.
10. Bowen, P., "Characterization of Crack Growth Resistance Under Cyclic Loading in the Presence of an Unbridged Defect in Fiber-Reinforced Titanium Metal Matrix Composite," *Life Prediction Methodology for Titanium Matrix Composites, ASTM STP 1253*, W.S. Johnson, J.M. Larsen, and B.N. Cox, Eds., American Society for Testing and Materials, West Conshohocken, PA, USA, 1996, pp. 461-479.
11. Bao, G. and McMeeking, R. M., "Fatigue Crack Growth in Fiber-Reinforced Metal-Matrix Composites," *Acta Metallurgica et Materialia*, Vol. 42, No. 7, 1994, pp. 2415-2425.
12. Jira, J. R. and Larsen, J. M., "Fatigue of Unidirectional SCS-6/Ti-24Al-11Nb Composite Containing a Circular Hole," *Metallurgical and Materials Transactions A*, Vol. 25A, 1994, pp. 1413-1424.
13. Larsen, J.M., Jira, J.R., John, R., and Ashbaugh, N.E., "Crack-Bridging Effects in Notch Fatigue of SCS-6/TIMETAL21S Composite Laminates," *Life Prediction Methodology for Titanium Matrix Composites, ASTM STP 1253*, W.S. Johnson, J.M. Larsen, and B.N. Cox, Eds., American Society for Testing and Materials, West Conshohocken, PA, USA, 1996, pp. 114-136.
14. John, R., Jira, J. R., Larsen, J. M., and Ashbaugh, N. E., "Analysis of Bridged Fatigue Cracks in Unidirectional SCS-6/Ti-24Al-11Nb Composite," *FATIGUE 93, Vol. 2*, J.-P. Bailon and I. J. Dickson, Eds., Engineering Materials Advisory Services, Ltd., U. K., 1993, pp. 1091-1096.
15. John, R., Kaldon, S. G., and Ashbaugh, N. E., "Applicability of Fiber Bridging Models to Describe Crack Growth in Unidirectional Titanium Matrix Composites," *Titanium Metal Matrix Composites II, WL-TR-93-4105*, P. R. Smith and W. C. Revelos, Eds., Wright-Patterson Air Force Base, OH, 1993, pp. 233-250.
16. John, R., Stibich, P.R., Johnson, D.A., and Ashbaugh, N.E., "Bridging Fiber Stress Distribution During Fatigue Crack Growth in $[0]_4$ SCS-6/TIMETAL®21S," *Scripta Metallurgica et Materialia*, Vol. 33, No. 1, 1995, pp. 75-80.
17. Buchanan, D., John, R., and Johnson, D.A., "Determination of Crack Bridging Stresses From Crack Opening Displacement Profiles," *International Journal of Fracture,* Accepted for publication (Paper # FRAC4191), March 1997.
18. Zheng, D. and Ghonem, H., "High Temperature/High Frequency Fatigue Crack Growth in Titanium Metal Matrix Composites," *Life Prediction Methodology for Titanium Matrix Composites, ASTM STP 1253*, W.S. Johnson, J.M. Larsen, and B.N. Cox, Eds., American Society for Testing and Materials, West Conshohocken, PA, USA, 1996, pp. 137-163.
19. Cox, B.N., "Life Prediction for Bridged Fatigue Cracks," *Life Prediction Methodology for Titanium Matrix Composites, ASTM STP 1253*, W.S. Johnson, J.M. Larsen, and B.N. Cox, Eds., American Society for Testing and Materials, West Conshohocken, PA, USA, 1996, pp. 552-572.
20. Zok, F.W., Connell, S.J., and Du, Z.-Z., "Fatigue Maps for Titanium Matrix Composites," *Life Prediction Methodology for Titanium Matrix Composites, ASTM STP 1253*, W.S. Johnson, J.M. Larsen, and B.N. Cox, Eds., American Society for Testing and Materials, West Conshohocken, PA, USA, 1996, pp. 432-460.

21. Connell, S.J. and Zok, F.W., "Measurement of the Cyclic Bridging Law in a Titanium Matrix Composite and it's Application to Simulating Crack Growth," *Acta Materialia*, Submitted for publication, January 1997.
22. Walls, D. P., Bao, G., and Zok, F. W., "Mode I Fatigue Cracking in a Fiber Reinforced Metal Matrix Composite," *Acta Metallurgica et Materialia*, Vol. 41, No. 7, 1993, pp. 2061-2071.
23. Nguyen, T.-H.B and Yang, J.-M., "Elastic Bridging For Modeling Fatigue Crack Propagation in a Fiber-Reinforced Titanium Matrix Composite," *Fatigue and Fracture of Engineering Materials and Structures*, Vol. 17, No. 2, 1994, pp. 119-131.
24. Herrmann, D.J. and Hillberry, B.M., "A New Approach to the Analysis of Unidirectional Titanium Matrix Composites With Bridged and Unbridged Cracks", *Engineering Fracture Mechanics*, Vol. 56, No. 5, 1997, pp. 711-726.
25. Bakuckas, J.G., Jr. and Johnson, W.S. "A Methodology to Predict Damage Initiation, Damage Growth, and Residual Strength in Titanium Matrix Composites," *Life Prediction Methodology for Titanium Matrix Composites, ASTM STP 1253*, W.S. Johnson, J.M. Larsen, and B.N. Cox, Eds., American Society for Testing and Materials, West Conshohocken, PA, USA, 1996, pp. 497-519.
26. Larsen, J.M., Jira, J.R., John, R., and Blatt, D., "Temperature Dependent Crack Bridging Effects in SCS-6/TIMETAL®21S Composite," *Materials Science and Engineering*, Accepted for publication, 1997.
27. Hutson, A., John, R., and Jira, J.R., "The Effect of Temperature on Fiber/Matrix Interface Sliding in SCS-6/Timetal 21S," *Scripta Metallurgica et Materialia*, To be submitted for publication, 1997.
28. Nicholas, T. and Kroupa, J.L., "Micromechanics Analysis and Life Prediction of Titanium Matrix Composites," *Journal of Composites and Technology and Research*, Submitted for publication, 1997.
29. Coker, D., Boller, F., Kroupa, J.L, and Ashbaugh, N.E, *FIDEP2: User Manual for Micromechanical Models for Thermoviscoplastic Behavior of Metal Matrix Composites*, University of Dayton Research Institute, Dayton, OH, USA, To be published, 1997.
30. Sharpe, W.N., Jr., Jira, J.R., and Larsen, J.M. "Real-Time Measurement of Small-Crack Opening Behavior Using an Interferometric Strain/Displacement Gage," *Small-Crack Test Methods, ASTM STP 1149*, American Society for Testing and Materials, Philadelphia, PA, 1992, pp. 92-115.
31. John, R., Kaldon, S.G., Johnson, D.A. and Coker, D., "Weight Function For A Single Edge Cracked Geometry With Clamped Ends," *International Journal of Fracture*, Vol. 72, No. 2, 1995, pp. 145-158.
32. John, R. and Rigling, B., "Effect of Height to Width Ratio on K and CMOD Solutions for Single Edge Cracked Geometry With Clamped Ends," *Engineering Fracture Mechanics*, Submitted for publication, March 1997.
33. Miller, M. S. and Gallagher, J. P., "An Analysis of Several Fatigue Crack Growth Rate (FCGR) Descriptions," *Fatigue Crack Growth Measurement and Data Analysis, ASTM STP 738*, American Society for Testing and Materials, Philadelphia, PA, 1981, pp. 205-251.
34. Marshall, D. B., Cox, B. N., and Evans, A. G., "The Mechanics of Matrix Cracking in Brittle-Matrix Fiber Composites," *Acta Metallurgica*, Vol. 33, No. 11, 1985, pp. 2013-2021.
35. McCartney, L.N., "Mechanics of Matrix Cracking in Brittle-Matrix Fibre-Reinforced Composites," *Proceedings of Royal Society of London A*, Vol. A409, 1987, pp. 329-350.
36. Cox, B.N. and Marshall, D.B., "Concepts for Bridged Cracks in Fracture and Fatigue," *Acta Metallurgica et Materialia*, Vol. 42, 1994, pp. 341-363.
37. Cox, B.N. and Marshall, D.B., "Crack Bridging in the Fatigue of Fibrous Composites," *Fatigue and Fracture of Engineering Materials and Structures*, Vol. 14, No. 8, 1991, pp. 847-861.
38. Cox, B. N. and Lo, C. S., "Simple Approximations for Bridged Cracks in Fibrous Composites," *Acta Metallurgica et Materialia*, Vol. 40, No. 7, 1992, pp. 1487-1496.
39. Tada, H., Paris, P.C., and Irwin, G.R., *The Stress Analysis of Cracks Handbook*, Del Research Corporation, St. Louis, MO, USA, 1985.
40. X.-R. Wu and A.J. Carlsson, *Weight Functions and Stress Intensity Factor Solutions*, Pergamon Press, Inc., Elmsford, New York, USA, 1991.

41. John, R., Larsen, J.M., and Jira, J.R., "Effective Stress Intensity Factor at the Matrix Crack Tip During Fatigue Crack Growth in a Metal Matrix Composite", *Scripta Metallurgica et Materialia*, To be submitted for publication, 1997.

42. Petitcorps, Y.L., Lahaye, M., Pailler, R., and Naslain, R., "Modern Boron and SiC CVD Filaments: A Comparitive Study," *Composites Science and Technology*, Vol. 32, 1988, pp. 31-55.

43. Ashbaugh, N.E., Metzcar, J., and Rosenberger, A.H., "Deformation and Rupture Model of [0] Metal Matrix Composite Under Sustained Load," To be submitted for publication, 1997.

44. Kantzos, P., Eldridge, J., Koss, D.A., and Ghosn, L.J., "The Effect of Fatigue Loading on the Interfacial Shear Properties of SCS-6/Ti-Based MMCs," *Intermetallic Composites II*, D.B. Miracle, D.L. Anton, and J.A. Graves, Eds., MRS Proceedings, Pittsburgh, PA, Vol. 273, 1992, pp. 135-142.

Table I. Fatigue Crack Growth Data Used for Analysis *

Fiber	Matrix	Layup	V_f	Geometry	Maximum Stress (MPa)	Stress Ratio	Width, W (mm)	Unbridged Notch / Width	Reference
SCS-6 **	Ti-6Al-4V	$[0]_8$	0.35 0.33 0.33	Center-cracked in tension, M(T)	400 400 700	0.1 0.1 0.1	19.0 19.1 18.9	0.11 # 0.11 0.11	This Study
SCS-6 **	Ti-6Al-4V	$[0]_4$	≈ 0.42	Center-cracked in tension, M(T)	171	0.1	24.0	0.25 #	Davidson [6]
SM1240 ++ (Sigma)	Ti-6Al-4V	$[0]_6$	≈ 0.32	Center-cracked in tension, M(T)	844 889	0.1	15.0	0.20	Zok, Connell and Du [20]
SM1240 ++ (Sigma)	Ti-6Al-4V	$[0]_6$	≈ 0.32	Center-cracked in tension, M(T)	222 278 333 389 444	0.1	15.0	0.20	Connell and Zok [21]
SM1240 ++ (Sigma)	Ti-6Al-4V	$[0]_6$	≈ 0.31	Single edge in bending, SE(B)	330 + 404 + 453 +	0.1	4.5	0.24	Cardona, Barney and Bowen [9]

Note:

* All the data were obtained at room temperature (23-25°C) in laboratory air.

\+ Maximum stress calculated at the outermost surface for a three-point bend configuration.

** SCS-6 is a SiC fiber (diameter=142μm) with a carbon core and dual coatings of carbon on the surface. Manufactured by Textron Specialty Materials Division (SMD), Lowell, MA, USA.

++ SM1240 is a SiC fiber (diameter=100μm) with a tungsten core, and dual coatings of carbon and boron-rich TiB_2 on the surface. Manufactured by BP Metal Composites Limited, Hampshire, UK.

\# Crack opening displacement profile measured during crack growth.

Table II. Constituent Properties Used in FCG Analysis

Property	Ti-6Al-4V Matrix	SCS-6™ Fiber	SM1240™ Fiber
Modulus, E (GPa)	117	393	400
Poisson's Ratio, ν	0.31	0.25	0.25

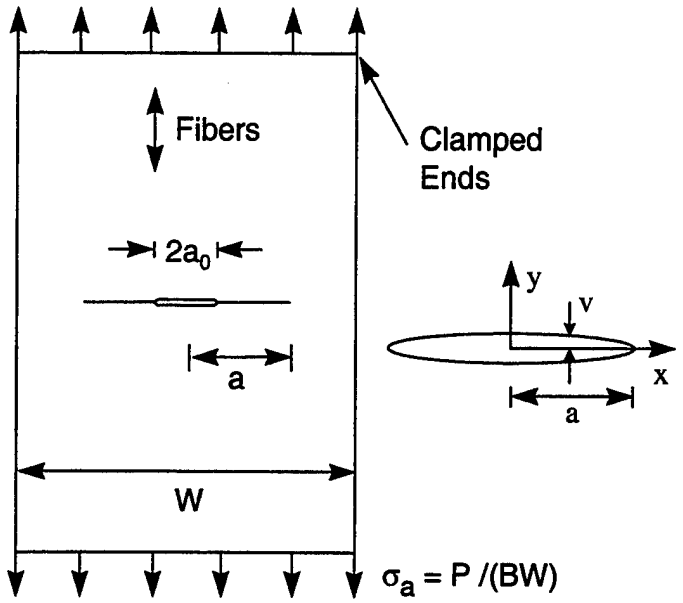


Fig. 1. Schematic of center-cracked-tension specimen, M(T) used for testing $[0]_8$ SCS-6/Ti-6Al-4V.

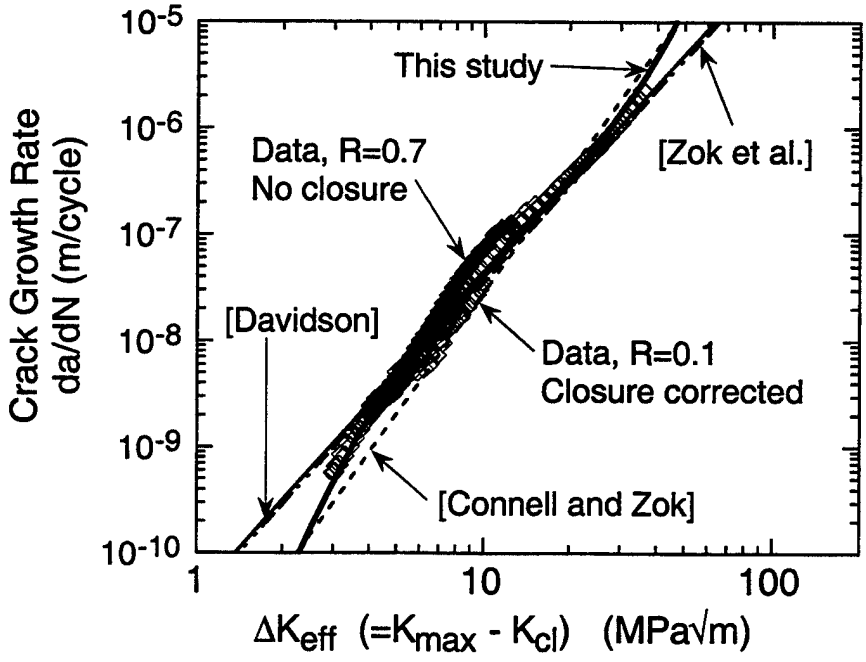


Fig. 2. Crack growth rate behavior of neat Ti-6Al-4V at room temperature

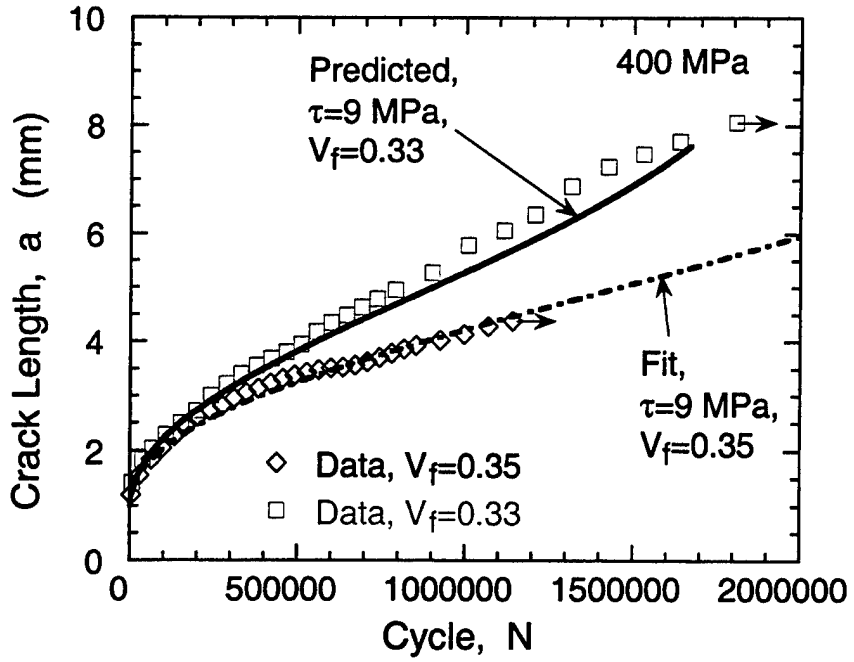


Fig. 3. Comparison of predicted and measured crack growth response in $[0]_8$ SCS-6/Ti-6Al-4V tested under tension fatigue loading at σ_{max}=400 MPa. Prediction assumes fully bridged crack growth.

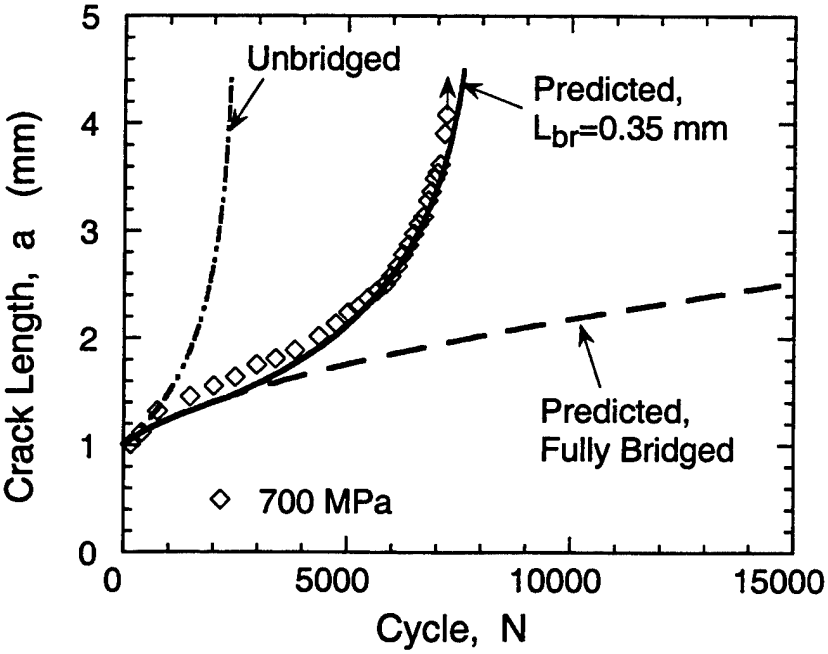


Fig. 4. Comparison of predicted and measured crack growth response in $[0]_8$ SCS-6/Ti-6Al-4V tested under tension fatigue loading at σ_{max}=700 MPa.

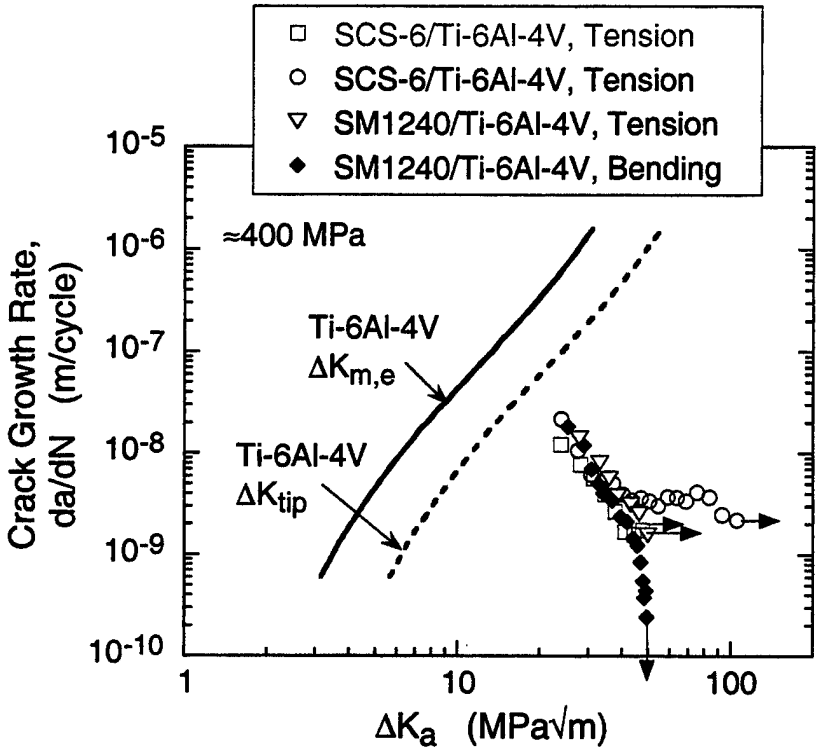


Fig. 5. Crack growth rate versus applied stress intensity factor range behavior of $[0]_8$ SCS-6/Ti-6Al-4V and $[0]_6$ SM1240/Ti-6Al-4V at maximum stress level of ≈400 MPa.

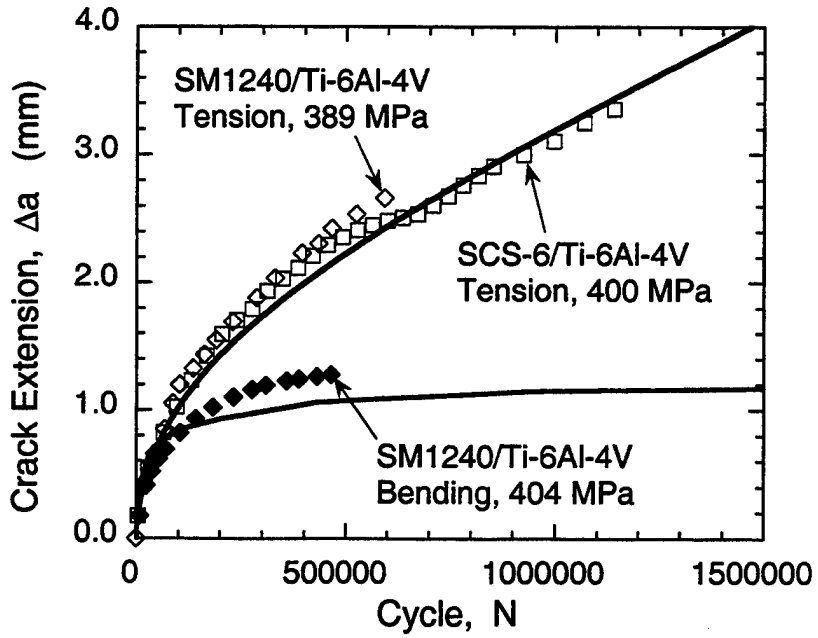


Fig. 6. Effect of type of loading on crack extension from an initial unbridged notch in $[0]_8$ SCS-6/Ti-6Al-4V and $[0]_6$ SM1240/Ti-6Al-4V. (Data = Symbols; Predictions = Lines)

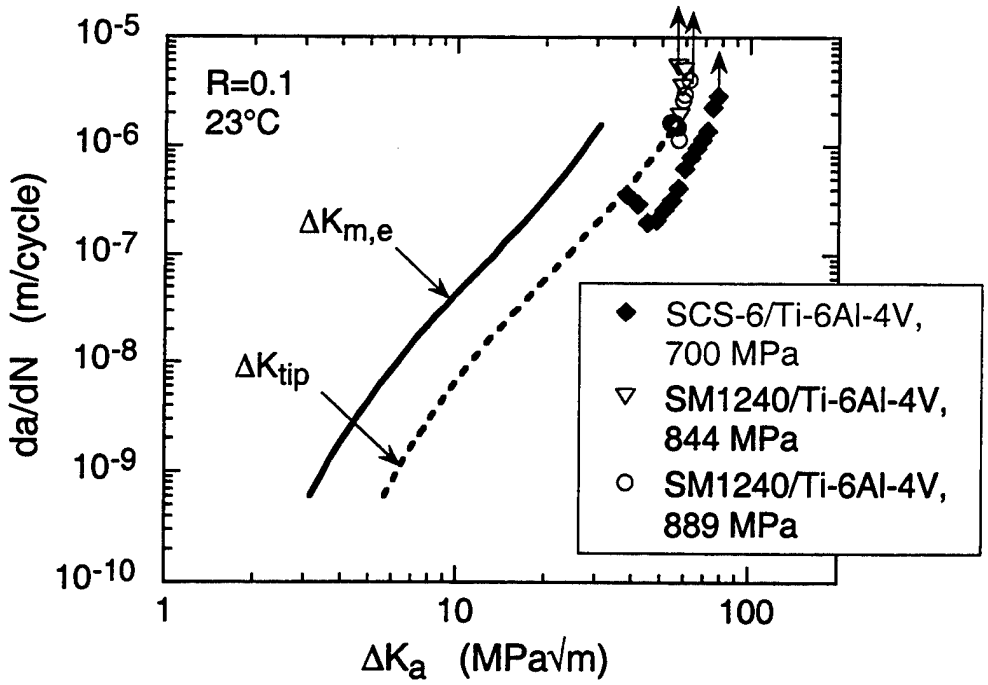


Fig. 7. Crack growth rate versus applied stress intensity factor range behavior of $[0]_8$ SCS-6/Ti-6Al-4V and $[0]_6$ SM1240/Ti-6Al-4V at high stresses.

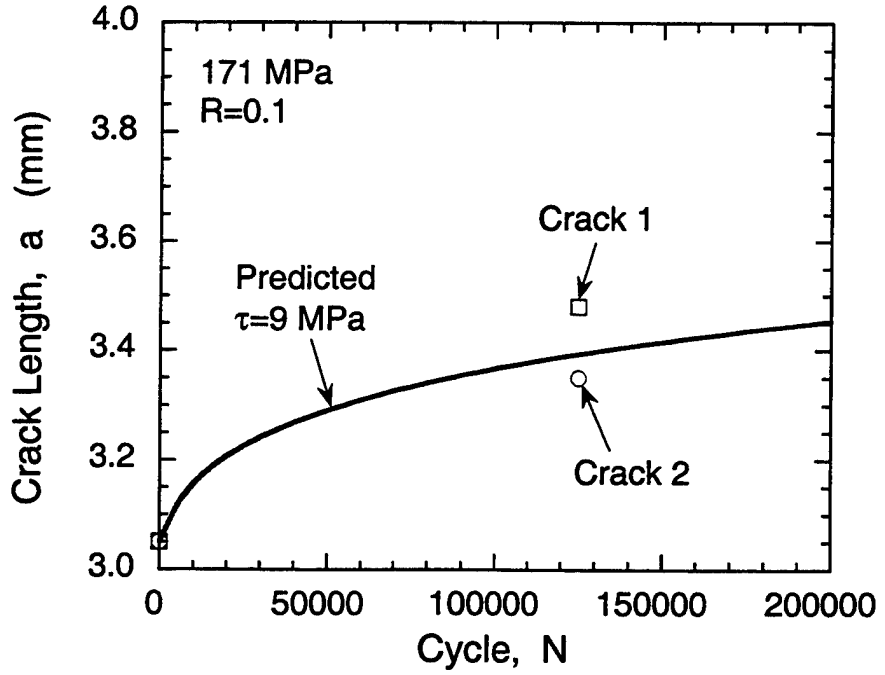


Fig. 8. Comparison of predicted and measured crack growth response in $[0]_4$ SCS-6/Ti-6Al-4V tested under tension fatigue loading at σ_{max}=171 MPa. Prediction assumes fully bridged crack growth. Data from Davidson [6].

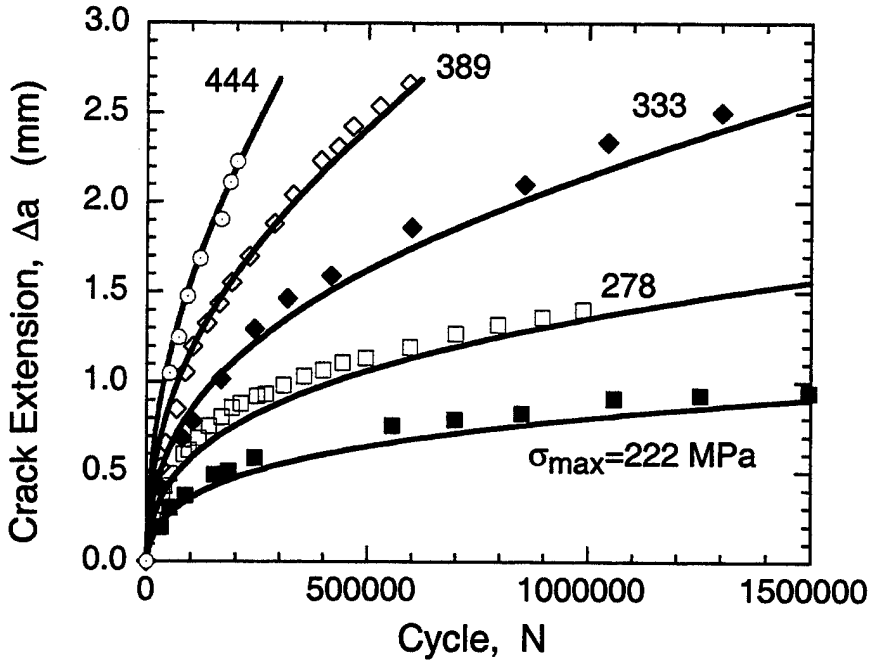


Fig. 9. Comparison of predicted (lines) and measured (symbols) crack growth response in $[0]_6$ SM1240/Ti-6Al-4V tested under tension fatigue loading at maximum stress, σ_{max}=222 to 444 MPa. Prediction assumes fully bridged crack growth. Data from Connell and Zok [21].

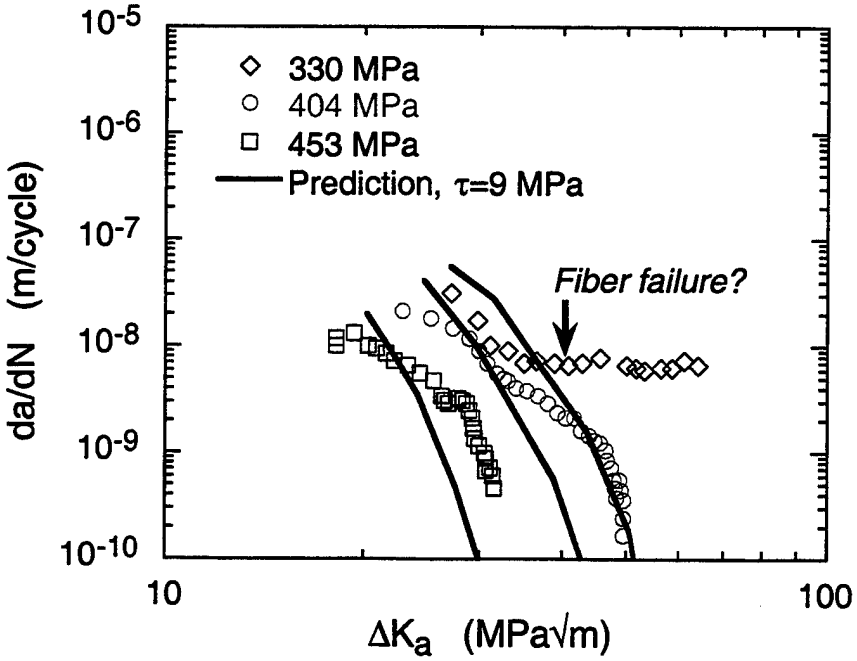


Fig. 10. Comparison of predicted and measured crack growth response in $[0]_6$ SM1240/Ti-6Al-4V tested under bending fatigue loading at σ_{max}=330 to 453 MPa. Prediction assumes fully bridged crack growth. Data obtained from Cardona, Barney and Bowen [9].

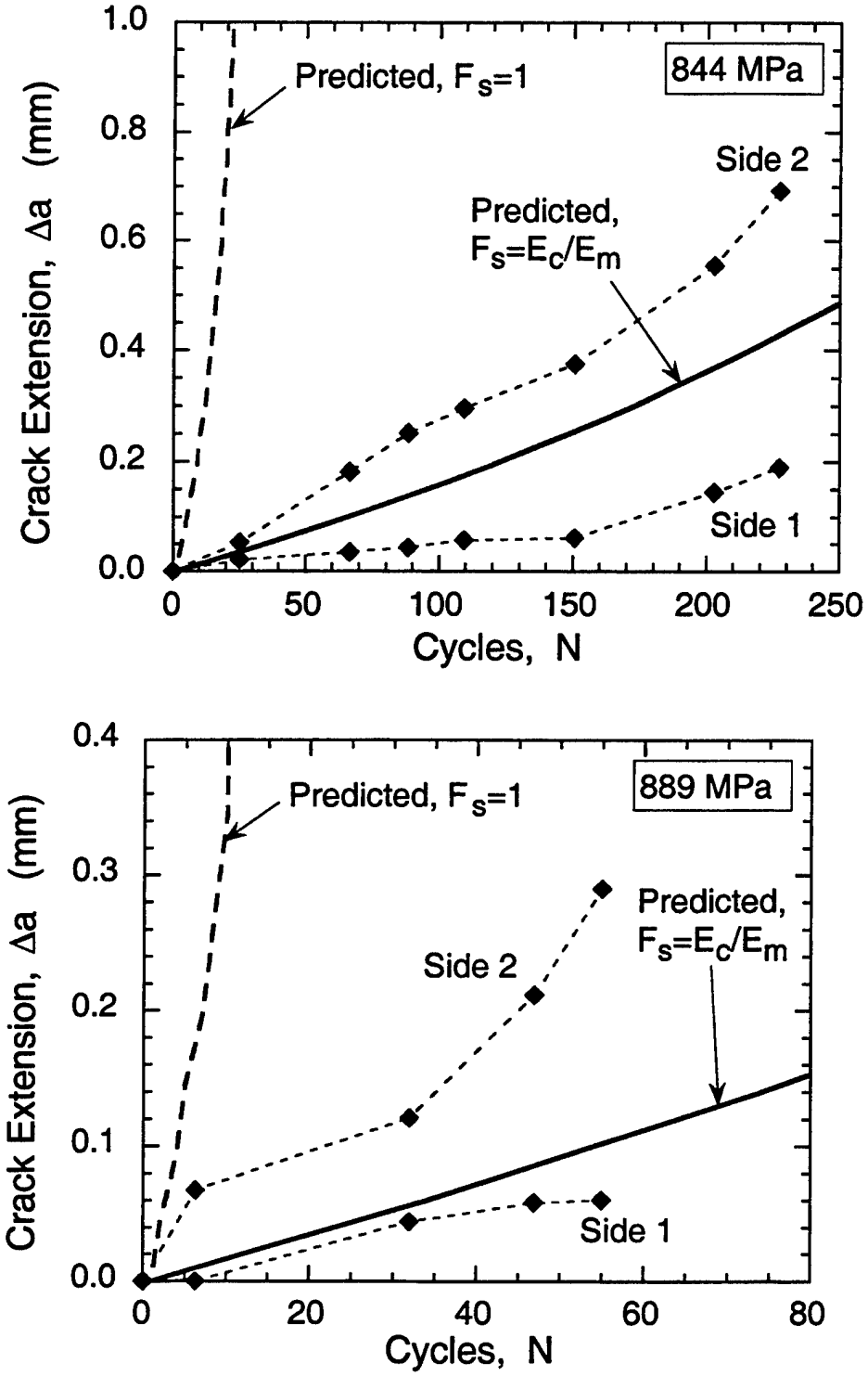


Fig. 11. Comparison of predicted and measured crack growth response in $[0]_6$ SM1240/Ti-6Al-4V tested under tension fatigue loading at σ_{max}=844 and 889 MPa. Prediction assumes unbridged crack growth. Data obtained from Zok, Connell and Du [20].

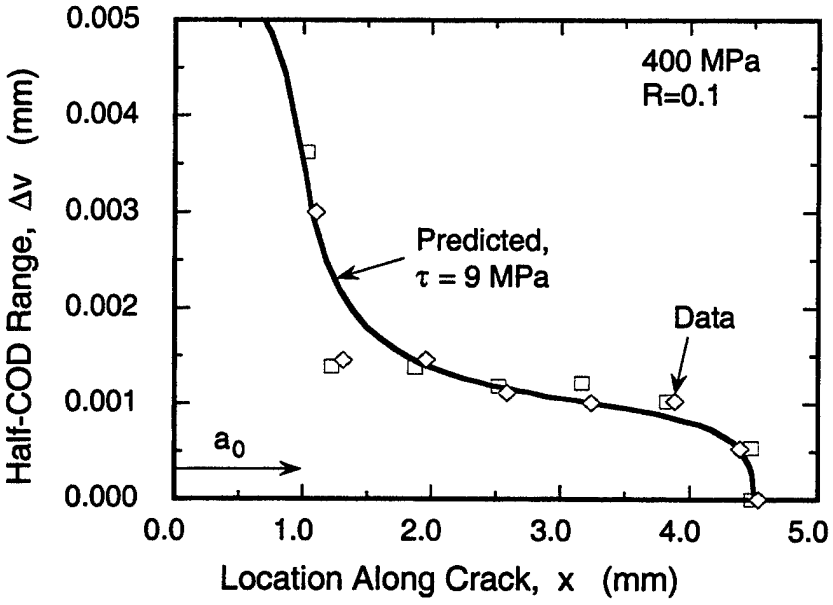


Fig. 12. Comparison of predicted half-crack opening displacement range with that measured during crack growth in $[0]_8$ SCS-6/Ti-6Al-4V tested at σ_{max}=400 MPa.

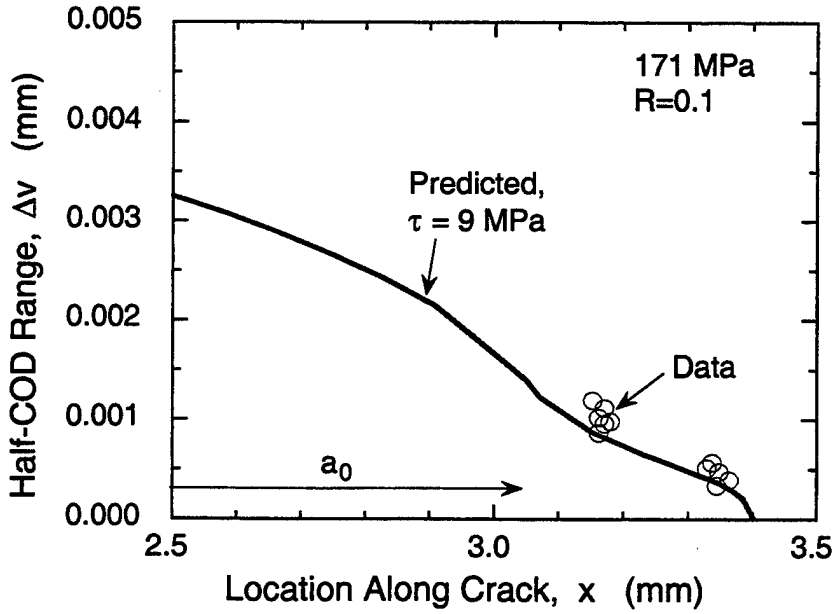


Fig. 13. Comparison of predicted half-crack opening displacement range with that measured during crack growth in $[0]_4$ SCS-6/Ti-6Al-4V tested at σ_{max}=171 MPa. Data from Davidson [6].

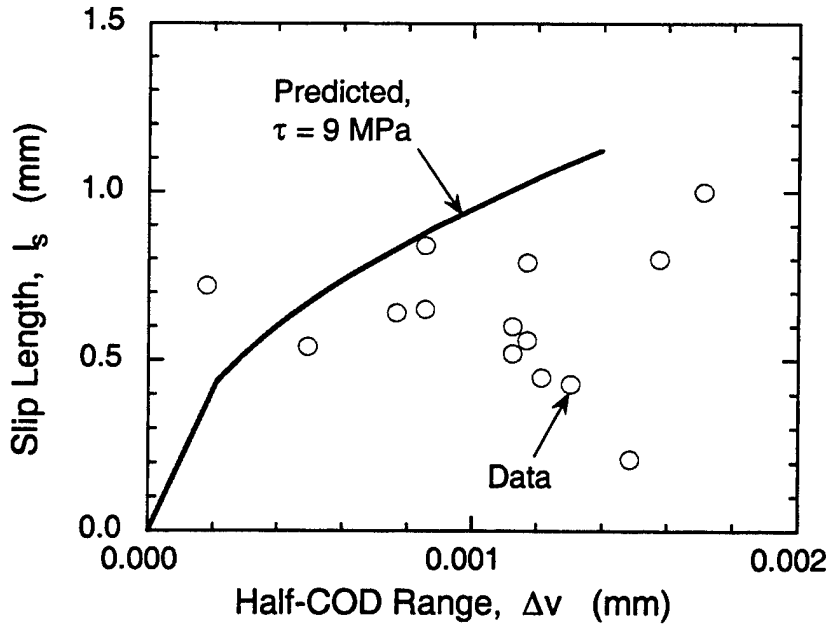


Fig. 14. Comparison of predicted slip length with that measured during crack growth in $[0]_4$ SCS-6/Ti-6Al-4V. Data from Davidson [6].

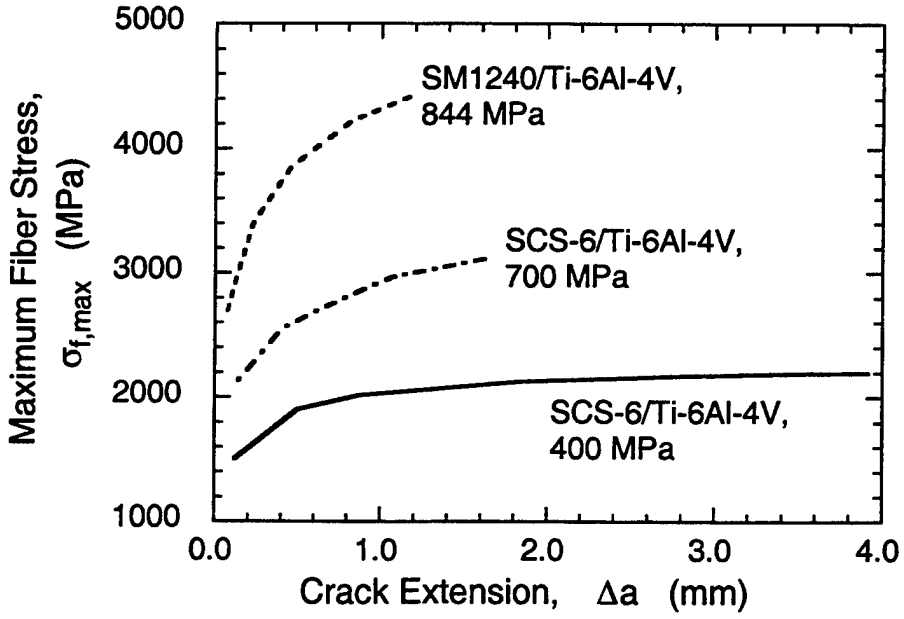


Fig. 15. Predicted variation of maximum fiber stress during crack growth in $[0]_8$ SCS-6/Ti-6Al-4V and $[0]_6$ SM1240/Ti-6Al-4V tested under tension fatigue loading.

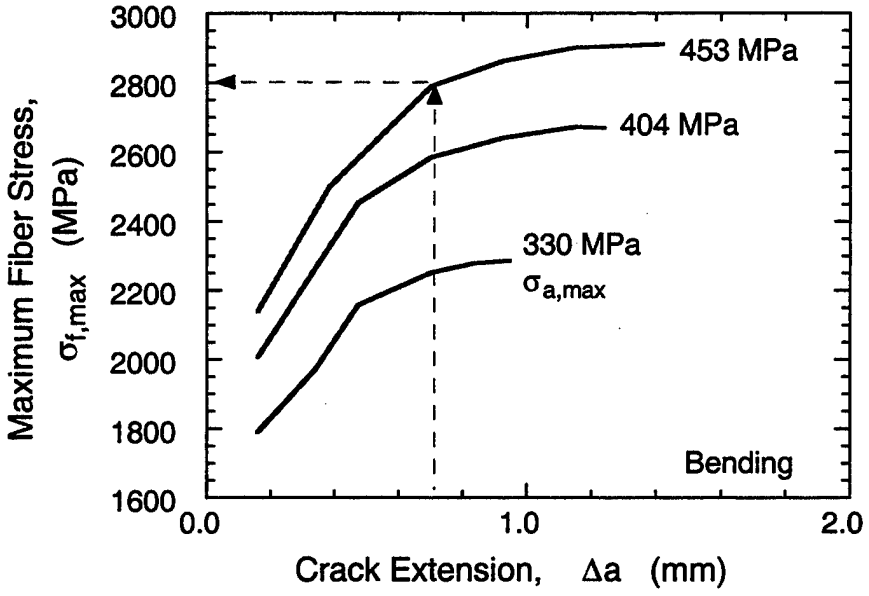


Fig. 16. Predicted variation of maximum fiber stress during crack growth in $[0]_6$ SM1240/Ti-6Al-4V tested under bending fatigue loading.

This page intentionally left blank

Modeling the Deformation and Failure of a Unidirectional Metal Matrix Composite Under Sustained Load

Jeff Metzcar[1], Materials Directorate, Wright Laboratory, WL/MLLN, Wright-Patterson AFB, OH 45433-7817

Technical Advisor: Noel E. Ashbaugh, PhD, University of Dayton Research Institute, Structural Integrity Division

Thesis Advisor: Fred K. Bogner, PhD, University of Dayton, Department of Civil Engineering

[1]University of Dayton, Department of Mechanical Engineering;
Submitted to the University of Dayton Honors Program October 1996.

ABSTRACT

A creep model utilizing the two bar composite representation was developed in order to characterize the deformation and failure of a unidirectionally reinforced Ti-6Al-4V/SCS-6 composite. This model is capable of simulating loading, taking into account residual stresses in the composite and allowing for fiber failure according to a Weibull statistical strength distribution. The validity of the model was evaluated by comparing predicted strains and lifetimes to measurements of strains and lifetimes taken from a range of creep tests. The model's sensitivity was also investigated using a parameter study. Through extensive fiber tracking of an interrupted creep test, the model's primary assumptions were evaluated and found to be true.

1. INTRODUCTION

Ceramic materials exhibit a number of distinct advantages over metals including higher specific strength, creep resistance at high temperatures, and resistance to corrosion. The primary downfall in their use, however, is that tiny flaws which result during their production coupled with their very brittle nature make ceramic components very unpredictable with respect to their ultimate strength. Clearly, this property severely limits the use of ceramics in applications where safety is an issue.

The design of continuous ceramic fiber reinforced MMCs is an effort to take advantage of the favorable properties of ceramics while limiting the risk associated with their use. While a single continuous ceramic part, such as a ceramic turbine blade, has a wide range of possible strengths, the same part if constructed using a metal matrix composite is in theory more predictable. Because the MMC is constructed using many ceramic fibers, some of which are unexpectedly weak and others which are strong, the risk of an unforeseen failure is reduced.

While the ceramic fibers provide the real strength and creep resistance of the composite, the titanium alloy matrix material serves several important purposes of its own. First, it gives the composite shape and holds the fibers in their proper orientation. Second, it protects the fibers, not only from environmental damage, but also from impact damage that could break fibers or at the very least severely reduce their strength. Lastly, the matrix provides a medium through which load can be transferred from one fiber to the next. This property of the matrix is critical to the strength of the composite.

Because of their high specific strength and creep resistance at elevated temperatures, continuous ceramic fiber reinforced MMCs are of considerable interest to the aerospace industry. In an aircraft, where the failure of a single part may result in the loss of the entire plane or worse the loss of life, the limitations of every component must be thoroughly

understood. In order to use ceramics safely, their properties must be exhaustively tested so that a designer may say with confidence exactly when and under what conditions a particular component will fail. The following study was conducted as part of a much larger effort for the purpose of accurately predicting the life of a Ti-6Al-4V/SCS-6 composite under any conditions which it might see. In particular this study was to model the deformation and failure of a unidirectional Ti-6Al-4V/SCS-6 composite under sustained load which is the primary design driver in turbine airfoil and rotor applications where these materials may be implemented.

1.1 Previous Work

Models of a unidirectional MMC under sustained load have already been proposed. One of the best known models and one upon which this study is loosely based is the McLean Model [1]. In this model the two bar concept is used to establish the framework within which a composite is permitted to deform and share its load. Using a very simple power law to approximate the creep rate of the matrix, McLean's model predicts a relaxation of the matrix which sheds its load to the non creeping fibers [2-4]. This accumulation of load on the fibers results in a time dependent deformation of the composite resembling creep.

Building upon McLean's model is the Curtin-McLean Model [2,3,5]. This model like McLean's original is based upon the two bar concept and a power law creeping matrix. The major improvement of the Curtin-McLean Model is the inclusion of fiber failure according to a shear lag analysis proposed by Curtin. By allowing the fibers in the composite to fail as the load which they must carry is gradually increased, the Curtin-McLean Model provides a rationale for and perhaps an accurate prediction of final composite rupture.

1.2 Goal

The goal of this work was threefold. First a model was to be developed in order to characterize the creep behavior of a unidirectional MMC. Then, the validity of the model's primary assumptions were to be evaluated using extensive fiber tracking of an interrupted creep test. Lastly, the Weibull parameters which are used to characterize the strengths of SCS-6 fibers were to be determined experimentally and compared to other values which have been reported.

2. MATERIAL

The creep tests which were used to evaluate the model were performed on unidirectionally-reinforced eight-ply Ti-6Al-4V/SCS-6 composites that were cut into dogbone specimens. The gage sections of these specimens on average were 7.5 mm wide and 1.9 mm thick.

2.1 SCS-6

The SCS-6 fiber which is manufactured by Textron Specialty Materials is a continuous 142mm diameter fiber. Starting with a 33mm diameter carbon core, approximately 55mm of SiC is built up using a process known as chemical vapor deposition. On top of this layer two additional carbon-rich layers totaling three to five microns are added to protect the fiber not only from mechanical damage but also from chemical reactions between the SiC and the matrix during consolidation of the composite. The SCS-6 fiber mats which are used for the consolidation of the composite are spaced at 51±1 fibers per centimeter. For a more complete description of the SCS-6 fiber see Reference 6.

2.2 Ti-6Al-4V

The bulk chemistry of the Ti-6Al-4V matrix material utilized in this study is presented below in Table 1 [7].

TABLE 1. Chemistry of Ti-6Al-4V

ELEMENT	WEIGHT PERCENT	
	Minimum	Maximum
Aluminum	5.5	6.75
Vanadium	3.5	4.5
Nitrogen	-	0.05
Carbon	-	0.10
Hydrogen	-	0.015
Iron	-	0.4
Oxygen	-	0.20
Others (each)	-	0.1
Others Total	-	0.5
Titanium	Remaining	

2.3 Timetal®21S

The specimen that was used to assess the one break per fiber assumption was a unidirectionally reinforced four-ply Timetal®21S/SCS-6 composite cut into a six inch long straight sided specimen. The bulk chemistry for the Timetal®21S matrix material is presented below in Table 2 [6].

TABLE 2. Chemistry of Timetal®21S

ELEMENT	WEIGHT PERCENT	
	Minimum	Maximum
Molybdenum	14.0	16.0
Niobium	2.2	3.2
Aluminum	2.5	3.6
Silicon	0.15	0.25
Iron	0.20	0.40
Oxygen	0.11	0.15
Carbon	-	0.05
Nitrogen	-	0.05
Hydrogen	-	0.015
Titanium	Remainder	

2.4 Consolidation

All of the composites that were used in this study were produced by Textron Systems Division and were consolidated by hot isostatic pressing a foil/fiber/foil layout. The consolidation conditions, for proprietary reasons, are not given.

3. MODEL DEVELOPMENT / PROCEDURE

3.1 Weibull Analysis

One of the valuable characteristics of the model which has been developed is its ability to predict composite failure based upon the strengths of its reinforcing fibers. As suggested before, ceramics which exhibit brittle behavior often possess a wide range of possible strengths. In order to characterize the strengths of a particular population of ceramic components Waloddi Weibull suggested a statistical treatment which is commonly accepted and used today [8]. In the case of a population of brittle ceramic fibers Weibull's statistical analysis may be applied to predict the probability of survival,

$$P_s = \exp\left(-\frac{L}{L_o}\left(\frac{\sigma_f}{\sigma_o}\right)^m\right), \qquad (1)$$

where L is the length of the fibers, s_f is the current stress in the fibers, L_o and s_o are scaling factors and m is the Weibull modulus which relates to the variability of the strengths. What this probability of survival indicates is that if given a population of 100 fibers with L/L_o=1, m=10 and s_o=3500 MPa, when a fiber stress of 2600.6 MPa is reached 95 fibers will have survived and 5 fibers will have failed. In order to determine the proper Weibull parameters to characterize a population of ceramic fibers the following routine may be used. Although it may strongly resemble magic to anyone not schooled in statistical methods, the Weibull characterization is widely accepted and more importantly it appears to work. With only minimal understanding, curve fitting the correct fiber data on the correct Weibull plot can produce excellent results.

3.1.1 *Weibull Plot*

The axes of a Weibull plot arise out of some manipulation of Equation 1. The inverse of Equation 1 yields

$$\frac{1}{P_s} = \exp\left(\frac{L}{L_o}\left(\frac{\sigma_f}{\sigma_o}\right)^m\right). \qquad (2)$$

Taking the natural logarithm of Equation 2 twice gives

$$\ln\left(\ln\left(\frac{1}{P_s}\right)\right) = m\ln\sigma_f - m\ln\sigma_o + \ln\left(\frac{L}{L_o}\right). \qquad (3)$$

Because a set of Weibull parameters, m and σ_0, can be determined for any given L_0, simply set L_0 equal to L, the fiber test length. Using this simplification Equation 3 is now of the form y = M x + b which is a straight line. If data can be plotted on a graph whose y axis corresponds to $\ln(\ln(1/P_s))$ and whose x axis corresponds to $\ln(s_f)$ and if that data appears linear then the slope of the data will be the Weibull modulus m and the y intercept will be $-m*\ln(s_o)$. In this way, curve fitting a Weibull plot will reveal the Weibull parameters m and s_o

3.1.2 *Generating Weibull Data*

To create the data which is to be plotted on the Weibull axes a series of tension tests must be conducted on a population of fibers. These failure tests are conducted at a constant gage length L. The stress level at which each fiber fails is recorded as s_f (corresponding to the s_f plotted on the x axis of a Weibull plot) and is ordered from the lowest failure stress to the highest. If valid fiber strengths were determined for every fiber in a population of n fibers, the tension tests would be said to be complete and each failure in ascending order would be given an order number 1,2,3,...,n. If, however, some of the tension tests were not performed properly and understandably produced less than optimal results, those tests would be recorded as suspended tests and the highest stress which was reached during such a test would be recorded in place of a failure stress. The most common example of a suspended test is a grip failure where the full load carrying potential of the fiber's gage section is assumed to have not yet been reached. These suspended tests may not be ignored since they do provide information for the fiber strength distribution. At the same time ,however, they cannot carry the same importance as a true failed item. Consequently, a series of tension tests which includes suspensions cannot be ordered simply 1,2,3,...,n. Rather, the order increment must be altered

each time a suspended test is encountered. The new order increment as given by Johnson [9] is,

$$\text{New Increment} = \frac{(n+1) - (\text{previous mean order number})}{1 + (\text{number of items beyond present suspended set})}.$$

In Table 3 a data set presented by Johnson [9] has been reproduced for the sake of clarity.

TABLE 3. The Proper Assignment Of Order Number In A Data Set Including Suspensions

Stress (MPa)	Status	Mean Order Number
21	Failed	1.00000
33	Suspended	
40	Failed	2.11111
66	Failed	3.22222
70	Suspended	
84	Failed	4.51852
100	Suspended	
110	Suspended	
150	Failed	6.67901
200	Failed	8.83950

For the first failure in Table 3 the mean order number is simply 1. For the second item in Table 3 a new order number increment must be calculated though no mean order number has been assigned since it is not itself a failure. The relevant calculation is

$$\text{New Increment} = \frac{(10+1) - 1.00000}{1+8} = 1.11111.$$

This new increment has been added to the previous mean order number to produce the mean order number of the second failure.

Now that the failures have been ordered, their mean order numbers must be converted into rankings that have some physical meaning. This ranking is accomplished by using the median rank which can be thought of as a probability of failure rather than of survival. One example of a simple median rank estimator is [8]

$$\text{Median Rank} = P_f = \frac{\text{mean order number} - 0.5}{n}.$$

For the case of large populations, however, when n is greater than 20, Johnson [10] suggests using the estimator,

$$\text{median rank} = P_f = \frac{\text{mean order number} - (1 - \ln 2) - (2\ln 2 - 1)\left(\frac{\text{mean order number} - 1}{n-1}\right)}{n}.$$

The estimated median ranks which are calculated for failures can easily be converted into probabilities of survival using the relation $P_s=1-P_f$. With a corresponding P_s for each stress at failure the data can be plotted on the correct Weibull axes and linearly fit to determine the Weibull parameters.

3.1.3 *Concurrent Weibull Distributions*

The simple Weibull distribution presented above is adequate in many cases for characterizing the range of strengths found in a fiber population. Inevitably, however, exceptions to the rule occur. In situations where a fiber population is exposed to additional damage, whether it be from exposure to high temperatures, handling or consolidation in a composite, flaw types beyond those originally present in the population are introduced. The simultaneous presence of two or more distinct flaw types in some or all of the fibers comprising a population leads to a complex Weibull strength distribution whereby some fibers will fail from one flaw type while others fail from another. Several variations of the simple Weibull distribution function attempt to account for the presence of simultaneous flaws within a population but the one which is most often applicable and most often used is the concurrent Weibull distribution [11],

$$Ps = \exp\left(-\frac{L}{L_0}\left(\frac{\sigma_f}{\sigma_{01}}\right)^{m1} - \frac{L}{L_0}\left(\frac{\sigma_f}{\sigma_{02}}\right)^{m2} \right).$$

This type of distribution which includes a second pair of Weibull parameters has been found to be useful in describing the strengths of fibers which have been removed from a consolidated composite. As shown in Figure* 1, a concurrent distribution is characterized by two distinct yet joined linear sections of data while a simple Weibull distribution is approximated by a single straight line. The steeper of the two linear sections in the concurrent distribution represents the stronger portion of fibers while the other section represents those fibers which have seen their strength degraded. In order to determine the effects of a concurrent distribution on composite strength the current model which has been developed has been altered so that it is capable of handling either a simple or a concurrent Weibull distribution of fiber strengths.

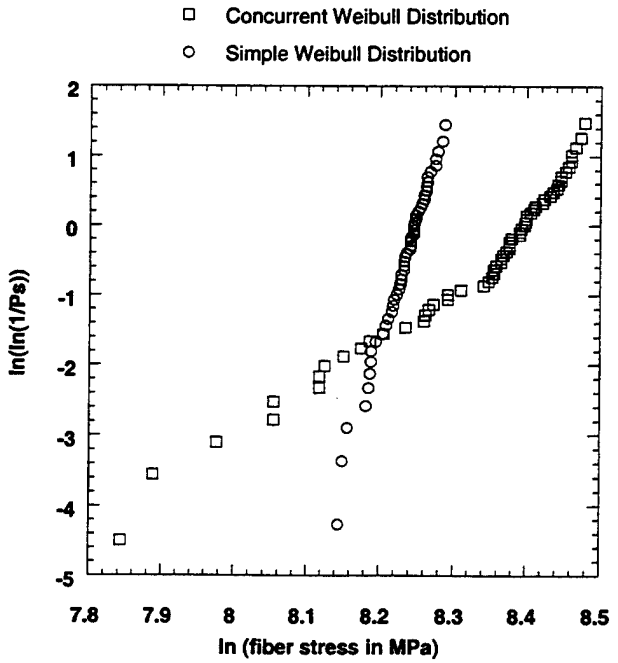


Figure 1. Comparison of Weibull Distributions

* Because the graphing program that was used cannot simultaneously handle symbols along with regular text in a title or legend, the words "fiber stress" have been used in the place of σ_f.

3.2 Two Bar Model Representation of a Composite

The fundamental device that is commonly used to characterize composites is called the two bar model. The visual representation of this device, for which it is named, is shown in Figure 2 where f is the bundle of fibers reinforcing the composite, m is the matrix material and P_c is the load which has been applied to the composite. The goal of the two bar model is to predict the response of a composite given the properties of its constituents. To facilitate such a prediction two assumptions are made. First, the condition of isostrain,

$$e_c = e_m = e_f,$$

is assumed for the deformation of the composite, where e_c is the strain in the composite, e_m is the strain in the matrix and e_f is the strain in the fibers. Second, the response of both components is assumed to be perfectly elastic,

$$e_m = \frac{\sigma_m}{E_m} = e_f = \frac{\sigma_f}{E_f},$$

where E is a component's elastic modulus, and σ is the stress in a component. In addition to these assumptions a static force balance is used,

$$\sigma_c = \sigma_f v_f + \sigma_m v_m,$$

where v is a component's volume fraction content. By manipulating these governing equations of the two bar representation, the initial stress state of the matrix in a composite, a value which is of great importance for each model presented in this paper, is predicted to be

$$\sigma_{m_o} = \frac{\sigma_c}{\left(v_m + \frac{E_f}{E_m} v_f\right)}. \qquad (4)$$

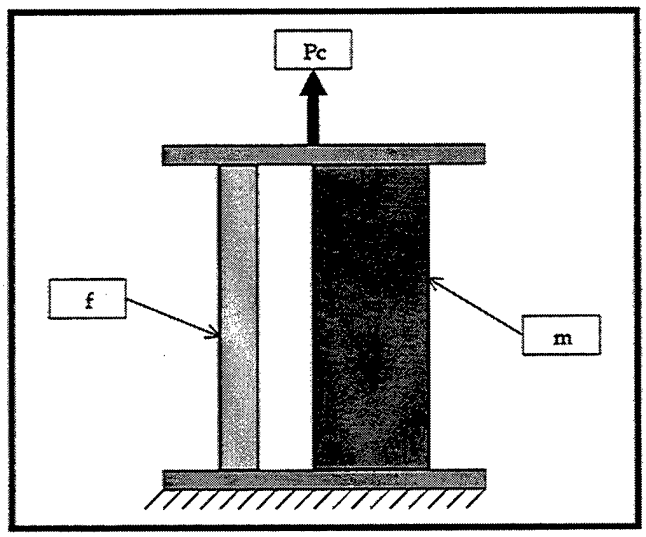


Figure 2. Schematic of Two Bar Model

3.3 McLean's Composite Creep Model

While the strength of the reinforcing fibers is ultimately responsible for determining whether or not a composite will fail under load, the properties of the matrix govern how quickly

the strength of those fibers may be called upon. The matrix material, unlike the ceramic fibers, creeps easily in the temperature range in which MMCs are to be used. Because the isostrain condition has been imposed, however, the matrix is not permitted to deform over time unless the fibers do so as well. The coupling of a creeping and a non creeping material constrained by the isostrain condition results in a relaxation phenomenon such that the matrix sheds its load to the reinforcing fibers. The result is that the elastic fibers accumulate load with time and deform accordingly, giving the composite the appearance of creep. The response of the fibers to loading is given by

$$e_f = \frac{\sigma_f}{E_f} \equiv e_f^E .$$

In contrast, the matrix response consists of an elastic and inelastic portion,

$$e_m = e_m^E + e_m^I = \frac{\sigma_m}{E_m} + e_m^I .$$

This inelastic portion of the matrix strain, called creep strain, controls the transfer of load from the matrix to the fibers. For simplicities sake, McLean approximated the creep stain rate to be governed by a power law,

$$\dot{e}_m^I = B(\sigma_m)^n , \qquad (5)$$

where B and n are constants which characterize the secondary or linear creep of the matrix.

Because McLean's Model does not take into account the gradual failure of fibers as load is redistributed within the composite, the model may be solved in closed form to produce exact solutions. Capitalizing upon the two bar representation of a composite, the governing equations in McLean's model are

$$\dot{e}_f^E = \dot{e}_m^E + \dot{e}_m^I = \frac{\dot{\sigma}_f}{E_f} = \frac{\dot{\sigma}_m}{E_m} + \dot{e}_m^I ,$$

the time derivative of the two bar equation,

$$\dot{\sigma}_c = 0 = \dot{\sigma}_f v_f + \dot{\sigma}_m v_m ,$$

and the power law creep expressed in Equation 5. The resulting composite strain as a function of time is given by

$$e_c = \frac{\sigma_c + (v_f - 1)\sigma_m}{v_f E_f} ,$$

where σ_m is given by

$$\sigma_m = \left\{(1-n)\left[\frac{Bt}{\left(\frac{1}{E_f}\left(\frac{v_f-1}{v_f}\right)-\frac{1}{E_m}\right)}+\frac{\left(\frac{\sigma_c}{\left(v_m+\frac{E_f}{E_m}v_f\right)}\right)^{(1-n)}}{1-n}\right]\right\}^{\left(\frac{1}{1-n}\right)}.$$

3.4 Curtin-McLean Model

The Curtin-McLean Model which utilizes the same two bar representation and power law creep conditions as the original McLean Model is mentioned here only because it demonstrates a method by which fiber fracture may be accounted for. Using Curtin's analysis of how much load a broken fiber can carry as a result of shear forces between the fiber and the matrix, the two bar equation is modified as shown [2,3,5],

$$\sigma_c = \sigma_f v_f\left[1-\tfrac{1}{2}\left(\frac{\sigma_f}{\sigma_o}\right)^{(m+1)}\right]+\sigma_m\left(1-v_f\right), \qquad (6)$$

where σ_o and m are the Weibull parameters of a simple Weibull distribution. Analysis of Equation 6 reveals that the addition of the bracketed shear lag term limits the amount of stress that the fibers may carry. While the stress in the composite must be maintained (constant load creep condition), the combination of a relaxing matrix and a limited fiber stress may lead to situations where no solution to Equation 6 exists. In the event that no solution is possible, the composite has failed by exceeding the maximum stress which is allowable for the fibers.

3.5 Single-Break Model

3.5.1 *Assumptions*

The model which is presented here and which shall be referred to as the Single-Break Model is based upon several simplifying assumptions. The first assumption is that once a fiber breaks it releases all of its load and cannot be reloaded again. Therefore, no fiber is expected to break more than once in the composite. In truth this assumption is most likely valid only for high temperatures but in any event, as will be demonstrated later, this assumption is very conservative in composite life predictions. The second assumption which has been made, one which if wrong potentially over-predicts the composite's capabilities, is that of a global load sharing regime. Under this regime the sliding resistance of the fibers in the matrix is taken to be low so that no stress concentrations may be built up at the tips of a broken fiber. In contrast, the condition under which stress concentrations do arise leading to failure of neighboring fibers along a single plane is called local load sharing and it results in a much weaker composite. Under global load sharing the load shed by a broken fiber is redistributed equally among he remaining fibers so that the full bundle strength of the reinforcing fibers can be achieved. This assumption like the first is most likely valid only at elevated temperatures. In order to assess the plausibility of global load sharing and "one break per fiber", work was conducted within this study to track the fiber breaks in a composite.

3.5.2 *Ti-6Al-4V Creep Law*

One advancement that the Single-Break Model shows over the original McLean Model is the use of a more accurate matrix creep law which incorporates primary creep. While this is an advancement it is also a limitation in that the matrix creep model does not lend itself to a simple closed form solution. In order to reap the rewards of a more accurate matrix creep law, such as the one presented here, a good deal more time and effort must be expended in determining the material constants than would otherwise be required for the simple McLean power law approximation. The Ti-6Al-4V creep law which is used in the Single-Break Model was developed by the University of Dayton Research Institute Structural Integrity Division, and is summarized below:

$$e_m^I = 0.5e^*\left[\left(t/t^*\right)^p + \left(t/t^*\right)^q\right], \tag{7}$$

where

$$p = 0.3857,$$

$$q = 586.9\left[1/(600 - Temp)\right]^{1.4373},$$

$$e^* = 0.02\left[1 - \exp\left\{-c\left(\frac{\sigma_m}{\sigma_u}\right)^{1.2}\left(1+\left(\frac{\sigma_m}{\sigma_u}\right)^2\right)^5\right\}\right],$$

$$t^* = 10^6\left[1 - \left(e^*/0.02\right)\right],$$

$$c = \left(5.6475\times10^{-7}\right)(Temp)\exp\left[\left(Temp/100\right)^{1.3751}\right],$$

and

$$\sigma_u = 962.77 - 0.80203(Temp).$$

In the previous expressions, p, q, c, and σ_u are material parameters and the variable Temp refers to the temperature in °C. Taking the time derivative of Equation 7 yields

$$\dot{e}_m^I = 0.5\left[\left(\frac{t}{t^*}\right)^p + \left(\frac{t}{t^*}\right)^q\right]\frac{de^*}{dt} - 0.5e^*\left[p\left(\frac{t}{t^*}\right)^p + q\left(\frac{t}{t^*}\right)^q\right]\frac{1}{t^*}\frac{dt^*}{dt} + 0.5e^*\left[p\left(\frac{t}{t^*}\right)^{p-1} + q\left(\frac{t}{t^*}\right)^{q-1}\right]\frac{1}{t^*}. \tag{8}$$

This expression is essentially a more accurate replacement for the power law and is used in an identical manner. The expressions for de*/dt and dt*/dt are

$$\frac{de^*}{dt} = 0.02\exp\left\{-c\left(\frac{\sigma_m}{\sigma_u}\right)^{1.2}\left(1+\left(\frac{\sigma_m}{\sigma_u}\right)^2\right)^5\right\}\cdot\left[c\frac{\sigma_m^{0.2}}{\sigma_u^{1.2}}\left(1+\left(\frac{\sigma_m}{\sigma_u}\right)^2\right)^4\left\{1.2+11.2\left(\frac{\sigma_m}{\sigma_u}\right)^2\right\}\frac{d\sigma_m}{dt}\right],$$

$$\frac{dt^*}{dt} = -50\times10^6\frac{de*}{dt}.$$

3.5.3 *Fiber Failure*

A second improvement upon the McLean Model which has previously been attempted by the Curtin-McLean Model is the inclusion of damage. As the matrix relaxes, the load which it carried is shed to the reinforcing fibers as a function of time. This accumulation of load permits the fibers, assuming a global load sharing regime, to fail from weakest to strongest according to a statistical distribution of their strengths. According to Curtin's shear lag analysis, even though a fiber may break within the composite the interaction between fiber and matrix permits even fiber fragments to carry a portion of the load. The Single-Break Model is more conservative, stating that once a fiber breaks it can carry no more load. The mathematical representation of this condition, which is very similar to the modified two bar equation given for the Curtin-McLean Model in Equation 6, is [4]

$$\sigma_c = v_f \sigma_f P_s + \left(1 - v_f\right)\sigma_m . \qquad (9)$$

In Equation 9, the limiting factor placed upon the fiber stress is Weibull's probability of survival shown in Equation 1. To demonstrate that the Single-Break Model is in fact more conservative than the Curtin-McLean Model the maximum fiber stress which is allowable for each model is determined below. Substitution of Equation 1 with $L/L_0=1$ into Equation 9 yields

$$\sigma_f \exp\left(-\left(\frac{\sigma_f}{\sigma_o}\right)^m\right) = \frac{\sigma_c - \left(1 - v_f\right)\sigma_m}{v_f} . \qquad (10)$$

Because the term on the right side of 10 increases with time until a limiting value of σ_o/v_f is reached, the left side must also increase to a maximum at least as large; otherwise no solution to the equation is possible and the composite is assumed to have failed. In order to determine the maximum value of the left side of Equation 10, which will be called the bundle strength of the reinforcing fibers, the derivative was taken and set equal to zero. After some simplification the maximum fiber stress that could be achieved is found to be

$$\sigma_{f_{max}} = \sigma_o \left(\frac{1}{m}\right)^{\left(\frac{1}{m}\right)} . \qquad (11)$$

By the same procedure the maximum attainable fiber stress in the Curtin-McLean Model is found to be [2]

$$\sigma_{f_{max}} = \sigma_o \left(\frac{2}{m+2}\right)^{\left(\frac{1}{m+1}\right)} . \qquad (12)$$

A comparison of Equation11 (Single-Break), to Equation 12 (Curtin-McLean), shows that the Curtin-McLean result predicts a greater maximum fiber stress than the Single-Break result. Thus, given the same conditions, longer composite lifetimes would be predicted by the Curtin-McLean Model. If in fact the Single-Break assumptions are in error at least they produce more conservative predictions than the Curtin-McLean Model.

3.5.4 *Residual Stresses*

One of the most critical errors which can be made in developing a model is to neglect the effects of residual stresses in the composite. The practice of pre-loading mechanical components is common and has a significant effect upon the range of stresses and strains within which components may be used. In the case of the Ti-6Al-4V/SCS-6 composites utilized in this study, the pre-load which is found on the various components is a natural result of a mismatch in the coefficients of thermal expansion of the constituents [12]. As the composite is

cooled down from consolidation temperatures to room temperatures, the matrix material which possesses a higher CTE than the fibers contracts to a greater extent than the fibers. The result is that the matrix clamps down on the fibers radially and attempts to shorten them axially. The consequence is an equal and opposite force applied by the matrix on the fibers and the fibers on the matrix. The effects of the residual stresses on the model are expressed below. The initial matrix stress from which relaxation will begin,

$$\sigma_{m_0} = \frac{\sigma_c}{\left(\nu_m + \frac{E_f}{E_m}\nu_f\right)} + \sigma_{m_{res}},$$

is shown to be the result predicted by the two bar model, see Equation 4, with the addition of the matrix residual stress. The residual stresses in the matrix and fibers are opposed to one another and are related by their volumetric content,

$$\sigma_{m_{res}} = -\sigma_{f_{res}} \frac{\nu_f}{\left(1-\nu_f\right)}.$$

Perhaps most importantly, the stress in the fibers must be adjusted for the purpose of calculating composite strains,

$$e_c = e_f = \frac{\sigma_f - \sigma_{f_{res}}}{E_f}.$$

3.5.5 *Loading*

In order to account for possible fiber failure prior to attaining the constant test load, a simulated loading has been included in the program which runs the Single-Break Model. No creep/relaxation is permitted during the loading which is perhaps an oversimplification given that at high temperatures creep/relaxation can occur very quickly, but nonetheless, the model is a more accurate simulation with at least the simple loading history included. In an effort to minimize any such relaxation during loading each of the creep tests which were performed for this study were loaded rapidly.

In conjunction with the simulation of loading, the Single-Break Model takes into account the ability of the matrix to yield. In the event that yielding does occur any further loading on the composite must be completely accepted by the reinforcing fibers. The effect of a yielding matrix on the composite stress-strain curve is shown in Figures 3 and 4 with and without residual stresses, respectively.

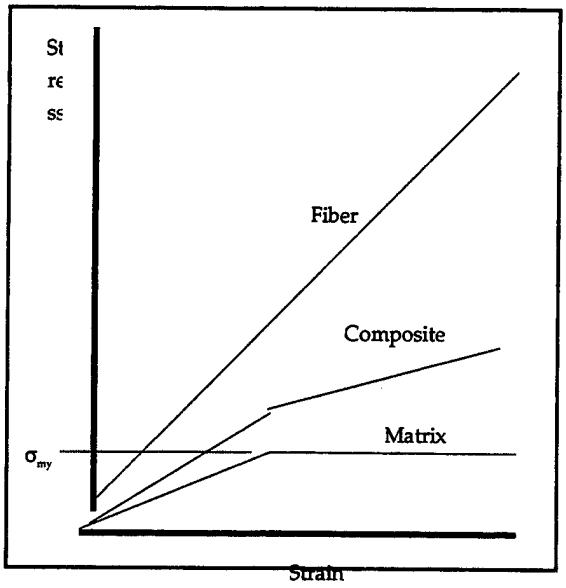
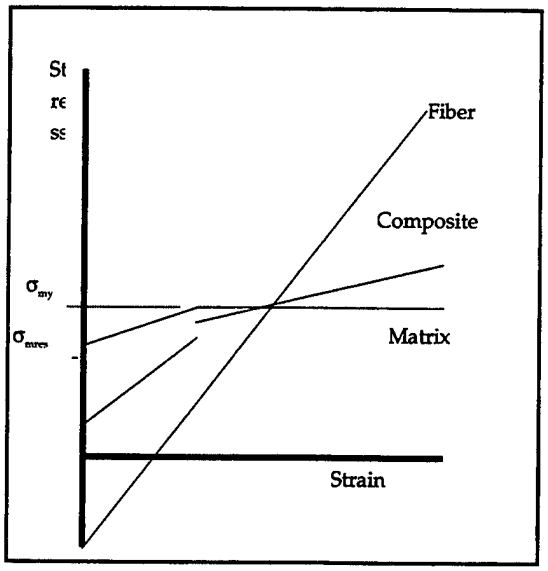


Figure 3. Effect Yielding Matrix



σ_{fres}

Figure 4. Effect of Yielding Matrix and Residual Stresses

3.5.6 *Governing Equations*

The governing equations for the Single-Break Model are

$$\dot{e}_f = \dot{e}_m^E + \dot{e}_m^I = \frac{\dot{\sigma}_m}{E_m} + \dot{e}_m^I = \frac{\dot{\sigma}_f}{E_f},$$

$$\sigma_c = v_f \sigma_f P_s + \left(1 - v_f\right)\sigma_m,$$

and the expression for the matrix creep rate given in Equation 8. Because the Single-Break Model accounts for fiber failure this system of equations cannot be solved in closed form. The code which simultaneously solves the governing equations of the Single-Break Model is presented in the Appendix.

3.6 Ti-6Al-4V/SCS-6 Creep Tests

The experimental data with which the Single-Break Model was evaluated was provided by the University of Dayton Research Institute in the form of a series of creep tests performed at various loads and temperatures on unidirectional Ti-6Al-4V/SCS-6 composites. The test conditions for these tests are shown below in Table 4. Along with the stress-strain data acquired from the creep tests, sensitive acoustic emission (AE) detection devices were employed in order to monitor and record fiber fractures during the tests. Depending upon the particular test set up, the cut off amplitude that was used to identify a "hit" as a fiber failure varied from 97dB to 99dB.

TABLE 4. Creep Test Conditions for Unidirectional Ti-6Al-4V/SCS-6 Composites

Specimen	Temp (°C)	Composite Stress (MPa)	Volume Fraction of Fiber	E_m (GPa)	E_f (GPa)	Matrix Yield Stress (MPa)	Matrix Residual Stress (MPa)
A	427	827	0.340	100	385	510	72
B	427	1170	0.340	100	385	510	72
C	538	827	0.333	89	370	390	30
D	538	1170	0.349	89	370	390	30
E	427	1170	0.328	100	385	510	72

3.7 Timetal®21S Specimen

In order to evaluate the assumptions of the model, global load sharing and one break per fiber, an extensive amount of fiber tracking was done to a six inch long, four ply, straight sided, unidirectional, Timetal®21S/SCS-6 specimen. This specimen was of limited use in evaluating the stain predictions of the Single-Break Model since only the matrix creep behavior of Ti-6Al-4V has been accurately defined for this study but because of the similarities in CTE's of the two matrix materials the Timetal®21S specimen could be used in assessing the model's assumptions. Prior to any testing, photographic montages were made of every cut surface on the specimen using a scanning electron microscope. With the aid of the photos, detailed mapping of damage to edge fibers resulting from the swimming of fibers in and out of the cut edges was possible as shown in Figure 5. The compiled results of this mapping are shown in Figrure 6 where the angled line segments indicate a fiber which has either entered or exited the composite and been cut off. In layers 1, 3 and 4 a systematic swimming of the fibers is apparent which is most likely the result of "fisheyes," a consolidation artifact that is commonly observed, while in layer 2 an obvious though slight misalignment of the fiber mat can be seen. From this information a fairly accurate estimate of the total length of fiber contained in the

composite along with the total number of load bearing fibers was made. The specimen was then creep tested at 700 MPa and 650°C.

The heating configuration for the Timetal®21S specimen is shown in Figure 7. The purpose of the off center heating was to allow for a hot and a cold zone on the specimen with the expectation that any fiber failures would occur in the hot zone where the matrix shed its load to the fibers most quickly. Also, because the amount of material available for testing was limited, the cold section of the specimen provided intact fibers for the purpose of characterizing consolidated fiber strengths. AE monitoring was also employed during the creep test so that damage assessments could continually be made and the creep test could be interrupted prior to the ultimate failure of the composite.

After more than 800 hours the creep test of the Timetal®21S specimen was interrupted and the composite's matrix material was slowly dissolved away one layer at a time using a bromine/methanol solution. This solution has been shown in other studies to not be harmful to the SCS-6 fibers although it does have the ability to eat away titanium. The method, although slow, was employed for the purpose of carefully tracking fiber breaks layer by layer. In theory only fiber fragments from the first layer of fibers should fall out after removal of just the first layer of matrix. Those fibers which were not damaged during the creep test were extracted, separated into heated and non-heated segments and then tensile tested to failure at room temperature in order to determine their proper Weibull parameters.

After tracking and tensile testing the first layer of fibers, the Timetal®21S specimen was severely damaged so that the remaining fibers could not be tensile tested. Fiber break tracking was still possible however, and was completed for all four layers. Using the collected fiber fragments and extracted lengths of fiber, one-for-one matches were attempted in order to prove the assumption of one break per fiber. In 11 out of 13 cases this match up was possible indicating that at 650°C "one break per fiber" is a reasonable assumption. In order to judge the assumption of global load sharing, each fiber break was tracked according to its location within the specimen. As expected all of the fibers breaks occurred within the heated section of the specimen and in only one case were two fibers broken side by side at the same length. This non-localized dispersion of fiber breaks gives no indication of stress concentrations within the composite and supports the assumption of global load sharing.

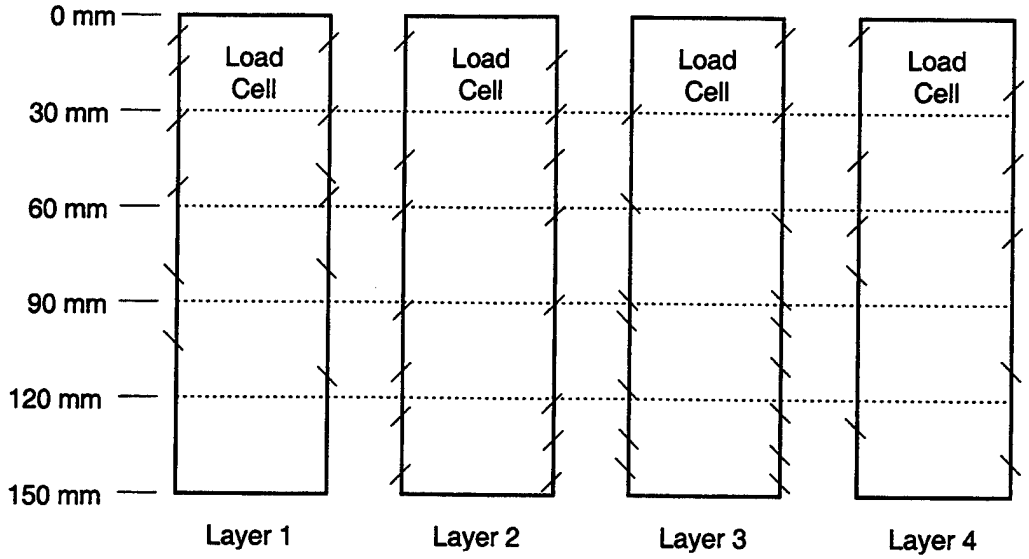


Figure 6. Results of Fiber Mapping for Timetal®21S Specimen

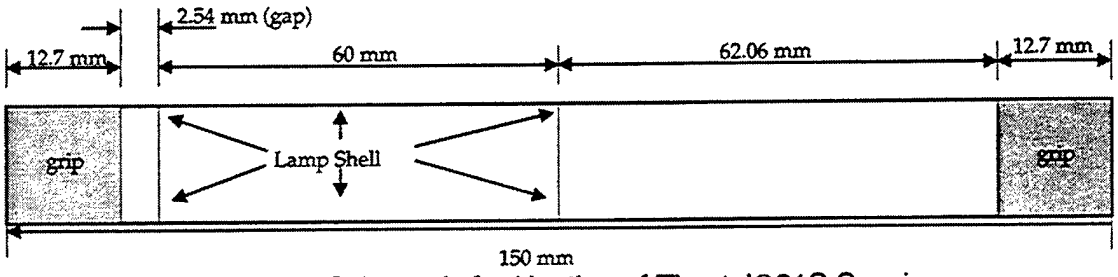


Figure 7. Schematic for Heating of Timetal®21S Specimen

3.7.1 *Additional Fiber Tracking*

Because the Timetal®21S specimen was tested at the high end temperature of 650°C and because its chemical composition did vary from the Ti-6Al-4V, additional fiber break tracking, albeit less extensive, was performed on a Ti-6Al-4V/SCS-6 composite as a check. This specimen, designated specimen C, again showed good dispersion among its fiber breaks and in 15 out of 15 breaks "one-for-one" match-ups were possible supporting the two assumptions of global load sharing and one break per fiber.

3.7.2 *Fiber Tensile Testing Procedure*

The test machine which was used to conduct tension tests on the extracted fibers uses a screw driven mechanism for loading and a laser/platinum flag system to measure displacement. After any undamaged fibers were extracted from the composite they were clipped into two segments; a segment which had been exposed to the full test temperature and a segment which had remained outside of the lamps. These segments were then individually tested to failure in the fiber tester at room temperature. In order to avoid slipping or breaking of the fibers in the grips, smoothed aluminum foil liners were used for protection along with a 13 to 14 inch pound torque on the screw driven grips. Each failure was recorded as either a simple gage failure, a high energy shatter or a grip failure. All grip failures were considered suspended items for the purposes of Weibull analysis since it is assumed that the full load carrying potential of the fiber's one inch gage length had not yet been reached.

3.7.3 *Weibull Parameters of Extracted and Virgin SCS-6 Fibers*

In order to demonstrate the damaging effect of consolidation on the SCS-6 fibers, two groups of virgin fibers, Population A and Population B, were tested along with the fibers that were extracted from the Timetal®21S specimen. Using the tensile data and the Weibull routine laid out earlier, the Weibull parameters for each population were determined and are shown below in Table 5. As shown in Figure** 8 the virgin fibers show a very steep slope on the Weibull plot indicating very little variability in their strengths. The average stress at failure for Population A (the sum of the failure stresses divided by the number of failures) was 3762 MPa and the bundle strength was found to be 3362 MPa.

For the extracted fibers that did not experience the full test temperature the appearance of two distinct linear sections on the Weibull plot, seen in Figure 9, indicates a concurrent strength distribution containing multiple flaw types. These additional flaw types as suggested before are incurred as a result of the high temperatures and pressures seen by the fibers during consolidation. For this population of extracted fibers the average stress at failure was 4149 MPa, which is higher than that of the virgin fibers, but their bundle strength was only 3212 MPa.

In the case of the fibers that were extracted from the fully heated test section, a simple Weibull distribution seems to be adequate for characterization but this does not mean that these fibers escaped damage during the consolidation process. The increased variability of the

** Because the graphing program that was used cannot simultaneously handle symbols along with regular text in a title or legend, the word sigma$_0$ has been used in place of σ_0. Unless reported differently every occurrence of the Weibull scaling strength, σ_0, is given in units of MPa.

strengths shown by the low Weibull modulus in Figure 10 suggests that perhaps all of the fibers were damaged during the course of consolidation and testing rather than just a portion of the fibers as in the case of the unheated extracted fibers. Like the unheated extracted fibers this population showed an average stress at failure higher than that of the virgin fibers at 4192 MPa. Again however the bundle strength was lower at 3129 MPa.

TABLE 5. Experimentally Determined Weibull Parameters

Population	m_1	σ_{01} (MPa)	m_2	σ_{02} (MPa)	L (in)	Average Failure Stress (MPa)	Bundle Strength (MPa)
Virgin (A)	36	3820	-	-	1	3762	3362
Virgin (B)	33	3730	-	-		3655	3255
Layer 1 Cold Section	7	4900	28	4650	1	4149	3212
Layer 1 Hot Section	9	4400	-	-	1	4192	3129

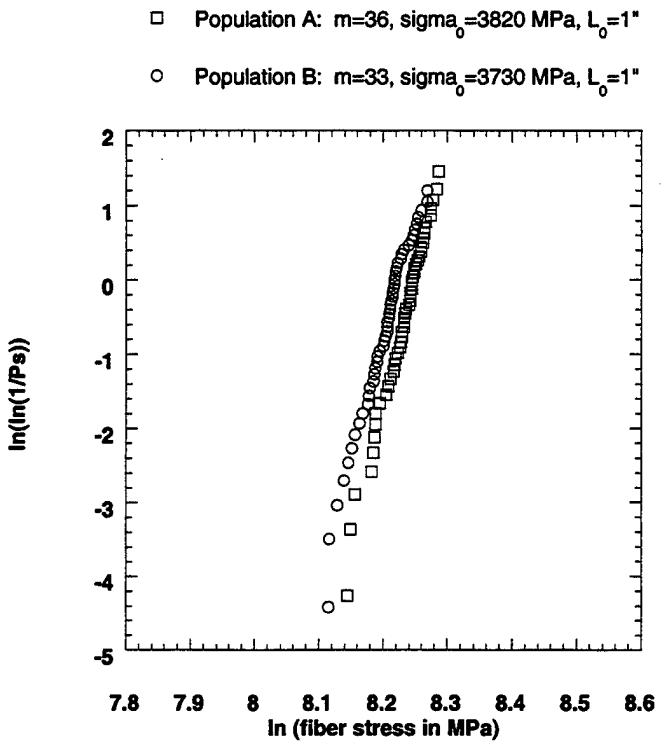


Figure 8. Weibull Plot for Virgin SCS-6 Fiber Strengths

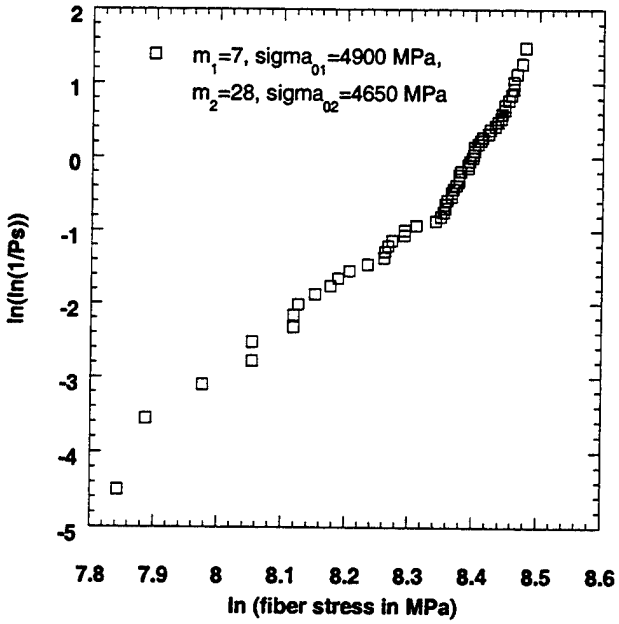


Figure 9. Weibull Plot for Fibers Extracted from the Non Heated Portion of Test Specimen

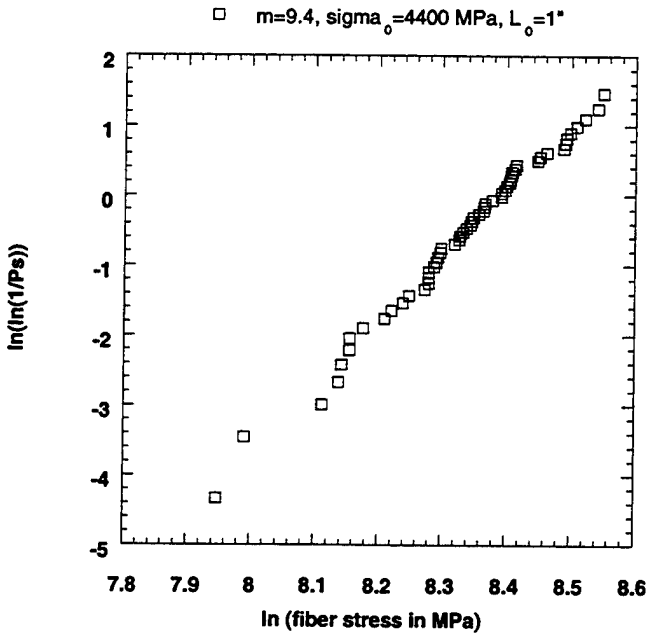


Figure 10. Weibull Plot for Fibers Extracted From Heated Test Section

Although the average and maximum strengths for fibers of the damaged populations are in fact higher than those of the virgin populations as shown by Figures 8 through 10, the bundle strengths of the populations are the true indicators of their capabilities. The virgin fibers as expected possess a higher bundle strength than the as-consolidated populations indicating the potential for better performance as a whole. While the extracted populations do contain some very strong fibers, they also contain a number of very weak fibers which once broken cease to carry any load at all, reducing the strength of the bundle.

The presence of fibers in the degraded populations which are stronger than the strongest fibers in the virgin populations is best explained by the variability of strengths from one

batch of fibers to the next. Because the virgin fibers which were consolidated in the Timetal®21S specimen did not come from the same batch as the virgin fibers for which the strengths have been reported here, it is possible that the fibers from the Timetal®21S specimen were initially stronger in their virgin state than the virgin fibers characterized in this study.

4. RESULTS

4.1 Parameter Study

The Single-Break Model has been developed in order to provide a more accurate characterization of deformation and failure than those offered by previous models. To aid in determining whether this goal was accomplished a parameter study was performed on the model and its results are presented below. This study reveals not only the effects of the individual variables on the model but also the sensitivity of the model itself to very slight changes in input. In every case presented below the model was run using the conditions shown in Table 6.

TABLE 6. Parameter Study Test Conditions

Parameter	Base Value	Additional Values
Composite Stress (constant)	1170 MPa	-
Temperature	427°C	-
Elastic Modulus of Fibers	385 GPa	-
Elastic Modulus of Matrix	100 GPa	-
Fiber Volume Fraction	0.34	-
Matrix Yield Stress	510 MPa	-
Original Number of Fibers	310	-
Weibull Modulus; m	10	15, 36
Weibull Scaling Parameter; σ_0	3500, 4000 MPa	3900, 4100 MPa
Weibull Length Ratio; L/L_0	1	1.5, 2
Matrix Residual Stress; σ_{mres}	72 MPa	25, 50, 100 MPa

The first variable that was investigated was the Weibull modulus m. As suggested before, this parameter describes the variability of the fiber strengths within a population and its value may vary as a result of handling or consolidation of the fibers. Reported values of m vary from as low as 4 or 5 for degraded fibers to as high as 16 for virgin fibers [13,14]. As part of this study a mat of virgin SCS-6 fibers was tested in order to independently determine some values for virgin Weibull parameters. Surprisingly a Weibull modulus as high as 36 was found. Although this number appears inconsistent with other reported values it most certainly represents a number that the manufacturers of SCS-6 fibers are aiming to achieve. The high Weibull modulus of 36 does not indicate that the fibers are unexpectedly strong, merely that all of the fibers cut from the same spool show good consistency in their strengths. As shown in Figure 11, with $L/L_0=1$, $\sigma_0=3500$ MPa and $\sigma_{mres}=72$ MPa, variations in the Weibull modulus have a tremendous effect upon the rupture time of the composite.

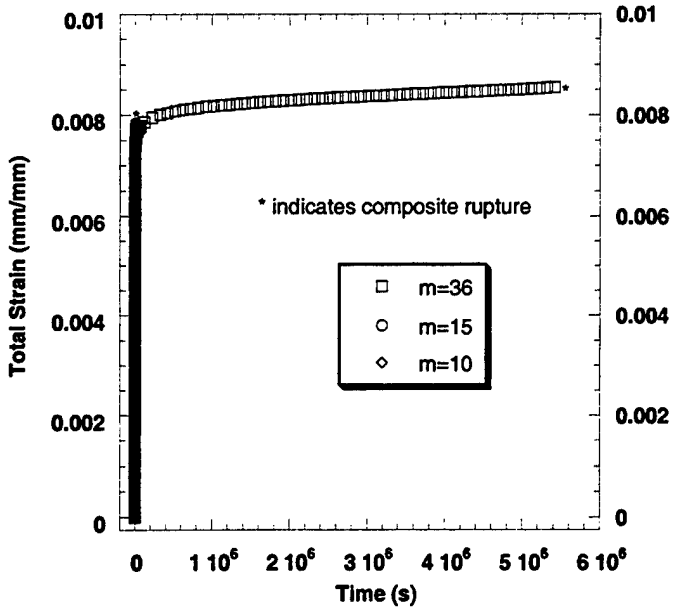


Figure 11. Influence of Weibull Modulus on Total Strain

Because the curves for the m=10 and m=15 cases appear very similar in Figure 11, Figure 12 has been included for the sake of clarity. In Figure 12 only the total strains starting immediately after loading are shown and the time axis has been shortened so that the rupture times of the weaker composites can be seen. Given that all of the test conditions besides m are the same for each curve in Figure 12, the McLean Model would have predicted an identical starting point for the strain curves but because the Single-Break Model accounts for fiber failure during loading, the weaker fiber distributions shown in Figure 12 have accumulated additional strains as a result of damage.

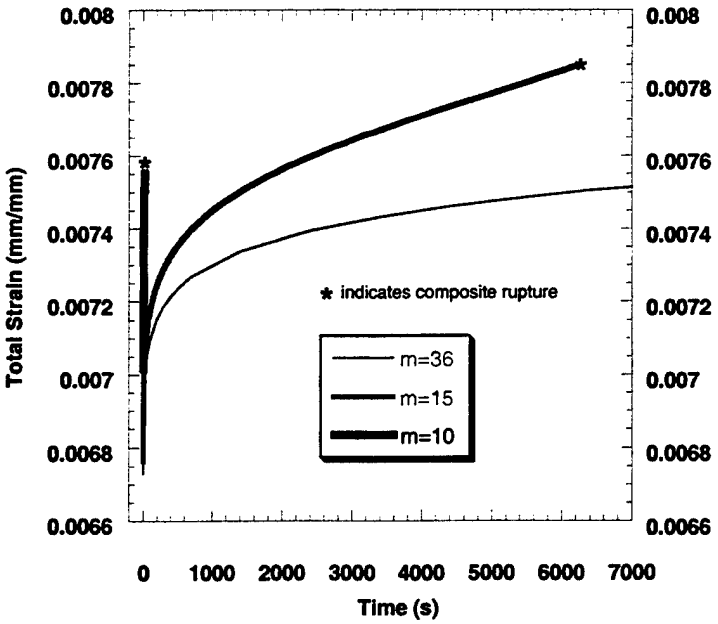


Figure 12. Influence of Weibull Modulus on Total Strain (for Short Time)

Perhaps even more instructive than the total strain curve in understanding the Weibull modulus m is the curve showing predicted fiber failures. As seen in Figure 13 the Weibull

modulus which describes the variability of a population's strengths establishes what percentage of the reinforcing fibers may fail before the composite finally ruptures. For low Weibull moduli weak fibers may fail harmlessly, shedding their load to other stronger fibers, while in the case of a high Weibull modulus where each fiber possesses approximately the same strength the failure of a single fiber means the failure of every fiber. For each curve shown below there were originally 310 load bearing fibers. For a Weibull modulus of 15 approximately 16 of those fibers failed prior to composite rupture while for the case of m=10 nearly 29 fibers failed.

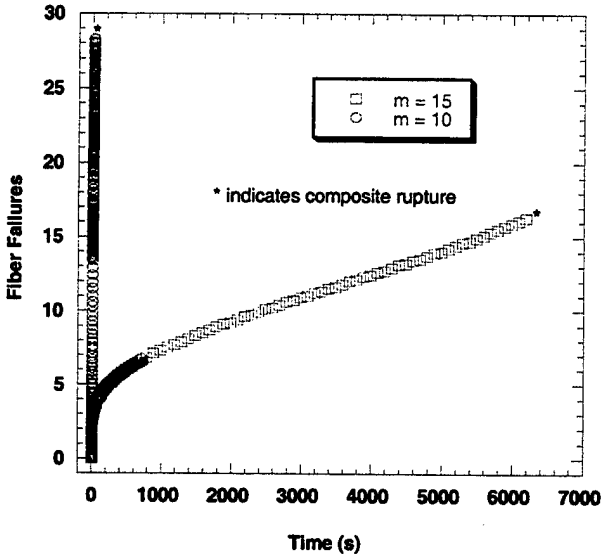


Figure 13. Influence of Weibull Modulus on Predicted Fiber Failure

In situations where extremely low or extremely high composite stresses are encountered the model loses its sensitivity to the value of the Weibull modulus. In the case of extremely low composite stresses even the weakest fibers in a population can withstand the condition of complete matrix relaxation and consequently no damage will be accumulated for either a strong or a weak reinforcing population. Likewise, if extremely high composite stresses are encountered so that even the strongest of fibers can barely support the initial fiber load, then the model will predict almost immediate failure for both a strong and a weak distribution.

The second parameter that was investigated was the Weibull scaling factor, σ_0. Using m=10, L/L_0=1 and σ_{mres}=72 MPa Figures 14 and 15 show the sensitivity of the Single-Break Model to only slight variations in σ_0. This variable relates directly to the strengths of the reinforcing fibers though it should not be considered an average strength. Reported values for σ_0 like the Weibull modulus m show wide variability not only between virgin and degraded values but also among the virgin and degraded values. In the case of virgin populations, scaling factors may range from as low as 3600 MPa to as high as 5100 MPa, while for the degraded (as-consolidated) populations values anywhere from 1500 MPa to 3900 MPa might be expected [13,14]. For the fibers tested in this study, the scaling strength of the degraded fibers was actually higher at 4400 MPa than that of the virgin fibers at 3800 MPa, reinforcing the notion that from batch to batch the SCS-6 fibers are very unpredictable.

The third parameter which was studied is the ratio L/L_0. Using m=10, σ_0=4000 MPa, and σ_{mres}=72 MPa the sensitivity of the Single-Break Model to the ratio L/L_0 can be seen in Figure 16. This variable relates the length of fiber to be loaded in a composite to the length of fiber which was tested when determining the Weibull parameters of the fiber. Because the flaws which weaken a ceramic fiber occur somewhere along its length, a fiber can be fragmented at the locations of its flaws until a small length can be produced which contains no weak points. The strength of this unflawed length is potentially much higher than the original flawed length of

fiber. For this reason the Weibull strength characterization must include the scaling length ratio L/L_0.

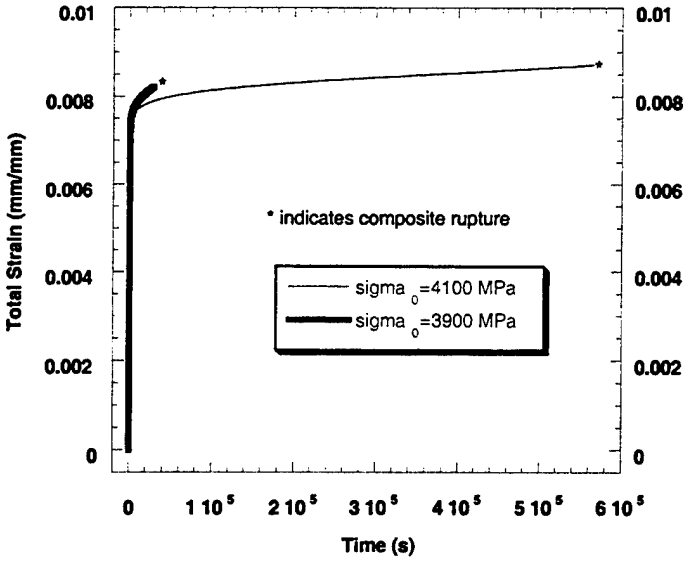


Figure 14. Influence of σ_0 on Total Strain

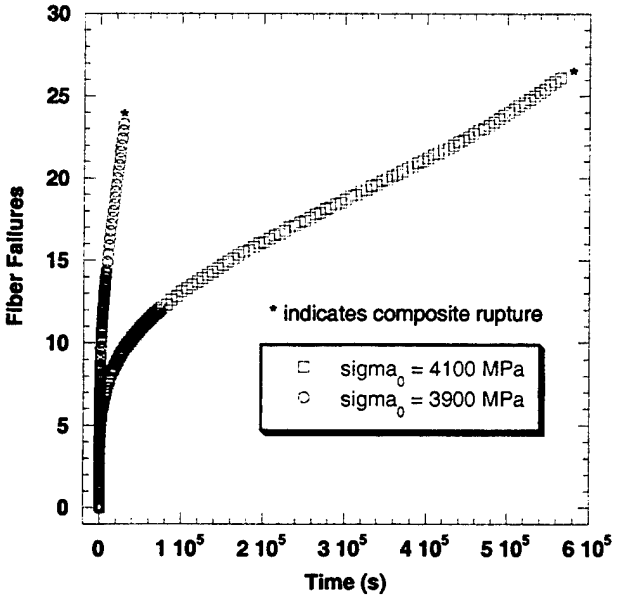


Figure 15. Influence of σ_0 on Predicted Fiber Failures

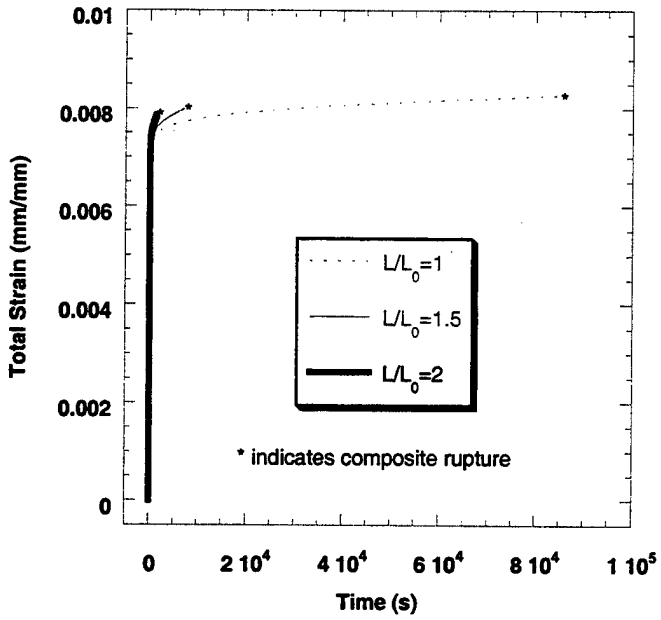


Figure 16. Influence of L/L_0 on Total Strain

The last parameter studied was σ_{mres}. This variable, unlike the others, is not used to characterize the strength of the reinforcing fibers and consequently has less of an effect upon the failure time of the composite. What the matrix residual stress does affect is the total initial strain of the composite. Using m=10, σ_0=4000 MPa and L/L_0=1 Figure 17 shows the sensitivity of the Single-Break Model to matrix residual stresses. Because a sufficiently high load was reached to cause matrix yielding for each case in Figure 17, the failure times are identical. In situations where yielding does not occur, matrix residual stresses can have an effect upon rupture time. Although it is not evident from Figure 17 the creep strains for each case are same.

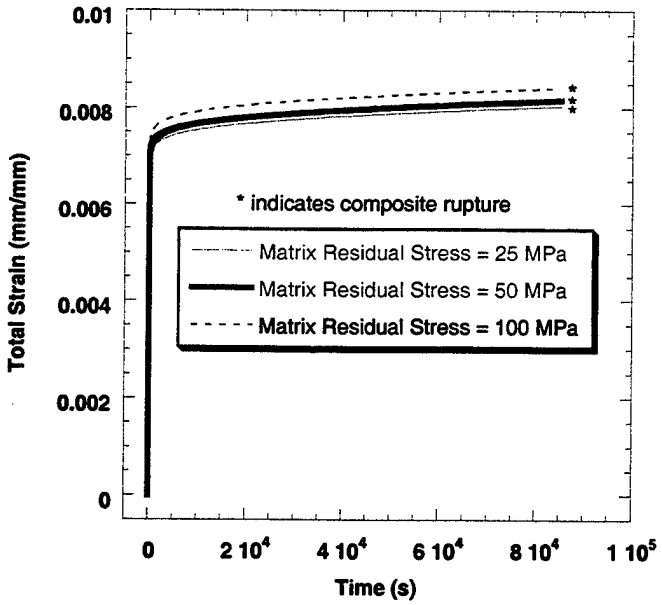


Figure 17. Influence of Residual Stresses on Total Strain

Because the variability in fiber strengths from one batch of fibers to the next is potentially very high, the results of the parameter study are discouraging. Both the Weibull modulus and the Weibull scaling strength effect the lifetime of a composite and both of these parameters possess values which are difficult to ascertain. Perhaps some additional piece of information is needed to reveal the true strength parameters of the reinforcing fibers in a composite.

4.2 Comparison to Experimental Data

As shown by the parameter study, the Single-Break Model demonstrates great sensitivity with respect to the Weibull parameters. Because of the possibility for wide variation in these parameters, any good correlation between the model's predictions and experimental data is probably serendipity. In the case of specimens A and B, see Table 4, no AE data exists and representative values for the Weibull parameters are not known. As a first approximation, the Weibull parameters which were determined for consolidated SCS-6 fibers in this study, see Table 5, were input into the model. The predicted strains and failure times using these parameters have been compared to the experimental data and are shown in Figure 18. In order to demonstrate the possible differences between the concurrent and simple Weibull distributions the model was run for both situations though no variation is apparent from Figure 18.

As seen in Figure 19 the creep strain prediction for specimen A differs drastically from the experimental data indicating either the data are incorrect or the model breaks down for the conditions of 427°C and 827 MPa. Clearly the Weibull parameters which have been input into the model are not the true Weibull parameters which characterize specimen A given that they result in failure times greater than three million seconds. This fact demonstrates both that the fiber parameters are variable from one population to the next and that this variation can have a tremendous effect upon the model's lifetime predictions.

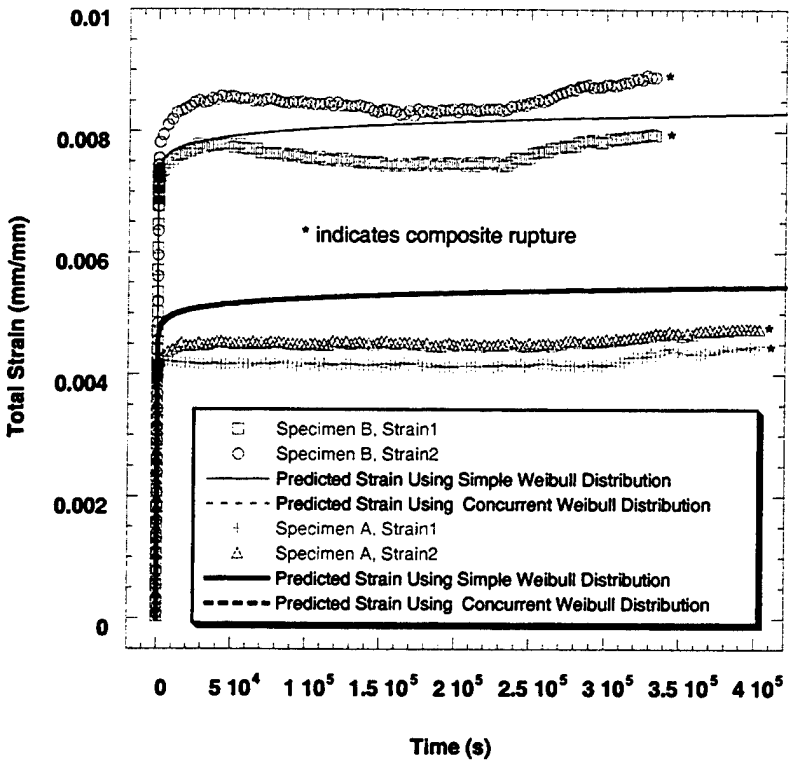


Figure 18. Comparison of Predicted and Measured Strain at 427°C

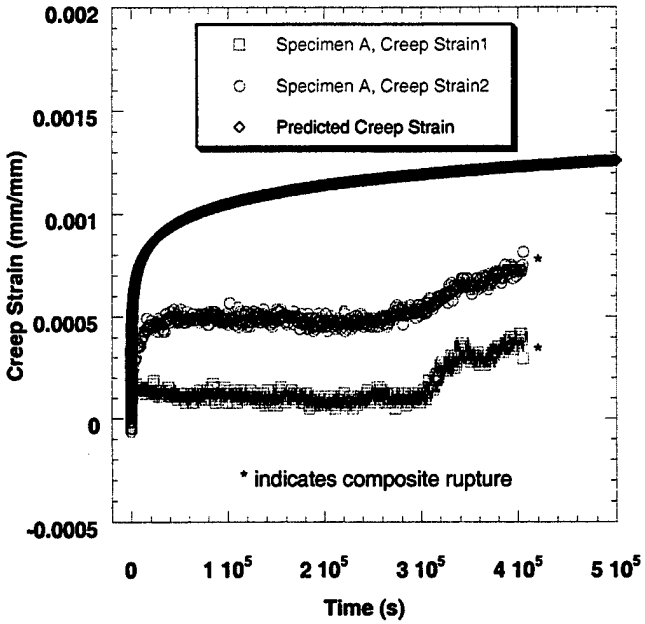


Figure 19. Comparison of Predicted and Measured Creep Strain at 427°C, 827 MPa

Although the model's predictions using the concurrent and simple Weibull distributions appear the same in Figure 18, they are not. As seen in Figure 20 which extends to three million seconds the different distributions do in fact diverge as expected.

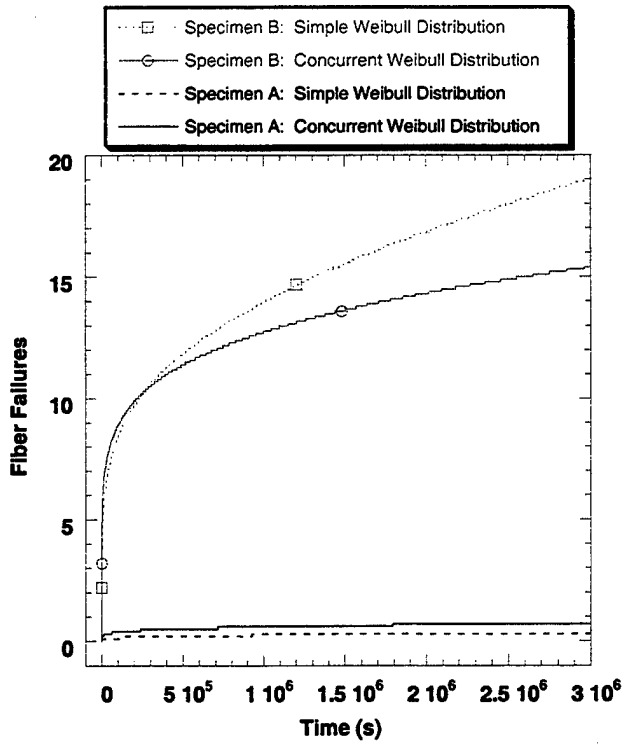
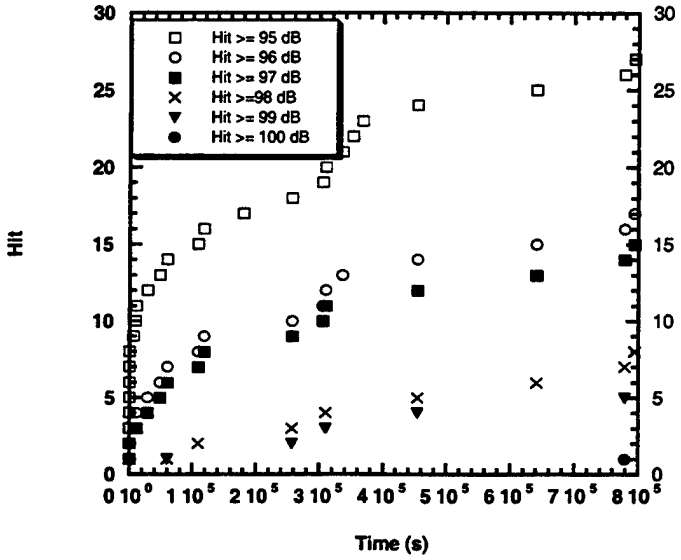


Figure 20. Comparison of Model's Predictions for Fiber Failure Using Concurrent and Simple Weibull Distributions

As explained previously, the concurrent distribution characterized by m_1=7, σ_0=4900 MPa, m_2=28 and σ_0=4650 MPa contains a number of degraded fibers which show very little strength and yet its overall bundle strength is higher than that of the simple distribution characterized by m=9 and σ_0=4400 MPa. As seen in Figure 20, the predicted fiber failure curve for specimen B, given a concurrent Weibull distribution and 310 fibers starting, is initially higher than that for the simple distribution though as time increases their positions reverse and the simple distribution predicts more failures. The explanation of this phenomenon is that the concurrent distribution contains some fibers that are weaker than the weakest fibers in the simple distribution. These fibers are the first to fail in either of the distributions but as relaxation continues and the fiber load accumulates fiber failures in the weaker simple distribution begin to outpace those in the stronger concurrent distribution and the curves switch positions. Similarly, in the case of specimen A where only low load levels are reached, the concurrent distribution which contains some of the very weakest fibers from either distribution predicts more fiber failures for the entire time range shown.

For specimens C, D and E acoustic emission data were taken in a "real time" manner so that the sounds of fibers breaking could be recorded and correlated with the relevant strain data. Although the exact sound amplitude of an emission which corresponds to a fiber break may vary slightly from one test to the next, examining the data may reveal extremely useful information. Specimen C which was tested for approximately 800,000 seconds, but not to failure, is the specimen mentioned previously which was used for additional fiber tracking. Upon digesting the matrix of specimen C, 15 fiber breaks were found within the test section of the specimen. Using Figure 21, which shows the real time hits recorded from the creep test of specimen C, the cutoff amplitude which corresponds to a fiber break can be firmly established as 97 dB.



Figrure 21. Acoustic Emission "Hits" Recorded During the Creep Test of Specimen C

The values, m=7.75 and σ_0=3725, yield 15 fiber breaks in 800,000 seconds as shown in Figure 22. Using this set of Weibull parameters, the strain predictions agree reasonably well with the experimental data seen in Figure 23.

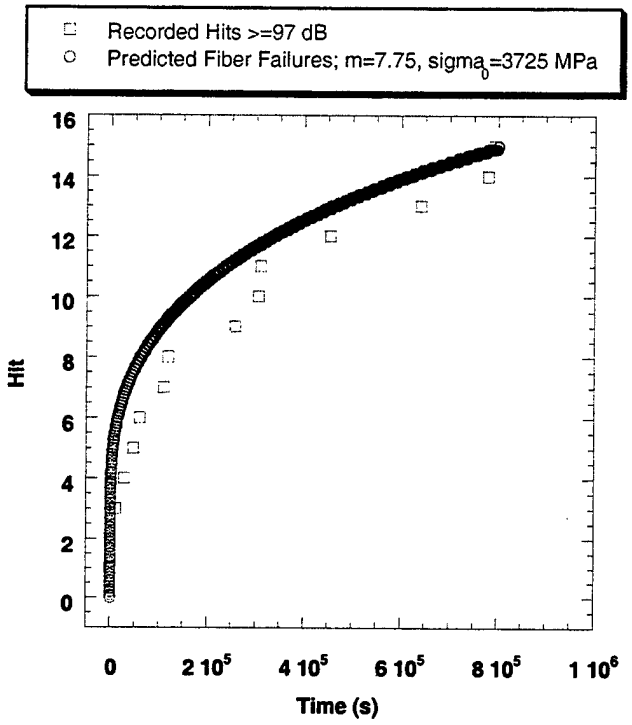


Figure 22. Comparison of Predicted and Observed Fiber Breaks

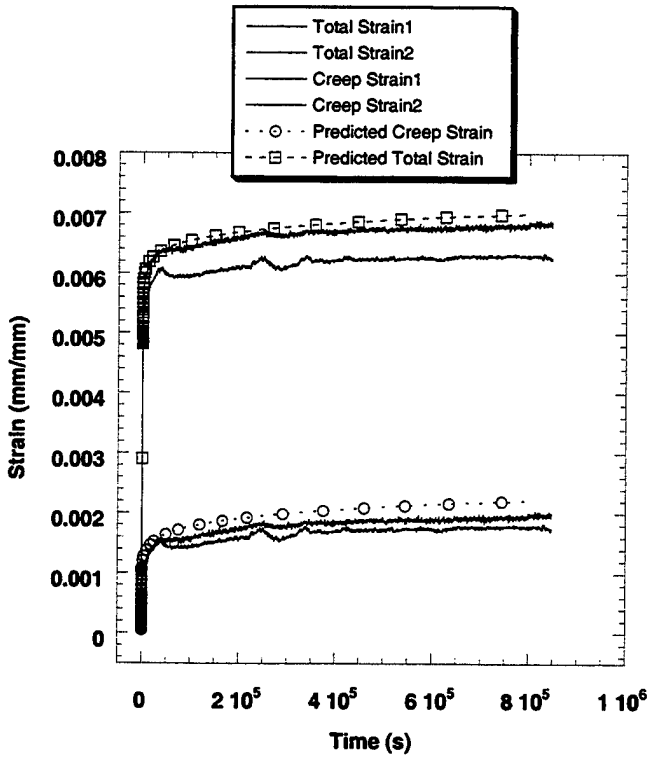


Figure 23. Comparison of Predicted and Measured Strains for Specimen C

For specimens D and E which were tested to failure, the acoustic emissions data provide an "after the fact" means for inferring the Weibull parameters of the reinforcing fibers. If the proper cutoff amplitude can be identified which corresponds to a breaking fiber then the AE data reveal how many fibers had broken prior to the composite's final rupture. Using this number a probable Weibull modulus can be "back" calculated, given that different Weibull moduli permit varying numbers of fibers to break before final composite rupture. For a low Weibull modulus the wide strength distribution of the fibers allows for many weak fiber failures while for a high Weibull modulus a single fiber failure may be enough to fail all of the others. Figure 24 shows the hits of various amplitudes recorded during the creep test of specimen D.

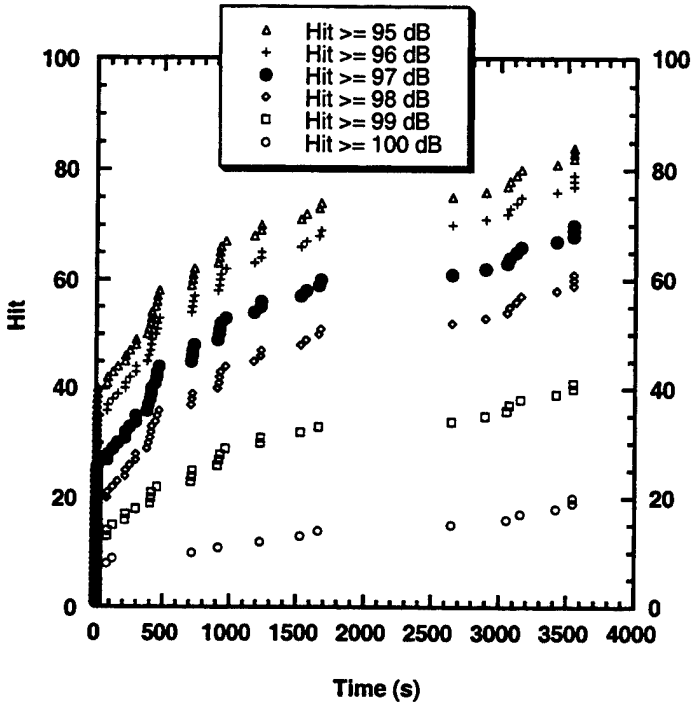


Figure 24. Acoustic Emission "Hits" Recorded During Creep Test of Specimen D

Although no obvious cutoff amplitude can be identified, 98 dB and 99 dB seem to be likely candidates. Assuming 98 dB and above indicates a fiber breaking then after 61 of approximately 310 fibers in specimen D failed, the composite ruptured. The maximum probability of survival would then be 0.80 for specimen D, corresponding to a Weibull modulus of approximately 5. Using a 99 dB cutoff just 41 fiber failures would result in composite rupture corresponding to a Weibull modulus of approximately 7.75. Knowing the actual failure time for the composite and the two likely Weibull moduli for the reinforcing fibers the model was run for a range of different σ_0 values until a similar failure time was predicted. The results of this "after the fact" investigation of Weibull parameters are shown below in Figures 25 and 26.

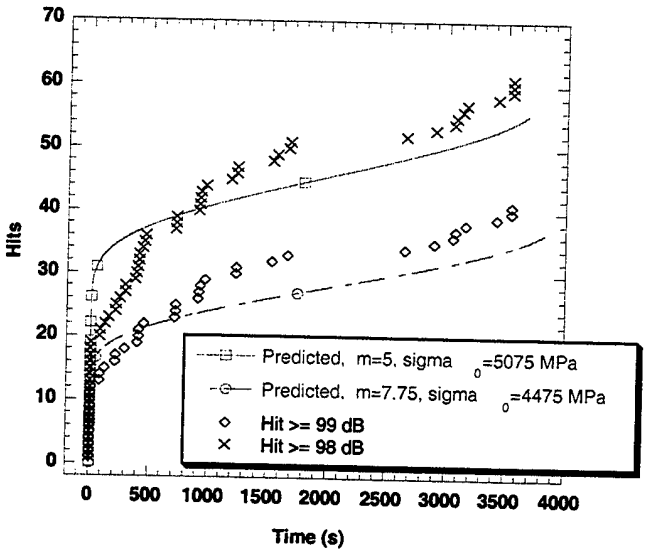


Figure 25. Comparison of Predicted and Recorded Hits for Specimen D

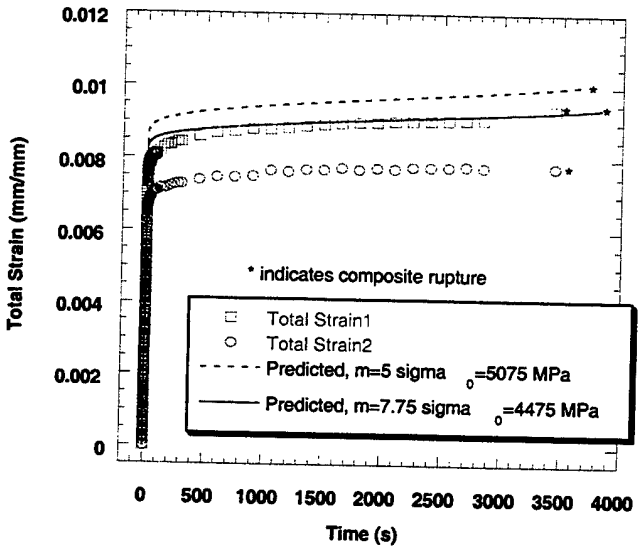


Figure 26. Comparison of Predicted and Measured Strains for Specimen D

Because the strain predictions using m=7.75 and σ_0= 4475 are closer to the experimentally measured strains and because this combination is more realistic in comparison to other referenced values of m and σ_0, the true cutoff amplitude corresponding to a fiber break is most likely 99 dB in this case.

Similarly for specimen E, the AE data provided at least some indication of the true Weibull parameters for the reinforcing fibers. Through an identical method of back calculation and trail and error a combination of Weibull parameters was identified to approximate the fiber properties. Using these fiber parameters the model's strain predictions were evaluated with much more reliable numbers than would otherwise be possible. As shown by the parameter study, to simply use some referenced values of Weibull parameters in order to evaluate the model is to neglect the possibility for wide variability from population to population and to ignore the obvious sensitivity of the model. Additionally, to determine the Weibull parameters through extraction and testing as was done for the Timetal®21S composite involves additional handling

which potentially alters the very properties which are being investigated, not to mention the fact that any Weibull parameters which are found characterize only the surviving fibers which were tested and in no way include the weakest fibers which fail very early in an interrupted test. In Figures 27 and 28 the results of the model's predictions using the approximated Weibull parameters are compared to the experimentally measured values. As shown by Figure 27 some additional fine tuning of the estimated Weibull parameters is necessary to match identically the number of fiber failures which leads to rupture but these parameters are a good approximation and for the sake of consistency a Weibull modulus of 7.75 has been utilized throughout.

In order to demonstrate the increased accuracy which is offered by the Single-Break Model, a side by side comparison has been made with the McLean Model in Figure 28. The McLean Model, as seen below, under predicts the composite strain as a result of neglecting the primary creep. Given long creep times this error would be minimized but initially the effect is significant.

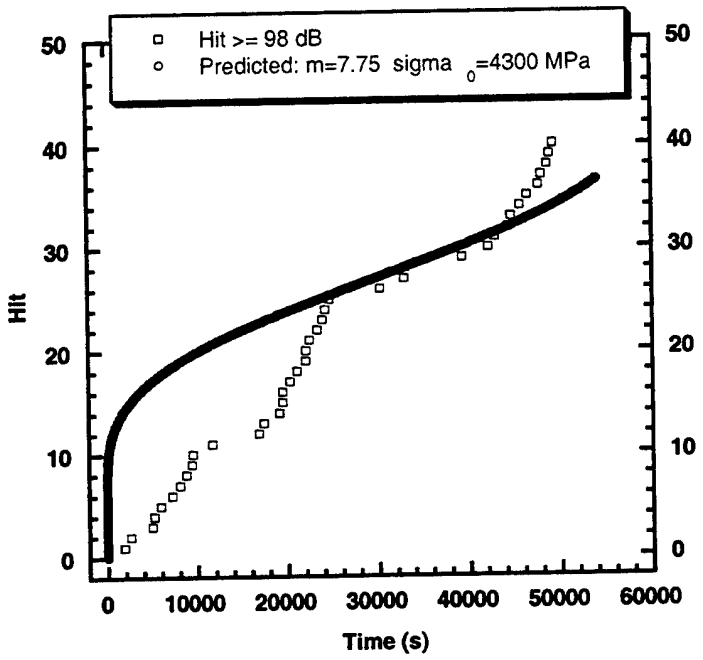


Figure 27. Comparison of Predicted Fiber Failures and Recorded Hits for Specimen E

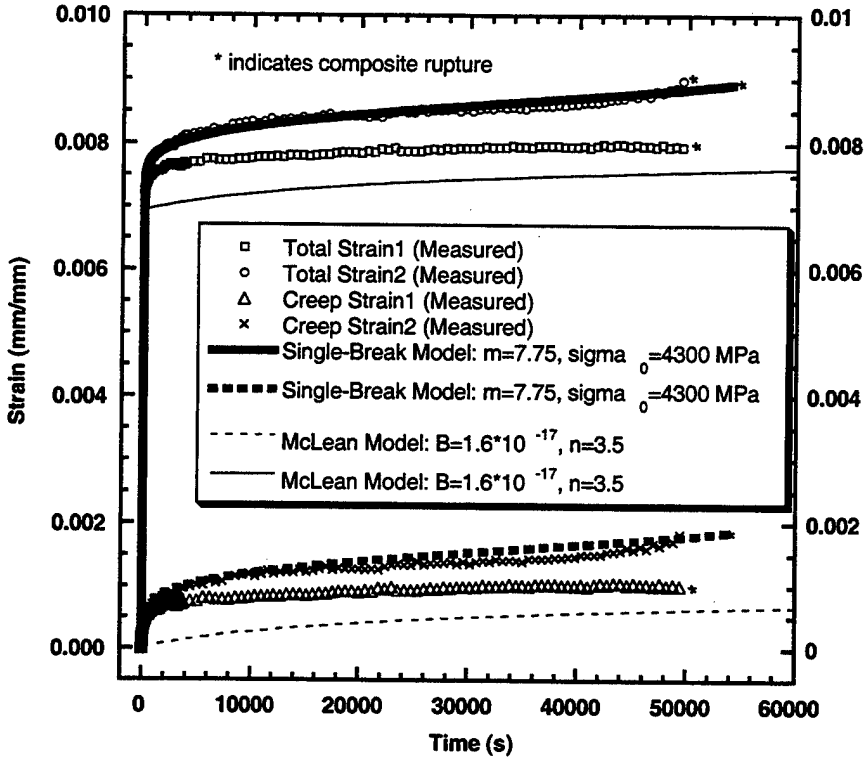


Figure 28. Comparison of Predicted and Measured Strains for Specimen E

In Table 7 the "after the fact" Weibull parameters which were inferred from the AE data and composite rupture times have been compiled. When compared to the experimentally determined Weibull parameters reported in Table 5, these estimated parameters appear to be reasonable. Although both Tables report parameter values for SCS-6 fibers, an exact agreement between the two should not be expected given that the consolidated fibers did not originate from the same spool and that the consolidation conditions were different for the Timetal®21S and Ti-6Al-4V composites. The fact that the Weibull parameters reported in Tables 5 and 7 are so similar indicates that the "after the fact" back calculation technique which was utilized may have some credibility. At the very least a further study is warranted.

TABLE 7. Practical Estimation of Weibull Parameters for Consolidated SCS-6 Fibers

Specimen	m	σ_0 (MPa)	Bundle Strength (MPa)
C	7.75	3725	2514
D	7.75	4475	3020
E	7.75	4300	2902

5. CONCLUSIONS

As a result of the extensive fiber tracking which was done within this study, the assumption of one break per fiber was concluded to be valid at elevated temperatures. Also the assumption of global load sharing was found to be valid. Thus, the reinforcing fibers of a composite may be considered to fail according to their Weibull strength distribution as they were in this study. What cannot be concluded is that absolutely no load is carried by a fiber fragment. Given, however, that a broken fiber cannot be reloaded enough to break again, any shear

forces which are exerted between a fiber and the matrix can be neglected compared to the load which is carried by intact fibers.

Perhaps one of the most useful results to come from this study is the development of the "after the fact" technique for estimating the Weibull parameters of the reinforcing fibers in a composite. While fiber strengths appear to show a wide and elusive variation from one population to the next, this method demonstrates real potential for getting a grasp on the characterizing Weibull parameters. Although a further study is necessary, it may be possible to test a sample specimen from a much larger plate and use a technique of back calculation to determine a representative pair of Weibull parameters, not only for that specimen but also for the entire plate. This method would enable designers to get a handle on the elusive Weibull parameters in a more cost and time effective manner than would otherwise be possible through extraction and testing of consolidated fibers.

As difficult as determining the simple Weibull parameters for a population of ceramic fibers may be, including the possibility of a concurrent distribution adds an additional level of uncertainty to the model's input. As demonstrated previously the differences in the two types of fiber characterizations do in fact have an effect upon the model's predictions but no simple comparison can be made between the two from this study. At this time, because no quick and easy way to determine the concurrent Weibull parameters which characterize a fiber population is apparent, a best estimate pair of simple Weibull parameters should be used instead as they were in this study. Perhaps in a perfect world the precision offered by the concurrent distribution would be useful. Given, however, that the strength characterization of the fibers is unpredictable, a problem only worsened by consolidation, the use of the concurrent Weibull distribution may well be wasted effort.

Using the estimated Weibull parameters which have been back calculated from the AE data, the model itself appears to be successful. The sensitivity of the Single-Break characterization which was demonstrated in the parameter study indicates that the model has excellent potential for predicting composite rupture but clearly the accuracy of the model's predictions is limited by the accuracy of the model's input. The variability of the Weibull parameters from one fiber population to the next is disheartening to say the least. In order to predict the composite's behavior with any degree of confidence, the true strengths of the consolidated SCS-6 fibers must be known. Although the goal of the MMC is to limit the risks associated with the use of ceramics, the immediate results of this study do not appear to demonstrate any satisfactory improvement. As suggested previously the "after the fact" estimation of Weibull parameters may prove to be useful but some criteria must be established to ensure that a particular specimen is identical in properties to a given sample specimen for which Weibull parameters have been estimated.

6. FUTURE WORK

In hindsight several improvements should be made to the model and these improvements are currently being pursued at the University of Dayton Research Institute. The first is the accommodating of creep during loading which may have a significant effect at high temperatures. Second is including a shear lag analysis similar to Curtin's for the case of the more realistic matrix creep law. This shear lag concept is important, especially at low temperatures where the one break per fiber assumption may not hold. Finally, is the more challenging task of accounting for eccentric loading due to a bow or misalignment in the composite. If a situation arises where one layer of the composite's reinforcing fibers sees a much higher stress than the others, the full bundle strength potential of the reinforcing fibers may never be achieved which could explain cases of premature failure.

Because the elusiveness of the fiber strengths appears to be the true obstacle in modeling these composites, if any future work is to be done at all it should involve a study of the Weibull parameters of consolidated fibers. Having already demonstrated the potential for wide

variability in virgin fiber strengths, any such further study into the strengths of consolidated fibers may be an exercise in futility.

One step to be taken which does hold the potential for producing meaningful results and one which perhaps should have been taken in this study is the careful control of composite consolidation. Although the consolidation conditions have been excluded from this report for proprietary reasons, they give some indication that the composites could have been fabricated with less threat of harm to the reinforcing fibers. Without giving exact numbers, the initial pressure which was placed upon the foil/fiber/foil layout while still at room temperature had the potential for damaging the fibers. The proper way to HIP a foil/fiber/foil layout is to maintain a very low pressure until the temperature is increased enough to soften the foils. Only then are pressures elevated enough to force together the fiber mats and now semi-flowing foils. In contrast, the consolidation schedules that were used in this study utilized high pressures before the foils were softened. Because the fiber mats use an over-under-over-under cross weave, the hipping pressure on the still solid foil/fiber/foil layout creates a three point bend on the SCS-6 fibers which is capable of severely damaging them [15]. In order to greatly reduce the damaging effect of consolidation on the fibers and potentially decrease the variability of consolidated fiber strengths, a gentler and more consistent consolidation schedule should be used in any further work.

REFERENCES

[1] McLean, M., Comp. Sci. & Tech., 1985, Vol. 23, pp 37-52.

[2] Du, Z.-Z. and McMeeking, R. M., "Creep Models for Metal Matrix Composites with Long Brittle Fibers," Journal of the Mechanics and Physics of Solids, Vol. 43, No. 5, May 1995, pp 701-726.

[3] Weber, C. H., Du, Z.-Z., and Zok, F. W., "High Temperature Deformation and Fracture of a Fiber Reinforced Titanium Matrix Composite," Acta Metallurgica et Materialia (submitted for publication 1994).

[4] Walls, D. P., "A Statistical Fiber Failure Model of Creep in Continuous Fiber Reinforced Composites" (unpublished work for United Technologies Pratt & Whitney).

[5] Curtin, W. A., "Theory of Mechanical Properties of Ceramic Matrix Composites," J. Am. Ceram. Soc., 74, pp 2837-2845.

[6] Larsen, J., Sanders, B., Gambone, M.L., and Khobaib, M., "Characterization of Titanium Matrix Composites", NASP Technical Memorandum 1199, Vol.II, June 1995.

[7] Metals Handbook, Ninth Edition , Vol. 3, American Society for Metals, Metals Park, OH, 44073

[8] Gambone, M.L., "The Fiber Strength Distribution and Its Effect on the Creep Behavior of a SiC/Ti-1100 Composite," Dissertation, University of Virginia, January 1995.

[9] Johnson, L. G., The Statistical Treatment of Fatigue Experiments, Elsevier, NY, 1964.

[10] Johnson, L. G., "The Median Ranks of Sample Values in Their Population with an Application to Certain Fatigue Studies," Industrial Mathematics, 2 (1951) pp 1-9.

[11] Service, T. H., Ritter, J. E., Jakus, K., and Sonderman, D., "Bimodal Strength Populations," American Ceramic Society Bulletin 64(9), pp1276-1280.

[12] Ohno, N., Toyoda, K., Okamoto, N., Miyake, T., and Nishide, S., "Creep Behavior of a Unidirectional SCS-6/Ti-15-3 Metal Matrix Composite at 450°C, Trans. ASME Series H. J. Engng. Mater. Techno. 116, 208.

[13] Gambone, M. L., Gundel, D. B. and Wawner, F. E., "The Effect of Isothermal Exposure on SiC Fibers," The 17th Conference on Metal Matrix, Carbon, and Ceramic Matrix Composites, edited by J. D. Buckley, NASA Conference Lpublication 3235, 1994, pp. 235-252.

[14] Gambone. M. L. and Wawner, F. E., "The Effect of Elevated Temperature Exposure of Composites on the Strength Distribuion of Reinforcing Fibers, "Intermetallic Matrix Composites III, 350, J. A. Graves, R. R. Bowman, and J. J. Lewandowski, eds., MRS, Pittsburgh, PA, 1994, pp 111-118.

[15] Nicolaou, P.D., Piehler, H.R., and Semiatin, S.L., "Fiber Fracture During Processing of Continuous Fiber, Metal-Matrix Composites Using the Foil/Fiber/Foil Technique," Metallurgical and Materials Transactions, Vol. 26A, May 1995, pp1129-1133.

APPENDIX

Numeric7.for

The following is a listing for the Fortran program which was created to run the Single-Break Model.

```
************************************************************************
*  PURPOSE: THE FOLLOWING PROGRAM IS USED TO MODEL THE DEFORMATION     *
*           AND FAILURE OF A UNIDIRECTIONAL METAL MATRIX COMPOSITE     *
*           UNDER A CONSTANT LOAD                                      *
************************************************************************
*  INPUT:   P - a constant which is used to characterize the creep     *
*               properties of Ti-6Al-4V                                *
*                                                                      *
*           COMPOSITE STRESS (MPa)                                     *
*                                                                      *
*           ELASTIC MODULUS OF THE FIBERS (MPa)                        *
*                                                                      *
*           ELASTIC MODULUS OF THE MATRIX MATERIAL (MPa)               *
*                                                                      *
*           VOLUME FRACTION OF THE FIBERS                              *
*                                                                      *
*           INCREMENTAL TIME STEP TO BE USED DURING CREEP (s)          *
*                                                                      *
*           FINAL TIME (s)                                             *
*                                                                      *
*           WEIBULL MODULUS m                                          *
*                                                                      *
*           WEIBULL STRENGTH SCALING FACTOR SIGMAo (MPa)               *
*                                                                      *
*           WEIBULL SCALING LENGTH Lo (same units as GAGE LENGTH)      *
*                                                                      *
*           NUMBER OF STEPS PER PRINTOUT                               *
*                                                                      *
*           ORIGINAL NUMBER OF FIBERS                                  *
*                                                                      *
*           TEST TEMPERATURE (DEGREES CELSIUS)                         *
*                                                                      *
*           MATRIX YIELD STRESS (MPa)                                  *
*                                                                      *
*           MATRIX RESIDUAL STRESS (MPa)                               *
*                                                                      *
*           LOADING TIME (S) - time during which the load will be      *
*                              applied linearly from zero to the       *
*                              full test load                          *
*                                                                      *
*           MIX FACTOR - variable used to aid in convergence at        *
*                        each time step (small values near 0.1 seem    *
*                        to work best)                                 *
*                                                                      *
*           GAGE LENGTH - length of fiber within which the maximun     *
*                         loads are expected to be seen (should be     *
*                         entered in the same units as Lo)             *
*                                                                      *
*                                                                      *
************************************************************************
*  OUTPUT:  TIME (s)                                                   *
*                                                                      *
*           MATRIX STRESS (MPa)                                        *
*                                                                      *
*           FIBER STRESS (MPa)                                         *
*                                                                      *
```

```
*           TOTAL STRAIN (mm/mm)                                        *
*                                                                       *
*           NUMBER OF FIBER FAILURES                                    *
*                                                                       *
************************************************************************
*                                                                       *
*  VARIABLES:                                                           *
*                                                                       *
*           SIGM     -matrix stress                                    *
*           SIGF     -fiber stress                                     *
*           T        -time                                             *
*           EF       -elastic modulus of fibers                        *
*           EM       -elastic modulus of matrix                        *
*           VF       -volume fraction of fibers                        *
*           VM       -volume fraction of matrix                        *
*           SIGC     -composite stress                                 *
*           STRAIN   -total composite strain                           *
*           TI       -time increment once loading is completed         *
*           TF       -final time                                       *
*           A        -initial guess for fiber stress (lower limit)     *
*           C        -initial guess for fiber stress (upper limit)     *
*           FA       -functional value calculated using A              *
*           FC       -functional value calculated using C              *
*           MIDPT    -midpoint of A and C                              *
*           FMIDPT   -functional value calculated using MIDPT          *
*           DSIGM1   -hold variable for the matrix stress increment    *
*           PROBS    -probability of survival                          *
*           DAMAGEF  -number of damaged fibers                         *
*           SIGMY    -matrix yield stress                              *
*           SIGFRES  -residual stress in fibers                        *
*           SIGMRES  -residual stress in matrix                        *
*           DESTARDT-derivative wrt time of estar                      *
*           SIGO     -Weibull strength scaling parameter               *
*           M        -Weibull modulus                                  *
*           SIGFO    -fiber stress of previous step                    *
*           DSIGMO   -initial guess for matrix stress increment        *
*           SIGMO    -original matrix stress                           *
*           DSIGM    -matrix stress increment                          *
*           TSTAR    -tstar                                            *
*           ESTAR    -estar                                            *
*           ERATE    -creep rate of matrix                             *
*           CONST    -c                                                *
*           SIGU     -ultimate stress for matrix                       *
*           TEMP     -test temperature                                 *
*           RTIME    -ramp time for loading                            *
*           CSIGC    -current composite stress during loading          *
*           RAMPR    -ramp rate                                        *
*           P        -p                                                *
*           Q        -q                                                *
*           DTSTARDT-derivative wrt time of tstar                      *
*           TILOAD   -time increment for loading                       *
*           CRPTM    -time over which creep has been accounted for     *
*           MIX      -aids in convergence at each step                 *
*           HOLD     -used to hold a value which might be needed       *
*           LO       -Weibull length scaling parameter                 *
*           GAGEL    -gage length                                      *
*       DONE       -true when the iteration for a step is finished *
*       PCOUNT   -counts the number of steps since last printout *
*       PNOW       -number of steps between printouts          *
*       FIBER0   -original number of fibers                      *
*       SCOUNT   -number of iterative steps changing mix factor  *
*       ENOUGH   -maximum number of iterative steps              *
************************************************************************

IMPLICIT NONE
```

```
*    declare all variables
DOUBLE PRECISION SIGM,SIGF,T,EF,EM,VF,SIGC,STRAIN,TI,TF,
     &   A,C,FA,FC,DSIGM1,PROBS,DAMAGEF,VM,SIGMY, SIGFRES,DESTARDT,
     &   MIDPT,FMIDPT,SIGO,M,SIGFO,DSIGMO,SIGMO,DSIGM,
     &   TSTAR,ESTAR, ERATE, CONST, SIGU, TEMP,RTIME, CSIGC, RAMPR,
     &   P,Q,SIGMRES,DTSTARDT,TILOAD,CRPTM,MIX,HOLD, LO,GAGEL

LOGICAL DONE

INTEGER PCOUNT, PNOW,FIBERO,SCOUNT,ENOUGH

*    open an output file
OPEN (UNIT =100, FILE='NUMERIC7.OUT', STATUS='OLD')

*    initialize the time, the strain and the composite stress
T=0.0
STRAIN = 0.0
       CSIGC=0.0

*    the time increment for loading is not an input value so it is
*    declared here
TILOAD=0.10000D-01

*    prompt the user for the necessary input
PRINT 1
 1   FORMAT(1X,'ASSUME THAT THE CREEP STRAIN IS GIVEN BY',/,
      &   ' e = 0.5e#(t/t#)^p + 0.5e#(t/t#)^q')
       PRINT 2
 2   FORMAT(1X,'ENTER THE REAL VALUE OF THE CONSTANT p.')
READ*, P
PRINT 3
 3   FORMAT(1X,'ENTER THE STRESS IN THE COMPOSITE (MPa).')
READ*, SIGC
PRINT 4
 4   FORMAT(1X,'ENTER THE ELASTIC MODULUS OF THE FIBER AND THE',/,
      &   ' MATRIX (MPa).')
READ*, EF, EM
PRINT 5
 5   FORMAT(1X,'ENTER THE VOLUME FRACTION OF THE FIBER.')
READ*, VF
PRINT 6
 6   FORMAT(1X,'ENTER THE TIME INCREMENT AND THE FINAL TIME (SEC).')
READ*,TI,TF
PRINT*,'ENTER WEIBULL PARAMETERS M, SIG0 AND LO'
READ*, M,SIGO,LO
PRINT 121
 121FORMAT(1X,'ENTER THE NUMBER OF STEPS PER PRINTOUT')
READ*, PNOW
PRINT 122
 122FORMAT(1X,'ENTER THE ORIGINAL NUMBER OF FIBERS')
READ*, FIBERO
PRINT 123
 123FORMAT(1X,'ENTER THE TEST TEMPERATURE')
READ*, TEMP
PRINT 124
 124FORMAT (1X,'ENTER THE YIELD STRESS OF THE MATRIX')
READ*, SIGMY
PRINT 125
 125FORMAT (1X,'ENTER THE RESIDUAL STRESS IN THE MATRIX')
READ*, SIGMRES
PRINT 126
 126FORMAT (1X,'ENTER THE TIME FOR LOADING')
READ *, RTIME
PRINT 127
```

```
 127FORMAT(1X,'ENTER THE MIX FACTOR')
READ*, MIX
PRINT 128
 128FORMAT(1X, 'ENTER THE GAGE LENGTH')
READ*, GAGEL

*   send a listing of the input to the output
WRITE (100,141)P
 141FORMAT(1X,'p = ', F5.4)
    WRITE (100,129) SIGC
 129  FORMAT(1X,'COMPOSITE STRESS = ',F7.2)
      WRITE (100,130) EF,EM
 130  FORMAT(1X,'EF = ',F7.0,'MPa',/,3X,'EM = ',F7.0,'MPa')
      WRITE (100,131) VF
 131  FORMAT(1X, 'VF = ',F4.3)
      WRITE (100,132) TI,TF
 132  FORMAT (1X,'TIME INCREMENT = ',E14.7,3X,'FINAL TIME = ',F10.0)
      WRITE (100,133) M,SIGO,LO
 133  FORMAT(1X,'M = ',F4.1,2X,'SIGO = ',F6.1,2X,'LO = ',F5.2)
      WRITE (100,134) FIBERO
 134  FORMAT(1X,'ORIGINAL NUMBER OF FIBERS = ',I3)
      WRITE(100,135) TEMP
 135  FORMAT(1X,'TEST TEMPERATURE = ',F6.1)
      WRITE(100,136) SIGMY
 136  FORMAT(1X,'SIGMY = ',F6.1)
      WRITE(100,137)SIGMRES
 137  FORMAT(1X,'RESIDUAL STRESS IN MATRIX = ',F6.1)
      WRITE(100,138)RTIME
 138  FORMAT(1X,'LOADING TIME = ',F5.1)
      WRITE(100,139)GAGEL
 139  FORMAT(1X,'GAGE LENGTH = ',F7.3)
      WRITE(100,140)MIX
 140  FORMAT(1X,'MIX = ',F3.2,///)


*   print column headings for the output
PRINT 7
WRITE(100, 7)
 7  FORMAT(1X,'   TIME(S)',T16,'MATRIX STRESS(MPa)',T35,
     &  'FIBER STESS(MPa)',T56,'STRAIN',T67,'BREAKS')

PRINT 8
WRITE(100, 8)
 8  FORMAT(1X,'    ----',T16,'------------------',T35,
     &      '----------------',T56,'------',T67,'-------')

**********************************************************************
*   loading portion of the model

RAMPR=SIGC/RTIME

VM=1-VF


 308SIGMO=(EM*CSIGC)/(EM*VM+EF*VF) + SIGMRES


SIGFRES= -(SIGMRES)*(VM/VF)

SIGFO=(EF*CSIGC)/(EM*VM+EF*VF) + SIGFRES

DAMAGEF=0
DSIGM1=0
DSIGMO =0
```

```
*    if the fiber stress is greater than 0 then there may be damage
*    use a root finder (bisection method) to the determine the
*    fiber stress given damage
IF (SIGFO.GE. 0.0)THEN

A=0
C=SIGO*(1/M)**(1/M)+1

DONE=.FALSE.

 310IF (.NOT. DONE)THEN
    MIDPT=(A+C)/2

FA=SIGMO*(1-VF)-CSIGC+VF*A*EXP(-(GAGEL/LO)*(A/SIGO)**M)
FC=SIGMO*(1-VF)-CSIGC+VF*C*EXP(-(GAGEL/LO)*(C/SIGO)**M)
FMIDPT=SIGMO*(1-VF)-CSIGC+VF*MIDPT*EXP(-(GAGEL/LO)*
     &   (MIDPT/SIGO)**M)

IF ((FA*FC).LT.0)THEN
IF (ABS(FMIDPT).LE.0.0001)THEN
    DONE=.TRUE.
ELSE IF ((FA*FMIDPT).LT.0)THEN
    C=MIDPT
ELSE
    A=MIDPT
END IF
ELSE
    C=C+10
END IF

GO TO 310
END IF

SIGFO=MIDPT

PROBS= EXP(-(GAGEL/LO)*(SIGFO/SIGO)**M)
DAMAGEF=FIBERO-FIBERO*PROBS

END IF

STRAIN =(SIGFO-SIGFRES)/EF


*    if the matrix is loaded beyond yield then treat it as an
*    elastic-perfectly plastic material
IF (SIGMO.GT.SIGMY)THEN
    SIGMO=SIGMY

A=0.0
C=SIGO*(1/M)**(1/M)+1

DONE=.FALSE.

 311IF (.NOT. DONE)THEN
    MIDPT=(A+C)/2

FA=SIGMO*(1-VF)-CSIGC+VF*A*EXP(-(GAGEL/LO)*(A/SIGO)**M)
FC=SIGMO*(1-VF)-CSIGC+VF*C*EXP(-(GAGEL/LO)*(C/SIGO)**M)
FMIDPT=SIGMO*(1-VF)-CSIGC+VF*MIDPT*EXP(-(GAGEL/LO)*
     &   (MIDPT/SIGO)**M)

IF ((FA*FC).LT.0)THEN
IF (ABS(FMIDPT).LE.0.0001)THEN
    DONE=.TRUE.
ELSE IF ((FA*FMIDPT).LT.0)THEN
```

```
    C=MIDPT
ELSE
    A=MIDPT
END IF
ELSE
    C=C+10
END IF

GO TO 311
END IF

SIGFO=MIDPT

PROBS= EXP(-(GAGEL/LO)*(SIGFO/SIGO)**M)
DAMAGEF=FIBERO-FIBERO*PROBS

    STRAIN=(SIGFO-SIGFRES)/EF

END IF

PRINT 11, T,SIGMO,SIGFO,STRAIN, DAMAGEF
WRITE(100, 11) T,SIGMO,SIGFO,STRAIN, DAMAGEF
 11 FORMAT(1X,F11.4,T14,F11.3,T35,F11.3,T56,F7.6,T67,F5.1)

T=T+TILOAD
CSIGC=T*RAMPR

IF (CSIGC.LE.(SIGC+.0000001))THEN

    GO TO 308
ELSE
*   initialize time back to zero (rounding errors occur for
*   non exact numbers other than zero and these errors may have
*   a significant effect when very small time increments are used)
    T=0.0

END IF
**********************************************************************
*   creep portion of model

SCOUNT=0
PCOUNT =0
ENOUGH=0
CONST=5.6475D-7*TEMP*EXP((TEMP/100.0D+0)**1.3751D+0)
SIGU=962.77D+0-.80203D+0*TEMP
*   the creep model only works below 600C
Q=586.9D+0*(1/(600.0D+0-TEMP))**1.4373D+0
HOLD=MIX

 12 IF (T.LE.TF+10D-18)THEN

      CRPTM=T+TI/2

      SCOUNT=SCOUNT+1
ENOUGH=ENOUGH+1

IF (ABS(DSIGMO).GE.SIGMO)THEN
    DSIGMO=SIGMO*(-.9)
END IF


      ESTAR=0.02D+00-0.02D+0*DEXP((-CONST)*((SIGMO+DSIGMO/2)/SIGU)**1.2
     &   *(1+((SIGMO+DSIGMO/2)/SIGU)**2)**5)

TSTAR=1.0D+6*DEXP((-CONST)*((SIGMO+DSIGMO/2)/SIGU)**1.2
```

```
     &   *(1+((SIGMO+DSIGMO/2)/SIGU)**2)**5)


IF (TI.GT.(TSTAR*0.001))THEN
    TI=TSTAR*0.001
END IF

DESTARDT=-0.02D+0*DEXP((-CONST)*((SIGMO+DSIGMO/2)/SIGU)**(1.2)*
     &   (1+((SIGMO+DSIGMO/2)/SIGU)**2)**5)*(- CONST*((SIGMO+DSIGMO/2)
     &   /SIGU)**(1.2)*5*(1+((SIGMO+DSIGMO/2)/SIGU)**2)**4
     &    *2*(SIGMO+DSIGMO/2)
     &   *DSIGMO/(TI*SIGU**2)-CONST*(1+((SIGMO+DSIGMO/2)/SIGU)**2)**5
     &   *1.2*((SIGMO+DSIGMO/2)/SIGU)**0.2*DSIGMO/(SIGU*TI))

DTSTARDT= -50.0D+6*DESTARDT

ERATE= 0.5*ESTAR*(T+TI/2)**P *(-P)*TSTAR**(-1-P)*DTSTARDT
     &   + 0.5*ESTAR
     &   *TSTAR**(-P)*P*(T+TI/2)**(P-1)+ 0.5*(T+TI/2)**P
     &   *TSTAR**(-P)*DESTARDT
     &   +0.5*ESTAR*(T+TI/2)**Q*(-Q*TSTAR**(-Q-1))*DTSTARDT
     &   + 0.5*ESTAR*
     &   TSTAR**(-Q)*Q*(T+TI/2)**(Q-1)+0.5*(T+TI/2)**Q
     &   *TSTAR**(-Q)*DESTARDT



DSIGM= -VF*EXP(-(SIGFO/SIGO)**M)*(1-M*(SIGFO/SIGO)**M)*
     &   EF*ERATE*TI/((1-VF)+(EF/EM)*VF*EXP(-(SIGFO/SIGO)**M)*
     &   (1-M*(SIGFO/SIGO)**M))

IF (ENOUGH.GE.10000) THEN
    PRINT 707
    WRITE (100,707)
 707    FORMAT (1X, 'ENOUGH')
    DSIGM=(DSIGM+DSIGMO)/2
    DSIGMO=DSIGM
    ENOUGH=0
    SCOUNT=0
    MIX=HOLD
END IF

        IF (SCOUNT.EQ. 1000) THEN
    HOLD=MIX
       MIX=MIX*1.113
    SCOUNT=0
    GO TO 12
END IF
*   the mix variable is used to speed up convergence (the iterative
*   process has a tendency to get hung up, calculating a value B
*   when using a value A and then calculating a value A when using
*   the value B)
    IF (ABS(DSIGM-DSIGMO).GE. 0.0001)THEN

    DSIGMO=(1-MIX)*DSIGMO+MIX*DSIGM

      GO TO 12

ELSE
        SCOUNT=0
        SIGM=SIGMO+DSIGM
        ENOUGH=0
        MIX=HOLD
END IF
```

```
      A=100
C=SIGO*(1/M)**(1/M)+1

DONE=.FALSE.

 61 IF (.NOT. DONE)THEN
    MIDPT=(A+C)/2

FA=SIGM*(1-VF)-SIGC+VF*A*EXP(-(GAGEL/LO)*(A/SIGO)**M)
FC=SIGM*(1-VF)-SIGC+VF*C*EXP(-(GAGEL/LO)*((C/SIGO)**M))
FMIDPT=SIGM*(1-VF)-SIGC+VF*MIDPT*EXP(-(GAGEL/LO)*
     &   ((MIDPT/SIGO)**M))

      IF ((FA*FC).LT.0)THEN
IF (ABS(FMIDPT).LE.0.0001)THEN
    DONE=.TRUE.
ELSE IF ((FA*FMIDPT).LT.0)THEN
    C=MIDPT
ELSE
    A=MIDPT
END IF
ELSE
    C=C+.1
END IF

GO TO 61
END IF

SIGF=MIDPT

PROBS= EXP(-(GAGEL/LO)*(SIGF/SIGO)**M)
DAMAGEF=FIBERO-FIBERO*PROBS

STRAIN =(SIGF-SIGFRES)/EF
PCOUNT=PCOUNT+1

T=T+TI

IF (PCOUNT.EQ.PNOW) THEN
PRINT 15, T,SIGM,SIGF,STRAIN,DAMAGEF
WRITE(100, 15) T,SIGM,SIGF,STRAIN,DAMAGEF
 15 FORMAT(1X,E14.7,T21,F11.7,T35,F11.3,T56,F8.6,T67,F5.1)

PCOUNT=0
END IF

*   as the strain curve becomes more linear the time increment is
*   changed in order to speed up the program
      IF (TI.LE.1000) THEN
IF (ABS(DSIGM1-DSIGM) .LE. ABS(0.001*DSIGM1)) THEN
    TI =TI*10
END IF
END IF

     DSIGM1=DSIGM
SIGMO=SIGM
SIGFO=SIGF

GO TO 12
END IF

END FILE (UNIT=100)
CLOSE (UNIT=100)
```

```
STOP
END
```

Weibull.for

The following is a listing of the Fortran program that was used to massage the Weibull data in this study.

```
PROGRAM WEIBULL

IMPLICIT NONE
REAL CHART(200,2),ROW,NUM,HOLD1,HOLD2,INCR,MEANON(200,3),MON
INTEGER N,K,FIRST,LAST,R,I,P
LOGICAL SORTED

        OPEN(UNIT=100, FILE='WEIBULL.OUT', STATUS='OLD')

PRINT 1
 1  FORMAT(1X,'ENTER THE NUMBER OF FIBERS INCLUDING SUSPENSIONS')
READ *, NUM
PRINT 2
 2  FORMAT(1X,'ENTER THE STRESS (MPa) AT FAILURE OR SUSPENSION',/,
     &  ' FOR A GIVEN FIBER FOLLOWED BY EITHER A "1" FOR FAILURE',/,
     &  ' OR A "0" FOR SUSPENSION. PRESS ENTER AFTER EACH.')


DO 10 N=1,NUM

READ *, CHART(N,1),CHART(N,2)

 10 CONTINUE

SORTED =.FALSE.
FIRST=1
LAST=NUM-1

 97 IF (.NOT. SORTED) THEN
    SORTED =.TRUE.

DO 99 K = FIRST,LAST
IF (CHART(K,1).GT.CHART(K+1,1))THEN
    HOLD1 = CHART(K,1)
    HOLD2 = CHART(K,2)
    CHART(K,1)=CHART(K+1,1)
    CHART(K,2)=CHART(K+1,2)
    CHART(K+1,1)=HOLD1
    CHART(K+1,2)=HOLD2
    SORTED =.FALSE.
END IF
 99 CONTINUE

LAST = LAST-1
GO TO 97
END IF

PRINT 56
 56 FORMAT(1X,'ORDERED DATA INCLUDING SUSPENSIONS',/)

DO 22 ROW =1,NUM

PRINT 20, CHART(ROW,1),CHART(ROW,2)
```

```
 20 FORMAT(1X,F6.1,1X,F6.1)

 22 CONTINUE


MON=0.0
INCR=1.0
P=0

DO 30 I=1,NUM
    IF (CHART(I,2).EQ. 0.0)THEN
        IF (CHART(I+1,2).EQ.1.0)THEN
        INCR = (NUM+1-MON)/(1+NUM-I)
        END IF
    ELSE
    P=P+1
    MEANON(P,1)=CHART(I,1)
    MEANON(P,2)=MON+INCR
    MEANON(P,3)=(MEANON(P,2)-(1.0-ALOG(2.0))-(2.0*ALOG(2.0)
     &      -1.0)*((MEANON(P,2)-1.0)/(NUM-1.0)))/NUM

    MON=MEANON(P,2)
    END IF
 30 CONTINUE

PRINT 72
        WRITE (100,72)
 72 FORMAT(1X,/,' FAILURES',5X,'MEAN ORDER #', 4X,'MEDIAN RANK',/)

DO 80 R = 1,P
            WRITE (100,19)MEANON(R,1),MEANON(R,2),MEANON(R,3)
    PRINT 19,MEANON(R,1),MEANON(R,2),MEANON(R,3)
 19 FORMAT(1X,F11.3,2X,F11.3,2X,F11.3)
 80 CONTINUE


        END FILE (UNIT=100)
        CLOSE (UNIT=100)

STOP
END
```

This page intentionally left blank

Reference: Smith, P.R., and Porter, W.J., "The Effect of Heat Treatment on the Tensile and Creep Behavior of 'Neat' Matrix Ti-22Al-23Nb," Journal of Materials Science, V.32, pp. 6215-6220.

THE EFFECT OF HEAT TREATMENT ON THE TENSILE AND CREEP BEHAVIOR OF 'NEAT' MATRIX Ti-22Al-23Nb

P.R. Smith[1] and W.J. Porter[2]

[1]Materials Directorate, Wright Laboratory, WPAFB, OH 45433
[2]University of Dayton Research Institute, Dayton, OH 45469

ABSTRACT

A study has been conducted to examine the effect of post-consolidation heat treatment on the longitudinal tensile and creep properties of an orthorhombic-based titanium aluminide, Ti-22Al-23Nb(a%), in neat matrix form. Heat treatment parameters were selected such that they would be consistent with future inclusion into the consolidation cycle for the fabrication of continuously-reinforced orthorhombic titanium matrix composites (O TMC's). The effects of heat treatment on microstructural evolution including type and morphology of the phase constituents was examined via scanning secondary electron microscopy and quantitative image analysis. Variations in microstructural features were correlated with resulting room temperature tensile properties including: ultimate tensile strength (UTS), yield strength (YS), total elongation (%El) and modulus (E), as well as isothermal creep response at 650°C/172MPa.

KEYWORDS

Orthorhombic; Ti_2AlNb; Ti-22Al-23Nb(a%); Titanium Aluminide; Creep; Titanium Matrix Composites

INTRODUCTION

Titanium aluminide composites based upon Ti_3Al (alpha-2, hexagonal DO_{19} structure) have been the subject of numerous investigations in recent years [1,2]. The majority of these studies have focused on a SiC-reinforced Ti-24Al-11Nb(at%) matrix alloy as representative of this class of materials. The deficiencies associated with this alloy as a matrix for compositing have been well documented, and include: poor fiber/matrix reactivity, modest low and elevated temperature tensile strength, low fracture resistance, poor creep response and high sensitivity to interstitial embrittlement [3,4]. Recent studies have begun to focus on an alternative titanium aluminide matrix alloy based upon the Ti_2AlNb (orthorhombic) phase [5]. Results from studies involving the orthorhombic composition, Ti-22Al-23Nb (at%) [6,7] seem to suggest that this matrix class offers the following benefits relative to Ti-24Al-11Nb: reduced fiber/matrix reactivity, improved fracture resistance, increased tensile strength and increased resistance to elevated temperature creep deformation. Unfortunately, the creep response obtained even for the Ti-22Al-23Nb alloy in its as-fabricated form, still falls short of the required 100 hours to 0.4% creep strain goal established for advanced propulsion applications currently under consideration. Therefore, the objective of the subject study is to utilize a post-consolidation heat treatment as a means to modify the matrix microstructure of the Ti-22Al-23Nb alloy, so as to improve its tensile and creep performance.

EXPERIMENTAL

The neat Ti-22Al-23Nb matrix material utilized in the subject study was produced using a conventional ingot to foil reduction approach. Atlantic Research/IMT fabricated the neat matrix material by hot isostatic pressing (HIP'ing) five foils laid up in the same orientation with respect to the foil rolling direction. Longitudinally oriented rectangular specimens measuring 10mm (w) x 100 mm (l) x 0.1mm (t) were machined from the neat panels using low speed diamond cutting. Specimens were wrapped in tantalum and heat treated in vacuum (10^{-6} torr) after flushing with high purity argon.

All heat treatments were applied after consolidation of the neat matrix. All of the solution heat treatment temperatures investigated were higher than the consolidation temperature. The beta transus of Ti-22Al-23Nb neat material was determined to be approximately 1100°C using the disappearing phase technique. A total of four solution heat treatment temperatures were examined: three sub-transus (1025°C, 1050°C and 1075°C) and one super-transus (1125°C). In addition, two cooling rates (direct from the solution heat treatment temperature to the aging temperature) were evaluated: 28°C/min and 2.8°C/min. The slower cooling rate was selected to be commensurate with those encountered during composite consolidation. Finally, three aging schemes were studied: 760°C/16hr, 815°C/8hr and 870°C/4hr. The baseline heat treatment selected for the study was: 1075°C/2hr + 28°C/min + 815°C/8hr/FC. The heat treatment conditions were selected such that they could be integrated into the composite fabrication cycle.

Microstructural analysis including determination of phase distribution, morphology and size was accomplished by secondary imaging of the as-fabricated and heat treated neat materials using a Leica 360FE scanning electron microscope (SEM) with a spatial resolution of 2nm at 25kV. Volume fraction determination of the constituent phases was accomplished using an image analysis program via a density slice function applied to stored digital backscattered SEM images. Microstructural characteristics were correlated with corresponding mechanical property levels.

Mechanical behavior examination included room temperature (23°C) tensile properties, as well as elevated temperature isothermal creep (650°C/172 MPa). A minimum of two tensile tests were conducted per heat treatment condition. Tensile tests were conducted under stroke-control at a constant crosshead speed of 0.0084 mm/s. Two creep tests were run per condition: 1) to 0.4% creep strain and 2) to at least 300 hours of creep life. All tests were conducted on a horizontal servo-hydraulic system. Details regarding the test system can be found elsewhere [8].

RESULTS AND DISCUSSION

Microstructure

The as-fabricated neat microstructure is displayed in Figure 1. It is seen to contain three ordered phases, consistent with previous results for orthorhombic alloys of similar chemistry containing high levels of oxygen [9]. The dark primary phase is alpha-2 (a_2) or Ti_3Al (hexagonal DO_{19} structure). This phase represents approximately 35v% of the structure, is fine-grained (5-10μm) and relatively equiaxed. The two phase mixture is a combination of orthorhombic "O" (light gray) platelets (~1μm x 5μm) in an ordered beta (B2) matrix (white). The "O" phase is based upon the Ti_2AlNb composition and represents a distortion of the a_2 structure by changing slightly the magnitude of the Burger's vectors of equivalent a and c+a dislocations in the a_2 structure. Note: Graves et al., [10] had previously determined that the beta phase was ordered for this composition. In addition, the perimeter of the primary a_2 phase is encased by a thin layer (~0.5μm) of "O" phase, however, it has not been determined if this is the same variant as the "O" platelets formed from the B2 phase. Previous studies [5] have indicated that the "O" phase can form as a transformation product from the B2 phase after solution treatment during aging, or by a phase separation reaction within the a_2 phase (i.e. Nb segregates to the

perimeter of the a_2). The corresponding volume fractions of the "O" and B2 phases were found to be 34v% and 31v%, respectively, with the B2 phase being continuous.

Figure 2 contains SEM micrographs showing the effects of solution heat treatment on microstructural response. In this instance the cooling rate and aging treatment conditions were held constant at 28°C/min and 815°C/8hr/FC, respectively. It can be seen that the primary a_2 phase content decreases continually up through the 1075°C solution treatment, after which it is totally dissolved as the beta transus is exceeded at 1125°C. An inverse relationship was found for the "O" phase content in that it is seen to be continually increasing with increasing solution treatment temperature. The B2 phase content appears to be relatively unchanged, and thus, the increase in "O" appears associated with a corresponding decrease in a_2. Previous studies [11] have indicated that the a_2 phase has poor ductility below ~600°C due to the anisotropy of slip associated with the DO_{19} structure. <a> Slip is seen to occur relatively easily on the prism plane, while <c+a/2> slip is very difficult. As a result, large incompatibility stresses can build up at a_2/ a_2 interfaces. As the solution heat treatment temperature increases, the number of a_2/ a_2 interfaces decrease, and the surrounding B2 phase acts to accommodate these stresses. In addition, Banerjee [11] has demonstrated that the amount of c+a slip available for the "O" phase is significantly more than for the a_2 phase.

Tensile Behavior

Table I contains the tensile properties corresponding to the solution heat treatment conditions previously discussed. In almost all instances the UTS, YS, %El and modulus have increased relative to the as-fabricated condition. The only exception to this being the ductility (elastic + plastic) after the 1125°C solution treatment. The 1050°C solution treatment appears to provide the best combination of UTS, %El and modulus. It would appear that the increase in tensile properties is associated with an increase in the volume fraction of the lenticular "O" phase and a corresponding decrease in the equiaxed a_2 phase.

properties, the effects of cooling rate and aging treatment were independently examined. First, the effect of reducing the cooling rate by a factor of 10 from 28°C/min to 2.8°C/min was evaluated by selecting a constant solution heat treatment of 1075°C/2hr and a constant aging treatment of 815°C/8hr/FC. The results are contrasted (Table II) with the as-fabricated condition, and the baseline heat treatment, wherein the later the cooling rate was 28°C/min. It can be noticed that the UTS and YS both drop with respect to both the as-fabricated and baseline conditions, that the ductility is similar to the baseline heat treatment, and the modulus is intermediate to the two conditions. The decrease in strength is most likely associated with increased lath size of the "O" platelets and hence the mean free slip length across individual platelets. Previous studies by Koss et al [12] suggest that strength is inversely proportional to this mean slip length. In addition, the volume fraction of the lower strength a_2 phase has increased.

In a similar fashion, the effect of aging treatment was evaluated by again holding the solution treatment condition (1075°C/2hr) and cooling rate (28°C/min) constant, while examining two additional (beyond the baseline 815°C/8hr) aging treatments of 760°C/16hr and 870°C/4hr. The results of the two aging treatments on tensile properties are also shown in Table II. The lower temperature age provides for a slight increase in UTS, and a relatively large increase in YS when compared to the as-fabricated and baseline heat treatment conditions. In addition, a significant decrease in ductility and an intermediate modulus value can be observed. These changes can be explained in terms of the resulting microstructure. It was noticed that the lower aging temperature resulted in a much finer O+B2 secondary structure, as well as, a semi-continuous layer of a_2. The finer scale of the secondary structure gives rise to increased strength levels due to Hall-Petch boundary strengthening, while in conjunction with the semi-continuous nature of the a_2, results in reduced ductility for reasons noted earlier. The higher temperature aging treatment results in UTS, YS and %EL values similar to that of the baseline heat treatment condition with an intermediate modulus value. It was observed that the resulting

microstructure had changed relative to the 815°C age, in that the volume fraction of a_2 increased, but it remained discontinuous. In addition, the "O" lath size had increased, while the B2 phase remained continuous. The fracture morphology of the 760°C age was dominated by transgranular cleavage of both the "O" platelets and a_2 grains with little evidence of ductile dimpling. Conversely, the material when aged at 870°C displayed a fracture exhibiting a significant amount of ductile dimpling produced by microvoid coalescence of primarily the B2 phase, while transgranular fracture of the a_2 and "O" phases was still observed.

The overall results of the effect of heat treatment on tensile behavior would seem to suggest that the Ti-22Al-23Nb alloy is heat treatable to improved combinations of UTS, YS, %El and modulus compared to the as-fabricated neat matrix. Furthermore, if a combination of good strength and ductility are required, a heat treatment incorporating a high sub-transus (btr-50°C) solution treatment followed by a rapid cool (28°C/min) and intermediate to high temperature (815-870°C) aging provide the best results.

Creep Behavior

The effects of solution heat treatment on isothermal creep behavior at 650°C/172 MPa are shown in Table III. As previously noted two tests per condition were run: 1) to 0.4% total creep strain and 2) to 300 hours of creep life. Therefore, the times shown to 0.4% creep strain are the average of two data points, while the 300 hour rupture criterion represents a singular value. Also shown are the minimum creep rates and the time spent in the primary transient creep regime as determined by the inflection of the creep curve to steady state conditions. It can be noticed as the solution heat treatment temperature increases, the time to 0.4% creep strain increases such that the super-transus treatment provides for an increase of >15x life extension compared to that for the as-fabricated condition. In addition, each of the solution treatments results in a rupture life which exceeds the 300 hour criterion. The super-transus excursion also results in approximately an order of magnitude increase in the minimum creep rate. Finally, all of the solution treatments result in a significant extension of the primary transient creep regime.

In an effort to understand the effect of microstructure on damage accumulation during creep, a neat sample which had been solution treated and direct aged (1025°C/2hr+28°C/min + 815°C/8hr/FC) was crept at 650°C/172MPa to a total creep strain of ~2.0%. The corresponding microstructure is shown in Figure 3. It can be noticed (Fig 3a) that the primary deformation mode appears to be by crack initiation at the interface between the "O" phase (at the rim of the primary a_2) and adjacent phase(s). Furthermore, there is little evidence of crack initiation at the lath "O"/B2 interfaces (Fig 3b). Therefore, one might deduce that if the volume fraction of the primary equiaxed a_2 phase was decreased (and hence the volume fraction of the rim "O" phase), and correspondingly, the volume fraction of the lath "O" phase was increased, that the creep resistance would increase. Figure 4 contains a plot of the time required to reach a creep strain of 0.4% versus the volume fraction of primary a_2 present in the microstructure. It is seen that as the volume fraction of primary a_2 decreases, the time to reach 0.4% creep strain steadily increases. Conversely, Figure 5 illustrates the effect of lath "O" phase content on time required to reach 0.4% creep strain. Here it is seen, that as the volume fraction of lath "O" phase increases, so does the creep resistance. It should be noted that in both instances, the volume fraction of B2 remains essentially constant, such that the increase in lath "O" is proportional to the decrease in equiaxed a_2. There are at least two possible explanations for this behavior. First, it has been previously demonstrated for a_2 + b alloys, Ti-25Al-10Nb-3V-1Mo and Ti-24Al-11Nb, that lath structures are stronger in creep than equiaxed structures [13-15]. Furthermore, Banerjee et al [16] have demonstrated that the "O" phase is substantially stronger in creep resistance than the a_2 phase.

The effect of aging treatment and cooling rate on the creep response of neat Ti-22Al-23Nb is depicted in Table IV. Comparisons are made against the as-fabricated condition and the baseline heat treatment condition (1075°C/2hr + 28°C/min + 815°C/8hr/FC). It can be seen

that all of the heat treatments resulted in improved creep resistance when compared to the as-fabricated condition. This is most likely the result of increased levels of "O" phase and lath microstructure and corresponding decreases in equiaxed a_2. It can be noticed that the effect of aging treatment on creep response was rather minimal. Both the high and low temperature aging temperatures resulted in very similar times to 0.4% creep strain, steady-state creep rates, and primary transient creep lives. This was true despite that fact that the volume fractions of the various phases were changing, as well as, the scale of the lath microstructure. This observation can be explained in terms of competing effects. The low temperature aging treatment resulted in a much finer lath size which would tend to favor increased creep rates. However, the same aging treatment produced decreased levels of a_2 with corresponding increases in lath "O", both of which tend to result in decreased creep rates. Similarly for the high temperature age, the scale of the lath structure has increased, while the volume fraction of a_2 increases and the "O" phase decreases. The net result is that the creep performance remains essentially unchanged when compared to the baseline aging condition. The effect of cooling rate was more dramatic. It is noticed that reducing the cooling rate by an order of magnitude to 2.8°C/min results in a two-fold decrease in the time to 0.4% creep strain, although the steady state creep rate and primary transient creep life remain essentially unchanged. This result can be rationalized by noting that the slower cooling rate produced a lath structure similar in width to that observed for the faster cooling rate, but reduced in length, while the relative volume fractions of a_2 increased and "O" decreased.

CONCLUDING REMARKS

This study has demonstrated the effects of post consolidation heat treatments on the longitudinal tensile and creep performance of a neat "orthorhombic" titanium aluminide composition, Ti-22Al-23Nb(a%). The heat treatments were chosen such that they might eventually be incorporated into the consolidation cycle for continuous fiber reinforced composites. It was found that this composition, much like conventional a+b titanium alloys can be heat treated to improved combinations of tensile and creep performance.

All of the sub-transus heat treatments resulted in an increase in UTS, YS, %El and modulus with respect to the as-fabricated condition, with the exception of the slower cooling rate which had slightly inferior UTS and YS values. The best balance of properties was produced by the b_{tr}-50°C (i.e. 1050°C) solution treatment. These increases were rationalized in terms of increases in lath "O" phase content, decreases in equiaxed a_2, and refinement in microstructural features. A super-transus solution treatment resulted in significant improvements in UTS, YS and modulus, again compared to the as-fabricated condition, but with reduced ductility as a result of aligned a_2 or "O" platelet formation at or near prior beta grain boundaries. The isothermal creep performance (650°C/172 MPa) provided by each of the heat treatments was also improved compared to the as-fabricated condition. The effect of solution treatment on time to reach 0.4% creep strain was correlated with volume fractions of equiaxed a_2 and lath "O". It was found that increases in lath "O" and associated decreases in equiaxed a_2, increased creep performance. The best creep results were afforded by the super-transus solution treatment, b_{tr}+25°C (i.e. 1125°C), which provided for a 15x life extension to 0.4% creep strain. The effect of aging temperature on creep was found to be minimal over the range of temperatures examined (760-870°C). This was rationalized based upon competing effects of relative volume fractions of phases and "O" lath size. The effect of decreasing the cooling rate (between solution treatment and aging temperatures) by an order of magnitude, reduced the time to 0.4% creep strain by a factor of ~2, as a result of increased equiaxed a_2 and decreased lath "O" volume fractions. While all of the heat treatments surpassed a 300 hour rupture criterion, none exceeded the 100 hour to 0.4% creep strain requirement (although the super-transus solution treatment resulted in >87 hours). This would suggest that alloy modification in combination with heat treatment may be required. In addition, the effects of the subject heat treatments on transverse properties, as well as, cyclic response are the focus of continuing

studies. Finally, optimum heat treatment(s) must be applied to the fiber reinforced composite and evaluated for their effect on composite mechanical performance.

ACKNOWLEDGMENTS

The authors would like to gratefully acknowledge the contributions of Mr. Dan Knapke and Ms. Debra Garner of University of Dayton Research Institute for mechanical testing performed under AF Contract #F33615-91-C-5606, as well as, Mr. Mark Dodd for heat treatment and Mr. Eric Fletcher for specimen preparation, all of Universal Energy Systems working under AF Contract #33615-93-C-5663.

REFERENCES

1. LARSEN, J.M., REVELOS, W.C. and GAMBONE, M.L., 'in Intermetallic Matrix Composites II, edited by D.B. Miracle, D.L. Anton and J.A. Graves (Materials Research Society, Pittsburgh, PA, 1992) p. 3.
2. MACKAY, R.A., BRINDLEY, P.K. and FROES, F.H., *JOM* **43**, No. 5 (1991) p. 23.
3. SMITH, P.R. and REVELOS, W.C., in Fatigue 90, edited by H. Kitagawa and T. Tanaka (MCE Publications LTD, Birmingham, UK, 1990) p. 1711.
4. REVELOS, W.C. and SMITH, P.R., *Metall. Trans. A* **23** (1992) 587.
5. BANERJEE, D., GOGIA, A.K., NANDY, T.K. and JOSHI, V.A, *Acta Metall* **36**, (1988) 871.
6. SMITH, P.R., GRAVES, J.A. and RHODES, C.G., in Intermetallic Matrix Composites II, edited by D.B. Miracle, D.L. Anton and J.A. Graves (Materials Research Society, Pittsburgh, PA, 1992) p. 43.
7. SMITH, P.R., GRAVES, J.A. and RHODES, C.G., *Metall. Trans. A* **25** (1994) 1267.
8. HARTMAN, G.A. and RUSS, S.M., in Metal Matrix Composites: Testing, Analysis and Failure Modes, edited by W.S. Johnson (ASTM, Philadelphia, PA, 1989) p. 43.
9. RHODES, C.G., GRAVES, J.A., SMITH, P.R. and JAMES, M.R., in Structural Intermetallics, edited by R. Darolia et al. (TMS-AIME, Warrendale, PA, 1993) p. 45.
10. GRAVES, J.A., SMITH, P.R. and RHODES, C.G,. in Intermetallic Matrix Composites II, edited by D.B. Miracle, D.L. Anton and J.A. Graves (Materials Research Society, Pittsburgh, PA, 1992) p. 31.
11. KOSS, D.A., BANERJEE, D., LUKASAK, D.A. and GOGIA, A.K. in High Temperature Titanium Aluminides and Intermetallics, edited by S.H. Whang et al., (TMS-AIME, Warrendale, PA, 1990) p. 175.
12. PANK, D.R. et al., 'Titanium Aluminide Composites', Report WL-TR-91-4020, Materials Directorate, Wright Laboratory, Wright-Patterson AFB, 1991.
13. ALBERT, D.E. and THOMPSON, A.W., *Metall. Trans. A* **23** (1992) 3035.
14. CHO, W., THOMPSON, A.W. and WILLIAMS, J.C., *Metall. Trans. A* **21** (1990) 641.
15. HAYES, R.W., *Acta. Metall.* **39** (1991) 569.
16. BANERJEE, D., et al., in Structural Intermetallics, edited by R. Darolia, et al (TMS-AIME, Warrendale, PA, 1993) 19.

Table I. Effect of Solution Heat Treatment Temperature on Tensile Properties

Condition	UTS(MPa)	YS(MPa)	%El	Modulus(GPa)
As-Fab'd	972	805	8.4	105
1025°C/2hr*	1096	848	9.0	119
1050°C/2hr*	1111	836	14.8	121
1075°C/2hr*	1059	810	11.5	120
1125°C/2hr	1053	926	4.0	135

*Solution Heat Treatment + 28°C/min + 815°C/8hr/FC

Table II. Effect of Cooling Rate and Aging Treatment on Tensile Behavior

Condition	UTS(MPa)	YS(MPa)	%El	Modulus(GPa)
As-Fab'd	972	805	8.4	105
Baseline HT*	1059	810	11.5	120
2.8°C/min**	946	725	11.2	114
760°C/16hr/FC#	1098	931	5.5	109
870°C/4hr/FC#	1062	810	12.3	113

* 1075°C/2hr+28°C/min to 815°C/8hr/FC
**Sol'n HT = 1075°C/2hr; Age = 815°C/8hr/FC
Sol'n HT = 1075°C/2hr; Cooling Rate = 28°C/min

Table III. Effect of Solution Treatment Temperature on 650°C/172MPa Isothermal Creep

Condition	Time (hr)			300 hr	S.S. Creep	Primary Creep
0.2%	0.4%	1.0%		Rate	(hrs)	
As-fab'd	1.4	5.4	28	No(147hrs)	3.1E-08	57
1025°C	3.0	12.4	63	Yes	1.6E-08	180
1050°C	8.7	31.1	179	Yes	1.2E-08	200
1075°C	8.5	41.0	290	Yes	1.2E-08	220
1125°C	22.5	87.5	*	Yes	5.9E-09	225

*Did not reach 1.0% creep strain before 300hr criterion was met

Table IV. Effect of Aging Treatment and Cooling Rate on 650°C/172MPa Isothermal Creep

Condition	Time (hr)			300 hr	S.S. Creep	Primary
0.2%	0.4%	1.0%	Rupture Criterion?	Rate	Life (hr)	
As-fab'd	1.4	5.4	28	No(147hrs)	3.1E-08	57
Baseline	8.5	41.0	290	Yes	1.2E-08	220
Lo Temp Age[1]	9.4	36.8	214	Yes	6.8E-09	230
Hi Temp Age[2]	6.9	36.8	226	Yes	8.2E-09	240
Slo Cool Rate[3]	3.8	19.6	129	Yes	9.0E-09	230

[1]1075°C/2hr+28°C/min+760°C/16hr/FC
[2]1075°C/2hr+28°C/min+870°C/4hr/FC
[3]1075°C/2hr+2.8°C/min+815°C/8hr/FC

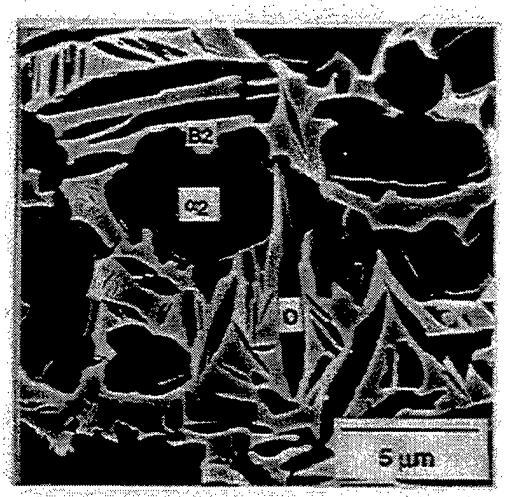


Figure 1. As-fabricated neat microstructure containing three ordered phases: O, B2 and a_2.

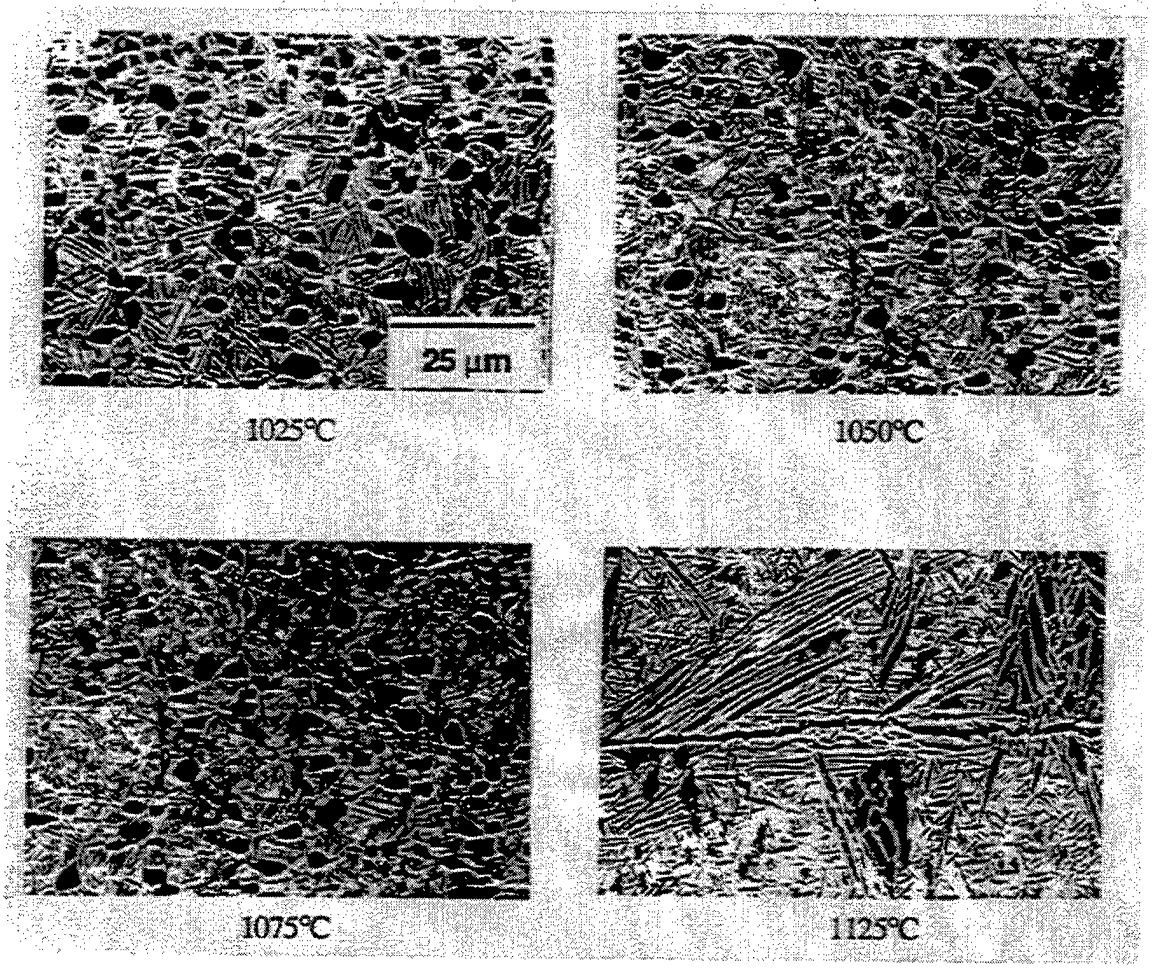


Figure 2. Effect of solution heat treatment temperature on microstructure (cooling rate = 28°C/min; age = 815°C/8hr/FC).

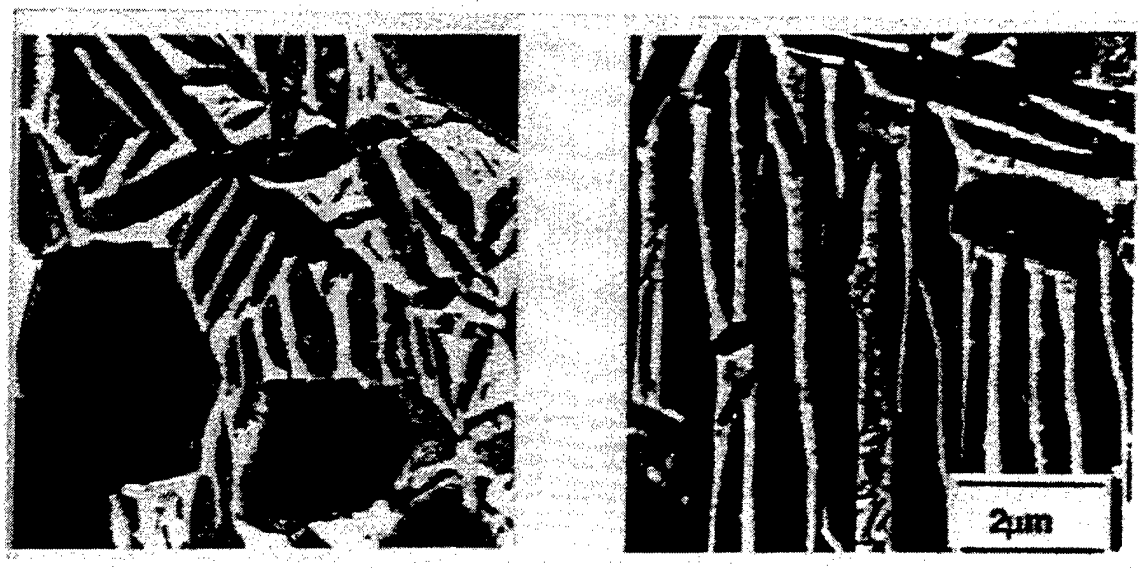


Figure 3. Creep damage accumulation at 650°C/172MPa to 2.0% creep strain indicating (a) crack initiation at interface of rim "O" and adjacent phases and (b) no cracking at lath "O"/B2 interfaces.

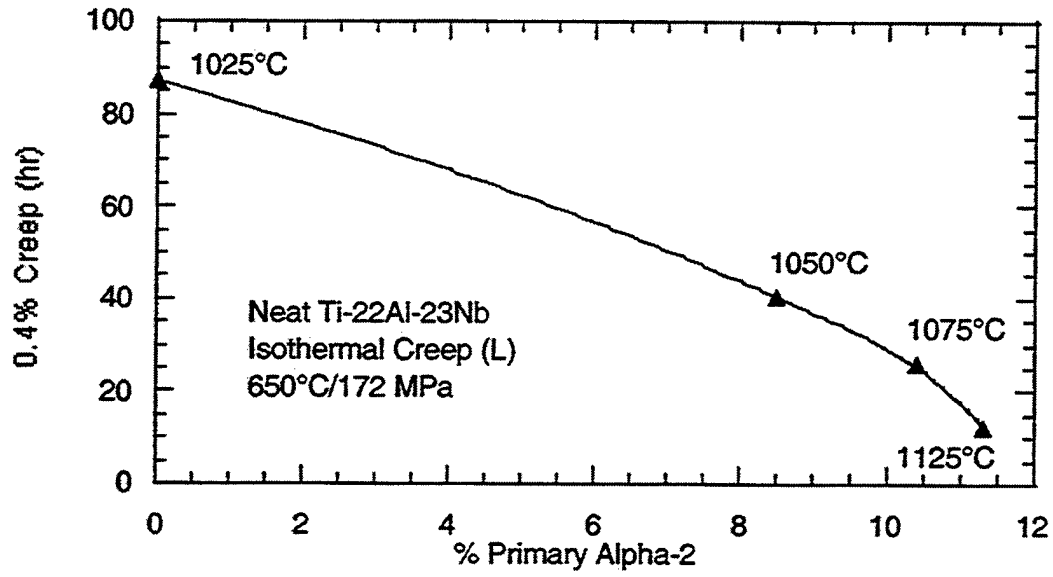


Figure 4. Effect of volume fraction of primary a_2 phase on time required to reach 0.4% creep strain at 650°C/172MPa.

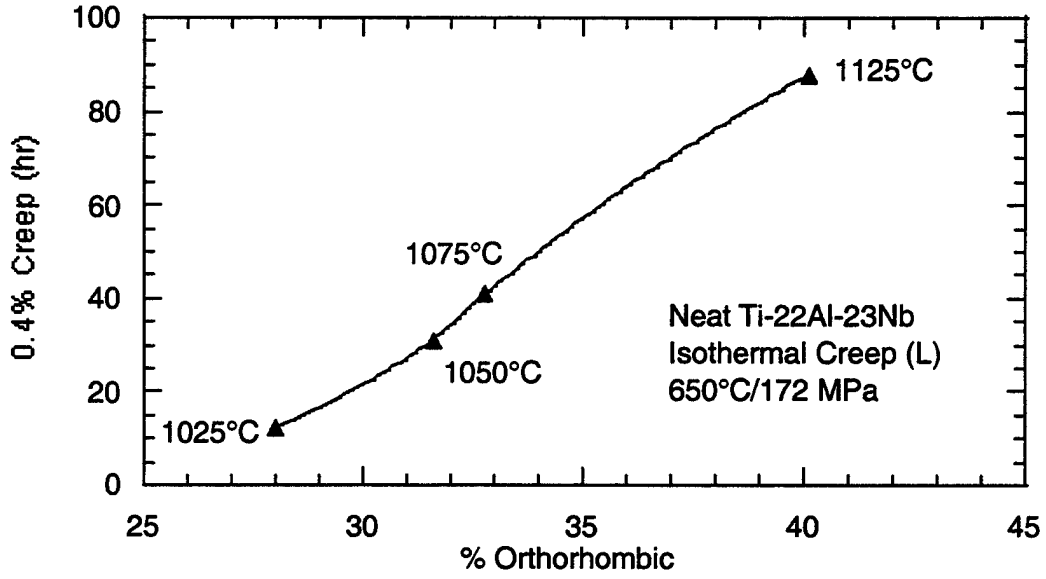


Figure 5. Effect of volume fraction of "O" phase on time required to reach 0.4% creep strain at 650°C/172MPa.

This page intentionally left blank

Submitted for publication to Journal of Materials Science, April 1997.

HEAT TREATMENT EFFECTS ON SiC FIBER

P.R. Smith[1], M.L. Gambone[1], D.S. Williams[2] and D.I. Garner[3]

[1]Materials Directorate, Wright Laboratory, WL/MLLM, WPAFB, OH 45433
[2] Southwestern Ohio Council for Higher Education (SOCHE), Dayton, OH 45420
[3] University of Dayton Research Institute, Dayton, OH 45469

ABSTRACT

The Wright Laboratory Materials Directorate at Wright-Patterson AFB has been spearheading the development and evaluation of a new class of metal matrix composites based upon continuous SiC fiber reinforcement of orthorhombic phase containing titanium aluminide matrices. These composites (O TMCs) will be necessarily subjected to thermal exposures during primary and secondary component processing, and possibly also to optimize matrix-dominated mechanical performance through heat treatment. It is imperative that such thermal excursions do not degrade the SiC fiber reinforcement, hence compromising resulting composite properties. As such, a study has been undertaken to examine the effects of heat treatment on the room temperature tensile strength of continuous SiC fibers. The fibers examined in the subject investigation included: Trimarc 1®, SCS-6, Ultra SCS and an experimental large diameter version of Ultra SCS. The fibers were subjected to two heat treatment conditions being below (subtransus) and above (supertransus) the beta solvus temperature of the orthorhombic matrix alloy utilized for this study, Ti-22Al-23Nb (at%). The fibers were evaluated for ambient temperature tensile strength in the following conditions: 1) as-received: 2) heat treated in vacuum; and 3) consolidated into Ti-22Al-23Nb, heat treated in vacuum, and chemically extracted. Fiber microstructure and fracture analysis was accomplished via secondary scanning electron microscopy (SEM). In addition, chemical reactions between fiber core and the SiC, and between the SiC fiber and the Ti-22Al-23Nb matrix, were also studied using SEM analysis.

INTRODUCTION

Since 1992, the Materials Directorate has been investigating a class of titanium aluminide matrix composites (i.e. O TMCs) based upon the ordered orthorhombic phase, Ti_2AlNb. These orthorhombic titanium matrices have as their main attributes: improved chemical compatibility with SiC reinforcing fibers, increased room and elevated temperature tensile strength, improved fracture resistance and enhanced elevated temperature creep performance when compared to their alpha-2 based predecessors (1-3). However, upon fabrication into structural components, it is expected that these O TMCs will undergo multiple thermal exposures during primary and secondary processing. In addition, it is possible that these composite matrices may require heat treatment in order to maximize matrix-dominated mechanical performance. It is imperative that the thermal excursions associated with either heat treatment and/or the component processing cycles do not degrade the load carrying capabilities of the reinforcing SiC fibers. The objective of the subject study is to examine the effect of thermal treatments on the residual room temperature tensile strength of a variety of continuous SiC fibers being considered as potential reinforcements for O TMCs.

EXPERIMENTAL PROCEDURE

Four continuous SiC fibers were selected for the subject study: Trimarc 1®, SCS-6, Ultra SCS and large diameter Ultra SCS. The first of these fibers, Trimarc 1® is a ~127μm diameter fiber deposited by chemical vapor deposition (CVD) onto a 12.5μm tungsten core and was manufactured by Amercom Inc. (Chatsworth, CA). The remaining three fibers were all manufactured by Textron Specialty Materials (Lowell, MA) using CVD processing. The SCS-6 fiber is ~142μm in diameter and is produced via single-stage CVD deposition onto a 33μm diameter carbon monfilament (CMF). The Ultra SCS fiber was developed as a higher strength alternative to the SCS-6 fiber. It is roughly the same diameter as the SCS-6 fiber (~140μm) and it too is deposited in a single stage CVD process upon a 33μm CMF. The last fiber, the large diameter Ultra SCS was at the time of this study in the preliminary stages of experimental development. This fiber is on the order of ~184μm in diameter and has been CVD deposited again in a single stage reactor on a 42μm CMF. Microstructural details for each fiber are provided later.

The matrix selected for evaluation is the orthorhombic composition, Ti-22Al-23Nb (at%) which the Materials Directorate has been examining as a baseline representative of this class of titanium aluminides. This alloy was obtained in thin foil (~125μm) form from Texas Instruments via conventional ingot reduction practices incorporating as a final step, unidirectional cold rolling. The details of the ingot to foil processing can be found elsewhere (4). These cold rolled foils were stacked in an alternating fashion with SiC fiber mats and hot isostatically press consolidated into four-ply, unidirectional composites at temperatures well below the beta solvus of the Ti-22Al-23Nb foil, which was determined to be ~1125°C. Recent studies (5) on "neat" (i.e. unreinforced consolidated foils) Ti-22Al-23Nb had indicated that this alloy could be heat treated to increased levels of room temperature strength, creep resistance and in some cases improved room temperature ductility. These heat treatments were modified in the present study to account for increases in the beta solvus temperature due to carbon dissolution from the SiC fiber during composite fabrication (6). The two heat treatments selected include solutionizing just below the beta solvus (subtransus) and just above the beta solvus (supertransus) of the Ti-22Al-23Nb matrix, followed by slow cooling directly to an isothermal aging condition. The subtransus heat treatment had been shown to provide the best balance of "neat" mechanical properties, while the supertransus treatment yielded the best high temperature creep performance. It should be noted that the heat treatments were selected to be compatible with (and possibly incorporated into) the composite/component fabrication cycle. The fibers were encapsulated in quartz glass tubing, backfilled with high purity helium (99.9999%), and heat treated in vacuum (~10E-06 torr). The specific heat treatments utilized were:

1085°C/2hr + cool @ 2.8°C/m to 815°C/8hr/FC (subtransus)
1160°C/2hr + cool @ 2.8°C/m to 815°C/8hr/FC (supertransus)

Each type of SiC fiber examined was produced in a single reactor run. In order to assess the effects of fiber/matrix chemical interaction during composite consolidation and subsequent heat treatment, small specimens (12.5 mm x 510 mm) were cut from SiC/Ti-22Al-23Nb panels and were subjected to heat treatment. Fibers from these composite samples were chemically extracted using 10% bromine in methanol saturated with tartaric acid. This solution had previously been shown to be successful in extracting SiC fibers from a titanium matrix without any change in tensile strength distribution (7).

The four types of SiC fibers were tensile tested at room temperature using 25 mm gage section at a constant cross-head speed of 20mm/min. The tests were conducted on a compact horizontal test machine which was developed by the University of Dayton Research Institute under USAF Contract No. F33615-94-C-5200 at Wright-Patterson Air Force Base, Ohio. Closed-loop computer control was used to acquire data during testing, as well as to control test conditions. Displacement was measured with a commercial scanning laser system by using

platinum wire "flags" that were hung 15-20 mm apart in the gage length. The load was measured using a 100 kg load cell, while the fibers were held in place by a compressive force applied through the use of aluminum foil-lined grips. The aluminum foil was used to prevent damage to the fiber surface during testing. This rigid grip system also acted to minimize bending stresses during testing. In order to obtain statistically meaningful results, approximately 50 tests were run per condition for each fiber type. (Note: only ~25 tests/condition could be run on the large diameter Ultra SCS due to limited fiber availability). Tests were conducted on each fiber type under the five aforementioned conditions (i.e. as-received, 1085°C Solution HT, 1085°C Solution HT + Extracted, 1160°C Solution HT and 1160°C Solution HT + Extracted). Fiber tensile strength was calculated from the maximum measured load and the cross-sectional area determined from a mean fiber diameter assuming that the fibers were cylindrical. The mean fiber diameter for each fiber type and condition was measured using a non-contact digital micrometer at a magnification of 200x. Only failures which occurred in the gage length were used in the data analysis.

When possible, one or both of the fracture surfaces were preserved and inventoried for examination by scanning electron microscopy (SEM) using secondary electron imaging to assess fracture type and initiation site. However, in some instances the fibers would shatter, particularly for the high strength tests, and in these instances, no information regarding the origin of fracture could be obtained. (Fracture site identification was considerably easier for the weaker Trimarc 1® fiber, than for the higher strength SCS-6, Ultra SCS and large diameter Ultra SCS fibers. As such, correspondingly more fractographic analysis is provided for the Trimarc 1® fiber during the discussion which follows.)

Transverse cross-sections for each of the fibers were mounted, polished, etched and examined by SEM to characterize their microstructural features and assess their thermal stability. Sample preparation for the fibers included: etching in boiling $NaOH:KNO_3$ for 2 minutes, washing in boiling water for 5 minutes, and immersing in ethanol. In addition, the Ti-22Al-23Nb matrix microstructure and fiber/matrix interface were also examined for effects of heat treatment using backscattered electron imaging (BSE) SEM.

RESULTS AND DISCUSSION

Matrix Characterization

Figure 1 displays the microstructure of the Ti-22Al-23Nb matrix in the as-consolidated and as-consolidated + heat treated conditions. The as-consolidated microstructure (Figure 1a) consists of three ordered phases (8): alpha-2 (dark equiaxed); orthorhombic (gray lenticular); and beta/B2 (light). The microstructure is in a metastable state in that the orthorhombic phase is very fine and has not fully precipitated from the B2. The relatively high volume fraction of the alpha-2 is due in part to the high levels of oxygen (~1700 wppm) in the starting foil (9), and possibly due to carbon dissolution from the SiC fiber into the matrix during consolidation. The subtranus heat treatment also results in a three phase microstructure (Figure 1b). In this case the orthorhombic phase has more fully precipitated from the B2 and has undergone grain growth. As previously noted, this microstructure resulted in the best balance of mechanical properties for neat Ti-22Al-23Nb. The supertransus heat treatment produces a fully transformed two-phase microstructure (Figure 1c). The large lenticular gray phase is orthorhombic, while the light continuous phase is B2. This microstructure resulted in the best creep resistance for neat matrix studies in Ti-22Al-23Nb.

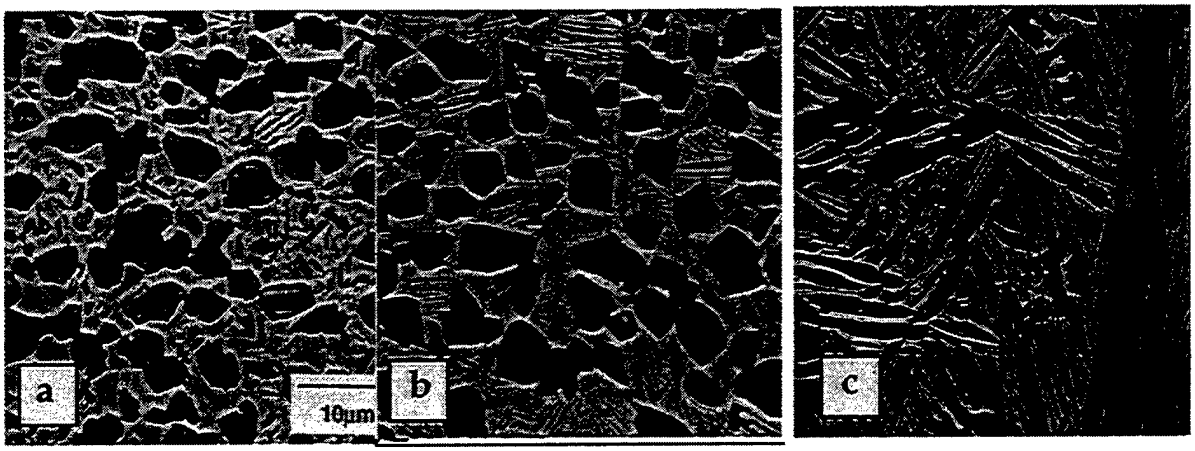


Figure 1. Ti-22Al-23Nb Neat Matrix in: a) As-Consolidated; b) 1085°C Solution HT and c) 1160°C Solution HT Conditions

Trimarc 1®

Fiber Structure

This ~127μm fiber was produced by CVD processing in a multi-stage "flexible" reactor at Amercom Inc. The salient features of the fiber architecture include a 12.5μm tungsten core upon which stoichiometric b SiC is deposited. The SiC grows in a columnar fashion and is protected at the surface by the application of a triplex coating system (~ 4 μm), which is applied in-line at the end of the CVD process. This coating consists of three alternating layers of "hard" and "soft" carbon with individual layer thicknesses ranging from 0.5-2.0μm. The degree of hardness associated with each of these layers has been suggested to be dictated by the level of and size of the dopent SiC particles. Details concerning the development and production of the Trimarc 1® fiber can be found elsewhere (10).

Tensile Properties, Microstructure and Fracture Analysis

As-Received

Figure 2a shows an SEM image of the b SiC portion of the as-received Trimarc 1® fiber wherein it can be seen that the microstructure grows radially outward in a columnar fashion from the tungsten core. Fry (10) has shown that during fiber production, typically {111} close-packed planes of the cubic b SiC orient normal to the radial direction. An as-received fracture surface (Figure 3a) shows that a chemical reaction takes place between the tungsten core and the SiC during fiber manufacturing, forming a layer of tungsten carbide (~ 0.38μm). This outer portion of this reaction layer also contains Kirkendall porosity formed as the result of the diffusion of carbon into and reaction with the tungsten core. Previous studies (11) have indicated this porosity within the tungsten carbide layer acts as a source for crack initiation and fiber strength degradation. In addition to this internal reaction zone, a chemical reaction also takes place at the SiC fiber/matrix interface (~ 0.51μm) as shown in Figure 4a, upon consolidation of the Trimarc 1® fiber into the Ti-22Al-23Nb matrix. The fiber/matrix reaction products have previously been shown to consist primarily of a complex combination of titanium and aluminum carbides, as well as, titanium silicides (12,13). These reaction products are extremely brittle in nature and are prone to cracking when loaded either by internally generated residual stresses or by externally applied forces leading to composite mechanical property degradation. It is therefore desirable to limit the size of this reaction layer from the standpoint of composite mechanical performance. The room temperature tensile strength of the as-received fiber is depicted in Figure 5 as a function of probability of survival at a given stress level. It can be seen that the distribution is very tight with 98% of failures at strengths between 2800-3200 MPa. The mean strength for the as-received condition is on the order of 3080 MPa

with most failures initiating in or near the tungsten core region of the fiber (Figure 6a). Indeed, >86% of the failures which could be identified initiated in or near the fiber core. There were a few failures (13.5%) identified near the mid-radius of the fiber (Figure 6b), however, the failure strengths associated with this location (3053 MPa) were very similar to those attributed to core failure (3050 MPa).

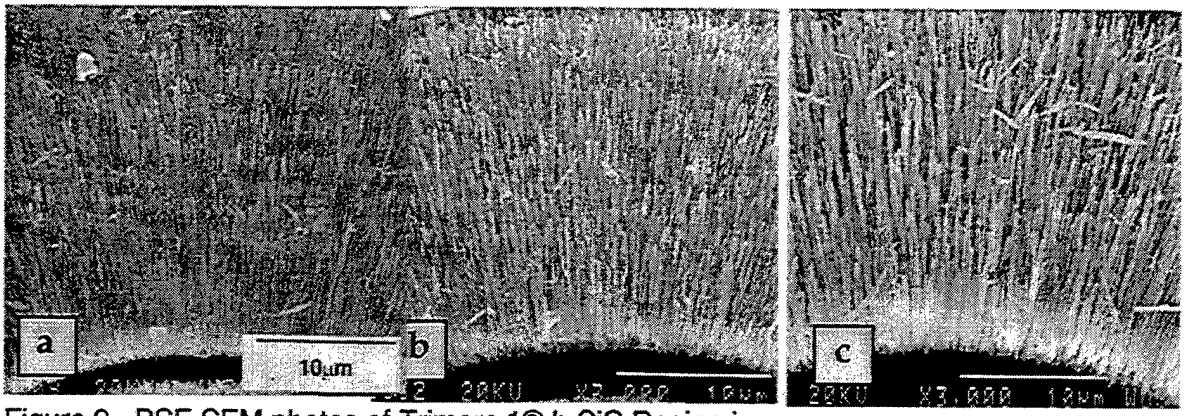
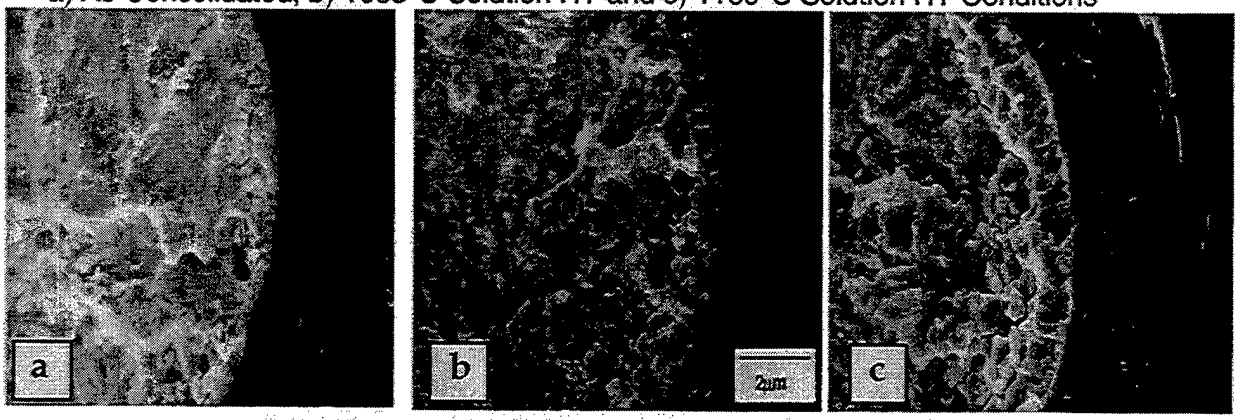


Figure 2. BSE SEM photos of Trimarc 1® b SiC Region in:
a) As-Consolidated; b) 1085°C Solution HT and c) 1160°C Solution HT Conditions



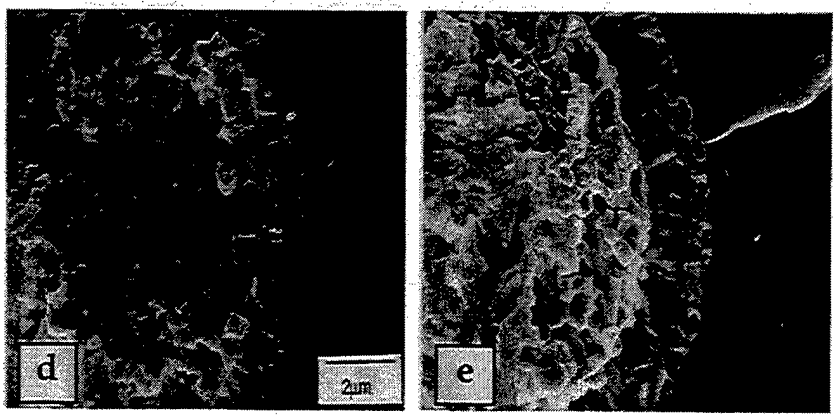


Figure 3. Tungsten Core/SiC Reaction in Trimarc 1® Fiber for a) As-Received; b) 1085°C Solution HT; c) 1085°C Solution HT + Extracted; d) 1160°C Solution HT and e) 1160°C Solution HT + Extracted Conditions

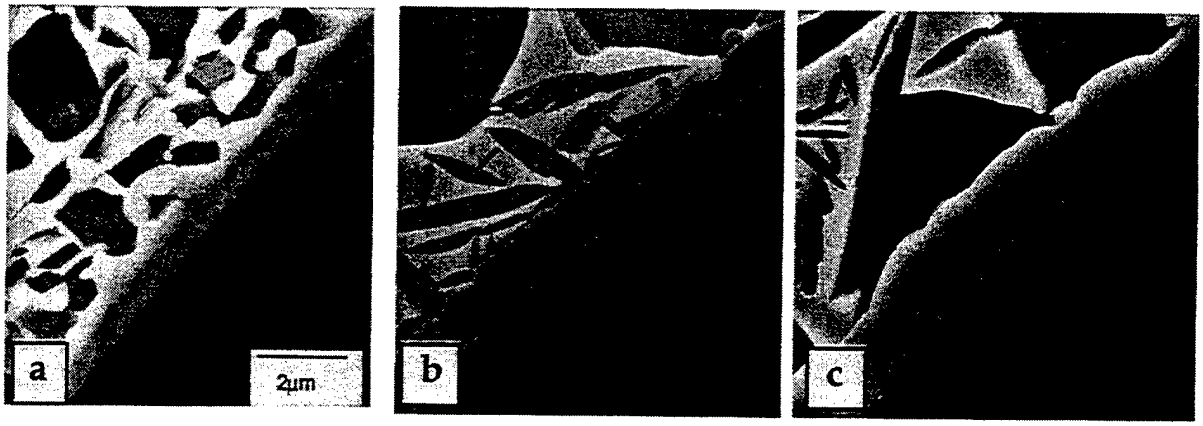


Figure 4. Trimarc 1®/Ti-22Al-23Nb Reaction for: a) As-Consolidated; b) As -Consolidated + 1085°C Solution HT and c) As-Consolidated + 1160°C Solution HT Conditions

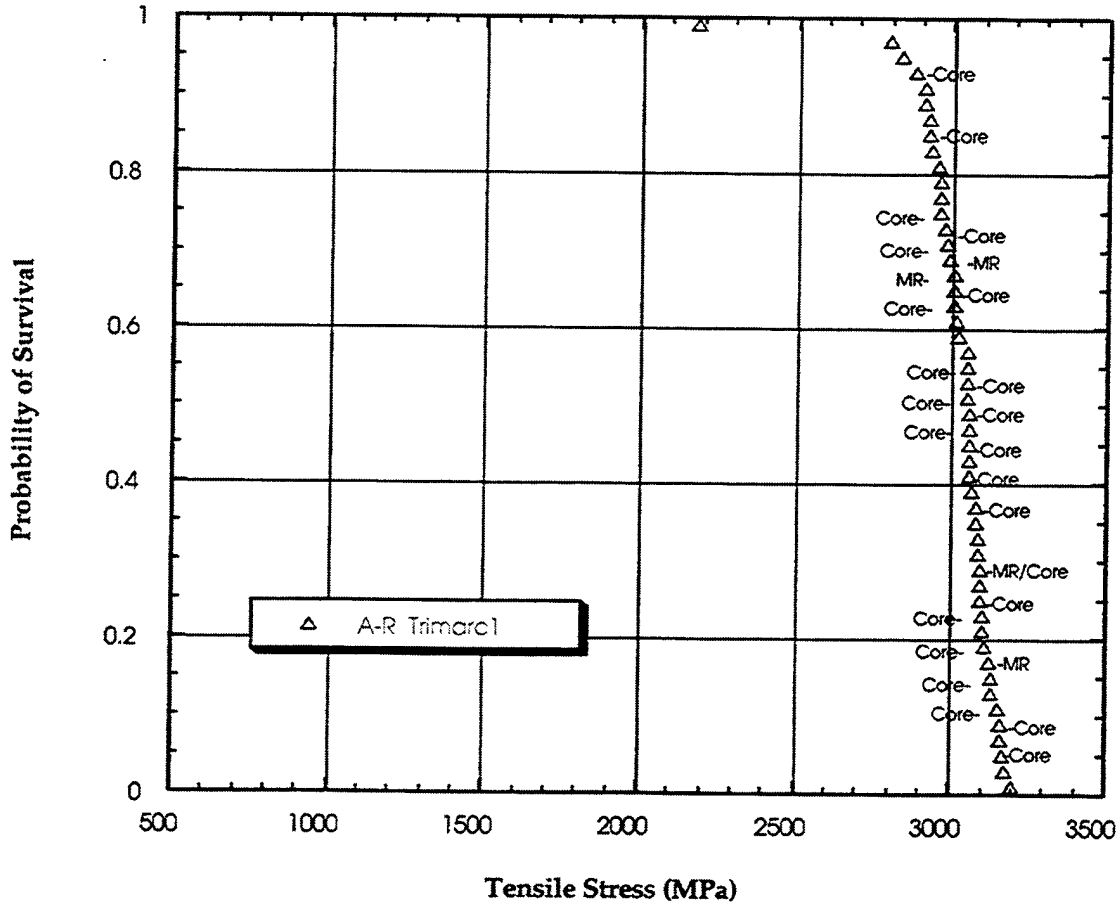


Figure 5. As-Received Trimarc 1® Strength

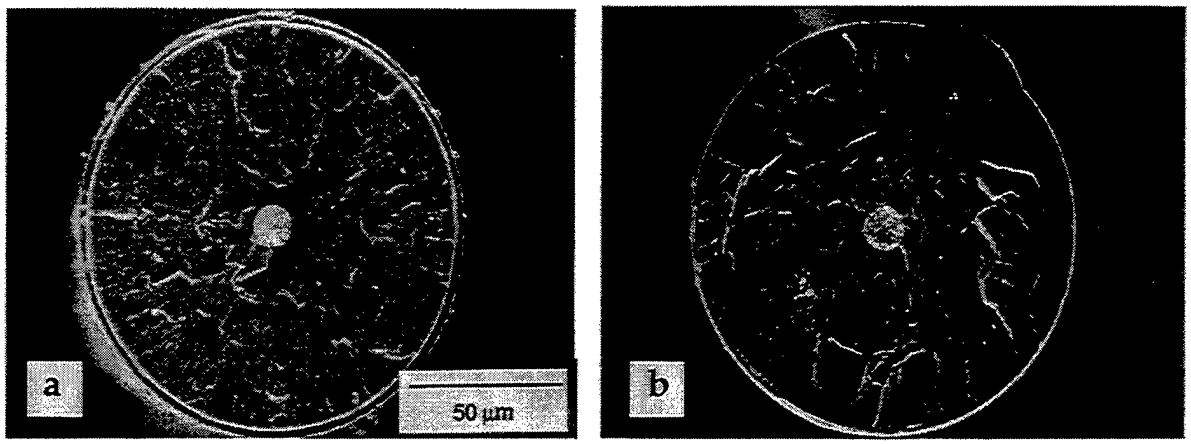


Figure 6. Secondary SEM Images of Trimarc 1® Fracture Surface for As-Received Condition Illustrating a) Core Initiation and b) Mid-Radius Initiation

Subtransus Heat Treated

The tensile strength for the 1085°C solution HT condition for Trimarc 1® fiber is shown in Figure 7. The mean strength has dropped relative to the as-received condition (to 2766 MPa), with the percentage of core failures actually increasing to >96%. The width of the b SiC columnar grain structure has increased slightly (Figure 2b), suggesting that the structure of the fiber may not be totally stable at this heat treatment temperature (i.e. 1085°C). Figure 3b shows that the reaction between the tungsten core and SiC has essentially doubled (~0.74μm) compared to the as-received condition. There was only one failure identified with the surface of the fiber and its strength value (2707 MPa) was very similar to that observed for core initiations (2741 MPa). Since the primary failure site appears to be at or near the tungsten core, it can be concluded that increased reaction at the core/SiC interface is the controlling factor in the observed strength reduction.

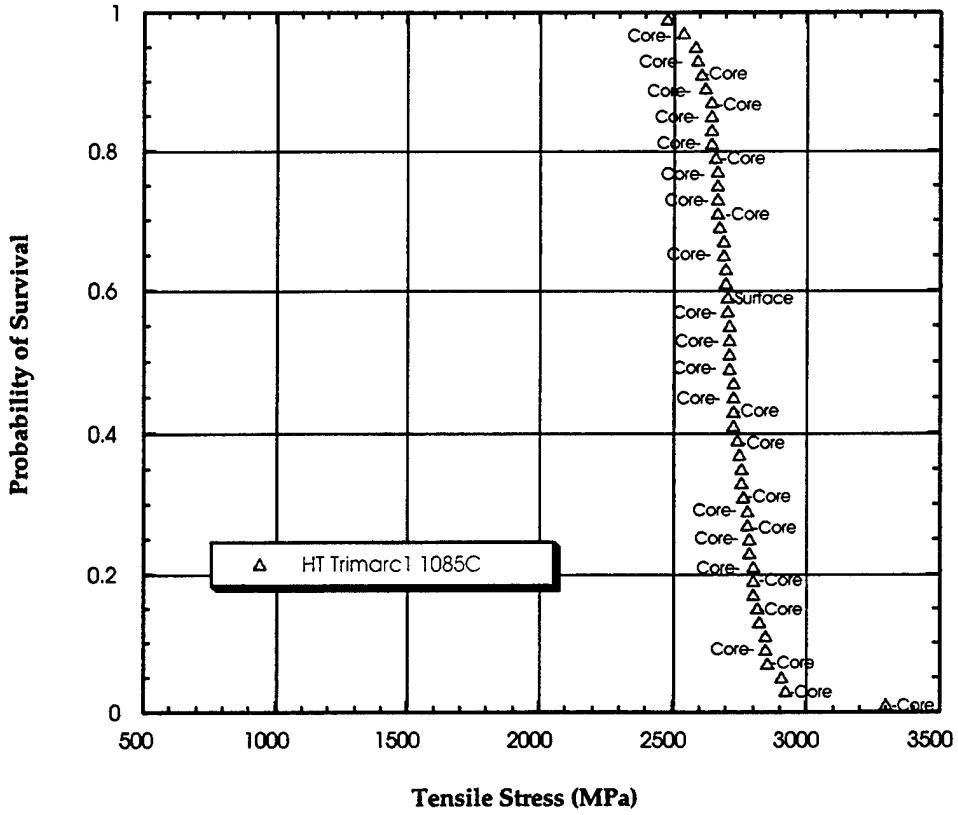


Figure 7. Trimarc 1® Fiber Strength after 1085°C Solution HT

Subtransus Heat Treated+ Extracted

The Trimarc 1® fiber tensile strength in the 1085°C Solution HT + extracted condition is shown in Figure 8. In this case the fiber was consolidated into a Ti-22Al-23Nb matrix, heat treated and chemically extracted for testing. The mean fiber strength has dropped to 2272 MPa. Furthermore, the fiber appears to fail both at regions near and around the core (47%), and also near the mid-radius of the of the fiber (46%). The average strength values associated with the mid-radius failures (2006 MPa) was noticeably less than for core failures (2334 MPa). The core/SiC reaction zone has increased to 1.05μm (Figure 3c) when compared to the subtransus heat treated condition (0.74 μm) due to the additional thermal exposure required for composite fabrication. Furthermore, the reaction zone at the fiber/matrix interface (Figure 4b) has increased by a factor of 3x (to 1.15μm) when compared to the as-fabricated condition. There were two failures identified at the surface of the fiber whose strength values were very low (1476 MPa). However, the most prominent failure site for low strength failures appears to be near or at the mid-radius of the SiC fiber. The propensity for increased number of low strength failures at the mid-radius may be related to manufacturing defects in the fiber in combination with residual stresses arising during composite fabrication. The CTE of the matrix is roughly 3x that of the fiber at room temperature. As such, during cool-down from the composite consolidation temperature the fiber is subjected to a large radial compressive residual stress. It is hypothesized that this stress tends to exacerbate the effect of defects near the mid-radius location of the SiC fiber.

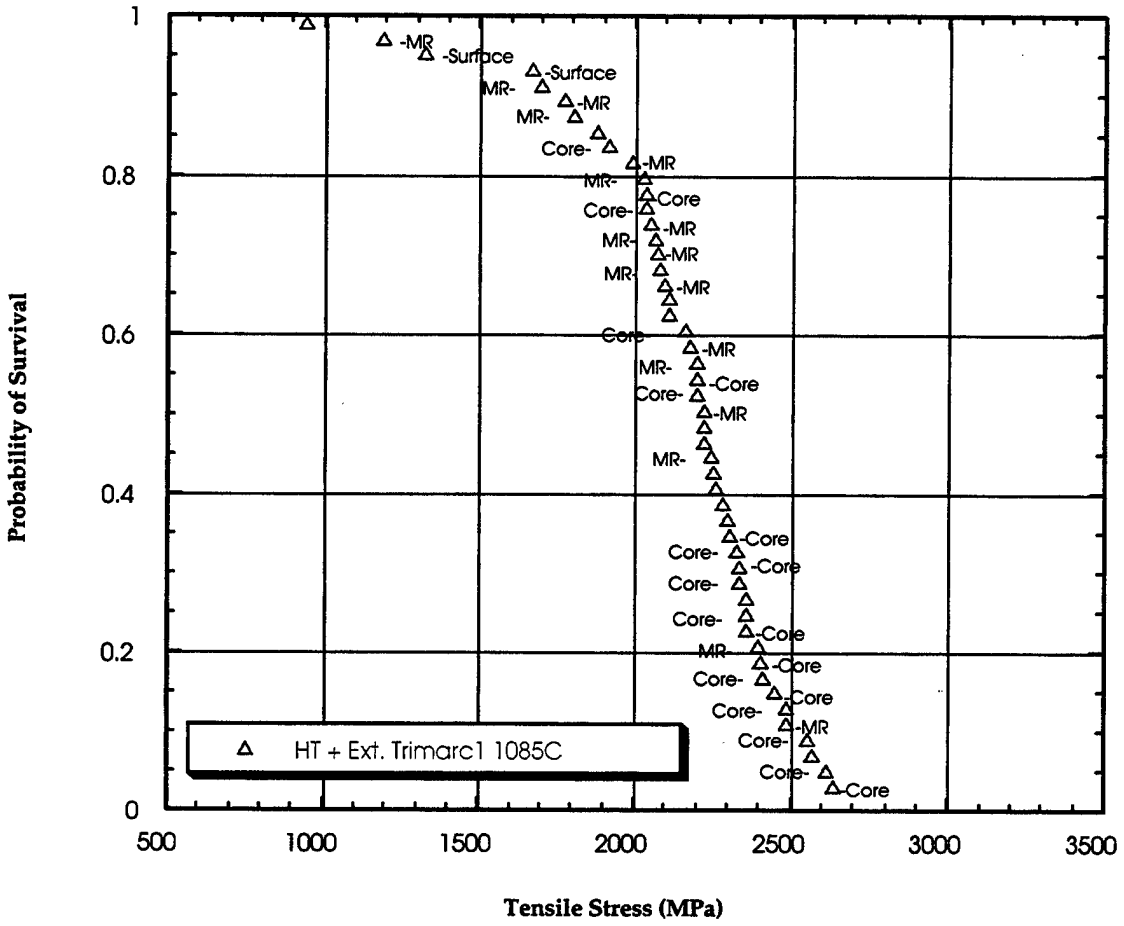


Figure 8. Trimarc 1® Fiber Strength in 1085°C Solution HT + Extracted Condition

Supertransus Heat Treatment

The fiber strength data for Trimarc 1® subjected to a supertransus heat treatment in vacuum is shown in Figure 9. The mean fiber strength continues to be degraded (to 2175 MPa). Almost all identifiable failures (>97%) occurred at or near the tungsten core with strength levels (2098 MPa) correspondingly close to the mean strength. In addition, there was very little scatter in the data set with 97% of the failures occurring within a 475 MPa band (1850-2325 MPa). The b SiC grains experience additional growth (Figure 2c) continuing to suggest that the SiC microstructure is not stable at 1160°C, however there were no failures identified at the mid-radius region of the SiC layer. The core/SiC reaction zone has increased to 1.21μm (Figure 3d), and is likely the controlling mechanism for the additional strength degradation which is observed. There was only a single failure identified with the surface of the Trimarc 1® fiber, however, like most failures of this type, it occurred at a relatively low strength level (1939 MPa).

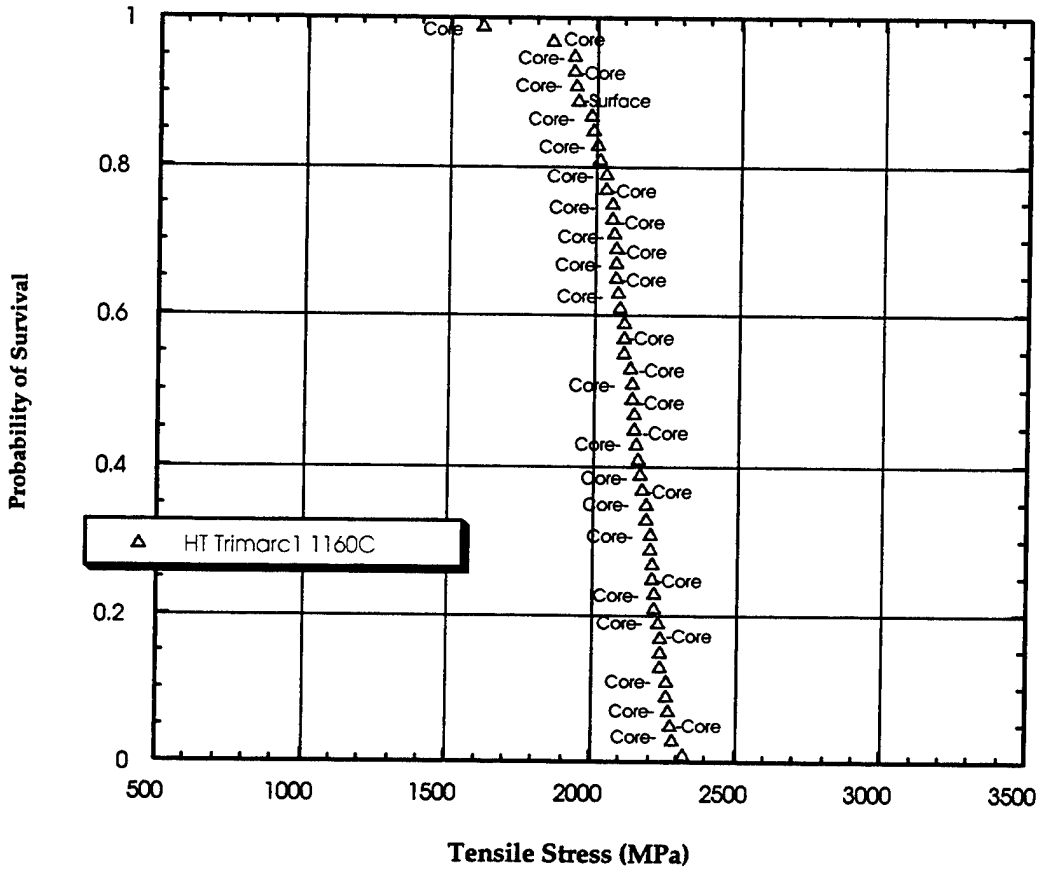


Figure 9. Trimarc1 Fiber Strength in 1160°C Solution HT Condition

Supertransus Heat Treated + Extracted

The Trimarc 1® fiber tensile strength for the 1160°C solution HT + extracted condition is shown in Figure 10. The mean fiber strength has dropped to 1639 MPa, which represents a 45% decrease when compared to the as-received strength condition. Furthermore, it is noticed that the fiber appears to fail primarily at regions near and around the core (81%). In addition, there were a few low strength failures (10%) in locations found near the mid-radius of the SiC layer of the fiber, and also at the surface the fiber surface (9%). The highest strength failures are associated with the core/SiC reaction zone (1782 MPa). This reaction zone has increased in size to 1.92μm (Figure 3e) when compared to the supertransus condition (1.21μm) due to the additional thermal exposure required for composite consolidation. The failures associated with the mid-radius (1410 MPa) suggest once again that compressive residual stresses arising from CTE mismatch due to composite fabrication may play a role as they had for the subtransus heat treated and extracted condition. Furthermore, the lowest strength failures (1255 MPa) occurred at the fiber surface, and may be associated with growth of the fiber/matrix reaction zone (Figure 4c), which has increased by a factor of 4x (to 1.98μm) when compared to the as-fabricated condition.

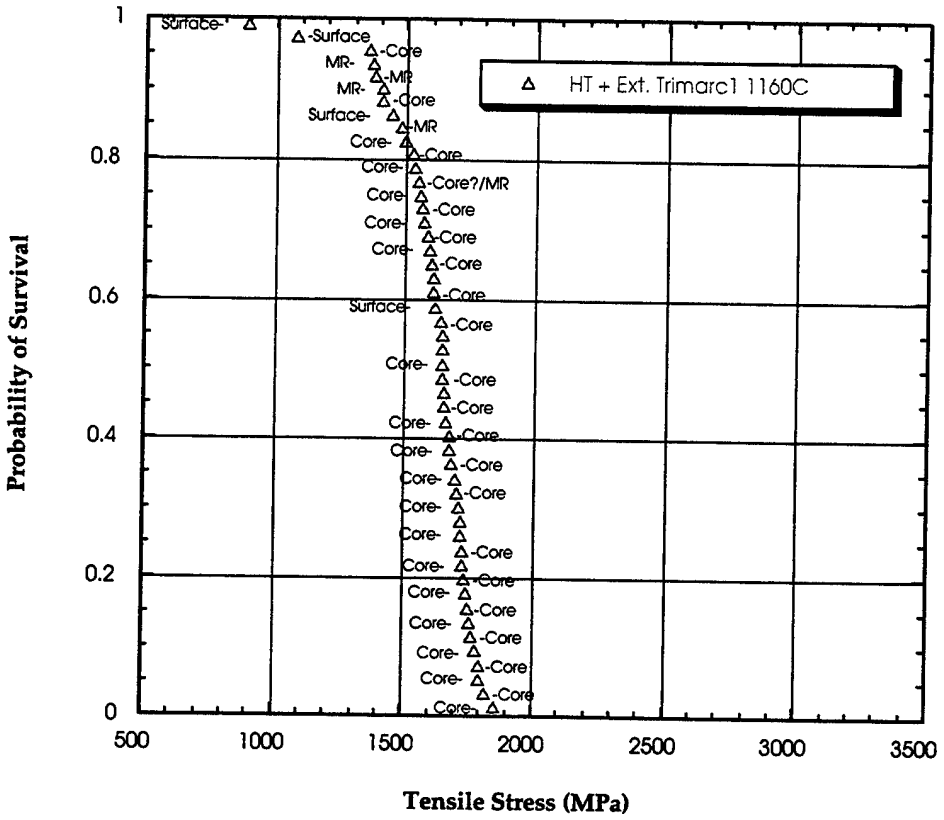


Figure 10. Trimarc 1® Fiber Strength in 1160°C Solution HT + Extracted Condition

Summary Trimarc 1®

Figure 11 displays a summary of the effect of heat treatment on the tensile strength of the Trimarc 1® fiber for all conditions, while Table I contains a summary of the fracture analysis data. All heat treatments are seen to degrade the fiber strength below as-received values (up to 45% for the 1160°C solution HT + extracted condition). In each case a significant number of core initiations are observed with the average strength value for those initiations decreasing with increased thermal exposure. This strength degradation is attributable to the increased reaction between the tungsten core and the SiC during composite consolidation an/or heat treatment. With respect to tungsten core/SiC reaction effects on fiber tensile strength, the Griffith criterion for cracks in brittle materials is thought to apply [i.e. s = C/• x; wherein s = fiber strength (GPa), x= crack length (reaction zone thickness (μm)) and C is a constant determined for the as-processed condition]. Table II contains core/SiC reaction zone data along with experimentally determined and calculated values of s (for core failures) using the Griffith criterion. Although this criterion does predict a strength debit, it would appear it consistently over-estimates the magnitude of the debit by 15-20%.

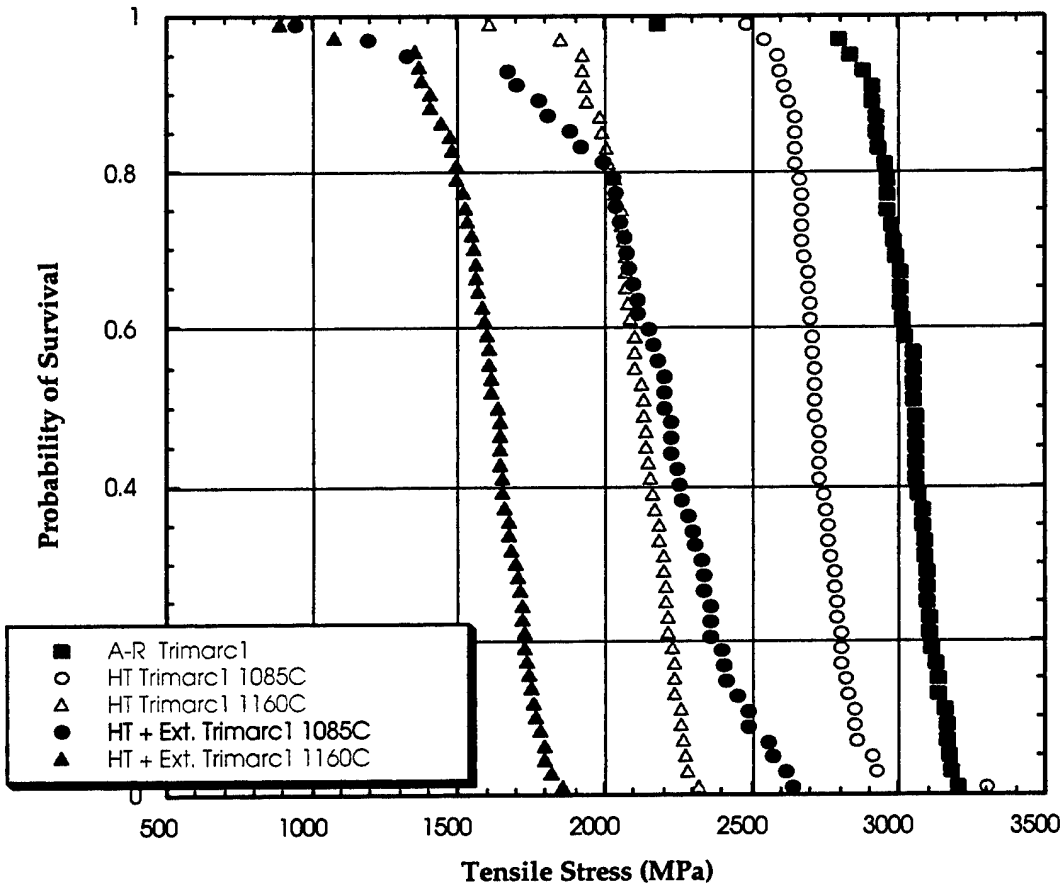


Figure 11. Summary of Effect of Heat Treatment on Trimarc1 Strength

Table I: Fracture Summary for Trimarc 1®

	As-Rec'd	1085°C	1085°C+Ext	1160°C	1160°C+Ext
# Fractures Identified	26/50	30/50	38/52	35/50	45/50
Mean Strength (MPa)	3079	2766	2272	2175	1639
% Core	86.5	96.6	47.4	97.1	81.1
M. Strength (MPa)	3059	2741	2334	2098	1782
% Mid Radius	13.5	0	46.1	0	10
M. Strength (MPa)	3053	-------	2006	-------	1410
% Surface	0	3.4	6.5	2.9	8.9
M. Strength (MPa)	-------	2707	1476	1937	1255

Similarly, Gambone and Gundel (14) performed a kinetic analysis for Trimarc 1® fiber wherein they were able to determine regions of time at temperature wherein degradation of the fiber tensile strength is expected to occur. The solution heat treatment conditions used in the current study fall in a region very near to where strength degradation would be expected.

In addition, high compressive radial residual stresses due to CTE mismatch between the fiber and matrix act to catalyze mid-radius failures for the heat treated + extracted conditions. There also appears to be a thermal instability of the b SiC microstructure which might be an

issue to consider for future development of this fiber. Finally, the increased fiber/matrix reaction associated with the heat treatments within the Ti-22Al-23Nb, may be responsible for the few very low strength failures occurring at the surface of the fiber for the heat treated + extracted conditions.

Table II: Effect of Core/SiC Reaction on Trimarc 1® Fiber Strength

Condition	Rxn. Zone (μm)	St. Dev. (μm)	s,core (GPa) Experimental	s,core (GPa) Calculated
As-Fabricated	0.38	0.03	3.059	3.080
1085°C	0.74	0.03	2.766	2.192
1085°C+Ext'd	1.05	0.06	2.272	1.840
1160°C	1.21	0.07	2.175	1.714
1160°C+Ext'd	1.92	0.11	1.639	1.361

In conclusion, the degradation observed for the Trimarc 1® fiber suggests this fiber as currently produced is unsuitable for use as a reinforcement in an orthorhombic titanium aluminide matrix for metal matrix composite applications wherein processing and/or heat treatment temperatures are comparable to, or exceed those examined in the subject study.

SCS-6

Fiber Structure

A schematic of the SCS-6 fiber is displayed in Figure 12. Microstructural and chemistry details for this fiber have been described elsewhere (15-18) and are summarized here. This 142μm diameter fiber is produced by CVD processing in a single-stage reactor. The salient features of the fiber architecture are that the core consists of a 33μm diameter carbon monofilament (CMF) originally spun from a pitch-based material, which is then sealed by a 1.5μm thick overcoat of pyrolytic carbon. The b SiC grows in columnar fashion outward from the CMF core forming two distinct zones. The zones consists of subgrains of b SiC with close-packed {111} planes oriented radially. These subgrains have a large aspect ratio with their length in the radial direction. The first zone which extends approximately 15μm is relatively fine grained (10-60 nm) and from a compositional standpoint, is slightly carbon rich (19). Although not depicted in Figure 12, Ning (15) has determined that the inner zone actually consists of three subzones with thicknesses starting at the pyrolytic coating of 6μm, 4.5μm and 4.5μm, respectively. The second zone is approximately 35μm wide and exhibits a coarser grain structure (70-140 nm) and is essentially stoichiometric in composition. The change in grain size is attributed to this change in chemistry. The interface between the two growth layers forms what is referred to as the mid-radius of the SiC. Unlike the tungsten core for the Trimarc 1® fiber, the CMF and the SiC are in chemical equilibrium, and as such, there is no observable reaction between the two. The external surface of the fiber is coated with three carbonaceous layers totaling ~3μm in thickness, which is used to protect the fiber during handling and to reduce its susceptibility to strength degradation due to chemical reaction within titanium matrices. The first coating layer is amorphous carbon which is approximately 0.5μm thick and which acts to "seal" the ends of the columnar b SiC. The fiber is then coated with two carbon layers (i.e. double pass) which are doped with b SiC crystallites. The thicknesses of the inner and outer c-rich layers are ~1.0μm and 1.5μm, respectively. The SCS-6 fiber has essentially been adopted as the industry standard for reinforcement of titanium over the last 15+ years, particularly for those instances wherein elevated temperatures (application or processing) preclude the use of tungsten core fibers due to SiC/core reactions.

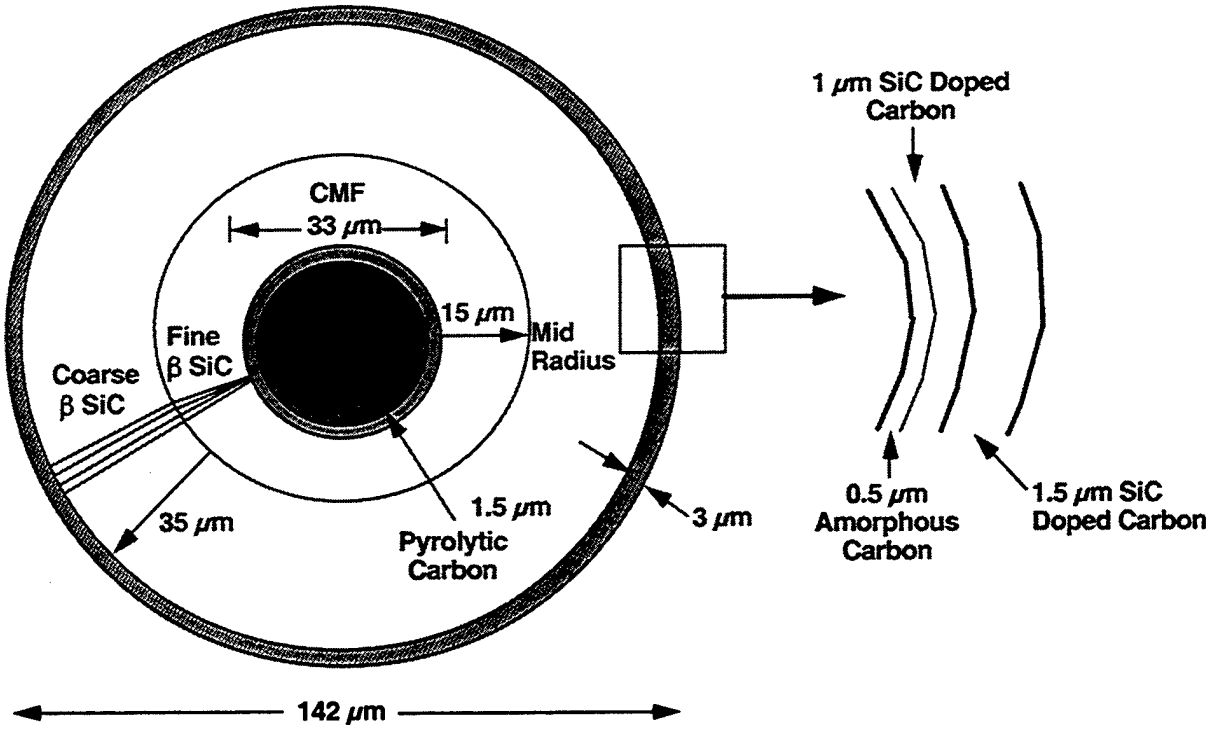


Figure 12. Schematic of SCS-6 Fiber

Tensile Properties, Microstructure and Fracture Analysis

Figure 13 contains a summary of the heat treatment effect on the tensile strength of SCS-6. The mean strength for the as-received fiber is 4403 MPa, which represents a >40% increase when compared to the as-received Trimarc 1®. Previous results (20) for SCS-6 fiber had indicated isothermal exposures in an inert environment at 1000°C for up to 700 hours resulted in no strength loss, and no signs of thermal instability in either the fiber coating or b SiC. In the present study, there also appears to be little or no discernible effect of any of the heat treatment conditions on the strength retention of the SCS-6 fiber, including those within the Ti-22Al-23Nb matrix. In fact, 93% of all failures occurred at strength levels in excess of 3000 MPa. Unlike the Trimarc 1® fiber, identification of the primary initiation site via fracture analysis was difficult, in that most of the higher strength fractures tended to be secondary in nature. However, for those fracture surfaces that were retained, the following observations could be made. The highest strength failures were located internally near the core of the fiber (Figure 14a). There were total of 18 failures which occurred at strength values • 3000 MPa. Of these, 16 initiation sites were identified, and 15 of those occurred at the surface of the fiber (Figure 14b). (Note: the remaining low strength failure appeared to be associated with a mid-radius initiation.) The fact that the low strength fibers had initiations near the fiber surface might seem to suggest that chemical reaction at the fiber/matrix interface played a role in the strength degradation. Figure 15 shows the SCS-6/matrix reactions for the as-consolidated, consolidated + 1085°C solution HT, and consolidated + 1160°C solution HT conditions. Although the reaction zone increases as the thermal conditions become more extreme, the protective carbon coating system remains essentially intact (i.e. >2.0 μm of coating remains). In fact, half of the surface failures occurred for conditions wherein the fiber was not exposed to the matrix at all (i.e. as-received, 1085°C solution HT and 1160°C solution HT conditions). It appears then, that the low strengths associated with the surface failures are a result of manufacturing defects, as opposed to chemical reaction with the matrix. Fry (10) has identified several classes of manufacturing surface defects which tend to reduce SiC fiber strength: CVD growth cones, surface nodules, SiC grains protruding from the fiber surface, surface damage from electrode

arcing, and abrasive surface damage during handling. One or more of these defects may have contributed to the low strength values found for the surface failures.

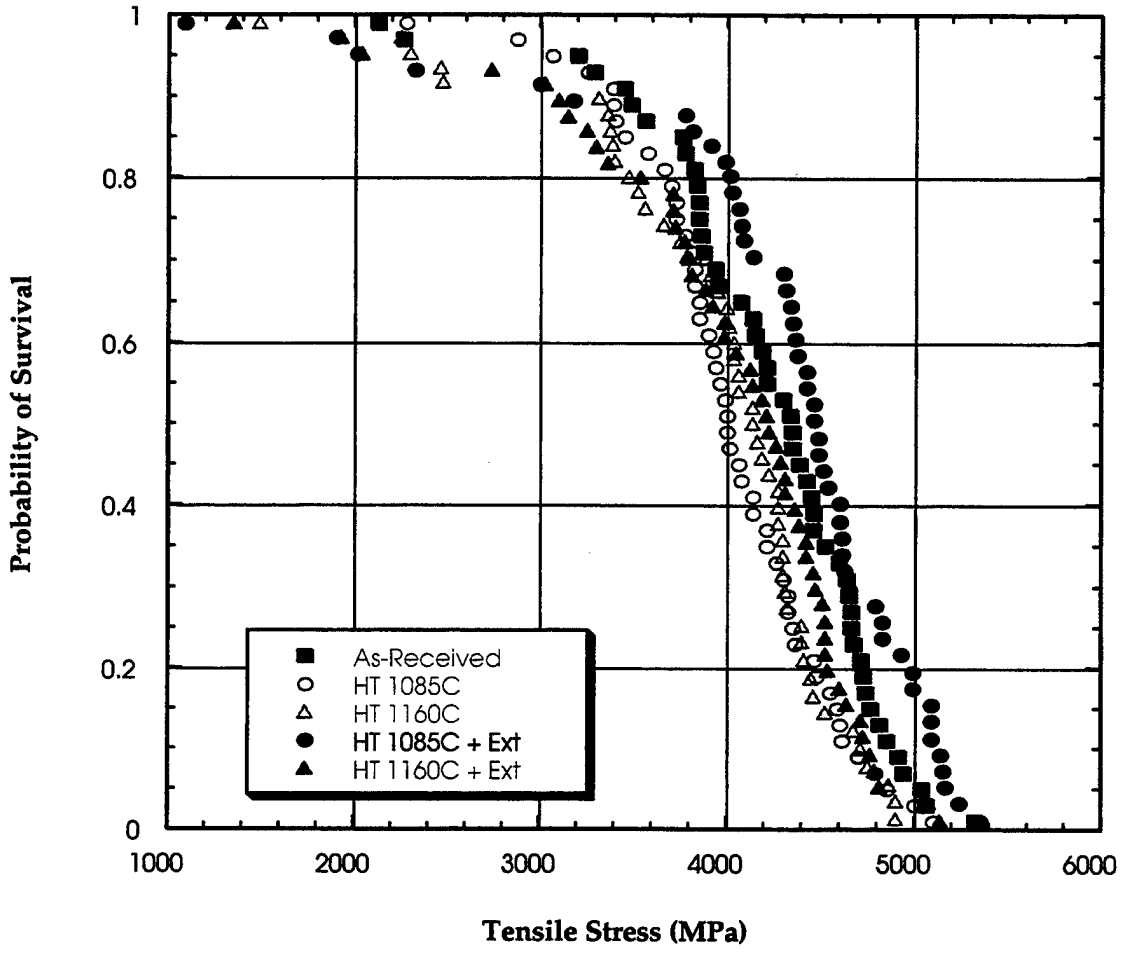


Figure 13. Summary of Effect of Heat Treatment on SCS-6 Fiber Strength

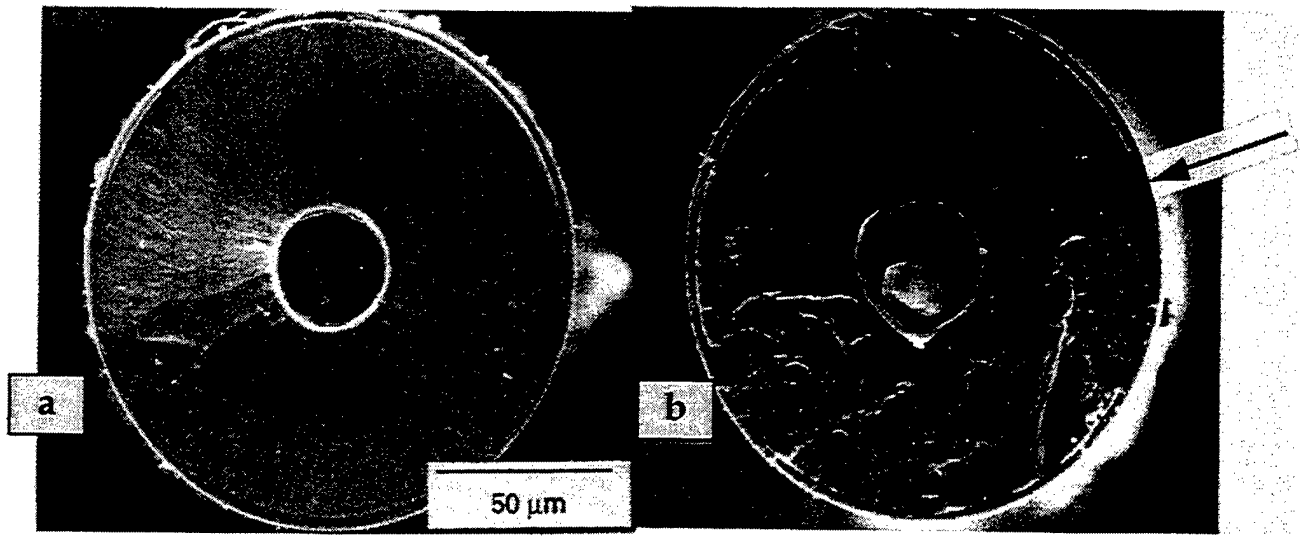


Figure 14. Fracture Surface of SCS-6 Fiber Illustrating: a) Core and b) Surface Initiations

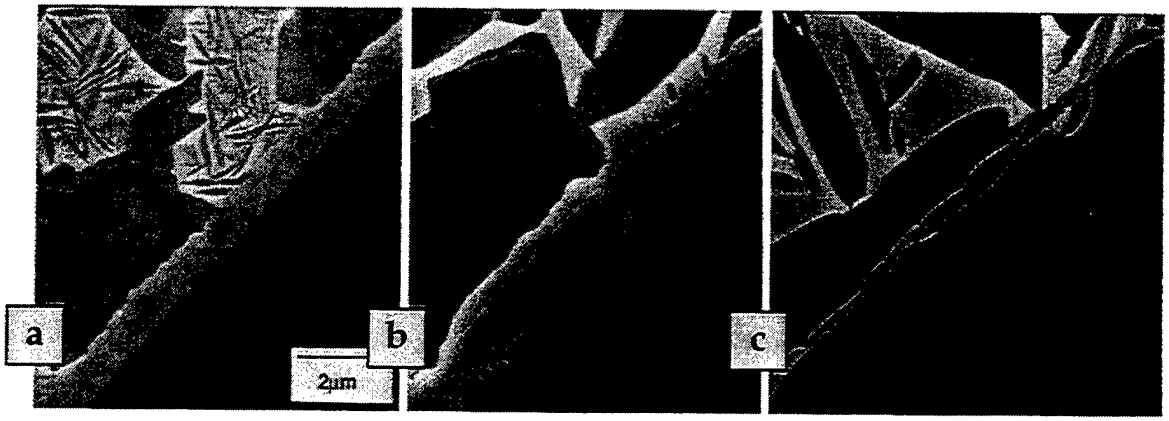


Figure 15. SCS-6/Ti-22Al-23Nb Interface Reactions for: a) As-Consolidated; b) Consolidated + 1085°C Solution HT and c) Consolidated + 1160°C Solution HT Conditions

With respect to SiC microstructural stability, Figure 16 shows the structure of the b SiC as a function of thermal exposure for the SCS-6 fiber. There appears to be only a very slight grain growth even after the supertransus heat treatment.

In conclusion, the SCS-6 fiber retains essentially all of its as-received strength under the heat treatment conditions evaluated, and as such, is suitable for use as a reinforcement in an orthorhombic titanium aluminide matrix for metal matrix composite applications wherein processing and/or heat treatment temperatures are comparable to those used in the subject study.

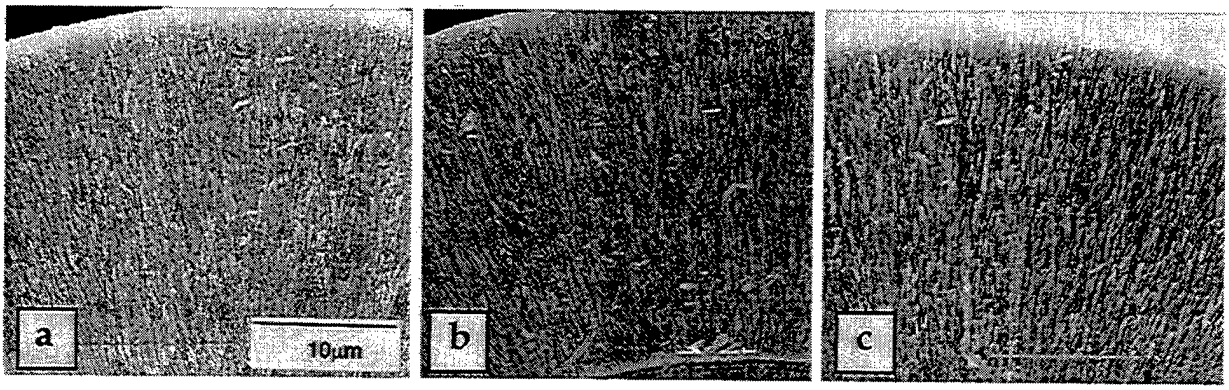


Figure 16. Secondary SEM Imaging of b SiC Portion of SCS-6 for: a) As-Received; b) 1085°C Subtranus HT and c) 1160°C Supertransus HT

Ultra SCS

Fiber Structure

A schematic of the Ultra SCS fiber is displayed in Figure 17. This 140μm fiber was developed to replace SCS-6 for those applications requiring increased fiber strength. Unlike the Trimarc 1® which is produced in a multi-stage reactor, the Ultra SCS fiber is produced via single stage CVD processing. The architecture of the Ultra SCS fiber is in some ways similar to that of the SCS-6 fiber. Like the SCS-6 fiber, the deposition of Ultra SCS takes place upon a 33μm CMF, which again is over-coated with a 1.5μm thick pyrolytic carbon layer. However, aside from the diameter of the fiber, this is where the similarities end. The microstructure of the SiC portion of the fiber is significantly different in that the grain size is relatively equiaxed and extremely fine in scale (Figure 18). Furthermore, since the fiber is produced in a single stage reactor, the growth process is continuous with this fine grain structure observed transcending the entire fiber diameter, (i.e. from the pyrolytic carbon coating on the core to the external surface coating). As such, there is no mid-radius grain size increase as was observed for the SCS-6 fiber. The surface of the fiber is protected for handlability and chemical reaction with the matrix by a ~3.3μm thick multi-layered coating. Not only is this coating layer thicker than for SCS-6, but there may also be some chemistry and structural differences as well. However, these and other details were not available from Textron at the time of this writing.

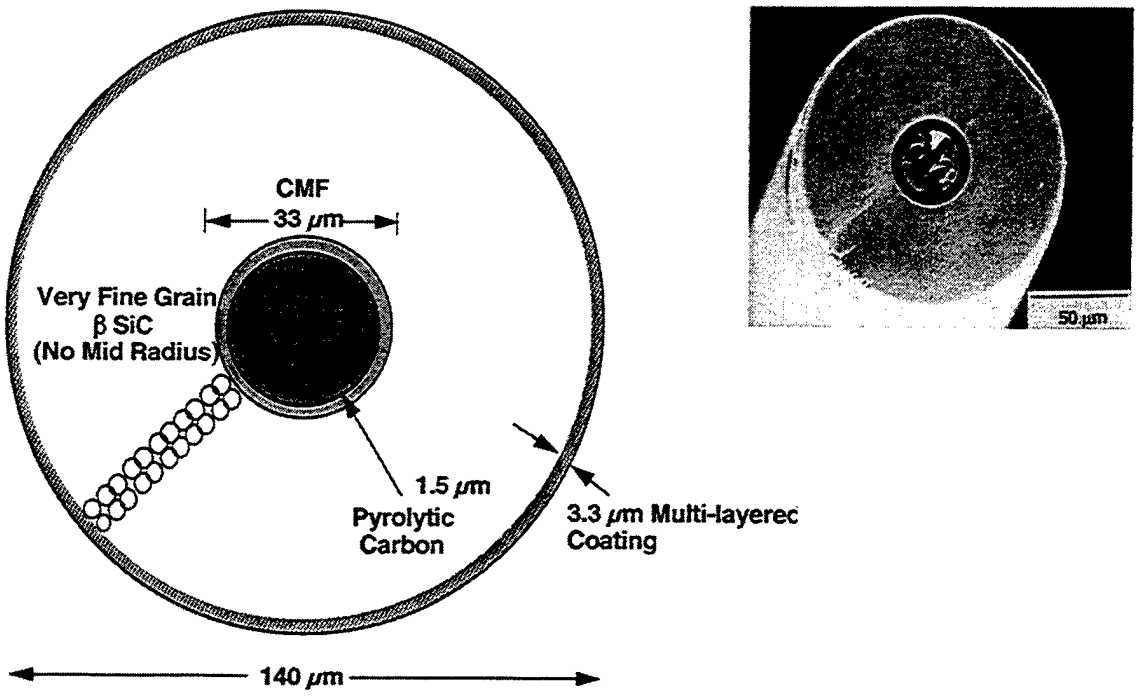


Figure 17. Schematic and Secondary SEM Image of Ultra SCS Fiber

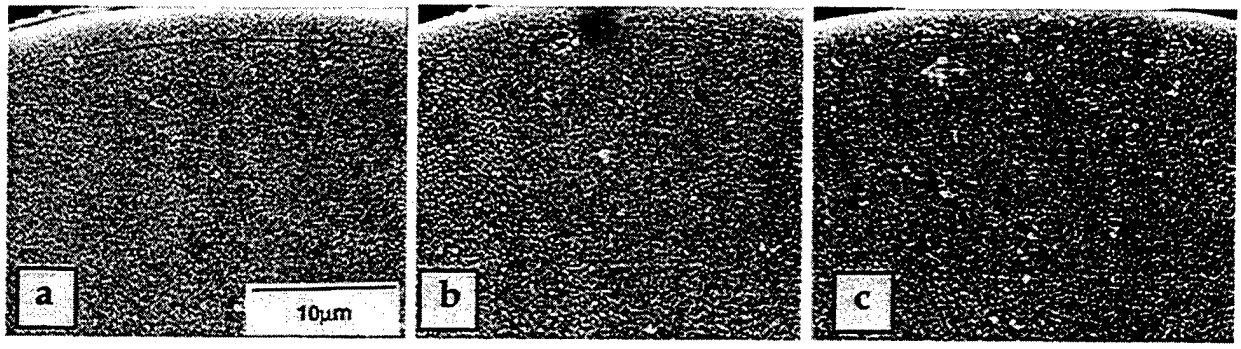


Figure 18. Secondary SEM Image of b SiC Portion of Ultra SCS Fiber in: a) As-Received; b) 1085°C Solution HT and c) 1160°C Solution HT Conditions

Tensile Properties, Microstructure and Fracture Analysis

Figure 19 contains a summary of the heat treatment effect on the tensile strength of Ultra SCS for all conditions. The mean strength for the as-received condition is 5610 MPa, which represents a >25% increase over SCS-6, and >80% over the Trimarc 1® fiber. The source of this high strength is thought to be the fine grained microstructure, and perhaps a modification to the surface coating system. There appears there might be a very modest effect of heat treatment on strength retention, however, 80% of the failures occurred at strengths in excess of 4800 MPa, and 96% in excess of 4000 MPa.

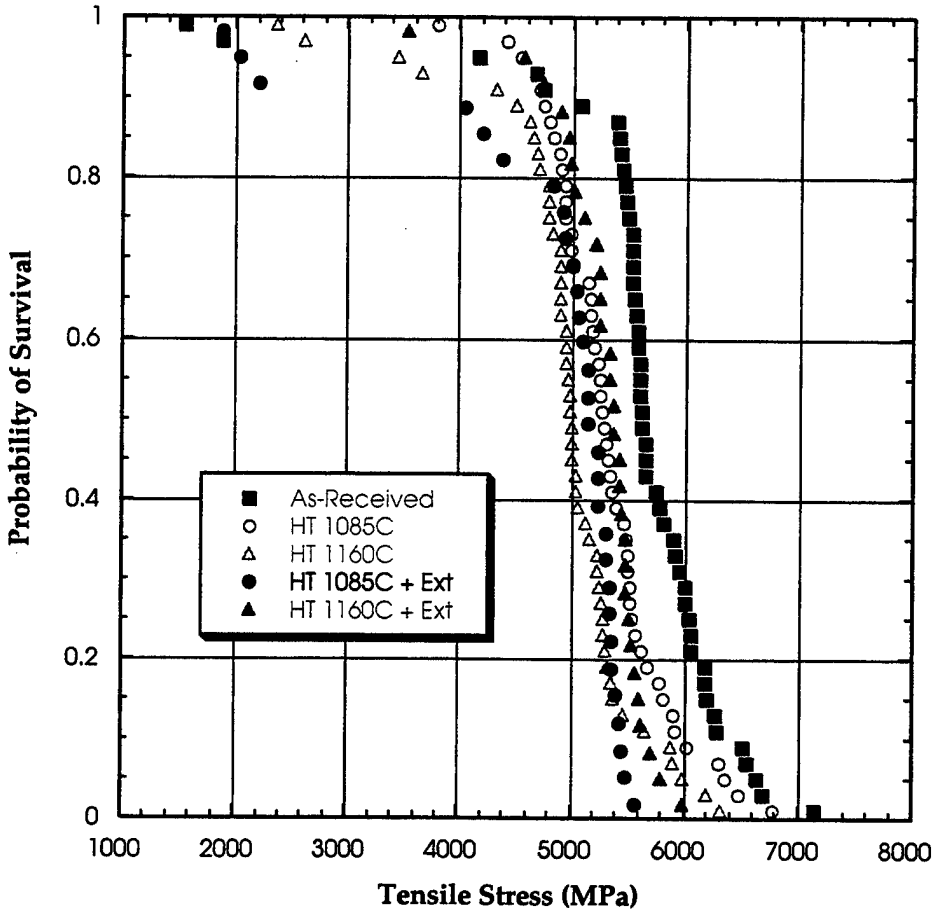


Figure 19. Summary of Effect of Heat Treatment on Ultra SCS Strength

Much like the SCS-6 fiber, the high strength associated with this fiber and the corresponding high energy of fracture make it very difficult to retain and identify fracture surfaces and primary initiation. Most of the failures were secondary in nature (Figure 20a), however, of the 10 failures occurring at strength levels <4000 MPa, 8 were identifiable, and all originated at the surface of the fiber (Figure 20b). As for the SCS-6, these surface failures do not appear to be related to chemical reaction with the matrix, as 5 of the 8 were for conditions for which the fiber was not in contact with the matrix. With regard to fiber/matrix chemical reaction, the effect of thermal exposure of reaction zone growth is depicted in Figure 21. Here is can be seen that the reaction zone is somewhat less uniform and grows at a slightly more rapid rate than for the SCS-6 fiber, lending credence to the possibility that the chemical make-up of the coating may have been modified for the Ultra SCS fiber. It was observed that a significant thickness of coating remains (~2.75μm) even after the supertranus heat treatment. Therefore, it is not surprising that the fiber is not significantly degraded by chemical reaction with the matrix during thermal treatment. The SiC microstructure appears to be relatively stable (within the limits of detectability) during thermal exposure. There were no failures identified that appeared to initiate within the SiC (i.e. mid-radius).

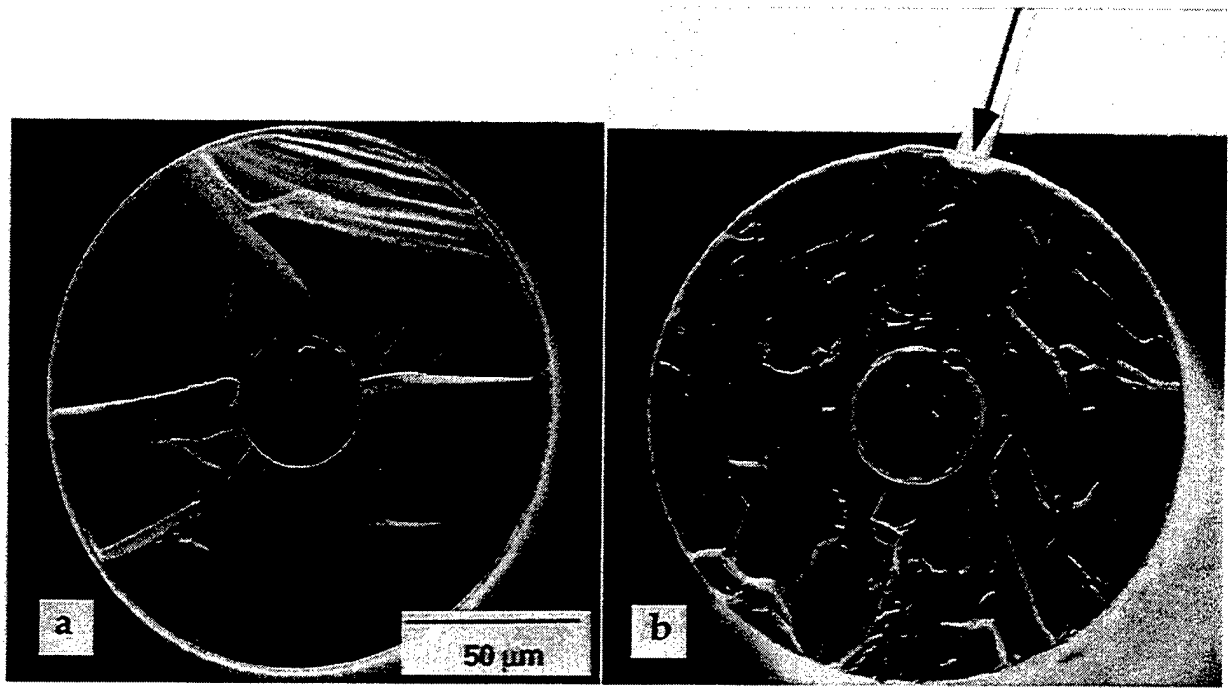


Figure 20. Secondary SEM Images of Fracture Surface for Ultra SCS Fiber Depicting: a) Secondary and b) Surface Initiations



Figure 21. SCS-6/Ti-22Al-23Nb Interface Reactions for : a) As-Consolidated; b) Consolidated + 1085°C Solution HT and c) Consolidated + 1160°C Solution HT Conditions

In conclusion, the Ultra SCS fiber exhibits the highest post-heat treatment strength of all fibers examined in the present study, and as such, is considered the best candidate for use as a reinforcement in an orthorhombic titanium aluminide matrix for metal matrix composite applications wherein processing and/or heat treatment temperatures are comparable to those used in the subject study.

Large Diameter Ultra SCS

At the time of this study, this 184μm diameter fiber was in the very preliminary stages of development at Textron Systems Division (formerly, Textron Specialty Materials). Indeed, only a single batch of fiber (totaling < 500 g) had been made at the time of this study. The primary benefits associated with a larger diameter fiber include the following: 1) an increased foil

thickness can be used for the same fiber volume loading with potential of decreasing foil processing costs and hence composite costs; 2) increased inter-fiber spacing can be realized which may enable higher off-axis strengths to be obtained; and 3) since the CMF does not carry significant load, higher volume fractions of the SiC portion of the fiber may result in even higher fiber tensile strength values. A schematic of the large diameter Ultra SCS fiber is shown in Figure 22. As for the Ultra SCS fiber, this fiber is manufactured using a single stage CVD reactor. The architecture of the fiber is in many ways analogous to the Ultra SCS fiber. The primary differences between the two fibers include the fiber diameter, a larger diameter CMF (42 μm vs. 33 μm), and a thinner external coating system (2.4 μm vs. 3.3 μm). Note: this coating system has not been optimized and its thickness and chemistry may eventually be modified. Details concerning the chemistry and structure of coating system were not available from Textron at the time of this writing. The most important similarity to Ultra SCS is a very finebSiC grain size that extends from the CMF to the external coating (with no mid-radius present), and which is thought to provide the very high tensile strengths associated with these fibers.

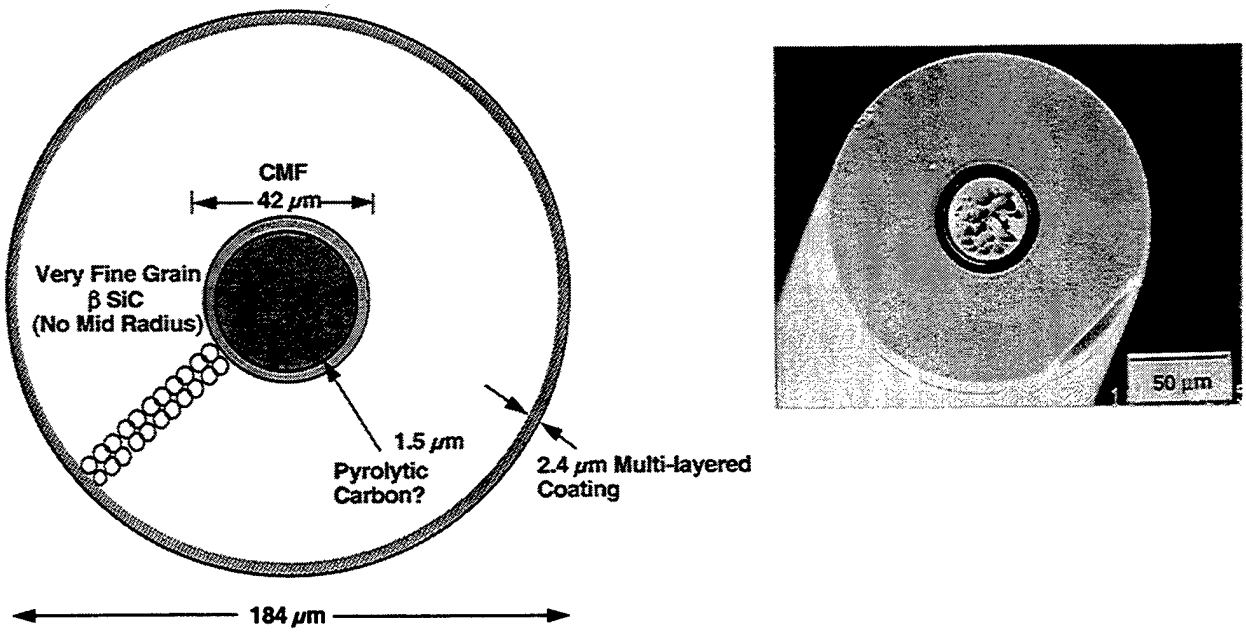


Figure 22. Schematic and Secondary SEM Image of Large Diameter Ultra SCS

Tensile Properties, Microstructure and Fracture Analysis

Figure 23 contains a summary of the heat treatment effect on the tensile strength of large diameter Ultra SCS for all conditions. The mean strength for the as-received condition is 6313 MPa, which was by far the highest strength observed for any of the fibers studied. In fact, 100% of all as-received failures occurred at strength levels > 5700 MPa. (Note: once again, these results need to be viewed in the context of this being a single, in fact, first batch of an experimental fiber). This strength value represents an increase of 12.5%, 43% and 103% when compared to the as-received values for Ultra SCS, SCS-6 and Trimarc 1®, respectively. As in the case of the Ultra SCS fiber, the source of the high strength is thought to be the fine grain size of theb SiC (Figure 24a) and perhaps a modification to the external coating system. The increase in strength over the Ultra SCS is thought to be due in part to the higher volume ratio of the b SiC/CMF core. There appears to be a measurable effect of heat treatment on the fiber itself in vacuum. The subtransus heat treated mean strength drops to 5450 MPa (-13%), while the supertransus heat treated strength drops to 5071 MPa (-20%), and for both heat

treatments, and there are a fair number of failures (~ 20%) at strength levels < 5000 MPa. Unfortunately, due to the very high strength and associated energies of fracture, none of the primary fracture surfaces were retained. The b SiC grain structure appears within the detection limits of SEM imaging to be relatively stable with respect to thermal exposure (Figure 24), and thus, it cannot be conclusively identified as the source of this debit. In addition, since the fiber is deposited upon a CMF, one would not expect reaction between the b SiC and the CMF to have occurred. Therefore, it was not possible to identify the source of this at this time.

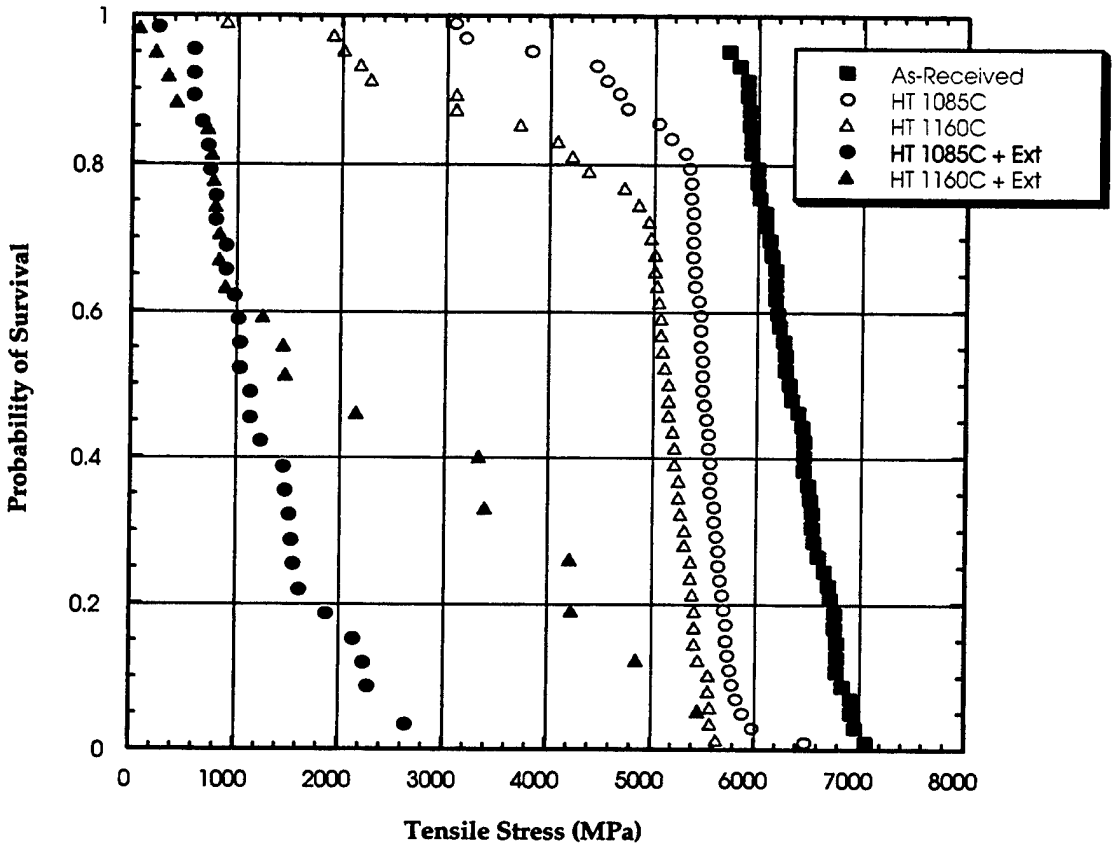


Figure 23. Summary of Effect of Heat Treatment on Large Diameter Ultra SCS Strength

The effect of both of the heat treatment + extracted conditions is extremely significant. In both conditions a large number of failures (~80%) occurred at strength levels < 2000 MPa. Although as previously noted, the fracture initiation sites could not be identified, one might logically conclude that the reaction with the titanium aluminide matrix may have played a significant role in the degradation observed. Figure 25 shows the fiber/matrix reaction for this system. The rate of reaction proceeds in a fashion very similar to the Ultra SCS system, but since the initial coating thickness was thinner, the amount of protective coating remaining after exposure is correspondingly less. It is thought that the coating thickness for this experimental fiber may be too thin to provide adequate protection from chemical reaction with the Ti-22Al-23Nb matrix during heat treatment.

In conclusion, the large diameter fiber shows great potential in terms of as-produced strengths, but in its present experimental form, is unsuitable for use as a reinforcement in an orthorhombic titanium aluminide matrix for metal matrix composite applications wherein processing and/or heat treatment temperatures meet or exceed those used in the subject study.

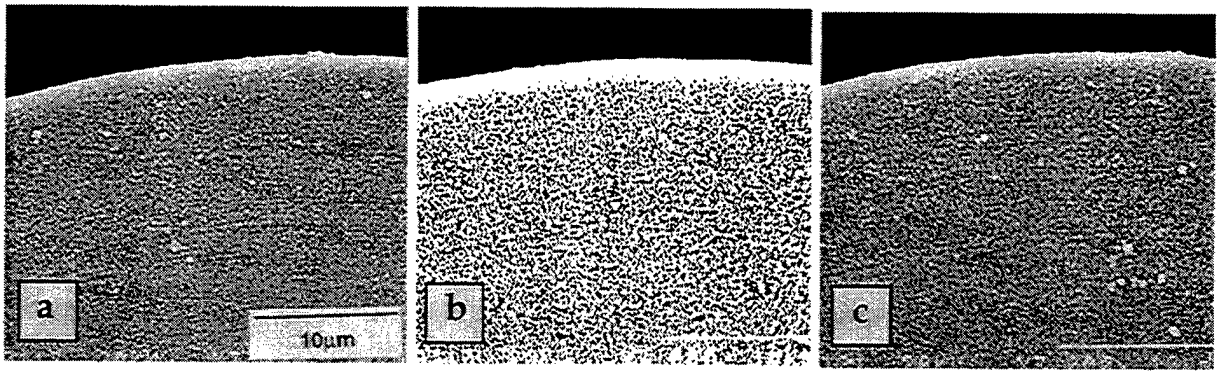


Figure 24. BSE SEM Image of b SiC Portion of Large Diameter Ultra SCS Fiber for: a) As-Received; b) 1085°C Subtransus HT and c) 1160°C Supertransus HT Conditions

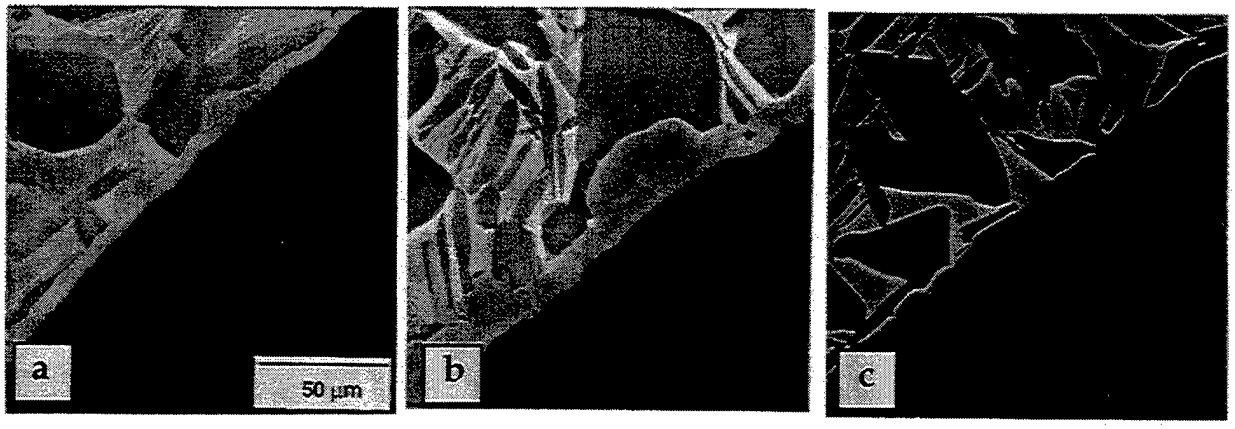


Figure 25. Large Diameter Ultra SCS/Ti-22Al-23Nb Reaction Zone for: a) As-Consolidated; b) Consolidated + !085°C Solution HT and c) Consolidated + 1160°C Solution HT Conditions

CONCLUSIONS

Trimarc 1®

- Trimarc 1® exhibited the lowest as-produced tensile strength values for all the fibers evaluated (mean strength = 3080 MPa).
- Significant fiber strength degradation occurred for all heat treatments due primarily to tungsten core/SiC reaction and possibly fiber/matrix chemical reaction.
- The b SiC microstructure appeared to be thermally unstable upon subtransus and supertransus heat treatment.
- This fiber should not be considered as a candidate reinforcement in orthorhombic titanium aluminide composites (O TMCs).

SCS-6

- The SCS-6 fiber exhibits good as-produced room temperature tensile strength (mean strength = 4303 MPa).
- There was no discernible effect of heat treatment on the tensile strength of the SCS-6 fiber (93% of failures > 3000 MPa).
- Almost all low strength failures were associated with surface flaws, which were likely not a result of fiber/matrix chemical reaction, but instead due to manufacturing/handling.

- There may be a very slight thermal instability of the b SiC structure, however, there was no effect on the fiber tensile strength.
- The SCS-6 fiber should be considered a good candidate for the reinforcement of O TMCs.

Ultra SCS

- The Ultra SCS fiber exhibits excellent as-produced room temperature tensile strength (mean strength = 5610 MPa).
- There was only a very modest effect of heat treatment on the tensile strength of the Ultra SCS fiber (96% of failures > 4000 MPa).
- Almost all low strength failures were associated surface flaws which were likely not a result of fiber/matrix chemical reaction, but due to manufacturing/ handling.
- Single stage CVD processing in combination with possibly a slight chemistry modification result in a very fine equiaxed b SiC structure, which is most likely responsible for the very high tensile strength for this fiber.
- The Ultra SCS fiber should be considered as an excellent candidate for the reinforcement of O TMCs.

Large Diameter Ultra SCS

- The large diameter (184 μm) Ultra SCS fiber exhibits outstanding as-produced room temperature tensile strength (mean strength = 6313 MPa; 100% of failures > 5700 MPa).
- This fiber exhibits significant reductions in tensile strength when heat treated, particularly within the orthorhombic matrix alloy (0.5 Probability of Survival • 1500 MPa).
- The strength debits are suspected to be the result of an unoptimized fiber surface coating, which may be too thin to protect the fiber from chemical reaction with the orthorhombic matrix alloy.
- Although offering tremendous potential in terms of as-produced strength, the large diameter Ultra SCS fiber should not be considered a candidate for the reinforcement of O TMCs in its present form.

ACKNOWLEDGMENTS

The authors would like to thank Textron Specialty Materials Division and Atlantic Research Corp. for supplying the continuous SiC fibers and composite materials for this study. Special thanks to Prof. Frank Wawner of the Univ. of Virginia for sample preparation and SEM examination of the SiC fibers for microstructural analysis. Additionally, the authors would like to express their gratitude to Mr. Mark Dodd of Universal Energy Systems who performed the fiber heat treatments.

REFERENCES

1. Smith, P.R., Graves, J.A. and Rhodes, C.G., "Preliminary Mechanical Property Assessment of a SiC/Orthorhombic Titanium Aluminide Composite", in Structural Intermetallics, eds. R. Darolia, et. al., TMS, Warendale, PA, 1993, pp. 765-771.

2. Smith, P.R., Graves, J.A. and Rhodes, C.G., "Evaluation of an SCS-6/Ti-22Al-23Nb Orthorhombic Composite", in Intermetallic Matrix Composites II, eds. D.B. Miracle, D.L. Anton and J.A. Graves, **Vol. 273**, MRS Sym Proc., Pittsburgh, PA, 1994, pp. 43-52.

3. Miracle, D.B., Smith, P.R. and Graves, J.A., "A Review of the Status and Developmental Issues for Continuously-Reinforced Ti-Aluminide Composites for Structural Applications", in Intermetallics Composites III, eds. J.A. Graves, R.R. Bowman and J.J. Lewandowski, **Vol. 350**, MRS Sym Proc., Pittsburgh, PA, 1994, pp. 133-142.

4. Graves, J.A., Smith, P.R. and Rhodes, C.G., "Evaluation of a Ti-22Al-23Nb Orthorhombic Alloy for Use as the Matrix in a High Temperature Ti-Based Composite", in Intermetallic Matrix Composites II, eds. D.B. Miracle, D.L. Anton and J.A. Graves, **Vol. 273**, MRS Sym Proc., Pittsburgh, PA, 1994, pp. 31-42.

5. Smith, P.R. and Porter, W.J., "The Effect of a Post-Consolidation Heat Treatment on the Tensile and Creep Behavior of Neat Matrix Ti-22Al-23Nb", submitted to J. Mat. Sci.

6. Krishnamurthy, K. and Miracle, D.B., "On the Role of Carbon Diffusion During Fiber/Matrix Reaction in SiC Fiber Reinforced Ti-Based MMCs", to be presented at Eleventh International Conference on Composite Materials (ICCM-11), Gold Coast, Queensland, Australia, 14-17 July 1997 (published in proceedings).

7. Gambone, M.L. and Wawner, F.E., "The Effect of Elevated Temperature Exposure of Composites on the Strength Distribution of the Reinforcing Fibers", in Intermetallics Composites III, eds. J.A. Graves, R.R. Bowman and J.J. Lewandowski, **Vol. 350**, MRS Sym Proc., Pittsburgh, PA, 1994, pp. 111-118.

8. Rhodes, C.G., Graves, J.A., Smith, P.R. and James, M.R., "Characterization of Orthorhombic Titanium Aluminde Alloys", in Structural Intermetallics, eds. R. Darolia, et. al., TMS, Warendale, PA, 1993, pp. 45-52.

9. Sukonnik, I.M., Smith, P.R., Graves, J.A., Rhodes, C.G., Shaw, M.C., Krishnamurthy, S. and Pandey, A., "Advances in Thermomechanical Processing of Titanium Aluminide Orthorhombic Foils", in Proc. Titanium Matrix Composites Workshop, eds., P.R. Smith and W.C. Revelos, Report No. WL-TR-92-4035, Materials Directorate, Wright Laboratory, WPAFB, OH, April 1992, pp. 98-114.

10. Fry, V., "Advanced Chemical Vapor Deposition (CVD) Fibers for Metal Matrix Composites", Report No. WL-TR-93-4050, Materials Directorate, Wright Laboratory, WPAFB, OH, April 1993.

11. Gambone, M.L., Materials Directorate, WPAFB, OH, unpublished research, 1996.

12. Smith, P.R., Rhodes, C.G. and Revelos, W.C., "Interfacial Evaluation of a Ti-25Al-17Nb/SCS-6 Composite", in Proc. Titanium Aluminide Composite Workshop, eds. P.R. Smith, S.J. Balsone and T. Nicholas, Report No. WL-Tr-91-4020, Materials Directorate, Wright Laboratory, WPAFB, OH, Feb. 1991, pp. 178-201.

13. Rhodes, C.G. "Charactrerization of Fiber/Matrix Interfaces by Transmission Electron Microscopy in Titanium Aluminide/SiC Composites", in Intermetallic Matrix Composites II, eds. D.B. Miracle, D.L. Anton and J.A. Graves, **Vol. 273**, MRS Sym Proc., Pittsburgh, PA, 1994, pp. 17-31.

14. Gambone, M.L. and Gundel, D.B., "The Effect of W-Core Reaction on the Strength of SiC Fibers in SiC/Ti-Alloy Composites", Proc. CMMC'96, San Sebastian, Spain (Sept. 1996).

15. Ning, X. J., Pirouz, P. and Lagerlof, K.P.D., "The Structure of Carbon in Chemically Vapor Deposited SiC Monofilaments", J. Mater. Res., **5**, No. 12, Dec. 1990, 2865-2876.

16. Ning, X.J. and Pirouz, P., "The Microstructure of SCS-6 Fiber", J. Mater. Res., **6**, No. 10, Oct. 1991, 2234-2248.

17. Wawner, F.E., in Fibre Reinforcements for Composite Materials, ed. A.R. Bunsell (Elsevier Science Publishers, N.Y., 1988), 371-425.

18. Nutt, S.R. and Wawner, F.E., J. Mat. Sci. 20, 1953 (1985).

19. Casey, J.D. and Geller, J., "Elemental Composition Profiles of SCS-6 SiC Fiber as Determined by Auger Electron Spectroscopy", in Proc. Titanium Aluminide Composite Workshop, eds. P.R. Smith, S.J. Balsone and T. Nicholas, Report No. WL-Tr-91-4020, Materials Directorate, Wright Laboratory, WPAFB, OH, Feb. 1991, pp. 59-72.

20. Gambone, M.L., Gundel, D.B. and Wawner, F.E., "The Effect of Isothermal Exposure on SiC Fibers", in proceedings of 17th Conference on Metal Matrix, Carbon, and Ceramic Matrix Composites, NASA Conf. Pub. # 3225, Part 1, May 1994, 235-252.

This page intentionally left blank

Reference: John, R., Zawada, L.P., and Kroupa, J.L, "Stresses Due to Temperature Gradients in CMC Aerospace Components," Journal of American Ceramic Society, V. 82, No. 1, pp. 161-168.

Stresses Due to Temperature Gradients in CMC Aerospace Components

Reji John[1], Larry P. Zawada, and Joseph L. Kroupa[1]

Wright Laboratory (WL/MLLN), Materials Directorate,
Wright-Patterson Air Force Base, OH 45433-7817, USA.

[1] University of Dayton Research Institute, Dayton, OH 45469-0128, USA.

Abstract

Ceramic matrix composites (CMC) are being considered as replacement materials for divergent flaps and seals in advanced aerospace turbine engines. During service, these components are subjected to severe temperature gradients across the width of the flaps. This papers discusses an analytical procedure to estimate the stresses generated in the CMC flaps due to the temperature gradients. The analytical procedure can be used for a material with non-linear temperature-dependent stress-strain behavior. This procedure was used to predict the thermal stresses in four candidate CMC systems due to temperature gradients. The thermal stresses along the edges typically exceed the proportional limit, and sometimes the fatigue limit of the CMC.

I. Introduction

Ceramic matrix composites (CMC) are targeted for use in advanced aerospace turbine engine components which are exposed to temperatures ≥ 1000°C [1-3]. Under the direction of the Advanced Research Projects Agency (ARPA), various CMC systems are under consideration as replacement materials for divergent flaps and seals in engines [4,5]. The typical flaps and seals currently in use are made of Rene'41. A live engine test with exposed flaps and seals is shown in Fig. 1. As shown by the distinct colors in the flaps, severe temperature gradients exist in the flaps and seals. The schematic of the flap and seal assembly is shown in Figs. 2(a) and 2(b). As shown in Fig. 2(a), during various stages of engine operation, the effective diameter of the nozzle can be expanded or contracted by moving the flaps and seals. Under these conditions, the seals cover significant areas of the flaps ranging from ≈10 to ≈50% of the flap area. The planar view shown in Fig. 2(b) highlights the uniform overlapping along the edges of the flaps. The overlapped region of the flaps is about 700°C cooler than the central one-third of the flap. Consequently, severe temperature gradients occur in the flaps during service. The temperature gradients are associated with temperatures as high as 800-1000°C and temperature gradients of 20°C/mm across 40 mm close to the ends of the flap.

Temperature gradients have been shown to cause significant thermal stresses in materials such as polymethacrylate (PMMA), polycarbonate and steel [6-10]. Yagawa et al. [7], Kokini and Long [8], John et al. [9] and Kuo and John [10] showed experimentally that local heating or cooling can generate severe temperature gradients which will generate thermal stresses high enough to initiate fracture. These studies [6-10] were conducted for materials which exhibit linear isotropic behavior. In contrast, the candidate CMC systems under

consideration for use as divergent flaps typically show non-linear stress-strain behavior [11,12]. Even though the candidate CMC systems can withstand up to ≈ 1000°C under tensile loading without significant degradation of properties [11,12], the temperature gradients could possibly generate stresses well above the proportional limit. In addition, the temperature gradients are expected to be cyclic during service. Hence, accurate design of the CMC flaps and seals requires a simple analytical tool to estimate the stresses due to temperature gradients. This paper describes an analytical procedure to determine the stresses due to temperature gradients in non-linear CMC systems. The proposed procedure was verified using finite element analysis. The analytical procedure was used to predict the thermal stresses in the candidate CMC systems subjected to the estimated temperature gradients. The paper also discusses the significance of using the non-linear analysis to predict the thermal stresses, deformation and fracture behavior of the CMC flaps due to the temperature gradients, and influence of length of plate on the predicted stress distribution in the CMC flap.

II. Candidate CMC Systems

The four CMC systems under consideration by ARPA as replacement materials for existing metallic divergent flaps are described in Table I. All the CMC systems have the same fiber architecture (8HSW, 8 harness satin weave). These CMC systems were fabricated using different techniques and contain different fibers, matrices, and interfaces. Additional details about these CMC systems can be found in Refs. [11] and [12]. The effect of temperature on the coefficient of thermal expansion, α, and conductivity, k, is shown in Fig. 3 [13,14]. The four CMC systems exhibit a wide range of α and k. The tension stress-strain curves [11,12] for Nicalon/Al_2O_3 and Nicalon/C are shown in Fig. 4, and that for Nicalon/SiNC and N610/AS are shown in Fig. 5. The data show that the tension stress-strain does change significantly with temperature up to ≈ 1000°C, except for the 25% decrease in failure strain of Nicalon/Al_2O_3. N610/AS is near-linear at room temperature and 1000°C, whereas Nicalon/Al_2O_3 is non-linear at room temperature and 1000°C. The dashed lines in Figs. 4 and 5, show the bilinear approximation used to represent the tension stress-strain response of the various CMC systems. A schematic of the bilinear representation of tension stress-strain response is shown in Fig. 6(a). The initial modulus is denoted as the elastic modulus, E_e, the second modulus as the plastic modulus, E_p, and the elastic strain limit as ε_e. The bilinear stress-strain parameters used in this study for the candidate CMC systems are reported in Table II. Due to the lack of extensive data, the stress-strain behavior of the CMC systems under compressive loading was assumed to be linear as shown in Fig. 6(b). Results from other CMC systems with similar fiber architecture [15,16] indicate that the assumption of a linear stress-strain response under compressive loading is valid. The data shown in Figs. 3-5 were used for the prediction of thermal stresses as discussed next.

III. Analytical Procedure

The CMC flap is modeled as an infinitely long (large H) and thin plate with uniform width (W) and thickness (B) as shown in Fig. 7. The thermal stresses generated by an arbitrary temperature distribution was derived using the procedure described by Boley and Weiner [17]. The analysis is based on the assumption that cross-sections remain plane after loading. In addition, the effect of lateral contraction is neglected. Under these conditions, the axial displacement can be represented as a linear function of the transverse coordinate. Thus we can represent the axial displacement, v(x,y) as,

$$v = f_0(y) + x\, f_1(y) \ . \qquad (1)$$

The corresponding axial total strain, $\varepsilon_{yy,t}$ and mechanical strain, $\varepsilon_{yy,m}$ can be derived as,

$$\varepsilon_{yy,t} = \frac{\partial v}{\partial y} = f_0'(y) + x\, f_1'(y) \text{ , and} \tag{2}$$

$$\varepsilon_{yy,m} = \varepsilon_{yy} - \alpha T \text{ ,} \tag{3}$$

where α = coefficient of thermal expansion, T is the temperature, T=T(x,y), and primes indicate derivatives with respect to y. Knowing $\varepsilon_{yy,m}$, the thermal stress, $\sigma_{yy,th}$ can be obtained as,

$$\sigma_{yy,th} = E_s\, \varepsilon_{yy,m} \text{ ,} \tag{4}$$

where $E_S = E_S(\varepsilon_{yy,m})$ = secant modulus which is a function of the current mechanical strain. The unknown functions f_0 and f_1 were determined using the force and moment equilibrium equations given by Eqn. (5) and Eqn. (6), respectively.

$$\int_0^W \sigma_{yy,th}\, B\, dx = 0 \text{ , and} \tag{5}$$

$$\int_0^W \sigma_{yy,th}\, x\, B\, dx = 0 \text{ .} \tag{6}$$

Substituting Eqns.(2)-(4) in Eqns. (5) and (6), we can solve for f_0' and f_1' as

$$f_0'(y) = \frac{I_1 - f_1'(y)\, I_4}{I_3} \text{ , and} \tag{7}$$

$$f_1'(y) = \frac{I_2 - \dfrac{I_4\, I_1}{I_3}}{I_5 - \dfrac{I_4\, I_4}{I_3}} \text{ .} \tag{8}$$

The integrals I_1 to I_5 are given by the following equations.

$$I_1 = \int_0^W \alpha\, E_s\, T\, dx \text{ , } \quad I_2 = \int_0^W \alpha\, E_s\, T\, x\, dx \text{ , } \quad I_3 = \int_0^W E_s\, dx \text{ ,} \tag{9}$$

$$I_4 = \int_0^W E_s\, x\, dx \text{ , and } \quad I_5 = \int_0^W E_s\, x^2\, dx \text{ .}$$

For an elastic material with temperature independent properties, the above equations can be simplified to,

$$\sigma_{yy,th} = -E\,\alpha\,T + \frac{1}{W}\int_0^W E\,\alpha\,T\,dx + \frac{12x}{W^3}\int_0^W E\,\alpha\,T\,x\,dx \tag{10}$$

for an asymmetric temperature distribution. Equation (10) is identical to the expressions derived by Boley and Weiner [17] and Timoshenko and Goodier [18].

Using Eqns. (8) and (9), $\varepsilon_{yy,t}$, $\varepsilon_{yy,m}$, and $\sigma_{yy,th}$ due to arbitrary temperature gradients across a plate can be calculated for non-linear materials. In addition, this procedure can also be used for materials with temperature-dependent properties. A FORTRAN code was developed based on the above equations such that the temperature dependency of α, and the tension and compression stress-strain behavior can be input in tabular form. The temperature distribution could also be input in tabular form for ease of use with results from finite element or rigorous thermal analysis of components.

The non-linear stress-strain behavior necessitates the use of an iterative scheme to predict the thermal stresses. The analysis is initiated assuming elastic behavior ($E=E_e$) and using Eqn. (10) to obtain the elastic strain distribution. Knowing the elastic strain distribution, and the current E_s, T and α at a given location, the five integrals I_1-I_5 in Eqn. (9) are calculated. The new total and mechanical strain distribution can be determined knowing the integrals I_i , and using Eqns. (2), (3), (7) and (8). If the difference between the current and previous strains at specified locations is not within ±0.05%, the current solution replaces the previous strain distribution and the analysis is repeated to calculate the next strain distribution. This iterative procedure is repeated until convergence (±0.05%) is achieved. During this study, the Chebyshev integration scheme [19] was used for the numerical integration of the integrals I_1-I_5.

IV. Verification of Analytical Procedure

The accuracy of the above analytical procedure was verified by comparing the predictions with the results from finite element analysis. The temperature distribution used for the verification of the analytical procedure discussed above is shown in Fig. 8. The magnitude of the temperature and the temperature gradient shown in Fig. 8 was based on the temperature distribution expected under service conditions as discussed later. The width of the plate, W was assumed equal to 128 mm based on the average width of CMC flaps. Using 8-node quadrilateral elements, the finite element analysis was conducted for plates with H/W = 2 and 10. The finite element code ABAQUS [20] was used for the analysis. The properties for Nicalon/Al_2O_3 and N610/AS given in Figs. 3-5 were used for the analysis. The stress-strain behavior was assumed to change linearly between room temperature and 1000°C. More accurate analysis could be conducted using the stress-strain data at intermediate temperatures if available.

Figure 9 compares the finite element results with the predictions using the analytical procedure described earlier. The predictions correlate well with the finite element results across the entire width of the specimen. The difference between the finite element results and the predictions from this study was within ±3.4 and ±1.0% for Nicalon/Al_2O_3 and N610/AS, respectively. The maximum stress at the edge and the center is about 238 and -231 MPa, respectively, which corresponds to about 70-110% of the ultimate strength depending on the CMC system. Hence, the thermal stresses can be very significant in the CMC flaps during service. The predicted total strain, ε_{yy} is compared with finite element results in Fig. 10 for N610/AS and Nicalon/Al_2O_3. The total strain, ε_{yy} is constant across the width of the flap. The difference between the prediction and the finite element result is within ±0.5%. The excellent correlation between the predictions and the finite element results validates the accuracy of the proposed non-linear analytical procedure.

V. Results and Discussion

The proposed non-linear analysis tool was used to predict the response of the four candidate CMC systems to various loading conditions. The predictions and the finite element results are used to discuss the following issues: (1) the significance of using the non-linear analysis to predict the thermal stresses, (2) stresses in the candidate CMC systems due to the estimated temperature distribution, (3) potential buckling of the CMC flaps due to compressive stresses, (4) behavior of small flaws in the presence of tensile stresses along the edges of the plate, and (5) influence of length of plate on the predicted stress distribution in the CMC flap.

(1) Non-Linear Analysis With Temperature Dependent Properties

Simple elastic analysis using Eqn. (10) could be used to estimate the stresses due to temperature gradients. Figure 11 compares the predictions for Nicalon/Al_2O_3 using elastic properties and temperature-dependent non-linear properties corresponding to the temperature distribution shown in Fig. 8. The elastic analysis grossly overestimates the tensile stresses at the edge by ≈ 63% while the compressive stress at the center is within 3% of the non-linear results. Hence, analysis using non-linear properties is essential to accurately predict the stress state in CMC which exhibit significant non-linear behavior.

The magnitude and shape of the stress distribution also depend on the variations in the temperature distribution. Figure 12(a) shows two types of temperature distributions used to evaluate the influence of the shape of the distribution. The difference between the maximum and minimum temperature is the same for both the distributions, but the solid line corresponds to a weaker temperature gradient. The predicted stress distributions for Nicalon/Al_2O_3 corresponding to the two temperature distributions are shown in Fig. 11(b). The narrow temperature distribution resulted in higher compressive stresses and lower tensile stresses along the edge of the flap. Note that all the thermal stress distributions discussed in this paper satisfy the load and moment equilibrium conditions given Eqns. (5) and (6). The predictions shown in Fig. 12 indicate that the thermal stress distribution is extremely sensitive to the temperature distribution. Hence, reliable predictions of thermal stresses require an accurate determination of the temperature distribution experienced by the CMC components.

(2) Stresses Due to Expected Temperature Distribution in CMC Flaps

The expected temperature distribution in a CMC divergent flap during an afterburner operation is shown in Fig. 13 [21]. The temperature distribution is symmetric with a maximum temperature of ≈ 810°C and minimum temperature of ≈ 79°C. The temperature distribution was obtained [21] from a 3-dimensional thermal finite element analysis of the engine components. The material properties of N610/AS was used for the finite element analysis. During service, the temperature distributions are expected to be dependent on the CMC systems because of the inherent differences in their thermal properties as shown in Fig. 3. Due to lack of additional data, the temperature distribution shown in Fig. 13 was assumed to act on all the CMC systems. The distribution shown in Fig. 13 corresponds to the maximum difference between the temperatures at the center and edge of the plate, i.e. the maximum temperature gradient expected during service. The corresponding thermal stress distribution was predicted for the four CMC systems and plotted in Fig. 14.

The maximum tensile stress at the edge of the plate ranges from 104 to 233 MPa and the maximum compressive stress ranges from -72 to -168 MPa, depending on the CMC system. The oxide/oxide CMC (N610/AS) has the highest stresses while Nicalon/C has the lowest stresses. Nicalon/Al_2O_3 does not experience the maximum tensile stresses despite its high elastic modulus (see Table II). The low stresses in Nicalon/Al_2O_3 can be attributed to the low plastic modulus, which is ≈ $1/6^{th}$ of the elastic modulus. In contrast, the plastic modulus of

N610/AS is significantly higher than that of the other CMC systems. Hence, N610/AS exhibits the highest thermal stresses.

The stress distributions shown in Fig. 14 correspond to the specific temperature distribution in Fig. 13. During various stages of engine operation, the temperature gradients in the CMC flaps will be cyclic such that the difference between the maximum and minimum temperatures varies over a wide range. Consequently, the CMC component will be subjected to fatigue loading with thermal stresses as shown in Fig. 14. Thus, the survivability of the CMC component can be evaluated by comparing the thermal stresses with proportional limit, tensile strength, and tensile fatigue limit of the composite. Figure 15 shows the ratio of the thermal stress at the edge to the tensile strength ($\sigma_{yy,th}/\sigma_u$), ratio of thermal stress at the edge to the fatigue limit ($\sigma_{yy,th}/\sigma_f$), and ratio of thermal stress at the edge to the proportional limit ($\sigma_{yy,th}/\sigma_{PL}$). Since the temperature at the edge was 79°C, σ_u, σ_f, and σ_{PL} obtained [11,12] at room temperature was used (see Table II) to calculate the ratios in Fig. 15. The predictions show that N610/AS could potentially fail because $\sigma_{yy,th}/\sigma_u$ and $\sigma_{yy,th}/\sigma_f > 1$ at the edge. For the other CMC systems, $\sigma_{yy,th}/\sigma_u$ and $\sigma_{yy,th}/\sigma_f$ at the edge range from 45% to 80%. For all the CMC systems the thermal stress at the edge, $\sigma_{yy,th}$ was significantly higher than the proportional limit, σ_{PL}. This implies that matrix cracks will occur at the edges of all the CMC flaps. During service, the CMC flaps are expected to be subjected to additional stresses due to constrained deformation of the flap, mechanical loading, etc. Hence, the combination of the mechanical and thermal stresses could result in total stresses close to the fatigue limit or ultimate strength of the composite.

As shown in Fig. 14, the thermal stresses in Nicalon/Al_2O_3 are lower than that in N610/AS. But the mechanical strain in Nicalon/Al_2O_3 is equal to or larger than that in N610/AS. Figure 15 also shows that $\sigma_{yy,th}/\sigma_{PL}$ for Nicalon/Al_2O_3 is significantly higher than that in N610/AS. Thus Nicalon/Al_2O_3 can be expected to exhibit larger amounts of cracking leading to environmentally induced degradation of the composite. Recently, Staehler et al. [22] showed that, after an engine test, Nicalon/Al_2O_3 exhibited significant strength degradation as compared to the negligible strength loss of the other CMC systems. Note that the continual degradation of the ultimate strength increases the ratio $\sigma_{yy,th}/\sigma_u$ to ≈ 1.0 implying potential failure of the component. This highlights the need to characterize the time-dependent change in residual strength of the CMC.

As discussed above, the proposed analytical procedure predicts very high stresses in some CMC components subjected to temperature gradients. Experimental verification of the analysis is necessary to determine the applicability of the procedure to screen materials for use in such applications. The development of an unique test system and the verification of the predictions of stresses/strains due to temperature gradients in CMC sub-components is described in Ref. [23].

(3) Buckling Due to Compressive Stresses

Figure 14 shows that the CMC flap could be subjected to compressive stresses ranging from -72 to -168 MPa. Such high compressive stresses could result in buckling of the flap. For an elastic column with hinges at both ends, the critical buckling stress, $\sigma_{b,cr}$ is given by,

$$\sigma_{b,cr} = \frac{\pi^2 E_e}{12\left(\frac{H}{B}\right)^2} \qquad (11)$$

in which E_e = Elastic modulus, H = height of column, B = thickness, and H/B = slenderness ratio. For typical CMC flaps, B ≈ 2.5 mm and H/B ≈ 100. Hence, $\sigma_{b,cr}$ ranges from 5.5 to 14.8 MPa for the candidate CMC systems. Equation 11 is not "exactly" valid for a column subjected to the stress distribution shown in Fig. 14, but the calculation shows that the compressive stresses in the central region of the flap could be significantly higher than the critical buckling load. The CMC flaps are designed to be held in place using rails with a gap of ≈ 1 mm between the rails and the flap. Since the compressive stresses could exceed the critical buckling stress, the flap can be expected to bend due to temperature gradients, as shown in Ref. [23]. If the resulting deformation of the flap is restrained by the rails, additional stresses will be introduced in the flap. More rigorous analysis and detailed experiments are required to verify this potential deformation mode [23].

(4) Small Flaws in the Region of Tensile Stresses

The [0/90] type fiber architecture in the four CMC systems and the fabrication process used to manufacture the CMC flaps could result in the existence of small unbridged flaws (≈ 2 mm) along the edges of the CMC flaps. The thermal stress intensity factor, $K_{I,th}$ due to the non-uniform stress distribution shown in Fig. 13 can be calculated using the weight function method given by,

$$K_{I,th}(a) = \int_0^a \sigma_{yy,th}(x)\, h(x,a)\, dx \ , \qquad (12)$$

in which $K_{I,th}$ = mode I stress intensity factor, a = crack length from the edge, $\sigma_{yy,th}(x)$ = thermal stress distribution, and h(x,a) = weight function. The weight function for a single edge cracked geometry [24,25] was used to calculate $K_{I,th}$ as a function of crack length as shown in Figs. 16(a) and 16(b).

The high stresses shown in Fig. 14 results in correspondingly high values of $K_{I,th}$. $K_{I,th}$ reaches a maximum at ≈ 20 mm followed by a continuous decrease consistent with the sudden decrease in thermal stresses from tensile to compressive as seen in Fig. 13. This implies that a crack initiating at the edge of the plate will propagate straight into the plate and reach arrest conditions when $K_{I,th}$ becomes very low close to the center of the plate. Hence, crack initiation at the edge may not result in a totally fractured component. Figure 16(b) shows $K_{I,th}$ predicted for very short crack lengths. For flaws of the order of 2 mm, $K_{I,th}$ varies from 9 MPa$\sqrt{m}$ for Nicalon/C to 20 MPa$\sqrt{m}$ for N610/AS. Experiments conducted at room temperature indicate that the fracture toughness, K_{If} , of the four CMC systems varies from 15-28 MPa$\sqrt{m}$ [26,27]. Hence, small flaws or defects present in the CMC flaps along the edges could lead to crack growth or fracture under repeated thermal loading with temperature gradients similar to that shown in Fig. 13. Since, the driving force for crack growth is the temperature gradient, crack growth will cease when the temperature gradient vanishes.

(5) Influence of H/W on Predicted Thermal Stresses

The analytical procedure used during this study was developed for an infinitely long plate. The proposed procedure was verified with finite element analysis conducted for plates with height to width ratio, H/W=10 as shown in Figs. 9 and 10. The CMC flaps targeted for use in engines are typically designed with H/W ≈ 2. Figure 17 compares the stress distribution predicted in N610/AS and Nicalon/Al_2O_3 flaps corresponding to the temperature distribution shown in Fig. 8 for flaps with H/W=2 and 10. The maximum tensile and compressive stresses

in the flap with H/W=2 is within ±1.5% of the stresses in the flap with H/W=10. Hence, thermal stresses and K_I in an actual CMC flap can be expected to be within ±1.5% of the stresses and K_I shown in Figs. 13 and 15, respectively.

V. Conclusions

i. We developed a procedure to determine the stresses due to temperature gradients in a CMC plate. The generalized procedure can be used for asymmetric temperature distributions in a non-linear material with temperature-dependent properties. This analytical tool can be used to design engine components subjected to temperature gradients.

ii. Divergent flaps made of CMC can be expected to experience tensile stresses along the edge which are about 47-110% of the ultimate strength or 55-130% of the fatigue limit. The magnitude of the compressive stresses near the center of the flap are as high as that of the tensile stresses at the edge. Hence, additional analytical and experimental evaluation is required to accurately assess the durability of the CMC components.

iii. For the same temperature distribution, the oxide/oxide CMC N610/AS experiences thermal stresses which exceed the ultimate strength. The thermal stresses are about 80, 75 and 55% of the fatigue limit in Nicalon/Al_2O_3, Nicalon/SiNC and Nicalon/C, respectively. Additional mechanical stresses could easily shorten the life of the CMC components.

iv. Presence of small unbridged flaws (≈ 2 mm) along the edges could lead to crack growth in the CMC systems subjected to cyclic thermal loading with temperature gradients. However, the crack driving force is diminished significantly as the crack grows towards the center of the component.

ACKNOWLEDGMENTS

This research was conducted at Wright Laboratory (WL/MLLN), Materials Directorate, Wright-Patterson Air Force Base, OH 45433-7817. R. John and J.L. Kroupa were supported under on-site contract no: F33615-94-C-5200. L.P. Zawada received partial financial support from Dr. W.S. Coblenz at DARPA under contract no: in-house and order number A565. The authors gratefully acknowledge the assistance of Ms. Jennifer Finch and Mr. Roger Gural in amassing some of the data used in the analysis.

REFERENCES:

1. Integrated High Performance Turbine Technology (IHPTET) Brochure, Edited by C. Lykins and K. Watson, Wright Laboratory (WL/POT), Materials Directorate, Wright-Patterson Air Force Base, OH, 1995.
2. D.M. Dix and J.S. Petty, "Aircraft Engine Technology Gets a Second Wind," *Aerospace America*, 36-39 (1990).
3. Lamicq, P.J. and Jamet, J.F., "Thermostructural CMCs: An Overview of the French Experience," pp. 1-11 in High-Temperature Ceramic-Matrix Composites I: Design, Durability and Performance, Edited by A.G. Evans and R. Naslain, Ceramic Transactions, **57**, American Ceramic Society, Westerville, OH, 1995.
4. R.J. Hill, "The Challenge of Integrated High Performance Turbine Engine Technology (IHPTET)," in Eleventh International Symposium on Air Breathing Engines, Edited by F.S. Billig, American Institute of Aeronautics and Astronautics, 19 September 1993.
5. W.R. Fohey, J.M. Battison, T.A. Nielsen, and S. Hastings, "Ceramic Composite Turbine Engine Component Evaluation," in Ceramic Engineering & Science Proceedings, Edited by G.N. Pfendt, American Ceramic Society, Westerville, OH, July-August 1995.
6. H.F. Nied, "Thermal Shock in an Edge Cracked Plate Subjected to Uniform Surface Heating," *Eng. Frac. Mech.*, **26** [2], 239-46 (1987).

7. G. Yagawa, M. Ichimaya, and Y. Ando, "Theoretical and Experimental Analysis of Semi-Elliptical Cracks Subject to Thermal Shock"; pp. 381-98 in Fracture Mechanics, ASTM STP 677, Edited by C.W. Smith, American Society for Testing and Materials, Philadelphia, PA, 1979.
8. R. John, G.A. Hartman, and J.P. Gallagher, "Crack Growth Induced by Thermal-mechanical Loading," *Exp. Mech.*, **32** [2], 102-08 (1992).
9. A.-Y. Kuo and R. John, "Analytical and Experimental Treatment of a Single Edge-Crack Plate Subjected to Arbitrary Point Heat Sources"; pp. 342-66 in Fracture Mechanics: Twenty-Second Symposium (Volume 1), ASTM STP 1131, Edited by H.A. Ernst, A. Saxena, and D.L., McDowell, American Society for Testing and Materials, Philadelphia, PA, 1992.
10. K. Kokini and M.A. Long, "Transient and Thermal Fracture of Cracked Plates," *Exp. Mech.*, **28** [4], 373-81 (1988).
11. L.P. Zawada and S.S. Lee, "Mechanical Behavior of CMCs For Flaps and Seals," Proceedings of ARPA Ceramic Technology Insertion Program (ACTIP) Annual Review, Annapolis, MD, August 15-16, 1994.
12. L.P. Zawada, "Mechanical Behavior of CMCs For Flaps and Seals," Technical Report, Wright Laboratory, Materials Directorate, Wright-Patterson Air Force Base, OH, To be published, 1997.
13. C. Farral, "F110 Divergent Flap Inserts and Divergent Seals For CMC Candidate Materials," Proceedings of ARPA Ceramic Technology Insertion Program (ACTIP) Annual Review, Annapolis, MD, August 15-16, 1994.
14. D. Carper, "Gen4(N610/AS) Mechanical/Thermal/Physical Properties," unpublished results, GE Aircraft Engines, Cincinnati, OH, January 1995.
15. P. Ladeveze, "Modeling and Simulation of the Mechanical Behavior of CMCs," pp. 53-63 in High-Temperature Ceramic-Matrix Composites I: Design, Durability and Performance, Edited by A.G. Evans and R. Naslain, Ceramic Transactions, **57**, American Ceramic Society, Westerville, OH, 1995.
16. T.R. Barnett and H.S. Starrett, "Room and Elevated Temperature Mechanical and Thermal Properties of Corning Nicalon/CAS," WRDC-TR-90-4131, Materials Directorate, Wright Laboratory, Wright-Patterson Air Force Base, OH, 1990.
17. B.A. Boley and J.H. Weiner, Theory of Thermal Stresses, John Wiley & Sons, Inc., New York, NY, 1960.
18. S.P. Timoshenko and J.N. Goodier, Theory of Elasticity, McGraw-Hill Book Company, New York, NY, 1970.
19. M. Abramowitz and I.A. Stegun, Handbook of Mathematical Functions, Dover Publications, Inc., New York, NY, 1972.
20. ABAQUS Version 5.5, Hibbit, Karlsson & Sorensen, Inc., Pawtucket, RI, 1995.
21. J. Lee, unpublished results, GE Aircraft Engines, Cincinnati, OH, January 1995.
22. J. M. Staehler and L.P. Zawada, "Retained Ultimate Strength of Engine Tested CMC Flaps," To be submitted for publication, 1997.
23. R. John, L.P. Zawada, A.F. Lackey, and J. M. Staehler, "Stresses Due to Temperature Gradients Along the Width of a Ceramic Matrix Composite Plate" To be submitted for publication, 1997.
24. A.C. Kaya and F. Eredogan, "Stress Intensity Factors and COD in an Orthotropic Strip," *Int. J. of Frac.*, **16** , 171-90 (1980).
25. H. Tada, The Stress Analysis of Cracks Handbook, Paris Productions Inc., St. Louis, MO, USA, 1985.
26. V. Kramb and R. John, "Fracture Toughness of Advanced CMC Materials"; unpublished results, University of Dayton Research Institute, Dayton, OH, 1995.
27. A.S. Fareed, B. Sonuparlak, P.A. Craig, and J.E. Garnier, "Effect of Sustained High Temperature Exposure on the Mechanical Properties of Nicalon/Al_2O_3 Composites," pp. 804-18 in Ceramic Engineering & Science Proceedings, **13** [9-10], American Ceramic Society, Westerville, OH, 1992.

Table I. Candidate CMC Systems

Material	Fiber	Matrix	Fiber Architecture	Process	Material Supplier
N610/AS	Nextel610™	Alumino-silicate (AS)	8HSW*	Polymer Pyrolysis	General Electric
Nicalon/ Al_2O_3	Nicalon™	Al_2O_3 (+ SiC_p)	8HSW	DIMOX	Dupont Lanxide
Nicalon/ C	Nicalon™	C	8HSW	CVI	Hitco Technologies
Nicalon/ SiNC	Nicalon™	SiNC	8HSW	Polymer Pyrolysis	Kaiser Ceramics

Note: * 8 Harness Satin Weave

Table II. Bilinear Stress-Strain Properties of the Candidate CMC Systems

CMC System	Elastic Modulus E_e (GPa)		Plastic Modulus E_p (GPa)		Elastic Strain Limit ε_e (m/m)		Ultimate Strength σ_u (MPa)		Fatigue Limit (10^6 cycles) σ_f (MPa)	Proportional Limit σ_{PL} (MPa)
	23°C	1000°C	23°C	1000°C	23°C	1000°C	23°C	1000°C	23°C	23°C
N610/AS	73	77	58	59	0.00110	0.00110	206	175	170	80
Nicalon/ Al_2O_3	180	160	23.5	32	0.00045	0.00060	196	194	170	81
Nicalon/ C	73	67	42	40	0.00080	0.00080	221	254	185	58
Nicalon/ SiNC	107	101	45	41	0.00080	0.00080	200	216	160	86

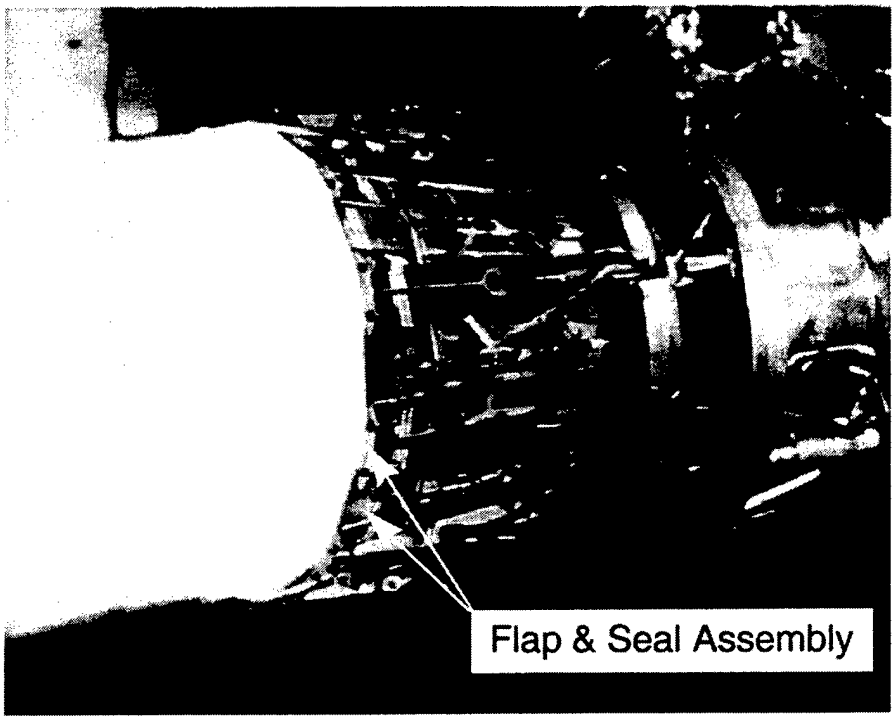
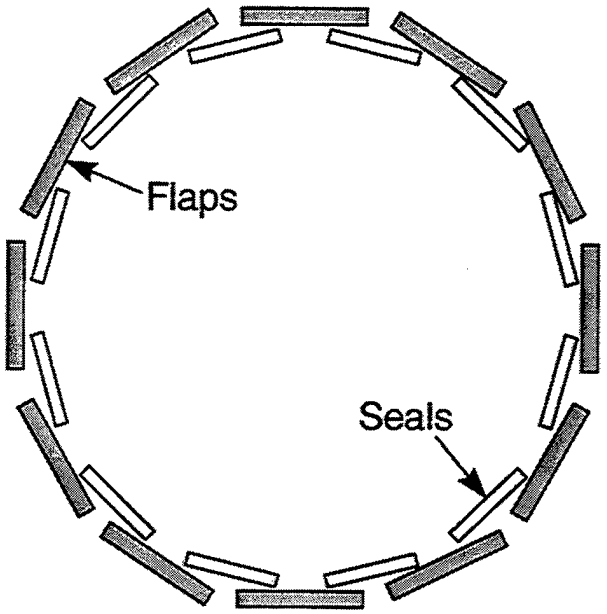
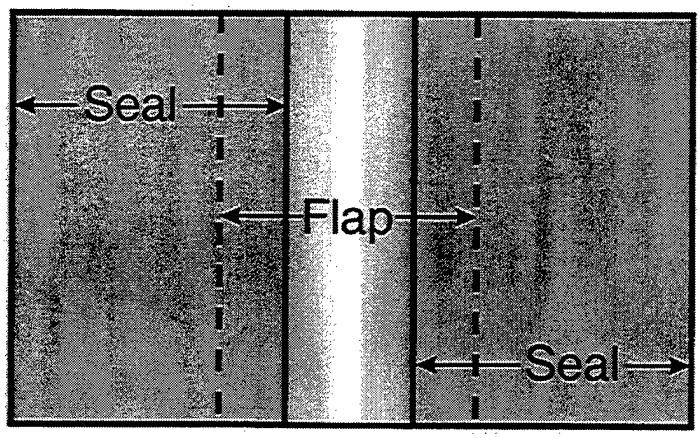


Figure 1. Photograph of a divergent flap and seal assembly in an aerospace engine.



(a)



(b)

Figure 2. (a) Schematic of the flap and seal assembly in the engine, and (b) Planar view highlighting the overlap between the flaps and seals.

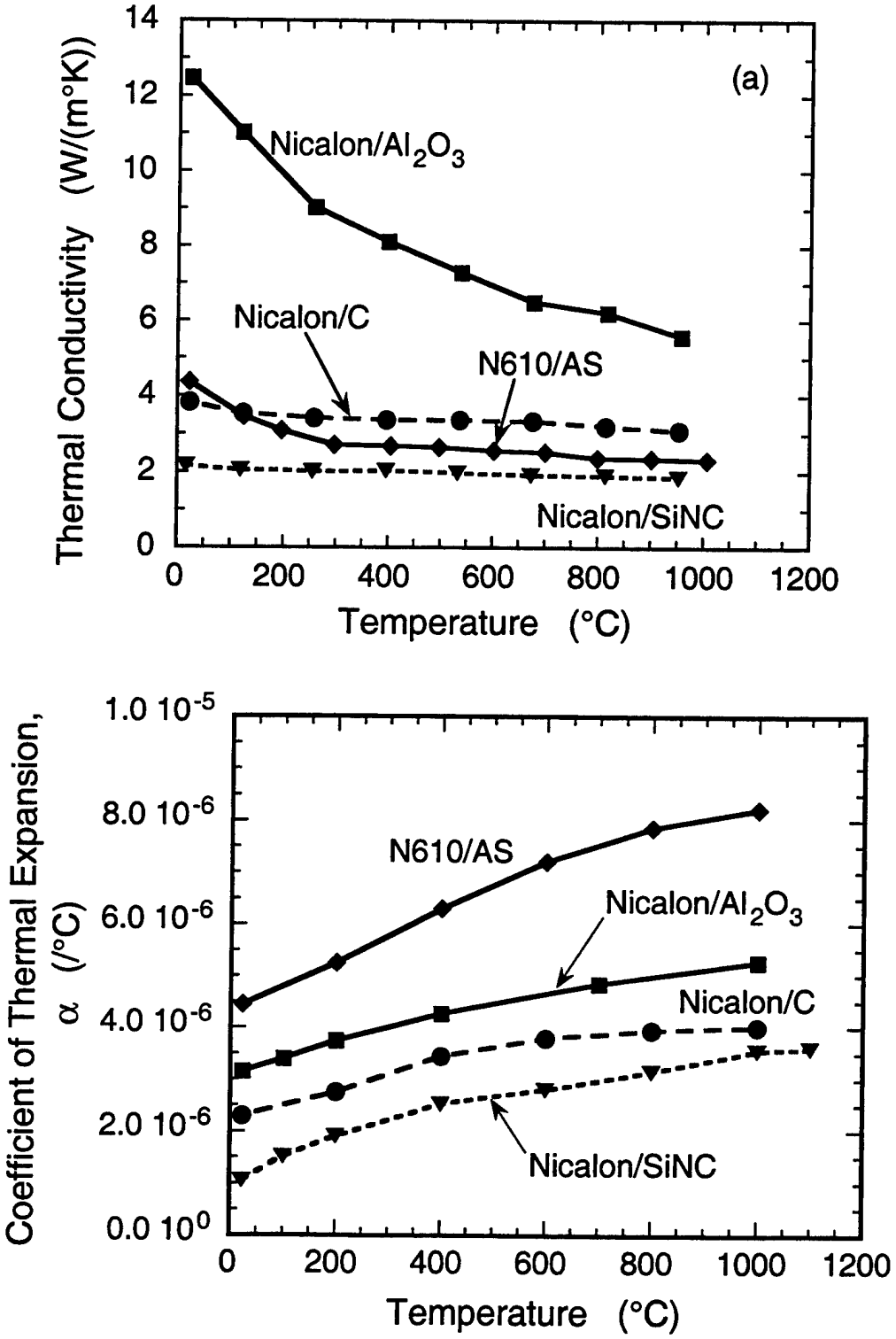


Figure 3. (a) Thermal conductivity, and (b) Coefficient of Thermal Expansion of the candidate CMC systems.

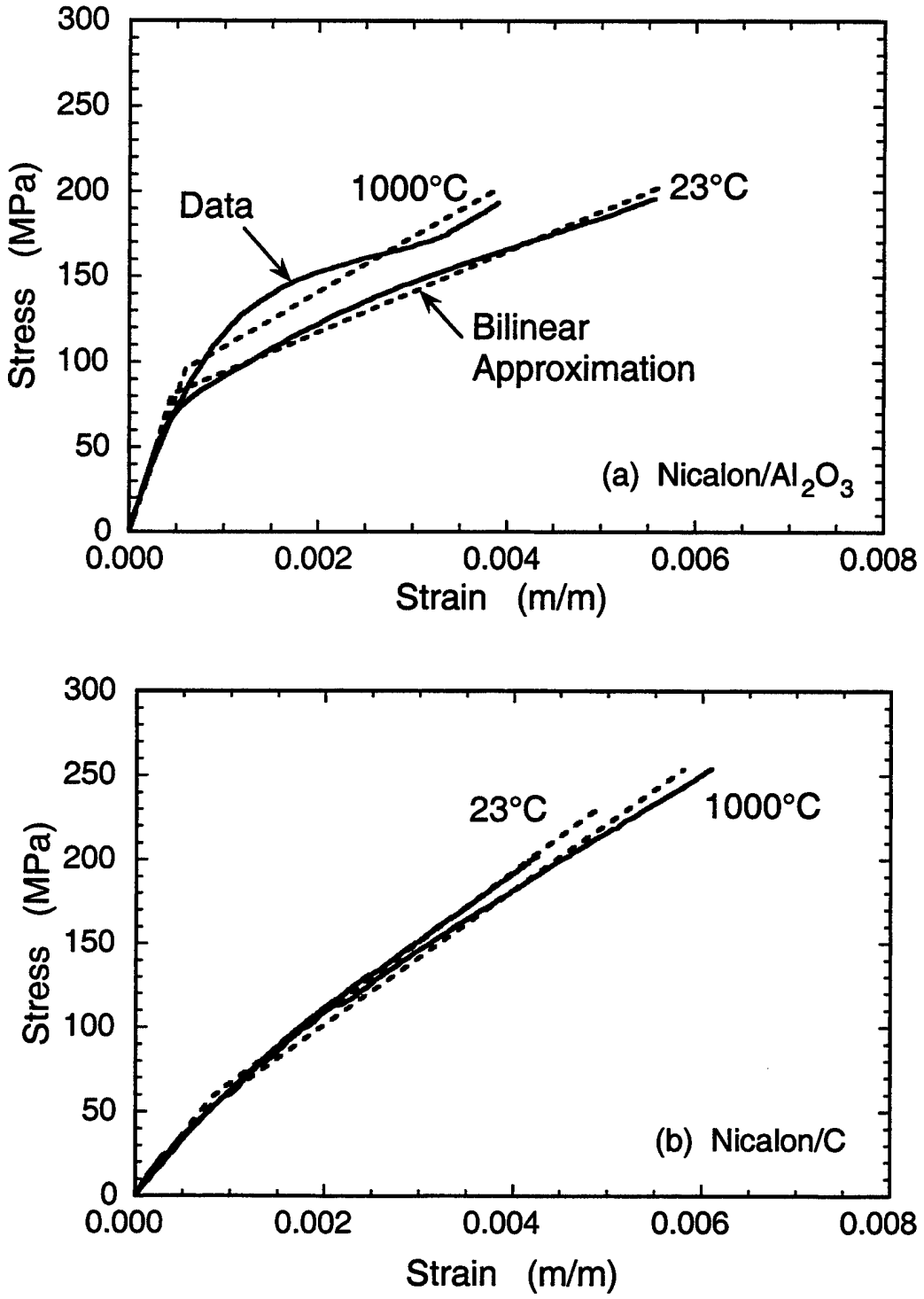


Figure 4. Tensile stress-strain behavior of (a) Nicalon/Al_2O_3 and (b) Nicalon/C systems at room temperature and 1000°C.

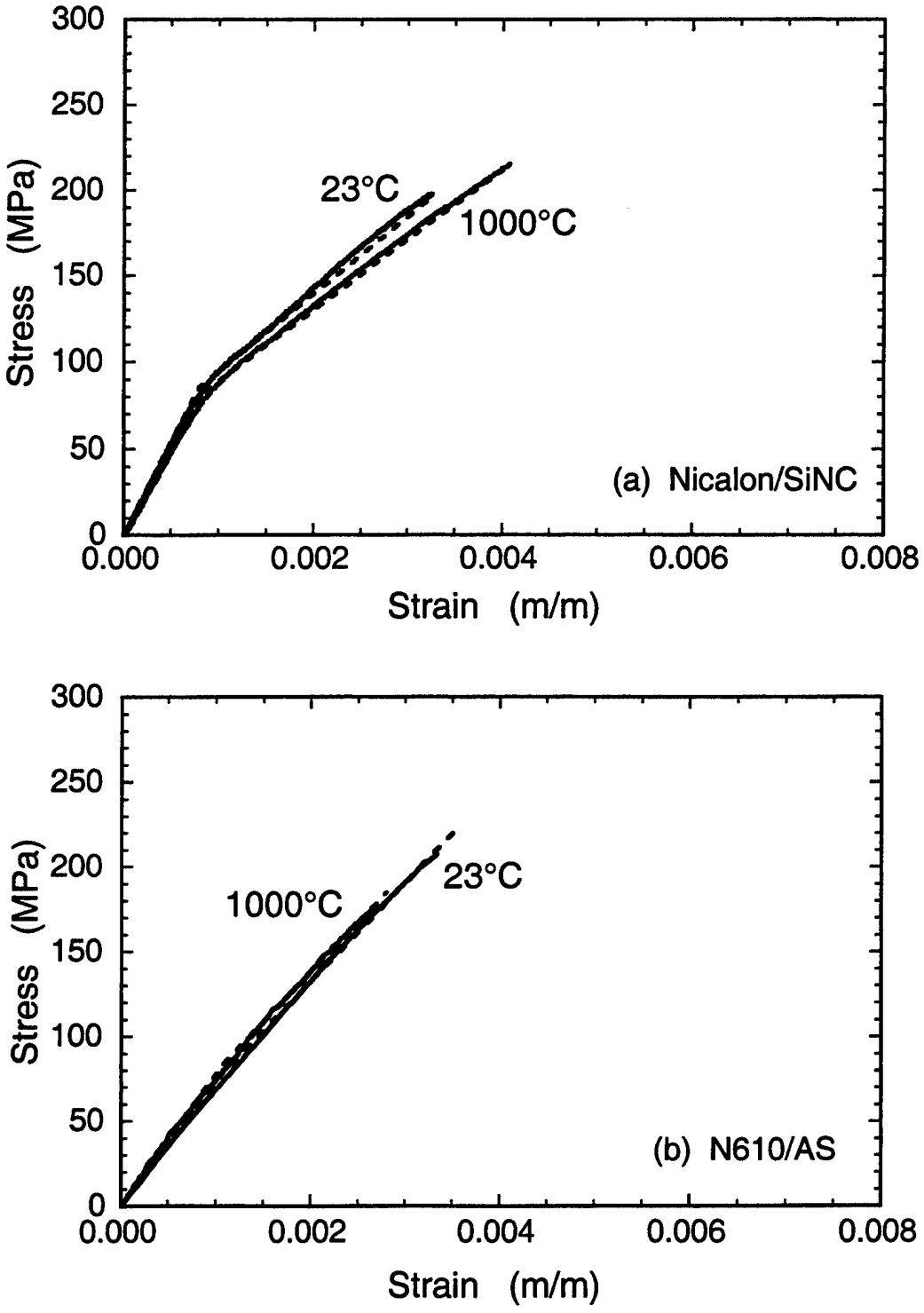


Figure 5. Tensile stress-strain behavior of (a) Nicalon/SiNC and (b) N610/AS systems at room temperature and 1000°C.

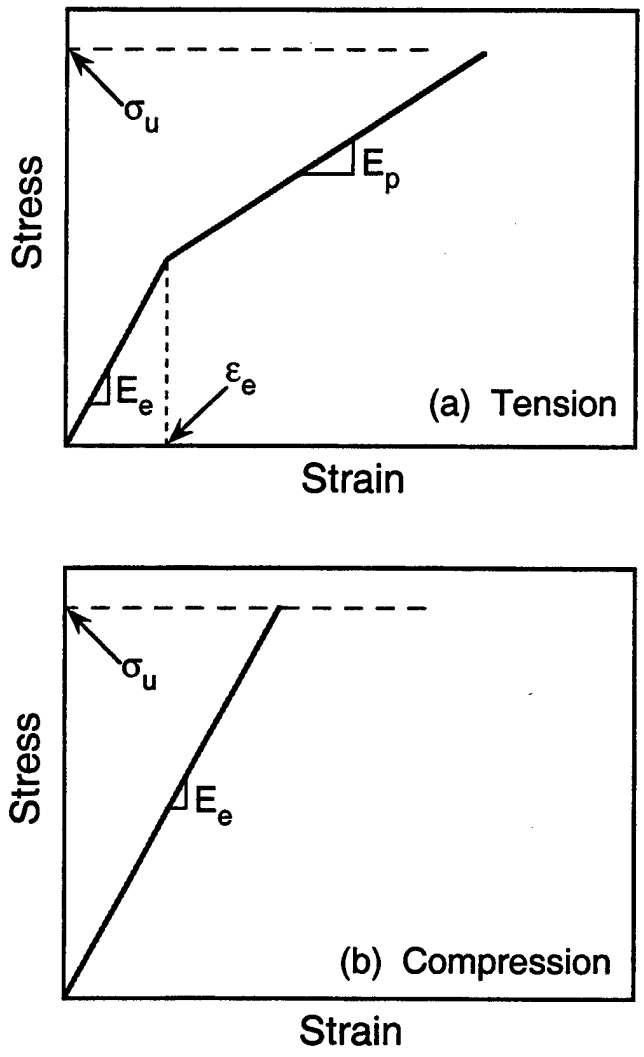


Figure 6. Bi-linear stress-strain response used to simulate the (a) tension and (b) compression stress-strain behavior of the candidate CMC systems.

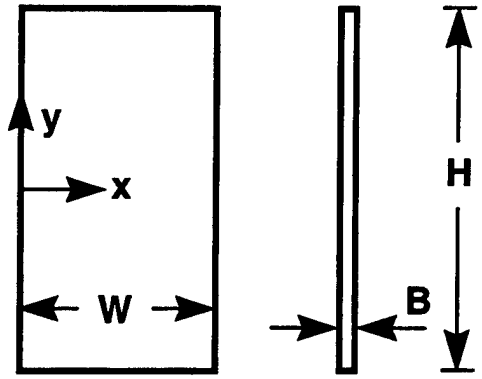


Figure 7. Two-dimensional plate approximation of the CMC flap.

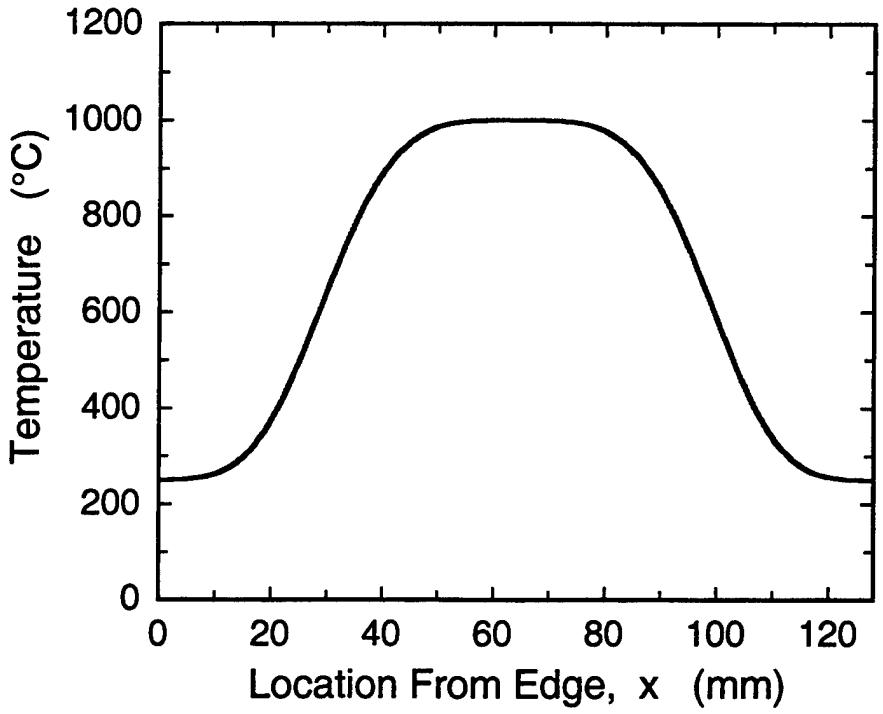


Figure 8. Temperature distribution assumed for verification of the analytical procedure.

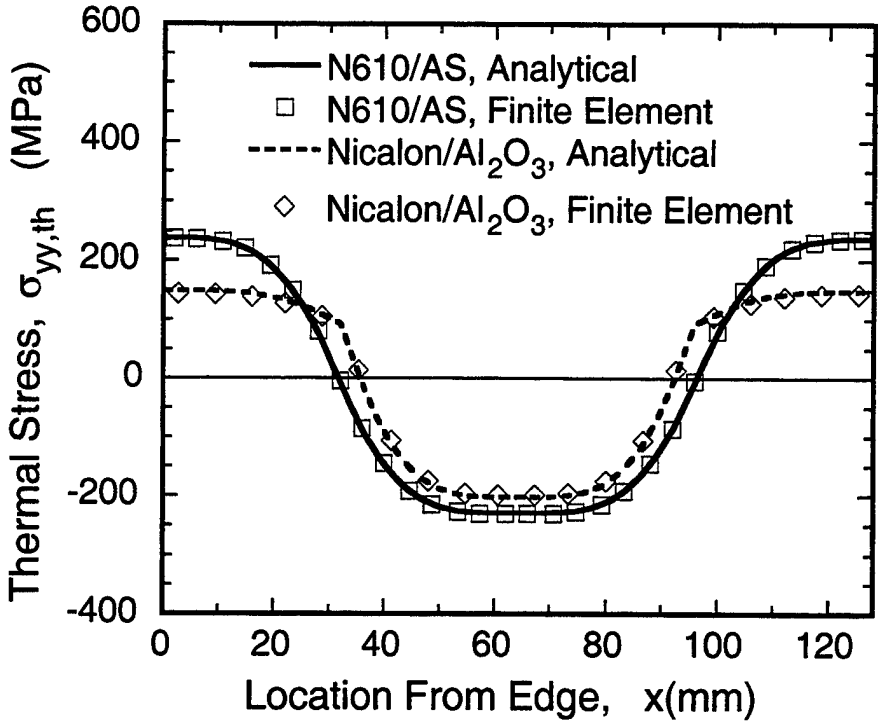


Figure 9. Comparison of stress distribution in Nicalon/Al_2O_3 and N610/AS predicted using Eqn. 4 with that obtained from finite element analysis.

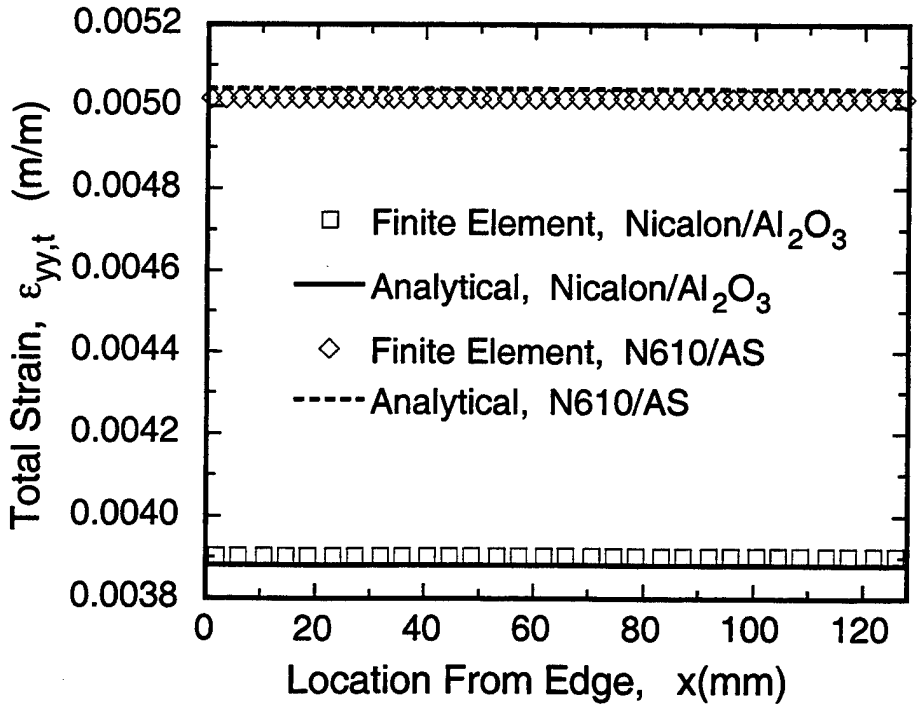


Figure 10. Total strain distribution across the width of Nicalon/Al_2O_3 and N610/AS plates subjected to the temperature distribution shown in Fig. 8.

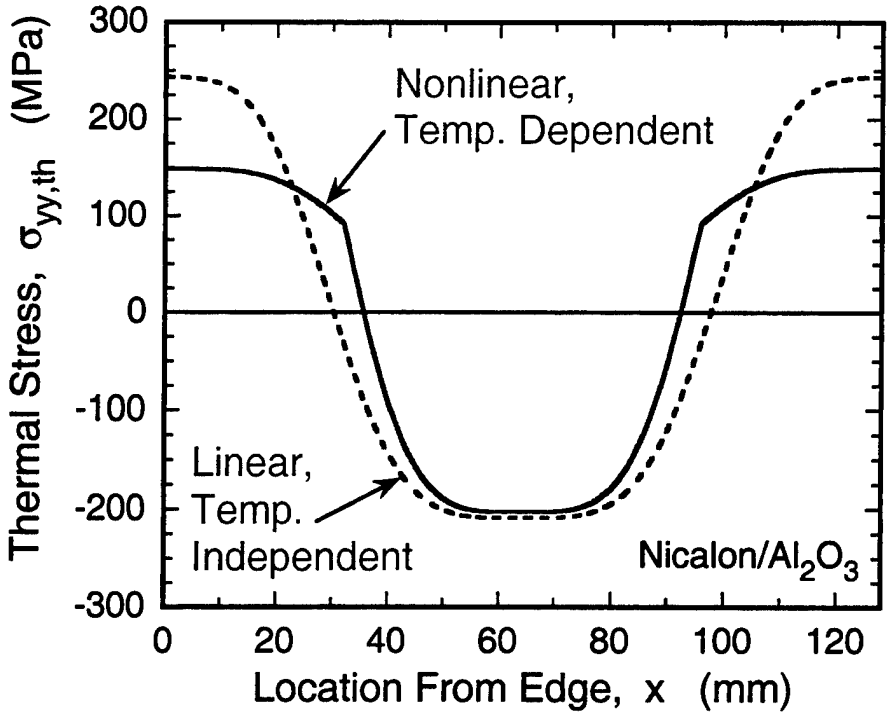


Figure 11. Thermal stress distribution predicted by linear and non-linear analyses for Nicalon/Al_2O_3 subjected to the temperature distribution shown in Fig. 8.

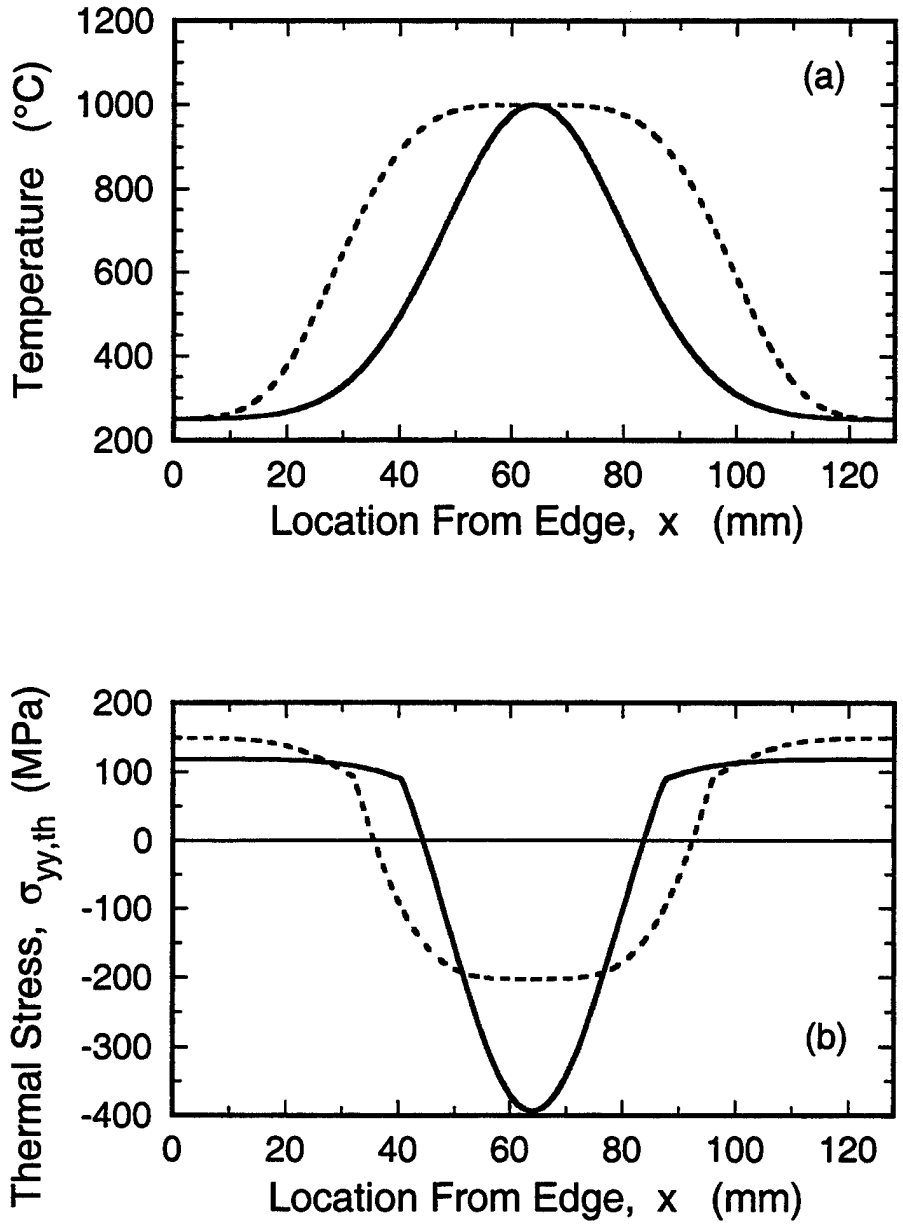


Figure 12. (a) Two types of temperature distributions, and (b) corresponding thermal stress distributions in Nicalon/Al_2O_3.

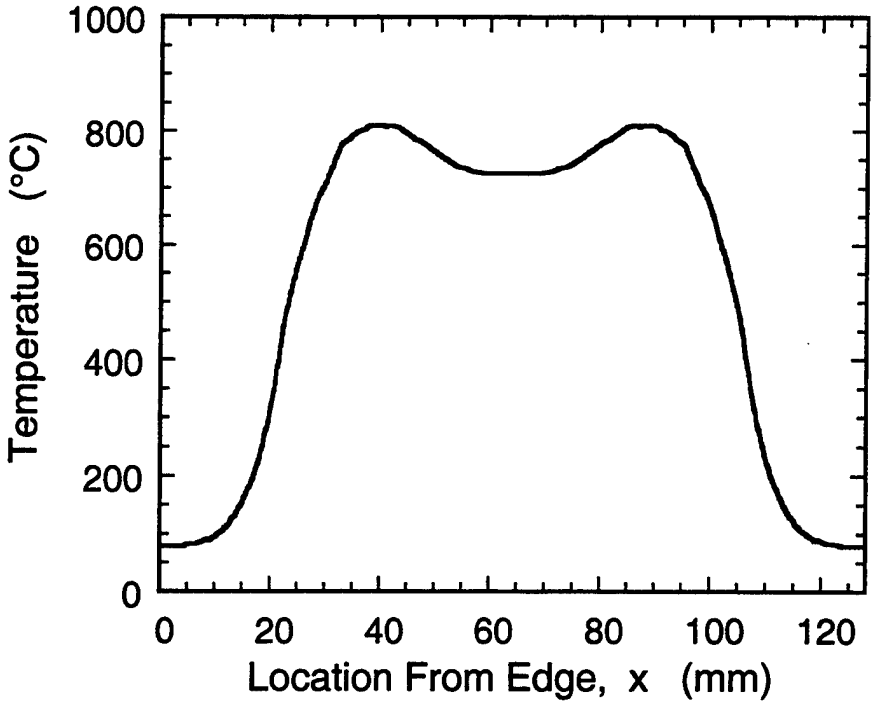


Figure 13. Temperature distribution in a divergent flap as predicted using 3-dimensional thermal analysis [J. Lee].

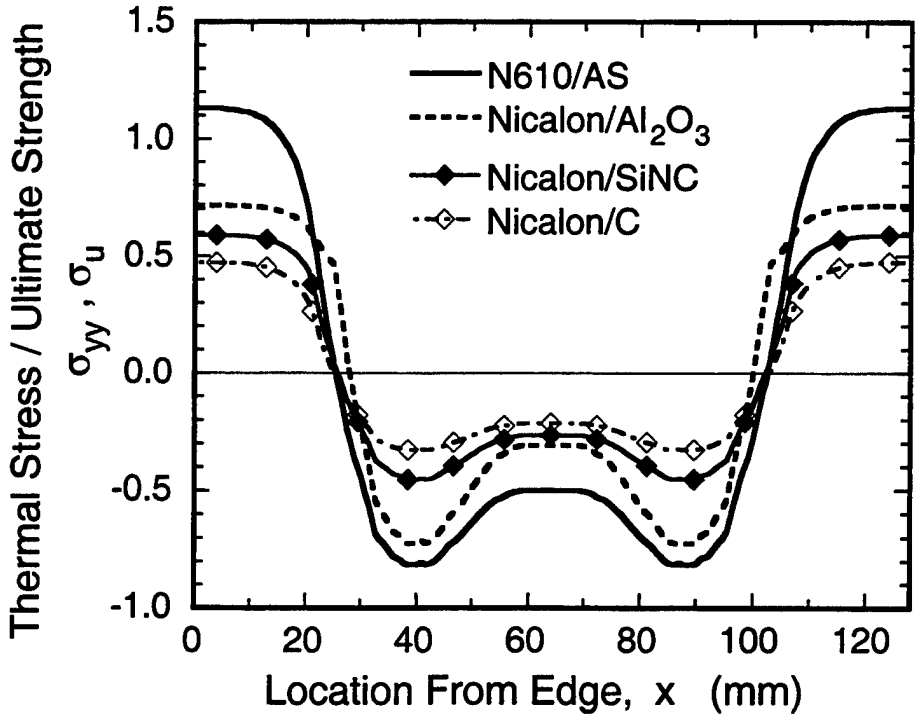


Figure 14. Thermal stress distribution predicted for the candidate CMC systems subjected to the temperature distribution shown in Fig. 12.

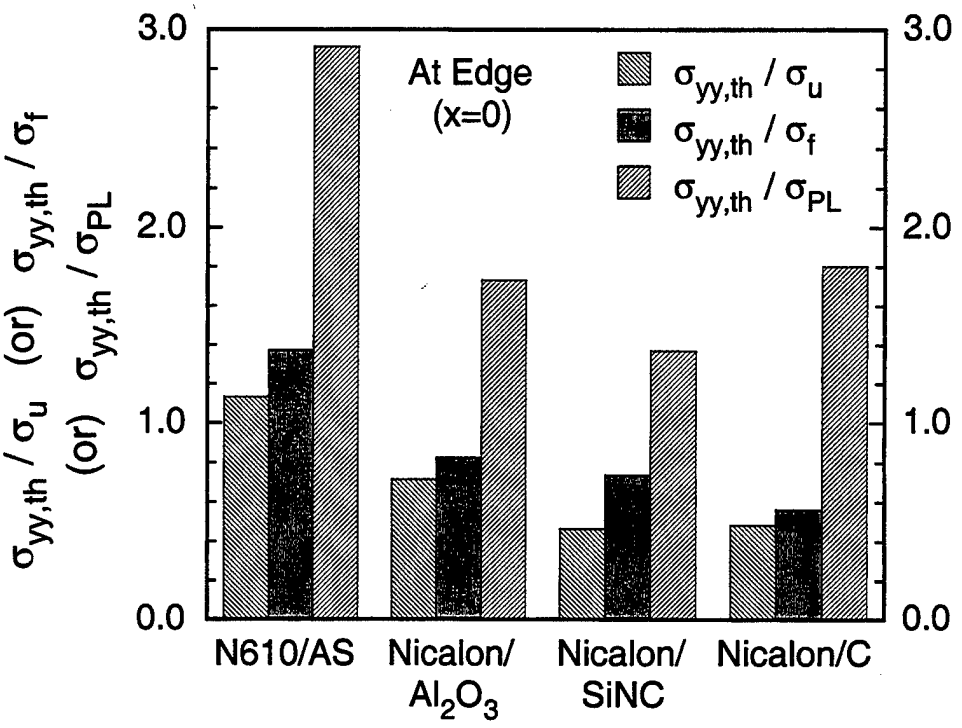


Figure 15. Normalized thermal stresses at the edge of the flaps the candidate CMC systems subjected to the temperature distribution shown in Fig. 12.

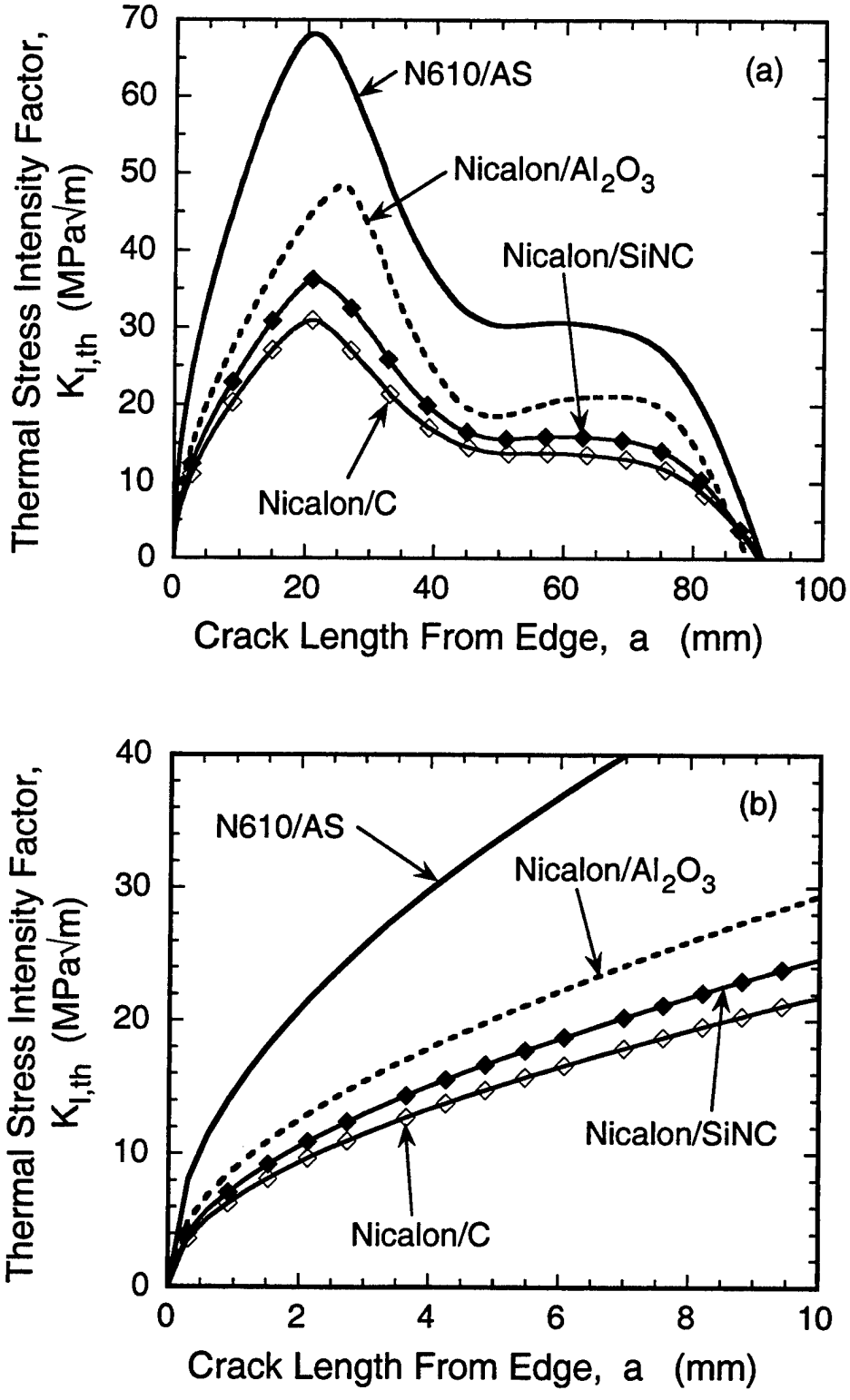


Figure 16. Thermal stress intensity factor versus crack length for the candidate CMC systems subjected to the stress distributions shown in Fig. 12.

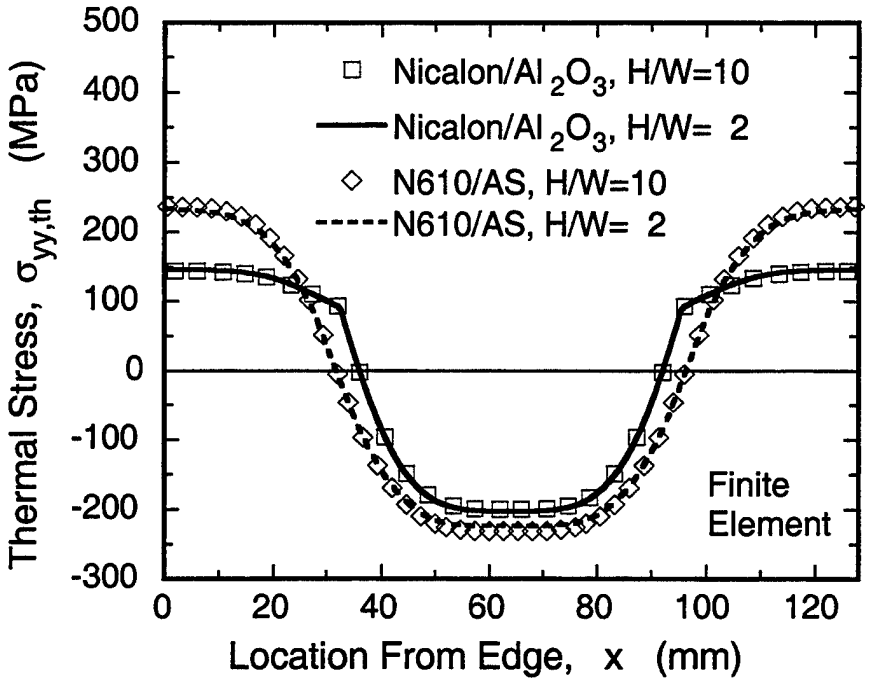


Figure 17. Effect of length of plate on the stress distribution across the width of a Nicalon/Al_2O_3 plate subjected to the temperature distribution shown in Fig. 8.

This page intentionally left blank

Reference: Sunder, R., Porter, J., and Ashbaugh, N.E., "The Effect of Stress Ratio on Fatigue Crack Growth Rate in the Absence of Closure," Int. J. Fatigue, V.9, Supp. No. 1, pp. S211-S221.

The Effect of Stress Ratio on Fatigue Crack Growth Rate in the Absence of Closure

R. Sunder[1], J. Porter[2] and N.E. Ashbaugh[2]

Abstract

A fractographic study[1] was performed on Al-alloy fatigue fracture surfaces produced by programmed load sequences. The load sequences included steps of constant amplitude cycles at three different stress ratios, each step is preceded by a small number of high amplitude cycles designed to avoid the influence of crack closure and to serve as fractographic markers. The experiments were conducted on different specimen geometries to produce conditions associated with a long crack under *fully elastic* conditions and a short crack in a notched coupon seeing *high local post yield* stress conditions. Crack sizes, covered in the study, ranged from 0.02 to 12 mm and growth rates ranged from $2x10^{-7}$ to $4x10^{-5}$ mm/cycle. Fractographic evidence from the study suggests that crack growth rate can vary by up to a factor of five with applied stress ratio change from 0.64 to 0.73. In the case of the long crack, the effect is less noticeable or totally absent. In the case of naturally initiating notch root cracks, the effect is more pronounced at higher stress level and lower crack growth rate.

Keywords

Fractography, fatigue crack growth, stress ratio, crack closure, small cracks.

Introduction

Load history effects in metal fatigue under random service loading are closely linked with mean stress effects in crack formation and stress ratio effects in fatigue crack growth. Most predictive models would indicate that in the absence of mean stress or stress ratio effects, cumulative fatigue damage will be load sequence (history) insensitive. In general, stress ratio effects in fatigue crack growth have been associated with fatigue crack closure [1]. Crack growth rate (da/dN) equations also account for the rapid increase in da/dN as K_{max} approaches K_{1c} [2,3].

Several mechanisms may be responsible for the stress ratio effect on fatigue crack growth rate [4,5,6]. Of these, fatigue crack closure has emerged as by the far most 'popular' one to explain the effect in terms of truncation of applied stress intensity range, DK, to an effective range, DK_{eff}. This reduction in DK is a consequence of closure in the wake of the crack, effectively working like a wedge, that does not allow stress intensity to drop below a certain level. The closure of the fatigue crack can be attributed to one or more mechanisms - crack tip plasticity, roughness, asperities, oxide layer formation, etc. [1,7]. The first three of these are load history sensitive, making crack closure a widely accepted phenomenon to model load interaction effects in fatigue life prediction for random, service load conditions [3]. Oxide layer formation can have a major influence on stress ratio effects on threshold stress intensity, DK_{th}.

---

[1]BiSS Research, 99, 14A Cross, Malleswaram, Bangalore 560 003, India

[2]University of Dayton Research Institute, 300 College Park, Dayton, OH 45469 , USA

[1]This investigation was conducted at the Materials Directorate of Wright Laboratory at Wright-Patterson Air Force Base, OH, USA, under contract F33615-94-C-5200.

The objective of this study was to fractographically examine the effect of stress ratio on crack growth rate in the absence of fatigue crack closure. For ease of measurements, a 'fractography friendly' Al-alloy 2014-T6511 with an average grain size of approximately 15 mm was chosen for the study. The tests were conducted on different specimen types to cover a wide range of stress levels.

Experimental Procedure

Two different coupons were tested. One was a 5 mm thick, 45 mm wide single edge tension, SE(T), coupon. The other was a specially designed 10 mm thick, 23 mm wide notched SE(T) coupon with a K_t = 2.5. Fig. 1 shows drawings of the two specimens used in testing.

The load sequence used in the experiments appears in Fig. 2. Each block consists of three steps of 2000 load cycles, each step is preceded by 10 marker cycles. The stress range for each of the steps is the same. Step #1 is at applied stress ratio, R = 0.73, Step #2 at R = 0.69 and Step #3 at R = 0.64. Thus, even at the lowest of these stress ratios, the fatigue crack is unlikely to see any closure. As a further 'insurance' against closure, the marker cycles were applied with a much lower minimum stress, designed to take crack closure stress even lower. Repeated blocks of the sequence described above were applied to the test specimen through to failure. Due to potential backlash in the pin loading arrangement on the notched SE(T) specimen, minimum load in the block for that specimen was increased from 0% to 4.67% of maximum load.

Previous work had suggested that at R = 0, crack closure stress in this material varies between 0% and 50% of S_{max} and depends on net stress levels. S_{max} in the marker cycles is the same as S_{max} during the first step at R = 0.73. This precludes any load interaction effects associated with overloads. Even the cycles at the lowest stress ratio of R = 0.64 see an overload ratio of just 36% due to the markers. Overloads under 50% of baseline loading have generally been found to cause only negligible retardation effects on crack growth.

Approximate calculations of plane strain plastic zone size suggest fatigue crack extension in a single step of 2000 cycles would be under 5% of the plastic zone size due to the preceding markers. This calculation also supports the possibility that plasticity induced retardation effects if any, would apply uniformly to all three steps.

All three sets of marker loads contain ten cycles. This number was selected to ensure discernible marker bands on the fracture surface even at very low crack growth rates of 10^{-5} mm/cycle due to the marker cycles. The step size of 2000 cycles for each of the stress ratios was selected to improve chances of measurable crack extension even at growth rates as low as 10^{-7} mm/cycle. Step size serves as a 'resolution amplifier' in microscopy. At very low growth rates, individual striations may be too fine to be picked up under the microscope. Ref. 8 noted that striation spacings indicating crack growth rate under 10^{-4} mm/cycle have not been observed. However, a band of multiple such striations are more readily identified, when spaced with marker cycles that leave behind their own bands with contrasting morphology.

In the process of ensuring minimum load interaction effects and absence of fatigue crack closure, variation of applied stress ratio was restricted to between 0.64 and 0.73. It was assumed however, that even this interval is wide enough to show any stress ratio effect on crack growth rate.

A total of three tests were conducted. Applied load levels and estimated stress responses are listed in Table 1. The da/dN measurements are shown in Table 2. A plot of these results is shown in Fig. 3. The material constants on the same material from Ref. 9 are given in Table 3. The constants E, s_f, and e_f are Young's modulus, tensile strength and failure strain, respectively. K' and n' are the cyclic strength coefficient and cyclic strain hardening exponent, respectively. For the K levels considered in Table 2, C and m are the coefficient and exponent, respectively, for the Paris crack growth law and K_c is the operational fracture toughness. These constants were used in analysis of inelastic specimen response and fatigue crack growth

analysis. Due to inelastic response, the effective stress ratios in the tests on the notched SE(T) specimens were slightly different from applied stress ratios. When the material yields under tensile loading and subsequent stress reversal are totally elastic, the effective stress ratio will be less than applied stress ratio.

Test 1 was on an SE(T) specimen with an edge crack. A 3 mm saw cut served as the crack initiator. The test was at S_{max} = 100 MPa to simulate long crack fully elastic conditions. Tests 2 and 3 were conducted on a specially designed notched coupon (see Fig. 1 for details) with K_t = 2.5. The purpose of these tests was to simulate the behavior of real engineering components with stress raiser and associated stress gradient. The specimen was designed with a notch enforcing natural crack initiation under conditions of controlled local inelasticity. The maximum applied load (50 kN) in Test 2 was selected to induce notch root yield, with estimated notch root maximum stress reaching 515 MPa compared to a material yield stress of 420 MPa. This maximum load caused limited residual stresses upon unloading, thereby reducing effective stress ratio from 0.73 to 0.72 in Step #1. Test 3 used a higher maximum applied load (75 kN), thereby producing considerable inelastic deformation of the notch root, leading to formation of noticeable residual stresses and associated reduction in effective stress ratio (see Table 1).

Table 1 summarizes the estimated stress response of the test coupon in the three tests. Stress levels for Tests 2 and 3 were estimated as notch surface local stresses after Neuber conversion. The maximum stress varied from 100 to 670 MPa to cover both fully elastic and inelastic loading conditions. As mentioned earlier, subsequent cycling after after initial inelastic deformation produced a purely elastic response. As seen from Table 1 and Fig. 2, the programmed pattern of loading in all three tests was identical, though stress levels varied considerably. A minor difference was the minimum 4.67% tensile load component in the notched coupons to avoid loading pin backlash at zero load. The other difference was in crack initiation. The SE(T) specimen had a saw-cut crack initiator, while the notched coupons saw natural crack initiation.

In all the tests, the specimen was cycled to failure through repeated cycling with the programmed load sequence shown in Fig. 2. After the test, the fracture surface was trimmed for observation on a Leica Cambridge 360FE 0303 Scanning Electron Microscope.

Results & Discussion

Test 1: Long crack under elastic loading

All the fractographs from this test show the fatigue crack growing from right to left. For consistency in measurements, they are all from the mid-thickness region, at least 1 mm from the specimen surfaces.

At crack size of 4.5 mm (DK = 3.6 MPa$\sqrt{m}$), the mid thickness area largely shows uniformly spaced striation bands, that in fact make it difficult to identify the band corresponding to the highest stress ratio (see Fig. 4). Crack growth rate over each of the 2000 cycle steps was estimated to be 1.891×10^{-6} mm/cycle. In Fig. 4, we find crevices along some of the marker bands, indicating the fatigue crack attempted to change direction during the 10 marker cycles. This was not apparent at lower crack growth rates and appears to indicate a point where the preferred plane of crack extension is no longer the same for the marker cycles and those in Steps #1-3.

Fig. 5 shows equally spaced striation bands from all three steps. This fractograph is from a mid-thickness site corresponding to a = 7.8 mm. Towards the left end of the fractograph, we find an increasing contribution of the marker cycles to fatigue crack extension. The marker bands now show a width of their own. The growth rate in each of the 2000 cycle steps is 1.207×10^{-5} mm/cycle, while in the marker cycles, it is 6.03×10^{-4} mm/cycle. These do not differ greatly from the computed values of 1.549×10^{-5} and 4.53×10^{-4} mm/cycle from material constants. However, the marker cycle component is steadily increasing and appears to always

exceed estimates from DK, while da/dN in the 2000 cycle steps is less than estimates. Schijve [10] has observed that due to crack front incompatibility, a crack grown in flat mode at low DK will show accelerated growth rate at high DK, until the new shear plane is established. Conversely when a crack already in the shear plane is forced to grow in flat plane, it will show reduced growth rates until the flat plane is re-established. The striation bands in the middle of the fractograph in Fig. 5 clearly appear to reflect such incompatibility.

The fractograph in Fig. 6 is from a site corresponding to crack length, a = 11.9 mm in the mid-thickness area. Crack growth rate is identical in Steps #1 and #2 (from the right) at 3.55×10^{-5} mm/cycle and somewhat less in Step 3 (2.65×10^{-5}). The growth rate during the marker cycles is 1.9×10^{-3} mm/cycle or 70 times greater than in the smaller cycles. This is in contrast to the 50:1 ratio at a = 7.8 mm. Individual striations from the marker cycles are now clearly visible.

Test 2: Notched coupon at 50 kN maximum loading

Figs. 7-12 show fractographs from Test 2 covering crack growth from a size of 0.04 mm up to 3 mm. A single fatigue crack initiated at a point about 0.025 mm from the notch root and grew to failure.

Fig. 7 shows the origin of the naturally initiating fatigue crack. After growing along a 45 deg. plane over the first 10-15 mm, further growth occurs along the horizontal plane. Fig. 8 shows the first discernible striation patterns that appear at a crack depth of about 0.04 mm. As reasoned earlier, the gradual decrease in striation spacing appears to indicate non-closure related stress ratio effect. As K_{max} at this point is under 15% of K_{1c}, one would have to assume that the effect is local stress related. Notch root S_{max} in the three steps reduces from a post yield value of 515 MPa in the first step, through near yield value of 442 MPa in the second and down to a fully elastic 370 MPa in the third step. Crack growth rate in the first step was estimated from striation band width to be 2.69×10^{-7} mm/cycle, while in the third step it was 2.8 times less at 9.6×10^{-8} mm/cycle, which is the lowest recorded crack growth rate in this study.

For the crack shown in Fig. 8, the calculated DK value over Steps #1-3 is 1.1 MPa$\sqrt{\text{m}}$. Assuming the material constants in Table 3 and the absence of a threshold, da/dN = 1.37×10^{-7} mm/cycle. The long crack data described earlier always showed calculated growth rates to be in excess of observed striation spacings. This had been attributed to the retardation effect due to crack front incompatibility caused by the marker loads. In contrast, the data from Fig. 8 indicate that crack growth rate in Step 1 is twice the estimated value. This may be attributed to the small crack effect, and the local stresses that are close to yield and ultimate stress. As S_{max} in Steps 2 and 3 recedes, growth rate drops to even less than the estimate. Fig. 9 shows the fatigue crack extending across two planes at a = 0.065 mm, with a clear and consistent reduction in crack growth rate over the three steps.

Fig. 10 shows a fractograph corresponding to a = 0.12 mm. At this particular point, we find crack growth rate to be identical in Steps #1 and #2 and down to a third in Step #3. The same argument advanced earlier may be suggested to apply with regard to the long crack under elastic conditions. Crack growth in the Step #3 is retarded by closure in the crack extension mode that is currently active. Just 30 mm away, at a crack size of 0.15 mm, crack growth rates over all three steps even out (see Fig. 10). This trend continued right through to a = 3.5mm, just before failure (see Fig. 11).

Test 3: Notched coupon at 75kN maximum loading

In contrast to Test 2, which initiated a single crack at the notch root, at least seven crack initiation sites were observed on the fracture surface from Test 3. Five of these sites appear in Figs. 12-14. An enlarged local area from one of the sites are also shown to give a clear indication of crack growth rates.

It has been observed earlier [11] that under a given load spectrum, the number of crack

initiation sites will increase with applied stress level. As multiple crack initiation would not have occurred simultaneously, one may expect to see differences in observed crack growth rates across multiple sites, given same crack size. The site showing the lowest growth rate may be assumed to have initiated first [11]. From these considerations, it would appear that the site shown in Fig. 12 served as the first initiation site. The crack appears to have grown out of an inclusion site seen at bottom left as a semicircular crack. The left half of the crack surface appears to have been obliterated due to rubbing. However, the right half has enough clear regions from which to measure crack growth rate.

Fig. 13 shows an enlarged segment of the fracture surface, clearly indicating gradual decrease in crack growth with decreasing stress ratio. The ratio of the largest to smallest striation band spacing is 4.33 at a crack size of about 0.06 mm. It may be recalled that the ratio had been 2.8 in Test 2 at a crack size of 0.04 mm. This more dramatic stress ratio effect may be attributed to the higher stress level in this test (see Table 1). The ratio may have been larger at smaller crack size. It diminishes with crack size and as seen in Fig. 14 from another site, appears to even out as crack size exceeds 0.1 mm.

The crack size at which growth rates over the three different stress ratios evened out in Test 2 was about 0.15 mm, which may be explained by the reduced stress level in that test. In terms of notch root response to applied stress level, both these dimensions are negligible when viewed in terms of the stress gradient. It would follow that even at a crack size around 0.15 mm, local stresses would be of the same order than those estimated for the notch factor. Why then does the stress ratio cease to strongly influence crack growth rate? The answer may lie in growth rate sensitivity to stress ratio: one may argue that at lower (near threshold) stress intensity (and growth rate), when the fatigue crack barely extends in a single cycle, the effect of large cyclic applied stress levels will be significant. Over this interval the S_{max} / S_f ratio may be crucial as indicated by the larger R effect in Test 3 as opposed to Test 2 (reduction in da/dN by a factor of 4.33 as opposed to 2.8 in Test 2). Indeed, the same trend would also be indicated by expressions for crack initiation life from LCF concepts [12,13]. As crack driving force due to the DK component increases, the stress-related R-effect component diminishes and crack closure starts playing its well documented role. Further, as K_{max} approaches K_c, the quasi-static component takes over and toughness-related stress ratio effects dominate (Forman equation in Ref. 2 and 3).

Concluding Remarks

In summary, the results from the study suggest that in the process of fatigue damage over its different stages, fatigue crack growth rates will be dominated by both stress as well as stress intensity parameters. There is some analog in the way stress ratio affects fatigue damage in the early and late stages of fatigue. In both cases, the ratio of the maximum to ultimate (S_{max} /S_f or K_{max}/K_c) increases the damaging power of the driving variable (DS or DK) in a way that cannot be described from first principles. The effect is to be empirically established from testing. In contrast, the intermediate stage of DK-dominated damage accumulation is controlled by crack closure that induces the stress ratio effect by *directly* controlling the *range* of the damaging parameter (DK_{eff}). The stress ratio effect over this stage can therefore be modeled analytically.

Specially designed load sequences permitted fractographic measurement of crack growth rates down to 10^{-7} mm/cycle and up to 10^{-3} mm/cycle. Further modifications to the load program are likely to extend the capability of fractography to even lower crack growth rates and smaller crack sizes.

Fractographic evidence from this study indicates the possibility of noticeable stress ratio effects in the absence of fatigue crack closure. These effects will be more significant at lower crack growth rates and as applied and net (local) stress levels approach ultimate stress. Thus, fatigue thresholds are stress level sensitive. However, with increase in crack growth rate above

near threshold levels (~2.10^{-6} mm/cycle), the stress ratio effect could be influenced more strongly by fatigue crack closure.

The present study was conducted using a very limited range of stress ratio variation (R=0.64-0.73). Given a wider range of stress ratios, the above effects are likely to be more dramatic.

The techniques used in this study appear to hold the potential for more fundamental research work in the area of notch root fatigue crack initiation, stress ratio effects and notch sensitivity studies.

Acknowledgments

The authors would like to acknowledge the helpful technical guidance and support provided by Dr. Ted Nicholas of the Materials Directorate, Wright-Patterson Air Force Base. The first author also appreciates the useful discussions with Dr. Raghu V. Prakash of the National Aerospace Laboratories, Bangalore, India. Excellent test support and guidance on SEM for the fractographs have been provided by Mr. Andy Lackey and Ms. Luann Piazza, respectively.

REFERENCES

[1] Elber, W., "The Significance of Fatigue Crack Closure," Damage Tolerance in Aircraft Structures, STP 486, American Society for Testing and Materials, Philadelphia, 1971.

[2] Forman, R. G., Kearney, V. E., and Engle, R. M., "Numerical Analysis of Crack Propagation in Cyclic Loaded Structures," J. Basic Engrg., Trans. ASME, 39, 1967, p. 459.

[3] Newman, "A Crack-Closure Model for Predicting Fatigue Crack Growth under Aircraft Spectrum Loading," Methods and Models for Predicting Fatigue Crack Growth under Random Loading, ASTM STP 748, J. B. Chang and C. M. Hudson, Eds., American Society for Testing and Materials, 1981, pp. 53-84.

[4] Booth, G. S. and Maddox, S. J., "Correlation of Fatigue Crack Growth Data Obtained at Different Stress Ratios," Mechanics of Fatigue Crack Closure, ASTM STP 982, J. C. Newman, Jr. And W. Elber, Eds., American Society for Testing and Materials, Philadelphia, 1988, pp. 516-527.

[5] Walker, K., "The Effect of Stress Ratio During Crack Propagation and Fatigue for 2024-T3 and 7075-T6 Aluminium," Effects of Environment and Complex Load History on Fatigue Life, STP 462, American Society for Testing and Materials, Philadelphia, 1970.

[6] Maddox, S. J., "The Effect of Mean Stress on Fatigue Crack Propagation: A Literature Review," International Journal of Fracture, Vol. 11, No. 3, June 1975.

[7] Elber, W., "Fatigue Crack Closure Under Cyclic Tension," Engineering Fracture Mechanics, Vol. 2, 1970, pp. 37-45.

[8] Davidson, D. L. and Lankford, J., "Fatigue Crack Growth in Metals and Alloys: Mechanisms and Micromechanisms," International Materials Reviews, Vol. 37, No. 2, 1977, pp. 45-76.

[9] Sunder, R., Prakash, R. V., and Mitchenko, E. I., "Calculation of Spectrum Load Notch Root Crack Growth Rate Under Elastic and Inelastic Conditions," Advances in Fatigue Lifetime Predictive Techniques: Second Volume, ASTM STP 1211, M. R. Mitchell and R. W. Landgraf, Eds., American Society for Testing and Materials, Philadelphia, 1993, pp. 30-44.

[10] Schijve, J., "Fatigue Damage Accumulation and Incompatible Crack Front Orientation," Engineering Fracture Mechanics, Vol. 6, 1974, pp. 245-252.

[11] Prakash, R. V., Sunder, R., and Mitchenko, E. I., "A Study of Naturally Initiating Notch Root Fatigue Cracks Under Spectrum Loading," Advances in Fatigue Lifetime Predictive Techniques: 3rd Volume, ASTM STP 1292, M. R. Mitchell and R. W. Landgraf, Eds., American Society for Testing and Materials, Philadelphia, 1995, pp. 136-160.

[12] Manson, S. S. and Muralidharan, U., "A Single Expression Formula for Inverting Strain-Life and Stress-Strain Relationships," Fatigue Fracture Engineering Materials Structures, Vol. 9, No. 5, 1987, pp. 343-356.

[13] Morrow, J. D., "Fatigue Properties of Metals," Fatigue Design Handbook, Section 3.2, Society of Automotive Engineers, 1968.

Table 1: Loading conditions and estimated specimen response. Refer to Fig. 2 for load sequence.

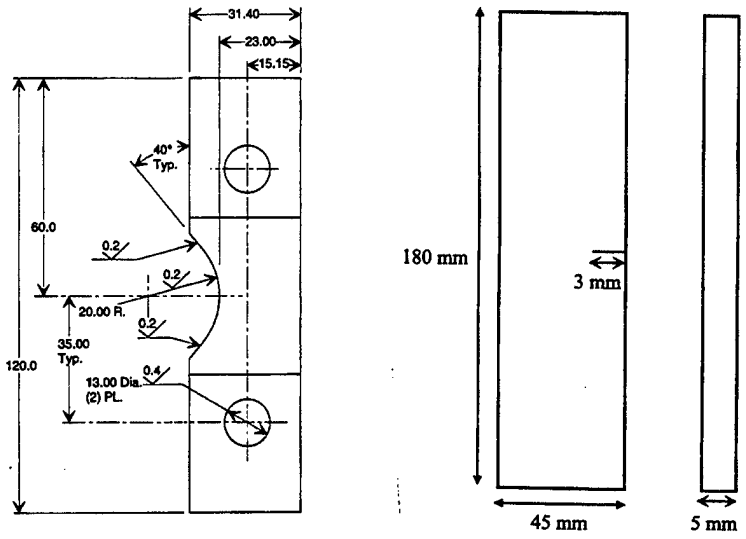
Test:	**1**	**2**	**3**
Specimen geometry:	SE(T) W45/T5 mm	Notched SE(T) (K_t = 2.5) W23/T10 mm	Notched SE(T) (K_t = 2.5) W23/T10 mm
Reference loading (100%)	100 MPa	50 kN	75 kN
Maximum net stress, MPa	100	217	326
Max. notch local stress, MPa	-	515	670
	Step #1 (2000 cycles)		
Applied stress ratio	R = 0.73		
Effective stress ratio	0.73	0.72	0.683
S_{max}, MPa	100	515	670
DS, MPa	26.67	145	217
	Step #2 (2000 cycles)		
Applied stress ratio	R = 0.69		
Effective stress ratio	0.69	0.67	0.624
S_{max}, MPa	86.66	442.5	564
DS, MPa	26.67	145	217
	Step #3 (2000 cycles)		
Applied stress ratio	R = 0.64		
Effective stress ratio	0.64	0.61	0.537
S_{max}, MPa	73.33	370	458
DS, MPa	26.67	145	217
	Step #4 (10 cycles)		
Applied stress ratio	R = 0.		R = 0.0467
Effective stress ratio	0.00	0	-0.16
S_{max}, MPa	100	515	670
DS, MPa	100	518	777

Table 2: da/dN data.

a (mm)	DK MPa $\sqrt{m}$	da/dN (mm/cycle)		Test
		Step #1	Step #3	
4.5	3.55	1.89×10^{-6}	1.89×10^{-6}	1
7.8	4.68	1.21×10^{-5}	1.21×10^{-5}	
11.9	5.77	3.68×10^{-5}	2.65×10^{-5}	
0.04	1.1	2.69×10^{-7}	9.6×10^{-8}	2
0.05	1.27	5.17×10^{-7}	1.55×10^{-7}	
0.065	1.4	8.18×10^{-7}	3.73×10^{-7}	
0.15	2.18	1.97×10^{-6}	1.64×10^{-6}	
0.024	1.3	6.25×10^{-7}	2.4×10^{-7}	3
0.028	1.4	7.69×10^{-7}	2.89×10^{-7}	
0.032	1.48	1.06×10^{-6}	3.85×10^{-7}	
0.037	1.6	1.15×10^{-6}	4.81×10^{-7}	
0.042	1.7	1.35×10^{-6}	6.73×10^{-7}	
0.049	1.9	1.44×10^{-6}	8.65×10^{-7}	
0.058	2.08	1.46×10^{-6}	9.0×10^{-7}	
0.066	2.15	1.49×10^{-6}	9.33×10^{-7}	
0.076	2.3	1.87×10^{-6}	1.31×10^{-6}	
0.087	2.5	2.24×10^{-6}	1.49×10^{-6}	
0.099	2.7	2.43×10^{-6}	1.68×10^{-6}	
0.11	2.8	2.61×10^{-6}	1.87×10^{-6}	
0.125	3.1	2.61×10^{-6}	2.43×10^{-6}	
0.136	3.2	2.49×10^{-6}	2.49×10^{-6}	

Table 3: Material constants 2014-T6511 [9]

E MPa	S_f MPa	e_f	K' MPa	n'	C mm/MPa $\sqrt{m}$	m	K_c MPa $\sqrt{m}$
70,800	1075.0	0.25	1479	0.148	10^{-7}	3.27	60



Short Crack Specimen **Long Crack Specimen**

Fig. 1 Test coupons used in experiments

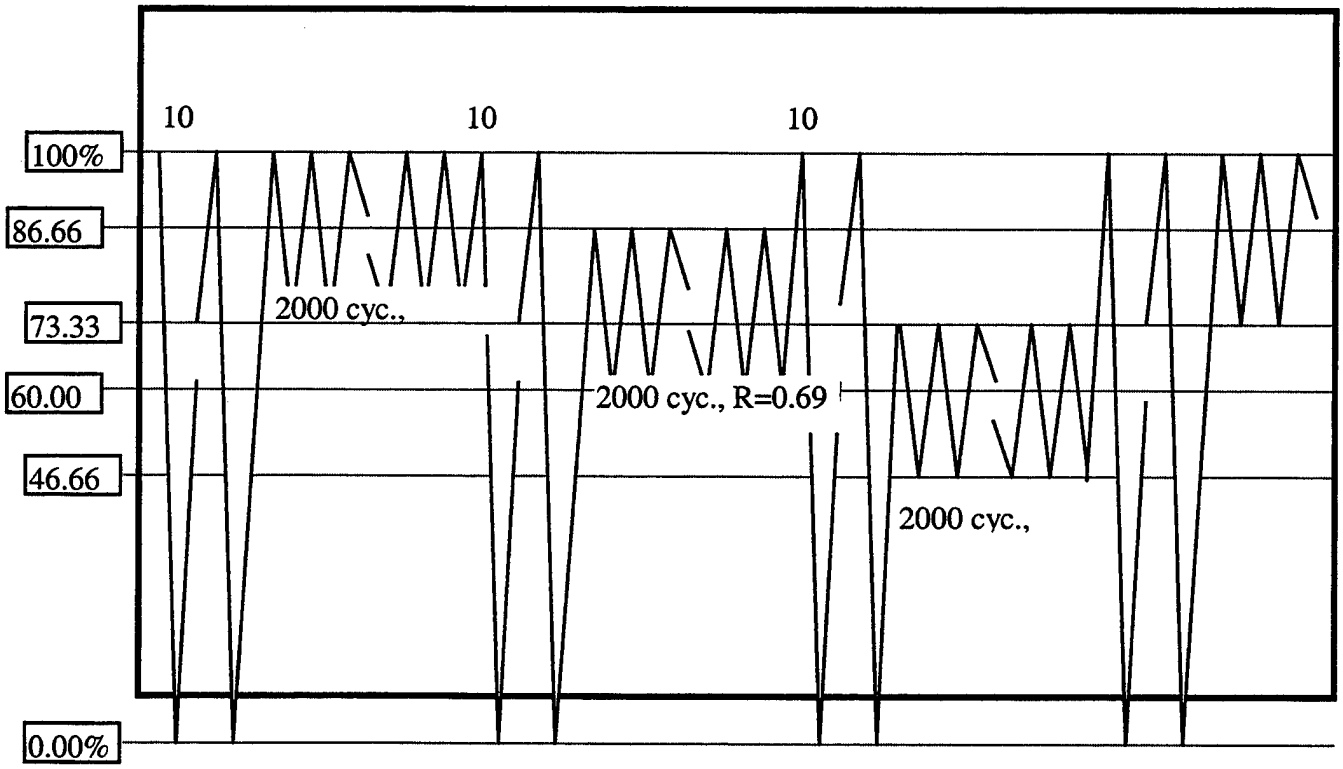


FIG.2 - Schematic of load sequence used in testing.

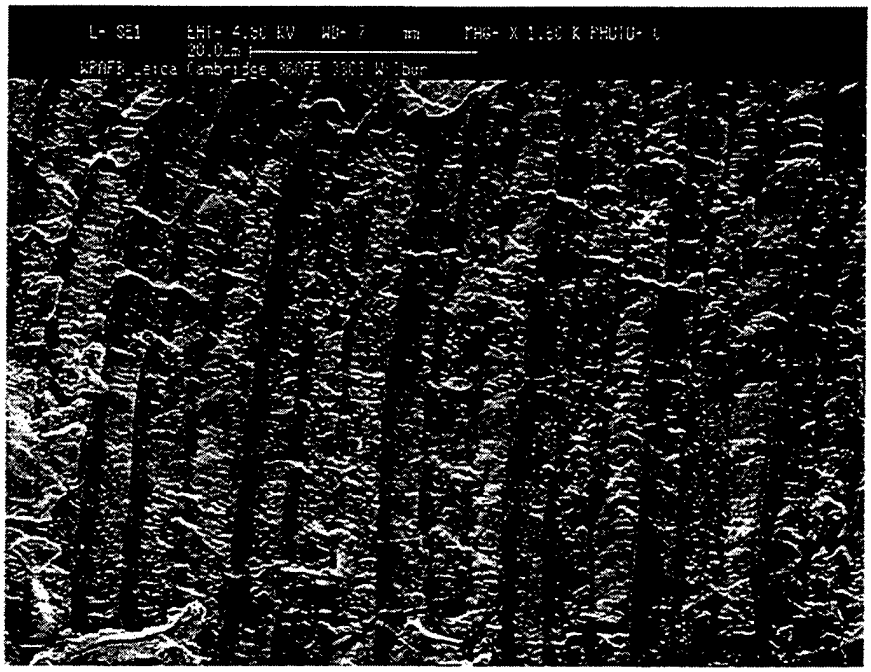


Fig. 4 SE(T) specimen at S_{max} = 100 MPa. Mid-thickness region. a ~ 4.5 mm. DK = 3.6 MPa$\sqrt{m}$ in Steps 1, 2, 3. da/dN ~ 1.89x10-6 mm/cycle (Steps 1-3)

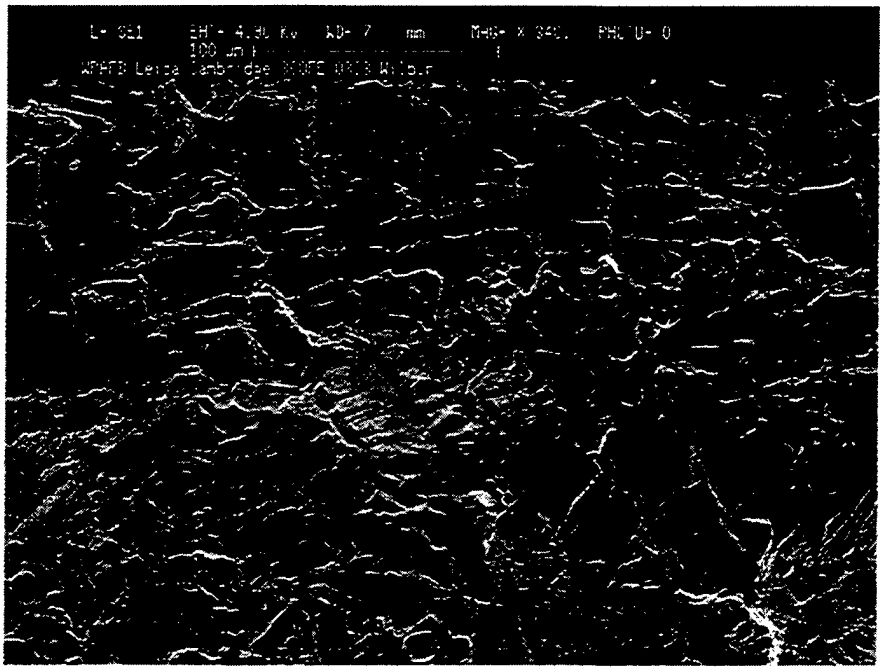


Fig. 5 SE(T) specimen at S_{max} = 100 MPa. Mid-thickness region. a ~ 7.8 mm. DK = 4.17 MPa$\sqrt{m}$ in Steps 1, 2, 3. da/dN ~ 1.21x10-5 mm/cycle (Steps 1-3) and 6x10-4 mm/cycle in marker cycles (Step 4)

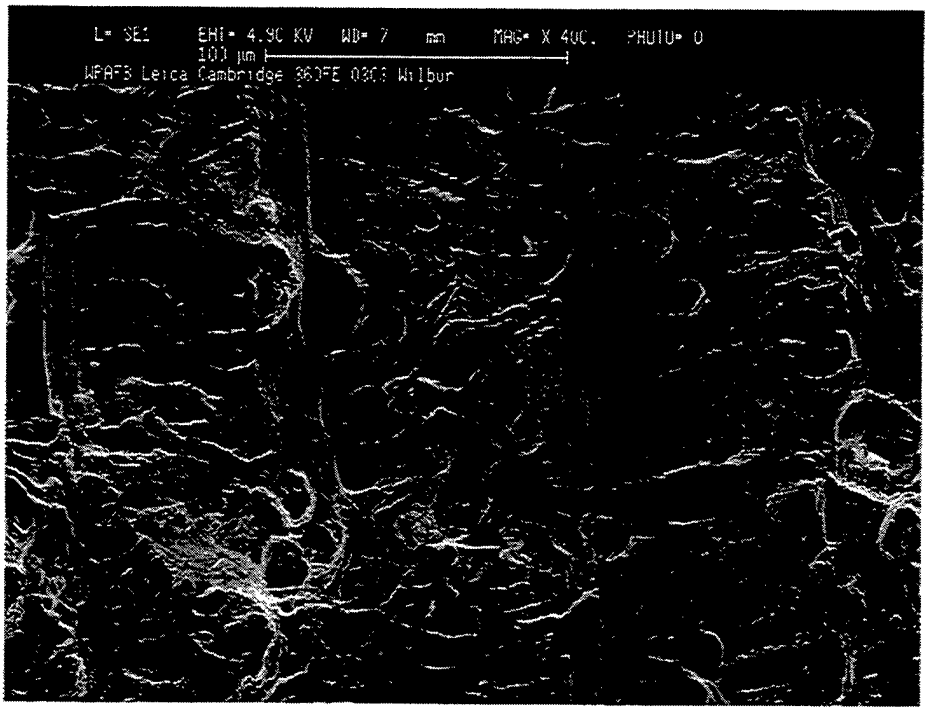


Fig. 6 SE(T) specimen at S_{max} = 100 MPa. Mid-thickness region. a ~ 12 mm. DK = 5.18 MPa$\sqrt{m}$ in Steps 1, 2, 3. da/dN ~ 3.55x10-5 mm/cycle (Steps 1-2), 2.65x10-5 mm/cycle in Step 3, 1.9x10-3 mm/cycle in Step 4.



Fig. 7 Notched SE(T) specimen tested at P_{max} = 50 kN. Origin of naturally initiating fatigue crack on the notch surface about 0.02 mm from the specimen side.

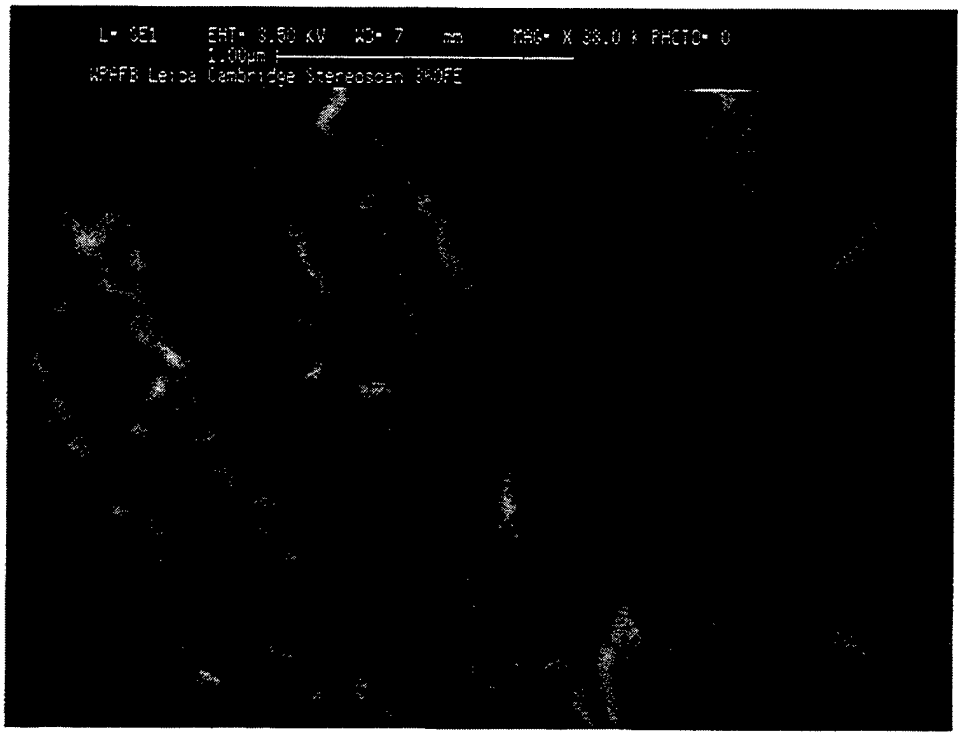


Fig. 8 Notched SE(T) specimen tested at P_{max} = 50 kN. First discernible striation bands at a crack depth of 0.04 mm. . DK = 1.1 MPa$\sqrt{m}$ in Steps 1, 2, 3. da/dN ~ 2.69x10-7 in Steps 1 and 0.96x10-7 in Step 3.

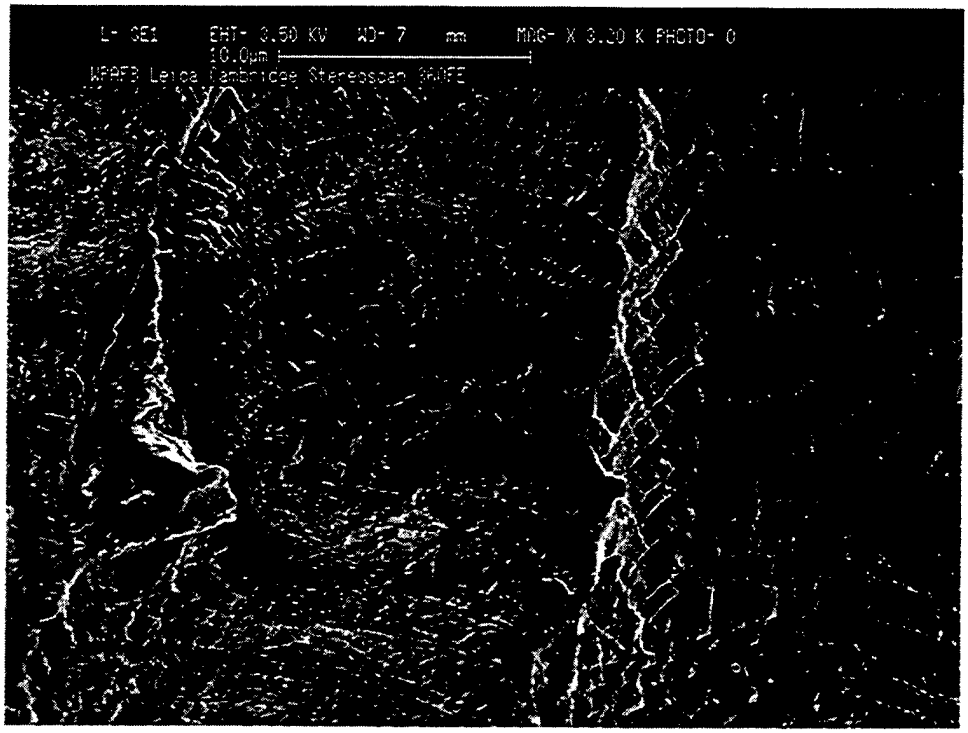


Fig. 9 Notched SE(T) specimen tested at P_{max} = 50 kN. Striation bands at a crack depth of 0.065 mm. DK = 1.1 MPa$\sqrt{m}$ in Steps 1, 2, 3. da/dN ~ 2.69x10-7 in Step 1 and 0.96x10-7 in Step 3.

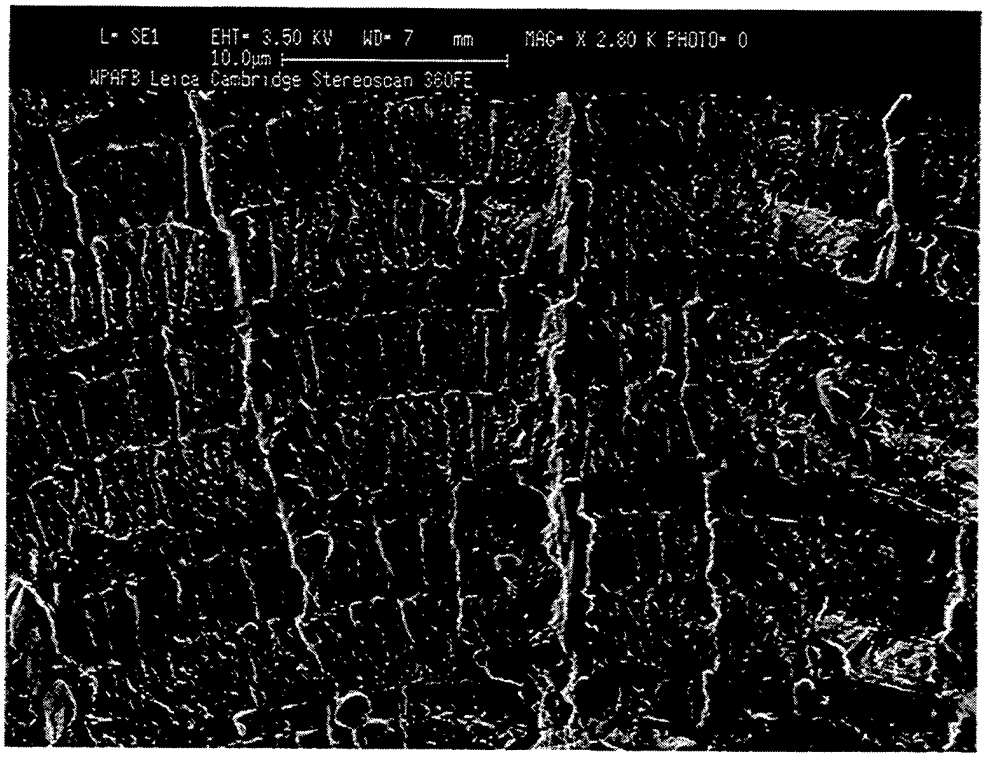


Fig. 10 Notched SE(T) specimen tested at P_{max} = 50 kN. Mid-thickness region. a~0.12 mm.

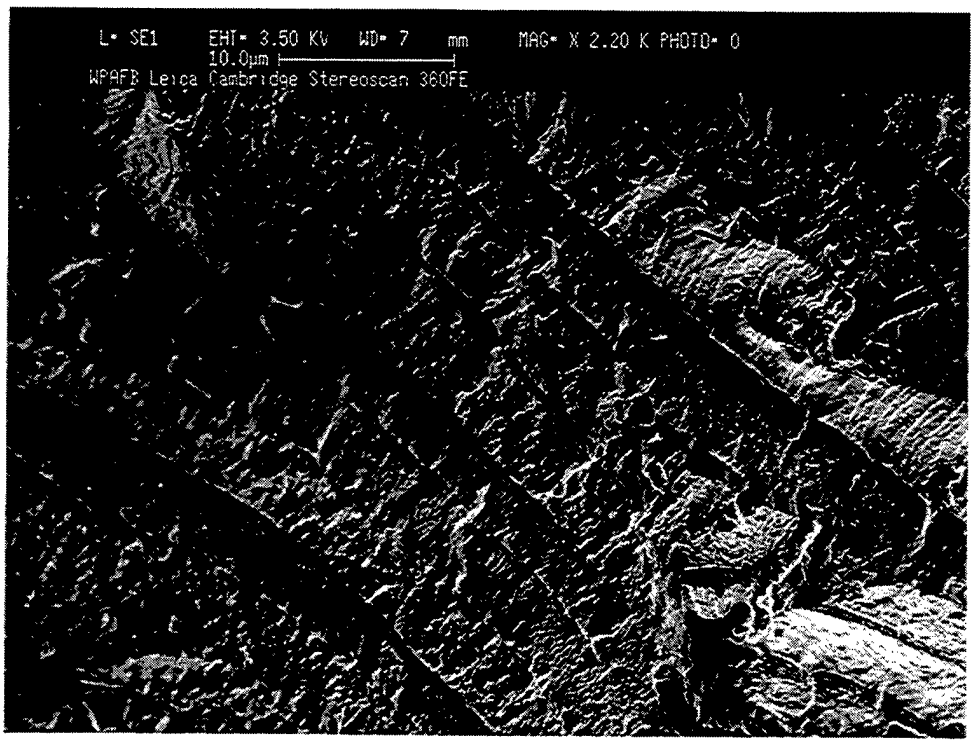


Fig. 11 Notched SE(T) specimen tested at P_{max} = 50 kN. a=3.5 mm.

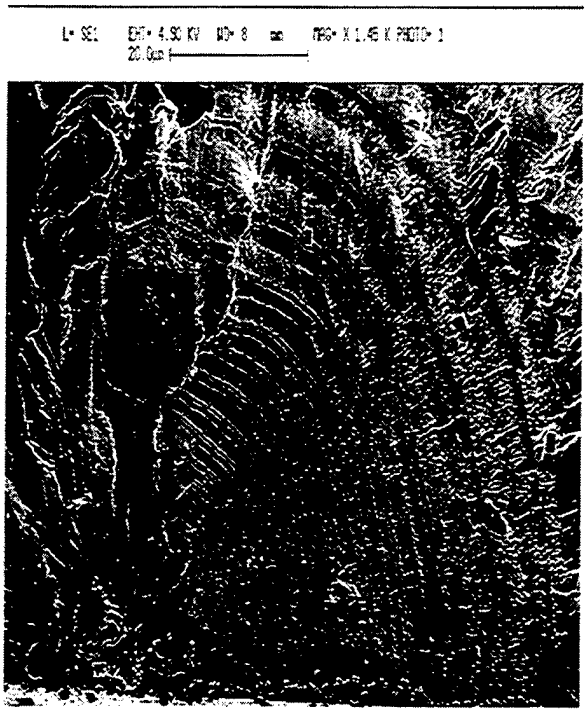


Fig. 12 Notched SE(T) specimen tested at P_{max} = 75 kN. Original initiation site of the seven identified on this sample.

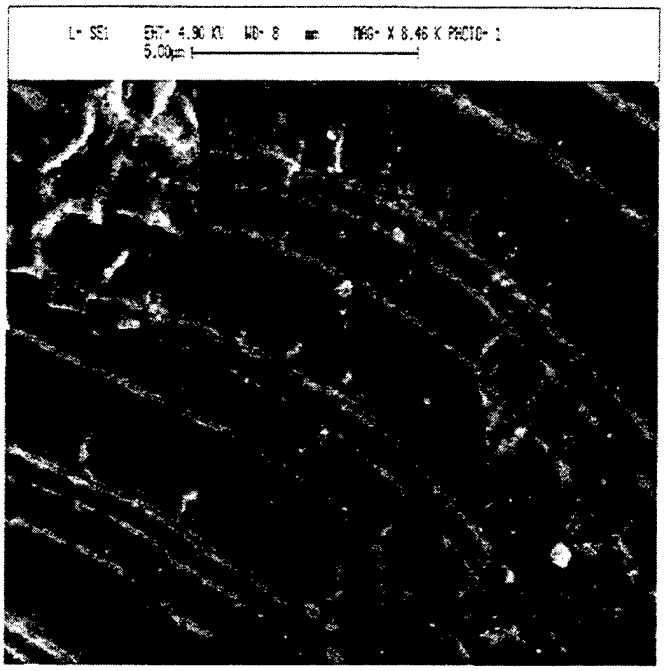


Fig. 13 Notched SE(T) specimen tested at P_{max} = 75 kN. a=0.06mm.



Fig. 14 Notched SE(T) specimen tested at P_{max} = 75 kN. a~0.1mm.

This page intentionally left blank

Reference: Lykins, C. and John, R., "Prediction Of Crack Growth In A Laser Shock Peened Zone," Proceedings of International Symposium on Inelastic Deformation, Damage and Life Analysis, Ed. V.K. Arya, Springer-Verlag Publishers, 4-9 May 1997.

PREDICTION OF CRACK GROWTH IN A LASER SHOCK PEENED ZONE

Chris Lykins
Components Branch, Turbine Engine Division, Aero Propulsion and Power Directorate
Wright Laboratory, Wright-Patterson Air Force Base, Ohio 45433, USA

Reji John
Advanced Materials Characterization Group, Structural Integrity Division
University of Dayton Research Institute, Dayton, Ohio 45469, USA

INTRODUCTION

Laser shock peening (LSP) has demonstrated the ability to significantly increase the damage tolerance of turbine engine airfoils. This process utilizes an impact event to generate a compressive residual stress field similar to that of shot peening. The LSP process uses a high intensity, short pulse duration laser to plastically deform the surface and subsurface of the target. The resulting compressive residual stress field is typically 5-10 times deeper than that achieved during shot peening and the surface remains relatively unscathed. These characteristics translate into significant damage tolerance improvements over competing technologies. The LSP process is being considered for improving the damage tolerance of aerospace engine fan blades [1]. The leading edge of the engine fan blade, which is susceptible to damage due to foreign objects, is subjected to the LSP treatment. The high compressive stresses generated by the LSP process is expected to retard the crack growth from the edges, thus increasing the damage tolerance of the engine blade.

This paper describes an analytical investigation of the effect of the LSP process on crack growth behavior of Ti-6Al-4V. A notched three point bend specimen with varying thickness was used to simulate the leading edge of a fan blade. Data from constant amplitude crack growth tests by Thompson, Ruschau and Nicholas [2] were used during this study. The weight function method was used to analyze the crack growth in the three point bend specimen subjected to the LSP process. An iterative scheme to deduce the residual stress distribution is also discussed.

LASER SHOCK PEENING

The LSP process uses a high intensity, short pulse duration laser to create the impact event, which plastically deforms the material and creates the residual stress state [3]. When the laser beam strikes the impact site, a sequence of events occurs identified as the three steps in Figure 1. Initially, the laser beam passes through a water overlay transparent to the beam striking the paint layer on the surface of the specimen as in step (1). The thin layer of the paint is immediately vaporized and rapidly expands by absorbing energy from the incoming laser beam. The vapor is transformed into a plasma, which continues to absorb the laser energy. The gas and plasma are confined against the surface of the blade by the water overlay, creating a localized rapid increase in pressure against the specimen as in step (2). The confinement by the water overlay increases the attainable pressures to very high levels ranging from 6-10 GPa. The confined pressure is transmitted partially into the specimen and partially out through the water as high amplitude shock waves as in step (3). When the peak pressure

of the shock wave exceeds the dynamic yield strength of the material, the specimen surface is plastically deformed. Thus the LSP process generates a relatively deep plastically deformed zone resulting in regions with deep compressive residual stresses. The depth of the compressive residual stress region depends on the magnitude and length of the pressure pulse. In the LSP process, the processed spot diameter is typically ≈ 5 to 10 mm. Hence, the process has to be repeated several times to induce residual stresses across large areas [3].

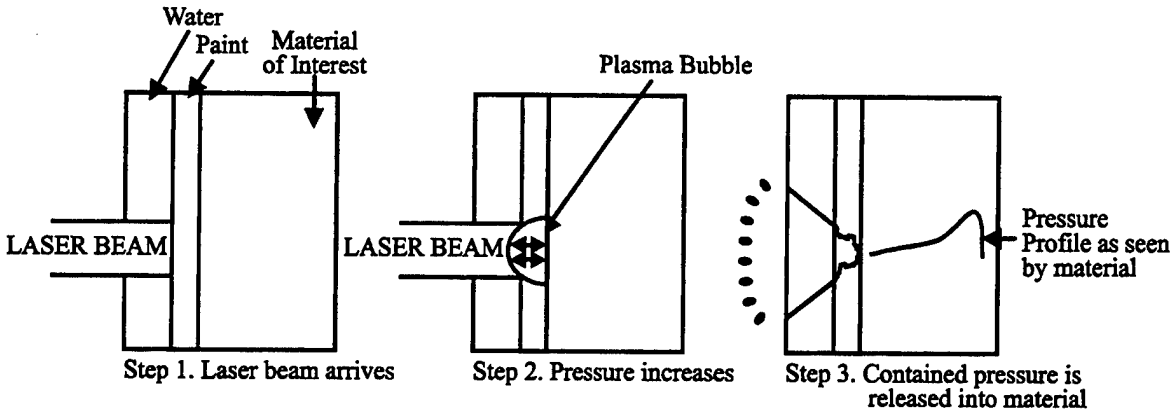


Figure 1. Laser Shock Peening Process

Based on the x-ray diffraction analysis on the leading edge of a turbine engine fan blade, Lykins, Prevey and Mason [1] reported that the compressive region is about 0.5 to 1.3 mm deep. In contrast, the region of compressive residual stresses generated using the shot peening process is ≈ 0.3 to 0.5 mm deep. The narrow half bandwidth revealed during the x-ray diffraction analysis suggested that negligible crystalline deformation occurred during the LSP process. Thus, the most significant advantage of the LSP process is the creation of deep regions with compressive residual stresses in the material without inducing large amounts of crystalline deformation [1].

EXPERIMENTAL PROCEDURE AND RESULTS

Recent experimental work [2] has shown that the tapered three point bend specimen, TSE(B) can be used to study the crack growth behavior in the leading edge of a turbine engine blade. A schematic of the TSE(B) specimen is shown in Fig. 2. Note that the thickness ranges from 0.76 mm at the bottom edge to 9.52 mm at the top edge. The leading edge of an engine blade is rounded but a square edge as shown in Fig. 2 was used during this study. The laser shock peened zone is shown as the region with overlapping circles in Fig. 2. Both sides of the specimen were subjected to the LSP process. An initial notch of ≈0.9 mm was machined at the center-span of the specimen using a diamond saw.

The TSE(B) specimens were machined from forged Ti-6Al-4V [2]. Crack growth tests were conducted at room temperature under constant load (P_{max}) and constant load ratio conditions. The load ratio, R (=minimum load/maximum load) was maintained at R = 0.1 for all the tests. The baseline specimen tested at constant load = 2.6 kN and zero residual stresses exhibited a typical crack growth behavior with crack growth rate increasing with increasing crack length. This specimen failed in ≈ 180000 cycles. In contrast, the specimen with residual stresses showed crack extension from the machined notch at a similar load level, immediately followed by near-arrest behavior as shown in Fig. 3. After reaching near-arrest conditions, the loads were increased by 10% and the test continued until the crack extension again reached the near-arrest condition. This procedure was repeated until the maximum load was = 4.6 kN resulting in final crack extension of ≈2.5 mm from the machined notch. The LSP process enabled the TSE(B) specimen to exhibit crack arrest behavior even at load levels which were ≈

77% greater than the load level required for unarrested crack growth in the unprocessed specimen. This crack growth behavior highlights the significant increase in the damage tolerance due to the LSP treatment.

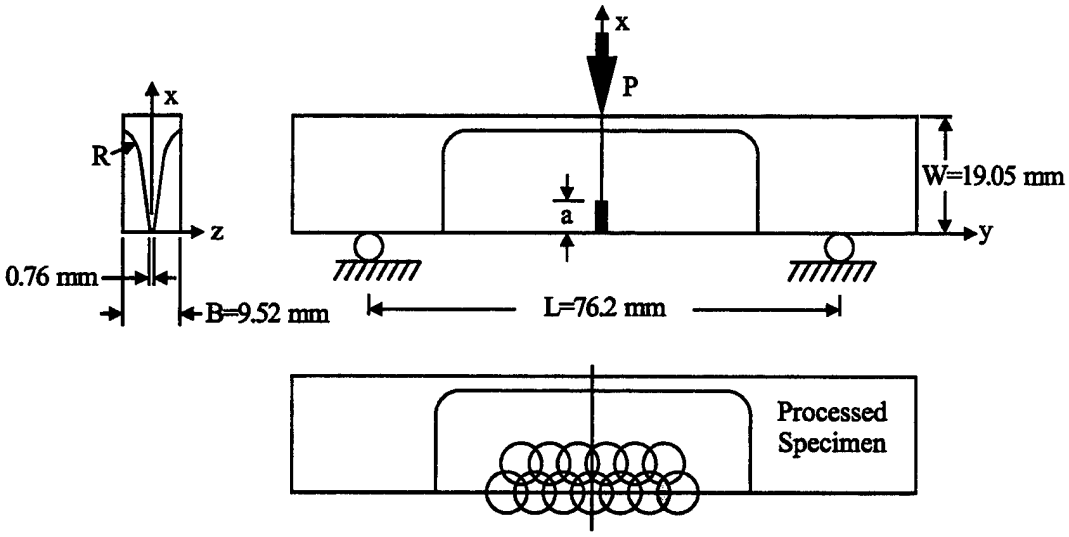


Figure 2. Schematic of the tapered 3-point bend specimen geometry, TSE(B).

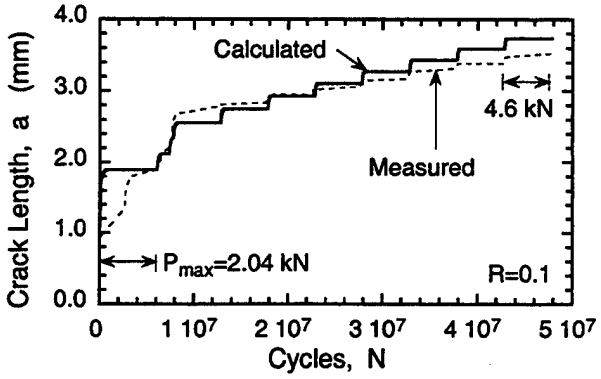


Figure 3. Crack growth behavior of a TSE(B) specimen subjected to the LSP process.

ANALYSIS OF CRACK GROWTH BEHAVIOR

Damage tolerance based design of fan blades requires reliable tools to predict the crack growth behavior in the presence of residual stresses. Linear elastic fracture mechanics based models are commonly used to predict the crack growth in components with residual stresses [4]. The measurement of the residual stress distribution using the x-ray diffraction technique for the TSE(B) geometry and processing conditions used during this study is in progress. This residual profile will typically posses a gradient profile, with high compressive stresses at the surface and tensile stresses in the interior regions of the specimen. In addition, the residual stress profile exists on both sides of the specimen. Hence, the residual stress distribution in the center of the LSP process zone can be expected to be 2-dimensional, i.e. function of x and z. During this study, as a first approximation, the residual stress distribution was assumed to be 1-dimensional (1-D), i.e. function of x only.

As discussed earlier, the residual stresses are non-uniform with steep gradients near the surface. The residual stress intensity factor, K_{res} due to non-uniform stress distributions can be calculated using the weight function method as,

$$K_{res} = \int_0^a \sigma_{res}(x)\ h(x,a)\ dx\,, \tag{1}$$

where x and a are defined in Figure 2, $\sigma_{res}(x)$ is the arbitrary residual stress distribution on the crack surface, and h(x,a) is the weight function. The development of the weight function for the TSE(B) geometry using three dimensional finite element results is discussed in Ref. [5].

Fatigue crack propagation in a residual stress field is usually analyzed using the principle of superposition to calculate an effective stress intensity factor range, ΔK_{eff} and an effective stress ratio, R_{eff} as given by [4],

$$R_{eff} = \frac{K_{min,eff}}{K_{max,eff}} = \frac{K_{min,a} + K_{res}}{K_{min,a} + K_{res}}\,, \tag{2}$$

$$\Delta K_{eff} = K_{max,eff} - K_{min,eff}\,, \qquad \text{for} \quad R_{eff} > 0 \tag{3}$$

$$\Delta K_{eff} = K_{max,eff}\,, \qquad \text{for} \quad R_{eff} \le 0 \tag{4}$$

in which, $K_{max,a}$ = maximum applied stress intensity factor, $K_{min,a}$ = minimum applied stress intensity factor, $K_{max,eff}$ = maximum effective stress intensity factor, and $K_{min,eff}$ = minimum effective stress intensity factor. Note that during a cycle, $K_{max,a}$ and $K_{min,a}$ are proportional to the applied load while K_{res} is independent of the applied load.

The analytical procedure requires the baseline description of the crack growth behavior of monolithic Ti-6Al-4V at different stress ratios. Equation (5) was used to describe the crack growth behavior for crack growth rates (da/dN) ranging from 10^{-10} to 10^{-5} m/cycle. The constants C_i in Eqn. (5) were determined as functions of stress ratio, R using the data from Ref. [6].

$$\log\left(\frac{da}{dN}\right) = C_1 \sinh\left[C_2\left(\log\left(\Delta K_{eff} + C_3\right)\right)\right] + C_4 \tag{5}$$

The available data [6] indicate that the crack growth behavior at R = -0.5 is identical to that at R = -1.0. Accordingly, during this study, we assumed that the crack growth behavior of baseline Ti-6Al-4V was independent of stress ratio for $R \le -0.5$. The threshold stress intensity factor, K_{th} for Ti-6Al-4V was assumed = 6.0 MPa$\sqrt{m}$ for $R \le -0.5$. Note that $K_{th} = \Delta K_{th}$ for $R \le 0.0$ as given by Eqn. (4). The near-arrest conditions for crack growth was assumed to be equivalent to growth rate of 10^{-10} m/cycle.

Using the measured crack length versus cycles response (Fig. 3), $K_{max,a}$ was calculated at the near-arrest conditions for various load levels and plotted as a function of crack length in Fig. 4. The compressive residual stresses due to the LSP process resulted in a negative K_{res} thus reducing the effective $K_{max,a}$ at the crack tip (Eqn. 2). Consequently, ΔK_{eff} also decreased to near-threshold values resulting in near-arrest conditions of crack growth. Hence, under these conditions, ΔK_{eff} at the crack tip can be assumed = ΔK_{th} of baseline Ti-6Al-4V. Since K_{res} is typically < 0.0 and $K_{min,a} \approx 0.0$, R_{eff} can be expected to be < 0.0 for the

crack growth shown in Fig. 3. Accordingly we assumed that ΔK_{th} (=K_{th}) is independent of crack length as shown in Fig. 4. Thus, at near-arrest conditions, K_{res} is given by,

$$K_{res} = -K_{max,a} + K_{th} \quad . \tag{6}$$

K_{res} deduced using Eqn. (6) is shown in Fig. 4. The magnitude of K_{res} increases with increasing crack length consistent with the near-arrest behavior exhibited in Fig. 3 up to ≈ 48 x 10^6 cycles.

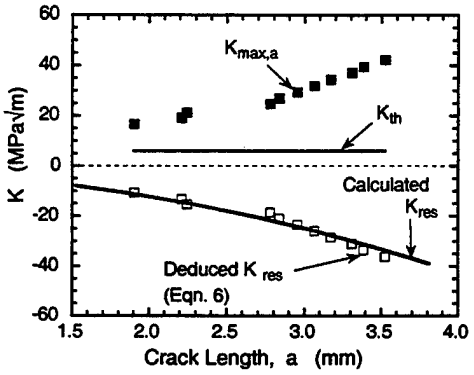


Figure 4. $K_{max,a}$ and K_{res} versus crack length.

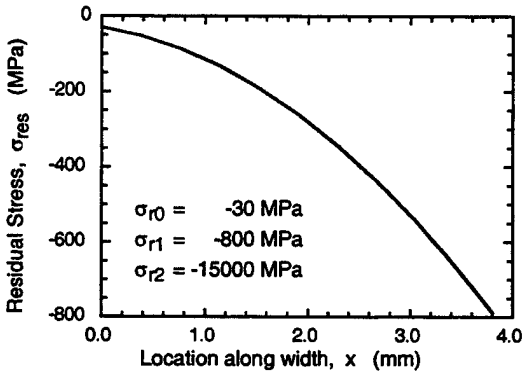


Figure 5. Calculated residual stress distribution.

An iterative procedure was used to determine the equivalent one-dimensional residual stress distribution, $\sigma_{res}(x)$. A polynomial form, given by Eqn. (7) was assumed for $\sigma_{res}(x)$.

$$\sigma_{res}(x) = \sigma_{r0} + \sigma_{r1}\left(\frac{x}{W}\right) + \sigma_{r2}\left(\frac{x}{W}\right)^2 \quad . \tag{7}$$

Equations (1) and (7) were used to correlate the calculated K_{res} with the deduced K_{res} as shown in Fig. 4. The best fit (visual) resulted in the residual stress distribution shown in Fig. 5. The corresponding K_{res} is shown as a solid line in Fig. 4. Figure 5 shows that the magnitude of the deduced σ_{res} increases with increase in location for ≈3.8 mm from the leading edge. The distribution shown in Fig. 5 is different from the measured 1-D residual stress profile with near-yield stress at the surface and 0.0 at ≈0.5 mm from the surface [1]. As discussed earlier, the true distribution of σ_{res} in the TSE(B) can be expected to be two-dimensional. The distribution shown in Fig. 5 represents a simple 1-D approximation of the actual σ_{res}.

The residual stress distribution shown in Fig. 5 was deduced based on K values at near-arrest conditions and assuming that $R_{eff} \leq -0.5$. The applicability of the deduced σ_{res} was verified by predicting the crack length versus cycles response for all the load levels using Eqns. (1)-(7). As shown in Fig. 3, the calculated crack growth response agrees satisfactorily with the measured data for all load levels. During these calculations, R_{eff} ranged from -5.3 to -1.3 consistent with the assumption that $R_{eff} \leq -0.5$.

Analytical and experimental investigations are in progress to verify the applicability of the equivalent 1-D residual stress distribution to predict the crack growth in a laser shock peened component. Tests at various applied stress ratios and detailed 2-D measurements of σ_{res} are in progress to verify the simplified analytical procedure.

ACKNOWLEDGMENT

This research was conducted at Wright Laboratory (WL/POTC and WL/MLLN), Wright-Patterson Air Force Base, OH 45433-7817, USA. R. John was supported under on-site contract number F33615-94-C-5200. The authors gratefully acknowledge the numerous discussions with Dr. T. Nicholas, Wright Laboratory (WL/MLLN), Wright-Patterson AFB, Ohio 45433, USA.

REFERENCES

1. Lykins C., Prevey P. and Mason P. (1995): *Laser Shock Peened Compressive Residual Profile after Exposure to Temperature*, WL-TR-95-2108, Wright-Patterson Air Force Base, Ohio 45433, USA.
2. Thompson S., Rushcau J. and Nicholas T. (1996), *Material Characterization of Laser-Shock Peened Titanium for Turbine Engine Applications*, Presented at Air Force Structural Integrity Program Conference, San Antonio, TX, USA.
3. Clauer A. and Holbrok J. (1981): *Effects of Laser Induced Shock Waves on Metals*, in Shock Waves and High Strain Rate Phenomena in Metals, Plenum Publishing Inc., New York, NY, USA.
4. Glinka, G.(1979): *Effect of Residual Stresses on Fatigue Crack Growth in Steel Weldments under Constant and Variable Amplitude Load*, Fracture Mechanics, ASTM STP 677, American Society for Testing and Materials, West Conshohocken, PA, USA, pp. 198-218.
5. Lykins C., John R. and Kroupa J. (1997): *Weight Function for a Tapered Three Point Bend Specimen*, to be published.
6. Skinn D., Gallagher J., Berens A., Huber P. and Smith J. (1994): Damage Tolerant Design Handbook, WL-TR-94-4052, Vol. 2, pp 278-332, Wright-Patterson Air Force Base, Ohio 45433, USA.

Reference: John, R. and Rigling, B., "Effect of Height to Width Ratio on K and CMOD Solutions for a Single Edge Cracked Geometry with Clamped Ends,", Engineering Fracture Mechanics, V. 60, No. 2, pp. 147-156.

EFFECT OF HEIGHT TO WIDTH RATIO ON K AND CMOD SOLUTIONS FOR A SINGLE EDGE CRACKED GEOMETRY WITH CLAMPED ENDS

Reji John[1] and Brian Rigling[2]
Materials Directorate, Wright Laboratory (WL/MLLN),
Wright-Patterson AFB, OH 45433-7817, U.S.A.
[1] University of Dayton Research Institute, Dayton, OH 45469-0128, U.S.A.
[2] Department of Physics, University of Dayton, Dayton, OH 45469, U.S.A.

ABSTRACT

Series expressions for the stress intensity factor (K) and crack mouth opening displacement (CMOD) were developed for a single edge cracked geometry with clamped ends using finite element analysis. The solutions are valid for crack length to width ratio (a/W) in the range $0 \le a/W \le 0.9$ and height to width ratio (H/W) in the range $2 \le H/W \le 10$. Experiments conducted using MSE(T) specimens with H/W = 3, 6 and 9 and compact tension specimens verified the applicability of the proposed solutions.

INTRODUCTION

Experimental work in the past has demonstrated the feasibility of testing metal matrix composites [1-3], ceramic matrix composites [4], and thin monolithic materials [3] using the single edge cracked geometry with clamped ends. Traditionally, the single edge crack geometry specimens were pin-loaded, allowing free rotation at the ends. Unfortunately, testing continuous fiber-reinforced composites using the pin-loaded geometry could result in bearing failure at the hole. Such failure at the hole can be avoided by using friction grips to load the single edge cracked geometry resulting in a clamped end condition. A schematic of a single edge crack geometry with clamped ends is shown in Fig. 1, where a = crack length, B = thickness, H = height, W = width, and P = load applied at the clamped ends. Note that H corresponds to the clear distance between the grips. The average far-field stress, σ can be calculated as,

$$\sigma = \frac{P}{BW} \quad . \qquad (1)$$

Automated fatigue crack growth testing requires a nonvisual method of measuring crack length (a) and an expression for the stress intensity factor (K). The load versus crack mouth opening displacement (CMOD) response of the specimen can be used to monitor the changes in the compliance of the specimen during testing. Knowing the solutions for CMOD, the current crack length can be calculated from the specimen compliance (=CMOD/P). Several investigators [5-8] have determined linear elastic fracture mechanics solutions of K for the MSE(T) geometry. The solutions for CMOD were not reported in these references [5-8]. Using finite element analysis, Blatt et al. [9] and John et al. [10] developed K and compliance solutions for the MSE(T) geometry with H/W = 4.0. The requirement of H/W = 4.0 is sometimes

restrictive especially when testing new expensive advanced materials such as composites. Hence, new K and compliance solutions are required for the MSE(T) geometry applicable over a wide range of H/W.

This paper describes the development of expressions for K and compliance for the MSE(T) geometry applicable in the range $2 \leq H/W \leq 10$ and $0.0 \leq a/W \leq 0.9$. Extensive finite element analysis was conducted to generate K and compliance results. Experiments were also conducted using MSE(T) specimens with H/W = 3, 6 and 9 and the compact tension geometry to verify the applicability of the proposed solutions.

AVAILABLE LEFM SOLUTIONS

As shown in Fig. 1, the clamped end condition implies rotationally constrained ends with uniform end displacements. Marchand [6] and Ahmad [7] derived K solutions for a wide range of H/W and a/W. The solution was based on the superposition of K due to uniform stress and bending stress distributions such that the resultant rotations of the edges were zero, and the displacements (v) at $y = \pm H/2$ were uniform. The expression for K was derived as [6,7]:

$$K = \sigma\sqrt{\pi a}\, F, \tag{2}$$

where

$$F = F_T - 6\xi_1 F_B \tag{3}$$

F_T and F_B correspond to geometry correction factors found in Ref. 11 for pin-loaded single edge cracked geometry subjected to uniform stress and pure bending distributions, respectively. The term x_1 can be obtained as [7]:

$$\xi_1 = \frac{\xi_2}{\xi_3 + 12\dfrac{H}{W}}, \tag{4}$$

where

$$\xi_2 = \frac{12\pi}{W^2}\int_0^a a' F_T(a'/W) F_B(a'/W)\, da' \text{ , and} \tag{5}$$

$$\xi_3 = \frac{72\pi}{W^2}\int_0^a a' F_B^2(a'/W)\, da' . \tag{6}$$

Solving Eqns. (1)-(6), we obtain the stress intensity factors for any a/W and $H/W \geq 2.0$. Figure 2 highlights the effect of the ratio H/W on normalized K for the MSE(T) geometry. The results obtained using Eqns. (1)-(6) for H/W=4 and 24 are compared with the solutions for a pin-loaded single edge cracked geometry, SE(T) [11] and a double edge cracked geometry, DE(T) [11]. The K solution for a MSE(T) geometry is bounded by the solutions for SE(T) and DE(T) geometries. For deep crack lengths, i.e. $a/W \approx 0.7$-0.8, the MSE(T) solution is within 15% of that of SE(T) geometry only if $H/W \geq 100$ [9]. The normalized K for the MSE(T) geometry is approximately independent (within ±20%) of H/W only for $a/W \leq 0.20$. Similarly, the solution for CMOD can also be expected very sensitive to the ratio H/W. Hence, finite element analysis was conducted to generate the K and CMOD values for a wide range of a/W and H/W as discussed next.

FINITE ELEMENT ANALYSIS

The finite element analysis program ADINA® [12] was used to generate the K and compliance solutions for a/W ranging from 0.1 to 0.9, and H/W ranging from 2.0 to 10.0. Eight-noded plane stress quadrilateral elements were used in the finite element model. Around the crack tip, quarter-point singular elements [13] were utilized to simulate the singularity at the crack tip. The typical mesh contained about 1500 elements. The number of nodes along the crack ranged from 100 for a/W=0.1 to 1000 for a/W=0.9. The mesh was made more refined along the crack for automating the generation of data corresponding to numerous crack lengths. John et al. [10] developed the automated finite element analysis procedure using ADINA® [12] and Mathematica® [14].

The accuracy of the finite element mesh used in this study was verified by simulating the pin-loaded end condition with constant stress. The K from the finite element analysis were within ± 1% of the handbook solutions [11]. In the finite element analysis conducted by Dao and Mettu [8], a uniform displacement was applied at the clamped ends and the average stress along the ends was used to normalize the stress intensity factors. In this study, a constant stress distribution was applied along the crack surface and the multipoint constraint (MPC) feature available in ADINA was used to ensure uniform displacement along the ends. The MPC condition forced the nodes along the top edge to displace the same amount as the corner node in the loading direction. An additional condition ensuring zero displacement in the x-direction along the top edge was imposed consistent with a clamped end condition.

K was calculated from the crack tip quarter-point displacements [13,15,16] using,

$$K = \frac{E}{4}\sqrt{\frac{8\pi}{L}}v_b \,, \tag{7}$$

where v_b is the displacement of the quarter-point node of the crack-tip element on the crack surface, L is the length of the quarter-point element, and E is the Young's modulus. The non-dimensionalized stress intensity factor, F was obtained as,

$$F = \frac{K}{\sigma\sqrt{\pi a}} \,. \tag{8}$$

The crack mouth opening displacement (CMOD) is defined as the total crack opening displacement at x = 0. The non-dimensionalized CMOD was calculated as,

$$G = \frac{E\,CMOD}{2\sigma\,a} \,. \tag{9}$$

F and G obtained using finite element analysis for various a/W and H/W are reported in Tables 1 and 2, respectively. The results in these tables correspond to the ranges $0 \le a/W \le 0.90$ and $2 \le H/W \le 10$. The limiting solutions for F and G at $a/W \to 0$ [11] are also shown in these tables. The values of F obtained during this study correlate well with those reported by Bowie et al. [5], Dao and Mettu [8] and Blatt et al. [9].

EXPRESSIONS FOR K, CMOD AND NORMALIZED CRACK LENGTH

F and G shown in Tables 1 and 2 are plotted in Figs. 3 and 4, respectively. As discussed earlier, F and G depend on a/W and H/W. For a given crack length to width ratio, F and G increase with increase in H/W. The change in G is significantly higher than that in F. The value of is approximately independent (within ±20%) of H/W for $a/W \le 0.2$. The results in Tables 1 and 2 were used to develop expressions for F and G as described below. The expression for F is given by Eqn. (10).

$$F = \frac{1.1215 + \sum_{i=1}^{6} A_i \left(\frac{a}{W}\right)^i}{\left(1 - \frac{a}{W}\right)^{3/2}} \qquad (10)$$

where

$$A_i = \sum_{j=0}^{2} B_{ij} \left[\log\left(\frac{H}{W}\right)\right]^j . \qquad (11)$$

The constants B_{ij} are listed in Table 3. Equation (10) is valid in the ranges $0 \le a/W \le 0.9$ and $2 \le H/W \le 10$, and agrees with the finite element results within ± 0.7%. The expression for G is given by Eqn. (12).

$$G = \frac{2.9086 + \sum_{i=1}^{6} C_i \left(\frac{a}{W}\right)^i}{\left(1 - \frac{a}{W}\right)^{2}} \qquad (12)$$

where

$$C_i = \sum_{j=0}^{3} D_{ij} \left[\log\left(\frac{H}{W}\right)\right]^j . \qquad (13)$$

The constants D_{ij} are listed in Table 4. Equation (12) is valid in the ranges $0 \le a/W \le 0.9$ and $2 \le H/W \le 10$, and agrees with the finite element results within ± 0.9%.

Compliance based automated crack growth and fracture testing requires an expression for a/W in terms of the normalized compliance of the specimen. The compliance of the specimen is given by C = CMOD / P and the normalized compliance is given by EBC. Note that EBC = 2Ga/W. Typically EBC ranges from 0.0 to ∞. Hence, we define a new variable, ψ as given by Eqn. (14) [17,18] such that ψ ranges from 1 to 0 corresponding to $0 \le EBC \le \infty$.

$$\psi = \frac{1}{1 + \sqrt{EBC}} \qquad (14)$$

Knowing ψ, the crack length can be calculated using Eqn. (15).

$$\frac{a}{W} = \sum_{i=1}^{6} M_i \left(\frac{1}{\psi}\right)^i \qquad (15)$$

where

$$M_i = \sum_{j=0}^{2} N_{ij} \left(\frac{W}{H}\right)^j . \qquad (16)$$

The constants N_{ij} are listed in Table 5. Equation (15) is valid in the ranges $0.1 \le a/W \le 0.9$ and $2 \le H/W \le 10$, and agrees with the finite element results within ± 1.5%.

EXPERIMENTAL PROCEDURE

Fatigue crack growth tests were conducted using MSE(T) and compact tension, C(T) specimens to verify the applicability of the expressions for normalized K, CMOD and crack length as described next.

Material and Test Specifications

Aluminum 6061-T651 was used as the model material during this study. Three MSE(T) specimens were machined with W = 18.7 mm, and H/W = 3, 6 and 9. Two C(T) specimens were also machined with W = 20.3 mm in accordance with ASTM E647-91 [17]. All the specimens were machined from the same plate with a nominal thickness = 3.0 mm. The initial machined notch length to width ratio (a_0/W) was ≈0.2. The total length of the MSE(T) specimens was equal to the sum of H and grip zones (≈ 19 mm at each end). All the tests were conducted using a closed-loop servo-hydraulic automated testing system [19]. The tests were conducted at room temperature in laboratory air at a frequency of 3 Hz with a load ratio, R (= minimum load / maximum load) of 0.5. During the tests, the CMOD was measured using a high-resolution extensometer for the MSE(T) specimens and a clip gage for the C(T) specimens. The ends of the MSE(T) specimens were clamped using hydraulic friction grips, which did not allow rotation or transverse displacement (u) at the ends.

Test Procedure

Each specimen was precracked using the ASTM procedure [17]. Accordingly, the crack extension from the initial notch was ≈ 1 mm at the end of precracking. After precracking, the MSE(T) specimens were tested under constant maximum load and stress ratio conditions. The C(T) specimens were tested under decreasing maximum K and constant maximum load conditions. All the tests were continued until failure.

Crack length measurement

During the automated tests, the load versus CMOD response of the specimen was measured at regular intervals based on equal crack extensions. A typical load versus CMOD plot is shown in Fig. 5. This figure includes a plot of load versus CMOD (a) and the load versus differential CMOD (b). A least square procedure was used to fit a straight line (c) to the unloading data between the upper and lower windows (UW and LW, respectively). The inverse slope of this line is equal to the elastic unloading compliance of the specimen, which when substituted in Eqn. (15) yields the compliance crack length. The deviation of the measured displacement from the least squares fit is magnified three times and plotted as the load versus differential CMOD data in the same figure. Thus during the tests, the compliance crack length was monitored as a function of applied cycles.

Optical measurements of crack length were recorded periodically using traveling microscopes to verify the accuracy of the compliance technique, i.e. Eqn. (15). The optical crack lengths were measured on both sides of the specimen and the average value is reported in the following sections.

RESULTS

Validation of Compliance Solution

The crack growth history of the MSE(T) specimen with H/W=3 is shown in Fig. 6. The compliance crack length correlates well with the periodic optical measurements during the entire test. The normalized optical and compliance crack length data are compared in Fig. 7 for the MSE(T) specimens with H/W=3, 6 and 9. The compliance crack length values are within 5% of the optical measurements for a/W ranging from 0.2 to 0.9. As given in Eqns. (14) and

(15), the compliance crack length is calculated assuming a value for the elastic modulus, E. In Figs. 6 and 7, the compliance crack length was calculated assuming E = 68-70 GPa which is very close to the reported value of E for Al 6061-T651. Thus, the results shown in Figs. 6 and 7 validate the compliance solutions given by Eqns. (12) and (15) for crack lengths up to a/W = 0.9.

Validation of K Solution

Using the crack length versus cycles response, the crack growth rate (da/dN) versus applied stress intensity factor range (ΔK) behavior was determined for the MSE(T) and C(T) specimens. Note that ΔK was calculated = K_{max} - K_{min}, where K_{max} = maximum K and K_{min} = minimum K. The crack growth rate behavior obtained from the different geometries is shown in Fig. 8. The data from the MSE(T) specimen with H/W = 3, 6 and 9 are identical and correlate well with that from the C(T) specimens. The good correlation between the results from the different geometries validates the general expression for K given by Eqn. (2) and (10).

Discussion

Note that in Fig. 1, H = clear distance between clamped ends and H ≠ length of the specimen. Since the K and CMOD solutions are very sensitive to H/W, especially for long cracks (a/W ≥ 0.2), accurate measurement of H/W is required. The single edge cracked geometry with clamped ends is ideally suited for testing thin materials since the loading is devoid of bending and the CMOD can be measured easily using extensometers. This technique has been successfully used for fatigue crack growth testing of titanium alloy specimens with thicknesses ranging from 0.2 to 3.0 mm [20].

As discussed earlier, the boundary conditions at the clamped ends enforce zero rotation and zero transverse displacement. The K and CMOD values are extremely sensitive to the end condition. Hence, the clamped end condition should be maintained throughout the test duration. Slippage at the grips is a potential problem. Using strain gages glued along the edges (x=0 and W) close to the clamped ends, the strains can be monitored. The strain along the edges close to the ends should be equal during the entire test. An alternate approach is to measure the CMOD during the test and monitor the compliance crack length from the measured load versus CMOD response. The modulus (E) to calculate the compliance crack length should be close to that obtained from conventional tension tests for monolithic materials. Good correlation between the compliance and optical crack lengths implies that the clamped end condition was maintained during the test.

SUMMARY

Series expressions for were developed for the stress intensity factor (K) and the crack mouth opening displacement (CMOD) of a single edge cracked geometry with clamped ends. The solutions are valid for crack length to width ratio (a/W) in the range 0 ≤ a/W ≤ 0.9 and height to width ratio (H/W) in the range 2 ≤ H/W ≤ 10. An expression was also developed to calculate the crack length from the measured compliance. Experiments conducted using MSE(T) specimens with H/W = 3, 6 and 9 and compact tension specimens verified the applicability of the K and CMOD solutions. The proposed equations can be used for fracture and fatigue crack testing of monolithic and composite materials.

ACKNOWLEDGMENT

The research was conducted at the Materials Directorate, Wright Laboratory, Wright-Patterson Air Force Base, OH 45433-7817, USA under on-site contract number F33615-94-C-5200. The second author was supported by the Southwestern Ohio Council For Higher Education (SOCHE) program under US Air Force contract number F33615-92-C-5904 as an

Undergraduate Student Assistant. Mr. David A. Johnson, currently a Graduate Research Assistant at Harvard University, Cambridge, MA, assisted in conducting the finite element analysis. The authors also gratefully acknowledge the assistance of Mr. A. F. Lackey in conducting the experiments.

REFERENCES

1. M. L. Gambone, Fatigue and fracture of titanium aluminides. WRDC-TR-89-4145, Vol. 2. Materials Laboratory, Wright-Patterson AFB, OH 45433-6533 (Feb. 1990).
2. L.J. Ghosn, P. Kantzos and J. Telesman, Modeling of crack bridging in a unidirectional metal matrix composite. *Int. J. Fracture* **54**, 345-357 (1992).
3. R. John, A.F. Lackey and N.E. Ashbaugh, Fatigue crack growth parallel to fibers in unidirectionally reinforced SCS-6/Timetal®21S, *Scripta Metallurgica et Materialia*, **35**, 711-716 (1996).
4. V.A. Kramb and R. John, Fatigue crack growth behavior of a woven silicon carbide/silicon carbide ceramic matrix composite, *Thermal and Mechanical Test Methods and Behavior of Continuous-Fiber Ceramic Matrix Composites*, ASTM STP **1309**, Accepted for publication, (1996).
5. O. L. Bowie, C. E. Freese and D. M. Neal, Solution of plane problems of elasticity utilizing partitioning concepts. *J. Appl. Mech.* **40**, 767-772 (Sept. 1973).
6. N. Marchand, D. M. Parks and R. M. Pelloux, K_i-solutions for single edge notch specimens under fixed end displacements. *Int. J. Fracture* **31**, 53-65 (1986).
7. J. Ahmad, V. Papaspyropoulos and A. T. Hopper, Elastic-plastic analysis of edge-notched panels subjected to fixed grip loading. *Engineering Fracture Mech.* **38**, 283-294 (1991).
8. T. X. Dao and S. R. Mettu, Analysis of an edge-cracked specimen subjected to rotationally-constrained end displacements. NASA JSC 32171 (Aug. 1991).
9. D. Blatt, R. John, and D. Coker, *Engineering Fracture Mechanics* 47 (1994) 521-532.
10. R. John, S.G. Kaldon, D.A. Johnson and D. Coker, *International Journal of Fracture*, **72**, 145-158 (1995).
11. H. Tada, P. C. Paris and G. R. Irwin, *The Stress Analysis of Cracks Handbook*. Del Research Corporation, St. Louis, MO (1985).
12. ADINA--A finite element program for automatic dynamic incremental nonlinear analysis. Report ARD 89-1, ADINA R & D, Inc., Watertown, MA (1989).
13. R. S. Barsoum, On the use of isoparametric finite elements in linear elastic fracture mechanics. *Int. J. Numer. Meth. Engng* **10**, 25-37 (1976).
14. Mathematica, Wolfram Research, Inc., Champaign, IL (1991).
15. A. R. Ingraffea and C. Manu, Stress intensity factor computation in three dimensions with quarter point elements. *Int. J. Numer. Meth. Engng* **15**, 1427-1445 (1980).
16. N. A. B. Yehia and M. S. Shephard, On the effect of quarter-point element size on fracture criteria. *Int. J. Numer. Meth. Engng* **21**, 1911-1924 (1985).
17. ASTM E647-91, Standard test method for measurement of fatigue crack growth rates. *Annual book of ASTM Standards*, Section3, Vol. 03.01. American Society for Testing and Materials, Philadelphia, PA (1991).
18. R. John, Stress intensity factor and compliance solutions for an eccentrically loaded single edge cracked geometry, *Engineering Fracture Mechanics*, Submitted for publication (1997).
19. G. A. Hartman, N. E. Ashbaugh and D. J. Buchanan, A sampling of mechanical test automation methodologies used in a basic research laboratory. *Automation in Fatigue and Fracture Testing and Analysis*, ASTM STP **1231**, 36-50 (1994)
20. R. John, A.F. Lackey and N.E. Ashbaugh, Cyclic crack propagation parallel to fibers in unidirectionally reinforced metal matrix composite, To be submitted for publication (1997).

Table 1. Normalized stress intensity factor, F obtained using finite element analysis.

a/W	H/W = 2	H/W = 3	H/W = 4	H/W = 4.5	H/W = 5	H/W = 5.5	H/W = 6	H/W = 6.5	H/W = 7	H/W = 8	H/W = 9	H/W = 10
0.00	1.12150	1.12150	1.12150	1.12150	1.12150	1.12150	1.12150	1.12150	1.12150	1.12150	1.12150	1.12150
0.10	1.12523	1.14394	1.15342	1.15661	1.15919	1.16127	1.16306	1.16454	1.16586	1.16793	1.16961	1.17091
0.15	1.13343	1.17223	1.19249	1.19943	1.20501	1.20961	1.21352	1.21680	1.21967	1.22430	1.22798	1.23090
0.20	1.14345	1.20703	1.24154	1.25354	1.26330	1.27140	1.27825	1.28410	1.28920	1.29751	1.30408	1.30938
0.25	1.15555	1.24704	1.29893	1.31733	1.33245	1.34510	1.35589	1.36515	1.37322	1.38651	1.39709	1.40564
0.30	1.17062	1.29170	1.36377	1.38993	1.41166	1.43005	1.44582	1.45945	1.47140	1.49125	1.50716	1.52012
0.35	1.18985	1.34097	1.43559	1.47084	1.50053	1.52588	1.54784	1.56698	1.58387	1.61216	1.63506	1.65388
0.40	1.21468	1.39513	1.51423	1.55985	1.59881	1.63251	1.66198	1.68789	1.71096	1.75000	1.78193	1.80845
0.45	1.24665	1.45486	1.59973	1.65682	1.70642	1.74985	1.78826	1.82241	1.85305	1.90554	1.94904	1.98558
0.50	1.28757	1.52112	1.69233	1.76192	1.82327	1.87781	1.92666	1.97057	2.01037	2.07946	2.13758	2.18702
0.55	1.33956	1.59535	1.79257	1.87521	1.94932	2.01618	2.07688	2.13213	2.18274	2.27192	2.34819	2.41405
0.60	1.40538	1.67957	1.90135	1.99713	2.08452	2.16461	2.23834	2.30634	2.36938	2.48224	2.58061	2.66695
0.65	1.48886	1.77679	2.02035	2.12864	2.22918	2.32276	2.41022	2.49194	2.56867	2.70840	2.83274	2.94390
0.70	1.59575	1.89183	2.15268	2.27193	2.38446	2.49088	2.59175	2.68735	2.77825	2.94683	3.10017	3.23999
0.75	1.73562	2.03299	2.30460	2.43192	2.55397	2.67109	2.78371	2.89187	2.99605	3.19278	3.37580	3.54623
0.80	1.92614	2.21619	2.48940	2.62033	2.74757	2.87134	2.99190	3.10918	3.22350	3.44320	3.65215	3.85083
0.85	2.20485	2.47644	2.73863	2.86660	2.99241	3.11620	3.23816	3.35805	3.47624	3.70687	3.93062	4.14762
0.90	2.67101	2.90858	3.14207	3.25761	3.37220	3.48593	3.59899	3.71107	3.82253	4.04266	4.25978	4.47372

Note: F for a/W=0 corresponds to the limiting solution.

Table 2. Normalized crack mouth opening displacement, G obtained using finite element analysis.

a/W	H/W = 2	H/W = 3	H/W = 4	H/W = 4.5	H/W = 5	H/W = 5.5	H/W = 6	H/W = 6.5	H/W = 7	H/W = 8	H/W = 9	H/W = 10
0.00	2.90860	2.90860	2.90860	2.90860	2.90860	2.90860	2.90860	2.90860	2.90860	2.90860	2.90860	2.90860
0.10	2.93521	2.98742	3.01388	3.02283	3.02998	3.03583	3.04079	3.04495	3.04861	3.05442	3.05905	3.06268
0.15	2.96413	3.07682	3.13572	3.15586	3.17208	3.18546	3.19678	3.20634	3.21467	3.22813	3.23878	3.24727
0.20	2.99830	3.19137	3.29616	3.33256	3.36218	3.38678	3.40760	3.42536	3.44076	3.46600	3.48593	3.50197
0.25	3.03784	3.32940	3.49465	3.55321	3.60138	3.64170	3.67600	3.70546	3.73111	3.77344	3.80705	3.83430
0.30	3.08365	3.49013	3.73177	3.81943	3.89235	3.95398	4.00681	4.05251	4.09253	4.15908	4.21232	4.25581
0.35	3.13741	3.67370	4.00909	4.13395	4.23916	4.32906	4.40680	4.47462	4.53439	4.63470	4.71572	4.78244
0.40	3.20146	3.88109	4.32898	4.50045	4.64697	4.77369	4.88444	4.98191	5.06853	5.21537	5.33529	5.43501
0.45	3.27880	4.11408	4.69448	4.92320	5.12180	5.29580	5.44960	5.58640	5.70900	5.91932	6.09344	6.23976
0.50	3.37308	4.37533	5.10919	5.40734	5.67032	5.90407	6.11334	6.30155	6.47194	6.76811	7.01698	7.22887
0.55	3.48886	4.66851	5.57725	5.95790	6.29941	6.60754	6.88709	7.14168	7.37470	7.78562	8.13688	8.44033
0.60	3.63186	4.99842	6.10341	6.58050	7.01592	7.41495	7.78218	8.12094	8.43474	8.99703	9.48684	9.91704
0.65	3.80963	5.37173	6.69323	7.28075	7.82621	8.33406	8.80829	9.25175	9.66774	10.42596	11.10024	11.70338
0.70	4.03267	5.79772	7.35375	8.06487	8.73617	9.37098	9.97246	10.54273	11.08463	12.09021	13.00433	13.83837
0.75	4.31657	6.29035	8.09508	8.94091	9.75187	10.53019	11.27813	11.99688	12.68870	13.99594	15.21142	16.34378
0.80	4.68666	6.87274	8.93470	9.92261	10.88307	11.81736	12.72688	13.61201	14.47436	16.13246	17.70863	19.20791
0.85	5.18989	7.58884	9.90889	11.04080	12.15415	13.24963	14.32806	15.38911	16.43402	18.47461	20.45380	22.37336
0.90	5.93208	8.54064	11.11012	12.38078	13.64176	14.89338	16.13628	17.36962	18.59448	21.01660	23.40460	25.75780

Note: G for a/W=0 corresponds to the limiting solution.

Table 3. Constants B_{ij} used in Equation (11).

i	j = 0	j = 1	j = 2
1	-1.6071E+00	-2.5295E-01	1.4856E-01
2	-4.0053E+00	1.9198E+01	-8.7311E+00
3	1.1513E+01	-5.0147E+01	2.1296E+01
4	-5.8413E+00	3.0109E+01	3.8125E+00
5	-4.6316E+00	1.4478E+01	-3.7584E+01
6	3.4420E+00	-1.3352E+01	2.1050E+01

Table 4. Constants D_{ij} used in Equation (13).

i	j = 0	j = 1	j = 2	j = 3
1	-6.0503E+00	1.4389E+00	-1.2694E+00	0.0000E+00
2	-1.4413E+00	2.2670E+01	-8.8785E-01	0.0000E+00
3	-6.4384E+00	4.7573E+00	-5.2142E+01	0.0000E+00
4	5.7307E+01	-2.0564E+02	2.4435E+02	0.0000E+00
5	-7.7132E+01	3.0193E+02	-3.2597E+02	0.0000E+00
6	3.0795E+01	-1.2485E+02	1.3534E+02	3.8746E-01

Table 5. Constants N_{ij} used in Equation (16).

i	j = 0	j = 1	j = 2
1	-4.0742E-01	-6.6430E-01	5.5044E+00
2	4.5795E-01	1.1923E+00	-9.1426E+00
3	-1.4013E-01	-8.2161E-01	5.6727E+00
4	1.7197E-02	2.6791E-01	-1.6349E+00
5	-5.4207E-04	-3.9546E-02	2.2108E-01
6	-2.7243E-05	2.1590E-03	-1.1376E-02

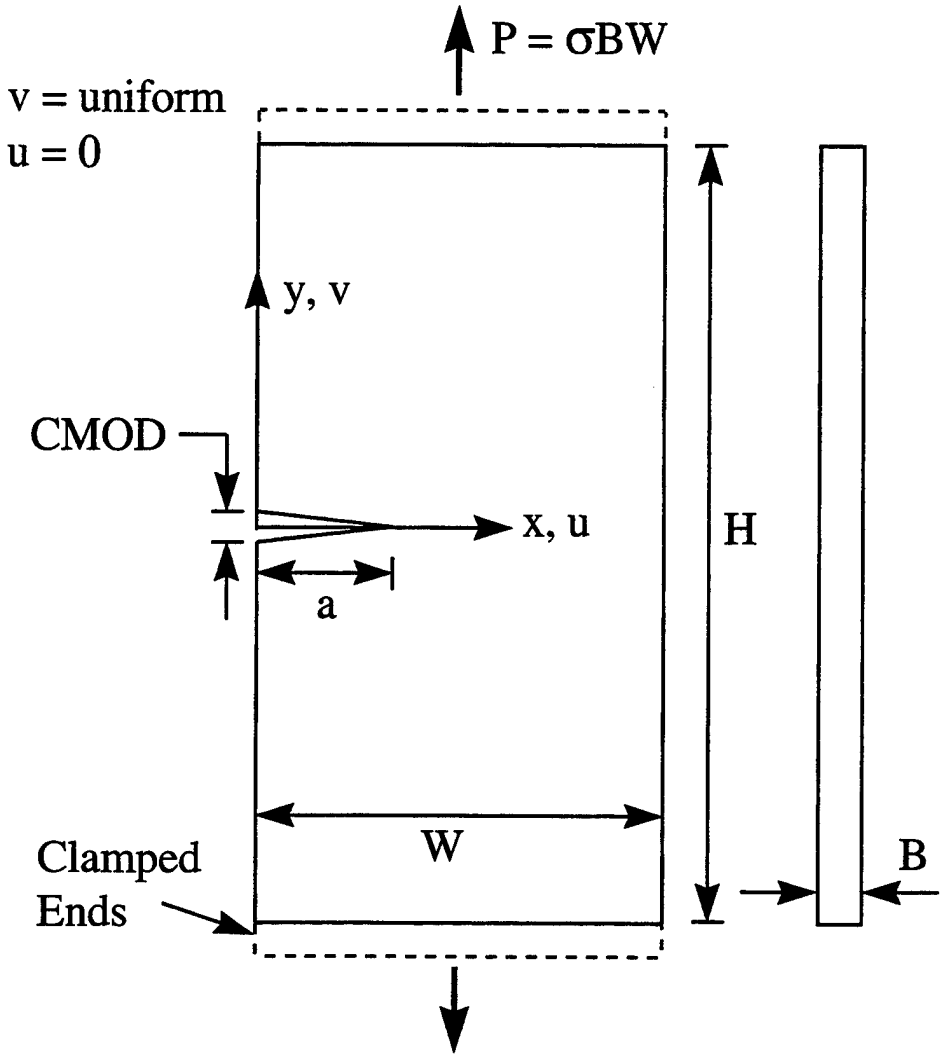


Fig. 1. Schematic of the single edge geometry with clamped ends, MSE(T).

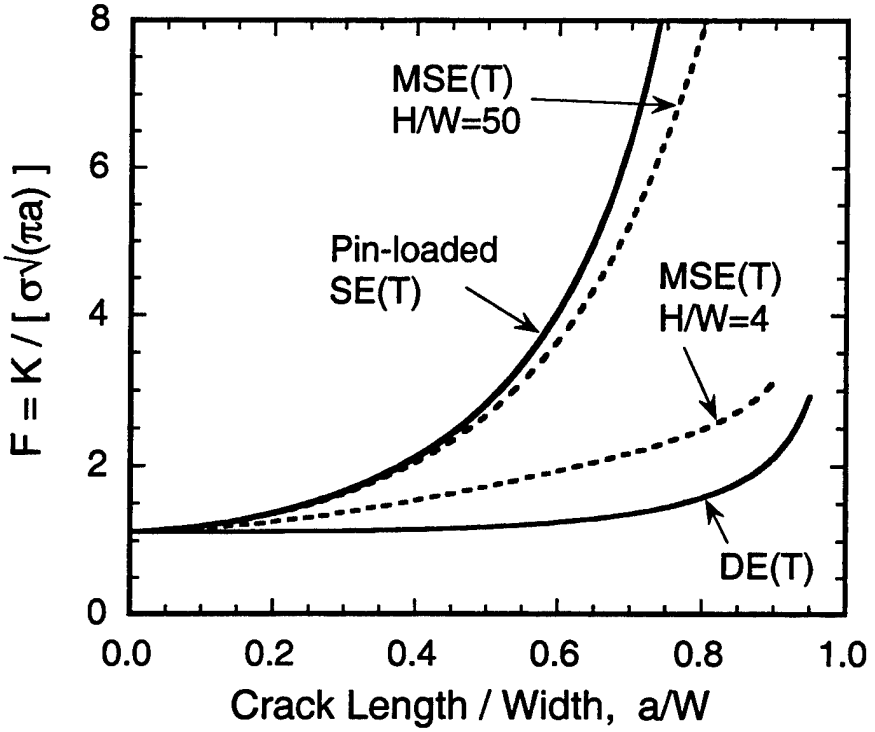


Fig. 2. Normalized K solutions for a single edge and double edge cracked geometries.

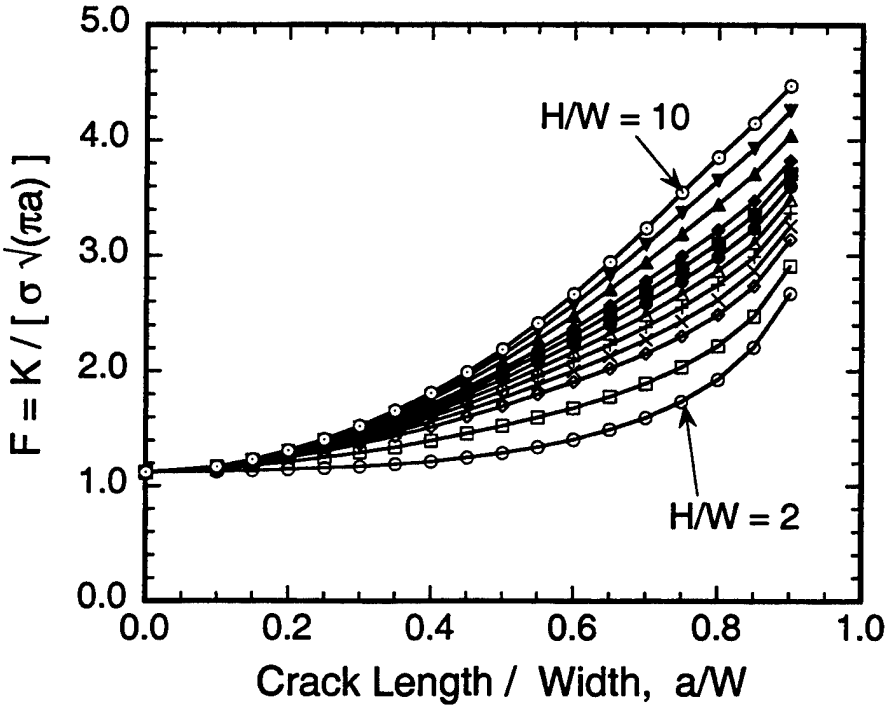


Fig. 3. Effect of a/W and H/W on the normalized stress intensity factor, F for the MSE(T) geometry.

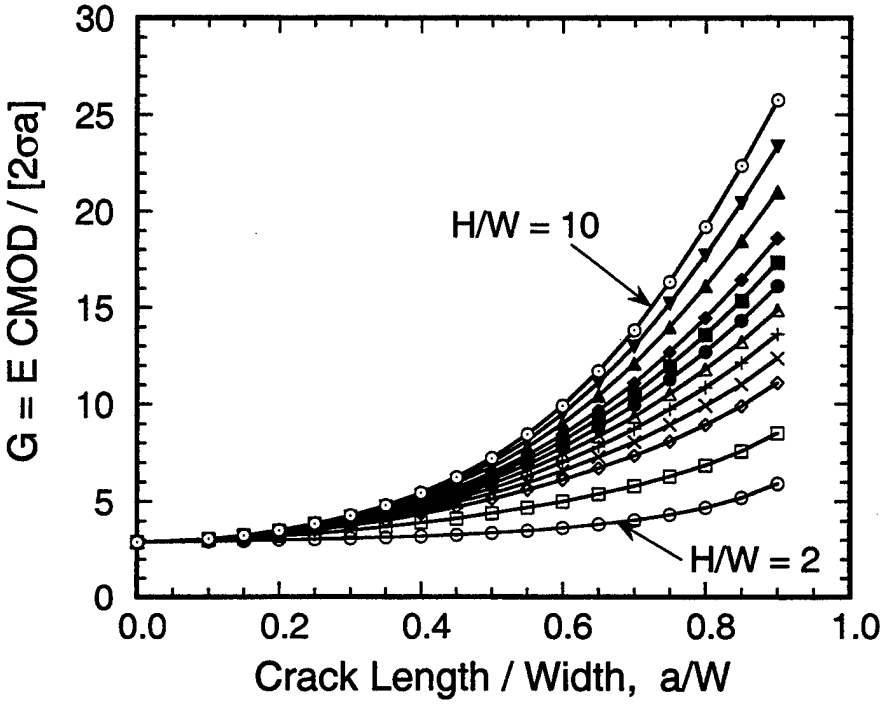


Fig. 4. Effect of a/W and H/W on the normalized crack mouth opening displacement, G for the MSE(T) geometry.

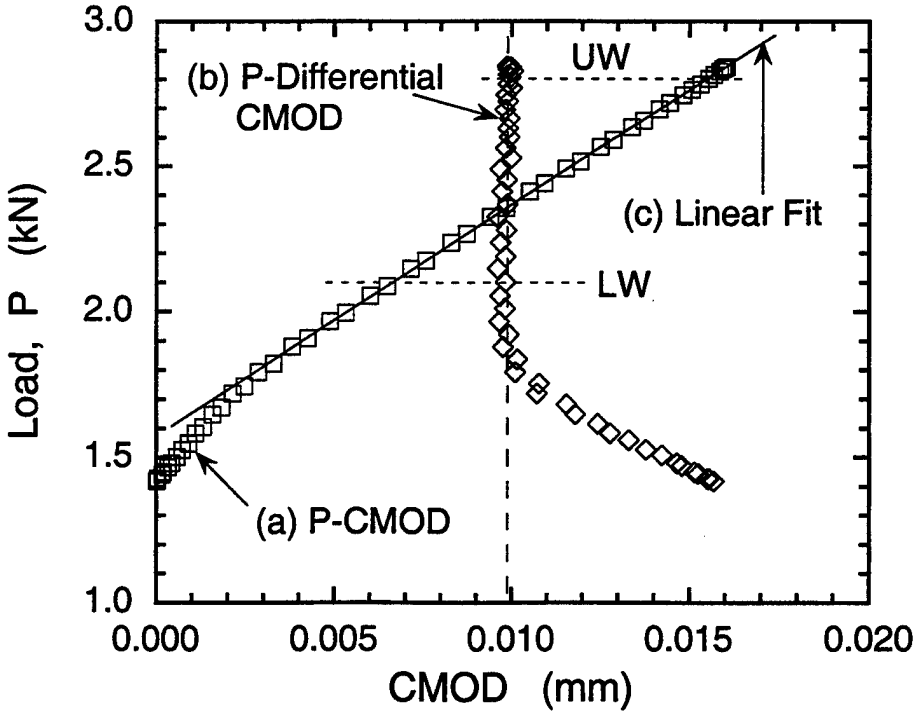


Fig. 5. (a) Typical load versus CMOD response measured during the test, (b) corresponding load versus differential CMOD response, and (c) linear fit to the initial portion of the unloading load versus CMOD response.

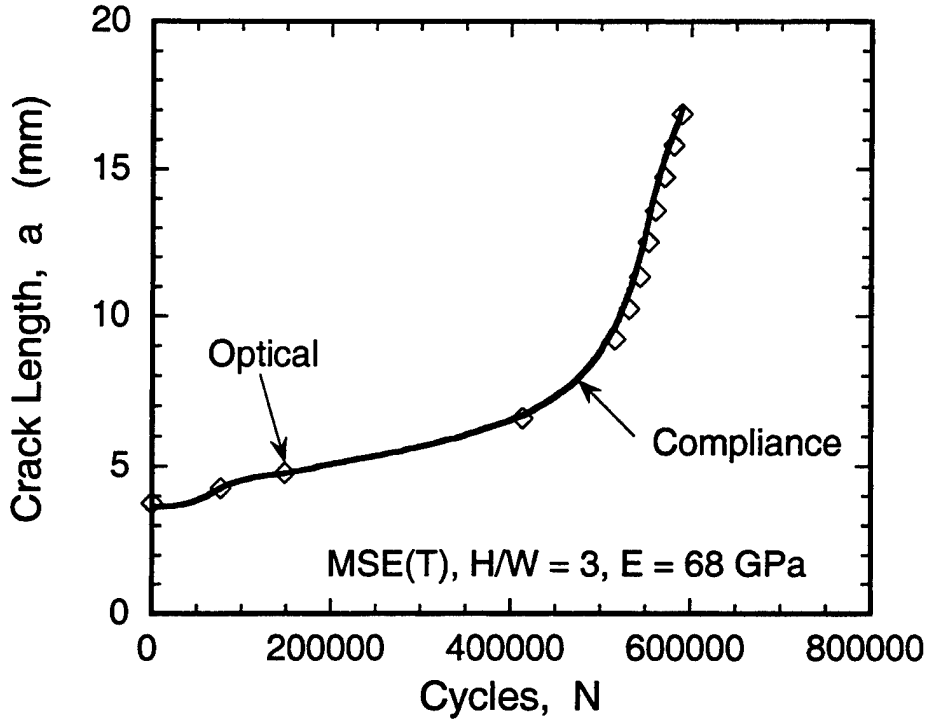


Fig. 6. Comparison of compliance and optical crack length versus cycles response for the MSE(T) specimen with H/W = 3.

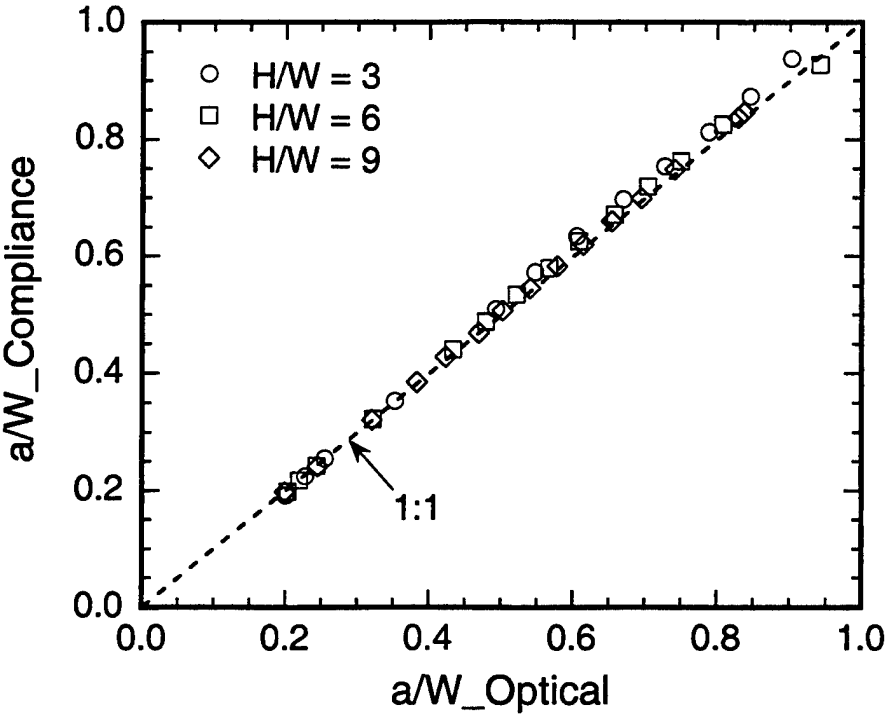


Fig. 7. Comparison of normalized compliance and optical crack lengths obtained from the MSE(T) specimens with H/W = 3, 6 and 9.

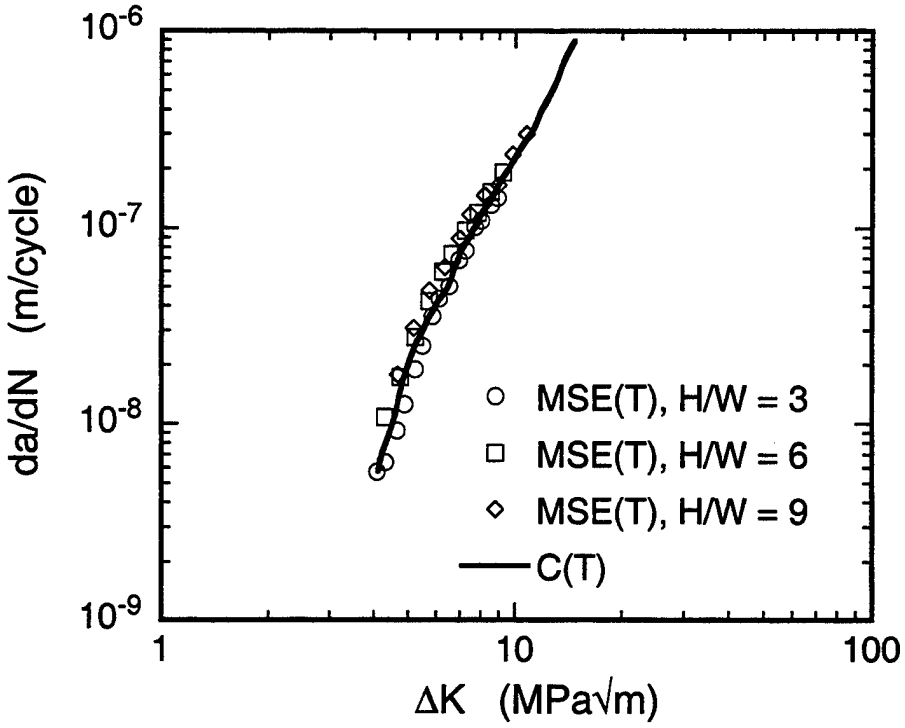


Fig. 8. Correlation of the crack growth rate versus applied stress intensity factor range behavior measured using the MSE(T) (H/W = 3, 6 & 9) and C(T) geometries.

This page intentionally left blank

Reference: John, R., "Stress Intensity Factor and Compliance Solutions For an Eccentrically Loaded Single Edge Cracked Geometry," Engineering Fracture Mechanics V. 58, No. 1/2, pp. 87-96.

Stress Intensity Factor and Compliance Solutions For an Eccentrically Loaded Single Edge Cracked Geometry

Reji John[1]

Materials Directorate, Wright Laboratory (WL/MLLN),
Wright-Patterson Air Force Base, OH 45433-7817 , USA
[1]University of Dayton Research Institute, Dayton, OH 45469-0128, USA

Abstract

Eccentrically pin-loaded single edge cracked geometries are an excellent alternative to compact tension type geometries for testing some advanced composite materials. This paper discusses the development of stress intensity factor and compliance solutions for an eccentrically pin-loaded single edge cracked geometry, ESE(T).

Keywords

Compliance, Eccentric load, Fracture, Fatigue Crack Growth, Single Edge Crack, Stress Intensity Factor, Test Geometry

Introduction

The schematic of an eccentrically pin-loaded single edge cracked geometry, ESE(T) is shown in Fig. 1. In this geometry, P = applied load, CMOD = crack mouth opening displacement, a = crack length, W = width of plate, d = distance of load-line from edge of plate, e = eccentricity of load-line = 0.5W - d, B = thickness, and H = distance between points of load application. This geometry was used by John et al. [1] for analyzing thermally induced crack growth in a steel plate with H = 2.9W and d = 0.33W. Recently, Piascik et al. [2,3] introduced a geometry identified as the Extended Compact Tension, EC(T). The EC(T) geometry [2,3] is similar to the ESE(T) geometry shown in Fig. 1 with H = 3W and d = 0.2W. Piascik and Willard [4] used the EC(T) geometry for investigating environmental fatigue crack propagation of small surface cracks and long through-the-thickness cracks in aluminum alloys. Underwood et al. [5] used the EC(T) geometry for characterizing the translaminar fracture toughness of carbon/epoxy laminates. Richardson and Goree [6] used a geometry similar to ESE(T) for fracture testing of polymethyl methacrylate (PMMA) to study the size effect on fracture toughness and evaluate a two-parameter fracture model.

John et al. [1] calculated the stress intensity factor, K for the ESE(T) geometry using tension and bending solutions [8] for a pin-loaded single edge cracked geometry for $a/W \approx 0.3$ and $d/W = 0.33$. Richardson and Goree [6] used a finite element alternating method [7] to calculate K for the ESE(T) geometry with d/W ranging from 0.13 to 0.5 and H/W from 0.6 to 3.3. Piascik et al. [2,3] used the boundary force method [9] to develop K and CMOD solutions for the EC(T) geometry with d = 0.2W applicable in the range $0 \leq a/W \leq 1$. This paper discusses the development of K and compliance solutions for the ESE(T) geometry with d/W ranging from 0 to 0.5. The solutions obtained during this study were also compared with the results from Piascik et al. [3] for d = 0.2W.

Analytical Procedure

The proposed procedure is based on the superposition of the results for a single edge cracked geometry subjected to tension and bending loads as shown in Fig. 2. The stress intensity factor the ESE(T) geometry, $K_{I,ESET}$ can be calculated as,

$$K_{I,ESET} = K_{I,Tension} + K_{I,Bending} \cdot \quad (1)$$

K solutions are available [8] for the single edge cracked geometry subjected to tension and bending loads, as given by Eqns. (2) and (3).

$$K_{I,Tension} = \sigma_T \sqrt{\pi a}\, F_T \quad , \text{and} \quad (2)$$

$$K_{I,Bending} = \sigma_B \sqrt{\pi a}\, F_B \quad (3)$$

Where σ_T and σ_B are the far-field tension and bending stresses along the edges, respectively, and the equations for F_T and F_B are given in the Appendix. The terms F_T and F_B in the Appendix are valid for any a/W and H/W ≥ 1.5 within ±0.5% [8]. In Eqns. (2) and (3) the far-field stresses σ_T and σ_B are calculated as,

$$\sigma_T = \frac{P}{BW} \quad , \text{and} \quad (4)$$

$$\sigma_B = \frac{6\,P\,e}{B\,W^2} \cdot \quad (5)$$

Combining Eqns. (1)-(5) we obtain K_I for the ESE(T) geometry as,

$$K_{I,ESET} = \frac{P}{B\,W} \sqrt{\pi a}\, F_{ESET} \,, \quad (6)$$

where

$$F_{ESET} = F_T + \frac{6\,e}{W} F_B = F_T + \left(3 - \frac{6\,d}{W}\right) F_B \quad (7)$$

Similar to the solution for $K_{I,ESET}$, the CMOD for the ESE(T) geometry can be calculated as,

$$CMOD_{ESET} = CMOD_{Tension} + CMOD_{Bending} \cdot \quad (8)$$

The solutions for CMOD are also available [8] for the single edge cracked geometry subjected to tension and bending loads, as given by Eqns. (9) and (10).

$$CMOD_{Tension} = \frac{\sigma_T\, a}{E} G_T \quad , \text{and} \quad (9)$$

$$CMOD_{Bending} = \frac{\sigma_B\, a}{E} G_B \quad (10)$$

where the equations for G_T and G_B are given in the Appendix. G_T and G_B in the Appendix are valid for any a/W and H/W ≥ 1.5 within ±1.0% [8]. Combining Eqns. (8)-(10), we obtain the CMOD for the ESE(T) geometry as,

$$CMOD_{ESET} = \frac{P\,a}{B\,W\,E}\,G_{ESET}\,, \qquad (11)$$

where

$$G_{ESET} = G_T + \frac{6\,e}{W}\,G_B = G_T + \left(3 - \frac{6\,d}{W}\right)G_B \qquad (12)$$

Equations (7) and (12) were used to generate F_{ESET} and G_{ESET} solutions for the ESE(T) geometry as discussed later.

Limited finite element analysis was also conducted during this study to verify the results from the above procedure. The finite element analysis was conducted for a single edge cracked geometry with H/W=1.5, a/W=0.5 and $0 \le d/W \le 0.5$. Eight-node quadrilateral elements were used for the finite element mesh and collapsed quadrilateral singular elements with quarter-point nodes were used at the crack tip. These results were used to verify the effect of d/W on F_{ESET} and G_{ESET} as discussed later.

Results and Discussion

Effect of Eccentricity on K and CMOD

Using Eqns. (7) and (12), F_{ESET} and G_{ESET} were generated for a/W ranging from 0 to 1, and d/W from 0 to 0.5. These values of F_{ESET} and G_{ESET} are shown as solid lines in Figs. 3 and 4, respectively. Note that d = 0.5W corresponds to a single edge cracked geometry subjected to tension, and d = 0 to a specimen with the load-line coincident with the edge of the plate. When d = 0.5W, $F_{ESET} = F_T$ and $G_{ESET} = G_T$. As d/W decreases, the load-line moves from the center towards the edge of the specimen. The decrease in d/W corresponds to an increase in the bending component of the loading. Consequently, for a given crack length, F_{ESET} and G_{ESET} increase with decrease in d/W.

The effect of eccentricity of loading on F_{ESET} and G_{ESET} is shown in Fig. 5 for a/W = 0.2, 0.5 and 0.7. F_{ESET} and G_{ESET} decrease linearly with increase in d/W consistent with Eqns. (7) and (12). This implies that higher K and CMOD can be achieved for the same load as the load-line is moved towards the edge of the specimen. For example, at a/W=0.5, F_{ESET} increases by ≈85% when d/W decreases from 0.5 to 0.2. Such large increases in F_{ESET} significantly decreases the load required to conduct fracture and fatigue crack growth tests. Thus, a single specimen and test system configuration can be used to study the effect of tension and bending loading on the fracture and fatigue crack growth behavior of materials by varying the location of the load-line.

During compliance based fatigue crack growth tests, the changes in crack length can be monitored through changes in the compliance (C) of the specimen [10]. The normalized specimen compliance is defined as EBC, as given by,

$$EBC = EB\frac{CMOD}{P} = \frac{a}{W}G_{ESET}\,. \qquad (13)$$

Since the compliance can range from 0 to ∞, a convenient form of expressing EBC is achieved by defining a new variable U [3,10] as given by,

$$U = \frac{1}{1+\sqrt{EBC}}\,. \qquad (14)$$

Figure 6 shows a plot of the normalized crack length, a/W versus U for various values of d/W. Knowing U through measurement of the load-CMOD response, the corresponding a/W can be calculated using the equations developed later.

Comparison With Other Solutions

As discussed earlier, Piascik et al. [2,3] determined F_{ESET} and G_{ESET} for d/W = 0.2 and $0.1 \leq a/W \leq 0.92$ using the boundary force method. The solutions obtained during this study for d = 0.2W correlates well with the results from Piascik et al. [2,3] as shown in Figs. 3 and 4. The percentage difference between the results from this study and that from Piascik et al. [2,3] is within ±1.3% for F_{ESET} and G_{ESET}. Figures 3-5 also compares the solutions obtained using the principle of superposition with finite element results for d/W ranging from 0 to 0.5 and a/W = 0.5. The linear dependency of F_{ESET} and G_{ESET} on d/W is confirmed by the finite element results.

Expressions for Normalized K, CMOD and Crack Length

Using the results for d/W = 0 and 0.5, new expressions were developed for F_{ESET} as a function of a/W and d/W. F_{ESET} is given as,

$$F_{ESET} = \sum_{i=0}^{7} \frac{p_i \left(\frac{a}{W}\right)^i}{\left(1-\frac{a}{W}\right)^{3/2}} \quad . \tag{15}$$

where

$$p_0 = 1.1215 + 6.7328\left(0.5-\frac{d}{W}\right), \tag{16a}$$

$$p_1 = -1.3923 - 17.518\left(0.5-\frac{d}{W}\right), \tag{16b}$$

$$p_2 = 4.316 + 41.1028\left(0.5-\frac{d}{W}\right), \tag{16c}$$

$$p_3 = -5.1009 - 64.082\left(0.5-\frac{d}{W}\right), \tag{16d}$$

$$p_4 = 0.6692 + 57.9826\left(0.5-\frac{d}{W}\right), \tag{16e}$$

$$p_5 = 5.1684 - 23.3734\left(0.5-\frac{d}{W}\right), \tag{16f}$$

$$p_6 = -5.4702 - 1.7092\left(0.5-\frac{d}{W}\right), \text{ and} \tag{16g}$$

$$p_7 = 1.8135 + 3.114\left(0.5-\frac{d}{W}\right). \tag{16h}$$

The limiting solutions at a/W=0 and a/W=1 were satisfied automatically because the solutions F_T and F_B [8] contained the limiting solutions for tension and bending loads, respectively. When d = 0.5W, Eqns. (15) and (16) are identical to the solution for SE(T) geometry. The constants, p_i are linear with d/W consistent with the linear dependence of the stress distribution on d/W. Equations (15) and (16) are valid in the range $0 \le a/W \le 1$, $0 \le d/W \le 0.5$, and $H/W \ge 3.0$.

Similarly, the expression for G_{ESET} is given as,

$$G_{ESET} = \sum_{i=0}^{7} \frac{q_i \left(\frac{a}{W}\right)^i}{\left(1-\frac{a}{W}\right)^2} \quad . \tag{17}$$

where

$$q_0 = 5.8399 + 35.0392\left(0.5 - \frac{d}{W}\right), \tag{18a}$$

$$q_1 = -11.5467 - 79.0168\left(0.5 - \frac{d}{W}\right), \tag{18b}$$

$$q_2 = 34.3928 + 155.4186\left(0.5 - \frac{d}{W}\right), \tag{18c}$$

$$q_3 = -42.4544 - 138.2746\left(0.5 - \frac{d}{W}\right), \tag{18d}$$

$$q_4 = 20.5012 + 7.3128\left(0.5 - \frac{d}{W}\right), \tag{18e}$$

$$q_5 = 24.3695 + 73.4932\left(0.5 - \frac{d}{W}\right), \tag{18f}$$

$$q_6 = -38.1176 - 53.3828\left(0.5 - \frac{d}{W}\right), \text{ and} \tag{18g}$$

$$q_7 = 14.9641 + 15.2504\left(0.5 - \frac{d}{W}\right). \tag{18h}$$

The limiting solutions at a/W=0 and a/W=1 were satisfied automatically because the solutions G_T and G_B [8] contained the limiting solutions for tension and bending loads, respectively. When d = 0.5W, Eqns. (15) and (16) are identical to the solution for the SE(T) geometry. Similar to p_i in Eqn. (15), the constants q_i are linear with d/W. Equations (17) and (18) are valid in the range $0 \le a/W \le 1$, $0 \le d/W \le 0.5$, and $H/W \ge 3.0$.

Compliance based fatigue crack growth testing requires the equations to calculate a/W knowing the measured compliance of the specimen. As discussed earlier, the normalized compliance of the specimen is given by U, i.e. Eqn. (14). The expression for a/W is given as,

$$\frac{a}{W} = \sum_{i=0}^{4} r_i \, U^i \quad , \tag{19}$$

where

$$r_0 = 0.99146 + 0.042148\left(\frac{d}{W}\right) - 0.091724\left(\frac{d}{W}\right)^2 , \tag{20a}$$

$$r_1 = -3.8183 + 1.1826\left(\frac{d}{W}\right) + 2.5002\left(\frac{d}{W}\right)^2 , \tag{20b}$$

$$r_2 = 4.9522 + 0.021518\left(\frac{d}{W}\right) - 5.9794\left(\frac{d}{W}\right)^2 , \tag{20c}$$

$$r_3 = -5.2085 - 6.163\left(\frac{d}{W}\right) + 0.11636\left(\frac{d}{W}\right)^2 + 21.967\left(\frac{d}{W}\right)^3 , \text{ and} \tag{20d}$$

$$r_4 = 6.7559 + 0.035694\left(\frac{d}{W}\right) + 5.2758\left(\frac{d}{W}\right)^2 - 28.294\left(\frac{d}{W}\right)^3 . \tag{20e}$$

Equations (19) and (20) are valid in the range $0.1 \le a/W \le 0.95$, $0 \le d/W \le 0.5$, and $H/W \ge 3.0$.

Equations (15)-(20) were developed based on values generated at discrete values of d/W. Equations (15)-(18) were developed using results obtained for d/W = 0.0 and 0.5. Equations (19) and (20) were developed using results for d/W = 0.0, 0.1, 0.2, 0.3, 0.4, and 0.5. The accuracy of the Eqns. (15)-(20) at intermediate values of a/W and d/W was evaluated by comparing these equations with those calculated using Eqns. (7), (12) and (14). During this comparison, d/W was varied from 0.0 to 0.5 in increments of 0.01 and a/W from 0.0 to 1.0 in increments of 0.01. The difference between the proposed Eqns. (15)-(20) and those obtained using the principle of superposition is plotted as a function of a/W in Fig. 7. At each value of a/W, the range of results corresponds to $0 \le d/W \le 0.5$. The error is within ± 0.2%, 0.4% and 1.0 % for F_{ESET}, G_{ESET} and a/W, respectively. Hence, Eqns. (15)-(20) can be used for fracture and fatigue crack growth testing with acceptable accuracy.

Conclusions

Stress intensity factor (K) and crack mouth opening displacement (CMOD) solutions were developed for an eccentrically pin-loaded single edge cracked geometry, ESE(T). The expressions for K and CMOD are valid over a wide range of crack length to width ratio and eccentricity of loading. An expression was also developed to calculate the crack length from the specimen compliance for a practical range of a/W (= 0.1 to 0.95). The proposed equations can be used for fracture and fatigue crack growth testing.

Acknowledgment

This research was partially conducted at Materials Directorate, Wright Laboratory (WL/MLLN), Wright-Patterson Air Force Base, OH 45433-7817 under on-site contract number F33615-94-C-5200. The author is grateful to Dr. J.C. Newman, Jr. and Dr. J.H. Underwood for providing the results prior to the publication of their papers.

Appendix

The expressions for F_T , F_B , G_T and G_B used in Eqns. (2), (3), (9) and (10) are given in the following equations [8].

$$F_T = \sqrt{\frac{2W}{\pi a}\tan\frac{\pi a}{2W}}\,\frac{\left[0.752 + 2.02\left(\frac{a}{W}\right) + 0.37\left(1-\sin\frac{\pi a}{2W}\right)^3\right]}{\cos\frac{\pi a}{2W}}, \tag{21}$$

$$F_B = \sqrt{\frac{2W}{\pi a}\tan\frac{\pi a}{2W}}\,\frac{\left[0.923 + 0.199\left(1-\sin\frac{\pi a}{2W}\right)^4\right]}{\cos\frac{\pi a}{2W}}, \tag{22}$$

$$G_T = \frac{4\left[1.46 + 3.42\left(1-\cos\frac{\pi a}{2W}\right)\right]}{\left(\cos\frac{\pi a}{2W}\right)^2}, \text{ and} \tag{23}$$

$$G_B = 4\left[0.8 - 1.7\left(\frac{a}{W}\right) + 2.4\left(\frac{a}{W}\right)^2 + \frac{0.66}{\left(1-\frac{a}{W}\right)^2}\right]. \tag{24}$$

References

1. John, R., Hartman, G.A., and J.P. Gallagher, J.P., Crack Growth Induced by Thermal-mechanical Loading, *Experimental Mechanics*, 1992, **32**, 102-108.
2. Piascik, R.S. and Newman, J.C., Jr., An Extended Compact Tension Specimen for Fatigue Crack Propagation and Fracture, *NASA-TM-110243*, 1996, NASA Langley Research Center, Hampton, VA, USA.
3. Piascik, R.S., Newman, J.C., Jr., and Underwood, J.H., The Extended Compact Tension Specimen, *Fatigue and Fracture of Engineering Materials and Structures*, 1997, Accepted for publication.
4. Piascik, R.S. and Willard, S.A., The Growth of Small Corrosion Fatigue Cracks in Alloy 2034, *Fatigue and Fracture of Engineering Materials and Structures*, 1994, **17**, 1247-1259.
5. Underwood, J.H., Kortschot, M.T., Lloyd, W.R., Eidinoff, H.L., Wilson, D.A, and Ashbaugh, N.E., Translaminar Fracture Toughness Test Methods and Results From Interlaboratory Tests of Carbon/Epoxy Laminates, *Fracture Mechanics: 26th Volume, ASTM STP 1256*, 1996, Edited by W.G. Reuter, J.H. Underwood and J.C. Newman, Jr., American Society for Testing and Materials, Philadelphia, PA, Accepted for publication.
6. Richardson, D.E. and Goree, J.G., Experimental Verification of a New Two-Parameter Fracture Model, *Fracture Mechanics: Twenty Third Symposium, ASTM STP 1189*, 1993, Edited by R. Chona, American Society for Testing and Materials, Philadelphia, PA, 738-750.
7. Raju, I.S. and Fichter, W.B., A Finite Element Alternating Method For Two-Dimensional Mode I Crack Configurations, *Engineering Fracture Mechanics*, 1989, **33**, 525-540.
8. Tada, H., *The Stress Analysis of Cracks Handbook*, 2nd Edition, Paris Productions, Inc., St. Louis, MO, USA, 1985.
9. Tan, P.W., Raju, I.S., and Newman, J.C., Jr., Boundary Force Method for Analyzing Two-Dimensional Cracked Plates, *ASTM STP 945*, 1988, Edited by D.T. Read and R.P. Reed, 259-277.
10. *Standard Test Method for Measurement of Fatigue Crack Growth Rates*, ASTM E647-95, Annual Book of ASTM Standards, American Society for Testing and Materials, Philadelphia, PA, 1995, **03.01**, 578-614.

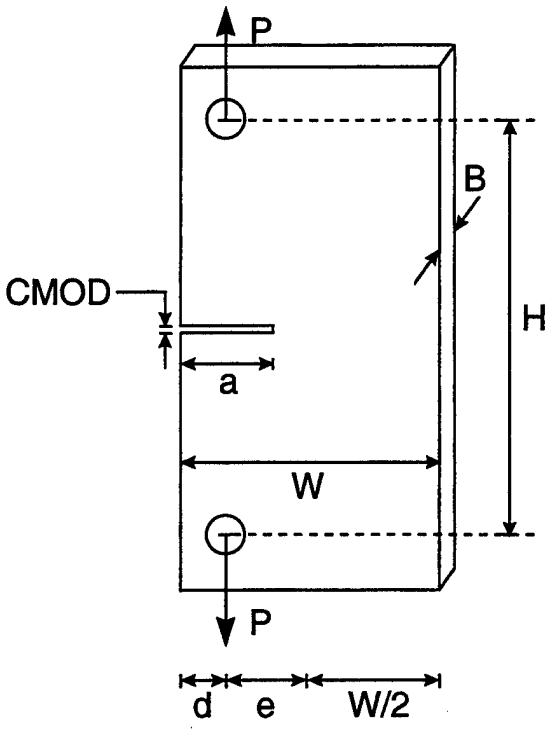


Figure 1. Schematic of an eccentrically loaded single edge cracked geometry.

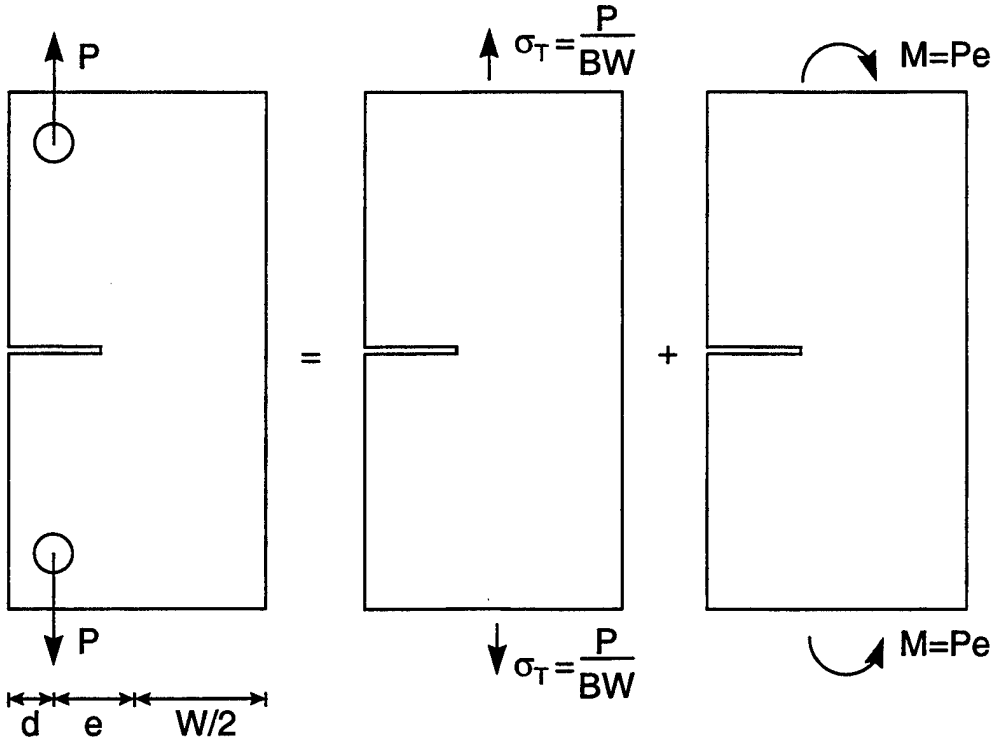


Figure 2. Schematic highlighting the principle of superposition used to calculate the stress intensity factor and compliance solutions for the eccentrically loaded single edge cracked geometry.

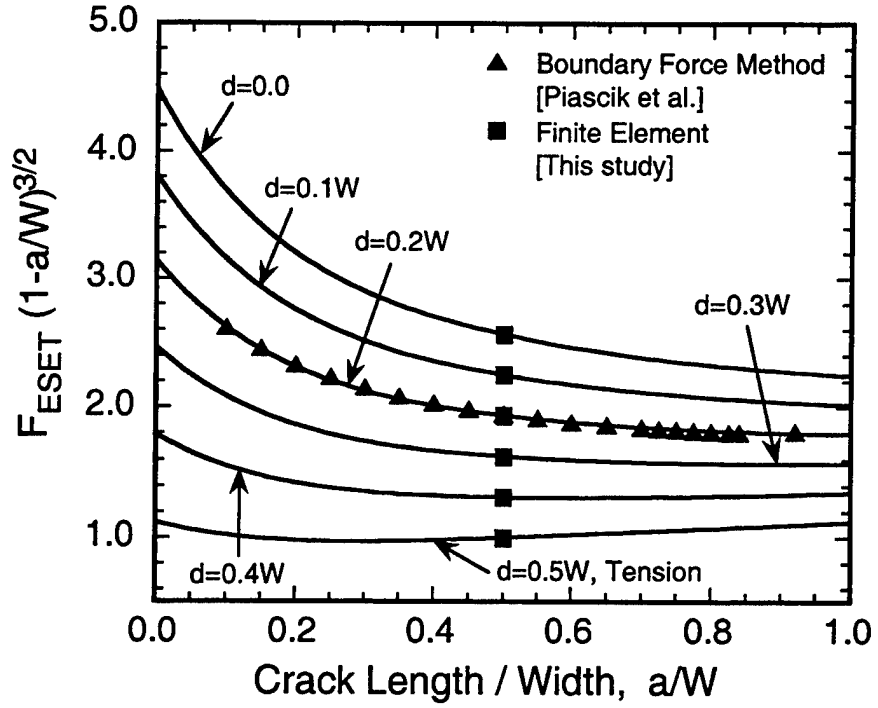


Figure 3. Normalized stress intensity factors for the eccentrically loaded single edge cracked geometry.

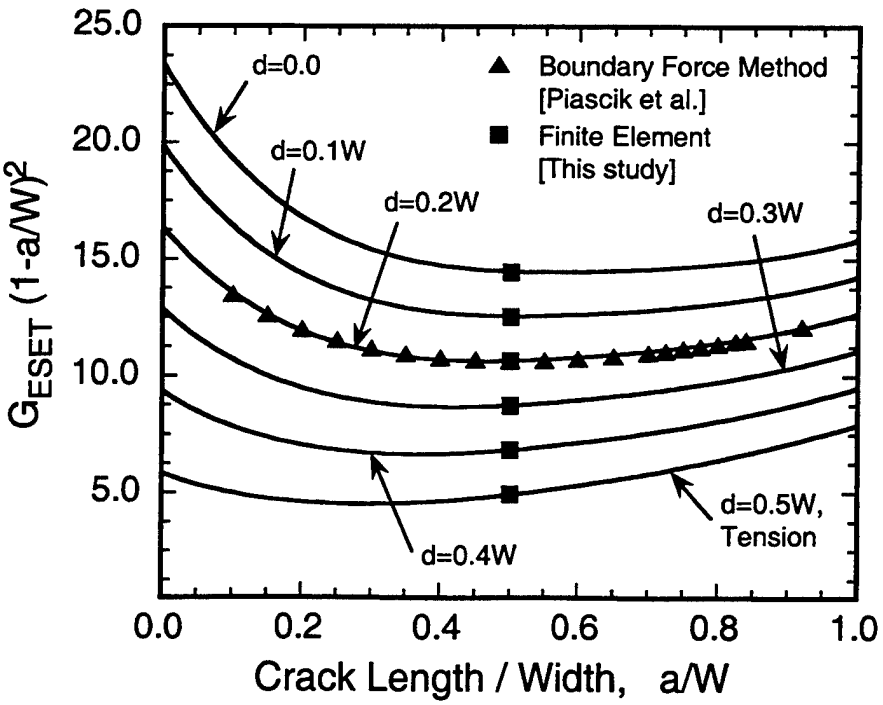


Figure 4. Normalized crack mouth opening displacements for the eccentrically loaded single edge cracked geometry.

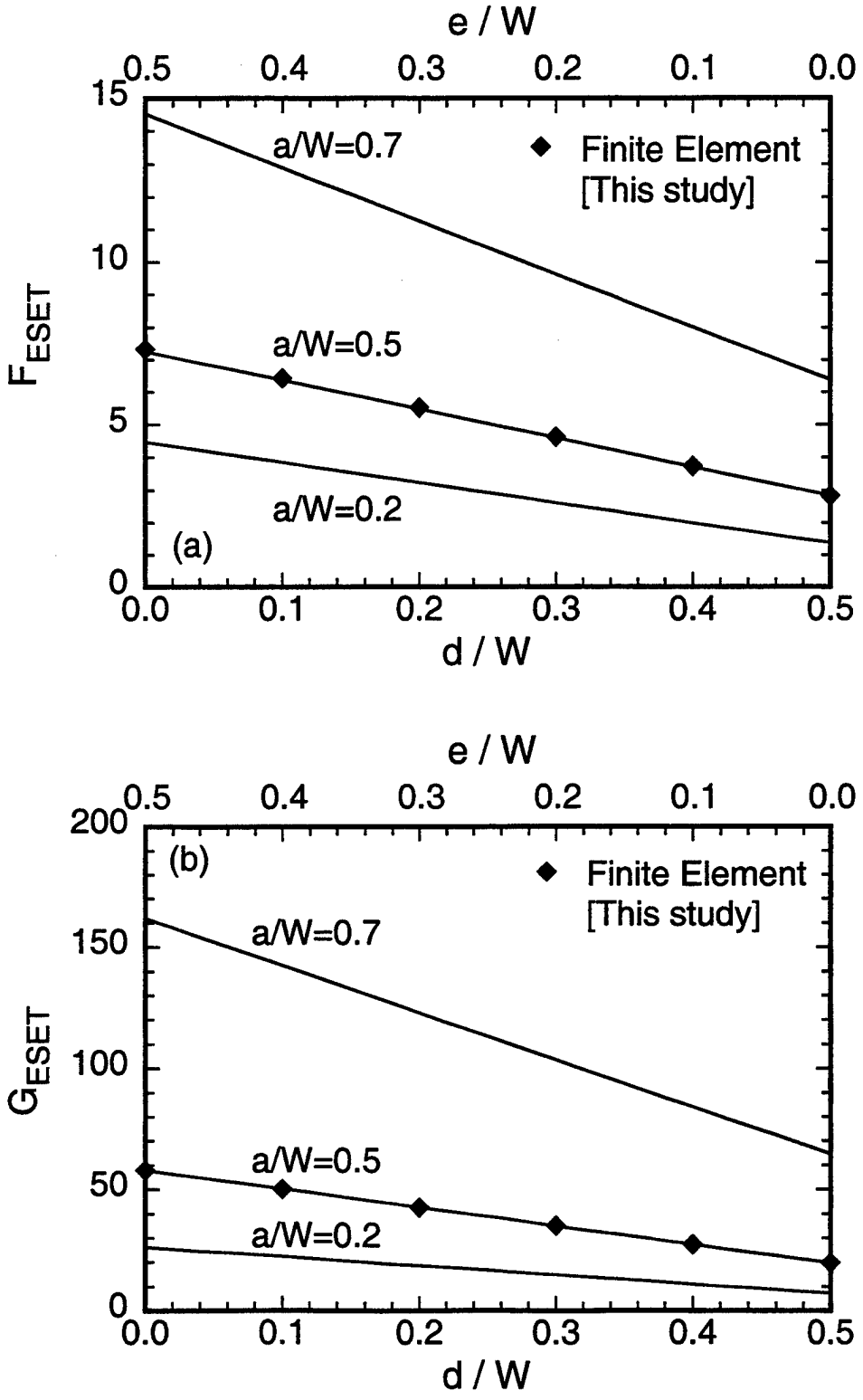


Figure 5. Effect of eccentricity of loading on the normalized stress intensity factor.

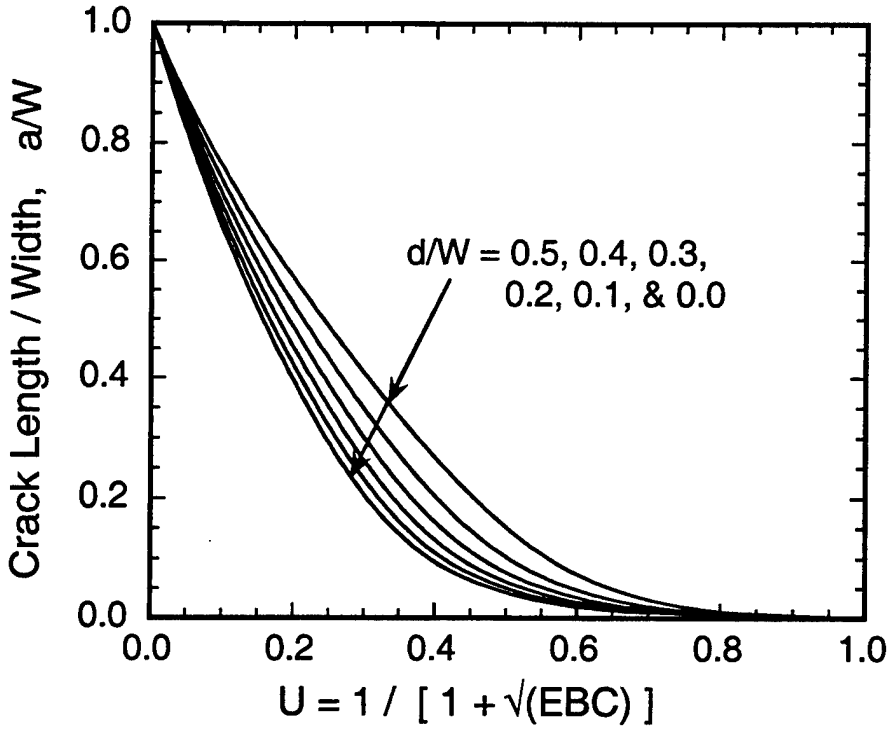


Figure 6. Normalized crack length (a/W) as a function of the specimen compliance (EBC) for the eccentrically loaded single edge cracked geometry.

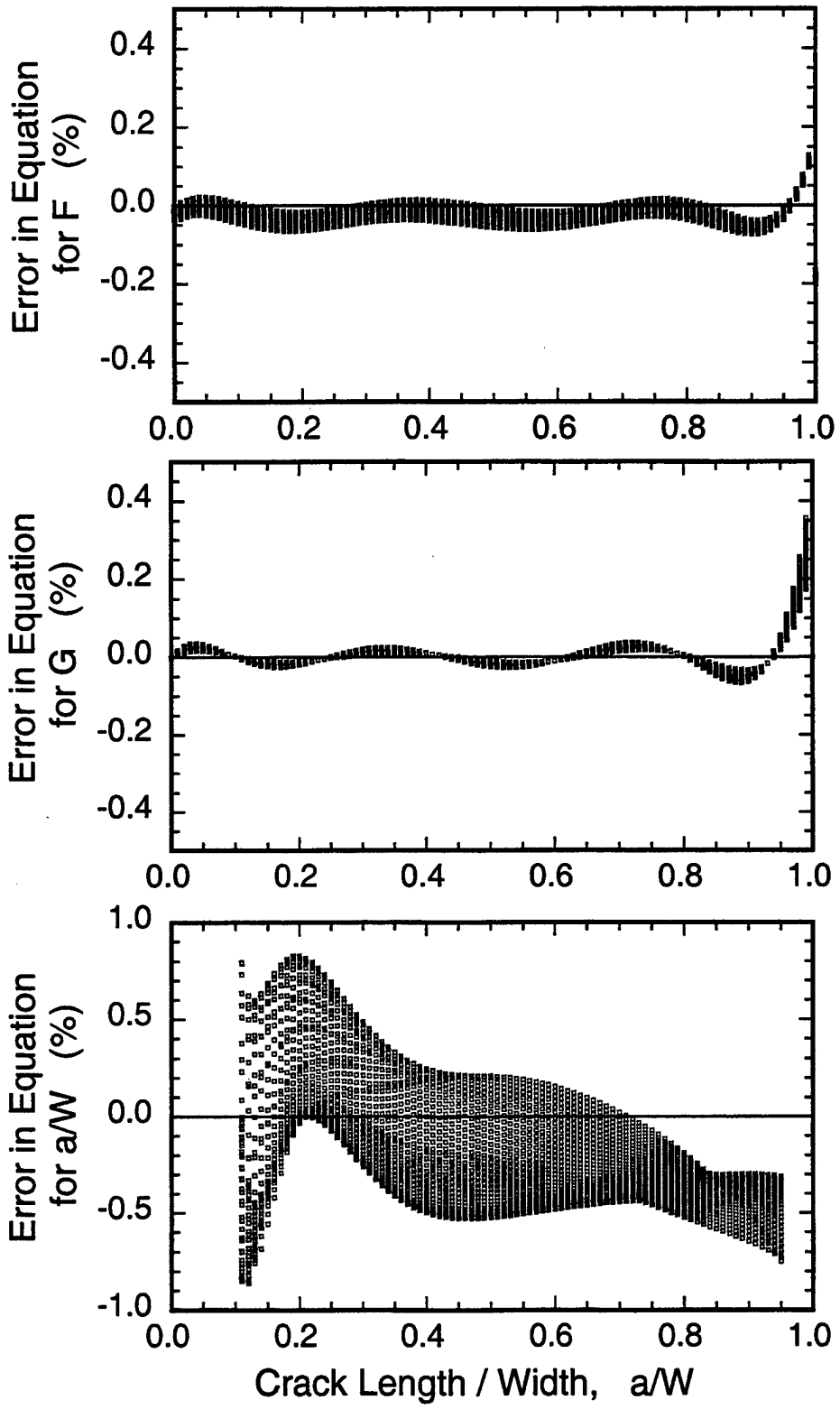


Figure 7. Error between proposed equations for F, G and a/W, and corresponding superposition solutions for $0.0 \leq d/W \leq 0.5$.